

Aus dem Bereich Medizinische Biochemie und Molekularbiologie
Theoretische Medizin und Biowissenschaften
der Medizinischen Fakultät
der Universität des Saarlandes, Homburg/Saar

The role of membrane property sensors and lipid fingerprints in endoplasmic reticulum stress and beyond

**Dissertation zur Erlangung des Grades eines Doktors der
Naturwissenschaften
der Medizinischen Fakultät
der UNIVERSITÄT DES SAARLANDES
2024**

vorgelegt von: John Matthias Reinhard
geboren am: 21. September 1988 in Halle (Saale)

Tag der Promotion: 25. November 2024
Dekan: Univ.-Prof. Dr. med. dent. M. Hannig

Berichterstatter: Prof. Dr. R. Ernst
Prof. Dr. F. Schmitz
Prof. Dr. S. Schuck

'More is different'

Philip Warren Anderson

Anderson, P. W. More is different: Broken symmetry and the nature of the hierarchical structure of science. *Science* **177**, 393-396 (1972).

INHALTSVERZEICHNIS

PUBLIKATIONEN	I
ZUSAMMENFASSUNG	III
SUMMARY	V
LIST OF ABBREVIATIONS	VII
1. INTRODUCTION	1
1.1. The origin of cellular life: Compartmentalization by self-assembling amphiphiles	1
1.2. Lipid diversity in eukaryotes	2
1.3. Collective biophysical membrane properties	6
1.4. How proteins interact with membranes	10
1.5. How cells sense and regulate lipid compositions and membrane properties	13
1.6. Organelle membrane lipid compositions and identities	19
1.7. Lipid bilayer stress in health and disease	24
2. PUBLICATION SUMMARIES AND PERSONAL CONTRIBUTIONS	27
2.1. Cysteine cross-linking in native membranes establishes the transmembrane architecture of Ire1	27
2.2. Regulation of lipid saturation without sensing membrane fluidity	30
2.3. A quantitative analysis of cellular lipid compositions during acute proteotoxic ER stress reveals specificity in the production of asymmetric lipids	34
2.4. MemPrep, a new technology for isolating organellar membranes provides fingerprints of lipid bilayer stress	38
2.5. Remodeling of yeast vacuole membrane lipidomes from the log (one phase) to stationary stage (two phases)	43
3. CONCLUDING REMARKS AND FUTURE DIRECTIONS	47
4. REFERENCES	53
5. APPENDIX	69
DANKSAGUNG	A
EIDESSTATTLICHE VERSICHERUNG	C
LEBENS LAUF	E

PUBLIKATIONEN

Diese kumulative Dissertation basiert auf den hier gelisteten Publikationen. Ich werde im Folgenden die Ergebnisse der Publikationen zusammenfassen, meinen eigenen Anteil an diesen darlegen und deren inhaltlichen Zusammenhang aufzeigen.

Reinhard, J., Starke, L., Klose, C., Haberkant, P., Hammarén, H., Stein, F., Klein, O., Berhorst, C., Stumpf, H., Sáenz, J. P., Hub, J., Schuldiner, M., Ernst, R. MemPrep, a new technology for isolating organellar membranes provides fingerprints of lipid bilayer stress. *The EMBO Journal* **8**, 1653-1685 (2024).

Reinhard, J.*, Leveille, C. L.*, Cornell, C. E., Merz, A. J., Klose, C., Ernst, R., Keller, S. L. Remodeling of yeast vacuole membrane lipidomes from the log (one phase) to stationary stage (two phases). *Biophysical Journal* **122**, 1-15 (2023).

(* these authors contributed equally)

Ballweg, S., Sezgin, E., Doktorova, M., Covino, R., Reinhard, J., Wunnicke, D., Hänelt, I., Levental, I., Hummer, G., Ernst, R. Regulation of lipid saturation without sensing membrane fluidity. *Nature Communications* **11**, 756 (2022).

Väth, K.*, Mattes, C.*, Reinhard, J.*, Covino, R., Stumpf, H., Hummer, G., Ernst, R. Cysteine cross-linking in native membranes establishes the transmembrane architecture of Ire1. *Journal of Cell Biology* **220**, e202011078 (2021).

(* these authors contributed equally)

Reinhard, J.*, Mattes, C.*, Väth, K.*, Radanović, T., Surma, M. A., Klose, C., Ernst, R. A quantitative analysis of cellular lipid compositions during acute proteotoxic ER stress reveals specificity in the production of asymmetric lipids. *Frontiers in Cell and Developmental Biology* **8**, 756 (2020).

(* these authors contributed equally)

ZUSAMMENFASSUNG

Biologische Membranen sind zelluläre Strukturen mit einer komplexen Zusammensetzung aus Lipiden und Proteinen. Sie bilden lebenswichtige Barrieren und einzigartige Umgebungen für vielfältige und essenzielle zelluläre Funktionen. Organellen von Eukaryoten bilden spezialisierte Reaktionsräume mit charakteristischen Membranzusammensetzungen. Diese Kompositionen sind von enormer Bedeutung für die Identität von Organellen und werden aufrechterhalten, trotz physikalischem Kontakt zu anderen Organellen und ständigem Austausch von molekularen Komponenten. *Saccharomyces cerevisiae* ist ein etablierter eukaryotischer Modellorganismus dessen Lipidmetabolismus gut erforscht ist. Er ist daher gut geeignet, um den Effekt von verschiedenen zellulären Stressbedingungen auf die Membranzusammensetzung und biophysikalischen Eigenschaften der Organellen zu untersuchen. Die *unfolded protein response (UPR)* und der *OLE pathway* sind homöostatische Programme, welche die zelluläre Proteinbiogenese und den Lipidstoffwechsel regulieren. Beide Signalwege hängen von Transmembranproteinen des endoplasmatischen Retikulums (ER) ab, die biophysikalische Membraneigenschaften als Eingangssignale wahrnehmen und verarbeiten. Aktuell verstehen wir nicht, wie kollektive Membraneigenschaften aus den Protein- und Lipidzusammensetzungen von komplexen Biomembranen entstehen. Veränderungen dieser Kompositionen, wie zum Beispiel ein erhöhter Sättigungsgrad von Lipid Acylketten in Membranen des sekretorischen Weges und des endosomalen und lysosomalen Systems, tragen entscheidend zu zellulärem Stress und pathologischen Konditionen bei.

Dieser kumulativen Dissertation liegen Publikationen zu Grunde, die durch zwei zentrale Fragen miteinander verknüpft sind: I) Was sind die molekularen Mechanismen der Sensoren von Membraneigenschaften? II) Welchen Einfluss hat zellulärer Stress auf die Zusammensetzung der Membran einzelner Organellen?

Zur Beantwortung dieser Fragen untersuchte ich zuerst die Transmembranarchitektur des *UPR*-aktivierenden Proteins Ire1. Durch Quervernetzungsexperimente in der komplexen Umgebung isolierter Membranvesikel und konfokale Fluoreszenzmikroskopie *in vivo* konnten wir zeigen, dass der Transmembranbereich von Ire1, unabhängig von der stressauslösenden Bedingung, eine X-förmige Konformation einnimmt. Um besser zu verstehen, wie biophysikalische Membraneigenschaften von Proteinsensoren erfasst werden, habe ich bei der Erforschung eines Lipid-Sättigungssensors mitgewirkt, dessen Sensitivität auf Helix-Helix Rotationen im Transmembranbereich beruht. Das ER-Protein Mga2 reguliert den Anteil von gesättigten und ungesättigten Acylketten in Membranlipiden.

Entgegen der verbreiteten Lehrmeinung, dass der Sättigungsgrad von Lipiden vornehmlich zur Aufrechterhaltung der Membranfluidität dient, zeigten unsere Daten, dass Mga2 auf die Packungsdichte der Lipide in einer bestimmten Tiefe im hydrophoben Kern der ER Membran reagiert, und nicht auf die Fluidität der Membran.

Um zu verstehen, welche Veränderungen in der ER Membran zu akuter und chronischer Aktivierung der *UPR* führen, muss der Einfluss von Stress auf die Zusammensetzung der ER Membran quantitativ analysiert werden. Chronischer ER Stress ist eng assoziiert mit komplexen metabolischen Erkrankungen. Die breite regulatorische Kapazität der *UPR*, welche eine Vielzahl von Genen des Lipidmetabolismus betrifft, impliziert eine Schlüsselrolle von ER Stress und *UPR* für die Membranbiogenese und die Regulation des Lipidstoffwechsels. Die Analyse quantitativer Lipidomdaten ergab, dass nach bestimmten akuten ER Stressbedingungen die Lipidzusammensetzung der Zelle nicht wesentlich verändert war. Ganzzell-basierte Lipidomdaten lassen jedoch keine Rückschlüsse auf die Lipidzusammensetzung der ER Membran zu, die für die molekularen Aktivierungsmechanismen der Sensoren Ire1 und Mga2 ausschlaggebend ist. Um bei quantitativen Lipidomanalysen eine subzelluläre Auflösung zu erreichen, und dadurch eine Verbindung zwischen veränderten Membranzusammensetzungen und molekularen Sensormechanismen herzustellen, entwickelte ich eine neuartige Methode zur Membranisolation, die MemPrep getauft wurde. Mit MemPrep konnten wir molekulare Signaturen von anhaltendem proteotoxischem und membranbasiertem Stress entschlüsseln. Basierend auf diesen Daten konnte eine Rolle der Membran-Dicke und -Kompressibilität, sowie der Oberflächenladung auf die Oligomerisierung von Ire1 und Aktivität der *UPR* identifiziert werden. Darüber hinaus adaptierte ich MemPrep zur Isolation der Vakuolenmembran. Bei limitiertem Angebot an Nährstoffen findet dort eine Phasentrennung, unter der Bildung zwei koexistierender flüssiger Membrandomänen, statt. Wir konnten zeigen, dass die phasengetrennte Vakuolenmembran eine erhöhte Konzentration von Phosphatidylcholin mit hohem Schmelzpunkt aufweist. Dies könnte zu einer Phasenseparation von flüssigen Domänen mit hoher Acylkettenordnung beitragen. Damit beschrieben wir das erste Mal, für einen physiologisch relevanten Kontext, die Lipidzusammensetzung einer phasengetrenten komplexen Biomembran.

Ire1 und Mga2 sind durch Evolution optimierte Sensoren, welche die Homöostase von biophysikalischen Membraneigenschaften sicherstellen. Meine Arbeiten zeigen: Die Lipidkomposition und die physikalischen Eigenschaften der ER- und Vakuolenmembran sind zwar abhängig vom zellulären Kontext, jedoch ist der Erhalt physiologischer Membranfunktionen und der Identität von Organellen von enormer Bedeutung für das Überleben von Zellen.

SUMMARY

Biological membranes are complex assemblies of lipids and proteins. They constitute unique environments for diverse and essential cellular functions. The membrane-bound organelles of eukaryotes are specialized compartments for biochemical reactions, featuring characteristic membrane compositions. These membrane lipid compositions are crucial for organellar identity and they are maintained despite physical contact to other organelles and constant exchange of molecular components. The yeast *Saccharomyces cerevisiae* is an established eukaryotic model organism, its lipid metabolism has been studied in great detail. Hence, it is well suited to study the effect of different cellular stress conditions on the lipid composition and collective properties of membranes. The unfolded protein response (UPR) and the OLE pathway are homeostatic programs that regulate cellular protein and lipid biogenesis. Both pathways depend on signal transduction from endoplasmic reticulum (ER) transmembrane proteins that sense collective biophysical membrane properties. How these collective properties emerge from the protein and lipid composition of a complex biomembrane, however, is not understood. Membrane aberrancies, such as increased levels of saturated lipid acyl chains, along the secretory pathway and the endosomal-lysosomal-system, contribute substantially to conditions of cellular stress and pathology.

The publications that constitute this cumulative thesis are centered around two central questions: I) What are the molecular sensing mechanisms of membrane property sensors? II) What is the effect of cellular stress on the membrane composition of individual organelles?

To answer these questions, I studied the transmembrane architecture of the UPR-activating protein Ire1. By *in vitro* crosslinking experiments, in the complex environment of isolated membrane vesicles, and *in vivo* fluorescence microscopy, we could show that Ire1's transmembrane domain adopts an X-shaped dimer conformation, independent of the stress-inducing condition. To better understand how biophysical membrane properties are sensed by proteins, I contributed to investigate the ER membrane protein Mga2, a lipid saturation sensor that relies on helix-helix rotations of its transmembrane domain. It regulates the abundance of saturated and unsaturated fatty acyl chains in membrane lipids. Against the common hypothesis, that lipid saturation mainly regulates membrane fluidity, our data suggest that Mga2 is sensitive to increased membrane packing density at a defined depth of the hydrophobic membrane core, and not to membrane fluidity.

To elucidate which membrane aberrancies lead to acute and chronic UPR activation, we must quantify the molecular composition of the ER membrane under diverse stress conditions. Chronic ER stress is tightly associated with complex metabolic diseases. The

broad regulatory capacity of the UPR, affecting many genes of lipid metabolism, implies a key role of ER stress and UPR activity in membrane biogenesis and the regulation of lipid metabolism. The analysis of quantitative lipidomics data revealed that, under certain acute ER stress conditions, the cellular lipid composition was not substantially altered. However, whole cell lipidome data does not allow conclusions on the composition of the ER membrane, which is decisive for the activation of the membrane property sensors Ire1 and Mga2. To gain subcellular resolution for our quantitative lipidomics analyses, and thereby build a connection between aberrant organelle membrane compositions and molecular sensing mechanisms, I developed the novel membrane isolation technique MemPrep. With MemPrep, we could elucidate the molecular fingerprints of prolonged proteotoxic and lipid bilayer stress. Based on these data, we identified a contribution of membrane thickness and membrane surface charge density to the oligomerization of Ire1 and UPR activation. Furthermore, I adapted MemPrep to determine the lipid composition of the vacuole membrane. Upon nutrient limitation, the vacuole membrane undergoes phase separation into different coexisting liquid membrane domains. We could show that the phase separating vacuole membrane contains increased levels of phosphatidylcholine lipids with high melting temperatures. These can contribute to the formation of liquid membrane domains with high acyl chain order. Our data presents, for the first time, the lipid composition of a phase separating complex biomembrane, in a physiologically relevant context.

Ire1 and Mga2 are evolutionarily optimized sensors that ensure homeostasis of collective biophysical membrane properties. My work demonstrates that the lipid composition and collective membrane properties of the ER and the vacuole membrane are context dependent. However, maintaining physiological membrane functions and organelle identities is crucial for cellular survival.

LIST OF ABBREVIATIONS

AH	amphipathic helix
APP	amyloid precursor protein
ATF6	activating transcription factor-6
CDP-DAG	cytidine diphosphate-diacylglycerol
CL	cardiolipin
cvt	cytoplasm-to-vacuole
DAG	diacylglycerol
Des	$\Delta 5$ -fatty acid desaturase
DOPC	dioleoylphosphatidylcholine
DPH	1,6-diphenyl-1,3,5-hexatriene
DTT	dithiothreitol
<i>E. coli</i>	<i>Escherichia coli</i>
ENTH	epsin N-terminal homology
ER	endoplasmic reticulum
ERAD	ER-associated degradation
FCS	fluorescence correlation spectroscopy
FRET	Förster resonance energy transfer
G3P	glycerol-3-phosphate
GPC	glycerophosphocholine
GPI	glycosylphosphatidylinositol
GPMVs	giant plasma membrane vesicles
HDL	high-density lipoproteins
IF2	interface 2
IPC	inositolphosphorylceramide
Ire1	inositol-requiring enzyme 1
<i>ISC1</i>	inositol phosphosphingolipid phospholipase C
L_{β}	gel phase membrane domain
L_d	liquid-disordered membrane domain
L_o	liquid-ordered membrane domain
$M(IP)_2C$	mannosyl-di-(inositolphosphoryl)ceramide
MD	molecular dynamics
MGL	membrane glycerolipids
MIPC	mannosyl-inositolphosphorylceramide
MLCL	Monolysocardiolipin

List of abbreviations

NAFLD	nonalcoholic fatty liver disease
NASH	nonalcoholic steatohepatitis
PA	phosphatidic acid
PC	phosphatidylcholine
PE	phosphatidylethanolamine
PERK	protein kinase R-like ER kinase
PG	phosphatidylglycerol
PH	pleckstrin homology
PI	phosphatidylinositol
PI3P	phosphatidylinositol-3-phosphate
PI4P	phosphatidylinositol-4-phosphate
PIPs	phosphatidylinositol phosphates
PKC	protein kinase C
POPC	palmitoyl-oleoyl-phosphatidylcholine
PS	phosphatidylserine
PX	phagocytic oxidase homology
RIDD	regulated Ire1-dependent mRNA decay
Rtn1	reticulon-1
SCD	synthetic complete dextrose, defined minimal medium
START	steroidogenic acute regulatory-related lipid transfer
T _{melt}	melting temperature
TAG	triacylglycerol
TGN	<i>trans</i> -Golgi network
TM	tunicamycin
TMD	transmembrane domain
TMH	transmembrane helix
TMHs	transmembrane helices
TOR	target of rapamycin
UAS _{ino}	inositol-sensitive upstream activating sequences
UPR	unfolded protein response
VLDL	very low-density lipoproteins
yeast	<i>Saccharomyces cerevisiae</i>
YPD	yeast extract peptone dextrose, rich medium

1. INTRODUCTION

1.1. The origin of cellular life: Compartmentalization by self-assembling amphiphiles

Compartmentalization has been an important factor in prebiotic chemical evolution. The origin of cellular life most likely involved the formation of protocellular vesicles by self-assembling amphiphilic molecules^{1,2}. Every cell we know today is surrounded by a membrane that contains lipids and proteins. This complex biomembrane defines the boundary between cellular life and the environment. Amphiphilic membranogenic molecules like fatty acids and long chain alcohols might have been available on the early earth by meteoritic infall³ or geochemical processes⁴. These compounds are capable of forming vesicular compartments with semipermeable bilayer boundaries that allow the concentration of biochemically important solutes for metabolism and replication^{5,6}. Furthermore, compartmentalization potentially led to the emergence of Darwinian evolution by generating individually replicating protocell units that are in competition to each other⁷. Self-assembly of amphiphiles in an aqueous solution is entropically driven by the hydrophobic effect. In the presence of amphiphilic lipids, dynamic hydrogen bonding networks of water molecules are disturbed. Instead, entropically unfavorable ordered water structures are formed. The free energy of the system is minimized by minimizing the interface between the aqueous solvent and the hydrophobic part of the amphiphil. This is facilitated by the aggregation of the amphiphile into larger structures⁸⁻¹⁰.

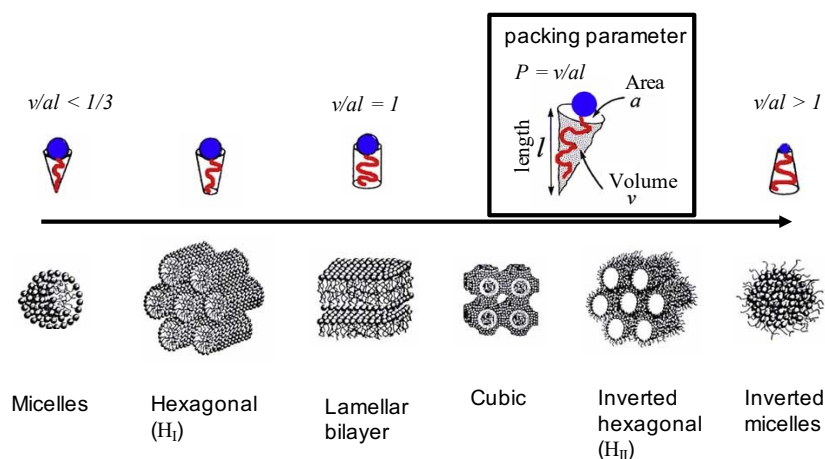


Figure 1: Lipid polymorphism. The apparent geometry of lipid molecules can be described as a packing parameter P , calculated as the volume v divided by the amphiphile length l times the area a of the lipid headgroup region. Depending on the P value, amphiphiles form different non-bilayer and bilayer aggregates in water. Adapted from⁸⁸.

Besides environmental parameters like the degree of hydration, ionic strength and temperature, the type and shape of the assembly depends on the intrinsic average shape of the amphiphilic molecule, which is described by its packing parameter P . Inverted-cone-shaped molecules with packing parameters $< 1/3$, typically found for detergents and some biologically relevant lipids with only a single hydrocarbon chain, form spherical micelles. Packing parameters greater than 1 correspond to cone-shaped molecules with a small hydrophilic head and two, often unsaturated, hydrocarbon tails. Such amphiphiles can form inverted hexagonal phases (H_{II}), in the shape of elongated tubes with hydrocarbon tails pointing outwards towards the aqueous solution, and inverted micelles (Figure 1). However, the vast majority of biological lipid aggregates are lamellar bilayer membranes, typically formed by molecules with packing parameters ranging from $1/2$ to 1 ^{11,12}. Hexagonal (H_I) and cubic phases are transitional forms from micelles to bilayers and bilayers to H_{II} , respectively. Whether non-bilayer phases play a role *in vivo* is a matter of active debate^{13,14}. Evidence has been presented for a role of local H_{II} phases in the inner mitochondrial and thylakoid membrane and more generally for membrane fusion events¹⁵⁻¹⁸.

1.2. Lipid diversity in eukaryotes

Considering that, in principle, one type of amphiphilic lipid molecule is sufficient to form a lipid bilayer membrane, it is astonishing that even relatively simple organisms contain hundreds of different lipid species¹⁹⁻²¹. The complexity of representative lipidomes ranges from 27 distinct lipid species in the prokaryote *Methylobacterium extorquens*²² to over 250 in the single-celled eukaryote *Saccharomyces cerevisiae* (yeast)¹⁹ and over 1100 in the mouse liver^{23,24}. A thought-provoking counter example is the result of a synthetic biology approach where a viable strain of *Mycoplasma mycoides* was generated that contained only 2 lipid species²⁵. This raises the question: Why do naturally evolved cellular membrane systems contain so many different lipid species?

Eukaryotic lipids are categorized into three major groups: I) glycerolipids, including glycerophospholipids and neutral lipids, II) sphingolipids, and III) sterols²¹. Prokaryotic and especially archaeal lipids are structurally distinct and deserve their own in-depth reviews^{26,27}.

Glycerophospholipids are characterized by a glycerol-3-phosphate (G3P) backbone with one or two fatty acids esterified to its *sn-1* and *sn-2* positions and a headgroup bound via the *sn-3* phosphate. They are considered the main structural lipids of cellular membranes. Bacterial lipids have the same G3P backbone, archaeal lipids however, contain glycerol-1-phosphate, the 'mirror image' molecule of G3P. This so-called lipid divide is

amongst the most fundamental unresolved questions in evolutionary biology^{28,29}. Attached to the *sn*-3 phosphate can be a number of class-defining headgroups with the most abundant classes in yeast, as well as in mammals³⁰ or plants³¹, being phosphatidylcholine (PC), phosphatidylethanolamine (PE), phosphatidylinositol (PI), phosphatidylserine (PS), phosphatidic acid (PA) and phosphatidylglycerol (PG) (Figure 2)³². These hydrophilic lipid headgroups differ in their size, charge, and polarity, which greatly influence the contribution to collective physicochemical properties of the resulting membrane surface. PI lipids can be phosphorylated to yield phosphatidylinositol phosphates (PIPs), which play an important role in signal transduction processes and as energy source for intracellular lipid transport^{33–37}. PA is a central node in the lipid metabolic network. When the phosphate is removed by a phosphatase, the resulting neutral diacylglycerol (DAG) is being generated. DAG serves as structural component of membranes, as a precursor for triacylglycerol (TAG) biosynthesis, or as a precursor for the biosynthesis of PC and PE lipids via the Kennedy pathway^{32,38}. Plants contain two additional classes of non-phosphate glycerolipids in their photosynthetically active chloroplast membranes. Galactolipids and sulpholipids have galactosyl or sulfoquinovosyl moieties, respectively, fused to the *sn*-3 headgroup position of DAG³¹.

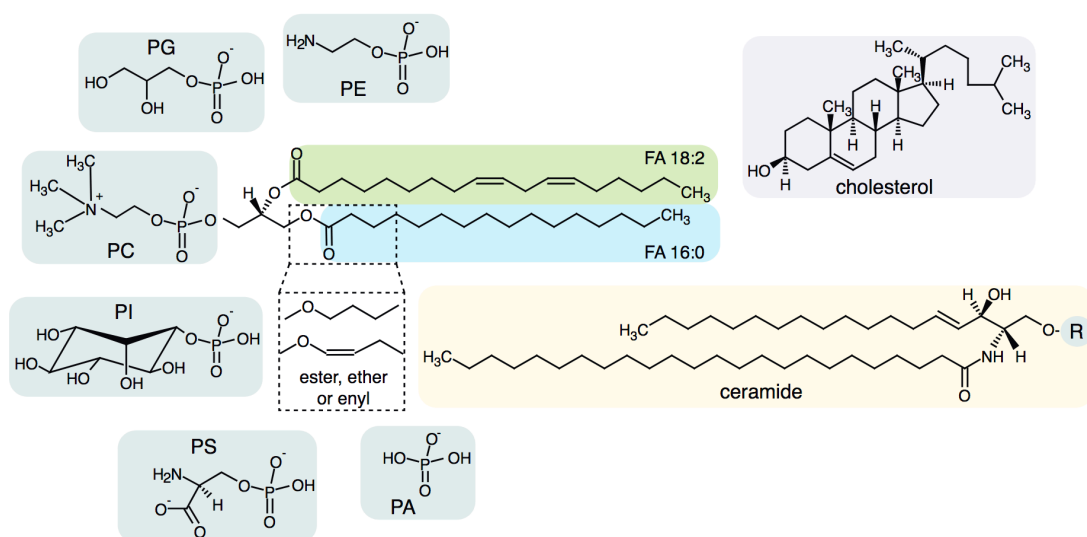


Figure 2: Chemical lipid diversity. Lipids are categorized into three major groups i) glycerophospholipids, sub-categorized into classes depending on the headgroup moiety (PE, phosphatidylethanolamine; PG, phosphatidylglycerol; PC, phosphatidylcholine; PI, phosphatidylinositol; PS, phosphatidylserine; PA, phosphatidic acid), ii) sphingolipids, like ceramide, with a sphinganine base built from serine and a saturated fatty acid, and iii) sterols like cholesterol, which is the main sterol species in animals. The figure was taken from²⁴⁹.

Glycerolipids contain either one (lysolipids), two, or three (TAG) hydrocarbon chains attached to the glycerol backbone. In yeast, these chains are always derived from fatty acids and are joined to glycerol via an ester bond (Figure 2).

Furthermore, in archaea, some bacteria, proto- and metazoans, etherlipids can be formed by the condensation of an alcohol with the glycerol base of the lipid. Plasmalogens, a subgroup of ether lipids with an *sn*-1 vinyl ether-linked alkenyl chain, are abundant phospholipids in human and mouse brain tissue³⁹. Reduced levels of PE plasmalogens have been found in Alzheimer's disease patients^{39,40}, and an inhibitory effect of plasmalogens on the disease-promoting enzymatic activity of the membrane-bound γ -secretase has been suggested^{40,41}.

In glycerolipids, the length of fatty acyl chains and the number and position of double bonds dramatically influences their physicochemical properties. Most cellular fatty acyl chains range from 10 to 26 C-atoms with 0 (saturated) to 6 (polyunsaturated) double bonds. However, in yeast, only saturated and monounsaturated fatty acids with a single *cis* double bond at the Δ 9-position can be synthesized⁴². The most abundant acyl chains found in yeast are myristoyl (14:0; 14 C-atoms, saturated), palmitoyl (16:0; 16 C-atoms, saturated), palmitoleoyl (16:1; 16 C-atoms, one *cis* double bond at Δ 9), oleoyl (18:1; 18 C-atoms, one *cis* double bond at Δ 9) and stearoyl (18:0; 18 C-atoms, saturated)⁴³. The many different possible combinations of these building blocks lead to a large chemical diversity of glycerol(phospho)lipid molecules. Nevertheless, acyl chains are not randomly distributed among the different phospholipid classes. In yeast, a remarkable selectivity of the lipid metabolic machinery leads to the enrichment of unsaturated acyl chains in PE and the four acyl chains-containing mitochondrial lipid cardiolipin (CL), while saturated acyl chains are enriched in PI^{19,44}. Besides *de novo* biosynthesis, acyl chain remodeling determines the composition of acyl chains in the different phospholipid classes^{45,46}. A two-step process known as Lands' cycle features deacylation by a phospholipase A and reacylation in an acyl-CoA-dependent fashion by an acyltransferase⁴⁷. The remodeling of PC lipids in yeast involves the removal of both acyl chains by the B-type phospholipases Plb1 and Nte1 to form free fatty acids and glycerophosphocholine (GPC)⁴⁸. Subsequently, PC is formed first via lyso-PC by the atypical acyltransferase activity of Gpc1⁴⁹ and then by activity of the broad spectrum lysophospholipid acyltransferase Ale1⁵⁰. Substrate-specific enzymes, e.g. the acyltransferase Cst26, which preferentially incorporates C18:0 at the *sn*-1 position of PI⁵¹ or the mitochondrial-located CL-specific phospholipase A Cld1⁵², contribute to the observed characteristic steady-state acyl chain compositions of phospholipid classes. Monolysocardiolipin (MLCL), which results from Cld1 activity, is reacylated by Taz1⁵³. Mutations in the human ortholog tafazzin cause the Barth syndrome, via dysfunctional mitochondria with altered CL compositions and the accumulation of MLCL^{54,55}.

Sphingolipids, the second major lipid category, are built from the profoundly different sphingoid base, which is synthesized by fusing the amino acid serine to a 16:0 fatty acid. This sphingoid base can be modified by introduction of a double bond and / or hydroxylations at few defined positions along the carbon chain⁵⁶. A very long chain fatty acid is then fused to the sphingoid base by N-acyl linkage to form a ceramide (Figure 2). The characteristic hydroxylations of sphingolipids are thought to stabilize lipid-lipid interactions, e.g. by hydrogen bonding to sterols, and potentially lipid-protein interactions in a similar manner to organize and stabilize membrane domains⁵⁷. Yeast synthesizes three classes of complex sphingolipids, categorized by their hydrophilic headgroups, which are based on inositolphosphate and mannose that are added to the ceramide moiety. These classes are inositolphosphorylceramide (IPC), mannosyl-inositolphosphorylceramide (MIPC), and mannosyl-di-(inositolphosphoryl)ceramide (M(IP)₂C)⁵⁶. In mammals, many more classes of complex sphingolipids are generated by addition of a phosphocholine headgroup (sphingomyelins), a single sugar (cerebrosides), or even complex branched oligosaccharides (gangliosides) that are located in the outer leaflet of the plasma membrane and have important roles in cell signaling^{58,59}.

The third major category of membrane lipids are sterols, composed of a 4-ring-system entirely made from carbon atoms that is planar and rigid in conformation. The biosynthetic precursor is squalene and depending on the exact sterol species that is formed, the ring system can have double bonds and feature distinct modifications with alkyl chains⁶⁰. However, the C3-atom always carries the eponymous hydroxyl group (Figure 2). In yeast, the main sterol species is ergosterol, with an abundance of circa 15 mol%^{19,20,32}, and minor levels of other sterols like zymosterol and episterol⁶¹. Cholesterol is the most important mammalian membrane sterol. In vertebrates, a broad spectrum of substances (sterol-based hormones and vitamins including steroids, mineralcorticoids, bile salts, and vitamin D) is derived from sterols like cholesterol⁶². Sterols can be esterified with fatty acids at their C3-hydroxyl group, forming steryl esters, which serve as intracellular storage⁶³. The extracellular synthesis of cholesteryl esters in mammals on the surface of high-density lipoproteins (HDL) is an important process for the delivery of peripheral cholesterol to hepatocytes. Low HDL cholesterol level have been widely accepted as important risk factors for arteriosclerosis and coronary heart disease⁶⁴.

Recent advances in mass-spectrometry based lipidomics enabled unprecedented insights into the chemical complexity and dynamics of cellular lipidomes, in particular for yeast and mammalian systems^{19,20,32,65,66}.

1.3. Collective biophysical membrane properties

The chemical diversity of lipid molecules, their organization in bilayers, and the compositional complexity of biological membranes, including the protein content, comprise an environment with emergent biophysical properties. Despite being only about 4 nm in width, lipid bilayers are unique environments for complex biochemical activity. The earliest model of the lipid bilayer was proposed by Gorter and Grendel in 1925, notably, based on monolayer techniques developed by Langmuir in 1917^{67,68}. The most influential model of our current understanding of biological membranes is the fluid mosaic model by Singer and Nicolson from 1972 (Figure 3 A)⁶⁹. It initially described membranes as flat, fluid solvent in which proteins can freely rotate, diffuse, and function.

A central aspect, which is unfortunately often ill-used and ill-defined in today's life sciences, is the fluidity of the membrane²⁴. Fluidity is the inverse of viscosity and refers to diffusion and rotational motion of molecules. Typical diffusion coefficients found for lipids in fluid synthetic bilayer systems are 2-19 $\mu\text{m}^2/\text{s}$ ⁷⁰⁻⁷³ and approximately one order of magnitude slower for lipids in cell membranes (0.9-2.0 $\mu\text{m}^2/\text{s}$)^{74,75}. Protein diffusion measured in fluid synthetic membranes is in a similar range as lipid diffusion (3-4 $\mu\text{m}^2/\text{s}$)^{72,73}. Interestingly, diffusion coefficients determined for membrane proteins in cells are one to two orders of magnitude smaller than their lipid counterparts (0.02-0.40 $\mu\text{m}^2/\text{s}$)⁷⁴⁻⁷⁶. However, protein diffusion measured in cell membranes is highly dependent on the protein that is observed, and the length and time-scale at which motion is being recorded, hence the overall experimental setup⁷⁷. Short-ranged diffusion of 10 $\mu\text{m}^2/\text{s}$ has been reported⁷⁸. The anchoring of larger protein complexes and the cytoskeleton to cell membranes can lead to the phenomenon of confined diffusion, or hop diffusion, due to steric hindrance by these relatively immobile structures^{79,80}. The fluid mosaic model has been updated throughout the decades to account for experimental evidence for lateral heterogeneity and an intricate anchoring of the cytoskeleton (Figure 3 A)^{81,82}. Nevertheless, complementary models have been developed that focus on the physical forces at play in lipid-lipid, lipid-protein, and lipid-water interactions (Figure 3 B,C)⁸³⁻⁸⁵.

The lateral pressure profile describes the differences in pressure that would be experienced by an imaginary probe traversing through the lipid bilayer, orthogonal to the membrane plane (Figure 3 B)^{83,84,86}. These pressure differences are hundreds of atmospheres in magnitude and result in forces acting on lipids and membrane embedded proteins^{84,87}. The headgroup region contributes positive pressure originating from repulsive forces between lipids. Strong interfacial tension, i.e. negative pressure at the hydrophobic-hydrophilic interface of the bilayer, results from the hydrophobic effect that minimizes the contact between hydrophobic hydrocarbon chains and water from the aqueous solvent. Crowding of the hydrocarbon chains in the hydrophobic core of the bilayer contributes positive

pressure. When integrated over the width of the bilayer, the net pressure is zero for a mechanically equilibrated membrane (Figure 3 B)^{86,87}.

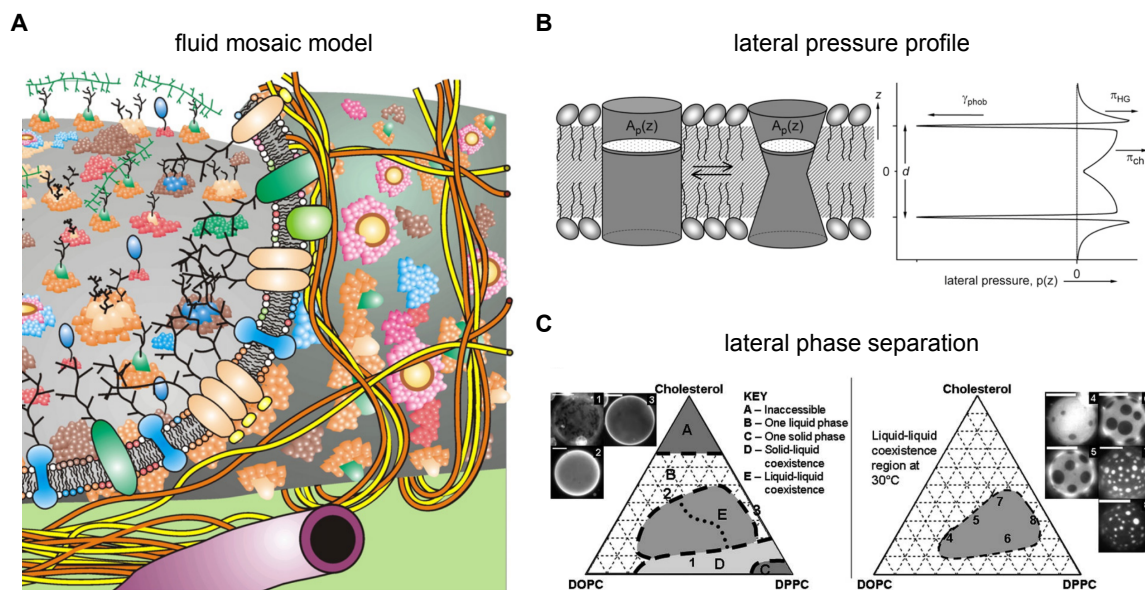


Figure 3: Membrane models and biophysical membrane properties. A) The fluid mosaic model of biological membranes. This scheme depicts an updated version of the model that includes lateral heterogeneity and an intricate association with the cytoskeleton, besides proteins being embedded in a fluid lipid bilayer. Figure was taken from⁸¹. **B)** The lateral pressure profile shows the distribution of positive and negative pressures, $p(z)$, across the width d of the bilayer. Depending on the distance z from the bilayer mid-plane, repulsive forces in the lipid headgroup region contribute positive pressure (π_{HG}), interfacial tension contributes large negative pressure due to the hydrophobic effect that minimizes hydrocarbon chain contact with water (γ_{phob}), and π_{ch} is a positive pressure contribution from crowding of hydrocarbon chains in the hydrophobic core of the bilayer. The differences of these pressures and tensions can be in the order of several hundred atmospheres. The integral of $p(z)$ across the complete width of the membrane is zero for a membrane in mechanical equilibrium. $A_p(z)$ is the cross-sectional profile that differs for two hypothetical states of a transmembrane protein. Figure was taken from⁸⁶. **C)** Phase diagrams of ternary lipid mixtures indicating regions where bilayers consist of one liquid phase (B), one solid phase (C) or show coexistence of solid and liquid (D) or liquid-ordered and liquid-disordered (E) domains. Inlets 1-8 show fluorescence micrographs of giant unilamellar vesicles generated with indicated ternary mixtures (scale bar = 20 μm). DOPC, dioleoylphosphatidylcholine; DPPC, dipalmitoylphosphatidylcholine. Figure was taken from¹⁰⁶.

Directly connected to the lateral pressure profile is the description of intrinsic or spontaneous curvature. It describes the tendency of each individual monolayer to curve if it would not be confined in a bilayer structure. Repulsive and attractive forces between lipids and their average molecular shapes, described by the packing parameter P (Figure 1), are important determinants of intrinsic curvature. When a monolayer consists of, on average, cylindrical lipids ($P = 1$), intrinsic curvature is zero. A high abundance of lipids with packing

parameters substantially different from 1 can manifest morphologically in non-bilayer lipid phases^{82,88}.

Beside fluidity and the lateral pressure profile, there are other bulk membrane properties that describe the physical state of a bilayer membrane. Packing density describes how tightly lipid molecules are packed within a given membrane area⁸⁹. Many if not all bulk properties are interconnected and interdependent, a high packing density for example often correlates with less fluid, thicker, more rigid and/or less permeable membranes²⁴. It can be achieved by different chemical changes within the lipidome of a membrane, e.g. more saturated acyl chains, longer hydrocarbon chains of lipids, or higher sterol content^{90,91}.

In contrast, the size and number density of lipid packing defects, especially in the headgroup region, increase with the abundance of lipids containing small headgroups, e.g. PA or DAG, or increased level of unsaturated acyl chains and can facilitate binding of membrane associated proteins^{91–93}. Packing defects can also be induced by membrane curvature that exists in diverse subcellular structures⁹⁴ and is often associated with and stabilized by specialized proteins, e.g. in endoplasmic reticulum (ER) tubules⁹⁵, the nuclear pore complex⁹⁶, tight bends of the inner mitochondrial membrane^{97,98}, or the stacks of thylakoid membranes⁹⁹.

How much energy is needed to bend a membrane into a curved structure is described by the bending rigidity^{100,101}. Another bulk property associated with energetic costs of deformations is the transverse compressibility which describes the ability of a membrane to change its thickness in response to external or internal forces, for example by an embedded protein²⁴.

Considering the vast chemical diversity of lipids and proteins, the thickness of biological membranes is astonishingly uniform across the tree of life. Within eukaryotic cells organelle membranes range in thickness from 35–45 Å¹⁰². Nevertheless, differences in thickness, besides other properties discussed earlier, influence the permeability of a membrane for solutes¹⁰³.

A fascinating aspect of collective biophysical membrane properties is the phenomenon of lateral phase separation (Figure 3 C). Bilayers can show lateral heterogeneities of lipids, segregating *in vitro* into membrane domains, with compositional bias and distinct physical properties. Such membrane phase separation phenomena have been extensively studied in model lipid bilayers^{104–112}. A tripartite system, i.e. a model membrane consisting of only three lipid species, is sufficient to provide the coexistence of two fluid domains¹⁰⁶. Robust phase separation at a range of temperatures can be achieved by mixing a low-melting lipid (often containing unsaturated acyl chains), a high-melting lipid (usually with saturated acyl chains), and a sterol. The melting point of a lipid is defined as the temperature where the transition from a highly viscous, rigidly packed gel with fully extended hydrocarbon chains

(referred to as L_{β}) to a fluid liquid phase occurs, where lipids can freely rotate and translate¹¹³. Lipid phase separation can feature two coexisting liquid domains, a liquid-disordered domain (L_d) and a liquid-ordered domain (L_o) where *gauche* rotamers of the hydrocarbon chain are restricted, e.g. by an ordering effect of cholesterol (Figure 3 C [E])¹¹⁰. Sterols have an ordering and water-expelling effect in liquid bilayers. Hence, sterols reduce lipid acyl chain motion and water content in the membrane interface and thereby increase microviscosity^{114,115}. However, both domains are fluid (L_d and L_o) and feature high rotational and translational mobility. Depending on the lipid composition and the temperature, coexistence of a liquid and a solid L_{β} domain is also possible, at least *in vitro* (Figure 3 C [D])¹⁰⁶.

The concept of physiologically relevant, or even essential, laterally segregated membrane domains has been introduced by the membrane raft hypothesis¹¹⁶. It predicts the existence of membrane domains, rich in cholesterol, sphingolipids, saturated phospholipids and specialized membrane proteins, that are formed by lipid-lipid and lipid-protein interactions^{117,118}. Membrane rafts are thought to play a role in sterol-rich membranes like the plasma membrane with implications for the activity of transmembrane receptor proteins and cellular signaling^{119,120}. Furthermore, it has been suggested that rafts regulate intracellular trafficking along the secretory pathway by providing platforms for protein and lipid sorting in the Golgi complex^{121,122}. Despite recent advances in direct imaging of lipid nano-domains¹²³⁻¹²⁷, the existence of rafts in the plasma membrane of living cells remains challenging to study¹²⁸⁻¹³⁰.

The probably clearest example of physiologically relevant membrane phase separation in living cells is the formation of coexisting micron-sized, stable L_d and L_o domains in the vacuole membrane of yeast¹³¹. Domains are formed under starvation conditions with functional importance for lipophagy¹³² and target of rapamycin (TOR) signaling¹³³. Yet, their molecular composition is unknown.

In conclusion, biological membranes can be described by a multitude of biophysical properties that each have to be maintained to ensure crucial membrane functions. Most of these membrane properties are interconnected and not directly encoded by the lipid composition. Furthermore, nonideal mixing and non-additivity of collective properties complicates their prediction based on the lipid composition^{134,135}. A chemical change on the level of lipid composition, e.g. the abundance of double bonds in lipid acyl chains, changes multiple biophysical membrane properties (decrease of packing, microviscosity, thickness or bending rigidity, increase of lateral diffusion speeds (fluidity), permeability or compressibility, and modulation of the lateral pressure profile, intrinsic curvature or phase behavior). These pleiotropic effects are hard to disentangle, especially in biomembranes that feature vastly complex lipidomes (and membrane proteomes).

1.4. How proteins interact with membranes

Cellular membranes are not just simple diffusion barriers, they harbor essential bioactivities on their surfaces, in their hydrophobic core and across the bilayer¹³⁶. The occupation of biomembranes with proteins is substantial and often underestimated. The sarcoplasmic reticulum, for example, contains 2 mol% of proteins, which means that there are only ~50 lipids (~25 in each leaflet) per protein¹³⁷. Another study found approximately 70 lipids per protein (~35 in each leaflet) in synaptic vesicles¹³⁸. An extreme example is the purple membrane of *Halobacterium salinarum* with only ~30 lipids (~15 per leaflet) lining a trimer of bacteriorhodopsin, rendering this membrane system a 2-dimensional crystal¹³⁹. Moreover, 20% of the cross-sectional area of the red blood cell membrane is occupied by protein¹⁴⁰. Similar observations have been made in synaptic vesicles in which 20% of the surface area is occupied by transmembrane protein¹³⁸.

The biological processes and protein structures that are part of membranes include transporters¹⁴¹, signal transduction by receptors¹⁴², the electron transport chain¹⁴³, lipid metabolic enzymes¹⁴⁴, intramembrane proteases¹⁴⁵, the cytoskeleton¹⁴⁶, pattern formation in space and time by Rho GTPases^{147,148} or the anchoring of the genome to the inner nuclear membrane¹⁴⁹.

Membrane protein structures are adapted to the unique environment of the lipid bilayer, e.g. featuring surface-exposed hydrophobic residues that can interact with the hydrophobic core of the membrane. They are generally divided into three major categories i) integral membrane proteins, ii) membrane-associated, and iii) peripheral membrane proteins³⁴. Integral membrane proteins, or transmembrane proteins, span the hydrophobic core of a membrane (Figure 4 A [1-3]). Their transmembrane domains (TMDs) consist of hydrophobic helices (single or multiple) or a β -barrel structure. Often, these proteins feature additional soluble domains on one or both sides of the bilayer.

Membrane-associated proteins are anchored to one side of a membrane either by a protein domain like an amphipathic helix (AH) (Figure 4 A [4]) or by lipidation of specific residues (Figure 4 A [5,6]). These lipid moieties attached to proteins include palmitate, farnesyl or the more complex glycosylphosphatidylinositol (GPI) anchors. GPI-anchors are typical for proteins that are located at the extracellular leaflet of the plasma membrane¹⁵⁰.

Peripheral membrane proteins, however, are recruited to the membrane by interactions with other membrane proteins (Figure 4 A [7]) or via lipid binding domains (Figure 4 B), which can be astonishingly specific for lipid headgroup features and the membrane context¹⁵¹. The C1 domain is circa 50 amino acids long and found in over 30 mammalian proteins. It was first identified as a DAG binding domain of protein kinase C (PKC) (Figure 4 B)¹⁵². The more prevalent C2 domain, which was also first described in PKC, is about 130 residues in size and mediates Ca^{2+} -dependent lipid binding. It has a wider selectivity of lipids with a

preference for anionic lipids like PS or PIPs which are phosphorylated PI derivatives^{153,154}. The pleckstrin homology (PH) domain is the most abundant lipid binding domain and it mediates a specific interaction with several PIPs¹⁵². The FYVE domain, named after the first proteins it has been described for (Fab1, YOTB (the uncharacterized *Caenorhabditis elegans* protein ZK632.12), Vac1, early endosome antigen 1) has been shown to bind phosphatidylinositol-3-phosphate (PI3P) in a pH-dependent manner¹⁵⁵. The molecular mechanism involves protonation of functionally important histidine residues¹⁵⁶. Phagocytic oxidase homology (PX) and epsin N-terminal homology (ENTH) domains are other examples of PIP binding domains, which underlines the importance of PIPs for determining membrane identity via the recruitment of cytosolic proteins (Figure 4 B)^{157,158}.

Membrane interacting proteins can also stabilize membrane curvature, and shape membrane architecture at the scale from ~30 nm to several μm . Membrane-shaping proteins include reticulon proteins, BAR (named after the proteins Bin/Amphiphysin/Rvs) domain-containing proteins, and sigma-1 receptor (SigmaR1). Reticulons are a class of evolutionarily conserved, wedge-shaped, proteins that insert from the cytosolic leaflet of the ER membrane, thereby inducing positive membrane curvature, which underlies the formation of ER tubules or the edges of ER sheets⁹⁵. In contrast, SigmaR1 is stabilizing flat membrane domains of the ER, presumably via an oligomerization mechanism. Its monomer structure contains both a single transmembrane helix (TMH) and an AH that are required for its function¹⁵⁹. BAR domains are banana shaped molecules that bind membranes at their concave face thereby stabilizing membrane curvature¹⁶⁰. They play an important role in membrane remodeling, e.g. during endocytosis or cytoskeletal reorganization^{161,162}.

The activity of membrane proteins is often dependent on the membrane lipid composition and the resulting biophysical properties. To fully understand these modulatory functions by the lipid environment it is important to consider specific protein-lipid interactions, the collective biophysical properties acting on embedded proteins, and the transmembrane architecture of proteins (Figure 4 C)^{87,163,164}. Well characterized examples include the activation of osmosensing and Ras-mediated signaling by thinning of the membrane¹⁶⁵, force-from-lipids gating of the mechanosensitive channel MscS¹⁶⁶, the length-based transmembrane proteins sorting along the secretory pathway, or receptor assembly based on differential thickness and packing density of disordered and ordered membrane nano-domains^{65,134,167,168}.

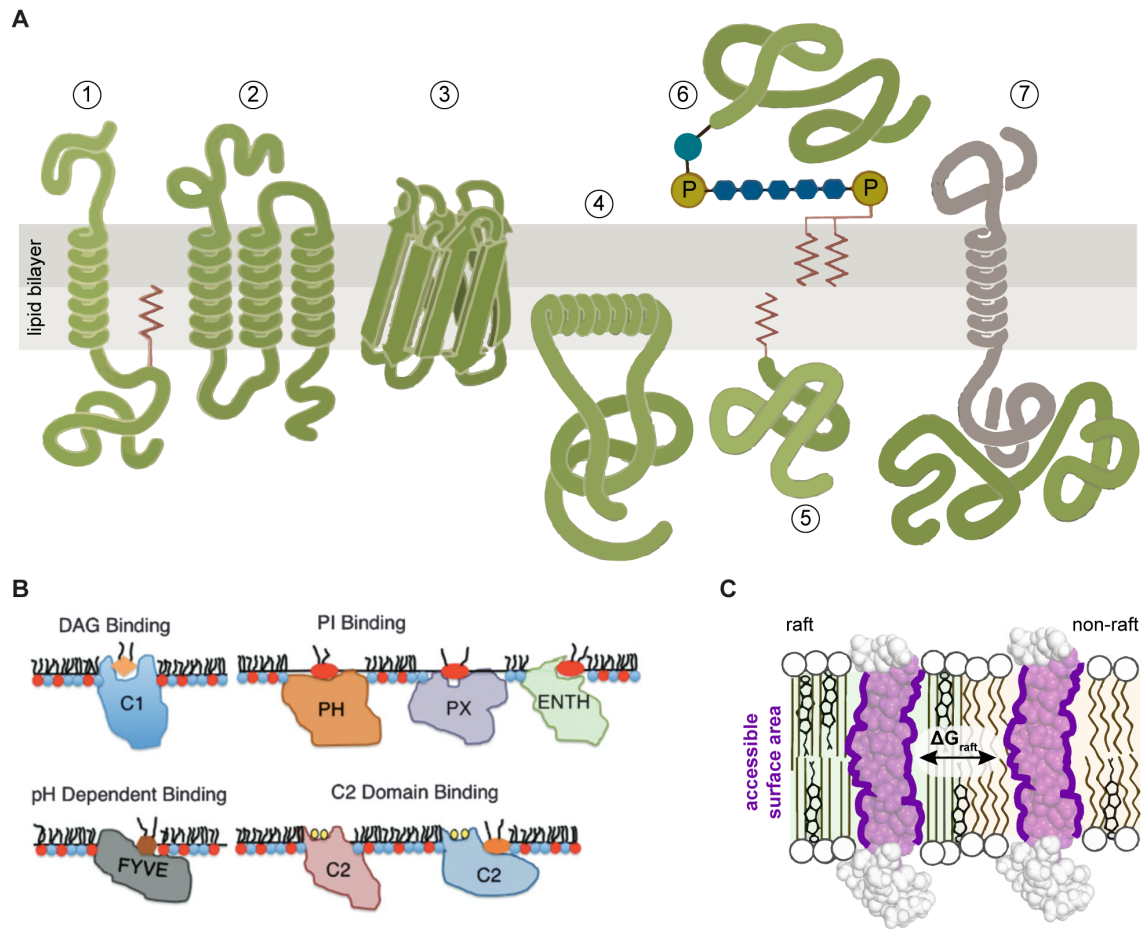


Figure 4: Modes of protein-membrane interaction. A) Major categories of membrane proteins include integral- or transmembrane proteins. Schematic examples for single-spanning (1), multi-spanning (2) and β -barrel (3) proteins. Membrane-associated proteins can be anchored to the membrane by amphipathic helices inserted into one leaflet of the bilayer (4), lipidations (5) or a GPI-anchor (6). Peripheral membrane proteins are indirectly bound to membranes via protein-protein interactions (7). Adapted from³⁴. **B)** Lipid / membrane binding domains mediate the recruitment of proteins to the surface of a membrane via specific protein-lipid interactions. The C1 domain binds diacylglycerol (DAG), PH, PX, and ENTH domains bind different phosphoinositides (PI), while FYVE domains bind phosphoinositides in a pH-codependent mechanism. C2 domains bind anionic lipids in a Ca^{2+} -dependent fashion. Adapted from¹⁵². **C)** Architectural features of transmembrane helices, like their accessible surface area, determine free energy costs (ΔG_{raft}) associated with lateral partitioning into different membrane domains (raft / non-raft). Adapted from¹⁶⁷.

1.5. How cells sense and regulate lipid compositions and membrane properties

The lipid composition and the resulting physical properties of a biomembrane have a crucial influence on the functions of membrane proteins and membrane associated processes. Eukaryotes maintain multiple different membrane compositions for functionality and identity of a multitude of membrane-bound organelles. Although all proteins that interact with membranes will be affected by the membrane environment, not all can be considered membrane property sensors. Genuine membrane property sensors are part of a homeostatic or adaptive sense and response pathway. A sensory protein interacts with the membrane in an environment-dependent fashion. Instead of a protein-lipid interaction with a specific lipid species or class, the sensory cue is usually a collective biophysical membrane property. Often, the homeostatic or adaptive response that is triggered is linked to a transcriptional program, with gene products that have the potential to alter membrane compositions and restore biophysical properties. Only few examples of membrane property sensors have been studied in mechanistic detail^{169–171}.

One of the best described adaptive response pathways is the temperature-controlled biosynthesis of unsaturated lipid fatty acyl chains in *Escherichia coli* (*E. coli*)¹⁷². In 1974, Sinensky suggested that the viscosity of *E. coli* membranes is maintained in response to a sudden drop of the ambient temperature. This homeostatic process has been termed homeoviscous adaptation¹⁷³. It marks the important conceptual breakthrough that membrane biophysics is actively maintained and serves as the prime example of adaptation of the membrane composition to physical cues. The molecular details of such a sense and response pathway have been studied in the two-component system DesK/DesR in *Bacillus subtilis*. The histidine kinase DesK, which features five transmembrane helices (TMHs), senses temperature-dependent changes in the bacterial membrane and initiates a response to cold shock (Figure 5 A). In the cold, DesK undergoes auto-phosphorylation at its cytosolic output domain, thereby switching from phosphatase to kinase activity. The main target of DesK is the response regulator DesR, which, when phosphorylated, upregulates the expression of the $\Delta 5$ -fatty acid desaturase (Des)^{174,175}. When membrane viscosity and other biophysical properties are restored by enzymatic activity of Des, the membrane sensor DesK falls back into the phosphatase state, dephosphorylating the response regulator DesR. Dissecting the molecular details of the interaction of a truncated chimeric version of DesK with its membrane environment revealed that DesK is most likely controlled by membrane thickness¹⁷⁶. In the minimal sensor construct, with a single TMH, DesK was functional as a constitutive dimer that switched between two preferred dimer states in a membrane thickness-dependent manner. Increase of membrane thickness led to

hydrophobic mismatch between lipids and the sensor protein, that was countered by elongation of the THM. This elongation led to the positioning of three serine residues, forming a new dimer interface that is stabilized by an intramembrane serine zipper (Figure 5 B). This alternative dimer conformation is associated with auto-phosphorylation and kinase activity, activating the downstream response regulator DesR and therefore increasing expression of the fatty acid desaturase Des¹⁷⁷.

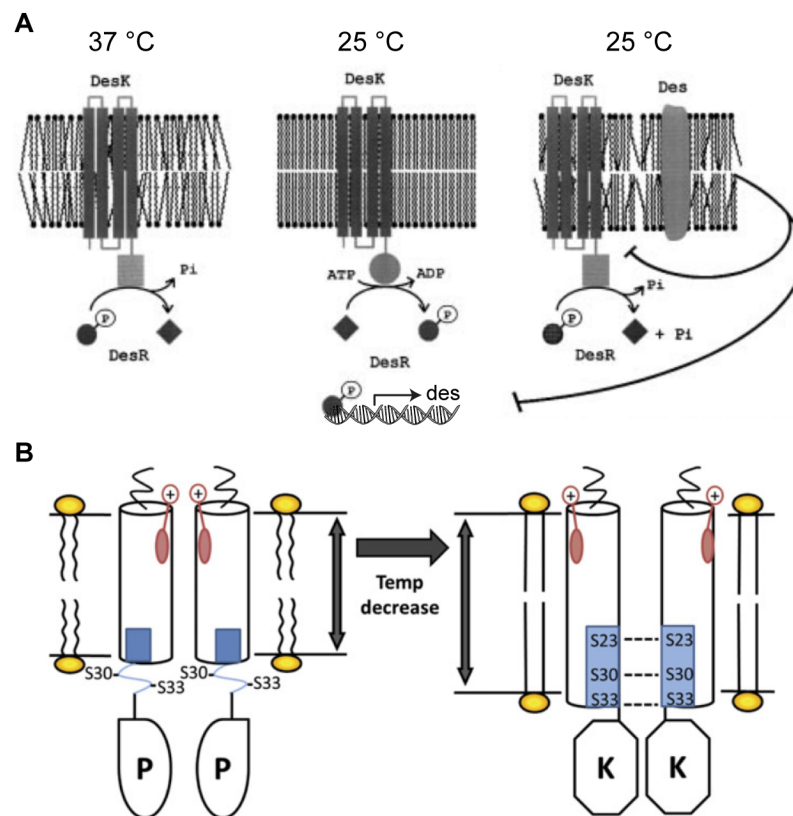


Figure 5: The cold shock and membrane thickness sensor DesK. A) At a growth temperature of 37 °C, the two-component histidine kinase DesK shows phosphatase activity towards the response regulator DesR. When temperature decreases, DesK switches to kinase activity, thereby phosphorylating DesR. Phosphorylated DesR activates the expression of the *des* gene, coding for Δ^5 -fatty acid desaturase (Des). Enzymatic activity of Des leads to feedback inhibition, by DesK returning to its phosphatase state. This panel was adapted from¹⁷⁴. **B)** The molecular mechanism of DesK-membrane interaction. Temperature decrease leads to hydrophobic mismatch between thicker membranes and the DesK-derived minimal sensor construct in its phosphatase (P) dimer conformation. This destabilization leads to the elongation of the transmembrane helix and the formation of an intramembrane serine zipper (residues S23, S30, and S33), stabilizing the kinase (K) dimer conformation. This panel was taken from¹⁷⁷.

Yeast also needs to adjust the levels of unsaturated membrane lipid acyl chains to the ambient temperature. Unlike in *Bacillus subtilis*, desaturation takes place during *de novo* synthesis of fatty acids. The ER membrane protein Mga2 is a membrane property sensor in yeast that regulates the expression of the gene *OLE1*, coding for yeasts sole fatty acid

desaturase (Ole1). The Δ^9 -fatty acid desaturase Ole1 is essential in the absence of exogenously provided unsaturated fatty acids. Mga2 is an unusual transcription factor that needs to be mobilized from the ER membrane before it can act in the nucleus. The OLE pathway describes the activation and processing of the 120 kDa transcription factor precursor which involves ubiquitylation of Mga2 by the E3 ubiquitin ligase Rsp5 (Figure 6 A). Subsequent recruitment of the segregase complex Cdc48/Ufd1/Npl4 by Ubx2 and proteolysis by the proteasome leads to the formation of a 90 kDa fragment that can enter the nucleus and upregulate *OLE1* expression (Figure 6 A)^{178,179}. The activity of the OLE pathway is dependent on the availability of unsaturated fatty acids, indicating the involvement of a potential lipid sensing mechanism^{178,180,181}.

The membrane sensing mechanism of Mga2 has been studied in molecular detail. Mga2 is an integral ER membrane protein spanning the membrane with a single TMH, featuring two crucial residues (W1042 and P1044). Minimal sensor constructs of Mga2 form dimers *in vitro* and molecular dynamics (MD) simulation has shown that the Mga2 dimer continuously explores all possible dimer interfaces (Figure 6 B)¹⁸¹. The occupation of distinct rotational orientations is affected by the degree of lipid saturation in the membrane environment and relative dimer orientations are not separated by high energetic barriers. A tightly packed membrane consisting of PC 16:0/18:1 (POPC) stabilizes a rotational orientation where the two W1042 residues of an Mga2 dimer, residing deep within the hydrophobic membrane core, hide in the dimer interface¹⁸¹. In more unsaturated membranes consisting of PC 16:1/18:1, an inversed orientation with both W1042 residues facing away from each other is stabilized (Figure 6 B). Despite this dependency on the membrane environment, dimers of Mga2 remain highly dynamic, exploring many different rotational orientations¹⁸¹. This rotational mechanism, featuring the relatively bulky tryptophan sensory residue, suggests that lipid packing might be the biophysical parameter that is sensed by the membrane property sensor Mga2 and maintained by regulation of the Ole1 enzyme level^{181,182}. Although *Bacillus subtilis* and yeast both regulate the levels of unsaturated membrane lipid acyl chains, the transmembrane sensor architectures and the sensory cues are fundamentally different.

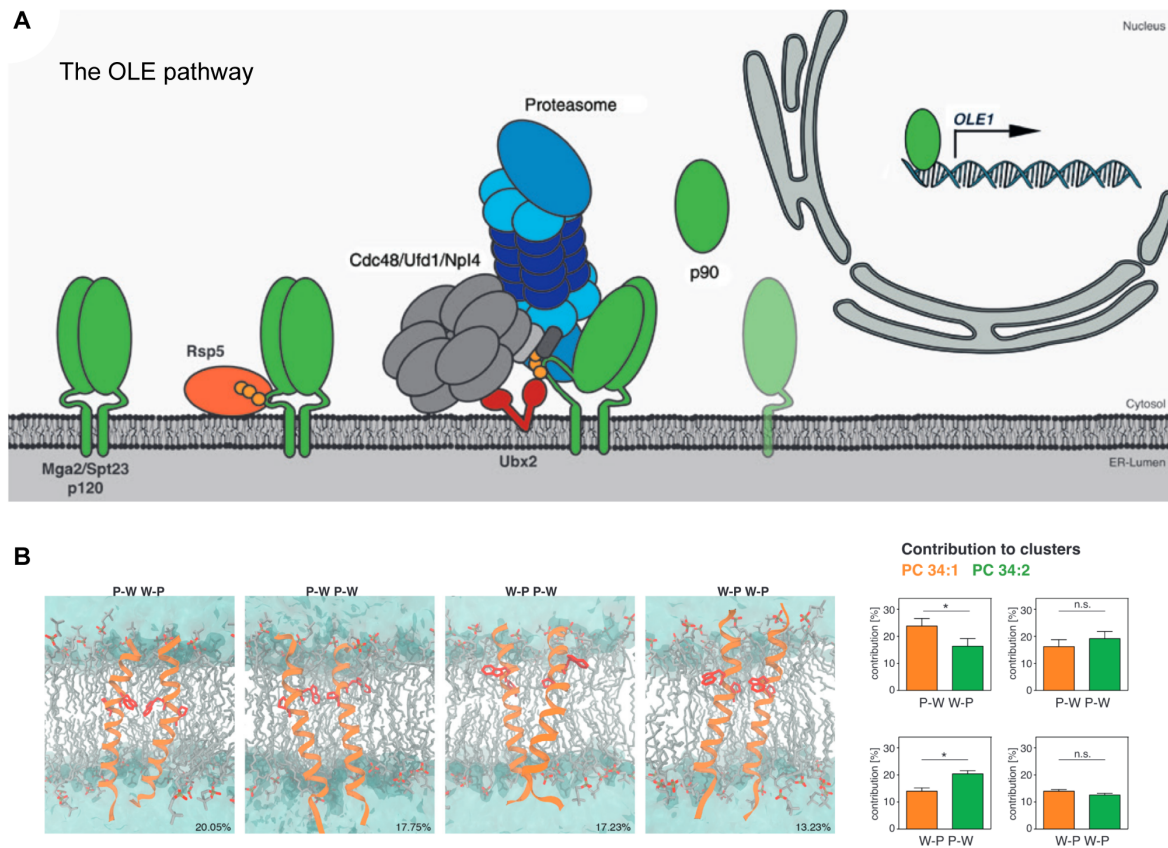


Figure 6: The OLE pathway and the molecular sensing mechanism of Mga2. A) The OLE pathway describes the processing of the transcription factors Mga2 and Spt23. Both proteins are 120 kDa ER transmembrane proteins with a single transmembrane helix (p120). Dependent on biophysical membrane properties, Mga2 gets ubiquitylated by the E3 ubiquitin ligase Rsp5. Subsequent recruitment of the segregase complex Cdc48/Ufd1/Npl4 by the substrate recruiting factor Ubx2 precedes processing by the proteasome at the cytosolic side of the ER membrane. Proteasomal proteolysis releases a 90 kDa fragment that relocates to the nucleus and activates the expression of the *OLE1* gene. This panel was adapted from¹⁸². **B)** Atomistic molecular dynamics simulation of a minimal sensor construct of Mga2 in POPC membranes. The Mga2 dimer continuously explores all possible dimer interfaces. However, a cluster analysis of structurally similar conformations revealed that the population of two clusters significantly changed in a membrane composition-dependent fashion. The conformation where both sensory tryptophan residues hide within the dimer interface (P-W W-P) was significantly more populated in tightly packing POPC membranes (PC 34:1, orange). Whereas in more loosely packing PC 34:2 membranes (green), featuring lipids with two unsaturated acyl chains, the conformation with sensory tryptophans pointing away from each other (W-P P-W) was more populated. This panel was adapted from¹⁸¹.

Not all membrane property sensor mechanisms act across or in the hydrophobic core of the membrane, like the mechanisms of DesK or Mga2 respectively. The yeast protein Opi1 represents a fundamentally different category of membrane property sensors. It regulates alternative transcriptional programs of membrane lipid and storage lipid production, that mark a central decision in cellular lipid metabolism. Opi1 is a peripheral membrane protein that interacts with the ER membrane indirectly via the ER transmembrane protein Scs2 and

directly in a PA-dependent manner¹⁸³. In contrast to DesK and Mga2, the sensing mechanism acts on the membrane surface and is more dependent on the abundance of a single phospholipid class in the ER membrane. *In vitro*, Opi1 binding to PA-containing model membranes is modulated by the lipid composition and collective membrane properties like curvature and packing¹⁸⁴. The molecular mechanism of PA recognition has been pinned down to an 18 amino acids long module that folds into an AH¹⁸⁵. The AH-fold explains the modulatory effects of membrane curvature and packing, as these parameters determine the probability of membrane insertion of an AH at the lipid headgroup region⁹¹. The sensory AH module features two 'three-finger grip' motifs, lysine-arginine-lysine and 3-lysine, which can intimately interact with the phosphate moieties of PA. MD simulation has suggested that these motifs recruit the anionic headgroups of PA and PS lipids¹⁸⁵. However, they strongly prefer PA over PS when both lipids are present in model membranes in equimolar amounts, suggesting the sensory modules specific recognition of PA in complex biomembranes¹⁸⁵.

When the PA level in cells is low, Opi1 is released from the ER membrane and relocates to the nucleus to act as transcriptional repressor of many glycerolipid biosynthesis genes. Specifically, those that are under the control of the transcriptional activators Ino2 and Ino4, at inositol-sensitive upstream activating sequences (UAS_{ino})^{186–188}. Hence, PA and inositol can be considered key regulators of lipid metabolism in yeast. Cells that lack either Ino2 or Ino4 require inositol supplementation for survival, while overproduction and secretion of inositol is observed in *OPI1* knockout cells^{189,190}. PA is a central precursor metabolite for both, membrane and storage lipid production^{187,191}. Opi1 regulates the balancing act between the two lipid metabolic pathways by sensing PA abundance in the ER membrane, with contributions of biophysical parameters that facilitate AH insertion.

The unfolded protein response (UPR) is a large transcriptional program that was initially discovered to restore the protein folding capacity of the ER¹⁹². However, the UPR is also activated by aberrant membrane compositions that potentially affect biophysical membrane properties and by depletion of inositol from the medium^{193–195}. The single-spanning ER transmembrane protein inositol-requiring enzyme 1 (Ire1) is the sole activator of the UPR in yeast and is evolutionarily conserved in humans. When unfolded proteins accumulate in the ER lumen, phosphorylation and oligomerization lead to the activation of a cytosolic RNase domain that initiates the unconventional splicing of the *HAC1* pre-mRNA (Figure 7 A)^{196–198}. The spliced *HAC1* mRNA is translated and the mature transcription factor Hac1 upregulates the expression of a large number of UPR target genes involved in protein folding, ER-associated degradation (ERAD), and lipid metabolism^{197,199}. Membrane sensing capabilities of Ire1 were suggested after the observation that cells with a dysfunctional Ire1 ER luminal domain, not able to bind unfolded proteins, still show UPR activity²⁰⁰. Many

The UPR transducer Ire1 contains a single alpha-helical transmembrane domain (TMD) that is crucial for its sensing capability for membrane aberrancies^{202,205}. Close inspection of the yeast TMD revealed an AH immediately adjacent to, and partly overlapping with, an unusually short hydrophobic TMH (Figure 7 B). This architecture leads to an overall tilted orientation of Ire1's TMD with the AH embedded in the luminal leaflet of the ER membrane²⁰⁵. Disruptive mutations of the AH's hydrophobic face showed severe loss of UPR-activating function. MD simulation measured the extent of local membrane compression around a TMD of Ire1 and suggested a sensory mechanism that is based on collective membrane properties, rather than the interaction of a specific lipid species²⁰⁵. Ire1 is a membrane property sensor that integrates a biophysical sensory cue, most likely membrane compressibility or thickness, into the UPR activity output. Increased energetic costs of compressing a thicker, stiffer, or more densely packed ER membrane might be minimized by coalescence of the compressed membrane areas in Ire1 oligomers, thus promoting the activation of its UPR effector domains²⁰⁵.

1.6. Organelle membrane lipid compositions and identities

Eukaryotic membrane-bound organelles are characterized by distinct proteomes and lipidomes. Subcellular biomembranes contain many hundreds of different lipid species in unique and context-dependent compositions that contribute to fingerprint-like organellar identities. This non-homogeneous subcellular distribution of lipids, with characteristic steady-state organelle compositions, is generated and maintained by spatially restricted biosynthesis, lipid sorting and selective vesicular transport, and active transport facilitated by lipid transfer proteins^{206–209}.

Particularly relevant and extreme is the distribution of sterols among organellar membranes. A sterol gradient along the secretory pathway is crucial for maintaining protein sorting and biophysical membrane properties. Cholesterol, or ergosterol in yeast, is found at low concentrations in the ER membrane and highly concentrated in the plasma membrane, despite its exclusive biosynthesis in the ER^{91,210}. In mammalian cells, the measured cholesterol concentration of the ER is dependent on the availability of cholesterol in the medium and ranges from 1 mol%, under conditions of acute cholesterol depletion, to 10 mol% when cholesterol is supplied externally in excess²¹¹. The SREBP/Scap sensory system that increases the expression of cholesterol biosynthesis genes was robustly activated when the ER cholesterol concentration fell below 5 mol%²¹¹. This suggests that the sterol concentration in the ER membrane is tightly regulated and actively maintained. Measurements of the yeast ER membrane sterol content have found a ratio of ergosterol

to phospholipids of 0.18, which corresponds to 13.5 mol%, assuming that 75% of all lipid molecules in the ER are phospholipids⁴⁴. A more recent study has suggested >20 mol% ergosterol in the ER of yeast grown in oleate-rich medium, while the purity of these preparations can be questioned²¹². These data demonstrate that organelle lipid compositions are species-specific and potentially context-dependent, however a sterol gradient along the secretory pathway is maintained in all examples. The sterol content of the plasma membrane has been determined for mammalian systems such as the apical side of a mouse endothelial cell (~33 mol%)²¹³, the apical side of a canine kidney cell (~45 mol%)²¹⁴, human erythrocytes (>40 mol%)⁶⁵, and in addition to this also for yeast (44 mol%)²¹⁵. For yeast, complementary lipidomics data of intermediate compartments suggest a steep step in membrane sterol concentrations only late in the secretory pathway. The *trans*-Golgi network and secretory vesicles contain 10 mol% - 14 mol% and 23 mol% - 30 mol% ergosterol respectively^{215,216}. The exact profile of the gradient has important implications for sorting and transport processes of lipids and membrane proteins. How is the sterol gradient generated and maintained? The observation of rapid equilibration of newly synthesized sterol with the pre-existing pools in the ER and the PM^{217,218}, suggests that, additional to vesicular transport, sterols are equilibrated by a multitude of non-vesicular sterol transfer proteins like NPC2²¹⁹, Osh4²²⁰, or steroidogenic acute regulatory-related lipid transfer (START) domain proteins^{221,222}. It is hypothesized that these proteins equilibrate sterol pools in the ER and the plasma membrane based on effective concentrations, that is the accessibility of membrane-bound sterol for these transfer proteins, modulated by the abundance of tightly packing, and therefore sterol shielding, saturated lipid acyl chains^{210,223}. Additionally, the mammalian sterol transporter OSBP shows counter-transport activity for phosphatidylinositol-4-phosphate (PI4P) from the plasma membrane to the ER, suggesting an energizing mechanism for the sterol transport by ATP-dependent Golgi- and plasma membrane-resident PI4-kinases^{37,224}.

Beside sterols, complex sphingolipids, saturated lipid acyl chains, and PS are enriched in the PM⁹¹. These compositional gradients manifest in a gradient of collective biophysical membrane properties (Figure 8 A)^{209,225}. Within the secretory pathway, biophysical properties range from mostly symmetric, thin, loosely packed membranes with low charge density at the ER surface, to asymmetric, thick, densely packed membranes with exposed charged surfaces at the plasma membrane (Figure 8 A). These membrane properties are reflected in the sequences and folds of transmembrane and membrane-interacting protein domains^{65,91,167,225,226}.

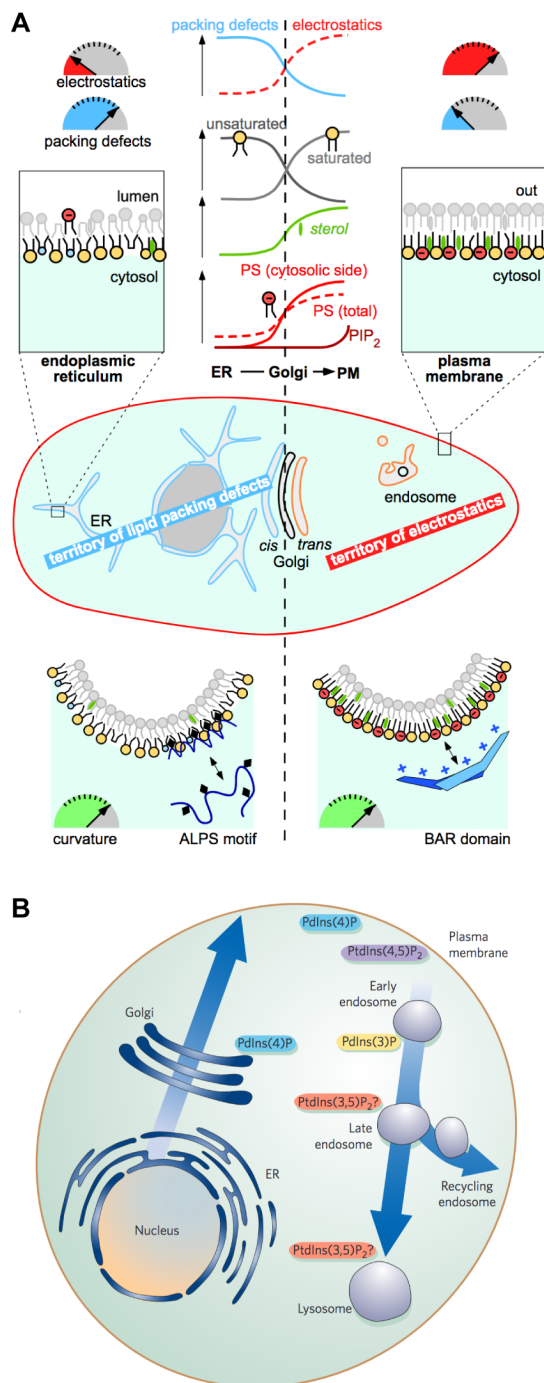


Figure 8: Two cellular territories present distinct membrane identities characterized by biophysical properties. A) There are compositional and biophysical gradients along the secretory pathway. The ER has abundant packing defects, unsaturated lipid acyl chains and a low level of sterol and PS. The plasma membrane (PM) is characterized by a high charge density, high level of saturated lipid acyl chains, sterols and the anionic lipids PS and the phosphoinositide PIP₂. Important sorting mechanisms that establish this unequal lipid distribution are located in the Golgi complex and endosomal system. The territory of lipid packing defects promotes the binding of proteins with amphipathic lipid packing sensor (ALPS) motifs. In the territory of electrostatics, proteins like BAR domain proteins interact with curved membranes via charged interactions. This panel was taken from⁹¹.

B) Organellar membranes in the secretory pathway and endosomal system contain identity-defining classes of phosphoinositides. The late secretory pathway (*trans* Golgi network and PM) is characterized by phosphatidylinositol-4-phosphate (PtdIns(4)P). Also found in the PM is the lipid phosphatidylinositol-4,5-diphosphate (PtdIns(4,5)P₂). Characteristic for endosomal membranes is the phosphoinositide phosphatidylinositol-3-phosphate (PtdIns(3)P). A PI(5)-kinase is located in late endosomes and the yeast vacuole, indicating the generation of phosphatidylinositol-3,5-diphosphate (PtdIns(3,5)P₂). This panel was adapted from²²⁸.

In mammalian cells, the targeting of tail-anchored proteins to different organelles depends on the hydrophobicity of the TMD and the charge of the adjacent tail region²²⁷. Cytoplasmic proteins need to distinguish between a multitude of diverse organelle membranes. In trafficking organelles of the endosomal and lysosomal system-specific identification and tethering is mediated by phosphoinositides and organelle-specific GTPases²²⁸. Such dynamic features allow the plasticity to lose old identities, e.g. after budding-off from a precursor organelle, or change identity during maturation processes by PI-kinase or

phosphatase activities (Figure 8 B)²²⁸. Besides phosphoinositides, sphingolipids play an important role in the sorting of vesicles in the endosomal system and the biogenesis of the lytic vacuole, the main catabolic compartment of yeast²²⁹. When sphingolipid metabolism is disturbed by knocking out inositol phosphosphingolipid phospholipase C (*ISC1*), which catalyzes the hydrolysis of complex sphingolipids to form ceramide, cytoplasm-to-vacuole (cvt) targeting of vesicles is dysfunctional, and the yeast vacuole appears fragmented²³⁰. This phenotype is mediated by the ceramide-activated protein phosphatase Sit4, that reacts to a shift in the ceramide acyl chain composition towards species with very long chain fatty acids of 26 C-atoms²³⁰. An important aspect of the vacuole's membrane identity is that it can phase separate into coexisting L_d and L_o membrane domains¹³¹. These domains are formed in the stationary growth stage and could be considered two separate membrane identities on the same organelle, as they show separate functionalities. The sterol enriched L_o domain serves as an essential docking platform, facilitating translocation of lipid droplets into the vacuole during micro-lipophagy^{132,231}. Changes of the yeast vacuole lipidome that might promote phase separation include increased ergosterol and complex sphingolipid level and a shift in sphingolipid composition to longer acyl chains and a higher degree of hydroxylation²³².

Organelle membrane lipid compositions have been estimated qualitatively by using lipid-sensitive probes that are partitioning to membranes that contain high levels of the lipid of interest, e.g. filipin binding to sterol-rich membranes or a diverse set of genetically encoded biosensors that bind membranes rich in DAG, PA, PS, or phosphoinositides^{233,234}. On the other hand, analytical methods based on cell fractionation and lipid extraction with downstream lipid chemical analyses, e.g. by thin layer chromatography or mass spectrometry, have revealed complete membrane lipidomes including class specific acyl chain compositions (Figure 9)^{208,235}. However, these data can only be as good as the cell fractionation that was performed before molecular analysis. Therefore, suitable isolation techniques are crucial to determine subcellular membrane lipid compositions. Most studies, even today, rely on classical cell fractionation techniques first described by Albert Claude²³⁶ and then further developed in the laboratory of George Palade^{237–239}. After cell lysis, subcellular components are separated by differential centrifugation and / or density gradient centrifugation. These techniques separate subcellular structures and particles based on physical properties, i.e. size, shape, and density²⁴⁰.

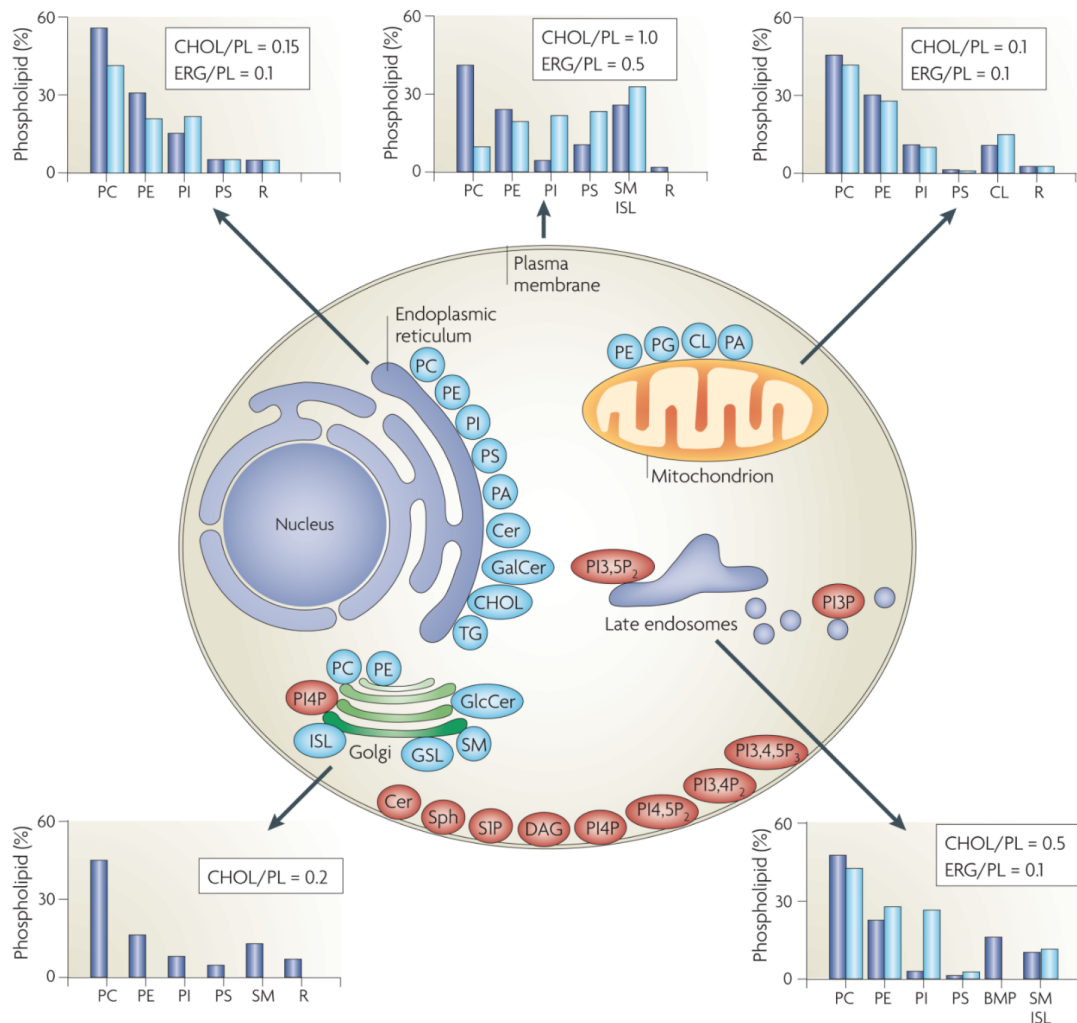


Figure 9: Subcellular membranes are locations of specific lipid biosynthesis and feature unique lipid compositions. The central scheme of a eukaryotic cell and its organelles shows the location of biosynthesis of diverse lipid classes. The ER produces all glycerophospholipid classes (PC, PE, PI, PS, PA), cholesterol (CHOL) or ergosterol (ERG), ceramide (Cer), galactosylceramide (GalCer) and the neutral storage lipid triacylglycerol (TG). Mitochondria generate PE, PG, cardiolipin (CL) and PA. The Golgi apparatus synthesizes complex inositol sphingolipids (ISL) in yeast and other complex sphingolipids in mammals (glucosylceramide (GlcCer), sphingomyelin (SM), glucosphingolipids (GSL)). Additionally, it generates the signaling lipid phosphatidylinositol-4-phosphate (PI4P). Phosphatidylinositol-3-phosphate (PI3P) and phosphatidylinositol-3,5-diphosphate (PI3,5P₂) are produced in late endosomes. The plasma membrane produces the phosphoinositides PI4P, phosphatidylinositol-4,5-diphosphate (PI4,5P₂), phosphatidylinositol-3,4-diphosphate (PI3,4P₂) and phosphatidylinositol-3,4,5-triphosphate (PI3,4,5P₃). Additional lipid classes that are generated at the PM are DAG, Cer, sphingosine (Sph) and sphingosine-1-phosphate (S1P). Surrounding bar graphs show characteristic lipid compositions of the ER, PM, mitochondria, Golgi apparatus and late endosomes. PL, phospholipids; R, remaining lipids; BMP, bis(monoacylglycero)phosphate. This figure was taken from²⁰⁸.

Systematic, pioneering cell fractionation studies in yeast, coupled to lipid analyses, have resulted in a series of publications from the Paltauf and Daum groups that established the

fundamentals of subcellular lipid compositions and distribution^{43,44,61,241,242}. They also pointed out the inherent linear anticorrelation between the abundance of an organelle in the cell and the achievable enrichment factor of this organelle in any isolation procedure. That means, the more abundant a type of membrane is in the intact cell, the lower is the achievable enrichment of these membranes²⁴². This fact and the vast physical interconnectedness with other organelles via membrane contact sites, makes the isolation of ER membranes particularly challenging^{243–245}.

A fundamentally different isolation strategy uses antibodies, raised against antigens with known localization at the subcellular membrane of interest. By this, organelles can be immobilized and then separated based on biochemical specificity and affinity. One of the earliest immuno-isolation protocols targeted endosomal vesicles from a mammalian cell culture system to study vesicle fusion events *in vitro*²⁴⁶. The methodology has been adapted to study the metabolite content of mammalian lysosomes and peroxisomes^{247,248} and the subcellular lipid composition of membranes in the late secretory pathway of yeast^{215,216}.

Despite early pioneering work and recent additions to the landscape of subcellular lipidomics^{208,235}, quantitative data are needed to understand the relation between lipid composition, membrane biophysics, and cellular homeostasis and pathology²⁴⁹.

1.7. Lipid bilayer stress in health and disease

The ER plays a crucial role in protein biogenesis, secretion, lipid metabolism and signaling. It handles a vast amount of different membrane and luminal proteins of the secretory pathway, especially in secretory cell types. Conditions that overload the protein folding and processing capacity of the ER are referred to as ER stress, which is tightly associated with the activation of the UPR. In human cells, the UPR signaling is initiated by three single-pass ER membrane proteins IRE1 α , Activating Transcription Factor-6 (ATF6), and Protein Kinase R-like ER kinase (PERK)²⁵⁰. In addition to the splicing of XBP1 mRNA, which resembles the splicing of the *HAC1* mRNA in yeast, mammalian IRE1 α supports protein folding homeostasis by reducing ER-targeted transcript levels via regulated Ire1-dependent mRNA decay (RIDD)²⁵¹. When activated, ATF6 is proteolytically processed in the Golgi complex to release the transcriptionally active fragment ATF6p50^{252–254}. Active PERK leads to the phosphorylation of the eukaryotic translation initiation factor 2 α resulting in a general downregulation of translation, while at the same time promoting the selective translation of the transcription factor ATF4^{255,256}. Severe or unresolved chronic ER stress can trigger apoptosis via the PERK branch. The ATF4 target C/EBPP homologous protein is a transcription factor that promotes pro-apoptotic signaling by upregulation of the death

receptor 5^{257,258}. Chronic activation of the IRE1 α branch has also been linked to programmed cell death via apoptosis signaling kinase 1 and RIDD activity²⁵⁹. Therefore, it is not surprising that ER stress, triggered by aberrant membrane compositions, i.e. lipid bilayer stress, is observed in many human disease conditions^{193,259–263}.

Saturated fatty acids can cause lipid bilayer stress, and eventually, cell death in pancreatic β -cells²⁶⁴. Exposure to palmitate leads to the activation of all three UPR branches and apoptosis in multiple mammalian pancreatic cell systems, including human islets²⁶⁵. The demise of pancreatic β -cells is a hallmark of the development of type II diabetes. When exogenous saturated fatty acids are supplied in excess, they are rapidly incorporated into membrane lipids. They pose a lipotoxic threat to the structural integrity of the ER membrane²⁶⁶ and potentially alter biophysical properties²⁶⁷ that could trigger lipid bilayer stress and IRE1 activation^{202,205,268}. Notably, unsaturated fatty acids show much lower lipotoxicity and can even counter the effects of palmitate²⁶⁵. It is possible that the other UPR transducers, PERK and ATF6, entail membrane-dependent activation mechanisms too. A PERK mutant missing its luminal, unfolded protein sensing domain was still capable of activating the UPR²⁰² and ATF6 activation was shown to be modulated by the abundance of the sphingolipids dihydrosphingosine and dihydroceramide²⁶⁹.

An intricate relation between lipid metabolism and ER stress is observed in hepatocytes with important implications for the pathology of nonalcoholic fatty liver disease (NAFLD)^{270–273}. In patients with NAFLD, lipids accumulate in hepatocytes, which progresses over time and can lead to conditions of liver dysfunction, nonalcoholic steatohepatitis (NASH) and cirrhosis. ER stress induces lipid accumulation in hepatocytes and steatosis in mice^{274,275}. The accumulating lipids might be originating from very low-density lipoproteins (VLDL), as the VLDL-receptor was shown to be upregulated via the PERK branch of the UPR²⁷⁶. Yet, other studies found evidence for an origin in fatty acid and TAG lipogenesis by hepatocytes, activated in an UPR-dependent fashion by SREBP-1c/2²⁷⁷. Notably, ER stress in cultured human hepatocytes can be induced by palmitate, or other saturated fatty acids, and sterols²⁷⁸. This lipotoxicity might lead to chronic ER stress and lead into a vicious circle by upregulation of hepatic lipogenesis. The importance of the glycerophospholipid content of hepatocyte membranes has been demonstrated in mice lacking the PE methyltransferase gene. These animals developed steatohepatitis and liver failure when choline was not provided with the diet²⁷⁹. This condition is characterized by lower PC to PE ratios and reduced membrane integrity in hepatocytes²⁸⁰. Notably, human NASH patients show similarly reduced PC to PE levels²⁸⁰. Lipid biomarkers that help distinguish between normal and diseased liver conditions can even be analyzed in the blood plasma²⁸¹.

Alzheimer's disease is characterized by progressing dementia and neurodegeneration with pathologically diagnosed accumulation of extracellular amyloid β plaques and intracellular aggregates of phosphorylated tau protein^{282,283}. Amyloid β is generated from the transmembrane amyloid precursor protein (APP) by proteolytic processing and it has been shown that overexpression of APP and the accumulation of amyloid β activate the UPR in neuronal cells²⁸⁴. It is thought that in early stages of Alzheimer's disease the initial accumulation of amyloid β and activation of the UPR can either lead to adaptation to alleviate ER stress or maladaptation that eventually triggers pro-apoptotic signals in cells with unresolved ER stress^{285,286}. Another line of evidence demonstrates aberrant lipid compositions in brains of patients with early Alzheimer's disease^{39,287} and a direct effect of plasmalogens on the activity of the APP-processing γ -secretase *in vitro*⁴⁰. It is tempting to speculate that there is crosstalk between these two pathologic processes, that is integrated by the UPR transducers, in the onset of Alzheimer's disease.

2. PUBLICATION SUMMARIES AND PERSONAL CONTRIBUTIONS

2.1. Cysteine cross-linking in native membranes establishes the transmembrane architecture of Ire1

The ER is the organelle at the base of the secretory pathway and therefore plays a crucial role in membrane and protein homeostasis. Every luminal and transmembrane protein of the endomembrane system is produced, inserted, and folded at the level of the ER²⁸⁸. Hence, the ER handles an exceptional number and abundance of proteins in every cell type and even more in professional secretory cells such as hepatocytes²⁷⁰. This protein load must be matched with appropriate folding and quality control capacities to prevent saturation of the folding machinery and increased protein misfolding and aggregates.

The UPR is a homeostatic program that surveilles protein folding activity in the ER¹⁹². When activated, the UPR downregulates protein synthesis and upregulates expression of a broad range of target genes involved in protein folding, ERAD, and lipid metabolism¹⁹⁹. When ER stress remains unresolved the UPR can trigger apoptosis and cell death by other means^{263,289–291}. Chronic ER stress has been linked to type II diabetes, cancer, and neurodegenerative diseases, thereby emphasizing the importance of the UPR to human health^{292,293}. In recent years it has been established that aberrant cellular membrane compositions can activate the UPR^{193,195,200}. Membrane-based ER stress is referred to as lipid bilayer stress²⁹⁴.

Ire1 is one of three UPR transducers and the only one that is evolutionarily conserved from yeast to humans. Ire1 is a type 1 transmembrane protein of the ER with a luminal domain that can bind unfolded proteins¹⁹⁸. When Ire1 is activated and forms signaling-active clusters, its C-terminal, cytosolic RNase domain cleaves the pre-mRNA of *HAC1* (XBP1 in mammalian cells) as the committed step in an unconventional splicing event. The spliced *HAC1* mRNA is translated, which produces a potent transcription factor that activates hundreds of UPR target genes^{295,296}. Ire1 contains an AH, which inserts into the luminal leaflet of the ER membrane, directly coupled to an unusually short TMH. This unique architecture of Ire1's TMD is the defining feature of its membrane-sensing capabilities²⁰⁵. Little is known how Ire1 TMDs are oriented with respect to each other in signaling-active clusters.

Here, we studied the transmembrane architecture of signaling active Ire1 under diverse ER stress conditions. We constructed a 'cysteine-less' GFP-tagged version of *IRE1* for expression in yeast cells. After characterizing its functionality *in vivo*, we introduced single-cysteine mutations along the TMD. Using copper ion-induced disulfide bridge formation along the TMD, we mapped the oligomeric Ire1 transmembrane architecture in microsomes

isolated from stressed cells^{297,298}. To probe the relative positioning of Ire1 molecules in dimers and oligomers we tested the cross-linking propensity of single cysteine residues along the TMD (E540C to C552). These data, together with MD simulations, indicated an X-shaped conformation of the dimeric Ire1 TMD in the ER membrane with F544 marking the point of crossover. This TMD architecture was observed both under conditions of proteotoxic and lipid bilayer stress.

As co-first author, I performed all microscopy experiments and subsequent image analyses. To address whether GFP-tagged *IRE1* constructs generated in this study were expressed and yielded functional proteins *in vivo*, I performed live cell fluorescence microscopy and quantified the clustering propensity. By targeting the genomic locus of *IRE1*, we achieved near endogenous expression levels which are exceptionally low (< 300 Ire1 molecules per cell²⁹⁹). As a consequence, under unstressed conditions Ire1-GFP signal was indistinguishable from background noise. Only in stressed cells, when Ire1-GFP formed signaling-active clusters, oligomers could be observed as dot-like structures of the ER (Appendix p. 73, Figure 1 D). To quantify these imaging data, I developed a custom analysis pipeline for automatic segmentation of cells and associated Ire1-GFP cluster. This allowed unbiased measurements of the clustering propensity of Ire1 and the associated cluster sizes.

My quantitative microscopy data suggested a tendency of cysteine-less Ire1 towards less cluster formation compared to Ire1 wildtype (Appendix p. 73, Figure 1 D). The dithiothreitol (DTT)-induced clusters of cysteine-less Ire1 were less prevalent and smaller in size (Appendix p. 91-92, Figure S3 G). Nevertheless, the data demonstrated the functionality of cysteine-less Ire1, which was capable of oligomerizing and cluster formation under ER stress conditions. In support of our immunoblotting data (Appendix p. 89, Figure S1 B, C), I could confirm that both wildtype and cysteine-less Ire1-GFP clusters colocalized with the ER marker ER-dsRed-HDEL (Appendix p. 89, Figure S1 F).

Taken together with other functional data (Appendix p. 73 and 89, Figure 1 B, C and Figure S1 A-D) we concluded that the cysteine-less version of Ire1 is functional and a suitable model to map the complex structure of Ire1's TMD in signaling-active oligomers via cysteine cross-linking.

Based on the cysteine-less version, cross-linkable mutants with single-cysteines located along the TMH were generated to investigate the transmembrane architecture of signaling-active Ire1 oligomers. To control for possible differences in cross-linking efficiency due to aberrant oligomerization of single-cysteine Ire1 versions, I measured their clustering propensity by live cell fluorescence microscopy. My data showed that all single-cysteine Ire1-GFP versions (E540C-C552) formed clusters in DTT-stressed cells (Appendix p. 91-92, Figure S3 E). Furthermore, the number and size of clusters formed in cells were the

same for all single-cysteine Ire1-GFP mutants and at the level of the cysteine-less version (Appendix p. 91-92, Figure S3 F, G). These data indicate that the observed cross-linking pattern reflects intermolecular proximity in the signaling-active Ire1 dimer and oligomer.

Next, we asked whether the observed cross-links are formed between Ire1 molecules in a dimer or between adjacent dimer units of the oligomer. To address this, we introduced a previously described Ire1 interface 2 (IF2) mutation (W426A) that interferes with higher oligomer formation³⁰⁰. In accordance with previous results³⁰⁰, I could show that the IF2 mutation completely abolished Ire1 cluster formation in cells that were treated with DTT (Appendix p. 79, Figure 6 A). Furthermore, Ire1 single-cysteine mutants, in the IF2 mutation background, showed no cluster formation under ER stress conditions (Appendix p. 79, Figure 6 B). Taken together with the dramatically reduced cross-linking efficiency in E540C+IF2 compared to E540C (Appendix p. 79, Figure 6 F), we concluded that TMD positions E540 of adjacent units of dimers are in close proximity within signaling-active clusters. In contrast, T541C+IF2 and F544C+IF2 did not show reduced cross-linking efficiency, when compared to T541C and F544C respectively. This indicated proximity of the respective TMD positions between the Ire1 molecules that form a dimer.

Based on our findings, we propose a membrane-sensing mechanism of Ire1 that is determined by its unique TMD characteristics. The combination of a short hydrophobic TMH and a partially overlapping AH, that inserts into the luminal leaflet, locally compresses the ER membrane²⁰⁵. Ire1's ellipsoid footprint in the ER membrane is associated with energetic costs that are dependent on biophysical membrane properties^{24,301}. When the thickness or transverse stiffness of the membrane increases, increased energetic costs of compression are minimized by overlapping footprint areas after side-to-side dimerization of Ire1 (Appendix p. 79, Figure 6 G). This model is compatible with the observation of elongated Ire1 clusters and a helical cluster ultrastructure in specialized ER subdomains^{302,303}.

Strikingly, Ire1 seems to converge into the same TMD architecture both under proteotoxic and lipid bilayer stress. Based on our findings, we speculate that instead of holding two separate sense-and-response modes, Ire1 integrates signals of protein folding capacity and membrane properties to trigger the UPR in a single signaling-active TMD conformation.

2.2. Regulation of lipid saturation without sensing membrane fluidity

Cellular membranes are complex and dynamic assemblies of lipids and proteins. The physicochemical properties of a membrane are dependent on its molecular composition. Furthermore, important bulk membrane properties like permeability, viscosity, and the lateral pressure profile are interdependent²⁴. Therefore, organisms can adjust the physicochemical characteristics of their cellular membranes by a multitude of different chemical features in a plethora of lipids and proteins²¹.

Poikilothermic organisms that cannot regulate their body temperature need to maintain membrane functions and membrane fluidity even under cold stress. The essential adaptation of the membrane composition to cold has been termed homeoviscous adaptation¹⁷³. Controlling the level of unsaturation in membrane hydrocarbon chains is a common strategy in cellular regulation of membrane fluidity^{304,305}. This mechanism has been described for bacteria^{306,307}, fungi^{20,182}, worms^{308,309}, flies³¹⁰, and vertebrates³¹¹. Furthermore, the level of unsaturated acyl chains in plankton inversely correlate with the ambient water temperature. In the context of global warming, this has important implications for marine food webs³¹².

Despite the importance of membrane acyl chain homeostasis, little is known about the molecular details by which cells sense physical membrane properties and maintain membrane fluidity. Based on topological considerations, one can distinguish three classes of membrane sensors that probe either the surface (class I), the hydrophobic core (class II) or across the thickness of the bilayer (class III)¹⁷¹. Class I sensors can measure charge or packing density in the headgroup region. This has been described for Opi1, which contains a sensory AH with binding motifs that are specific for the anionic lipid PA¹⁸⁵. Class II sensors, like the transmembrane protein Mga2, are susceptible to features of the lateral pressure profile or packing density in the hydrophobic core of the bilayer¹⁸¹. Class III sensors are transmembrane proteins that measure membrane properties like thickness or compressibility across the transversal axis of the bilayer^{176,205}.

The prototypical class II sensor Mga2 is a transmembrane protein that regulates the expression of the gene *OLE1* in yeast. The enzyme Ole1 is the only fatty acid desaturase in yeast and essential for *de novo* biosynthesis of unsaturated, *cis*- $\Delta 9$, CoA-activated fatty acids³¹³. Furthermore, without supplementation of external unsaturated fatty acids it is essential for yeast survival. The Ole1 regulator Mga2 is an ER membrane protein of 120 kDa that is processed by ubiquitylation, proteasome activity and is eventually released as a soluble 90 kDa transcription factor¹⁷⁸. This gene regulation circuit is known as the OLE pathway³¹⁴. Mga2's single TMH harbors the tryptophan residue W1042 deep in the membrane hydrophobic core. Recently, it has been demonstrated that W1042 is crucial to the sensing mechanism of Mga2¹⁸¹. Coarse-grained MD simulations have shown that two

adjacent TMHs in an Mga2 dimer explore rotational orientations with preferences for two conformations that are dependent on the membrane environment. In more saturated membranes, both W1042 residues spend more time facing each other (on-conformation, promoting the OLE pathway). In more loosely packed membranes containing more unsaturated lipids, the two W1042 residues are more likely to face away from each other (off-conformation)¹⁸¹. The minimal energetic barriers between rotational orientations present an inherently noisy signal and it remains unclear how a robust molecular signaling decision is generated¹⁸¹.

Here we investigated the signal propagation and functional coupling of Mga2's transmembrane sensor domain to its ubiquitylation sites. By carefully distinguishing different biophysical parameters of lipid bilayers *in silico* and *in vitro* we showed that despite regulating fatty acid desaturation in yeast, Mga2 is not *per se* sensitive to membrane viscosity. Instead, we suggest a sensing mechanism for the abundance of double bonds, at a defined region along the transverse of the bilayer, based on the lipid-packing density at a defined depth in the lipid bilayer.

We designed a minimal sense-and-response construct comprising an N-terminal leucine zipper, a maltose binding protein and residues 950-1062 of Mga2. The leucine zipper ensures the formation of a sensing-active dimer *in vitro* and therefore functionally mimics the IPT domain (Ig-like, plexin, transcription factor) of Mga2. The maltose binding protein acts as solubility and affinity tag for protein purification. Mga2 residues 950-1062 contain the E3 ligase binding site LPKY (967-970)³¹⁵, three lysine residues K980, K983, and K985 within a disordered loop that can be ubiquitylated³¹⁶, and the TMH with the sensory tryptophan W1042 (Appendix p. 100, Figure 2 A). This construct was reconstituted into liposomes with defined lipid compositions mimicking either physiological or aberrant concentrations of unsaturated acyl chains.

We followed the ubiquitylation of a minimal sense-and-response construct based on Mga2 in a variety of membrane environments. In a reaction mix with purified ubiquitin, yeast cytosol and an ATP regenerating system we observed significant ubiquitylation of Mga2 in saturated membranes (e.g. 100% palmitoyl-oleoyl-phosphatidylcholine, POPC), but no ubiquitylation was observed in more unsaturated membrane environments reflecting the physiological degree of lipid saturation (50% dioleoylphosphatidylcholine, DOPC plus 50% POPC) (Appendix p. 100, Figure 2 D, E).

We tested whether the relative positioning of the two E3 binding sites LPKY (967-970) in the dimer and each of the two ubiquitylation sites K980, K983, and K985 was dependent on the membrane composition. To this end, we introduced a pair of Förster resonance energy transfer (FRET)-capable fluorophores into dimers of the Mga2 sense-and-response construct. With a donor at the ubiquitylation site K983 and an acceptor at the E3 binding

site K969, we measured gradually increasing FRET efficiencies with increasing saturation of membrane lipid acyl chains. This indicated that the E3 binding site in one protomer and the ubiquitylation site of the opposing protomer approach each other with increased lipid saturation, thereby providing a possible explanation for the higher ubiquitylation efficiency in saturated membranes (Appendix p. 101, Figure 3 E-G).

Next, we asked if the conformational dynamics of Mga2 and its ubiquitylation propensity are directly dependent on membrane viscosity. By including PE in our model membrane systems we generated bilayers with higher viscosity, due to tighter lipid packing, while keeping the abundance of double bonds at physiological levels. We found that in this membrane environment, despite the higher viscosity, Mga2 ubiquitylation propensity was not increased when compared to the less viscous PC-only membrane composition (Appendix p. 103, Figure 4).

To this study, I contributed systematic fluorescence anisotropy measurements using the membrane probe 1,6-diphenyl-1,3,5-hexatriene (DPH). When incorporated into model membranes, DPH is thought to orient parallel to lipid acyl chains although measurements and *in silico* observations of orthogonal orientation have been reported^{317,318}. The flexibility of the DPH fluorophore dipole, and therefore the fluorescence anisotropy, is dependent on temperature and the local membrane environment. DPH is widely considered a fluidity or microviscosity probe. Notably, it is not sensitive to differences in lateral diffusivity¹¹⁵. My data suggests that DPH is probing the main phase transition between gel and liquid bilayer based on qualitative differences of acyl chain order, which is consistent with previous observations (Appendix p. 121-124, Supplementary Figure 4 B and Supplementary Figure 5 E)^{317,319}. Subtle, quantitative differences in fluidity can be measured directly as lateral diffusivity by fluorescence correlation spectroscopy (FCS) (Appendix p. 103-104, Figure 4 A and Figure 5 A)³²⁰. Hence, FCS measures the general viscosity of the model membrane as experienced by the probe molecule³²¹.

These data illustrate an important point. Every membrane probe is sensitive to specific biophysical cues^{322,323}. Measurements with fluorescent membrane probes should be described by appropriate terminology and conclusions from such data must be drawn with care. Membrane fluidity, the inverse of viscosity, is defined by rotational and translational mobility of molecules³²⁴. With the Mga2-based sense-and-response construct, we observed that the ubiquitylation of Mga2 does not correlate with the lateral diffusion constants of fluorescently labeled lipids (Appendix p. 103, Figure 4 A, F). Hence, we concluded that Mga2 is not measuring membrane fluidity.

Next, we tested the effect of the positioning (*cis*- Δ 6 / *cis*- Δ 9) and configuration (*trans*- Δ 9 / *cis*- Δ 9) of double bonds in lipid acyl chains. Membranes of *cis*- Δ 6 18:1-PC were only slightly more viscous than DOPC (which is the same as *cis*- Δ 9 18:1-PC) membranes (Appendix p.

104, Figure 5 A). Nevertheless, the Mga2 ubiquitylation efficiency in *cis*- Δ 6 18:1-PC membranes was the highest we observed in any of the tested conditions (Appendix p. 104, Figure 5 H). To test if Mga2 senses the double bond directly at the Δ 9 position rather than lipid packing, we measured viscosity and Mga2 ubiquitylation in *trans*- Δ 9 18:1-PC membranes, which also contains a double bond in the same position, but packs considerably better than DOPC. The ubiquitylation efficiency in *trans*- Δ 9 18:1-PC membranes was significantly higher than in DOPC membranes (Appendix p. 104, Figure 5 H). When compared to *cis*- Δ 6 18:1-PC membranes, *trans*- Δ 9 18:1-PC membranes lead to lower ubiquitylation efficiency of Mga2, despite presenting the more viscous environment (Appendix p. 104, Figure 5 H). Taken together, these data indicate that Mga2 is not directly sensing double bonds. Instead, it is most likely reacting to a collective biophysical membrane property that, in yeast, is greatly influenced by the introduction of *cis*- Δ 9 double bonds in lipid acyl chains.

Since the sensory tryptophan is a bulky residue, we asked whether a biophysical membrane property, at the position of the double bond, could serve as the sensory cue. In fact, we observed a correlation between residue size at the sensory TMH position 1042 and the signaling output of mutant Mga2 variants *in vivo* (Appendix p. 106, Figure 6). Previous data showed that the sensory W1042 of Mga2 is located between 3 - 10 Å from the bilayer center¹⁸¹. Here, we used MD simulations to characterize the differences in biophysical membrane properties between Mga2 ubiquitylation-promoting POPC and non-permissive DOPC membranes. We found that the atom number density is substantially increased in the POPC membrane, exactly at the region between 3 - 10 Å from the bilayer center where also the sensory W1042 resides (Appendix p. 107, Figure 7 B). This indicates that Mga2 is indeed sensitive to a biophysical parameter related to local lipid packing density in the hydrophobic core of the bilayer.

Additionally, proximity measurements by FRET and electron paramagnetic resonance in all tested membrane environments show that TMH conformation and ubiquitylation propensity follow a general positive correlation, indicative for information transfer from the signaling module embedded in the membrane core to the juxtaposed response module that eventually leads to the activation of the OLE pathway.

2.3. A quantitative analysis of cellular lipid compositions during acute proteotoxic ER stress reveals specificity in the production of asymmetric lipids

Cell membranes are more than simple barriers to the outside world. The plasma membrane, and organelle membranes in eukaryotes, are active, functional, and essential biological environments¹³⁶. Even the membranes of relatively simple eukaryotes like yeast contain hundreds of different lipid species¹⁹. The lipid composition of yeast membranes is highly dynamic. Cells remodel the lipidome depending on available nutrients, environmental conditions, or cellular stress^{20,32}. The ER is the central hub of lipid homeostasis and plays a key role in lipid biosynthesis¹⁸⁷, distribution^{209,325}, and regulation^{188,314}.

The UPR is an important example for the intricate relationship of membrane lipid composition and cellular stress²⁵⁰. In recent years it has become evident that the UPR can be activated by both, unfolded proteins in the ER lumen and aberrant lipid compositions^{195,200,205}. Active UPR leads to an expansion of the ER size³²⁶, a general attenuation of protein synthesis^{192,327}, and the upregulation of ERAD-components and chaperones^{194,196}. The UPR also activates a broad range of genes involved in membrane biogenesis¹⁹⁹. Probably because of this central role in the homeostasis of cellular protein and lipid production, a dysfunctional UPR has been firmly associated with pathological processes in the context of viral infections, neurodegenerative diseases, cancer, type II diabetes, and non-alcoholic steatohepatitis^{259,261,328,329}. However, it is not understood how the membrane lipid composition influences UPR activation and potentially disease conditions.

Many aspects of the UPR have been studied in yeast, where the evolutionarily conserved Ire1 is the sole UPR transducer. It consists of an N-terminal, ER-luminal, sensor domain that responds to deficiencies in protein folding, a single TMH, and cytosolic kinase and RNase effector domains³³⁰. When activated by the accumulation of unfolded proteins or lipid bilayer stress, Ire1 oligomerizes and its RNase effector domain initiates an unconventional splicing of the *HAC1* mRNA in the cytosol^{197,295}. The translation product of the spliced *HAC1* mRNA, Hac1, is a potent transcription factor that upregulates the expression of hundreds of target genes involved in protein folding, ERAD, and lipid metabolism¹⁹⁹.

ER stress in yeast is commonly triggered by the proteotoxic agents DTT or tunicamycin (TM), supplemented to the culture medium. DTT is a reducing agent that prevents the formation of disulfide bridges in the ER lumen, but it also removes palmitate from palmitoylated proteins. TM is a specific inhibitor of N-linked glycosylation in the ER lumen³³¹. However, how these treatments affect cellular lipidomes is unknown.

Here, we studied the yeast lipidome during acute proteotoxic stress, induced by DTT and TM. We found that DTT causes a rapid and substantial remodeling of the lipidome while TM causes much less pronounced changes. Therefore, we concluded that short TM treatment presents a clean proteotoxic stress, without major consequences on the level of lipids. Furthermore, we showed that the choice of medium, rich or minimal, has a dramatic impact on the cellular lipid composition. Combinatorial effects of DTT and TM treatment with rich or minimal media might indicate a context-dependent modulation of UPR activity. First, we tested the impact of DTT and TM on cellular growth by determining minimal inhibitory concentrations for both proteotoxic agents in rich (YPD) and minimal (SCD) media (Appendix p. 138, Figure 1 A-D). We found that DTT inhibited growth more effectively in SCD medium, while TM had a more potent effect in YPD (Appendix p. 138, Figure 1 A-D). An Ire1-knockout strain (*ire1* Δ) was more sensitive under both proteotoxic stress conditions, in both media, indicating an UPR-dependent gain in fitness. To study the effect of acute proteotoxic stress on the cellular lipidome, we chose concentrations of both proteotoxic agents that completely inhibited overnight growth. Hence, we used 8 mM and 2 mM DTT in YPD and SCD respectively. Likewise, TM concentration was adjusted to 1.0 μ g/ml and 1.5 μ g/ml in YPD and SCD respectively (Appendix p. 140, Figure 2 A). These concentrations are within the range of previously reported experimental conditions to study the UPR^{326,332,333}. Nevertheless, after 1 h of ER stress we did not observe a difference in cell growth, when compared to untreated control cultures (Appendix p. 152, Supplementary Figure S1 A, B) despite the fact that UPR activity leads to a substantial remodeling of the transcriptome within this time window^{199,200,334}.

As co-first author, I categorized and normalized the data to master the complex dataset, generated all figures, and performed statistical tests. Furthermore, I analyzed and interpreted all lipidomics data and made the unexpected discovery that yeast generates abundant asymmetric phospholipids with remarkably specific pairing of two saturated acyl chains of substantially different lengths. First, I studied the impact of the medium on the cellular lipidome by comparing data from cells cultivated in YPD and SCD medium. Yeast cells growing in minimal SCD medium showed a significantly higher content of complex sphingolipids compared to YPD-grown cells (Appendix p. 141, Figure 3 A). The composition of membrane glycerolipids (MGL) showed characteristic differences with lower level of PE and higher level of the anionic lipids PA, PI, and PS in SCD compared to YPD (Appendix p. 141, Figure 3 A). Next, I analyzed the acyl chain lengths and degree of lipid saturation of MGL. We found that MGL of cells cultivated in SCD had longer (Appendix p. 141, Figure 3 C) and more unsaturated acyl chains when compared to YPD-grown cells (Appendix p. 141, Figure 3 D). It is possible that these lipidome characteristics modulate UPR activity, as it has previously been shown that aberrant lipid saturation²⁰², PC-to-PE ratios^{201,335}, or

depletion of inositol²⁰⁰ can trigger the UPR. Additionally, it was demonstrated that Ire1 senses biophysical bilayer properties like membrane thickness or compressibility^{24,205}. Furthermore, cells cultivated in SCD contained more storage lipids such as TAG and ergosteryl ester (Appendix p. 141, Figure 3 A), thereby underscoring the vast impact of the medium on lipid droplet biogenesis, fatty acid storage, and membrane lipid biogenesis³³⁶. While analyzing the acyl chain composition of MGL from YPD cultures, I realized that a large fraction of DAG and PI lipids contained an unusually asymmetric combination of a saturated medium-length, C10:0 or C12:0, acyl chain with a saturated long, C16:0, acyl chain (Appendix p. 141, Figure 3 F). However, these lipid species were much less abundant in cells grown in SCD (Appendix p. 141, Figure 3 G). Nevertheless, the remarkable specificity of fatty acyl chain pairing in these asymmetric lipids suggests an exquisite selectivity in their biosynthesis and / or remodeling.

Next, I turned to analyze the species distribution of sphingolipids. Here, we identified a dramatic shift from 3 to 4 hydroxylations, associated with all sphingolipid species, when cells were cultivated in SCD (Appendix, p. 141, Figure 3 H). Taken together, we found a substantial influence of the culture medium on the cellular lipidome of yeast, with a multitude of potential implications for the properties of cellular membranes and their homeostasis.

Subsequently, I focused on the lipidomes of cells that were treated with either DTT or TM, two proteotoxic ER stress-inducing agents. Short-term treatments (1 h) with DTT had a significant impact on the lipidome of cells cultivated in YPD, compared to untreated control cells (Appendix p. 144, Figure 4 A, B). The lipidome from stressed cells featured significantly more PA, while PC, PS, and DAG were significantly decreased (Appendix p. 144, Figure 4 A, B). Especially the strong increase of the important signaling lipid PA is likely to impact transcriptional lipid homeostatic programs¹⁸⁷. Within the category of MGL, which accounts for approximately 75% of all lipids, we found significantly increased levels of lipids with only one unsaturated acyl chain, indicating potential changes in central biophysical membrane properties (Appendix p. 144, Figure 4 E)¹⁷¹.

Surprisingly, the lipidome changes were indistinguishable for wildtype and *ire1Δ* cells (Appendix p. 156-157, Supplementary Figure S4 B). This might indicate that the duration of stress was insufficient to remodel the proteome and substantially change the enzymatic activities of lipid metabolism. Furthermore, it could indicate that the UPR target genes of the lipid metabolism only lead to membrane expansion in a *more-of-the-same* mode instead of changing the composition. In fact, the expression of many key lipid metabolic enzymes is indirectly upregulated by UPR activity via the heterodimeric transcription factors Ino2 and Ino4 of which at least Ino4 is a direct target of the UPR^{199,326}.

Next, I analyzed the differences in cellular lipidomes by TM-induced ER stress. In contrast to the stark changes induced by DTT in YPD-cultured cells, lipidomes were much less

affected by TM (Appendix p. 144, Figure 4 B). In SCD medium, small lipidome changes during acute ER stress were similar in both, DTT- and TM-treated cells, with the exception of lower ergosterol level during DTT-induced stress (Appendix p. 145, Figure 5 B). With respect to the contribution of UPR activity to these lipidome changes, we made the same observation as for YPD medium, i.e. these changes are surprisingly independent of Ire1 (Appendix p. 158-159, Supplementary Figure S5 B).

The increase in lipid saturation, especially in stressed YPD-cultured cells, might modulate UPR activity. To this end, future experiments could be performed to directly measure the UPR activity in the conditions explored here. Increased levels of lipid saturation have been linked to UPR activation in previous studies^{195,203}. The faster growth rates of cells cultured in YPD, in combination with a potentially high content of saturated medium chain fatty acids in this medium, might present a challenge for the lipid metabolic network. Fatty acids from the culture medium are promiscuously taken up by yeast and are incorporated into membrane lipids⁴⁶. Competition of acyltransferases and Ole1 for the same substrates might lead to insufficient levels of lipid desaturation.

Based on our findings, we recommend the induction of a 'clean' acute proteotoxic stress by TM treatment in minimal SCD medium. The surprising result that lipidomes of the UPR-deficient *ire1Δ* strain were indistinguishable from wildtype cells, at least for this relatively short period of ER stress induction, indicates that the observed changes in lipid composition might be caused by direct effects of the proteotoxic stress and not by UPR activity. Such direct effects could be, e.g. the inactivation of lipid metabolic enzymes or defective targeting of vesicular traffic between organelles due to unfolding of the involved proteins. The discovery of highly asymmetric DAG and PI lipid species revealed a remarkable selectivity of the lipid metabolic network and yet the robustness to cope with varying, potentially adverse, growth conditions.

2.4. MemPrep, a new technology for isolating organellar membranes provides fingerprints of lipid bilayer stress

Biological membranes show a complex composition of lipids and proteins. The hundreds of lipid species found in cellular membranes are generated by a dynamic lipid metabolic network^{32,209}. Maintaining characteristic membrane compositions of organelles is a major regulatory challenge. Often, competing requirements of fluidity, compressibility, permeability, and other collective biophysical membrane properties, must be fulfilled to ensure homeostasis of cell functions^{170,172,188,208,209}. The central hub of cellular lipid metabolism and membrane protein biogenesis is the ER. Accordingly, it plays a crucial role in cellular adaptation and homeostasis and hosts important regulatory machinery and stress response pathways¹⁸⁷. The ER is a continuous membrane network that forms various structural domains such as the nuclear envelope, tubules and sheets³³⁷, and highly specialized subdomains involved in lipid droplet biogenesis³³⁸, peroxisome biogenesis³³⁹, and vesicular transport³⁴⁰. Furthermore, the ER forms membrane contact sites, physically connecting it to virtually every other organelle in the cell, to exchange small molecules such as ions and lipids³⁴¹. These physical contacts, however, make it particularly challenging to isolate the ER for studying its molecular composition and response to cellular stress.

Differential and density centrifugation separate organelles based on physical properties like size and density. These techniques have been the standard in cell fractionation for a long time²⁴². The systematic application of these classical approaches has established the main compositional characteristics of most organelles in yeast. Nevertheless, we are still lacking comprehensive and quantitative data on the ER membrane⁴⁴.

The ER is not only the central hub for lipid metabolism it is also the entry point for every soluble and transmembrane protein of the secretory pathway²⁸⁸. It harbors protein folding capacity which is maintained by the UPR^{192,250}. Ire1 is a UPR transducer that is evolutionarily conserved from yeast to *Homo sapiens*³⁴². In yeast, Ire1 senses the accumulation of unfolded proteins in the ER lumen^{196,198}. The binding of unfolded proteins induces oligomerization of Ire1, which activates its cytosolic effector domains. This initiates the unconventional splicing of the *HAC1* mRNA and facilitates the production of the transcription factor Hac1²⁹⁵. As a consequence, hundreds of downstream genes involved in protein folding, ERAD, and lipid metabolism are upregulated^{199,343}.

Furthermore, it has been shown that Ire1 is also sensitive to membrane aberrancies, referred to as lipid bilayer stress^{195,202,205}. A variety of lipid metabolic perturbations such as inositol depletion^{200,204}, increased lipid saturation^{195,203}, altered sterol levels²⁰³, impaired sphingolipid biosynthesis³⁴⁴ and deregulated ratios of PE to PC^{201,345} can activate the UPR. Interestingly, even prolonged proteotoxic stress manifests in a membrane-based cue that

contributes to UPR activation^{200,346,347}. This emphasizes the central role of Ire1 as an integrator of lipid and protein signals by sensing ER membrane properties^{205,347}.

Human pathological states like type II diabetes and NAFLD are firmly linked to chronic ER stress due to an unresolved UPR and aberrancies of the lipid metabolism^{264,271,348}. However, the molecular mechanisms by which ER membrane components contribute to the activation of the UPR are not understood^{250,349}.

Here we report the development of an isolation technique (MemPrep) for subcellular membranes that is based on both, differential centrifugation and affinity purification. Using quantitative proteomics, we demonstrate that MemPrep yields an unprecedented purity of ER membrane preparations. Further, we demonstrated its compatibility with quantitative shotgun lipidomics. Our data reveal characteristic molecular fingerprints of lipid bilayer stress on the subcellular level. We identified increased lipid saturation in the ER membrane as a possible contributor to UPR activation in prolonged proteotoxic stress. Unexpectedly, we uncovered a potential of anionic lipids as negative regulators of the UPR. We demonstrated the general applicability of our technique for other organelles by isolating the vacuole membrane. The most striking difference between the ER and the vacuole membrane is the almost complete absence of PA lipids in the vacuole membrane.

As the first author of this study, I developed the isolation strategy, including the design and cloning of the bait-tag, and the optimization of the MemPrep protocol. I performed all sample preparations via MemPrep for immunoblot analyses and for all subsequent lipidomics and proteomics experiments. Furthermore, I performed all microscopy experiments and established a sensitive FRET-assay to rule out the possibility of an unwanted fusion or lipid exchange between membrane vesicles during the isolation procedure. The immunolocalization is based on endogenously tagging a transmembrane protein that unambiguously resides in the organelle of interest. The bait-tag consists of a myc epitope, a specific cleavage site for the human rhinovirus 3C protease and a 3xFLAG epitope C-terminally fused to the bait protein. To isolate ER membranes via MemPrep, we chose the ER membrane protein reticulon-1 (Rtn1) because of its well-established ER localization and its abundance²⁹⁹. In contrast to many other fractionation protocols developed for yeast, we chose mechanical cell disruption, which is quick, can be performed at 4 °C and does not rely on any chemical or enzymatic treatment to digest the cell wall for generating spheroplasts (Appendix p. 163, Figure 1 A)²⁴². Differential centrifugation of the lysate resulted in a crude membrane fraction after sedimentation at 100,000 g for 1 h (P100) (Appendix p. 163, Figure 1 A, B). A central step in the MemPrep protocol is a brief sonication treatment that generated small, well-separated vesicles less likely to be attached to contaminating membranes from other organellar origins (Appendix p. 163, Figure 1 A, C). After specific binding of bait-tag-containing vesicles to an affinity matrix and stringent

washing steps, the ER membranes were selectively eluted by cleaving the bait tag with 3C protease. This selective and non-destructive elution unlocks a range of downstream analytical approaches including spectroscopic measurements using fluorescent membrane dyes. To assess the performance of our isolation technique we performed not only immunoblot analyses of individual fractions, but also untargeted proteomics. We calculated organelle enrichments based on unique cellular component gene ontology term annotations using hundreds of identified proteins. This provided a more rigorous determination of sample enrichment. To test whether the sonication treatment led to mixing of membranes from different origins, I performed a control experiment based on a FRET-pair of labelled lipids. If labelled liposomes fused with the excess of microsomal membranes during sonication, the fluorophore concentration, and therefore the FRET signal, would be reduced³⁵⁰. The data showed that the brief sonication applied during the MemPrep procedure is not causing membrane fusion or lipid exchange (Appendix p. 195, Appendix Figure S1 B).

Quantitative lipidomics analyses of ER membranes revealed its lipid characteristics. The ergosterol levels in the yeast ER of 9.7 mol% (Appendix p. 166, Figure 2 A) suggested a relatively flat gradient of sterols in the early secretory pathway. The sterol level does not increase substantially before the *trans*-Golgi network (TGN)/endosome system, which has been reported to have 9.8 mol% of ergosterol²¹⁶. Secretory vesicles pinching off from the TGN, however, feature significantly higher ergosterol level (30 mol%)²¹⁵, consistent with the formation of lipid raft-based transport carriers. The ergosterol level in the plasma membrane was determined with >44 mol%²¹⁵. Notably, the absence of a steep sterol gradient in the early secretory pathway has important implications for the trafficking of transmembrane proteins based on hydrophobic thickness^{351,352}. Compared to the cellular average, the ER contains significantly more DAG, PC and PE (Appendix p. 166, Figure 2 A). PC, PE, and PI each account for >20 mol% of the ER membranes lipidome. In sum, these three glycerophospholipid classes are the main structural components with >68 mol% of all ER membrane lipids. However, the abundance of PI, a glycerophospholipid class with typically at least one saturated acyl chain, is significantly less abundant in the ER compared to a whole cell lipidome. When analyzing the acyl chain composition of all membrane glycerolipids, we found significantly lower amounts of lipids with one or two saturated acyl chains. Instead, the data showed a high enrichment of loosely packing lipids, with two unsaturated acyl chains, in the ER membrane (Appendix p. 166, Figure 2 C). This is in accordance with the role of the highly flexible ER in membrane protein insertion and lipid biosynthesis^{24,187,288}.

A central motivation for the development of MemPrep was the determination of the ER membrane lipid composition in stressed cells. First, we wanted to measure the effect of a

well-established lipid bilayer stress, which is induced by inositol depletion. Inositol is an important lipid metabolite found in yeast sphingolipids and PI. Depletion of inositol from the medium robustly activates the UPR^{196,200,205,347}. Therefore, I removed inositol from the growth medium while cultures were in the logarithmic growth phase and isolated ER membranes via the Rtn1-bait using MemPrep. Expectedly, the level of PI is dramatically reduced in the ER under this condition (Appendix p. 168, Figure 3 A). The two metabolic precursors PA and cytidine diphosphate-diacylglycerol (CDP-DAG) were found at significantly increased levels, indicating precursor build-up. To our surprise, inositol-based sphingolipid levels were not reduced, suggesting a metabolic prioritization of sphingolipid biosynthesis or extremely different turnover rates (Appendix p. 168, Figure 3 B).

Next, we asked whether prolonged proteotoxic stress affects the lipid composition of the ER. I performed MemPrep immuno-isolation of ER membranes from cells that have been challenged by DTT or TM for 4 h. At this point, it is expected that the protein folding machinery has been adapted to the proteotoxic stress and that membrane-based cues dominate in activating Ire1²⁰⁰. The ER membrane exhibited significantly increased level of DAG and an increased PC-to-PE ratio under this condition (Appendix p. 170, Figure 4 D). Similar to the stress induced by inositol depletion stress, PI level were decreased (although more mildly upon prolonged proteotoxic stresses), and the precursors PA and CDP-DAG were increased. However, prolonged DTT and TM treatments lower the IPC and MIPC sphingolipid levels (Appendix p. 170, Figure 4 E). When analyzing the acyl chains of glycerophospholipids, we found a significantly increased abundance of saturated acyl chains. These data establish, for the first time, the lipid fingerprints of different forms of lipid bilayer stress in the ER.

Interestingly, both forms of lipid bilayer stress, inositol depletion and prolonged proteotoxic stress, feature reduced level of anionic lipids, particularly PI, which is also reflected in the calculated average charge per lipid (Appendix p. 192, Figure EV4).

Inferred from our lipidomics data, I composed a commercially available mix of lipids, which can be used to realistically mimic the ER membrane composition in biochemical reconstitution experiments and for MD simulations. MD simulations of these synthetic membranes, performed in collaboration with the Jochen Hub group, demonstrated that the ER membrane thickness is increased in the stressed ER membranes. Furthermore, we found that the charge density distribution in the water membrane interface differs substantially between the stressed and unstressed ER membrane mimics (Appendix p. 199, Appendix Figure S4).

Next, by untargeted proteomics experiments, we analyzed the impact of inositol depletion and DTT / TM treatment on the ER membrane proteome. By an additional sodium carbonate wash, prior to the immuno-isolation, we reduced the amount of cytosolic and loosely

associated peripheral membrane proteins to further enrich ER membrane proteins. Surprisingly, inositol depletion did only have a very mild effect on the ER membrane proteome, with only 12 out of 2655 detected proteins showing increased abundances in ER isolates (Appendix p. 168, Figure 3 A). On the other hand, prolonged proteotoxic stress, induced by DTT or TM treatment, led to a substantial remodeling of the ER membrane proteome involving hundreds of proteins. Overall, both types of proteotoxic stress led to similar changes in the proteome of ER membrane isolates (Appendix p. 193, Figure EV5 D). These included increased abundances of canonical UPR targets, lipid metabolic enzymes, components of the vesicular trafficking machinery of the secretory pathway and other non-ER proteins (Appendix p. 172, Figure 5 A ,B). Whether the accumulation of non-ER proteins contributes to UPR activation remains to be investigated. However, K-means clustering of the proteomics data revealed some differences between DTT- and TM-induced changes (Appendix p. 193, Figure EV5 E). Notably, the analysis of enriched gene ontology terms in these clusters identified the DTT-specific increased abundance of proteins involved in copper and iron transport. Iron homeostasis has been linked previously to Ire1 clustering and UPR signaling³⁵³.

To test the broader applicability of MemPrep, I adapted the isolation procedure to target the vacuole membrane via Vph1 as a bait protein. After the isolation of vacuole membranes via MemPrep, analysis of organelle enrichment by untargeted proteomics revealed a high purity of the sample (Appendix p. 173, Figure 6 B). This allowed us to determine the lipidome of the vacuole membrane isolates, which showed substantial differences compared to the ER membrane. The vacuole membrane contains significantly more ergosterol, DAG, and lysophospholipids and features a characteristic absence of PA (Appendix p. 173, Figure 6 C, D). These findings demonstrate the versatility of MemPrep to specifically and robustly target organelle membranes for lipidomics and proteomics analysis. MemPrep has the potential to drive future studies of membrane composition and homeostasis at subcellular resolution.

2.5. Remodeling of yeast vacuole membrane lipidomes from the log (one phase) to stationary stage (two phases)

When nutrient sources become limiting for yeast it adapts to the environment by a large-scale reprogramming of cellular metabolism³⁵⁴. Eventually, yeast enters a quiescent state, also referred to as the stationary growth phase, accompanied by a multitude of changes in cellular morphology and composition that collectively help to survive prolonged periods in adverse conditions.

The fusion of multiple small vacuoles, the lytic organelle of yeast that is functionally equivalent to mammalian lysosomes, to form a single large membrane-bound vacuole is a characteristic hallmark of entering the stationary stage³⁵⁵. Astonishingly, this morphological change is accompanied by micron-scale liquid-liquid phase separation of the vacuole membrane, with the membrane domains being stable for hours¹³¹. In fact, this is one of few and particularly prominent examples where membrane phase separation can be directly observed *in vivo* in a physiologically relevant context. Membrane phase separation can cause the segregation of membrane proteins, most likely depending on the composition and architecture of their transmembrane, or membrane-associated, domains^{109,167,356}. Both phases of the yeast vacuole membrane are in a fluid state as shown by the ability of individual domain patches to coalesce over time¹³¹. Our current understanding of membrane phase separation comes predominantly from the work with simplified artificial membrane systems including giant unilamellar vesicles and supported lipid bilayers^{104,105,109–111}. The lateral organization of membrane domains is driven by lipid-lipid interactions. It has been demonstrated that the simplest membrane composition that robustly undergoes liquid-liquid phase separation contains three components: A low melting lipid, a high melting lipid and a sterol¹⁰⁶. These mixtures can robustly support the formation of two coexisting liquid domains, a liquid-disordered (L_d) and a liquid-ordered (L_o) domain. The L_o domain is characterized by a high lipid acyl chain order with limited degrees of freedom for forming *gauche* rotamers. Fluorescent molecular probes have been used to visualize membrane domains *in vitro* and *in vivo*. Lipophilic dyes like FM4-64 and many labelled phospholipid and sterol derivatives show preferential partitioning to one of the two formed membrane domains, indicating different collective biophysical membrane properties^{109,323,357}.

Nevertheless, we know very little about the composition of membrane domains in complex cellular membranes. Biomembranes contain many hundreds of different lipid species and a wide variety of proteins, potentially contributing to phase separation. Early works postulated an important role of membrane domain formation for cellular trafficking and signaling processes¹¹⁶. However, the compositional complexity of biological membranes, and the submicroscopical size and short-lived nature of the membrane domains, led to

critical discussions about their existence and functional relevance¹³⁰. Nevertheless, recent studies established that phase separated domains of the vacuole membrane play an active role in cellular physiology. The degradation of lipid droplets by uptake from the vacuole (lipophagy) depends on the presence of phase separated membrane domains¹³². Furthermore, segregation of signaling components into phase separated membrane domains decreased the activity of TORC1 with important implications on downstream responses such as the regulation of cell-cycle progression and translation¹³³. These studies show that liquid-liquid phase separation in the yeast vacuole membrane, and potentially other biomembranes, is an important aspect of cell homeostasis. Membrane phase separation into stable large domains is not a yeast specific phenomenon. It was observed in giant plasma membrane vesicles (GPMVs) from various species, containing the full compositional complexity of a biomembrane^{358–360}. However, GPMVs are membrane systems that have been taken out of the non-equilibrium context of a living cell.

Here, we demonstrated the applicability of a recently developed membrane isolation technique (MemPrep) to determine the lipid composition of the phase separating vacuole membrane. We coupled cell fractionation to quantitative shotgun lipidomics to analyze the molecular composition of the vacuole from stationary cells. Notably, vacuole membranes from the logarithmic and the stationary growth stage have significantly different lipid compositions. The phase separating vacuole membrane from stationary cells was characterized by higher levels of PC lipids with saturated acyl chains, which were associated with higher melting temperatures (T_{melt}). Our data suggested that an increase in high- T_{melt} membrane components drives the formation of liquid membrane domains in the yeast vacuole.

As co-first author of this paper, I established and optimized the MemPrep technology for the vacuole. I identified Mam3 as a suitable bait for the immuno-isolation of the vacuole membrane. Furthermore, I performed all membrane isolations via MemPrep including the cultivation of yeast and the immunoblot analyses to document the isolation process. Subsequently, I analyzed and interpreted the lipidomics data, performed statistical tests, and described, for the first time, the lipid composition of the phase separating vacuole membrane. This work identified saturated PC lipids as a key driver of micron-scale membrane phase separation in the stationary vacuole.

First, we confirmed the expression level and vacuole localization of Mam3, a protein involved in magnesium homeostasis³⁶¹, in the logarithmic and stationary growth stage. Specific localization to the vacuole membrane, partitioning to the L_d domain when phase separated, and reasonably high²⁹⁹ and even expression in both growth stages make it a robust bait protein for MemPrep (Appendix p. 208, Figure 3). Next, I prepared crude membrane fractions from yeast expressing the Mam3-bait by differential centrifugation

(Appendix p. 209, Figure 4 A). Subsequent immuno-isolation via MemPrep yielded highly enriched vacuole membranes with low contaminations from ER or mitochondrial membranes (Appendix p. 209, Figure 4 B, C). Hence, we could determine the lipid composition of immuno-isolated vacuole membranes from logarithmic and stationary stage yeast. In the logarithmic stage, the vacuole membrane is characterized by similar concentrations of PC, PE, and PI, each accounting for >20 mol% of all measured lipid classes (Appendix p. 210, Figure 5). A striking feature of the vacuole membrane is the near complete absence of PA lipids. The stationary stage vacuole membrane exhibits significantly higher levels of PC and IPC, while PE, PI, DAG and lysolipid levels are significantly reduced (Appendix p. 210, Figure 5). Notably, we did not find any indication for changes in the ergosterol level, which was previously suggested to potentially play a role in membrane domain formation *in vivo*^{131,362}. When analyzing the number of double bonds in glycerolipids with two acyl chains (i.e. CDP-DAG, DAG, PA, PC, PE, PG, PI, PS), we found that lipids with one mono-unsaturated acyl chain were more abundant, while fully saturated lipids were less abundant, in phase separating vacuole membranes from stationary yeast (Appendix p. 212, Figure 6 A). Strikingly, an in-depth analysis of all identified PC lipids revealed a dramatic reduction of species with two unsaturated acyl chains, while species with one or two saturated acyl chains are significantly more abundant (Appendix p. 212, Figure 6 C). Nevertheless, the total pool of saturated acyl chains in glycerolipids was unchanged (Appendix p. 239, Figure S14). Notably, PI lipids were substantially longer in the stationary vacuole membrane (Appendix p. 236, Figure S11 A).

We looked at known data for lipid melting temperatures (T_{melt}), i.e. the main transition temperature from the gel phase (L_{β}) to the fluid phase, and extrapolated unknown T_{melt} values from experimental trends where applicable (Appendix p. 234 and 241-244, Figure S9 and Table S2 - Table S5). We found that the vacuole membrane from stationary yeast contains more PC lipids with higher melting temperatures (above -10 °C) and less lipids with intermediate or low T_{melt} (Appendix p. 213, Figure 7). In a complex biomembrane, that also contains ergosterol and lipids with low melting temperatures, this might facilitate the formation of liquid-ordered membrane domains. Notably, the abundance of PC 14:1_16:1 which has a very low T_{melt} of approximately -53 °C, was also increased in the stationary vacuole. This indicates the generation of a high and a low T_{melt} regime within the PC lipid class. In contrast, the same analysis for PE lipids showed no substantial changes in the distribution of melting temperatures (Appendix p. 214, Figure 8).

To sum up our findings, we measured the lipid composition of a phase separating complex biological membrane. Compared to the one-phase membrane of logarithmically growing yeast, the phase separated vacuole membrane of stationary cells contained significantly more PC with dramatically different properties. Acyl chains were found to be slightly longer

and substantially more saturated, resulting in higher weighted average melting temperatures of PC lipids (Appendix p. 215, Figure 9). Our data suggest that this specific remodeling of the yeast vacuole lipidome contributes to the formation of membrane domains *in vivo*.

3. CONCLUDING REMARKS AND FUTURE DIRECTIONS

In the publications that constitute this cumulative thesis, I investigated two central questions: I) What are the molecular sensing mechanisms of membrane property sensors? II) How do subcellular lipid compositions and collective biophysical membrane properties change in cellular stress conditions? These two questions strongly relate to each other since the membrane property sensors Ire1 and Mga2 in the ER membrane regulate the expression of lipid metabolic genes that will affect lipid biosynthesis and hence, the ER membrane lipid composition^{199,314}. *Vice versa*, Ire1 and Mga2 are activated in an ER membrane composition-, or property-, dependent manner^{181,205}. To understand cellular lipid homeostasis, we need to elucidate both the molecular mechanisms of the sensors and the steady-state lipid compositions of the ER membrane in both physiological and pathological contexts.

Previously, a hydrophobic mismatch-based model for the membrane sensing mechanism of Ire1's TMD has been established²⁰⁵. It features a short TMH that seamlessly transitions into an AH on the luminal side, thereby compressing the ER membrane²⁰⁵. However, the organization of dimers and oligomers remained unresolved. Under conditions of both, proteotoxic and lipid bilayer stress, two Ire1 TMDs adopt an X-shaped architecture with the residues F544 at the crossing point. Although we cannot fully exclude stress-specific conformational changes in other domains, Ire1's TMDs converge into the same architecture under both types of stress. Nevertheless, divergent transcriptional programs for each stress type have been proposed, which may be a direct impact of the different forms of stress and due to distinct temporal patterns of UPR activities³⁶³.

Because a relatively large surface area of the ER lipid bilayer is compressed, Ire1 harbors substantial membrane-deforming potential and seems particularly sensitive to membrane thickening or a reduced membrane compressibility. The energetic penalty from an increased hydrophobic mismatch in stressed ER membranes is minimized by dimerization along the longer axis of Ire1's ellipsoid membrane footprints^{301,364}, thereby maximizing the overlap of compressed areas upon dimerization. This mode of oligomerization is compatible with the observation that the mammalian IRE1 α forms elongated clusters in specialized narrow ER tubules³⁰². It is tempting to speculate that these lateral specializations of the ER membrane feature a characteristic lipid composition. The energetic costs associated with bilayer compression are affected by the lipid composition and collective biophysical properties of the ER membrane.

To establish lipid fingerprints of ER stress, I developed the organelle isolation technique MemPrep. It is grounded on a large body of previous studies that optimized cell fractionation

using differential and density gradient centrifugation which are indispensable tools to separate organelles. Pioneering studies in yeast have established many, in essence still widely used fractionation protocols, for various organelles, including the ER²⁴². However, we wanted to prevent that the composition of an organelle membrane changes during the preparation. Therefore, we omitted cell lysis by preparing spheroplasts. It involves lengthy incubation at elevated temperatures using reducing agents such as DTT, which rapidly activates the UPR²⁰⁰. Instead, we performed quick mechanical cell disruption using glass beads. Another key aspect of MemPrep is the use of an affinity-tagged bait protein, which is used to immuno-isolate ER membranes from a crude microsome fraction. MemPrep combines separation of subcellular membranes based on size, shape, and density by differential centrifugation with biochemical affinity and specificity-based separation. In contrast to other immuno-isolation techniques^{248,365,366}, it maximizes purity at the expense of yield, and the elution of isolated organelle-derived vesicles in MemPrep facilitates the application of downstream analytical methods. Although we cannot fully rule out the redistribution of certain lipid species, proteomics and lipidomics identify organelle-specific compositions, excluding general organelle mixing. Nevertheless, lateral specializations of the ER membrane, such as sheets and tubules, collapse, as our experiments with differently localized ER baits demonstrated (Appendix p. 189-190, Figure EV1 and Figure EV2). To determine the lipid composition of lateral specializations like membrane contact sites, selective solubilization is a promising approach³⁶⁷. MemPrep provides detailed and quantitative compositional snapshots of organelle membranes.

Based on our whole cell lipidomics data of acutely stressed yeast, that showed little perturbation of the lipidome (Appendix p. 145, Figure 5), we decided to establish fingerprints of the ER membrane upon prolonged proteotoxic and direct lipid bilayer stress. Despite the characteristic lipid fingerprints identified (Appendix p. 201, Appendix Figure S5), we were able to determine the bilayer thickness as common denominator of membrane-based UPR activation (Appendix p. 199, Appendix Figure S4 D). This is in line with the hydrophobic mismatch-based sensing mechanism of Ire1^{205,347}. Further, we identified increased levels of saturated lipid acyl chains as a feature of stressed ER membranes, in both lipid bilayer and proteotoxic stress conditions. Increased saturation of lipids has been previously reported to cause lipid bilayer stress^{195,203} and likely contributes to the increase of membrane thickness and lipid packing, and the reduction of membrane compressibility²⁴. The unexpected finding that anionic lipids may serve as negative modulators of the UPR should be investigated further *in vitro* to establish a direct mechanistic function. The ER membrane mimetic lipid mixes, that we propose based on our quantitative subcellular lipidomics data (Appendix p. 199, Appendix Figure S4 A), will help *in vitro* reconstitution

and *in silico* experiments to consider more realistic membrane environments. This is particularly important when studying membrane property sensors.

Anionic lipids as negative modulators of UPR activity would have important implications for cellular physiology as their levels change over the course of a typical yeast growth curve. In fact, they are lowest at the diauxic shift³², and this growth stage has been associated with temporal UPR activation³⁴⁶.

Anionic lipids like PS are potentially enriched in the luminal leaflet of the ER membrane, to allow a territory of electrostatics at later stages of the secretory pathway, even though lipid asymmetry in the ER membrane is still a matter of debate^{91,368}. Ire1's ER luminal AH contains several positively charged residues and is ideally positioned to interact with anionic lipid headgroups of the luminal leaflet. Hence, a loss of ER membrane asymmetry, or any type of transmembrane reorganization of lipids, would also cause a redistribution of anionic lipids with potential implications for UPR activity.

Astonishingly, DTT- and TM-induced prolonged proteotoxic stress feature virtually identical lipid fingerprints, despite having similar but clearly characteristic ER proteomes (Appendix p. 193, Figure EV5 D, E). Both types of stress cause a major remodeling of the ER membrane proteome that needs to be considered as important contributing factor to stress-induced changes of the biophysical ER membrane properties. However, it remains unclear whether quantity or quality of transmembrane proteins would influence biophysical properties of the ER membrane. Intriguingly, an accumulation of long transmembrane helices from plasma membrane proteins could lead to a thickening of the ER membrane²²⁶ and an increased membrane protein-to-lipid ratio would render membranes less compressible¹⁷¹. Hence, the remarkable sensitivity of Ire1 to reduced ER membrane compressibility may serve to sense global issues in the secretory pathway and mount an adaptive response²⁵⁰.

A fundamental conundrum is the causal relation between aberrant membrane compositions and the activity of the UPR. Is the observed steady-state lipid composition causing UPR activation or does it already contain response effects? What is the UPRs influence on the measured membrane lipid composition in conditions of ER stress? Here, our data suggests that the UPR does not have a significant influence on the cellular lipid composition, as an *IRE1* knockout strain showed whole cell lipidomes similar to wildtype, under the tested acute (Appendix p. 158-159, Supplementary Figure S5 B) and prolonged ER stress conditions (Appendix p. 170, Figure 4 A, B).

The high levels of unsaturated lipid acyl chains in the unstressed ER membrane confirm a low degree of lipid packing, which renders it highly compressible, as a major determinant for ER organelle identity^{24,91,209}. These are important collective properties of the ER membrane to facilitate the introduction of membrane proteins that differ substantially in their

hydrophobic thickness and surface roughness, depending on their final subcellular localization^{167,226}. Hence, it is not surprising that the ER bilayer compressibility is monitored by the membrane property sensor Ire1^{205,347}. Furthermore, the membrane property sensor Mga2 is susceptible for the membrane packing density at a defined depth in the hydrophobic ER membrane core. It integrates an inherently noisy signal from the hydrophobic core of the membrane to yield a discrete output in the production of a 90 kDa fragment that upregulates *OLE1* expression. Despite having a dramatic impact on membrane fluidity, Mga2 is not a fluidity sensor. Biophysical membrane properties are multifactorial characteristics, changing a particular chemical feature in lipids has multi-faceted effects on collective membrane properties. The term membrane fluidity is often imprecisely used for a multitude of distinguishable biophysical properties²⁴. Microenvironment-sensitive membrane probes usually report on very specific features like microviscosity or hydration, not on lateral diffusion^{115,323}. The fluorescent probe DPH is most often considered a fluidity or microviscosity sensor. However, additional to wiggling between the acyl chains of lipids, DPH was shown to flip orthogonally to the hydrophobic interface of membrane leaflets^{317,318}. DPH fluorescence anisotropy signal might therefore be difficult to interpret and first and foremost report on the probability of orthogonal flipping. In this context it would be interesting to study the effect of acyl chain interdigitation on the probability of orthogonal flipping of the DPH probe. Nevertheless, DPH fluorescence anisotropy clearly indicates the major phase transition from the fluid to the gel phase.

Our subcellular lipidomics data is compatible with the proposed gradients of saturated lipids and sterols along the secretory pathway^{91,209}. They are consistent with estimations of ergosterol concentrations in the yeast ER⁴⁴ and parallel findings in mammalian cells^{211,366}. Furthermore, they complement existing data on intermediate compartments of the secretory pathway and the plasma membrane^{215,216}. Taken together, these data support a model of a relatively flat gradient of sterols until the TGN/endosomal system and a steep step in sterol concentration towards secretory vesicles and the plasma membrane. This would have important implications for protein and lipid sorting along the secretory pathway^{167,226,352,369} and would be in favor of models that propose sterol-enriched vesicles³⁷⁰ and sterol-rich selective diffusion barriers in the early secretory pathway³⁷¹.

To demonstrate the broad applicability of MemPrep, I adapted it to isolate the vacuole membrane and determine its lipid composition. The vacuole membrane is dramatically different from the plasma membrane²¹⁵, despite substantial intake of plasma membrane material via the endocytic pathway³⁷². Our subcellular lipidomics data also shows that the vacuole is significantly different from the ER, featuring more saturated membrane glycerolipids and higher level of ergosterol (Appendix p. 202, Appendix Figure S6 C-E). A striking characteristic of the vacuole membrane is the absence of PA lipids, consistent with

observations from others^{232,373}. I further performed the MemPrep technique to investigate the lipid determinants of membrane domain formation in the stationary vacuole membrane. We could show that the lipidome differs substantially from the lipidome of non-phase separating vacuoles isolated from logarithmically growing yeast. The phase separating vacuole features significantly higher level of PC with high melting temperatures, indicating a contribution to the formation of L_o membrane domains (Appendix p. 215, Figure 9). Notably, increased levels of sphingolipids in the stationary vacuole membrane have also been proposed to drive membrane domain formation²³². A fascinating new development is the recent superresolution revolution in fluorescence microscopy, including methods like MINFLUX with 100-fold increase in resolution from conventional confocal microscopy^{374,375}. Since this technique is applicable to live cells, it holds enormous potential to study the fast dynamics of nanoscopic membrane domains³⁷⁶.

The two membrane property sensors Ire1 and Mga2 measure collective biophysical membrane properties and not individual chemical lipid features. This suggests that cells maintain collective biophysical properties of biomembranes rather than setting a distinct chemical composition. Several distinct membrane compositions may feature similar collective membrane properties, such that there are often several biological solutions and molecular compositions optimal to reach one set of collective membrane properties. In other words: Like the genetic code, the lipid code for biophysical membrane properties is degenerated. However, the downstream effectors that execute the adaptation by manipulating lipid metabolism can only give rise to lipids with distinct chemical features. Hence, membrane homeostasis is established by a complex, interconnected network of regulatory circuits, which provide redundancy and robustness to the system instead of 'just' adding complexity.

A serendipitous finding revealed a remarkably strong selectivity in the pairing of saturated medium-length fatty acyl chains with long saturated fatty acyl chains, particularly enriched in PI and DAG lipids. Open questions related to this discovery remain: Are these lipids generated by *de novo* biosynthesis after uptake of free fatty acids from the medium⁴³ or by acyl chain remodeling⁴⁶? Would there be any deleterious effects if this specificity would be disturbed?

MemPrep is a technique that will facilitate our understanding of homeostasis and adaptation of organellar membranes to metabolic perturbation and cellular stress. It can be used to study the subcellular redistribution of lipids in the adaptation to ER stress and lipotoxicity, and study the effects of gene deletions on the lipid composition of specific organelles.

4. REFERENCES

1. Szostak, J. W., Bartel, D. P. & Luisi, P. L. Synthesizing life. *Nature* **409**, 388–390 (2001).
2. Schrum, J. P., Zhu, T. F. & Szostak, J. W. The origins of cellular life. *Cold Spring Harb. Perspect. Biol.* **2**, a002212 (2010).
3. Deamer, D. W. Boundary structures are formed by organic components of the Murchison carbonaceous chondrite. *Nature* **317**, 792–794 (1985).
4. Mccollom, T. M., Ritter, G. & Simoneit, B. R. T. Lipid synthesis under hydrothermal conditions by Fischer-Tropsch-type reactions. *Orig. Life Evol. Biosph.* **29**, 153–166 (1999).
5. Black, R. A. *et al.* Nucleobases bind to and stabilize aggregates of a prebiotic amphiphile, providing a viable mechanism for the emergence of protocells. *Proc. Natl. Acad. Sci. U. S. A.* **110**, 13272–13276 (2013).
6. Cornell, C. E. *et al.* Prebiotic amino acids bind to and stabilize prebiotic fatty acid membranes. *Proc. Natl. Acad. Sci. U. S. A.* **116**, 17239–17244 (2019).
7. Chen, I. A., Roberts, R. W. & Szostak, J. W. The emergence of competition between model protocells. *Science* **305**, 1474–1476 (2004).
8. Kauzmann, W. Some factors in the interpretation of protein denaturation. in *Advances in Protein Chemistry* vol. 14 1–63 (Elsevier, 1959).
9. Tanford, C. The hydrophobic effect and the organization of living matter. *Sci. New Ser.* **200**, 1012–1018 (1978).
10. Voet, D., Voet, J. G. & Pratt, C. W. *Lehrbuch der Biochemie.* (Wiley-VCH, Weinheim, 2002).
11. Israelachvili, J. N., Marčelja, S. & Horn, R. G. Physical principles of membrane organization. *Q. Rev. Biophys.* **13**, 121–200 (1980).
12. Gruner, S. M., Cullis, P. R., Hope, M. J. & Tilcock, C. P. S. The Molecular Basis of Nonbilayer Phases. *Annu Rev Biophys Biophys Chem* **14**, 211–238 (1985).
13. Ortiz, A., Killian, J. A., Verkleij, A. J. & Wilschut, J. Membrane fusion and the lamellar-to-inverted-hexagonal phase transition in cardiolipin vesicle systems induced by divalent cations. *Biophys. J.* **77**, 2003–2014 (1999).
14. Jouhet, J. Importance of the hexagonal lipid phase in biological membrane organization. *Front. Plant Sci.* **4**, 494 (2013).
15. Gasanov, S. E., Kim, A. A., Yaguzhinsky, L. S. & Dagda, R. K. Non-bilayer structures in mitochondrial membranes regulate ATP synthase activity. *Biochim. Biophys. Acta - Biomembr.* **1860**, 586–599 (2018).
16. Dlouhy, O. *et al.* Modulation of non-bilayer lipid phases and the structure and functions of thylakoid membranes: effects on the water-soluble enzyme violaxanthin de-epoxidase. *Sci. Rep.* **10**, 11959 (2020).
17. Poojari, C. S., Scherer, K. C. & Hub, J. S. Free energies of membrane stalk formation from a lipidomics perspective. *Nat. Commun.* **12**, 6594 (2021).
18. Garab, G. *et al.* Structural and functional roles of non-bilayer lipid phases of chloroplast thylakoid membranes and mitochondrial inner membranes. *Prog. Lipid Res.* **86**, 101163 (2022).
19. Ejsing, C. S. *et al.* Global analysis of the yeast lipidome by quantitative shotgun mass spectrometry. *Proc. Natl. Acad. Sci. U. S. A.* **106**, 2136–2141 (2009).
20. Klose, C. *et al.* Flexibility of a eukaryotic lipidome - insights from yeast lipidomics. *PLoS ONE* **7**, e35063 (2012).
21. Harayama, T. & Riezman, H. Understanding the diversity of membrane lipid composition. *Nat. Rev. Mol. Cell Biol.* **19**, 281–296 (2018).
22. Chwastek, G. *et al.* Principles of membrane adaptation revealed through environmentally induced bacterial lipidome remodeling. *Cell Rep.* **32**, 108165 (2020).
23. Sprenger, R. R. *et al.* Lipid molecular timeline profiling reveals diurnal crosstalk between the liver and circulation. *Cell Rep.* **34**, 108710 (2021).
24. Renne, M. F. & Ernst, R. Membrane homeostasis beyond fluidity: control of membrane compressibility. *Trends Biochem. Sci.* **48**, 963–977 (2023).
25. Justice, I. & Saenz, J. P. A tuneable minimal cell membrane reveals that two lipids suffice for life. Preprint at <https://doi.org/10.1101/2023.10.24.563757> (2023).
26. Sohlenkamp, C. & Geiger, O. Bacterial membrane lipids: diversity in structures and pathways. *FEMS Microbiol. Rev.* **40**, 133–159 (2016).

References

27. Řezanka, T., Kyselová, L. & Murphy, D. J. Archaeal lipids. *Prog. Lipid Res.* **91**, 101237 (2023).
28. Villanueva, L. *et al.* Bridging the membrane lipid divide: bacteria of the FCB group superphylum have the potential to synthesize archaeal ether lipids. *ISME J.* **15**, 168–182 (2021).
29. Gould, S. B. Membranes and evolution. *Curr. Biol.* **28**, R381–R385 (2018).
30. Cockcroft, S. Mammalian lipids: structure, synthesis and function. *Essays Biochem.* **65**, 813–845 (2021).
31. Yu, L., Zhou, C., Fan, J., Shanklin, J. & Xu, C. Mechanisms and functions of membrane lipid remodeling in plants. *Plant J.* **107**, 37–53 (2021).
32. Casanovas, A. *et al.* Quantitative analysis of proteome and lipidome dynamics reveals functional regulation of global lipid metabolism. *Chem. Biol.* **22**, 412–425 (2015).
33. Di Paolo, G. & De Camilli, P. Phosphoinositides in cell regulation and membrane dynamics. *Nature* **443**, 651–657 (2006).
34. Alberts, B. *Molecular Biology of the Cell.* (Garland science, Taylor and Francis group, New York, 2015).
35. Katan, M. & Cockcroft, S. Phosphatidylinositol(4,5)bisphosphate: diverse functions at the plasma membrane. *Essays Biochem.* **64**, 513–531 (2020).
36. Hammond, G. R. V. & Burke, J. E. Novel roles of phosphoinositides in signaling, lipid transport, and disease. *Curr. Opin. Cell Biol.* **63**, 57–67 (2020).
37. Mesmin, B. & Antonny, B. The counterflow transport of sterols and PI4P. *Biochim. Biophys. Acta - Mol. Cell Biol. Lipids* **1861**, 940–951 (2016).
38. Kennedy, E. P. & Weiss, S. B. The function of cytidine coenzymes in the biosynthesis phospholipides. *J. Biol. Chem.* **222**, 193–214 (1956).
39. Han, X., Holtzman, D. M. & McKeel, D. W. Plasmalogen deficiency in early Alzheimer's disease subjects and in animal models: molecular characterization using electrospray ionization mass spectrometry. *J. Neurochem.* **77**, 1168–1180 (2001).
40. Rothhaar, T. L. *et al.* Plasmalogens inhibit APP processing by directly affecting γ -secretase activity in Alzheimer's disease. *Sci. World J.* **2012**, 141240 (2012).
41. Su, X. Q., Wang, J. & Sinclair, A. J. Plasmalogens and Alzheimer's disease: a review. *Lipids Health Dis.* **18**, 100 (2019).
42. Stukey, J. E., McDonough, V. M. & Martin, C. E. The *OLE1* gene of *Saccharomyces cerevisiae* encodes the $\Delta 9$ fatty acid desaturase and can be functionally replaced by the rat stearoyl-CoA desaturase gene. *J. Biol. Chem.* **265**, 20144–20149 (1990).
43. Wagner, S. & Paltauf, F. Generation of glycerophospholipid molecular species in the yeast *Saccharomyces cerevisiae*. Fatty acid pattern of phospholipid classes and selective acyl turnover at *sn*-1 and *sn*-2 positions. *Yeast* **10**, 1429–1437 (1994).
44. Schreier, R. *et al.* Electrospray ionization tandem mass spectrometry (ESI-MS/MS) analysis of the lipid molecular species composition of yeast subcellular membranes reveals acyl chain-based sorting/remodeling of distinct molecular species en route to the plasma membrane. *J. Cell Biol.* **146**, 741–754 (1999).
45. Renne, M. F., Bao, X., De Smet, C. H. & De Kroon, A. I. P. M. Lipid acyl chain remodeling in yeast. *Lipid Insights* **8**, 33–40 (2015).
46. Patton-Vogt, J. & De Kroon, A. I. P. M. Phospholipid turnover and acyl chain remodeling in the yeast ER. *Biochim. Biophys. Acta - Mol. Cell Biol. Lipids* **1865**, 158462 (2020).
47. Lands, W. E. Metabolism of glycerolipids - II. The enzymatic acylation of lysolecithin. *J Biol Chem* **235**, 2233–2237 (1960).
48. Lee, K. S. *et al.* The *Saccharomyces cerevisiae* *PLB1* gene encodes a protein required for lysophospholipase and phospholipase B activity. *J. Biol. Chem.* **269**, 19725–19730 (1994).
49. Ståhlberg, K., Neal, A. C., Ronne, H. & Ståhl, U. Identification of a novel GPCAT activity and a new pathway for phosphatidylcholine biosynthesis in *S. cerevisiae*. *J. Lipid Res.* **49**, 1794–1806 (2008).
50. Anaokar, S. *et al.* The glycerophosphocholine acyltransferase Gpc1 is part of a phosphatidylcholine (PC)-remodeling pathway that alters PC species in yeast. *J. Biol. Chem.* **294**, 1189–1201 (2019).
51. Le Guédard, M. *et al.* *PSI1* is responsible for the stearic acid enrichment that is characteristic of phosphatidylinositol in yeast. *FEBS J.* **276**, 6412–6424 (2009).
52. Beranek, A. *et al.* Identification of a cardiolipin-specific phospholipase encoded by the gene *CLD1* (YGR110W) in yeast. *J. Biol. Chem.* **284**, 11572–11578 (2009).

53. Gu, Z. *et al.* Aberrant cardiolipin metabolism in the yeast *taz1* mutant: a model for Barth syndrome. *Mol. Microbiol.* **51**, 149–158 (2004).
54. Valianpour, F. *et al.* Monolysocardiolipins accumulate in Barth syndrome but do not lead to enhanced apoptosis. *J. Lipid Res.* **46**, 1182–1195 (2005).
55. Vreken, P. *et al.* Defective remodeling of cardiolipin and phosphatidylglycerol in Barth syndrome. *Biochem. Biophys. Res. Commun.* **279**, 378–382 (2000).
56. Schneiter, R. Brave little yeast, please guide us to Thebes: Sphingolipid function in *S. cerevisiae*. *BioEssays* **21**, 1004–1010 (1999).
57. Sezgin, E., Levental, I., Mayor, S. & Eggeling, C. The mystery of membrane organization: Composition, regulation and roles of lipid rafts. *Nat. Rev. Mol. Cell Biol.* **18**, 361–374 (2017).
58. Montefusco, D. J., Matmati, N. & Hannun, Y. A. The yeast sphingolipid signaling landscape. *Chem. Phys. Lipids* **177**, 26–40 (2014).
59. Hannun, Y. A. & Obeid, L. M. Sphingolipids and their metabolism in physiology and disease. *Nat. Rev. Mol. Cell Biol.* **19**, 175–191 (2018).
60. Dufourc, E. J. Sterols and membrane dynamics. *J. Chem. Biol.* **1**, 63–77 (2008).
61. Zinser, E., Paltauf, F. & Daum, G. Sterol composition of yeast organelle membranes and subcellular distribution of enzymes involved in sterol metabolism. *J. Bacteriol.* **175**, 2853–2858 (1993).
62. Guerriero, G. Vertebrate sex steroid receptors: Evolution, ligands, and neurodistribution. *Ann. N. Y. Acad. Sci.* **1163**, 154–168 (2009).
63. Wagner, A., Grillitsch, K., Leitner, E. & Daum, G. Mobilization of steryl esters from lipid particles of the yeast *Saccharomyces cerevisiae*. *Biochim. Biophys. Acta - Mol. Cell Biol. Lipids* **1791**, 118–124 (2009).
64. Steinberg, D. Transport of cholesterol and cholesterol esters by HDL. in *Drugs affecting lipid metabolism* (eds. Paoletti, R., Kritchevsky, D. & Holmes, W. L.) 42–47 (Springer Berlin Heidelberg, 1987).
65. Lorent, J. H. *et al.* Plasma membranes are asymmetric in lipid unsaturation, packing and protein shape. *Nat. Chem. Biol.* **16**, 644–652 (2020).
66. Surma, M. A. *et al.* Mouse lipidomics reveals inherent flexibility of a mammalian lipidome. *Sci. Rep.* **11**, 19364 (2021).
67. Langmuir, I. The constitution and fundamental properties of solids and liquids. II. liquids. *J. Am. Chem. Soc.* **39**, 1848–1906 (1917).
68. Gorter, E. & Grendel, F. On bimolecular layers of lipoids on the chromocytes of the blood. *J. Exp. Med.* **41**, 439–443 (1925).
69. Singer, S. J. & Nicolson, G. L. The fluid mosaic model of the structure of cell membranes. *Science* **175**, 720–731 (1972).
70. Alecio, M. R., Golan, D. E., Veatch, W. R. & Rando, R. R. Use of a fluorescent cholesterol derivative to measure lateral mobility of cholesterol in membranes. *Proc Natl Acad Sci USA* **79**, 5171–5174 (1982).
71. Gaede, H. C. & Gawrisch, K. Lateral diffusion rates of lipid, water, and a hydrophobic drug in a multilamellar liposome. *Biophys. J.* **85**, 1734–1740 (2003).
72. Doeven, M. K. *et al.* Distribution, lateral mobility and function of membrane proteins incorporated into giant unilamellar vesicles. *Biophys. J.* **88**, 1134–1142 (2005).
73. Ramadurai, S. *et al.* Lateral diffusion of membrane proteins. *J. Am. Chem. Soc.* **131**, 12650–12656 (2009).
74. Schlessinger, J., Axelrod, D., Koppel, D. E., Webb, W. W. & Elson, E. L. Lateral transport of a lipid probe and labeled proteins on a cell membrane. *Science* **195**, 307–309 (1977).
75. Nennering, A. *et al.* Independent mobility of proteins and lipids in the plasma membrane of *Escherichia coli*. *Mol. Microbiol.* **92**, 1142–1153 (2014).
76. Kumar, M., Mommer, M. S. & Sourjik, V. Mobility of cytoplasmic, membrane, and DNA-binding proteins in *Escherichia coli*. *Biophys. J.* **98**, 552–559 (2010).
77. Worch, R., Petrášek, Z., Schwille, P. & Weidemann, T. Diffusion of single-pass transmembrane receptors: From the plasma membrane into giant liposomes. *J. Membr. Biol.* **250**, 393–406 (2017).
78. Chow, D., Guo, L., Gai, F. & Goulian, M. Fluorescence correlation spectroscopy measurements of the membrane protein TetA in *Escherichia coli* suggest rapid diffusion at short length scales. *PLoS ONE* **7**, e48600 (2012).
79. Sackmann, E. Biological membranes architecture and function. in *Handbook of biological physics* vol. 1 1–63 (Elsevier, 1995).

References

80. Alenghat, F. J. & Golan, D. E. Membrane protein dynamics and functional implications in mammalian cells. *Curr. Top. Membr.* **72**, 89–120 (2013).
81. Nicolson, G. L. The fluid - mosaic model of membrane structure: Still relevant to understanding the structure, function and dynamics of biological membranes after more than 40 years. *Biochim. Biophys. Acta - Biomembr.* **1838**, 1451–1466 (2014).
82. Bagatolli, L. A. & Mouritsen, O. G. Is the fluid mosaic (and the accompanying raft hypothesis) a suitable model to describe fundamental features of biological membranes? What may be missing? *Front. Plant Sci.* **4**, 1–6 (2013).
83. Cantor, R. S. Lateral pressures in cell membranes: A mechanism for modulation of protein function. *J. Phys. Chem. B* **101**, 1723–1725 (1997).
84. Cantor, R. S. Lipid composition and the lateral pressure profile in bilayers. *Biophys. J.* **76**, 2625–2639 (1999).
85. Bagatolli, L. A., Ipsen, J. H., Simonsen, A. C. & Mouritsen, O. G. An outlook on organization of lipids in membranes: Searching for a realistic connection with the organization of biological membranes. *Prog. Lipid Res.* **49**, 378–389 (2010).
86. Marsh, D. Lateral pressure profile, spontaneous curvature frustration, and the incorporation and conformation of proteins in membranes. *Biophys. J.* **93**, 3884–3899 (2007).
87. Marsh, D. Protein modulation of lipids, and vice-versa, in membranes. *Biochim. Biophys. Acta - Biomembr.* **1778**, 1545–1575 (2008).
88. Mouritsen, O. G. Lipids, curvature, and nano-medicine. *Eur. J. Lipid Sci. Technol.* **113**, 1174–1187 (2011).
89. White, S. H. & King, G. I. Molecular packing and area compressibility of lipid bilayers. *Proc. Natl. Acad. Sci. U. S. A.* **82**, 6532–6536 (1985).
90. Marsh, D. *Handbook of Lipid Bilayers*. (CRC Press, Boca Raton, FL, 2013).
91. Bigay, J. & Antonny, B. Curvature, lipid packing, and electrostatics of membrane organelles: Defining cellular territories in determining specificity. *Dev. Cell* **23**, 886–895 (2012).
92. Antonny, B., Huber, I., Paris, S., Chabre, M. & Cassel, D. Activation of ADP-ribosylation factor 1 GTPase-activating protein by phosphatidylcholine-derived diacylglycerols. *J. Biol. Chem.* **272**, 30848–30851 (1997).
93. Davies, S. M. A., Epand, R. M., Kraayenhof, R. & Cornell, R. B. Regulation of CTP: Phosphocholine cytidyltransferase activity by the physical properties of lipid membranes: An important role for stored curvature strain energy. *Biochemistry* **40**, 10522–10531 (2001).
94. Jarsch, I. K., Daste, F. & Gallop, J. L. Membrane curvature in cell biology: An integration of molecular mechanisms. *J. Cell Biol.* **214**, 375–387 (2016).
95. Voeltz, G. K., Prinz, W. A., Shibata, Y., Rist, J. M. & Rapoport, T. A. A class of membrane proteins shaping the tubular endoplasmic reticulum. *Cell* **124**, 573–586 (2006).
96. Vollmer, B. *et al.* Dimerization and direct membrane interaction of Nup53 contribute to nuclear pore complex assembly: Nup53 membrane binding promotes NPC assembly. *EMBO J.* **31**, 4072–4084 (2012).
97. Davies, K. M., Anselmi, C., Wittig, I., Faraldo-Gómez, J. D. & Kühlbrandt, W. Structure of the yeast F₁ F_o-ATP synthase dimer and its role in shaping the mitochondrial cristae. *Proc. Natl. Acad. Sci. U. S. A.* **109**, 13602–13607 (2012).
98. Jiko, C. *et al.* Bovine F₁ F_o-ATP synthase monomers bend the lipid bilayer in 2D membrane crystals. *eLife* **4**, e06119 (2015).
99. Armbruster, U. *et al.* *Arabidopsis* curvature thylakoid 1 proteins modify thylakoid architecture by inducing membrane curvature. *Plant Cell* **25**, 2661–2678 (2013).
100. Kummrow, M. & Helfrich, W. Deformation of giant lipid vesicles by electric fields. *Phys. Rev. A* **44**, 8356–8360 (1991).
101. Delabre, U. *et al.* Deformation of phospholipid vesicles in an optical stretcher. *Soft Matter* **11**, 6075–6088 (2015).
102. Mitra, K., Ubarretxena-Belandia, I., Taguchi, T., Warren, G. & Engelman, D. M. Modulation of the bilayer thickness of exocytic pathway membranes by membrane proteins rather than cholesterol. *Proc. Natl. Acad. Sci. U. S. A.* **101**, 4083–4088 (2004).
103. Frallicciardi, J., Melcr, J., Siginou, P., Marrink, S. J. & Poolman, B. Membrane thickness, lipid phase and sterol type are determining factors in the permeability of membranes to small solutes. *Nat. Commun.* **13**, 1605 (2022).
104. Silvius, J. R., Del Giudice, D. & Lafleur, M. Cholesterol at different bilayer concentrations can promote or antagonize lateral segregation of phospholipids of differing acyl chain length. *Biochemistry* **35**, 15198–15208 (1996).

105. Korlach, J., Schwille, P., Webb, W. W. & Feigenson, G. W. Characterization of lipid bilayer phases by confocal microscopy and fluorescence correlation spectroscopy. *Proc. Natl. Acad. Sci. U. S. A.* **96**, 8461–8466 (1999).
106. Veatch, S. L. & Keller, S. L. Separation of liquid phases in giant vesicles of ternary mixtures of phospholipids and cholesterol. *Biophys. J.* **85**, 3074–3083 (2003).
107. Baumgart, T., Hess, S. T. & Webb, W. W. Imaging coexisting fluid domains in biomembrane models coupling curvature and line tension. *Nature* **425**, 821–824 (2003).
108. Bacia, K., Schwille, P. & Kurzchalia, T. Sterol structure determines the separation of phases and the curvature of the liquid-ordered phase in model membranes. *Proc. Natl. Acad. Sci.* **102**, 3272–3277 (2005).
109. Baumgart, T. *et al.* Large-scale fluid/fluid phase separation of proteins and lipids in giant plasma membrane vesicles. *Proc. Natl. Acad. Sci.* **104**, 3165–3170 (2007).
110. Heberle, F. A. & Feigenson, G. W. Phase separation in lipid membranes. *Cold Spring Harb. Perspect. Biol.* **3**, a004630 (2011).
111. Cornell, C. E. *et al.* Tuning length scales of small domains in cell-derived membranes and synthetic model membranes. *Biophys. J.* **115**, 690–701 (2018).
112. Sych, T., Gurdap, C. O., Wedemann, L. & Sezgin, E. How does liquid-liquid phase separation in model membranes reflect cell membrane heterogeneity? *Membranes* **11**, 323 (2021).
113. Brown, D. A. & London, E. Structure and origin of ordered lipid domains in biological membranes. *J. Membr. Biol.* **164**, 103–114 (1998).
114. M'Baye, G., Mély, Y., Duportail, G. & Klymchenko, A. S. Liquid ordered and gel phases of lipid bilayers: Fluorescent probes reveal close fluidity but different Hydration. *Biophys. J.* **95**, 1217–1225 (2008).
115. Demchenko, A. P., Mély, Y., Duportail, G. & Klymchenko, A. S. Monitoring biophysical properties of lipid membranes by environment-sensitive fluorescent probes. *Biophys. J.* **96**, 3461–3470 (2009).
116. Simons, K. & Ikonen, E. Functional rafts in cell membranes. *Nature* **387**, 569–572 (1997).
117. Almeida, P. F. F. Thermodynamics of lipid interactions in complex bilayers. *Biochim. Biophys. Acta - Biomembr.* **1788**, 72–85 (2009).
118. Lingwood, D. & Simons, K. Lipid rafts as a membrane-organizing principle. *Science* **327**, 46–50 (2010).
119. Janosi, L., Li, Z., Hancock, J. F. & Gorfe, A. A. Organization, dynamics, and segregation of Ras nanoclusters in membrane domains. *Proc. Natl. Acad. Sci.* **109**, 8097–8102 (2012).
120. Zhou, Y. *et al.* Membrane potential modulates plasma membrane phospholipid dynamics and K-Ras signaling. *Science* **349**, 873–876 (2015).
121. Diaz-Rohrer, B. B., Levental, K. R., Simons, K. & Levental, I. Membrane raft association is a determinant of plasma membrane localization. *Proc. Natl. Acad. Sci.* **111**, 8500–8505 (2014).
122. Surma, M. A., Klose, C. & Simons, K. Lipid-dependent protein sorting at the trans-Golgi network. *Biochim. Biophys. Acta - Mol. Cell Biol. Lipids* **1821**, 1059–1067 (2012).
123. Eggeling, C. *et al.* Direct observation of the nanoscale dynamics of membrane lipids in a living cell. *Nature* **457**, 1159–1162 (2009).
124. Owen, D. M. & Gaus, K. Imaging lipid domains in cell membranes: the advent of super-resolution fluorescence microscopy. *Front. Plant Sci.* **4**, 503 (2013).
125. Saka, S. K. *et al.* Multi-protein assemblies underlie the mesoscale organization of the plasma membrane. *Nat. Commun.* **5**, 4509 (2014).
126. Huang, H., Simsek, M. F., Jin, W. & Pralle, A. Effect of receptor dimerization on membrane lipid raft structure continuously quantified on single cells by camera based fluorescence correlation spectroscopy. *PLOS ONE* **10**, e0121777 (2015).
127. Gohrbandt, M. *et al.* Low membrane fluidity triggers lipid phase separation and protein segregation in living bacteria. *EMBO J.* **41**, e109800 (2022).
128. Owen, D. M., Magenau, A., Williamson, D. & Gaus, K. The lipid raft hypothesis revisited - New insights on raft composition and function from super-resolution fluorescence microscopy. *BioEssays* **34**, 739–747 (2012).
129. Levental, I. & Veatch, S. L. The continuing mystery of lipid rafts. *J. Mol. Biol.* **428**, 4749–4764 (2016).
130. Levental, I., Levental, K. R. & Heberle, F. A. Lipid rafts: Controversies resolved, mysteries remain. *Trends Cell Biol.* **30**, 341–353 (2020).
131. Toulmay, A. & Prinz, W. A. Direct imaging reveals stable, micrometer-scale lipid domains that segregate proteins in live cells. *J. Cell Biol.* **202**, 35–44 (2013).

132. Wang, C.-W., Miao, Y.-H. & Chang, Y.-S. A sterol-enriched vacuolar microdomain mediates stationary phase lipophagy in budding yeast. *J. Cell Biol.* **206**, 357–366 (2014).
133. Murley, A. *et al.* Sterol transporters at membrane contact sites regulate TORC1 and TORC2 signaling. *J. Cell Biol.* **216**, 2679–2689 (2017).
134. Brown, M. F. Soft matter in lipid–protein interactions. *Annu. Rev. Biophys.* **46**, 379–410 (2017).
135. Sodt, A. J., Venable, R. M., Lyman, E. & Pastor, R. W. Nonadditive compositional curvature energetics of lipid bilayers. *Phys. Rev. Lett.* **117**, 138104 (2016).
136. Leonard, T. A., Loose, M. & Martens, S. The membrane surface as a platform that organizes cellular and biochemical processes. *Dev. Cell* **58**, 1315–1332 (2023).
137. Navarro, S., Borchman, D. & Bicknell-Brown, E. Lipid-protein ratios by infrared spectroscopy. *Anal. Biochem.* **136**, 382–389 (1984).
138. Takamori, S. *et al.* Molecular anatomy of a trafficking organelle. *Cell* **127**, 831–846 (2006).
139. Corcelli, A., Lattanzio, V. M. T., Mascolo, G., Papadia, P. & Fanizzi, F. Lipid-protein stoichiometries in a crystalline biological membrane: NMR quantitative analysis of the lipid extract of the purple membrane. *J. Lipid Res.* **43**, 132–140 (2002).
140. Dupuy, A. D. & Engelman, D. M. Protein area occupancy at the center of the red blood cell membrane. *Proc. Natl. Acad. Sci.* **105**, 2848–2852 (2008).
141. Stieger, B., Steiger, J. & Locher, K. P. Membrane lipids and transporter function. *Biochim. Biophys. Acta - Mol. Basis Dis.* **1867**, 166079 (2021).
142. Jones, A. J. Y., Gabriel, F., Tandale, A. & Nietlispach, D. Structure and dynamics of GPCRs in lipid membranes: Physical principles and experimental approaches. *Molecules* **25**, 4729 (2020).
143. Basu Ball, W., Neff, J. K. & Gohil, V. M. The role of nonbilayer phospholipids in mitochondrial structure and function. *FEBS Lett.* **592**, 1273–1290 (2018).
144. Jacquemyn, J., Cascalho, A. & Goodchild, R. E. The ins and outs of endoplasmic reticulum-controlled lipid biosynthesis. *EMBO Rep.* **18**, 1905–1921 (2017).
145. Kühnle, N., Dederer, V. & Lemberg, M. K. Intramembrane proteolysis at a glance: from signalling to protein degradation. *J. Cell Sci.* **132**, jcs217745 (2019).
146. Andrade, D. M. *et al.* Cortical actin networks induce spatio-temporal confinement of phospholipids in the plasma membrane – a minimally invasive investigation by STED-FCS. *Sci. Rep.* **5**, 11454 (2015).
147. Wigbers, M. C. *et al.* A hierarchy of protein patterns robustly decodes cell shape information. *Nat. Phys.* **17**, 578–584 (2021).
148. Olayioye, M. A., Noll, B. & Hausser, A. Spatiotemporal control of intracellular membrane trafficking by Rho GTPases. *Cells* **8**, 1478 (2019).
149. Czapiewski, R., Robson, M. I. & Schirmer, E. C. Anchoring a leviathan: How the nuclear membrane tethers the genome. *Front. Genet.* **7**, 82 (2016).
150. Chen, B., Sun, Y., Niu, J., Jarugumilli, G. K. & Wu, X. Protein lipidation in cell signaling and diseases: Function, regulation, and therapeutic opportunities. *Cell Chem. Biol.* **25**, 817–831 (2018).
151. Lemmon, M. A. Membrane recognition by phospholipid-binding domains. *Nat. Rev. Mol. Cell Biol.* **9**, 99–111 (2008).
152. Stahelin, R. V. Lipid binding domains: more than simple lipid effectors. *J. Lipid Res.* **50**, S299–S304 (2009).
153. Van Den Bogaart, G., Meyenberg, K., Diederichsen, U. & Jahn, R. Phosphatidylinositol 4,5-bisphosphate increases Ca²⁺ affinity of Synaptotagmin-1 by 40-fold. *J. Biol. Chem.* **287**, 16447–16453 (2012).
154. Corbin, J. A., Evans, J. H., Landgraf, K. E. & Falke, J. J. Mechanism of specific membrane targeting by C2 domains: Localized pools of target lipids enhance Ca²⁺ affinity. *Biochemistry* **46**, 4322–4336 (2007).
155. Stenmark, H., Aasland, R., Toh, B.-H. & D’Arrigo, A. Endosomal localization of the autoantigen EEA1 is mediated by a zinc-binding FYVE finger. *J. Biol. Chem.* **271**, 24048–24054 (1996).
156. Lee, S. A. *et al.* Targeting of the FYVE domain to endosomal membranes is regulated by a histidine switch. *Proc. Natl. Acad. Sci.* **102**, 13052–13057 (2005).
157. Kay, B. K., Yamabhai, M., Wendland, B. & Emr, S. D. Identification of a novel domain shared by putative components of the endocytic and cytoskeletal machinery. *Protein Sci.* **8**, 435–438 (1999).

158. Wishart, M. J., Taylor, G. S. & Dixon, J. E. Phoxy lipids: Revealing PX domains as phosphoinositide binding modules. *Cell* **105**, 817–820 (2001).
159. Sawyer, E. M. *et al.* A flat protein complex shapes rough ER membrane sheets. Preprint at <https://doi.org/10.1101/2023.10.06.559866> (2023).
160. Peter, B. J. *et al.* BAR domains as sensors of membrane curvature: The amphiphysin BAR structure. *Science* **303**, 495–499 (2004).
161. Qualmann, B., Koch, D. & Kessels, M. M. Let's go bananas: revisiting the endocytic BAR code. *EMBO J.* **30**, 3501–3515 (2011).
162. Heath, R. J. W. & Insall, R. H. F-BAR domains: multifunctional regulators of membrane curvature. *J. Cell Sci.* **121**, 1951–1954 (2008).
163. Lee, A. G. Lipid–protein interactions in biological membranes: a structural perspective. *Biochim. Biophys. Acta - Biomembr.* **1612**, 1–40 (2003).
164. Levental, I. & Lyman, E. Regulation of membrane protein structure and function by their lipid nano-environment. *Nat. Rev. Mol. Cell Biol.* **24**, 107–122 (2023).
165. Cohen, B. E. Membrane Thickness as a Key Factor Contributing to the Activation of Osmosensors and Essential Ras Signaling Pathways. *Front. Cell Dev. Biol.* **6**, 76 (2018).
166. Reddy, B., Bavi, N., Lu, A., Park, Y. & Perozo, E. Molecular basis of force-from-lipids gating in the mechanosensitive channel MscS. *eLife* **8**, e50486 (2019).
167. Lorent, J. H. *et al.* Structural determinants and functional consequences of protein affinity for membrane rafts. *Nat. Commun.* **8**, 1219 (2017).
168. Shelby, S. A., Castello-Serrano, I., Wisser, K. C., Levental, I. & Veatch, S. L. Membrane phase separation drives responsive assembly of receptor signaling domains. *Nat. Chem. Biol.* **19**, 750–758 (2023).
169. Radanović, T., Reinhard, J., Ballweg, S., Pesek, K. & Ernst, R. An emerging group of membrane property sensors controls the physical state of organellar membranes to maintain their identity. *BioEssays* **40**, 1700250 (2018).
170. Ernst, R., Ejsing, C. S. & Antonny, B. Homeoviscous adaptation and the regulation of membrane lipids. *J. Mol. Biol.* **428**, 4776–4791 (2016).
171. Covino, R., Hummer, G. & Ernst, R. Integrated functions of membrane property sensors and a hidden side of the unfolded protein response. *Mol. Cell* **71**, 458–467 (2018).
172. Sinensky, M. Temperature control of phospholipid biosynthesis in *Escherichia coli*. *J. Bacteriol.* **106**, 449–455 (1971).
173. Sinensky, M. Homeoviscous adaptation—a homeostatic process that regulates the viscosity of membrane lipids in *Escherichia coli*. *Proc. Natl. Acad. Sci.* **71**, 522–525 (1974).
174. Aguilar, P. S. Molecular basis of the thermosensing: a two-component signal transduction thermometer in *Bacillus subtilis*. *EMBO J.* **20**, 1681–1691 (2001).
175. Cybulski, L. E., Del Solar, G., Craig, P. O., Espinosa, M. & De Mendoza, D. *Bacillus subtilis* DesR functions as a phosphorylation-activated switch to control membrane lipid fluidity. *J. Biol. Chem.* **279**, 39340–39347 (2004).
176. Cybulski, L. E., Martín, M., Mansilla, M. C., Fernández, A. & De Mendoza, D. Membrane thickness cue for cold sensing in a bacterium. *Curr. Biol.* **20**, 1539–1544 (2010).
177. Cybulski, L. E. *et al.* Activation of the bacterial thermosensor DesK involves a serine zipper dimerization motif that is modulated by bilayer thickness. *Proc. Natl. Acad. Sci.* **112**, 6353–6358 (2015).
178. Hoppe, T. *et al.* Activation of a membrane-bound transcription factor by regulated ubiquitin/proteasome-dependent processing. *Cell* **102**, 577–586 (2000).
179. Auld, K. L., Brown, C. R., Casolari, J. M., Komili, S. & Silver, P. A. Genomic association of the proteasome demonstrates overlapping gene regulatory activity with transcription factor substrates. *Mol. Cell* **21**, 861–871 (2006).
180. Bossie, M. A. & Martin, C. E. Nutritional regulation of yeast Δ -9 fatty acid desaturase activity. *J. Bacteriol.* **171**, 6409–6413 (1989).
181. Covino, R. *et al.* A eukaryotic sensor for membrane lipid saturation. *Mol. Cell* **63**, 49–59 (2016).
182. Ballweg, S. & Ernst, R. Control of membrane fluidity: The OLE pathway in focus. *Biol. Chem.* **398**, 215–228 (2017).
183. Loewen, C. J. R. *et al.* Phospholipid metabolism regulated by a transcription factor sensing phosphatidic acid. *Science* **304**, 1644–1647 (2004).
184. Putta, P. *et al.* Phosphatidic acid binding proteins display differential binding as a function of membrane curvature stress and chemical properties. *Biochim. Biophys. Acta - Biomembr.* **1858**, 2709–2716 (2016).

185. Hofbauer, H. F. *et al.* The molecular recognition of phosphatidic acid by an amphipathic helix in Opi1. *J. Cell Biol.* **217**, 3109–3126 (2018).
186. Ambroziak, J. & Henry, S. A. *INO2* and *INO4* gene products, positive regulators of phospholipid biosynthesis in *Saccharomyces cerevisiae*, form a complex that binds to the *INO1* promoter. *J. Biol. Chem.* **269**, 15344–15349 (1994).
187. Henry, S. A., Kohlwein, S. D. & Carman, G. M. Metabolism and regulation of glycerolipids in the yeast *Saccharomyces cerevisiae*. *Genetics* **190**, 317–349 (2012).
188. Henry, S. A., Gaspar, M. L. & Jesch, S. A. The response to inositol: regulation of glycerolipid metabolism and stress response signaling in yeast. *Chem. Phys. Lipids* **180**, 23–43 (2014).
189. Greenberg, M. L., Reiner, B. & Henry, S. A. Regulatory mutations of inositol biosynthesis in yeast: isolation of inositol-excreting mutants. *Genetics* **100**, 19–33 (1982).
190. Loewy, B. S. & Henry, S. A. The *INO2* and *INO4* loci of *Saccharomyces cerevisiae* are pleiotropic regulatory genes. *Mol. Cell. Biol.* **4**, 2479–2485 (1984).
191. Athenstaedt, K. & Daum, G. Phosphatidic acid, a key intermediate in lipid metabolism. *Eur. J. Biochem.* **266**, 1–16 (1999).
192. Walter, P. & Ron, D. The unfolded protein response: from stress pathway to homeostatic regulation. *Science* **334**, 1081–1086 (2011).
193. Volmer, R. & Ron, D. Lipid-dependent regulation of the unfolded protein response. *Curr. Opin. Cell Biol.* **33**, 67–73 (2015).
194. Jonikas, M. C. *et al.* Comprehensive characterization of genes required for protein folding in the endoplasmic reticulum. *Science* **323**, 1693–1697 (2009).
195. Surma, M. A. *et al.* A lipid E-MAP identifies Ubx2 as a critical regulator of lipid saturation and lipid bilayer stress. *Mol. Cell* **51**, 519–530 (2013).
196. Cox, J. S., Shamu, C. E. & Walter, P. Transcriptional induction of genes encoding endoplasmic reticulum resident proteins requires a transmembrane protein kinase. *Cell* **73**, 1197–1206 (1993).
197. Mori, K., Kawahara, T., Yoshida, H., Yanagi, H. & Yura, T. Signalling from endoplasmic reticulum to nucleus: Transcription factor with a basic-leucine zipper motif is required for the unfolded protein-response pathway. *Genes Cells* **1**, 803–817 (1996).
198. Gardner, B. M. & Walter, P. Unfolded proteins are Ire1-activating ligands that directly induce the unfolded protein response. *Science* **333**, 1891–1894 (2011).
199. Travers, K. J. *et al.* Functional and genomic analyses reveal an essential coordination between the unfolded protein response and ER-associated degradation. *Cell* **101**, 249–258 (2000).
200. Promlek, T. *et al.* Membrane aberrancy and unfolded proteins activate the endoplasmic reticulum stress sensor Ire1 in different ways. *Mol. Biol. Cell* **22**, 3520–3532 (2011).
201. Thibault, G. *et al.* The membrane stress response buffers lethal effects of lipid disequilibrium by reprogramming the protein homeostasis network. *Mol. Cell* **48**, 16–27 (2012).
202. Volmer, R., Van Der Ploeg, K. & Ron, D. Membrane lipid saturation activates endoplasmic reticulum unfolded protein response transducers through their transmembrane domains. *Proc. Natl. Acad. Sci.* **110**, 4628–4633 (2013).
203. Pineau, L. *et al.* Lipid-induced ER stress: Synergistic effects of sterols and saturated fatty acids. *Traffic* **10**, 673–690 (2009).
204. Cox, J. S., Chapman, R. E. & Walter, P. The unfolded protein response coordinates the production of endoplasmic reticulum protein and endoplasmic reticulum membrane. *Mol. Biol. Cell* **8**, 1805–1814 (1997).
205. Halbleib, K. *et al.* Activation of the unfolded protein response by lipid bilayer stress. *Mol. Cell* **67**, 673–684 (2017).
206. Holthuis, J. C. M. & Levine, T. P. Lipid traffic: floppy drives and a superhighway. *Nat. Rev. Mol. Cell Biol.* **6**, 209–220 (2005).
207. Prinz, W. A. Non-vesicular sterol transport in cells. *Prog. Lipid Res.* **46**, 297–314 (2007).
208. van Meer, G., Voelker, D. R. & Feigenson, G. W. Membrane lipids: where they are and how they behave. *Nat. Rev. Mol. Cell Biol.* **9**, 112–124 (2008).
209. Holthuis, J. C. M. & Menon, A. K. Lipid landscapes and pipelines in membrane homeostasis. *Nature* **510**, 48–57 (2014).
210. Menon, A. K. Sterol gradients in cells. *Curr. Opin. Cell Biol.* **53**, 37–43 (2018).
211. Radhakrishnan, A., Goldstein, J. L., McDonald, J. G. & Brown, M. S. Switch-like control of SREBP-2 transport triggered by small changes in ER cholesterol: a delicate balance. *Cell Metab.* **8**, 512–521 (2008).

212. Reglinski, K. *et al.* Fluidity and lipid composition of membranes of peroxisomes, mitochondria and the ER from oleic acid-induced *Saccharomyces cerevisiae*. *Front. Cell Dev. Biol.* **8**, 574363 (2020).
213. Koichi, K., Michiya, F. & Makoto, N. Lipid components of two different regions of an intestinal epithelial cell membrane of mouse. *Biochim. Biophys. Acta BBA - Lipids Lipid Metab.* **369**, 222–233 (1974).
214. Gerl, M. J. *et al.* Quantitative analysis of the lipidomes of the influenza virus envelope and MDCK cell apical membrane. *J. Cell Biol.* **196**, 213–221 (2012).
215. Surma, M. A., Klose, C., Klemm, R. W., Ejsing, C. S. & Simons, K. Generic sorting of raft lipids into secretory vesicles in yeast. *Traffic* **12**, 1139–1147 (2011).
216. Klemm, R. W. *et al.* Segregation of sphingolipids and sterols during formation of secretory vesicles at the trans-Golgi network. *J. Cell Biol.* **185**, 601–612 (2009).
217. Baumann, N. A. *et al.* Transport of newly synthesized sterol to the sterol-enriched plasma membrane occurs via nonvesicular equilibration. *Biochemistry* **44**, 5816–5826 (2005).
218. Georgiev, A. G. *et al.* Osh proteins regulate membrane sterol organization but are not required for sterol movement between the ER and PM. *Traffic* **12**, 1341–1355 (2011).
219. Friedland, N., Liou, H.-L., Lobel, P. & Stock, A. M. Structure of a cholesterol-binding protein deficient in Niemann–Pick type C2 disease. *Proc. Natl. Acad. Sci.* **100**, 2512–2517 (2003).
220. Im, Y. J., Raychaudhuri, S., Prinz, W. A. & Hurley, J. H. Structural mechanism for sterol sensing and transport by OSBP-related proteins. *Nature* **437**, 154–158 (2005).
221. Hurley, J. H. & Tsujishita, Y. Structure and lipid transport mechanism of a StAR-related domain. *Nat. Struct. Biol.* **7**, 408–414 (2000).
222. Romanowski, M. J., Soccio, R. E., Breslow, J. L. & Burley, S. K. Crystal structure of the *Mus musculus* cholesterol-regulated START protein 4 (StarD4) containing a StAR-related lipid transfer domain. *Proc. Natl. Acad. Sci.* **99**, 6949–6954 (2002).
223. Mesmin, B. & Maxfield, F. R. Intracellular sterol dynamics. *Biochim. Biophys. Acta BBA - Mol. Cell Biol. Lipids* **1791**, 636–645 (2009).
224. Mesmin, B. *et al.* Sterol transfer, PI4P consumption, and control of membrane lipid order by endogenous OSBP. *EMBO J.* **36**, 3156–3174 (2017).
225. Antonny, B., Vanni, S., Shindou, H. & Ferreira, T. From zero to six double bonds: phospholipid unsaturation and organelle function. *Trends Cell Biol.* **25**, 427–436 (2015).
226. Sharpe, H. J., Stevens, T. J. & Munro, S. A comprehensive comparison of transmembrane domains reveals organelle-specific properties. *Cell* **142**, 158–169 (2010).
227. Costello, J. L. *et al.* Predicting the targeting of tail-anchored proteins to subcellular compartments in mammalian cells. *J. Cell Sci.* **130**, 1675–1687 (2017).
228. Behnia, R. & Munro, S. Organelle identity and the signposts for membrane traffic. *Nature* **438**, 597–604 (2005).
229. Hurst, L. R. & Fratti, R. A. Lipid rafts, sphingolipids, and ergosterol in yeast vacuole fusion and maturation. *Front. Cell Dev. Biol.* **8**, 539 (2020).
230. Teixeira, V. *et al.* Ceramide signaling targets the PP2A-like protein phosphatase Sit4p to impair vacuolar function, vesicular trafficking and autophagy in *Isc1p* deficient cells. *Biochim. Biophys. Acta BBA - Mol. Cell Biol. Lipids* **1861**, 21–33 (2016).
231. Seo, A. Y. *et al.* AMPK and vacuole-associated Atg14p orchestrate μ -lipophagy for energy production and long-term survival under glucose starvation. *eLife* **6**, e21690 (2017).
232. Kim, H. & Budin, I. Intracellular sphingolipid sorting drives membrane phase separation in the yeast vacuole. *J. Biol. Chem.* **300**, 105496 (2024).
233. Romanuska, A. & Köhler, A. The inner nuclear membrane is a metabolically active territory that generates nuclear lipid droplets. *Cell* **174**, 700–715 (2018).
234. Hammond, G. R. V., Ricci, M. M. C., Weckerly, C. C. & Wills, R. C. An update on genetically encoded lipid biosensors. *Mol. Biol. Cell* **33**, tp2 (2022).
235. Sarmiento, M. J. *et al.* The expanding organelle lipidomes: current knowledge and challenges. *Cell. Mol. Life Sci.* **80**, 237 (2023).
236. Claude, A. Fractionation of mammalian liver cells by differential centrifugation. I. Problems, methods and preparation of extract. *J. Exp. Med.* **84**, 51–59 (1946).
237. Hogeboom, G. H., Schneider, W. C. & Pallade, G. E. Cytochemical studies of mammalian tissues. I. Isolation of intact mitochondria from rat liver; some biochemical properties of mitochondria and submicroscopic particulate material. *J. Biol. Chem.* **172**, 619–635 (1948).
238. Palade, G. E. & Siekevitz, P. Liver microsomes. An integrated morphological and biochemical study. *J. Biophysic. and Biochem. Cytol.* **2**, 171–213 (1956).
239. De Duve, C. Tissue fractionation—Past and present. *J. Cell Biol.* **50**, 20–55 (1971).

240. Lottspeich, F. & Engels, J. W. *Bioanalytics: Analytical Methods and Concepts in Biochemistry and Molecular Biology*. (Wiley-VCH Verlag, Weinheim, 2018).
241. Zinser, E. *et al.* Phospholipid synthesis and lipid composition of subcellular membranes in the unicellular eukaryote *Saccharomyces cerevisiae*. *J. Bacteriol.* **173**, 2026–2034 (1991).
242. Zinser, E. & Daum, G. Isolation and biochemical characterization of organelles from the yeast, *Saccharomyces cerevisiae*. *Yeast* **11**, 493–536 (1995).
243. Scorrano, L. *et al.* Coming together to define membrane contact sites. *Nat. Commun.* **10**, 1287 (2019).
244. Castro, I. G. *et al.* Systematic analysis of membrane contact sites in *Saccharomyces cerevisiae* uncovers modulators of cellular lipid distribution. *eLife* **11**, e74602 (2022).
245. Voeltz, G. K., Sawyer, E. M., Hajnóczky, G. & Prinz, W. A. Making the connection: How membrane contact sites have changed our view of organelle biology. *Cell* **187**, 257–270 (2024).
246. Gruenberg, J. E. & Howell, K. E. Reconstitution of vesicle fusions occurring in endocytosis with a cell-free system. *EMBO J.* **5**, 3091–3101 (1986).
247. Abu-Remaileh, M. *et al.* Lysosomal metabolomics reveals V-ATPase- and mTOR-dependent regulation of amino acid efflux from lysosomes. *Science* **358**, 807–813 (2017).
248. Ray, G. J. *et al.* A PEROXO-tag enables rapid isolation of peroxisomes from human cells. *iScience* **23**, 101109 (2020).
249. Klose, C., Surma, M. A. & Simons, K. Organellar lipidomics-background and perspectives. *Curr. Opin. Cell Biol.* **25**, 406–413 (2013).
250. Radanović, T. & Ernst, R. The unfolded protein response as a guardian of the secretory pathway. *Cells* **10**, 2965 (2021).
251. Hollien, J. *et al.* Regulated Ire1-dependent decay of messenger RNAs in mammalian cells. *J. Cell Biol.* **186**, 323–331 (2009).
252. Haze, K., Yoshida, H., Yanagi, H., Yura, T. & Mori, K. Mammalian transcription factor ATF6 is synthesized as a transmembrane protein and activated by proteolysis in response to endoplasmic reticulum stress. *Mol. Biol. Cell* **10**, 3787–3799 (1999).
253. Ye, J. *et al.* ER stress induces cleavage of membrane-bound ATF6 by the same proteases that process SREBPs. *Mol. Cell* **6**, 1355–1364 (2000).
254. Wu, J. *et al.* ATF6 α optimizes long-term endoplasmic reticulum function to protect cells from chronic stress. *Dev. Cell* **13**, 351–364 (2007).
255. Harding, H. P. *et al.* Regulated translation initiation controls stress-induced gene expression in mammalian cells. *Mol. Cell* **6**, 1099–1108 (2000).
256. Harding, H. P., Zhang, Y., Bertolotti, A., Zeng, H. & Ron, D. Perk is essential for translational regulation and cell survival during the unfolded protein response. *Mol. Cell* **5**, 897–904 (2000).
257. Oyadomari, S., Araki, E. & Mori, M. Endoplasmic reticulum stress-mediated apoptosis in pancreatic beta-cells. *Apoptosis* **7**, 335–345 (2002).
258. Lu, M. *et al.* Opposing unfolded-protein-response signals converge on death receptor 5 to control apoptosis. *Science* **345**, 98–101 (2014).
259. Wang, S. & Kaufman, R. J. The impact of the unfolded protein response on human disease. *J. Cell Biol.* **197**, 857–867 (2012).
260. Ozcan, L. & Tabas, I. Role of endoplasmic reticulum stress in metabolic disease and other disorders. *Annu. Rev. Med.* **63**, 317–328 (2012).
261. Wang, M. & Kaufman, R. J. The impact of the endoplasmic reticulum protein-folding environment on cancer development. *Nat. Rev. Cancer* **14**, 581–597 (2014).
262. Han, J. & Kaufman, R. J. The role of ER stress in lipid metabolism and lipotoxicity. *J. Lipid Res.* **57**, 1329–1338 (2016).
263. Hetz, C. & Papa, F. R. The unfolded protein response and cell fate control. *Mol. Cell* **69**, 169–181 (2018).
264. Pineau, L. & Ferreira, T. Lipid-induced ER stress in yeast and β cells: parallel trails to a common fate. *FEMS Yeast Res.* **10**, 1035–1045 (2010).
265. Cunha, D. A. *et al.* Initiation and execution of lipotoxic ER stress in pancreatic β -cells. *J. Cell Sci.* **121**, 2308–2318 (2008).
266. Borradaile, N. M. *et al.* Disruption of endoplasmic reticulum structure and integrity in lipotoxic cell death. *J. Lipid Res.* **47**, 2726–2737 (2006).
267. Shen, Y. *et al.* Metabolic activity induces membrane phase separation in endoplasmic reticulum. *Proc. Natl. Acad. Sci.* **114**, 13394–13399 (2017).
268. Cho, H. *et al.* Intrinsic structural features of the human IRE1 α transmembrane domain sense membrane lipid saturation. *Cell Rep.* **27**, 307–320 (2019).

269. Tam, A. B. *et al.* The UPR activator ATF6 responds to proteotoxic and lipotoxic stress by distinct mechanisms. *Dev. Cell* **46**, 327–343 (2018).
270. Rutkowski, D. T. Liver function and dysfunction – a unique window into the physiological reach of ER stress and the unfolded protein response. *FEBS J.* **286**, 356–378 (2019).
271. Henkel, A. & Green, R. The unfolded protein response in fatty liver disease. *Semin. Liver Dis.* **33**, 321–329 (2013).
272. González-Rodríguez, Á. *et al.* Impaired autophagic flux is associated with increased endoplasmic reticulum stress during the development of NAFLD. *Cell Death Dis.* **5**, e1179 (2014).
273. Song, M. J. & Malhi, H. The unfolded protein response and hepatic lipid metabolism in non alcoholic fatty liver disease. *Pharmacol. Ther.* **203**, 107401 (2019).
274. Rutkowski, D. T. *et al.* UPR pathways combine to prevent hepatic steatosis caused by ER stress-mediated suppression of transcriptional master regulators. *Dev. Cell* **15**, 829–840 (2008).
275. Lee, J.-S., Mendez, R., Heng, H. H., Yang, Z.-Q. & Zhang, K. Pharmacological ER stress promotes hepatic lipogenesis and lipid droplet formation. *Am. J. Transl. Res.* **4**, 102–113 (2012).
276. Jo, H. *et al.* Endoplasmic reticulum stress induces hepatic steatosis via increased expression of the hepatic very low-density lipoprotein receptor. *Hepatology* **57**, 1366–1377 (2013).
277. Laressergues, E. *et al.* Does endoplasmic reticulum stress participate in APD-induced hepatic metabolic dysregulation? *Neuropharmacology* **62**, 784–796 (2012).
278. Cao, J. *et al.* Saturated fatty acid induction of endoplasmic reticulum stress and apoptosis in human liver cells via the PERK/ATF4/CHOP signaling pathway. *Mol. Cell. Biochem.* **364**, 115–129 (2012).
279. Walkey, C. J., Yu, L., Agellon, L. B. & Vance, D. E. Biochemical and evolutionary significance of phospholipid methylation. *J. Biol. Chem.* **273**, 27043–27046 (1998).
280. Li, Z. *et al.* The ratio of phosphatidylcholine to phosphatidylethanolamine influences membrane integrity and steatohepatitis. *Cell Metab.* **3**, 321–331 (2006).
281. Gordon, D. L. *et al.* Biomarkers of NAFLD progression: a lipidomics approach to an epidemic. *J. Lipid Res.* **56**, 722–736 (2015).
282. Gerakis, Y. & Hetz, C. Emerging roles of ER stress in the etiology and pathogenesis of Alzheimer's disease. *FEBS J.* **285**, 995–1011 (2018).
283. Ajoalabady, A., Lindholm, D., Ren, J. & Pratico, D. ER stress and UPR in Alzheimer's disease: mechanisms, pathogenesis, treatments. *Cell Death Dis.* **13**, 706 (2022).
284. Nishitsuji, K. *et al.* The E693Δ mutation in amyloid precursor protein increases intracellular accumulation of amyloid β oligomers and causes endoplasmic reticulum stress-induced apoptosis in cultured cells. *Am. J. Pathol.* **174**, 957–969 (2009).
285. Lee, D. Y. *et al.* Activation of PERK signaling attenuates Aβ-mediated ER stress. *PLoS ONE* **5**, e10489 (2010).
286. Duran-Aniotz, C. *et al.* IRE1 signaling exacerbates Alzheimer's disease pathogenesis. *Acta Neuropathol.* **134**, 489–506 (2017).
287. Chew, H., Solomon, V. A. & Fonteh, A. N. Involvement of lipids in Alzheimer's disease pathology and potential therapies. *Front. Physiol.* **11**, 598 (2020).
288. Barlowe, C. K. & Miller, E. A. Secretory protein biogenesis and traffic in the early secretory pathway. *Genetics* **193**, 383–410 (2013).
289. Tabas, I. & Ron, D. Integrating the mechanisms of apoptosis induced by endoplasmic reticulum stress. *Nat. Cell Biol.* **13**, 184–190 (2011).
290. Lebeaupin, C. *et al.* ER stress induces NLRP3 inflammasome activation and hepatocyte death. *Cell Death Dis.* **6**, e1879 (2015).
291. Iurlaro, R. & Muñoz-Pinedo, C. Cell death induced by endoplasmic reticulum stress. *FEBS J.* **283**, 2640–2652 (2016).
292. Kaufman, R. J. Orchestrating the unfolded protein response in health and disease. *J. Clin. Invest.* **110**, 1389–1398 (2002).
293. Hetz, C. The unfolded protein response: controlling cell fate decisions under ER stress and beyond. *Nat. Rev. Mol. Cell Biol.* **13**, 89–102 (2012).
294. Puth, K. *et al.* Homeostatic control of biological membranes by dedicated lipid and membrane packing sensors. *Biol. Chem.* **396**, 1043–58 (2015).
295. Cox, J. S. & Walter, P. A novel mechanism for regulating activity of a transcription factor that controls the unfolded protein response. *Cell* **87**, 391–404 (1996).

References

296. Sidrauski, C. & Walter, P. The transmembrane kinase Ire1p is a site-specific endonuclease that initiates mRNA splicing in the unfolded protein response. *Cell* **90**, 1031–1039 (1997).
297. Kobashi, K. Catalytic oxidation of sulfhydryl groups by o-phenanthroline copper complex. *Biochim. Biophys. Acta BBA - Gen. Subj.* **158**, 239–245 (1968).
298. McIntosh, P. R. & Freedman, R. B. Characteristics of a copper-dependent cross-linking reaction between two forms of cytochrome *P*-450 in rabbit-liver microsomal membranes. *Biochem. J.* **187**, 227–237 (1980).
299. Ghaemmaghami, S. *et al.* Global analysis of protein expression in yeast. *Nature* **425**, 737–741 (2003).
300. Kimata, Y. *et al.* Two regulatory steps of ER-stress sensor Ire1 involving its cluster formation and interaction with unfolded proteins. *J. Cell Biol.* **179**, 75–86 (2007).
301. Haselwandter, C. A. & MacKinnon, R. Piezo's membrane footprint and its contribution to mechanosensitivity. *eLife* **7**, e41968 (2018).
302. Tran, N.-H. *et al.* The stress-sensing domain of activated IRE1 α forms helical filaments in narrow ER membrane tubes. *Science* **374**, 52–57 (2021).
303. Belyy, V., Tran, N.-H. & Walter, P. Quantitative microscopy reveals dynamics and fate of clustered IRE1 α . *Proc. Natl. Acad. Sci.* **117**, 1533–1542 (2019).
304. Irving, L. *Arctic Life of Birds and Mammals*. (Springer Berlin Heidelberg, Berlin, Heidelberg, 1972).
305. Hazel, J. R. Thermal adaptation in biological membranes: Is homeoviscous adaptation the explanation? *Annu. Rev. Physiol.* **57**, 19–42 (1995).
306. Los, D. A. & Murata, N. Membrane fluidity and its roles in the perception of environmental signals. *Biochim. Biophys. Acta BBA - Biomembr.* **1666**, 142–157 (2004).
307. Mendoza, D. D. Temperature sensing by membranes. *Annu. Rev. Microbiol.* **68**, 101–116 (2014).
308. Ma, D. K. *et al.* Acyl-CoA dehydrogenase drives heat adaptation by sequestering fatty acids. *Cell* **161**, 1152–1163 (2015).
309. Svensk, E. *et al.* *Caenorhabditis elegans* PAQR-2 and IGLR-2 protect against glucose toxicity by modulating membrane lipid composition. *PLOS Genet.* **12**, e1005982 (2016).
310. Brankatschk, M. *et al.* A Temperature-dependent switch in feeding preference improves *Drosophila* development and survival in the cold. *Dev. Cell* **46**, 781–793 (2018).
311. Levental, K. R. *et al.* Lipidomic and biophysical homeostasis of mammalian membranes counteracts dietary lipid perturbations to maintain cellular fitness. *Nat. Commun.* **11**, 1339 (2020).
312. Holm, H. C. *et al.* Global ocean lipidomes show a universal relationship between temperature and lipid unsaturation. *Science* **376**, 1487–1491 (2022).
313. Zhang, S., Skalsky, Y. & Garfinkel, D. J. *MGA2* or *SPT23* is required for transcription of the $\Delta 9$ fatty acid desaturase gene, *OLE1*, and nuclear membrane integrity in *Saccharomyces cerevisiae*. *Genetics* **151**, 473–483 (1999).
314. Hoppe, T., Rape, M. & Jentsch, S. Membrane-bound transcription factors: regulated release by RIP or RUP. *Curr. Opin. Cell Biol.* **13**, 344–348 (2001).
315. Shcherbik, N., Kee, Y., Lyon, N., Huibregtse, J. M. & Haines, D. S. A single PXY motif located within the carboxyl terminus of Spt23p and Mga2p mediates a physical and functional interaction with ubiquitin ligase Rsp5p. *J. Biol. Chem.* **279**, 53892–53898 (2004).
316. Bhattacharya, S. *et al.* Identification of lysines within membrane-anchored Mga2p120 that are targets of Rsp5p ubiquitination and mediate mobilization of tethered Mga2p90. *J. Mol. Biol.* **385**, 718–725 (2009).
317. Ameloot, M. *et al.* Effect of orientational order on the decay of the fluorescence anisotropy in membrane suspensions. Experimental verification on unilamellar vesicles and lipid/ α -lactalbumin complexes. *Biophys. J.* **46**, 525–539 (1984).
318. Poojari, C. *et al.* Behavior of the DPH fluorescence probe in membranes perturbed by drugs. *Chem. Phys. Lipids* **223**, 104784 (2019).
319. Lentz, B. R. Membrane “fluidity” as detected by diphenylhexatriene probes. *Chem. Phys. Lipids* **50**, 171–190 (1989).
320. Chiantia, S., Ries, J. & Schwille, P. Fluorescence correlation spectroscopy in membrane structure elucidation. *Biochim. Biophys. Acta BBA - Biomembr.* **1788**, 225–233 (2009).
321. Honigsmann, A., Mueller, V., Hell, S. W. & Eggeling, C. STED microscopy detects and quantifies liquid phase separation in lipid membranes using a new far-red emitting fluorescent phosphoglycerolipid analogue. *Faraday Discuss* **161**, 77–89 (2013).

322. Cogan, U., Shinitzky, M., Weber, G. & Nishida, T. Microviscosity and order in the hydrocarbon region of phospholipid and phospholipid-cholesterol dispersions determined with fluorescent probes. *Biochemistry* **12**, 521–528 (1973).
323. Klymchenko, A. S. & Kreder, R. Fluorescent probes for lipid rafts: from model membranes to living cells. *Chem. Biol.* **21**, 97–113 (2014).
324. Edidin, M. Rotational and translational diffusion in membranes. *Annu. Rev. Biophys. Bioeng.* **3**, 179–201 (1974).
325. Quon, E. *et al.* Endoplasmic reticulum-plasma membrane contact sites integrate sterol and phospholipid regulation. *PLOS Biol.* **16**, e2003864 (2018).
326. Schuck, S., Prinz, W. A., Thorn, K. S., Voss, C. & Walter, P. Membrane expansion alleviates endoplasmic reticulum stress independently of the unfolded protein response. *J. Cell Biol.* **187**, 525–536 (2009).
327. Harding, H. P., Zhang, Y. & Ron, D. Protein translation and folding are coupled by an endoplasmic-reticulum-resident kinase. *Nature* **397**, 271–274 (1999).
328. Hetz, C., Zhang, K. & Kaufman, R. J. Mechanisms, regulation and functions of the unfolded protein response. *Nat. Rev. Mol. Cell Biol.* **21**, 421–438 (2020).
329. Fonseca, S. G., Gromada, J. & Urano, F. Endoplasmic reticulum stress and pancreatic β -cell death. *Trends Endocrinol. Metab.* **22**, 266–274 (2011).
330. Kimata, Y. & Kohno, K. Endoplasmic reticulum stress-sensing mechanisms in yeast and mammalian cells. *Curr. Opin. Cell Biol.* **23**, 135–142 (2011).
331. Surani, M. A. Glycoprotein synthesis and inhibition of glycosylation by tunicamycin in preimplantation mouse embryos: Compaction and trophoblast adhesion. *Cell* **18**, 217–227 (1979).
332. Bernales, S., Schuck, S. & Walter, P. ER-phagy: Selective autophagy of the endoplasmic reticulum. *Autophagy* **3**, 285–287 (2007).
333. Hsu, J.-W. *et al.* Unfolded protein response regulates yeast small GTPase Arl1p activation at late Golgi via phosphorylation of Arf GEF Syt1p. *Proc. Natl. Acad. Sci.* **113**, E1683–E1690 (2016).
334. Kawahara, T., Yanagi, H., Yura, T. & Mori, K. Endoplasmic reticulum stress-induced mRNA splicing permits synthesis of transcription factor Hac1p/Ern4p that activates the unfolded protein response. *Mol. Biol. Cell* **8**, 1845–1862 (1997).
335. Fu, S. *et al.* Aberrant lipid metabolism disrupts calcium homeostasis causing liver endoplasmic reticulum stress in obesity. *Nature* **473**, 528–531 (2011).
336. Gaspar, M. L., Hofbauer, H. F., Kohlwein, S. D. & Henry, S. A. Coordination of storage lipid synthesis and membrane biogenesis. *J. Biol. Chem.* **286**, 1696–1708 (2011).
337. West, M., Zurek, N., Hoenger, A. & Voeltz, G. K. A 3D analysis of yeast ER structure reveals how ER domains are organized by membrane curvature. *J. Cell Biol.* **193**, 333–346 (2011).
338. Choudhary, V., El Atab, O., Mizzon, G., Prinz, W. A. & Schneider, R. Seipin and Nem1 establish discrete ER subdomains to initiate yeast lipid droplet biogenesis. *J. Cell Biol.* **219**, e201910177 (2020).
339. Joshi, A. S. *et al.* Lipid droplet and peroxisome biogenesis occur at the same ER subdomains. *Nat. Commun.* **9**, 2940 (2018).
340. Lee, M. C. S., Miller, E. A., Goldberg, J., Orci, L. & Schekman, R. Bi-directional protein transport between the ER and Golgi. *Annu. Rev. Cell Dev. Biol.* **20**, 87–123 (2004).
341. Prinz, W. A., Toulmay, A. & Balla, T. The functional universe of membrane contact sites. *Nat. Rev. Mol. Cell Biol.* **21**, 7–24 (2020).
342. Hollien, J. Evolution of the unfolded protein response. *Biochim. Biophys. Acta BBA - Mol. Cell Res.* **1833**, 2458–2463 (2013).
343. Ho, N. *et al.* Stress sensor Ire1 deploys a divergent transcriptional program in response to lipid bilayer stress. *J. Cell Biol.* **219**, e201909165 (2020).
344. Han, S., Lone, M. A., Schneider, R. & Chang, A. Orm1 and Orm2 are conserved endoplasmic reticulum membrane proteins regulating lipid homeostasis and protein quality control. *Proc. Natl. Acad. Sci.* **107**, 5851–5856 (2010).
345. Ishiwata-Kimata, Y., Le, Q. G. & Kimata, Y. Induction and aggravation of the endoplasmic-reticulum stress by membrane-lipid metabolic intermediate phosphatidyl-N-monomethylethanolamine. *Front. Cell Dev. Biol.* **9**, 743018 (2022).
346. Tran, D. M., Ishiwata-Kimata, Y., Mai, T. C., Kubo, M. & Kimata, Y. The unfolded protein response alongside the diauxic shift of yeast cells and its involvement in mitochondria enlargement. *Sci. Rep.* **9**, 12780 (2019).

347. V  th, K. *et al.* Cysteine cross-linking in native membranes establishes the transmembrane architecture of Ire1. *J. Cell Biol.* **220**, e202011078 (2021).
348. Fonseca, S. G., Burcin, M., Gromada, J. & Urano, F. Endoplasmic reticulum stress in β -cells and development of diabetes. *Curr. Opin. Pharmacol.* **9**, 763–770 (2009).
349. Celik, C., Lee, S. Y. T., Yap, W. S. & Thibault, G. Endoplasmic reticulum stress and lipids in health and diseases. *Prog. Lipid Res.* **89**, 101198 (2023).
350. Weber, T. *et al.* SNAREpins: Minimal machinery for membrane fusion. *Cell* **92**, 759–772 (1998).
351. Bretscher, M. S. & Munro, S. Cholesterol and the Golgi apparatus. *Science* **261**, 1280–1281 (1993).
352. Herzig, Y., Sharpe, H. J., Elbaz, Y., Munro, S. & Schuldiner, M. A systematic approach to pair secretory cargo receptors with their cargo suggests a mechanism for cargo selection by Erv14. *PLoS Biol.* **10**, e1001329 (2012).
353. Cohen, N. *et al.* Iron affects Ire1 clustering propensity and the amplitude of endoplasmic reticulum stress signaling. *J. Cell Sci.* **130**, 3222–3233 (2017).
354. Werner-Washburne, M. & Singer, R. A. Stationary phase in the yeast *Saccharomyces cerevisiae*. *Microbiol. Rev.* **57**, 383–401 (1993).
355. Wiemken, A., Matile, P. & Moor, H. Vacuolar dynamics in synchronously budding yeast. *Arch. F  r Mikrobiol.* **70**, 89–103 (1970).
356. Levental, I. *et al.* Cholesterol-dependent phase separation in cell-derived giant plasma-membrane vesicles. *Biochem. J.* **424**, 163–167 (2009).
357. Sezgin, E. *et al.* Partitioning, diffusion, and ligand binding of raft lipid analogs in model and cellular plasma membranes. *Biochim. Biophys. Acta BBA - Biomembr.* **1818**, 1777–1784 (2012).
358. Keller, H., Lorizate, M. & Schwille, P. PI(4,5)P₂ degradation promotes the formation of cytoskeleton-free model membrane systems. *ChemPhysChem* **10**, 2805–2812 (2009).
359. Levental, K. R. & Levental, I. Giant plasma membrane vesicles: Models for understanding membrane organization. in *Current Topics in Membranes* vol. 75 25–57 (Elsevier, 2015).
360. Burns, M., Wisser, K., Wu, J., Levental, I. & Veatch, S. L. Miscibility transition temperature scales with growth temperature in a zebrafish cell line. *Biophys. J.* **113**, 1212–1222 (2017).
361. Tang, R.-J. *et al.* Conserved mechanism for vacuolar magnesium sequestration in yeast and plant cells. *Nat. Plants* **8**, 181–190 (2022).
362. Leveille, C. L., Cornell, C. E., Merz, A. J. & Keller, S. L. Yeast cells actively tune their membranes to phase separate at temperatures that scale with growth temperatures. *Proc. Natl. Acad. Sci. U. S. A.* **119**, e2116007119 (2022).
363. Fun, X. H. & Thibault, G. Lipid bilayer stress and proteotoxic stress-induced unfolded protein response deploy divergent transcriptional and non-transcriptional programmes. *Biochim. Biophys. Acta BBA - Mol. Cell Biol. Lipids* **1865**, 158449 (2020).
364. Phillips, R., Ursell, T., Wiggins, P. & Sens, P. Emerging roles for lipids in shaping membrane-protein function. *Nature* **459**, 379–385 (2009).
365. Liao, P.-C., Boldogh, I. R., Siegmund, S. E., Freyberg, Z. & Pon, L. A. Isolation of mitochondria from *Saccharomyces cerevisiae* using magnetic bead affinity purification. *PLOS ONE* **13**, e0196632 (2018).
366. Sokoya, T. *et al.* Pathogenic variants of sphingomyelin synthase SMS2 disrupt lipid landscapes in the secretory pathway. *eLife* **11**, e79278 (2022).
367. Van 'T Klooster, J. S. *et al.* Periprotein lipidomes of *Saccharomyces cerevisiae* provide a flexible environment for conformational changes of membrane proteins. *eLife* **9**, e57003 (2020).
368. Tsuji, T. *et al.* Predominant localization of phosphatidylserine at the cytoplasmic leaflet of the ER, and its TMEM16K-dependent redistribution. *Proc. Natl. Acad. Sci.* **116**, 13368–13373 (2019).
369. Quiroga, R., Trenchi, A., Montoro, A. G., Taubas, J. V. & Maccioni, H. J. F. Short length transmembrane domains having voluminous exoplasmic halves determine retention of Type II membrane proteins in the Golgi complex. *J. Cell Sci.* **126**, 5344–5349 (2013).
370. Borgese, N. Getting membrane proteins on and off the shuttle bus between the endoplasmic reticulum and the Golgi complex. *J. Cell Sci.* **129**, 1537–1545 (2016).
371. Weigel, A. V. *et al.* ER-to-Golgi protein delivery through an interwoven, tubular network extending from ER. *Cell* **184**, 2412–2429 (2021).
372. Wendland, B., Emr, S. D. & Riezman, H. Protein traffic in the yeast endocytic and vacuolar protein sorting pathways. *Curr. Opin. Cell Biol.* **10**, 513–522 (1998).

-
373. González Montoro, A. *et al.* Vps39 interacts with Tom40 to establish one of two functionally distinct vacuole-mitochondria contact sites. *Dev. Cell* **45**, 621–636 (2018).
 374. Gwosch, K. C. *et al.* MINFLUX nanoscopy delivers 3D multicolor nanometer resolution in cells. *Nat. Methods* **17**, 217–224 (2020).
 375. Schmidt, R. *et al.* MINFLUX nanometer-scale 3D imaging and microsecond-range tracking on a common fluorescence microscope. *Nat. Commun.* **12**, 1478 (2021).
 376. Deguchi, T. *et al.* Direct observation of motor protein stepping in living cells using MINFLUX. *Science* **379**, 1010–1015 (2023).

5. APPENDIX

These open-access articles are distributed under terms of the Creative Commons Attribution License (CC BY, <https://creativecommons.org/licenses/by/4.0/>):

Väth *et al.*, *Journal of Cell Biology* **220**, e202011078 (2021)
<https://doi.org/10.1083/jcb.202011078>

Ballweg *et al.*, *Nature Communications* **11**, 756 (2022)
<https://doi.org/10.1038/s41467-020-14528-1>

Reinhard *et al.*, *Frontiers in Cell and Developmental Biology* **8**, 756 (2020)
<https://doi.org/10.3389/fcell.2020.00756>

Reinhard *et al.*, *The EMBO Journal* **8**, 1653-1685 (2024)
<https://doi.org/10.1038/s44318-024-00063-y>

This open-access article is distributed under terms of the Creative Commons Attribution License (CC BY-NC-ND, <https://creativecommons.org/licenses/by-nc-nd/4.0/>):

Reinhard *et al.*, *Biophysical Journal* **122**, 1043–1057 (2023)
<https://doi.org/10.1016/j.bpj.2023.01.009>

ARTICLE

Cysteine cross-linking in native membranes establishes the transmembrane architecture of Ire1

Kristina Váth^{1,2*}, Carsten Mattes^{1,2*}, John Reinhard^{1,2*}, Roberto Covino³, Heike Stumpf^{1,2}, Gerhard Hummer^{4,5}, and Robert Ernst^{1,2}

The ER is a key organelle of membrane biogenesis and crucial for the folding of both membrane and secretory proteins. Sensors of the unfolded protein response (UPR) monitor the unfolded protein load in the ER and convey effector functions for maintaining ER homeostasis. Aberrant compositions of the ER membrane, referred to as lipid bilayer stress, are equally potent activators of the UPR. How the distinct signals from lipid bilayer stress and unfolded proteins are processed by the conserved UPR transducer Ire1 remains unknown. Here, we have generated a functional, cysteine-less variant of Ire1 and performed systematic cysteine cross-linking experiments in native membranes to establish its transmembrane architecture in signaling-active clusters. We show that the transmembrane helices of two neighboring Ire1 molecules adopt an X-shaped configuration independent of the primary cause for ER stress. This suggests that different forms of stress converge in a common, signaling-active transmembrane architecture of Ire1.

Introduction

The ER marks the entry point to the secretory pathway for soluble and membrane proteins. Under adverse conditions, accumulation of unfolded proteins causes ER stress and initiates the unfolded protein response (UPR). The UPR is mediated by the inositol-requiring enzyme 1 (Ire1) in budding yeast, and by the troika of IRE1 α , PKR-like ER kinase (PERK), and activating transcription factor 6 (ATF6) in vertebrates (Walter and Ron, 2011). Once activated, the UPR down-regulates the production of most proteins and initiates a wide transcriptional program to up-regulate ER chaperones, ER-associated degradation, and lipid biosynthesis (Travers et al., 2000). Through these mechanisms, the UPR is centrally involved in cell fate decisions between life, death, and differentiation (Hetz, 2012). Insulin-producing β -cells, for example, rely on UPR signals for their differentiation into professional secretory cells, while chronic ER stress caused by an excess of saturated fatty acids kills them (Fonseca et al., 2009). Consistent with its broad effector functions, the UPR is associated with numerous diseases including diabetes, cancer, and neurodegeneration (Kaufman, 2002).

Ire1 is highly conserved among eukaryotes and represents the only transducer of ER stress in budding yeast (Nikawa and Yamashita, 1992; Kimata and Kohno, 2011). It is a type I transmembrane protein equipped with an ER-luminal sensor domain and two cytosolic effector domains: a kinase and an RNase (Cox et al., 1993; Sidrauski and Walter, 1997; Mori et al., 1993). How exactly unfolded proteins activate the UPR via direct and

indirect mechanisms is a matter of active debate (Karagöz et al., 2017; Gardner and Walter, 2011; Adams et al., 2019; Amin-Wetzel et al., 2017; Le and Kimata, 2021). ER stress caused by the accumulation of unfolded proteins leads to the oligomerization of Ire1 (Kimata et al., 2007), which activates the cytosolic effector kinase and RNase domains (Korennykh et al., 2009). The unconventional splicing of the *HAC1* precursor mRNA initiated by the RNase domain facilitates the production of an active transcription factor that controls a broad spectrum of genes with unfolded protein response elements in their promoter regions (Travers et al., 2000; Mori et al., 1992). A regulated *IRE1*-dependent decay of mRNA has been suggested as a parallel mechanism to reduce the folding load of the ER. However, regulated *IRE1*-dependent decay of mRNA does not seem to play the same important role in *Saccharomyces cerevisiae* as it does in *Saccharomyces pombe* or mammalian cells (Travers et al., 2000; Hollien and Weissman, 2006; Frost et al., 2012; Tam et al., 2014; Li et al., 2018).

Lipid bilayer stress due to aberrant compositions of the ER membrane is equally potent in activating the UPR (Promlek et al., 2011; Volmer et al., 2013; Surma et al., 2013). This membrane-based mechanism is conserved throughout evolution (Ho et al., 2018; Hou et al., 2014; Volmer et al., 2013) and has been associated with pathogenesis of type II diabetes and the lipotoxicity associated with obesity (Fonseca et al., 2009; Pineau and Ferreira, 2010). We have shown that Ire1 from baker's yeast

¹Medical Biochemistry and Molecular Biology, Medical Faculty, Saarland University, Homburg, Germany; ²Preclinical Center for Molecular Signaling, Medical Faculty, Saarland University, Homburg, Germany; ³Frankfurt Institute of Advanced Sciences, Goethe-University, Frankfurt, Germany; ⁴Department of Theoretical Biophysics, Max Planck Institute of Biophysics, Frankfurt, Germany; ⁵Institute of Biophysics, Goethe-University, Frankfurt, Germany.

*K. Váth, C. Mattes, and J. Reinhard contributed equally to this paper; Correspondence to Robert Ernst: robert.ernst@uks.eu.

© 2021 Váth et al. This article is available under a Creative Commons License (Attribution 4.0 International, as described at <https://creativecommons.org/licenses/by/4.0/>).

inserts an amphipathic helix (AH) into the luminal leaflet of the ER membrane, thereby forcing the short, adjacent transmembrane helix (TMH) to tilt, which locally squeezes the bilayer (Halbleib et al., 2017). Aberrant stiffening of the ER membrane during lipid bilayer stress increases the free energy penalty for membrane deformations, thereby stabilizing oligomeric assemblies of Ire1 via a membrane-based mechanism (Halbleib et al., 2017; Ernst et al., 2018). Even though it is well-established that proteotoxic and lipid bilayer stress leads to the formation of Ire1 clusters (Kimata et al., 2007; Halbleib et al., 2017; Li et al., 2010; Belyy et al., 2020), it remains unexplored if these forms of ER stress have a distinct impact on the architecture of Ire1 within these clusters. It has been speculated that different forms of ER stress might induce conformational changes in the transmembrane region, thereby allowing Ire1/IRE1 α to mount custom-tailored adaptive programs (Hetz et al., 2020; Cho et al., 2019; Ho et al., 2020).

Here, we report on a systematic dissection of Ire1's TMH region in signaling-active clusters. We have engineered a cysteine-less variant for a genomic integration at the endogenous *IRE1* locus and generated a series of constructs featuring single cysteines in the TMH region. This enabled us to develop a cross-linking approach and to study the transmembrane configuration of Ire1 in the natural environment of ER-derived membrane vesicles featuring a native complexity of lipids and proteins. This approach uncovers the overall transmembrane architecture of Ire1 and suggests an X-shaped configuration of the TMHs of neighboring Ire1 molecules. Our findings underscore the crucial importance of Ire1's highly bent configuration in the TMH region for stabilizing an oligomeric state via a membrane-mediated mechanism. Most importantly, we provide direct evidence that proteotoxic and lipid bilayer stress converge in common architecture of the TMH region in signaling-active Ire1.

Results

We used systematic cysteine cross-linking in the TMH region of Ire1 to gain insight into the structural organization of signaling-active clusters during ER stress. Recognizing that Ire1 is activated by aberrant physicochemical membrane properties (Halbleib et al., 2017; Ernst et al., 2018), which are hard to mimic *in vitro*, we performed these experiments with microsomes exhibiting the natural complexity of ER proteins and lipids.

Cysteine-less Ire1 is functional

We have generated a cysteine-less version of Ire1 that allows us to introduce single-cysteine residues in the TMH region for subsequent cross-linking using copper sulfate (CuSO₄). The cysteine-less construct is based on a previously established knock-in construct of *IRE1* that provides homogeneous, near-endogenous expression (Halbleib et al., 2017) and encodes for a fully functional variant of Ire1 equipped with an 3xHA tag and a monomeric, yeast-enhanced GFP (yeGFP) inserted in a flexible loop at the position H875 (Fig. 1 A; van Anken et al., 2014; Halbleib et al., 2017). To generate a cysteine-less version, we substituted each of the 12 cysteines in the luminal,

transmembrane, and cytosolic domains with serine. Two cysteines in the signal sequence, which are cotranslationally removed, remained in the final construct to ensure correct ER targeting and membrane insertion (Fig. 1 A). Cysteine 48 of yeGFP (C48^{yeGFP}) was mutated to serine, while C70^{yeGFP} is present in the cysteine-less construct to ensure correct folding of the fluorescent protein (Costantini et al., 2015). Notably, C70^{yeGFP} is buried inside the GFP (Ormö et al., 1996) and thus inaccessible for cross-linking agents under non-denaturing conditions.

The steady-state levels of WT and cysteine-less Ire1 are comparable (Fig. S1 A). Cysteine-less Ire1 is properly integrated into the membrane as shown by subcellular fractionation (Fig. S1 B) and extraction assays (Fig. S1 C), thereby matching previous observations for WT Ire1 (Kimata et al., 2007; Halbleib et al., 2017). The functionality of cysteine-less Ire1 was analyzed using a sensitive assay scoring for the growth of cells exposed to inducers of ER stress (Halbleib et al., 2017). Liquid cultures in either minimal (synthetic complete dextrose [SCD]) or full (yeast peptone dextrose [YPD]) medium were exposed to different concentrations of the reducing agent DTT interfering with disulfide bridge formation in the ER. After 18 h of cultivation, the ODs of these cultures were determined. Cells producing either WT or cysteine-less Ire1 are phenotypically indistinguishable by this assay and substantially more resistant to DTT than cells lacking *IRE1* (Fig. 1 B). This suggests that cysteine-less Ire1 is functional and capable of mounting an adaptive UPR.

The functionality of cysteine-less Ire1 was further validated by quantifying the mRNA levels of spliced *HAC1* (Fig. 1 C) and the mRNA level of the UPR target gene *PDI1* (Fig. S1 D) in both stressed and unstressed cells. We used either DTT or tunicamycin (TM), an inhibitor of N-linked glycosylation, to induce proteotoxic stress for 1 h and analyzed lysates from stressed and unstressed cells by RT-quantitative PCR (RT-qPCR). As expected, the level of the spliced *HAC1* mRNA was several-fold higher in stressed versus unstressed cells, and this up-regulation is observed in both WT and cysteine-less Ire1-producing cells (Fig. 1 C). Control experiments also validated a comparable degree of *HAC1* mRNA splicing in WT or cysteine-less Ire1-producing cells stressed with DTT (Fig. S1 D). We also observed an up-regulation of the *PDI1* mRNA in response to ER stress, albeit to slightly lower extent for the cysteine-less version compared with the WT construct (Fig. S1 E). Using confocal microscopy and by applying an automated pipeline to identify cells with and without fluorescent clusters, we show that both cysteine-less and WT Ire1 cluster under conditions of ER stress, but not in unstressed cells (Fig. 1 D). Notably, confocal microscopy can only identify large clusters of Ire1, while dimers and smaller assemblies escape our detection. Furthermore, the detection of Ire1 in unstressed cells is particularly challenging in our case, because our knock-in strategy aims to provide a close to endogenous level of *IRE1* expression (Halbleib et al., 2017). This is important because even the mild degree of overexpression when using an endogenous promoter from a yeast centromere (*CEN*)-based plasmid (Karim et al., 2013) is likely to interfere with normal UPR function by favoring dimerization and oligomerization. Using our setup, we robustly detect GFP-positive clusters of Ire1 (Fig. 1 D) in stressed cells,

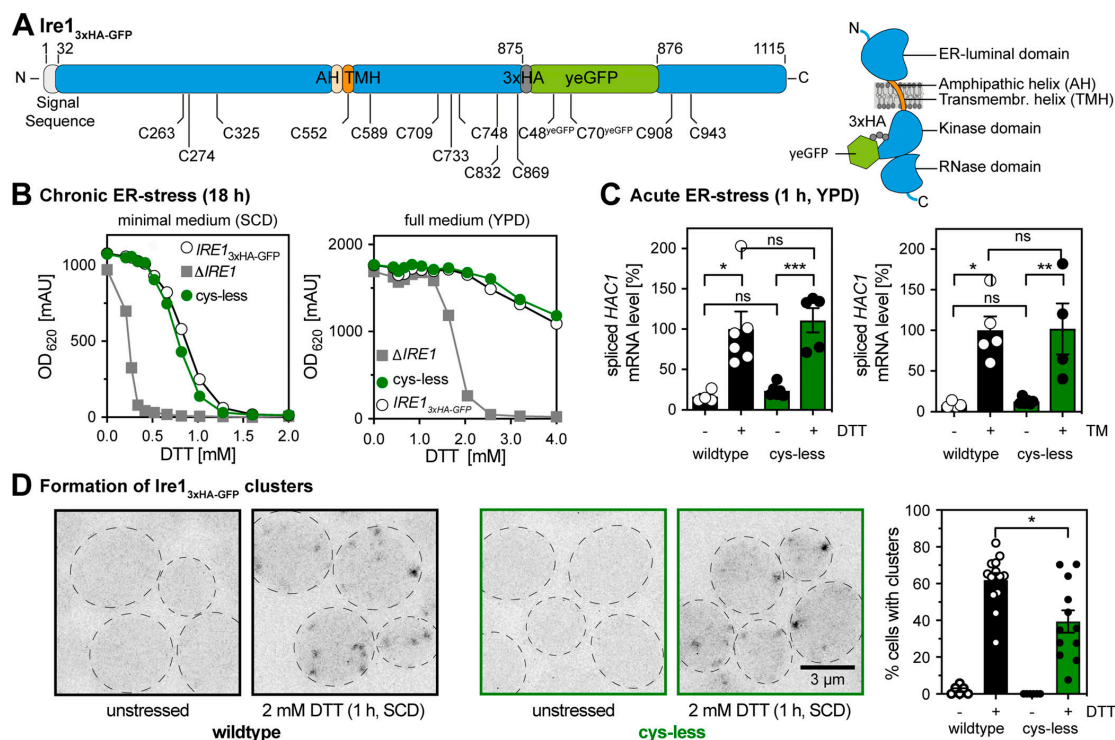


Figure 1. Cysteine-less Ire1 expressed from its endogenous locus is functional. (A) Schematic representations of the *IRE1*^{3xHA-GFP} construct indicating the position of cysteine residues and topology. All 12 cysteines of Ire1 and C48^{yeGFP} of yeGFP were substituted to serine to generate a cysteine-less variant. C70^{yeGFP} remains in the final construct. Two cysteines in the signal sequence of Ire1 are removed upon ER translocation. (B) Resistance of the indicated strains to prolonged ER stress. Stationary overnight cultures of the indicated strains were used to inoculate a fresh culture in full or minimal media to an OD₆₀₀ of 0.2. After cultivation for 5–7 h at 30°C, the cells were diluted with prewarmed full or minimal media to an OD₆₀₀ of 0.01. Cells were cultivated for 18 h at 30°C in the indicated media and stressed with DTT. The density of the resulting culture was determined using the OD₆₂₀ or OD₆₀₀. Number of experiments in SCD (left): Δ *IRE1*, WT ($n = 20$), and cysteine-less ($n = 12$, each from four individual colonies). Number of experiments in YPD (right): Δ *IRE1* ($n = 14$ from three colonies), cysteine-less ($n = 12$ from four colonies), and WT ($n = 9$ from three colonies). (C) The relative level of the spliced *HAC1* mRNA was determined by RT-qPCR in unstressed and acutely stressed cells. Exponentially growing cells of the indicated strains were used to inoculate a fresh culture in YPD medium to an OD₆₀₀ of 0.2. After cultivation to an OD₆₀₀ of 0.7, the cells were stressed for 1 h with either 4 mM DTT (left) or 1.0 μ g/ml TM (right). The data were normalized to the level of the spliced *HAC1* mRNA in DTT-stressed cells with the *IRE1*^{3xHA-GFP} WT construct. Number of experiments (left): WT -DTT: $n = 4$; WT +DTT: $n = 6$; cysteine-less -DTT: $n = 6$; cysteine-less +DTT: $n = 5$. Number of experiments (right): WT -TM: $n = 4$; WT +TM: $n = 5$; cysteine-less -TM: $n = 6$; cysteine-less +TM: $n = 4$. (D) Cells were cultivated from OD₆₀₀ of 0.2 to OD₆₀₀ of 0.7 in SCD medium and then either left untreated or stressed with 2 mM DTT for 1 h. Live cells were mounted on agar slides, and z-stacks were recorded using confocal microscopy. Cells and clusters of Ire1 were automatically detected and quantified. All data are represented as the mean \pm SEM of three independent experiments. WT -DTT: ($n = 6$ fields of view/172 cells); WT +DTT: ($n = 13/302$); cysteine-less -DTT: ($n = 6/209$); cysteine-less +DTT: ($n = 12/326$). Significance was tested by an unpaired, two-tailed Student's *t* test (data distribution was assumed to be normal, but this was not formally tested), except for C, which was analyzed using a Kolmogorov-Smirnov test. *, $P < 0.05$; **, $P < 0.01$; ***, $P < 0.001$.

while the tendency of clustering is somewhat lower for the cysteine-less Ire1 compared with the WT (Fig. 1 D). Colocalization of GFP-positive clusters with an ER-targeted variant of dsRed-HDEL confirms the ER localization of WT and cysteine-less Ire1 in DTT-stressed cells (Fig. S1 F). In line with the functional data (Fig. 1, B and C), we conclude that both WT and cysteine-less Ire1 can mount robust responses to acute and prolonged forms of ER stress.

Cross-linking of Ire1's TMH in ER-derived microsomes

We established a strategy to cross-link single-cysteine variants of Ire1 via CuSO₄ in microsomes derived from the ER of stressed

cells (Fig. 2, A–C). Our approach has several advantages over previous attempts: Ire1 is studied (i) as a full-length protein, (ii) at the near-endogenous level, (iii) in its natural, complex membrane environment, (iv) with a spatial resolution of one residue, and (v) in a signaling-active state. In contrast to mercury chloride (HgCl₂), which cross-links by forming covalent bonds with two nearby cysteines (Soskine et al., 2002), CuSO₄ is “traceless” by catalyzing the oxygen-dependent formation of a disulfide bond (Bass et al., 2007). We performed the cross-linking experiments on ice and with CuSO₄ (instead of the more reactive Cu²⁺-phenanthroline) to prevent the loss of signal from unspecific cross-linking and/or aggregation. Even though

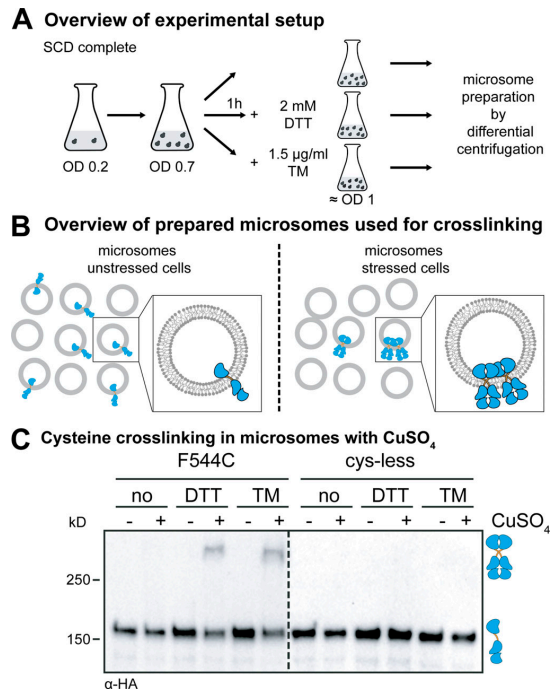


Figure 2. The cross-linking of Ire1 via single cysteines in microsomes requires CuSO₄ and preformed clusters. (A) Cultivation of yeast cells for cysteine cross-linking. A culture in SCD medium was inoculated with stationary cells to an OD₆₀₀ of 0.2. After cultivation at 30°C to an OD₆₀₀ of 0.7, the clustering of Ire1 was induced either by DTT (1 h, 2 mM, SCD) or TM (1 h, 1.5 µg/ml, SCD) as indicated. After harvesting, the cells were lysed and used to prepare microsomes. (B) Schematic representation of the cysteine cross-linking with CuSO₄. Only microsomes from stressed cells contain clusters of Ire1 clusters that can cross-link via cysteines using CuSO₄. (C) Cross-linking of a single-cysteine variant of Ire1 in microsomes. The indicated strains were cultivated in the presence and absence of ER stressors as described in A. 80 OD equivalents of cells were harvested, and microsomes were prepared. 8 µl microsomes (1 mg/ml protein) was mixed with 2 µl of 50 mM CuSO₄, and the sample was incubated on ice for 5 min to catalyze cysteine cross-linking. The reaction was stopped by the addition of 2 µl 1 M NEM, 2 µl 0.5 M EDTA, and 4 µl membrane sample buffer. The resulting samples were analyzed by SDS-PAGE and immunoblotting using anti-HA antibodies.

every cross-linking approach on membrane proteins faces the challenge of varying efficiencies at different depths in the membrane, Cu²⁺-mediated cross-linking has been successfully used to interrogate and establish structure–function relationships of membrane proteins (Falke and Koshland, 1987; Bass et al., 2007; Matthews et al., 2011; Lopez-Redondo et al., 2018). Here we have studied the configuration of Ire1's TMH in UPR-signaling clusters, which are long-lived and stable for minutes (Kimata et al., 2007; Cohen et al., 2017). Because CuSO₄-mediated cross-linking occurs on the same time scale, it can provide useful structural information even though it leads to the formation of covalent disulfide bonds under our experimental conditions.

Cells expressing either a cysteine-less variant of Ire1 or a variant with a single cysteine in the TMH region (F544C) were

cultivated to the mid-exponential phase in minimal medium (Fig. 2 A). These cells were either left untreated or stressed for 1 h with either DTT (2 mM) or TM (1.5 µg/ml) to cause ER stress, which leads to the formation of Ire1 clusters (Kimata et al., 2007; Halbleib et al., 2017; Belyy et al., 2020). We used such an early time point to minimize the contribution of secondary effects from stress- and UPR-dependent reprogramming of the cell. We then isolated crude microsomes from these cells and incubated them on ice for 5 min either in the presence or absence of 10 mM CuSO₄ to catalyze the formation of disulfide bonds by oxidizing nearby sulfhydryl groups (Kobashi, 1968). Given the low copy number of ~260 for Ire1 (Ghaemmaghami et al., 2003) and the fragmentation of the ER during microsome preparation, we expected to detect cross-linking of single-cysteine variants of Ire1 only when it was clustered before the preparation (Fig. 2 B).

Immunoblotting of the resulting samples revealed a prominent, HA-positive signal corresponding to monomeric Ire1 and a less-pronounced HA-positive signal from a band with lower electrophoretic mobility that was only observed when (i) Ire1 contained a single cysteine in the TMH region (F544C), (ii) the microsomes were prepared from stressed cells (either DTT or TM), and (iii) cross-linking was facilitated by CuSO₄ (Fig. 2 C). This suggests a remarkably specific formation of covalent, disulfide bonds between two Ire1 molecules in the TMH region, despite the presence of numerous other, potentially competing membrane proteins with exposed cysteines in the ER. The observed degree of cross-linking was somewhat low considering that up to 70–85% of Ire1 may reside in signaling-active clusters under conditions of ER stress (Aragón et al., 2009). For our cross-linking approach, however, we used a slightly milder condition to induce ER stress (2 mM DTT instead of 10 mM) and performed all experiments with an *IRE1* knock-in strain that provides a more native-like expression level (Halbleib et al., 2017; Aragón et al., 2009). Notably, the signal from the cross-linked species was increased by neither the use of more reactive cross-linking agents (e.g., HgCl₂ or Cu²⁺-phenanthroline) nor by harsher cross-linking conditions (higher temperatures or increased concentrations of the cross-linking agent). In fact, more reactive agents and harsher conditions only caused a loss of the total HA-positive signal, presumably due to an unspecific cross-linking and/or aggregation of Ire1 (data not shown). A co-immunoprecipitation analysis using Flag- and HA-tagged Ire1 variants produced in the same cell and cross-linked in microsomes via the native cysteine (C552) verified that the additional band with low electrophoretic mobility represents disulfide-linked, SDS-resistant dimers of Ire1 (Fig. S2 A). In fact, treating a cross-linked species of Ire1 with heat under reducing conditions revealed full reversibility of disulfide bond formation (Fig. S2 B). We conclude that CuSO₄ can catalyze the formation of disulfide bridges between two neighboring Ire1 molecules, when they are present in preformed clusters and isolated in microsomes from stressed cells.

A cross-linking screen in the TMH region of Ire1

Next, we generated a set of 13 mutant variants of Ire1, each containing a single cysteine in the TMH region starting with E540C at the transition between the AH and the TMH (Fig. 3 A)

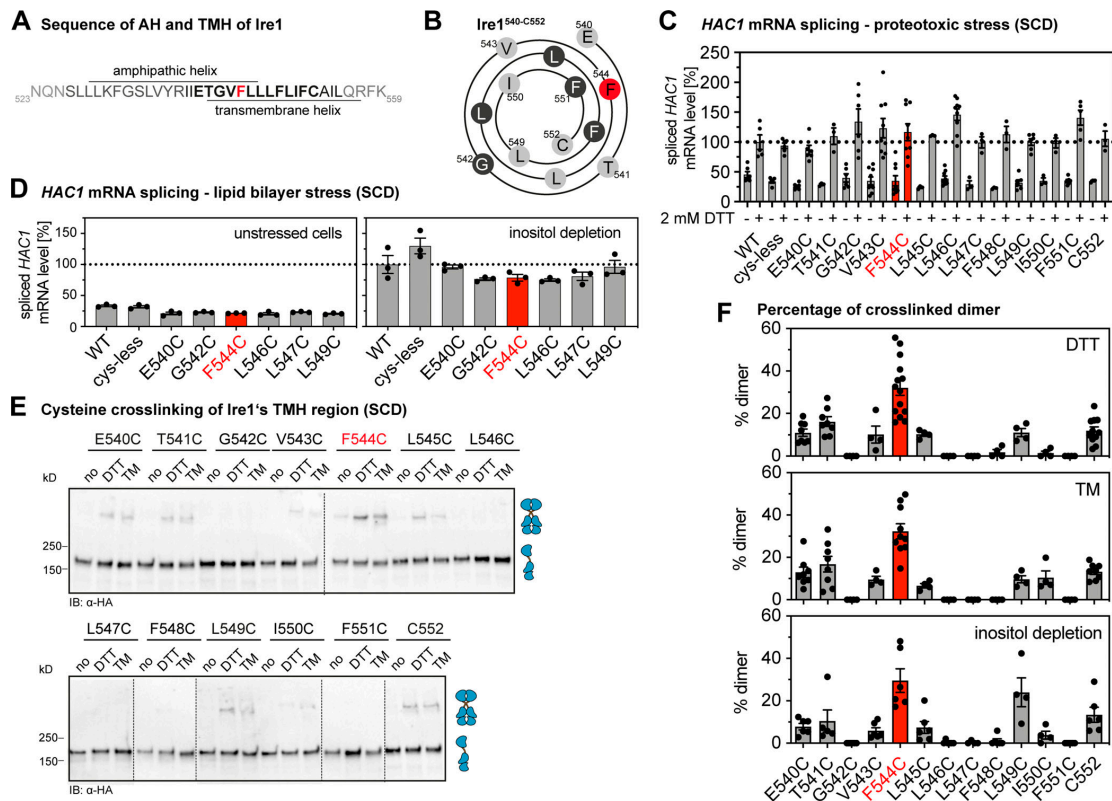


Figure 3. Systematic cross-linking of cysteines in the TMH region of Ire1 reveals a specific configuration during ER stress. (A) Primary structure of ER-luminal AH of Ire1 and the short TMH. Almost every residue of the short TMH (shown in bold) was substituted individually by cysteine for the cysteine cross-linking strategy. (B) Helical wheel representation of Ire1's TMH (Ire1⁵⁴⁰⁻⁵⁵²). (C) The level of the spliced *HAC1* mRNA was determined from the indicated strains by RT-qPCR for either unstressed cells or cells stressed with 2 mM DTT for 1 h (for details, see E). The data are normalized to the level of the spliced *HAC1* mRNA in stressed cells with a tagged, WT variant of Ire1. Number of independent experiments with technical duplicates for +DTT condition: WT: *n* = 5; cysteine-less: *n* = 6; E540C: *n* = 6; T541C: *n* = 3; G542C: *n* = 6; V543C: *n* = 9; F544C: *n* = 9; L545C: *n* = 3; L546C: *n* = 9; L547C: *n* = 3; F548C: *n* = 3; L549C: *n* = 6; I550C: *n* = 3; F551C: *n* = 5; C552: *n* = 3. Number of experiments with technical duplicates for the unstressed, -DTT condition: WT: *n* = 6; cysteine-less: *n* = 5; E540C: *n* = 6; T541C: *n* = 3; G542C: *n* = 6; V543C: *n* = 9; F544C: *n* = 9; L545C: *n* = 3; L546C: *n* = 9; L547C: *n* = 3; F548C: *n* = 3; L549C: *n* = 6; I550C: *n* = 3; F551C: *n* = 6; C552: *n* = 3. (D) The level of the spliced *HAC1* mRNA was determined from the indicated strains by qPCR using stressed (inositol-depleted) and unstressed cells. The data are normalized to the level of the spliced *HAC1* mRNA splicing caused by 2 mM DTT, as determined in C. Number of independent experiments with technical duplicates for the condition of inositol depletion: WT: *n* = 3; cysteine-less: *n* = 3; E540C: *n* = 3; G542C: *n* = 3; F544C: *n* = 3; L546C: *n* = 3; L547C: *n* = 3; L549C: *n* = 3. Number of independent experiments with technical duplicates for the unstressed condition: WT: *n* = 3; cysteine-less: *n* = 3; E540C: *n* = 3; G542C: *n* = 3; F544C: *n* = 3; L546C: *n* = 3; L547C: *n* = 3; L549C: *n* = 3. (E) A culture in SCD medium was inoculated with stationary cells to an OD₆₀₀ of 0.2. After cultivation at 30°C to an OD₆₀₀ of 0.7, Ire1 clustering was induced by either DTT (1 h, 2 mM, SCD) or TM (1 h, 1.5 μg/ml, SCD). 8 μl microsomes (1 mg/ml protein) from unstressed (no) and stressed cells was mixed with 2 μl of 50 mM CuSO₄, and the sample was incubated on ice for 5 min to catalyze cysteine cross-linking. The reaction was stopped, and the sample was analyzed by SDS-PAGE and immunoblotting using anti-HA antibodies. (F) Quantification of cysteine cross-linking of the indicated variants of Ire1 in microsomes isolated cells stressed by DTT, TM, or inositol depletion. Cells were cultivated and treated as described in E. For inositol depletion, a culture was inoculated with exponentially growing cells to an OD₆₀₀ of 0.5 and cultivated for 3 h at 30°C in inositol-free medium (a representative immunoblot after cross-linking is shown in Fig. S3 B). The percentage of cross-linked species was determined by densitometry. Data are represented as the mean ± SEM of at least three independent experiments. IB, immunoblot.

and ending at the native C552, which is substituted to serine in cysteine-less Ire1. Our scanning approach covered more than three helical turns and almost the entire short TMH of Ire1 (Fig. 3, A and B). Systematic cross-linking of these variants can provide important insight into the organization of Ire1's TMH in signaling-active clusters. An important prerequisite for a structural interpretation is that the single-cysteine substitutions

required to form the cross-links affect neither the oligomerization nor the activity of Ire1.

We therefore subjected all Ire1 variants with engineered cysteine residues (E540C to F551C) to a sensitive, cell-based assay to ascertain the functionality of the UPR under conditions of prolonged ER stress (Fig. S3 A). Consistent with the functional role of the AH adjacent to the short TMH (Halbleib

et al., 2017), we found that the substitution of AH residues to cysteine (E540C, T541C, or G542C) impaired the response to ER stress, as evident from an increased sensitivity of the respective cells to DTT (Fig. S3 A). The substitution of TMH residues (V543C-F551C), by contrast, did not cause any apparent functional defect (Fig. S3 A). Hence, these TMH variants are suitable to map the transmembrane architecture via cysteine cross-linking. To validate the functionality of these variants with a more direct assay, we systematically quantified the level of the spliced *HAC1* mRNA in stressed and unstressed cells under conditions of both proteotoxic (Fig. 3 C) and lipid bilayer stress (Fig. 3 D), which is caused by inositol depletion (Promlek et al., 2011; Surma et al., 2013). Because these data are normalized to the level of the spliced *HAC1* mRNA in DTT-stressed cells, it is possible to compare the UPR activity between these conditions (Fig. 3, C and D). We find a similar level of the *HAC1* mRNA in stressed cells and, consistently, a comparable degree of *HAC1* mRNA splicing in cells by either DTT or inositol depletion (Fig. S3 B). All single-cysteine variants were functional and responsive to proteotoxic stress (Fig. 3 C). Likewise, the subset of variants tested under conditions of lipid bilayer stress showed robust activation of the UPR (Fig. 3 D). Because the steady-state level of all Ire1 variants was also comparable (Fig. S3 C), we could proceed with mapping the TMH region.

We subjected the entire set of single-cysteine variants to the cysteine cross-linking procedure (Fig. 3 E and Fig. S3 D) and determined the fraction of cross-linked Ire1 for construct (Fig. 3 F). While some variants (e.g., G542C or L546C) showed no detectable cross-linking, a significant portion of them (e.g., T541C or L549C) could be cross-linked under the given experimental conditions (Fig. 3, E and F). The F544C variant consistently exhibited the highest cross-linking efficiency (Fig. 3 F). Notably, the differences in cross-linking are not caused by an aberrant oligomerization of Ire1, because confocal microscopy experiments with cells cultivated and treated as in the cross-linking experiments demonstrate the same degree of cluster formation of all single-cysteine variants upon ER stress as judged by cluster size and intensity and compared with cysteine-less Ire1 (Fig. S3, D-F).

Different forms of ER stress converge in a common architecture of the TMH region

Using the cross-linking assay, we could show that the overall pattern of cross-linking residues was independent of the condition of ER stress (Fig. 3 F). Lipid bilayer stress and proteotoxic stress induced by either DTT or TM show essentially the same cross-linking pattern (Fig. 3 F). These data strongly suggest that the overall structural organization of Ire1 is similar for different types of stress, at least in the TMH region. Notably, the L549C mutant showed significant cross-linking in cells stressed by DTT or TM, but even more during inositol depletion (Fig. 3 F). Because F544C, the best-cross-linking residue, and L549C seemingly lie on opposing sites of Ire1's TMH as judged from a helical wheel representation (Fig. 3 B), this raises the question of whether the corresponding residues in the native TMH can face each other at the same time. This point was addressed by molecular dynamics (MD) simulations further below.

Cysteine cross-linking can be used to infer structural models. The observed pattern of cross-linking residues in the TMH of Ire1 is very distinct from those observed in the TMH of the growth hormone receptor (Brooks et al., 2014) and the thrombopoietin receptor (Matthews et al., 2011), which form parallel dimers leading to a helical periodicity of cross-linking. Instead, our cross-linking data suggest an X-shaped configuration of the TMHs with the best cross-linking residue, F554, positioned at the crossing point. Intriguingly, such an arrangement would be consistent with the previously reported, highly tilted orientation of the monomeric TMH of Ire1, which is enforced by the adjacent, ER-luminal AH (Halbleib et al., 2017). However, it is important to realize that cross-links might occur either within dimers of Ire1 or across dimers in higher oligomeric assemblies.

To obtain a structural representation, we used an experimentally validated model of the monomeric TMH region of Ire1 (Halbleib et al., 2017), generated a model of the dimer based on extensive MD simulations in lipid membranes, and integrated the cross-linking data with a particular attention on the contact between the two F544 residues (Fig. 4, Video 1, and Video 2), which were restrained to face each other. The resulting model of the dimeric TMH region highlighted a highly bent configuration of each protomer leading to an X-shaped configuration of the dimer (Fig. 4, Video 1, and Video 2). A substantial membrane thinning (Fig. 4 B) and water penetration around the dimeric TMH region of Ire1 became apparent (Fig. S4 A and Video 1). It is tempting to speculate that this substantial degree of membrane deformation facilitates the access of Cu^{2+} ions to F544C for mediating efficient cross-linking (Fig. 3, E and F). A thorough inspection of the trajectories revealed that the residues at positions F544 and L549 can face their counterpart in an X-shaped dimer at the same time (Fig. S4 C), thereby rendering the corresponding single-cysteine variants capable of cross-linking (Fig. 3 B). This would be unlikely if the TMHs associated in a strictly parallel fashion. Inspecting the dynamics of Ire1's TMH region in a MD simulation over a period of 1,000 ns (Video 1) underscored the stability of the overall X-shaped configuration, which nevertheless allowed for significant relative motions of the TMHs. In summary, our combined approach of biochemical cross-linking and MD simulations established a surprising configuration of Ire1's TMH region with a particularly small interface between the TMHs.

Validating the structural model of the TMH region of Ire1

Our cross-linking approach indicates that the TMH residue F544 is part of a small interface between Ire1 protomers, which might stabilize the unusual X-shaped transmembrane configuration of Ire1. Aromatic residues TMH residues have been implicated in sensing lipid saturation by Mga2 (W1042; Covino et al., 2016; Ballweg et al., 2020) and lipid bilayer stress by the mammalian IRE1 α (W547; Cho et al., 2019). Despite a different position within the ER membrane, we wanted to test a similar role for F544 in Ire1 from baker's yeast. We generated a F544A variant of Ire1, which contained the native C552 in the TMH as the only accessible residue for Cu^{2+} -mediated cross-linking. A cell-based assay revealed that the F544A mutant was phenotypically indistinguishable from cysteine-less Ire1 (Fig. 5 A) and the F544C

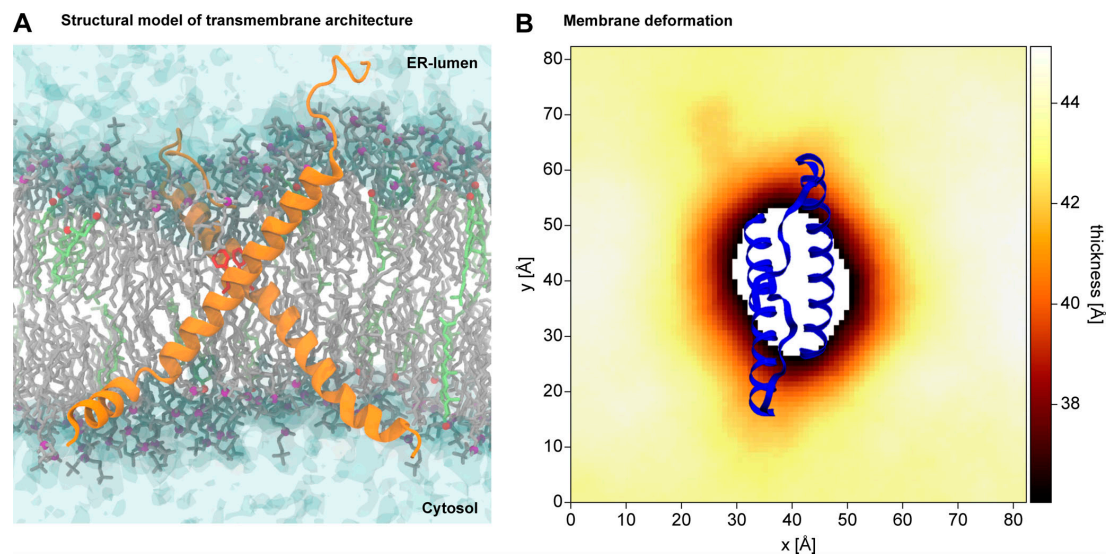


Figure 4. **Structural model of the TMH region of Ire1.** (A) Configuration of a model TMH dimer obtained from atomistic MD simulations. Protomers are shown as an orange ribbon with the two F544 residues highlighted in red. POPC lipids and their phosphate moieties are shown in gray and purple, respectively. Cholesterol molecules and their hydroxyl groups are shown in light green and red, respectively. Water is shown with a transparent surface representation. (B) Membrane thickness around the sensor peptide, defined as the average vertical distance between the two phosphate layers. A representative structure of the dimeric TMH region is shown in blue. For the SEM of the thickness profile, see Fig. S4 C.

mutant (Fig. 3 C and Fig. S1 A). This finding was corroborated by Cu^{2+} -mediated cross-linking of C552 in microsomes isolated from stressed cells (DTT or TM). The intensity of the band corresponding to cross-linked Ire1 was unaffected by the F544A mutation (Fig. 5 B). Thus, F544 does not contribute to the stability of Ire1 dimers and oligomers even though it is placed near the equivalent residue on the opposing Ire1 protomer.

Previously, we have proposed that a tilted configuration of the monomeric TMH region, which is stabilized by a proximal AH, facilitates Ire1 to sense aberrant membrane properties (Halbleib et al., 2017; Covino et al., 2018). In fact, disrupting the amphipathic character of the AH by an F531R mutation increases the cellular sensitivity to ER stress (Fig. 5 C) and reduces the cross-linking propensity via the native C552 residue in the TMH (Fig. 5 D). These findings provide biochemical evidence that the AH contributes to the stability of either dimeric or oligomeric forms of Ire1, which are challenging to distinguish.

Similarly, when the AH-disrupting mutation F531R was combined with the F544C mutation (at the crossing-point of the X-shaped TMH dimer), we observed only a very mild, yet significant functional defect (Fig. S5 A) and a strongly reduced cross-linking propensity (Fig. S5 B). This robust resistance to DTT is somewhat surprising considering the strongly reduced cross-linking propensity. However, the disruption of the AH changes the placement of the TMH in the membrane and the degree of membrane thinning and water penetration (Halbleib et al., 2017). We speculate that these combined changes would place the polar F544C residue more deeply in the hydrophobic core of the membrane, thereby affecting its propensity to

undergo a Cu^{2+} -catalyzed cross-linking, but at the same time favoring Ire1 dimerization. Notably, the F544C mutation alone does not lead to an increased UPR activity and ER stress resistance (Fig. 3, C and D; and Fig. S3 A). In fact, the primary sequence of Ire1's TMH can be systematically mutated (Fig. 3 C and Fig. S3 A), scrambled (in the case of the mammalian IRE1 α), or exchanged altogether (Halbleib et al., 2017; Volmer et al., 2013) without causing a detectable functional defect. It therefore seems that a suitably placed polar residue in the TMH, here through the F544C mutation, becomes phenotypically relevant only when Ire1 is otherwise compromised. Beyond that, our data suggest that the overall architecture of the TMH region with an intact AH is relevant for normal UPR function.

The TMH region of Ire1 makes dimer- and oligomer-specific contacts

Does the cross-linking of engineered cysteines in the TMH occur only within dimers of Ire1 or also across dimers in signaling-active clusters? The x-ray structure of the core ER-luminal domain of Ire1 revealed an interface-1 (IF1) required for dimerization, and an interface-2 (IF2) providing a platform for the back-to-back association of dimers in higher oligomeric assemblies (Credle et al., 2005; Korennykh and Walter, 2012). Consistent with a previous report (van Anken et al., 2014), the formation of microscopically visible clusters of Ire1 is abolished by disrupting either IF1 or IF2 by mutation (T226A/F247A and W426A for IF1 and IF2, respectively; Fig. 6 A). Expectedly, lack of clustering correlates with an increased cellular sensitivity to DTT (Fig. S6).

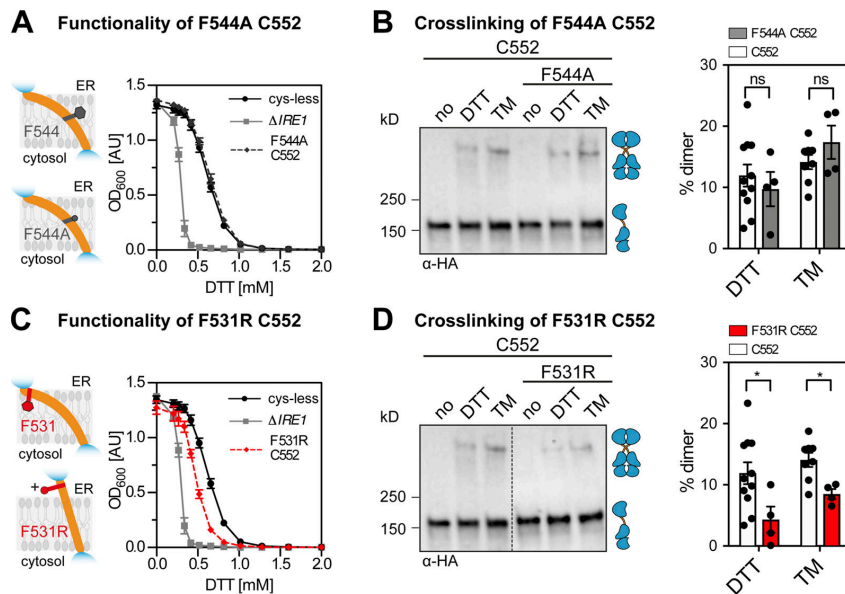


Figure 5. The impact of mutations in the TMH and the AH of Ire1 on its functionality and cross-linking propensity. (A) The ER stress resistance of cells expressing the F544A variant of *IRE1*_{3xHA-GFP} containing the native cysteine 552 was determined. Stationary overnight cultures of the indicated strains were used to inoculate a fresh culture minimal medium to an OD₆₀₀ of 0.2. After cultivation for 5 to 7 h at 30°C, the cells were diluted in 96-well plates to an OD₆₀₀ = 0.01 with prewarmed minimal medium and cultivated in the presence of the indicated concentrations of DTT for 18 h at 30°C. The density of the resulting culture was determined using the OD₆₀₀. Number of experiments including technical replicates: Δ *IRE1* ($n = 12$ from two colonies); cysteine-less ($n = 12$ from two colonies); F544A/C552 ($n = 12$ from four colonies). (B) The impact of the F544A mutation on Ire1 degree of cross-linking via cysteine 552 was analyzed. The indicated strains were subjected to the cross-linking procedure as outlined in Fig. 3 E. Data for the C552 variant are identical to the data in Fig. 3 F. Number of experiments from DTT-stressed cells including technical duplicates: C552 ($n = 11$ from 6 colonies); F531R/C552 ($n = 4$ from two colonies); cysteine-less ($n = 12$ from two colonies). Number of experiments from TM-stressed cells including technical duplicates: C552 ($n = 8$ from four colonies); F544A/C552 ($n = 4$ from two colonies). (C) ER stress resistance of indicated cells including a single-cysteine variant (C552) of *IRE1*_{3xHA-GFP} with an AH-disrupting F531R mutation was determined. The cells were cultivated and treated as in A. The data for Δ *IRE1* and cysteine-less *IRE1* are identical to the data in A. Number of experiments including technical triplicates for F531R/C552 ($n = 9$ from three colonies). (D) The impact of the AH-disrupting F531R mutation on Ire1 cross-linking via cysteine 552 was determined. The indicated strains were subjected to the same cross-linking procedure used for Fig. 3 E. Data for the C552 single-cysteine variant are identical to the data in Fig. 3 F. The immunoblot for the C552 single-cysteine variant is identical to that in B. Number of experiments including technical duplicates for DTT-stressed F531R/C552 cells ($n = 4$ from two colonies) and TM-stressed F531R/C552 cells ($n = 4$ from two colonies). All data are represented as the mean \pm SEM derived from at least three independent experiments. Significance was tested by an unpaired, two-tailed Student's *t* test. *, $P < 0.05$. Data distribution was assumed to be normal, but this was not formally tested.

By disrupting IF2 and leaving IF1 intact, we sought to uncover the contribution of dimeric and oligomeric assemblies to the cross-linking propensity in the TMH region. We focused on F544C marking the crossing-point of the X-shaped TMH region in dimeric Ire1, and on E540C and T541C in the vicinity. Upon disruption of IF2 (W426A), these single-cysteine variants failed to form microscopically visible clusters in stressed cells (Fig. 6 B). The positioning of the engineered cysteine, however, had profound impact on the cellular resistance to DTT in rich medium. The F544C/IF2 double mutant rendered the respective cells more resistant than the IF2 mutant alone, while the T541C/IF2 and E540C/IF2 mutants were highly sensitive to DTT and indistinguishable from cells lacking *IRE1* altogether (Fig. 6 C). Thus, the functional defect from the IF2 mutation can be alleviated or even aggravated by polar residues in the TMH region.

For interpreting these data, it is important to consider the time frame of the different assays. Cross-linking is performed with microsomes isolated from acutely stressed cells, which

were treated with either DTT or TM for only 1 h. Similarity, clustering of Ire1 is studied by confocal microscopy in acutely cells stressed after 1 h of treatment. The cellular resistance to DTT, however, is scored after 18 h of cultivation. The acute proteotoxic stress caused by DTT or TM treatments has barely any impact on the cellular lipid composition under given conditions (Reinhard et al., 2020). Prolonged treatments, however, cause membrane aberrancies, which can dominate Ire1 activation (Promlek et al., 2011) and which are likely to affect the resulting ER stress resistance phenotype.

To further characterize the impact of the single-cysteine variants on Ire1 function, we determined the level of the spliced *HAC1* mRNA in time course experiments with DTT-stressed cells (Fig. 6 D). We find that the level of the spliced *HAC1* mRNA is up-regulated in response to DTT-induced stress for cysteine-less Ire1 and F544C/IF2, but not for the E540C/IF2 and T541C/IF2 double mutants (Fig. 6 D). Notably, we find that UPR activation is delayed for the F544C/IF2 double mutant

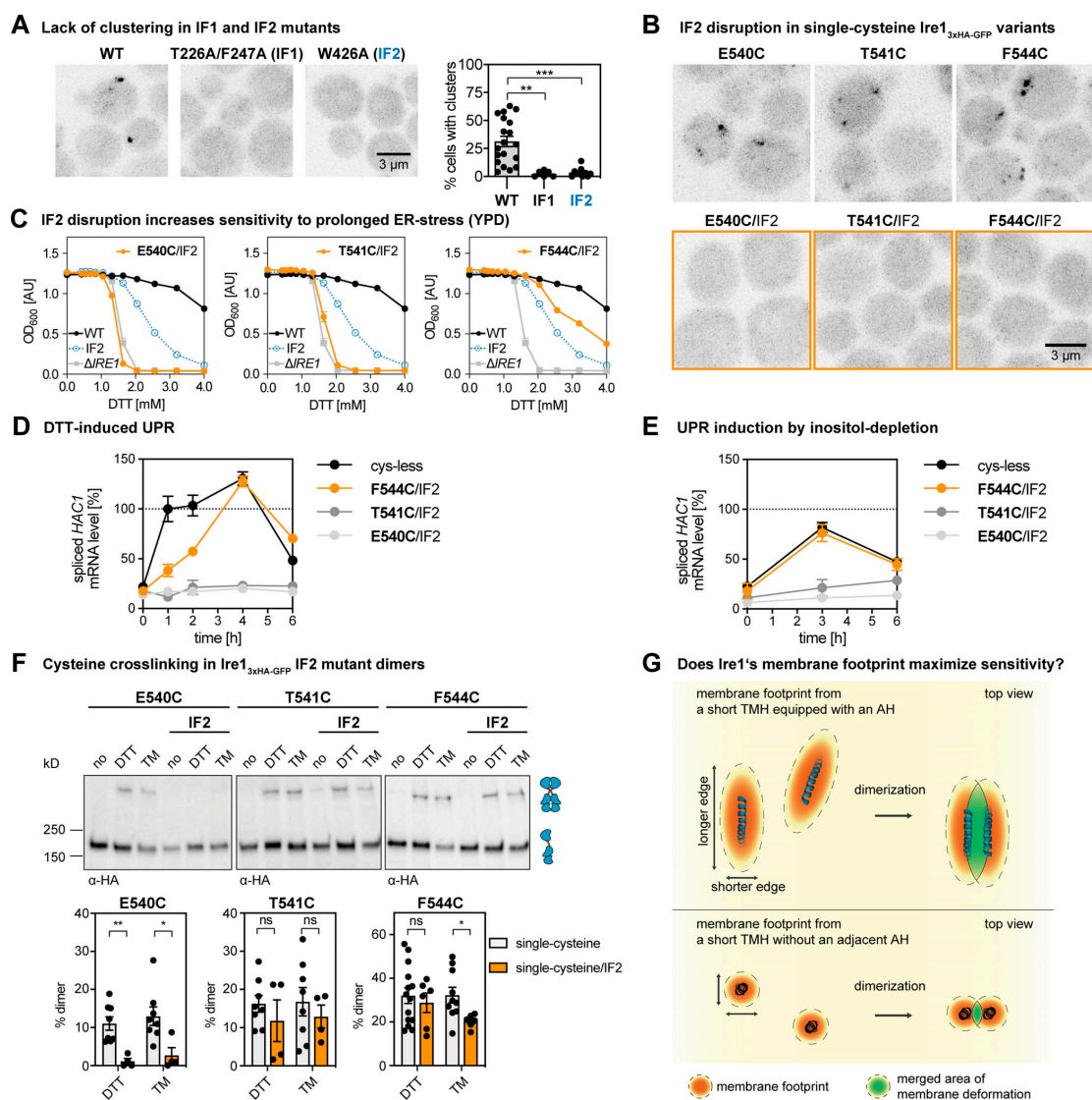


Figure 6. Cross-linking occurs within and across dimers of Ire1. (A) Indicated variants of an *IRE1* knock-in construct (Halbleib et al., 2017) were cultivated and stressed with 2 mM DTT for 1 h as described in Fig. 1 D. A refined, automated counting of Ire1-containing clusters was performed as described in the Online supplemental material. Data from Fig. 1 D were reanalyzed and pooled with new data to yield the following: WT ($n = 19$ fields of view/441 cells); T226A/F247A (IF1; $n = 6/154$); W426A (IF2; $n = 10/329$). All data are represented as the mean \pm SEM. Significance was tested by an unpaired, two-tailed Student's *t* test. **, $P < 0.01$; ***, $P < 0.001$. (B) Clustering in DTT-stressed cells was studied by confocal microscopy of the indicated single-cysteine variants with either an intact or disrupted IF2 (orange). Representative images from at least six independent fields of view are shown. For a quantitative analysis, see Fig. S6 B. (C) ER stress resistance of indicated cells was studied in rich medium containing different concentrations of DTT. Data from independent experiments for E540C/IF2 ($n = 4$), T541C/IF2 ($n = 5$), and F544C/IF2 ($n = 6$; IF2 indicates the W426A mutation) are plotted in orange. Reference datasets for Δ IRE1 ($n = 6$), Ire1_{3xHA-GFP} WT ($n = 6$ from two individual colonies), and the IF2 variant ($n = 12$ from two individual colonies) are plotted in gray, black, and blue, respectively. All data are represented as the mean \pm SEM. (D) The level of the spliced *HAC1* mRNA was determined from the indicated strains by RT-qPCR after treating the cells with 2 mM DTT for the indicated times. The data are normalized to the level of the spliced *HAC1* mRNA in cysteine-less Ire1 after 1 h of treatment and derive from three independent colonies with experimental duplicates ($n = 6$). (E) The level of the spliced *HAC1* mRNA was determined for the indicated strains cultivated under inositol-depletion conditions. The data are normalized to the level of the spliced *HAC1* mRNA splicing caused by 2 mM DTT, as determined in D. The data derive from three independent colonies with experimental duplicates ($n = 6$). (F) The impact of the IF2-disrupting W426A mutation on cross-linking via the indicated single cysteines was determined. Single- and double-mutant strains were subjected to the cross-linking procedure as in Fig. 3 E. Data for the single mutant variants are replotted from Fig. 3 F. All data are represented as the mean \pm SEM. Number of experiments including technical duplicates for DTT-stressed cells:

E540C ($n = 8$ from four colonies), T541C ($n = 8$ from four colonies), F544C ($n = 14$ from seven colonies; identical to data in Fig. 3 F), E540C/IF2 ($n = 4$ from two colonies), T541C/IF2 ($n = 4$ from two colonies), and for F544C/IF2 ($n = 6$ from three colonies). Number of experiments including technical duplicates for TM-stressed cells: E540C ($n = 8$ from four colonies), T541C ($n = 8$ from four colonies), F544C ($n = 10$ from five colonies; identical to data in Fig. 3 F), E540C/IF2 ($n = 4$ from two colonies), T541C/IF2 ($n = 4$ from two colonies), and F544C/IF2 ($n = 6$ from three colonies). Significance was tested by an unpaired, two-tailed Student's *t* test. *, $P < 0.05$; **, $P < 0.01$. Data distribution was assumed to be normal, but this was not formally tested. (G) Hypothetical model for Ire1's exquisite sensitivity. The membrane-based oligomerization of Ire1 (blue) and unrelated single-pass membrane proteins (black) leads to the coalescence of deformed membrane regions (green). In the case of Ire1, a larger portion of the deformed membrane region can be shared upon dimerization due to the ellipsoid membrane "footprint" and an association via the longer edge of deformation (parallel to the major axis of the ellipse). According to this model, this maximizes the sensitivity of Ire1 to aberrant membrane properties when compared with unrelated single-pass membrane proteins, which can merge only a relatively small portion of their circular membrane "footprint" upon dimerization.

compared with the cysteine-less control strain. Because membrane aberrancies caused by DTT manifest over a time course of several hours (Promlek et al., 2011), this suggests that the F544C/IF2 double mutant may respond predominantly to such membrane-based stresses. This interpretation is further confounded by the observation that the two other double mutants, E540C/IF2 and T541C/IF2, with mutations in the functionally critical AH (S526-V543) cannot respond to this type of prolonged DTT stress (Fig. 6 D). In order to cross-validate our interpretation, we studied the response of the same set of strains to lipid bilayer stress caused by inositol depletion (Fig. 6 E). While the F544C/IF2 mutation exhibited an almost identical response to inositol depletion as the control strain, the two E540/IF2 and T541/IF2 variants showed a massively impaired response (Fig. 6 E). Because E540 and T541 are part of the AH, these data underscore the central importance of the AH for sensing lipid bilayer stress. More importantly, however, these data suggest that membrane sensitivity of Ire1 may be particularly important for dealing with prolonged forms of ER stress caused by proteotoxic agents.

Next, we subjected these double mutant variants to the cross-linking procedure (Fig. 6 F). Cross-linking via E540C in DTT- and TM-stressed cells was abolished by the IF2 mutation, while the cross-links observed for the T541C and F544C variants were only marginally affected (Fig. 6 F). This suggests that the cross-links of T541C and F544C are formed within Ire1 dimers, while E540C cross-links across dimers. Importantly, these data not only validate the particular position of F544 at the crossing point of two TMHs in two adjacent Ire1 protomers, but also provide direct, biochemical evidence that the unusual X-shaped transmembrane architecture might laterally associate to form higher oligomers. Notably, such lateral "stacking" of the transmembrane domain in signaling-active clusters would be consistent with the complex, elongated organization of clusters as recently observed by super-resolution microscopy for IRE1 α (Belyy et al., 2020). On the functional level, our data show that the dimerization of Ire1 is not sufficient to mediate resistance to ER stress: the T541C/IF2 variant forms dimers that can be cross-linked (Fig. 6 D), but it does not render cells more resistant to DTT than cells lacking Ire1 (Fig. 6 C), nor does it up-regulate the level of the HAC1 mRNA in response to ER stress (Fig. 6, D and E). A suitably positioned polar residue (here F544C) leaves the membrane-sensitive AH intact and increases the cellular ER stress resistance in the IF2/F544C double mutant compared with a single IF2 mutant (Fig. 6 C). Thus, seemingly subtle changes in the TMH region can have substantial impact on the ER stress

resistance phenotype, especially when the normal function of Ire1 is compromised.

Discussion

Here, we establish a structural model of Ire1's TMH region in signaling-active clusters (Fig. 4). In a previous study, we have established a model of Ire1's monomeric TMH region (Halbleib et al., 2017), but its organization in dimers and higher oligomers, especially in the complex environment of the ER membrane, remained unexplored. Predicting a dimeric structure based on a model for the monomer is not trivial, as the two protomers can be arranged in various ways and might undergo substantial conformational changes upon oligomerization. Based on a systematic cysteine cross-linking approach in native membranes and aided by MD simulations, we show that the neighboring TMHs in clusters of Ire1 organize in an X-shaped configuration.

Our model of the transmembrane organization provides intriguing insights into the membrane-deforming potential of Ire1 (Fig. 4, A and B; Fig. S4; and Video 1). Positively charged residues at the cytosolic end of the TMH (Fig. 3 A) and the previously identified ER-luminal AH (Halbleib et al., 2017) cooperate in squeezing the lipid bilayer (Fig. 4, A and B; and Fig. S4 A). This deformation is most prominent at the intersection of the two protomers reaching almost to the level of the lipid bilayer center (Fig. 4 B and Video 1). Membrane squeezing and the associated disordering of lipid acyl chains come at energetic costs, which are affected by the composition and collective physicochemical properties of the surrounding bilayer (Radanović et al., 2018; Covino et al., 2018). The higher this cost (e.g., due to increased lipid saturation, inositol depletion, or membrane aberrancies from prolonged proteotoxic stresses), the higher the free energy gain from coalescing these regions and thus the propensity of Ire1 to oligomerize.

The specific way each membrane protein locally deforms the bilayer, referred to as membrane "footprints" (Haselwandter and MacKinnon, 2018) or "fingerprints" (Corradi et al., 2018), could be at the origin of membrane sensitivity and, more generally, could control the organization of supramolecular assemblies (Corradi et al., 2018). Is it possible that the unusual TMH region of Ire1 and its resulting footprint serve a specific function? We speculate that the combination of a short TMH with an AH inserting deep into the bilayer contributes to Ire1's exquisite sensitivity to aberrant ER membrane stiffening. The region of membrane compression around monomeric Ire1 is, when viewed from the top, not of circular shape but ellipsoid

due to the membrane-inserted AH (Fig. 6 G; Halbleib et al., 2017). Based on simple geometric considerations, it is conceivable that the total extent of membrane deformation contributing to the free energy of dimerization depends on how precisely the two TMH regions are arranged toward each other. Our structural model of the dimeric TMH suggests that the two protomers associate via the longer edge of membrane deformation (parallel to the major axis of the ellipse; Fig. 4, A and B), thereby maximizing the area of coalescence (Fig. 6 G, top) and minimizing the free energy. We speculate that Ire1 is more responsive to aberrant membrane stiffening than other single-pass transmembrane proteins with short TMHs but without AHs. Because these proteins also lack the characteristic ellipsoid shape of membrane deformation (Kaiser et al., 2011), they coalesce only a smaller area of their footprints upon dimerization (Fig. 6 G, bottom). It will be intriguing to study the membrane-driven dimerization and oligomerization of Ire1 side by side with other single-pass membrane proteins exhibiting distinct membrane footprints using advanced microscopic tools such as single-molecule photobleaching (Chadda et al., 2016).

Our data also provide evidence that cross-linking can occur across dimers of Ire1 (Fig. 6 F), thereby suggesting that the X-shaped dimeric arrangements of the TMH region can laterally associate and “stack” in the plane of the membrane. We propose that it is the characteristic, ellipsoid shape of membrane deformation by monomeric Ire1 and the unusual mode of dimerization and oligomerization that maximize the sensitivity of Ire1 to aberrant membrane properties.

Our structural and functional analyses suggest that the oligomeric state of Ire1 is stabilized by the overall transmembrane architecture and the membrane-embedded AH, but not by specific interactions between residues in the TMH. Disrupting the AH, which also disrupts transmembrane architecture (Covino et al., 2018), increases the cellular sensitivity to ER stress (Fig. 5 C). In contrast, the F544A mutation at the intersection of neighboring TMHs causes no functional defect (Fig. 5, A and B). Instead of maximizing the interface between the TMHs for forming a more stable protein:protein interaction, they are kept in a configuration where only a few TMH residues can contact the opposing protomer. However, they are driven together via a membrane-based mechanism and thus are particularly sensitive to the properties of the surrounding membrane (Covino et al., 2018).

Strikingly, our data provide evidence that different forms of ER stress converge in a single overall transmembrane architecture of Ire1. We observed remarkably similar cross-linking patterns in the context of lipid bilayer stress and proteotoxic stress (Fig. 3 F). This suggests that the X-shaped configuration in the TMH region is maintained in the signaling-active clusters even under largely distinct conditions of ER stress. Neither the oligomerization of Ire1 per se nor lipid bilayer stress seems to cause major conformational changes in the TMH region of the individual protomers. Based on our data, we speculate that Ire1 mounts a single response to different types of ER stress, but with distinct temporal patterns of activation. Proteotoxic stress caused by DTT or TM is characterized by two phases: an early phase of a rapid UPR activation with little to no changes in the lipid composition, and a second, slower phase characterized by

a build-up of membrane aberrancies (Promlek et al., 2011; Reinhard et al., 2020). While these membrane aberrancies remain poorly characterized, they serve as a robust signal for Ire1 activation (Fig. 6 D; Promlek et al., 2011). The lipid bilayer stress caused from inositol depletion, in contrast, lacks the early phase of UPR activation. It manifests slowly and causes a distinct temporal pattern of UPR activation (Fig. 6, D and E). It will be interesting to study whether different temporal patterns of UPR activation are sufficient to give rise to largely distinct transcriptional programs or if, alternatively, Ire1 can custom tailor its output via yet unknown mechanisms (Hetz et al., 2020; Ho et al., 2020; Fun and Thibault, 2020).

Our cross-linking data suggest a similar transmembrane architecture in Ire1 in response to proteotoxic and lipid bilayer stress (Gardner and Walter, 2011; Halbleib et al., 2017). While we cannot formally exclude conformational changes in other parts of the protein, we do not find evidence that Ire1 custom-tailors its signaling output via conformational changes in the TMH region. Based on our cross-linking data and the observed temporal patterns of activation for different mutants of Ire1 (Fig. 6 E), we suggest that the complex metabolic, transcriptional, and nontranscriptional adaptations to different forms of ER stress do not reflect distinct functional modes of Ire1. Instead, we propose that different degrees of oligomerization and different rates of Ire1 activation and inactivation are sufficient to drive differently stressed cells into distinct physiological states.

Our combined results lead to the following model of UPR activation. Both accumulating unfolded proteins and lipid bilayer stress lead to the oligomerization of Ire1 and the formation of signaling-active clusters (Korennykh and Walter, 2012). Under these conditions, the cytosolic effector domains “follow” the oligomerization of the ER-luminal domain and the TMH region. A large diversity of ER-luminal and cytosolic interactors including chaperones can tune and specify the activity of mammalian UPR transducers (Sepulveda et al., 2018; Amin-Wetzel et al., 2017). This may reflect a way to custom tailor the globally acting UPR to different cell types with distinct protein folding requirements at steady-state and during differentiation. Lipid bilayer stress activates the UPR in both yeast and mammals via a membrane-based mechanism and does not require the binding of unfolded proteins to the ER-luminal domain and/or associated chaperones (Promlek et al., 2011; Halbleib et al., 2017; Volmer et al., 2013). Furthermore, our findings underscore the importance of Ire1’s membrane sensitivity to deal with the stress caused by prolonged cellular treatments with proteotoxic agents (Promlek et al., 2011). Our data from direct, cross-linking experiments suggest that both proteotoxic and lipid bilayer stress converge in a single overall architecture of the TMH region. We propose that Ire1’s distinct signaling outputs to different forms of ER stress reflect a different temporal pattern of Ire1 activation rather than different qualities of signaling.

Materials and methods

Reagents, antibodies, strains, and plasmids

All chemicals and reagents used in this study were purchased from Sigma-Aldrich, Carl Roth, or Millipore and are of analytical

or higher grade. The following antibodies were used: mouse anti-Flag monoclonal (M2; Santa Cruz), rat anti-HA monoclonal (3F19; Roche), mouse anti-Dpml monoclonal (5C5A7; Life Technologies), mouse anti-Pgk1 (22C5D8; Life Technologies), mouse anti-MBP monoclonal (NEB), anti-mouse-HRP (Dianova), and anti-rat-HRP (Dianova). All strains and plasmids used in this study are listed in Table S1 and Table S2, respectively.

Generation of a cysteine-less construct and a Flag-tag variant of IRE1

A cysteine-less construct of IRE1 was generated based on a previously described knock-in construct (Halbleib et al., 2017). This construct comprises the IRE1 promoter (-1 to -551 bp), the IRE1 gene including a coding sequence for a 3xHA tag and a monomeric version of yeGFP (A206R^{yeGFP}) inserted at the position of H875, and the IRE1 endogenous 5' terminator on the plasmid pcDNA3.1-IRE1_{3xHA-GFP} (Halbleib et al., 2017). A cysteine-less variant was generated by site-directed mutagenesis. Cysteine 48 (C48^{yeGFP}) of the monomeric yeGFP was substituted to serine, while cysteine 70 (C70^{yeGFP}) remained in the final construct (Costantini et al., 2015; Ormö et al., 1996). Single-cysteine variants were generated by site-directed mutagenesis.

Plasmids encoding either single-cysteine variants or cysteine-less Ire1 (Table S2) were linearized using *HindIII* and *XhoI* restriction enzymes and used for transforming our previously established cloning strain lacking both the IRE1 gene and its promoter. Strains used in this study are listed in Table S1. Additionally, a Flag-tagged cysteine-less Ire1 version based on the *CEN*-based Ire1 construct from the pPW1628/pEv200 plasmid was generated. The 3xHA epitope tag in the knock-in construct was replaced by a 3xFlag epitope tag using the Q5 site-directed mutagenesis kit (NEB). The newly generated knock-in sequence was amplified in a multi-step PCR reaction adding the terminator sequence from the pEv200 plasmid and *BssHI* and *HindIII* restriction sites. The transfer of the IRE1_{3xFlag-GFP} sequence in the *CEN*-based pPW1628/pEv200 plasmid was performed using *BssHI*/*HindIII* restriction sites.

Cultivation and live cell confocal microscopy

The yeast strains were cultivated at 30°C on agar plates containing SCD complete medium or selection medium. Liquid yeast cultures either in SCD or YPD (the pH of the medium was not adjusted) were inoculated with a single colony and typically cultivated at 30°C for a minimum of 18 h to reach the stationary phase. This overnight culture was used to inoculate a fresh culture to an OD₆₀₀ = 0.2, which was cultivated until the mid-exponential phase. For microsomal membrane preparation, stationary cells were used to inoculate a fresh culture in SCD complete medium to an OD₆₀₀ of 0.2. After cultivation at 30°C to an OD₆₀₀ of 0.7, the cells were either left untreated or stressed with either 2 mM DTT or 1.5 µg/ml TM for 1 h. For inositol depletion, exponentially growing cells were washed with SCD complete without inositol and then used to inoculate the main culture to an OD₆₀₀ of 0.5 in SCD complete without inositol, which was further cultivated for 3 h.

Live cell confocal microscopy and image analysis

A fresh culture in SCD medium was inoculated to an OD₆₀₀ = 0.2 and cultivated for 5–5.5 h at 30°C and under constant agitation at 220 rpm. To induce ER stress, DTT was added to a final concentration of 2 mM followed by additional cultivation for 1 h. The cells were harvested by centrifugation and mounted on microscopic slides coated with a thin layer of SCD containing 1.5% agarose for immobilization. Microscopy was performed at 23 ± 2°C using a Zeiss LSM 780 confocal laser scanning microscope (Carl Zeiss Microscopy GmbH) with inverted stage and spectral detection, a Plan-Apochromat 63× 1.40 NA oil immersion objective with immersol 518 f, and the acquisition software ZEN2012 (Carl Zeiss Microscopy GmbH). GFP fluorescence was excited at 488 nm, and the emission was detected between 493 and 598 nm. Transmission images were simultaneously recorded using differential interference contrast optics. Z-stacks (450-nm step size, 62.1-µm pinhole size) were recorded. When multiple fluorophores were imaged (Fig. S6 F), GFP was excited at 488 nm and dsRed at 561 nm, and emission was detected at 493–557 nm and 592–704 nm, respectively. For multi-fluorophore images, a Z-stack step size of 372 nm with a pinhole diameter of 80.3 µm was used. Image stacks were corrected for potential x-y drift using the Fiji plugin StackReg (Thévenaz et al., 1998; Schindelin et al., 2012). Maximum intensity and sum projections were created, while the contrast was adjusted equally for all images using Fiji (Schindelin et al., 2012). Individual cells and clusters of Ire1 were identified by automated segmentation using CellProfiler (McQuinn et al., 2018). In brief, the cellular areas were determined for each image based on sum projections of recorded z-stacks and the cellular autofluorescence. After smoothing with a median filter, potential cells were identified by global thresholding (minimum cross-entropy). Objects outside the diameter restraint of 1.9c6.3 µm were discarded. Cells being too bright (a high autofluorescence indicates cell death) were omitted from further analysis if the mean intensity of a potential cell exceeded the mean intensity of all potential cells within an image by >30%. Clusters of Ire1 within cells were identified in maximum intensity projections using a threshold of 1.5 times the mean intensity of the identified cells. Potential clusters outside the diameter range 0.3–0.9 µm were discarded. The strain RE773 IRE1_{3xHA-yeGFP} E540C/IF2 showed substantial signs of cell death (increased autofluorescence) when challenged with DTT. Therefore, all microscopic images represented in and used for Fig. 6 and Fig. S6 B were reanalyzed and subjected to more stringent parameters to avoid false positive identifications of Ire1 clusters. Cells were not considered if their mean intensity was 10% above average. Structures with diameters from 0.3 to 1.2 µm were initially allowed as potential clusters, but only counted if their maximum intensity was at least 2.5 times higher than the mean intensity of the respective cell. Furthermore, if >3.5% of a cell area was covered by potential clusters, the cell was considered as unfit and counted as free of clusters.

Assaying the resistance to ER stress

The cellular resistance to ER stress caused by DTT was assayed using a sensitive growth assay (Halbleib et al., 2017). Stationary

overnight cultures were used to inoculate a fresh culture to an OD_{600} of 0.2. After cultivation for 5–7 h at 30°C, the cells were diluted with prewarmed medium to an OD_{600} of 0.05. 50 μ l of these diluted cultures was mixed in a 96-well plate with 180 μ l of medium and 20 μ l of a DTT dilution series leading to a final concentration of DTT between 0 and 2 mM and 0 and 4 mM, respectively. After incubation at 30°C for 18 h, the cultures were thoroughly mixed, and 200 μ l of the cell suspension was transferred to a fresh 96-well plate for determining the density of the culture via spectrophotometers using the OD_{600}/OD_{620} .

RNA preparation, cDNA synthesis, and qPCR analysis

The level of the spliced *HAC1* mRNA and the *PDI1* mRNA in stressed and unstressed cells was determined via RT-qPCR using Oligo(dT) primers, the Superscript II RT protocol (Invitrogen), the ORA qPCR Green ROX L Mix (HighQu), and a Piko Real PCR system (Thermo Fisher Scientific). The RNA was prepared from 5 OD equivalents of stressed and unstressed cells using the RNeasy Plus RNA Isolation Kit (Qiagen). 500 ng RNA of the total isolated RNA was used as a template for the synthesis of cDNA using Oligo(dT) primers and the Superscript II RT protocol (Invitrogen). qPCR was performed using ORA qPCR Green ROX L Mix (HighQu) in a Piko Real PCR system (Thermo Fisher Scientific). The following primers were used at a final concentration of 400 nM: *HAC1s* forward primer: 5'-CTTTGTCGCCCAAGAGTATGCG-3'; *HAC1s* reverse primer: 5'-ACTGCGCTTCTG GATTACGC-3'; *ACT1* forward primer: 5'-TGTCACCAACTGGGACGATA-3'; *ACT1* reverse primer: 5'-AACCAGCGTAAATTGGAA CG-3'; *PDI1* forward primer: 5'-GATCGATTACGAGGGACCTAG A-3'; and *PDI1* reverse primer: 5'-GCCGAGGGCAAGTAAATA GAA-3'.

The qPCR program included the following steps: (1) 95°C, 15 min; (2) 95°C, 20 s; (3) 58°C, 20 s; (4) 72°C, 30 s; and (5) 72°C, 5 min; steps 2–4 were repeated 40 times. For quantifying the level of the *PDI1* mRNA and the spliced *HAC1* mRNA, we used the comparative $\Delta\Delta CT$ method using normalization to *ACT1* levels (StepOnePlus user Manual, Applied Biosystems). For amplifying both cDNAs generated from the spliced and unspliced *HAC1* mRNA, we used the following primers at a final concentration of 400 nM and previously established PCR conditions (Promlek et al., 2011): *HAC1* splicing forward primer: 5'-TACAGGGATTC CAGAGCACG-3'; and *HAC1* splicing reverse primer: 5'-TGAAGT GATGAAGAAATCATTCATTC-3'.

Preparation of cell lysates and immunoblotting

Lysates were prepared from exponentially growing cells, which were harvested by centrifugation (3,000 $\times g$, 5 min, 4°C) and then washed once with double-distilled water and once with PBS. During washing, the cells were transferred into 1.5-ml reaction tubes, allowing for a more rapid centrifugation (8,000 $\times g$, 20 s, 4°C). The tubes with the washed cell pellet were placed in a –80°C freezer and stored until further use. For preparing the lysate, either 5 or 20 OD equivalents were resuspended in 400 μ l or 1,000 μ l lysis buffer (PBS containing 10 μ g/ml chymostatin, 10 μ g/ml antipain, and 10 μ g/ml pepstatin), respectively. After addition of either 100 μ l or 500 μ l of zirconia beads, respectively, the cells were disrupted by bead beating for 5 min at 4°C.

Four parts of the resulting lysate were mixed with one part of 5 \times reducing sample buffer (8 M urea, 0.1 M Tris-HCl, pH 6.8, 5 mM EDTA, 3.2% [wt/vol] SDS, 0.15% [wt/vol] bromophenol blue, 4% [vol/vol] glycerol, and 4% [vol/vol] β -mercaptoethanol) and then incubated at 95°C for 10 min to fully unfold and solubilize the proteins therein. 0.1 OD equivalents of the resulting sample was subjected to SDS-PAGE, and the proteins were separated on 4–15% Mini-PROTEAN-TGX strain-free gels (BioRad). For subsequent immunoblotting, proteins were transferred from the gel to methanol-activated polyvinylidene difluoride membranes using semi-dry Western blotting. Specific proteins were detected using antigen-specific primary antibodies, HRP-coupled secondary antibodies, and chemiluminescence.

Microsomal membrane preparation

80 OD_{600} equivalents were harvested from a mid-exponential culture by centrifugation (3,000 $\times g$, 5 min, 4°C), washed with PBS, and stored at –80°C. All steps of membrane fractionation were performed on ice or at 4°C. Cells were resuspended in 1.5 ml lysis buffer (50 mM Hepes, pH 7.0, 150 mM NaCl, 1 mM EDTA, 10 μ g/ml chymostatin, 10 μ g/ml antipain, and 10 μ g/ml pepstatin). For cysteine cross-linking experiments, a buffer without EDTA was used. After cell disruption using zirconia beads (Roth) and a bead beater (2 \times 5 min), cell debris was removed by centrifugation (800 $\times g$, 5 min, 4°C; and 5,000 $\times g$, 10 min, 4°C). The supernatant was centrifuged (100,000 $\times g$, 45 min, 4°C) to obtain crude microsomes in the pellet. Microsomes were resuspended in 1.4 ml lysis buffer, sonicated for homogenization (50%, 5 \times 1 s, MS72 tip on a sonifier cell disrupter from Branson Ultrasonic), snap-frozen in liquid N_2 , and stored in aliquots at –80°C.

Test of membrane integration

The cleared supernatant of a 5,000 $\times g$ step was divided into equal parts, which were then mixed with an equal volume of lysis buffer supplemented with 0.2 M Na_2CO_3 , resulting in a final pH of 11, 5 M urea, and 2% Triton X-100 or without additional additives. After incubation for 1 h on a rotator, these samples were centrifuged (100,000 $\times g$, 45 min, 4°C) to separate soluble from insoluble material. The supernatant and pellets from these fractions corresponding to 0.2 OD equivalents were further analyzed by SDS-PAGE and immunoblotting.

CuSO₄-induced cysteine cross-linking

Microsomes were thawed on ice. 8 μ l microsomes (1 \pm 0.2 mg/ml protein) were mixed either with 2 μ l of 50 mM $CuSO_4$ or 2 μ l double-distilled water and then incubated for 5 min on ice. The reaction was stopped with 8 μ l of membrane sample buffer (4 M urea, 50 mM Tris-HCl, pH 6.8, 1.6% [wt/vol] SDS, 0.01% [wt/vol] bromophenol blue, and 2% [vol/vol] glycerol) containing 125 mM EDTA and 250 mM *N*-Ethylmaleinimid (NEM). The samples were analyzed by SDS-PAGE and immunoblotting with chemiluminescence detection. The percentage of cross-linked dimer was determined via densitometry with Fiji (Schindelin et al., 2012) using the bands corresponding to the monomeric and covalently cross-linked protein.

Immunoprecipitation from microsomes after CuSO₄-induced cysteine cross-linking

300 μ l of microsomes with a typical protein concentration of 1 mg/ml were incubated with 12.5 μ l 250 mM CuSO₄ (final concentration of 10 mM) for 5 min on ice. The reaction was stopped by adjusting the sample to a final concentration of 50 mM EDTA and 111 mM NEM by adding 30 μ l of 0.5 M EDTA stock solution and 44 μ l of 1 M NEM stock solution, respectively. The final volume was adjusted to 1.3 ml with lysis buffer with a final concentration of 5 mM EDTA. The CuSO₄ concentration was thus reduced to 2.4 mM and the NEM concentration to 33.6 mM, respectively.

After cross-linking, the microsomes were solubilized using 2% Triton X-100 and incubated for 1 h at 4°C under constant agitation. Insoluble material was removed by centrifugation (20,000 \times g, 10 min, 4°C). The resulting supernatant was incubated with 8 μ l Flag beads (Sigma-Aldrich), equilibrated with immunoprecipitation (IP) wash buffer (lysis buffer + 5 mM EDTA + 0.2% Triton X-100), for 3 h under constant shaking. Flag beads were washed five times with IP wash buffer by centrifugation (8,000 \times g, 30 s, 4°C). For elution, the Flag beads were incubated with 10 μ l IP-Wash and 10 μ l 5 \times reducing sample buffer for 5 min at 95°C, which did not disrupt the disulfide bond formed between two protomers of Ire1. These samples were analyzed by SDS-PAGE and immunoblotting.

Modeling of the transmembrane dimer of Ire1 and MD simulations

The dimeric TMH region of Ire1 was modeled using a 56-amino acid-long peptide, 516-SRELD EKNQNSLLK FGSLVYRIIE TGVFLLFLI FCAILQRFKI LPPLYVLLSK I-571. We extracted an equilibrated, monomeric configuration of the peptide from a previously performed 10- μ s-long equilibrium MD simulation. We duplicated the configuration in order to create a new system containing two identical protomers. We then rotated and translated one of the two protomers to form a dimer structure, such that the two F544s faced each other with the distance between their C β atoms at around 0.7 nm. A short energy minimization in solution resolved all steric clashes between side chains. The structure of the model dimer was prepared by using gromacs/2019.3 tools (Abraham et al., 2015) and VMD (Humphrey et al., 1996). We used Charmm-GUI (Wu et al., 2014; Lee et al., 2016) to reconstitute the dimer in a bilayer containing 248 POPC and 62 cholesterol molecules modeled in the Charmm36m force field (Klauda et al., 2010; Best et al., 2012). We solvated the system with 24813 TIP3P water molecules and 72 chloride and 66 sodium ions, corresponding to a salt concentration of 150 mM.

Equilibrium and restrained simulations of the dimer model

After an initial energy minimization and quick relaxation, we equilibrated the dimer model in the bilayer. We first ran a 50-ns-long simulation restraining the position of protein atoms by using harmonic potentials with force-constants (in units of kJ mol⁻¹ nm⁻²) of 500 for backbone atoms and 200 for side chain atoms. We then ran further 50 ns lowering the force-constants to 200 and 50, respectively. After this equilibration, we relieved

all restraints and ran a 1,000-ns-long MD simulation, where the system evolved according to its unbiased dynamics. We ran both the restrained equilibration and unbiased production simulation in gromacs/2019.3 using a time step of 2 fs. Electrostatic interactions were evaluated with the Particle-Mesh-Ewald method (Essmann et al., 1995). We maintained a constant temperature of 303 K (Bussi et al., 2007), applying separate thermostats on the protein, membrane, and solvent with a characteristic time of 1 ps. We applied the semi-isotropic Berendsen barostat (Berendsen et al., 1984) for the restrained equilibration, and the Parrinello-Rahman barostat (Parrinello and Rahman, 1981) for the production runs, acting separately on the x-y plane and z direction to maintain a constant pressure of 1 atm, and with a characteristic time of 5 ps. We constrained all hydrogen bonds with the LINCS algorithm (Hess et al., 1998). Molecular visualizations were obtained with VMD and rendered with Tachyon.

Data representation and replicates

All data are represented as the average \pm SEM if not stated otherwise. The number of the biological and technical replicates are provided in the Online supplemental material. Statistical tests were performed with Prism 8 for macOS Version 8.4.0.

Online supplemental material

Fig. S1 shows protein levels of cysteine-less Ire1 and characterization of its membrane association. Fig. S2 shows validation of a covalent, reversible cross-linking of Ire1 homodimers via disulfide bridges. Fig. S3 shows functionality of cysteine mutants and their cross-linking potential in lipid bilayer stress conditions. Fig. S4 shows that the dimeric TMH region of Ire1 deforms the membrane. Fig. S5 shows that a mutation of the AH affects Ire1 function and cross-linking propensity. Fig. S6 shows that disrupting ER-luminal interfaces for dimerization (IF1) and oligomerization (IF2) of Ire1 impairs cellular ER-stress resistance and the formation of Ire1 clusters. In Video 1, a structural model of the TMH region of Ire1 highlights membrane thinning and water penetration into the bilayer. Video 2 shows dynamics of the TMH region of Ire1 dimers over a period of 600 ns. Table S1 lists yeast strains used in this study. Table S2 lists plasmids used in this study.

Data availability

All data discussed in the paper are included in this published article and in the online supplemental material. Additional materials including qPCR data, microscopy data, and the immunoblots contributing to the bar diagrams in Fig. 3 F; Fig. 5, B and D; and Fig. 6 F have been deposited to Mendeley Data (DOI: 10.17632/s52vt8sPMC1).

Acknowledgments

We thank Kristina Halbleib for her important contributions during the early phase of the project and David Ron for critically reading the manuscript and helpful discussions. We thank Sebastian Schuck and Dimitrios Papagiannidis (ZMBH, Heidelberg University, Germany) for providing the pSS455 plasmid.

This work was supported by the Deutsche Forschungsgemeinschaft (SFB807 "Transport and Communication



across Biological Membranes” to R. Ernst and G. Hummer; SFB894 “Ca²⁺-Signals: Molecular Mechanisms and Integrative Functions” to R. Ernst). R. Ernst was supported by the Volkswagen Foundation (Life?, 93089). This project has received funding from the European Research Council under the European Union’s Horizon 2020 research and innovation program (grant agreement no. 866011). R. Covino and G. Hummer were supported by the Max Planck Society and by the LOEWE CMMS program of the state of Hesse. R. Covino acknowledges the support of the Frankfurt Institute for Advanced Studies.

The authors declare no competing financial interests.

Author contributions: Conceptualization: R. Ernst and R. Covino; experimental design: K. V  th, J. Reinhard, C. Mattes, and R. Ernst; experiment performance: K. V  th, J. Reinhard, C. Mattes, and H. Stumpf; modeling, MD simulations, and rendering: R. Covino; microscopy and Segmentation: J. Reinhard; writing – original draft: K. V  th, R. Covino, and R. Ernst; writing – revised draft: K. V  th, R. Covino, J. Reinhard, C. Mattes, G. Hummer, and R. Ernst; figure design: K. V  th, J. Reinhard, C. Mattes, and R. Ernst; funding acquisition: R. Ernst and G. Hummer; supervision: R. Ernst, R. Covino, and G. Hummer.

Submitted: 12 November 2020

Revised: 28 April 2021

Accepted: 19 May 2021

References

- Abraham, M.J., T. Murtola, R. Schulz, S. P  ll, J.C. Smith, B. Hess, and E. Lindahl. 2015. Gromacs: High performance molecular simulations through multi-level parallelism from laptops to supercomputers. *SoftwareX*. 1–2:19–25. <https://doi.org/10.1016/j.softx.2015.06.001>
- Adams, C.J., M.C. Kopp, N. Larburu, P.R. Nowak, and M.M.U. Ali. 2019. Structure and Molecular Mechanism of ER Stress Signaling by the Unfolded Protein Response Signal Activator IRE1. *Front. Mol. Biosci.* 6:11. <https://doi.org/10.3389/fmolb.2019.00011>
- Amin-Wetzel, N., R.A. Saunders, M.J. Kamphuis, C. Rato, S. Preissler, H.P. Harding, and D. Ron. 2017. A J-Protein Co-chaperone Recruits BiP to Monomerize IRE1 and Repress the Unfolded Protein Response. *Cell*. 171:1625–1637.e13. <https://doi.org/10.1016/j.cell.2017.10.040>
- Arag  n, T., E. van Anken, D. Pincus, I.M. Serafimova, A.V. Korenykh, C.A. Rubio, and P. Walter. 2009. Messenger RNA targeting to endoplasmic reticulum stress signalling sites. *Nature*. 457:736–740. <https://doi.org/10.1038/nature07641>
- Ballweg, S., E. Sezgin, M. Doktorova, R. Covino, J. Reinhard, D. Wunnicke, I. H  nelt, I. Levental, G. Hummer, and R. Ernst. 2020. Regulation of lipid saturation without sensing membrane fluidity. *Nat. Commun.* 11:756. <https://doi.org/10.1038/s41467-020-14528-1>
- Bass, R.B., S.L. Butler, S.A. Chervitz, S.L. Gloor, and J.J. Falke. 2007. Use of Site-Directed Cysteine and Disulfide Chemistry to Probe Protein Structure and Dynamics: Applications to Soluble and Transmembrane Receptors of Bacterial Chemotaxis. In *Methods in Enzymology*. Academic Press Inc. pp. 25–51.
- Belyy, V., N.-H. Tran, and P. Walter. 2020. Quantitative microscopy reveals dynamics and fate of clustered IRE1a. *Proc. Natl. Acad. Sci. USA*. 117:1533–1542. <https://doi.org/10.1073/pnas.1915311117>
- Berendsen, H.J.C., J.P.M. Postma, W.F. Van Gunsteren, A. Dinola, and J.R. Haak. 1984. Molecular dynamics with coupling to an external bath. *J. Chem. Phys.* 81:3684–3690. <https://doi.org/10.1063/1.448118>
- Best, R.B., X. Zhu, J. Shim, P.E.M. Lopes, J. Mittal, M. Feig, and A.D. Mackerell Jr. 2012. Optimization of the additive CHARMM all-atom protein force field targeting improved sampling of the backbone ϕ , ψ and side-chain $\chi(1)$ and $\chi(2)$ dihedral angles. *J. Chem. Theory Comput.* 8:3257–3273. <https://doi.org/10.1021/ct300400x>
- Brooks, A.J., W. Dai, M.L. O’Mara, D. Abankwa, Y. Chhabra, R.A. Pelekanos, O. Gardon, K.A. Tunny, K.M. Blucher, C.J. Morton, et al. 2014. Mechanism of activation of protein kinase JAK2 by the growth hormone receptor. *Science*. 344:1249783. <https://doi.org/10.1126/science.1249783>
- Bussi, G., D. Donadio, and M. Parrinello. 2007. Canonical sampling through velocity rescaling. *J. Chem. Phys.* 126:014101. <https://doi.org/10.1063/1.2408420>
- Chadda, R., V. Krishnamani, K. Mersch, J. Wong, M. Brimberry, A. Chadda, L. Kolmakova-Partensky, L.J. Friedman, J. Gelles, and J.L. Robertson. 2016. The dimerization equilibrium of a ClC Cl(–)/H(+) antiporter in lipid bilayers. *eLife*. 5:e17438. <https://doi.org/10.7554/eLife.17438>
- Cho, H., F. Stanzione, A. Oak, G.H. Kim, S. Yermenli, L. Qi, A.K. Sum, and C. Chan. 2019. Intrinsic Structural Features of the Human IRE1a Transmembrane Domain Sense Membrane Lipid Saturation. *Cell Rep.* 27:307–320.e5. <https://doi.org/10.1016/j.celrep.2019.03.017>
- Cohen, N., M. Breker, A. Bakunts, K. Pesek, A. Chas, J. Argem  , A. Orsi, L. Gal, S. Chuartzman, Y. Wigelman, et al. 2017. Iron affects Ire1 clustering propensity and the amplitude of endoplasmic reticulum stress signaling. *J. Cell Sci.* 130:3222–3233. <https://doi.org/10.1242/jcs.201715>
- Corradi, V., E. Mendez-Villuendas, H.I. Ing  lfs  n, R.X. Gu, I. Siuda, M.N. Melo, A. Moussatova, L.J. DeGagn  , B.I. Sejdiu, G. Singh, et al. 2018. Lipid-Protein Interactions Are Unique Fingerprints for Membrane Proteins. *ACS Cent. Sci.* 4:709–717. <https://doi.org/10.1021/acscentsci.8b00143>
- Costantini, L.M., M. Baloban, M.L. Markwardt, M. Rizzo, F. Guo, V.V. Verkhusha, and E.L. Snapp. 2015. A palette of fluorescent proteins optimized for diverse cellular environments. *Nat. Commun.* 6:7670. <https://doi.org/10.1038/ncomms8670>
- Covino, R., S. Ballweg, C. Stordeur, J.B. Michaelis, K. Puth, F. Wernig, A. Bahrami, A.M. Ernst, G. Hummer, and R. Ernst. 2016. A eukaryotic sensor for membrane lipid saturation. *Mol. Cell*. 63:49–59. <https://doi.org/10.1016/j.molcel.2016.05.015>
- Covino, R., G. Hummer, and R. Ernst. 2018. Integrated Functions of Membrane Property Sensors and a Hidden Side of the Unfolded Protein Response. *Mol. Cell*. 71:458–467. <https://doi.org/10.1016/j.molcel.2018.07.019>
- Cox, J.S., C.E. Shamu, and P. Walter. 1993. Transcriptional induction of genes encoding endoplasmic reticulum resident proteins requires a transmembrane protein kinase. *Cell*. 73:1197–1206. [https://doi.org/10.1016/0092-8674\(93\)90648-A](https://doi.org/10.1016/0092-8674(93)90648-A)
- Credle, J.J., J.S. Finer-Moore, F.R. Papa, R.M. Stroud, and P. Walter. 2005. On the mechanism of sensing unfolded protein in the endoplasmic reticulum. *Proc. Natl. Acad. Sci. USA*. 102:18773–18784. <https://doi.org/10.1073/pnas.0509487102>
- Ernst, R., S. Ballweg, and I. Levental. 2018. Cellular mechanisms of physicochemical membrane homeostasis. *Curr. Opin. Cell Biol.* 53:44–51. <https://doi.org/10.1016/jceb.2018.04.013>
- Essmann, U., L. Perera, M.L. Berkowitz, T. Darden, H. Lee, and L.G. Pedersen. 1995. A smooth particle mesh Ewald method. *J. Chem. Phys.* 103:8577–8593. <https://doi.org/10.1063/1.470117>
- Falke, J.J., and D.E. Koshland. 1987. Global flexibility in a sensory receptor: A site-directed cross-linking approach. *Science*. 237:1596–1600. <https://doi.org/10.1126/science.2820061>
- Fonseca, S.G., M. Burcin, J. Gromada, and F. Uramo. 2009. Endoplasmic reticulum stress in β -cells and development of diabetes. *Curr. Opin. Pharmacol.* 9:763–770. <https://doi.org/10.1016/j.coph.2009.07.003>
- Frost, A., M.G. Elgort, O. Brandman, C. Ives, S.R. Collins, L. Miller-Vedam, J. Weibezahn, M.Y. Hein, I. Poser, M. Mann, et al. 2012. Functional repurposing revealed by comparing *S. pombe* and *S. cerevisiae* genetic interactions. *Cell*. 149:1339–1352. <https://doi.org/10.1016/j.cell.2012.04.028>
- Fun, X.H., and G. Thibault. 2020. Lipid bilayer stress and proteotoxic stress-induced unfolded protein response deploy divergent transcriptional and non-transcriptional programmes. *Biochim. Biophys. Acta Mol. Cell Biol. Lipids*. 1865:158449. <https://doi.org/10.1016/j.bbalip.2019.04.009>
- Gardner, B.M., and P. Walter. 2011. Unfolded proteins are Ire1-activating ligands that directly induce the unfolded protein response. *Science*. 333:1891–1894. <https://doi.org/10.1126/science.1209126>
- Ghaemmaghani, S., W.K. Huh, K. Bower, R.W. Howson, A. Belle, N. Dephore, E.K. O’Shea, and J.S. Weissman. 2003. Global analysis of protein expression in yeast. *Nature*. 425:737–741. <https://doi.org/10.1038/nature02046>
- Halbleib, K., K. Pesek, R. Covino, H.F. Hofbauer, D. Wunnicke, I. H  nelt, G. Hummer, and R. Ernst. 2017. Activation of the Unfolded Protein Response by Lipid Bilayer Stress. *Mol. Cell*. 67:673–684.e8. <https://doi.org/10.1016/j.molcel.2017.06.012>
- Haselwandter, C.A., and R. MacKinnon. 2018. Piezo’s membrane footprint and its contribution to mechanosensitivity. *eLife*. 7:e41968. <https://doi.org/10.7554/eLife.41968>

V  th et al.

Proteotoxic and lipid bilayer stress converge

Journal of Cell Biology

<https://doi.org/10.1083/jcb.202011078>

15 of 17

- Hess, B., H. Bekker, H.J.C. Berendsen, and J.G.E.M. Fraaije. 1998. LINC: A Linear Constraint Solver for molecular simulations. *J. Comput. Chem.* 18:1463-1472. [https://doi.org/10.1002/\(SICI\)1096-987X\(199709\)18:12<1463::AID-JCC4>3.0.CO;2-H](https://doi.org/10.1002/(SICI)1096-987X(199709)18:12<1463::AID-JCC4>3.0.CO;2-H)
- Hetz, C. 2012. The unfolded protein response: controlling cell fate decisions under ER stress and beyond. *Nat. Rev. Mol. Cell Biol.* 13:89-102. <https://doi.org/10.1038/nrm3270>
- Hetz, C., K. Zhang, and R.J. Kaufman. 2020. Mechanisms, regulation and functions of the unfolded protein response. *Nat. Rev. Mol. Cell Biol.* 21: 421-438. <https://doi.org/10.1038/s41580-020-0250-z>
- Ho, N., C. Xu, and G. Thibault. 2018. From the unfolded protein response to metabolic diseases - lipids under the spotlight. *J. Cell Sci.* 131:jcs199307. <https://doi.org/10.1242/jcs.199307>
- Ho, N., W.S. Yap, J. Xu, H. Wu, J.H. Koh, W.W.B. Goh, B. George, S.C. Chong, S. Taubert, and G. Thibault. 2020. Stress sensor Ire1 deploys a divergent transcriptional program in response to lipid bilayer stress. *J. Cell Biol.* 219:e201909165. <https://doi.org/10.1083/jcb.201909165>
- Hollien, J., and J.S. Weissman. 2006. Decay of endoplasmic reticulum-localized mRNAs during the unfolded protein response. *Science.* 313: 104-107. <https://doi.org/10.1126/science.1129631>
- Hou, N.S., A. Gutschmidt, D.Y. Choi, K. Pather, X. Shi, J.L. Watts, T. Hoppe, and S. Taubert. 2014. Activation of the endoplasmic reticulum unfolded protein response by lipid disequilibrium without disturbed proteostasis in vivo. *Proc. Natl. Acad. Sci. USA.* 111:E2271-E2280. <https://doi.org/10.1073/pnas.1318262111>
- Humphrey, W., A. Dalke, and K. Schulten. 1996. VMD: visual molecular dynamics. *J. Mol. Graph.* 14:33-38. [https://doi.org/10.1016/0263-7855\(96\)00018-5](https://doi.org/10.1016/0263-7855(96)00018-5)
- Kaiser, H.-J., A. Orlowski, T. Róg, T.K. Nyholm, W. Chai, T. Feizi, D. Lingwood, I. Vattulainen, and K. Simons. 2011. Lateral sorting in model membranes by cholesterol-mediated hydrophobic matching. *Proc. Natl. Acad. Sci. USA.* 108:16628-16633. <https://doi.org/10.1073/pnas.1103742108>
- Karagöz, G.E., D. Acosta-Alvear, H.T. Nguyen, C.P. Lee, F. Chu, and P. Walter. 2017. An unfolded protein-induced conformational switch activates mammalian IRE1. *eLife.* 6:e30700. <https://doi.org/10.7554/eLife.30700>
- Karim, A.S., K.A. Curran, and H.S. Alper. 2013. Characterization of plasmid burden and copy number in *Saccharomyces cerevisiae* for optimization of metabolic engineering applications. *FEMS Yeast Res.* 13:107-116. <https://doi.org/10.1111/1567-1364.12016>
- Kaufman, R.J. 2002. Orchestrating the unfolded protein response in health and disease. *J. Clin. Invest.* 110:1389-1398. <https://doi.org/10.1172/JCI0216886>
- Kimata, Y., and K. Kohno. 2011. Endoplasmic reticulum stress-sensing mechanisms in yeast and mammalian cells. *Curr. Opin. Cell Biol.* 23: 135-142. <https://doi.org/10.1016/j.cob.2010.10.008>
- Kimata, Y., Y. Ishiwata-Kimata, T. Ito, A. Hirata, T. Suzuki, D. Oikawa, M. Takeuchi, and K. Kohno. 2007. Two regulatory steps of ER-stress sensor Ire1 involving its cluster formation and interaction with unfolded proteins. *J. Cell Biol.* 179:75-86. <https://doi.org/10.1083/jcb.200704166>
- Klauda, J.B., R.M. Venable, J.A. Freites, J.W. O'Connor, D.J. Tobias, C. Mondragon-Ramirez, I. Vorobyov, A.D. MacKerell Jr., and R.W. Pastor. 2010. Update of the CHARMM all-atom additive force field for lipids: validation on six lipid types. *J. Phys. Chem. B.* 114:7830-7843. <https://doi.org/10.1021/jp101759q>
- Kobashi, K. 1968. Catalytic oxidation of sulfhydryl groups by o-phenanthroline copper complex. *Biochim. Biophys. Acta.* 158:239-245. [https://doi.org/10.1016/0304-4165\(68\)90136-0](https://doi.org/10.1016/0304-4165(68)90136-0)
- Korenykh, A., and P. Walter. 2012. Structural basis of the unfolded protein response. *Annu. Rev. Cell Dev. Biol.* 28:251-277. <https://doi.org/10.1146/annurev-cellbio-101011-155826>
- Korenykh, A.V., P.F. Egea, A.A. Korostelev, J. Finer-Moore, C. Zhang, K.M. Shokat, R.M. Stroud, and P. Walter. 2009. The unfolded protein response signals through high-order assembly of Ire1. *Nature.* 457: 687-693. <https://doi.org/10.1038/nature07661>
- Le, Q.G., and Y. Kimata. 2021. Multiple ways for stress sensing and regulation of the endoplasmic reticulum-stress sensors. *Cell Struct. Funct.* 46:37-49. <https://doi.org/10.1247/csf.21015>
- Lee, J., X. Cheng, J.M. Swails, M.S. Yeom, P.K. Eastman, J.A. Lemkul, S. Wei, J. Buckner, J.C. Jeong, Y. Qi, et al. 2016. CHARMM-GUI Input Generator for NAMD, GROMACS, AMBER, OpenMM, and CHARMM/OpenMM Simulations Using the CHARMM36 Additive Force Field. *J. Chem. Theory Comput.* 12:405-413. <https://doi.org/10.1021/acs.jctc.5b00935>
- Li, H., A.V. Korenykh, S.L. Behrman, and P. Walter. 2010. Mammalian endoplasmic reticulum stress sensor IRE1 signals by dynamic clustering. *Proc. Natl. Acad. Sci. USA.* 107:16113-16118. <https://doi.org/10.1073/pnas.1010580107>
- Li, W., V. Okreglak, J. Peschek, P. Kimmig, M. Zubradt, J.S. Weissman, and P. Walter. 2018. Engineering ER-stress dependent non-conventional mRNA splicing. *eLife.* 7:e35388. <https://doi.org/10.7554/eLife.35388>
- Lopez-Redondo, M.L., N. Coudray, Z. Zhang, J. Alexopoulos, and D.L. Stokes. 2018. Structural basis for the alternating access mechanism of the cation diffusion facilitator YipP. *Proc. Natl. Acad. Sci. USA.* 115: 3042-3047. <https://doi.org/10.1073/pnas.1715051115>
- Matthews, E.E., D. Thévenin, J.M. Rogers, L. Gotow, P.D. Lira, L.A. Reiter, W.H. Brissette, and D.M. Engelman. 2011. Thrombopoietin receptor activation: transmembrane helix dimerization, rotation, and allosteric modulation. *FASEB J.* 25:2234-2244. <https://doi.org/10.1096/fj.10-178673>
- McQuin, C., A. Goodman, V. Chernyshev, L. Kametsky, B.A. Cimini, K.W. Karhohs, M. Doan, L. Ding, S.M. Rafelski, D. Thirstrup, et al. 2018. CellProfiler 3.0: Next-generation image processing for biology. *PLoS Biol.* 16:e2005970. <https://doi.org/10.1371/journal.pbio.2005970>
- Mori, K., A. Sant, K. Kohno, K. Normington, M.J. Gething, and J.F. Sambrook. 1992. A 22 bp cis-acting element is necessary and sufficient for the induction of the yeast KAR2 (BiP) gene by unfolded proteins. *EMBO J.* 11: 2583-2593. <https://doi.org/10.1002/j.1460-2075.1992.tb05323.x>
- Mori, K., W. Ma, M.J. Gething, and J. Sambrook. 1993. A transmembrane protein with a cdc2+/CDC28-related kinase activity is required for signaling from the ER to the nucleus. *Cell.* 74:743-756. [https://doi.org/10.1016/0092-8674\(93\)90521-Q](https://doi.org/10.1016/0092-8674(93)90521-Q)
- Nikawa, J., and S. Yamashita. 1992. IRE1 encodes a putative protein kinase containing a membrane-spanning domain and is required for inositol phototrophy in *Saccharomyces cerevisiae*. *Mol. Microbiol.* 6:1441-1446. <https://doi.org/10.1111/j.1365-2958.1992.tb00864.x>
- Ormö, M., A.B. Cubitt, K. Kallio, L.A. Gross, R.Y. Tsien, and S.J. Remington. 1996. Crystal structure of the Aequorea victoria green fluorescent protein. *Science.* 273:1392-1395. <https://doi.org/10.1126/science.273.5280.1392>
- Parrinello, M., and A. Rahman. 1981. Polymorphic transitions in single crystals: A new molecular dynamics method. *J. Appl. Phys.* 52:7182-7190. <https://doi.org/10.1063/1.328693>
- Pineau, L., and T. Ferreira. 2010. Lipid-induced ER stress in yeast and β cells: parallel trails to a common fate. *FEMS Yeast Res.* 10:1035-1045. <https://doi.org/10.1111/j.1567-1364.2010.00674.x>
- Promlek, T., Y. Ishiwata-Kimata, M. Shido, M. Sakuramoto, K. Kohno, and Y. Kimata. 2011. Membrane aberrancy and unfolded proteins activate the endoplasmic reticulum stress sensor Ire1 in different ways. *Mol. Biol. Cell.* 22:3520-3532. <https://doi.org/10.1091/mbc.11-04-0295>
- Radanović, T., J. Reinhard, S. Ballweg, K. Pesek, and R. Ernst. 2018. An Emerging Group of Membrane Property Sensors Controls the Physical State of Organellar Membranes to Maintain Their Identity. *BioEssays.* 40:e1700250. <https://doi.org/10.1002/bies.201700250>
- Reinhard, J., C. Mattes, K. Váth, T. Radanović, M.A. Surma, C. Klose, and R. Ernst. 2020. A Quantitative Analysis of Cellular Lipid Compositions During Acute Proteotoxic ER Stress Reveals Specificity in the Production of Asymmetric Lipids. *Front. Cell Dev. Biol.* 8:756. <https://doi.org/10.3389/fcell.2020.00756>
- Schindelin, J., I. Arganda-Carreras, E. Frise, V. Kaynig, M. Longair, T. Pietzsch, S. Preibisch, C. Rueden, S. Saalfeld, B. Schmid, et al. 2012. Fiji: an open-source platform for biological-image analysis. *Nat. Methods.* 9: 676-682. <https://doi.org/10.1038/nmeth.2019>
- Sepulveda, D., D. Rojas-Rivera, D.A. Rodríguez, J. Groenendyk, A. Köhler, C. Lebeaupin, S. Ito, H. Urrea, A. Carreras-Sureda, Y. Hazari, et al. 2018. Interactome Screening Identifies the ER Luminal Chaperone Hsp47 as a Regulator of the Unfolded Protein Response Transducer IRE1 α . *Mol. Cell.* 69:238-252.e7. <https://doi.org/10.1016/j.molcel.2017.12.028>
- Sidrauski, C., and P. Walter. 1997. The transmembrane kinase Ire1p is a site-specific endonuclease that initiates mRNA splicing in the unfolded protein response. *Cell.* 90:1031-1039. [https://doi.org/10.1016/S0092-8674\(00\)80369-4](https://doi.org/10.1016/S0092-8674(00)80369-4)
- Soskine, M., S. Steiner-Mordoch, and S. Schuldiner. 2002. Crosslinking of membrane-embedded cysteines reveals contact points in the EmrE oligomer. *Proc. Natl. Acad. Sci. USA.* 99:12043-12048. <https://doi.org/10.1073/pnas.192392899>
- Surma, M.A., C. Klose, D. Peng, M. Shales, C. Mrejen, A. Stefanko, H. Braberg, D.E. Gordon, D. Vorkel, C.S. Ejsing, et al. 2013. A lipid E-MAP identifies Ubx2 as a critical regulator of lipid saturation and lipid bilayer stress. *Mol. Cell.* 51:519-530. <https://doi.org/10.1016/j.molcel.2013.06.014>



- Tam, A.B., A.C. Koong, and M. Niwa. 2014. Ire1 has distinct catalytic mechanisms for XBP1/HAC1 splicing and RIDD. *Cell Rep.* 9:850–858. <https://doi.org/10.1016/j.celrep.2014.09.016>
- Thévenaz, P., U.E. Ruttimann, and M. Unser. 1998. A pyramid approach to subpixel registration based on intensity. *IEEE Trans. Image Process.* 7: 27–41. <https://doi.org/10.1109/83.650848>
- Travers, K.J., C.K. Patil, L. Wodicka, D.J. Lockhart, J.S. Weissman, and P. Walter. 2000. Functional and genomic analyses reveal an essential coordination between the unfolded protein response and ER-associated degradation. *Cell.* 101:249–258. [https://doi.org/10.1016/S0092-8674\(00\)80835-1](https://doi.org/10.1016/S0092-8674(00)80835-1)
- van Anken, E., D. Pincus, S. Coyle, T. Aragón, C. Osman, F. Lari, S. Gómez Puerta, A.V. Korennykh, and P. Walter. 2014. Specificity in endoplasmic reticulum-stress signaling in yeast entails a step-wise engagement of HAC1 mRNA to clusters of the stress sensor Ire1. *eLife.* 3:e05031. <https://doi.org/10.7554/eLife.05031>
- Volmer, R., K. van der Ploeg, and D. Ron. 2013. Membrane lipid saturation activates endoplasmic reticulum unfolded protein response transducers through their transmembrane domains. *Proc. Natl. Acad. Sci. USA.* 110: 4628–4633. <https://doi.org/10.1073/pnas.1217611110>
- Walter, P., and D. Ron. 2011. The unfolded protein response: from stress pathway to homeostatic regulation. *Science.* 334:1081–1086. <https://doi.org/10.1126/science.1209038>
- Wu, E.L., X. Cheng, S. Jo, H. Rui, K.C. Song, E.M. Dávila-Contreras, Y. Qi, J. Lee, V. Monje-Galvan, R.M. Venable, et al. 2014. CHARMM-GUI Membrane Builder toward realistic biological membrane simulations. *J. Comput. Chem.* 35:1997–2004. <https://doi.org/10.1002/jcc.23702>

Downloaded from http://jcb.rupress.org/jcb/article-pdf/202/8/e202011078/1418855/jcb_202011078.pdf by guest on 31 January 2023



Supplemental material

Downloaded from http://rupress.org/jcb/article-pdf/2018/e202011078/1418855/jcb_202011078.pdf by guest on 31 January 2023

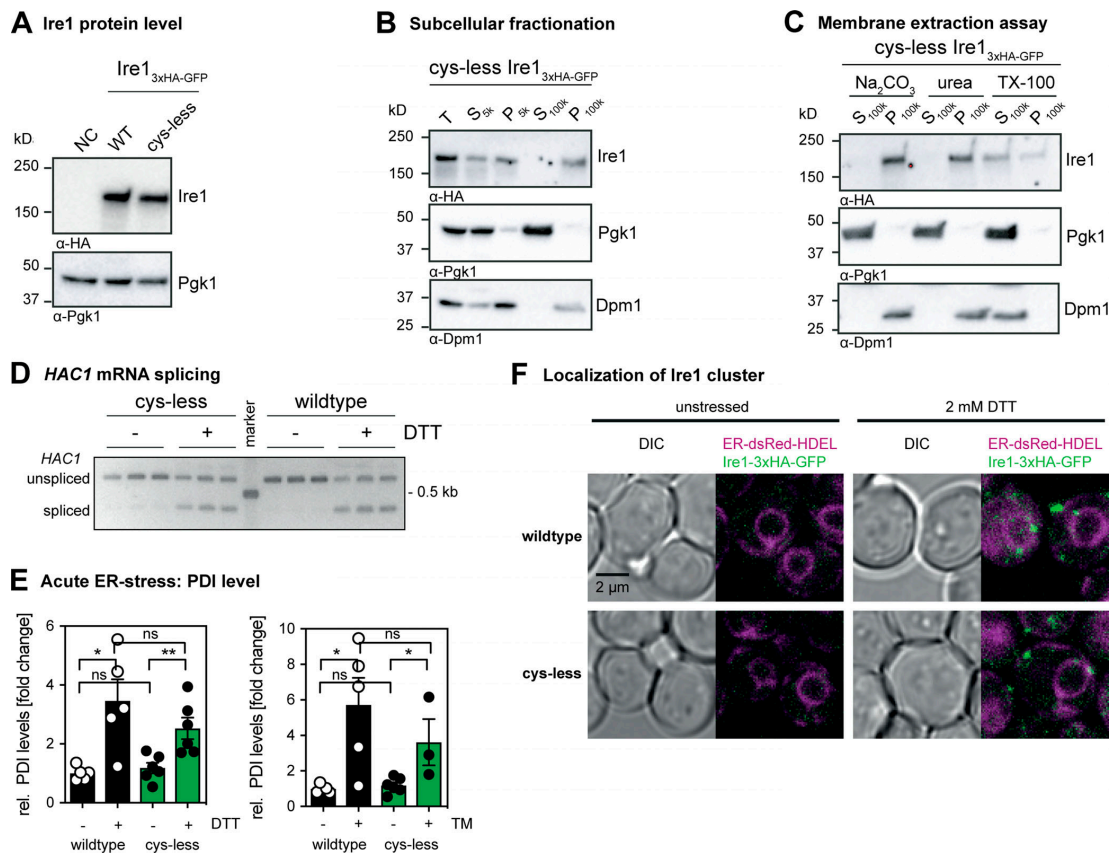


Figure S1. **Protein levels of cysteine-less Ire1 and characterization of its membrane association.** (A) Protein levels of cells expressing either *IRE1*_{3xHA-GFP} WT or the cysteine-less (*cys-less*) variant. The isogenic WT strain BY4741 that does not express a HA-tagged variant of *IRE1* was used as a negative control (NC). Stationary overnight cultures were used to inoculate a fresh culture in SCD complete to an OD_{600} of 0.2 and cultivated until an OD_{600} of 1 was reached. 0.1 OD equivalents of cell lysates were immunoblotted using anti-HA and anti-Pgk1 antibodies. (B) Subcellular fractionation of exponentially growing cells expressing cysteine-less *IRE1*_{3xHA-GFP} by differential centrifugation at 5,000 $\times g$ and 100,000 $\times g$. Stationary overnight cultures were used to inoculate a fresh culture in SCD complete to an OD_{600} of 0.2 and cultivated until an OD_{600} of 1 was reached. 80 OD_{600} equivalents were harvested, lysed, and served as total input (T) for microsomal membrane preparation. The total lysate (T), and the individual supernatant (S) and pellet (P) fractions from centrifugation steps at 5,000 $\times g$ (5k) and 100,000 $\times g$ (100k) were analyzed separately by immunoblotting using anti-HA, anti-Pgk1, and anti-Dpm1 antibodies. 0.4 OD equivalents were loaded per lane. (C) Extraction assay of microsomes. Carbonate and urea extraction validate proper membrane integration of cysteine-less *IRE1*_{3xHA-GFP} (*cys-less*). Samples of each step corresponding to 0.2 OD equivalents were analyzed by immunoblotting using anti-HA, anti-Pgk1, and anti-Dpm1 antibodies. (D) The indicated strains from a stationary culture were used to inoculate fresh culture in SCD to an OD_{600} of 0.2. After cultivation at 30°C to an OD_{600} of 0.7, cells were either left untreated or stressed with DTT (1 h, 2 mM, SCD). The level of the cDNA obtained from the spliced and unspliced HAC1 mRNA was amplified and separated by a 2% agarose gel. (E) PDI1 mRNA levels in acutely stressed cells normalized to the fold change of unstressed cells expressing *IRE1*_{3xHA-GFP} WT. Exponentially growing cells of the indicated strains were used to inoculate fresh YPD media to an OD_{600} of 0.2, cultivated in YPD, and acutely stressed with either 4 mM DTT (left) or 1.0 $\mu g/ml$ TM (right) for 1 h. The relative level of PDI1 in these cells was analyzed by RT-qPCR and quantitated using the comparative $\Delta\Delta CT$ method using normalization to ACT1 levels. The data were normalized to the PDI1 level in unstressed cells carrying the *IRE1*_{3xHA-GFP} WT construct. All error bars in this figure represent the mean \pm SEM. Number of independent experiments: (left) -DTT: WT ($n = 6$); -DTT: cysteine-less ($n = 6$); +DTT: WT ($n = 5$); cysteine-less ($n = 6$); (right) -TM: WT ($n = 5$); cysteine-less ($n = 6$); +TM: WT ($n = 5$); cysteine-less ($n = 3$). Significance was tested by an unpaired, two-tailed Student's *t* test. *, $P < 0.05$; **, $P < 0.01$. Data distribution was assumed to be normal, but this was not formally tested. (F) Cells were cultivated from OD_{600} of 0.2 to OD_{600} of 0.7 in SCD medium and then either left untreated or stressed with 2 mM DTT for 1 h. Live cells were mounted on agar slides, and z-stacks were recorded using confocal microscopy. Images show the center plane of indicated channels. DIC, differential interference contrast; rel., relative; TX-100, Triton X-100.

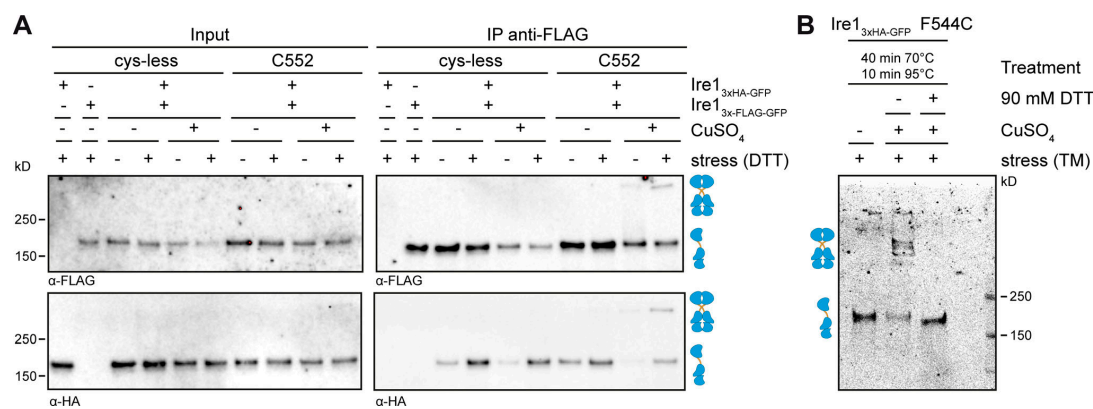
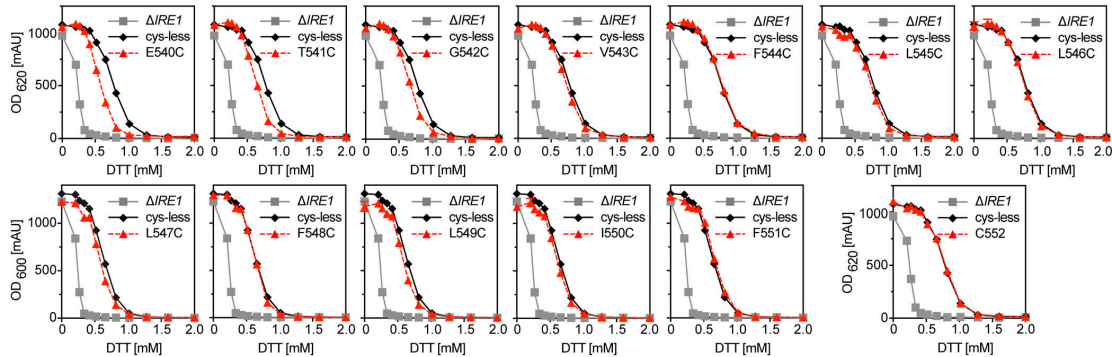
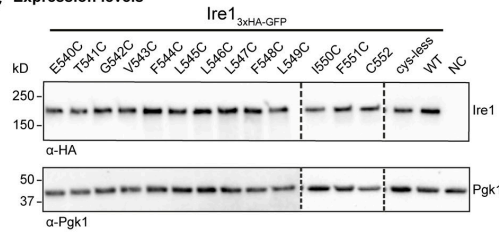


Figure S2. **Validation of a covalent, reversible cross-linking of Ire1 homodimers via disulfide bridges.** (A) A cross-linking experiment using CuSO₄ was performed with microsomes prepared from cells expressing a HA-tagged variant of Ire1 from endogenous locus (*Ire1*_{3xHA-GFP}) and a Flag-tagged variant (*Ire1*_{3xFLAG-GFP}) from a CEN-based plasmid. A yeast culture in selective medium without leucine was inoculated to an OD₆₀₀ of 0.2 from a stationary overnight culture and cultivated at 30°C until an OD₆₀₀ of 0.7 was reached. The cells were either stressed with 2 mM DTT or left untreated and were further cultivated for 1 h. 80 OD₆₀₀ equivalents from these cultures were harvested by centrifugation. Microsomal membranes were isolated by differential centrifugation. Microsomes prepared from cells expressing only one of the two tagged variants of Ire1 served as controls. Both constructs contained a single cysteine in the TMH region at the position 552 (C552). After incubation of the microsomes with 10 mM CuSO₄ on ice for 5 min, the cross-linking reaction was stopped by the addition of NEM in a final concentration of 111 mM and EDTA in a final concentration of 50 mM. The microsomes were then solubilized using 2% Triton X-100 and subjected to an IP using anti-Flag beads. Both the input and IP samples were analyzed by immunoblotting using anti-Flag and anti-HA antibodies. (B) The reversibility of the cysteine-mediated cross-link was validated using the indicated F544C variant of Ire1_{3xHA-GFP}. The cross-link was induced by CuSO₄ in microsomes prepared from cells stressed with TM as described in Fig. 3. The cross-link was reverted by treating the sample with 90 mM DTT and incubating at 70° and 95° as indicated. The monomeric and dimeric species of Ire1 are indicated by symbols.

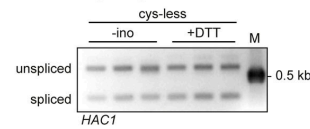
A Functionality of cysteine mutants



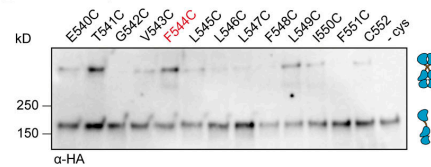
C Expression levels



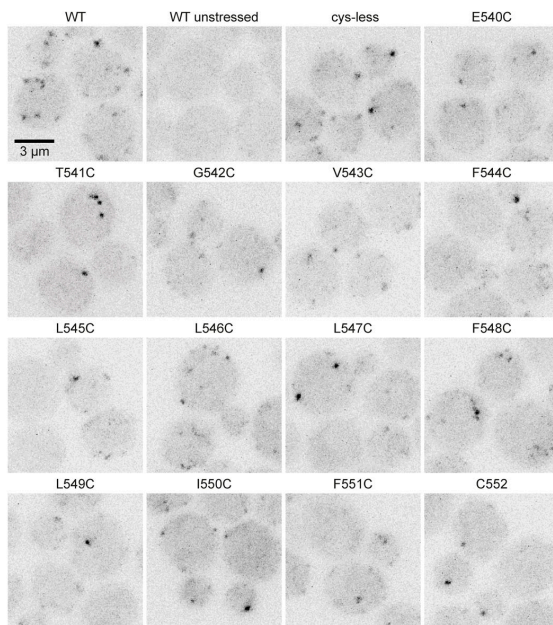
B HAC1 mRNA splicing



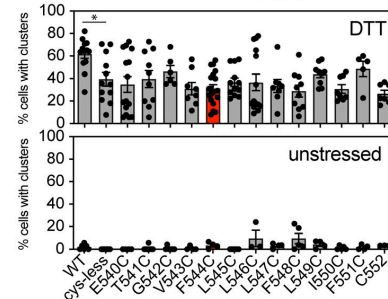
D Inositol depletion crosslinks



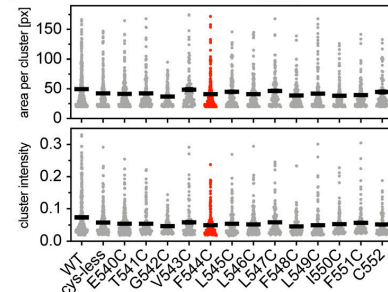
E Formation of Ire1^{3HA-GFP} clusters



F Quantification of cells with Ire1^{3HA-GFP} clusters



G Properties of DTT-induced Ire1^{3HA-GFP} clusters



Downloaded from <http://jcb.rupress.org/> at 2020/11/07 14:18:55 by guest on 31 January 2023

Figure S3. Functionality of cysteine mutants and their cross-linking potential in lipid bilayer stress conditions. (A) The resistance to ER stress was investigated for the indicated yeast strains. Stationary overnight cultures of the indicated yeast strains were used to inoculate a fresh culture in full or minimal media to an OD_{600} of 0.2. After cultivation for 5–7 h at 30°C, the cells were diluted with fresh minimal media to an OD_{600} of 0.1. Cells were cultivated for 18 h at 30°C and stressed with DTT. The density of the resulting culture was determined using the OD_{620} or OD_{600} . The error bars represent the mean \pm SEM of at least two independent clones. Number of experiments to yield OD_{620} : $\Delta IRE1$ ($n = 20$; identical to Fig. 1 B); cysteine-less ($n = 12$; identical to Fig. 1 B); E540C to L546C ($n = 6$; triplicates from two individual colonies); and C552 ($n = 12$; triplicates from two individual colonies). Number of experiments to yield OD_{600} : $\Delta IRE1$ ($n = 10$; replicates from three individual colonies); cysteine-less ($n = 22$; replicates from four individual colonies); L547C, L549C, I550C, and F551C ($n = 6$; triplicates from two individual colonies); and F548C ($n = 5$; replicates from two individual colonies). (B) The indicated strains were cultivated and treated as described in Fig. 3, C and D, using conditions of proteotoxic (+DD) and lipid bilayer stress (-ino), respectively. The level of the cDNA obtained from the spliced and unspliced *HAC1* mRNA was amplified and separated by a 2% agarose gel using a DNA ladder as size marker (M). (C) Protein levels of cells expressing different *IRE1*_{3xHA-GFP} variants. The lysates of exponentially growing cells were immunoblotted using anti-HA and anti-Pgk1 antibodies. (D) Cross-linking of single cysteine variants of Ire1 in microsomes derived from cells grown in lipid bilayer stress conditions. Exponentially growing cells in SCD complete media were washed and used to inoculate a fresh culture in SCD complete to an OD_{600} of 0.5. To induce lipid bilayer stress, the cells were washed and then cultivated in pre-warmed SCD complete without inositol medium for 3 h. 80 OD equivalents were harvested and used for microsomal membrane preparation. $CuSO_4$ -induced cross-link was performed by incubating 8 μ l of microsomes with 2 μ l of 50 mM $CuSO_4$ for 5 min on ice. After stopping the reaction with NEM and EDTA, samples were subjected to SDS-PAGE with a subsequent immunoblotting with anti-HA antibody. Notably, all samples subjected to SDS-PAGE underwent a cross-linking procedure. Differences in specific and unspecific cross-linking may falsely suggest differences in loading. (E) Cells were cultivated to the early exponential phase in SCD and either treated with 2 mM DTT for 1 h or left untreated. Representative images (maximum projections of z-stacks) recorded by confocal microscopy. (F) The percentage of cluster-containing cells was determined for stressed (2 mM DTT, 1 h) and unstressed cells using a custom-made CellProfiler pipeline. The percentage of cluster-containing cells with the cysteine-less variant of Ire1 is not significantly different from any of the cells with single-cysteine variants. All data for the WT and cysteine-less variant are identical to the data from Fig. 1 C and plotted as a reference. For stressed cells: E540C ($n = 12$ fields of view/359 cells); T541C ($n = 10/206$); G542C ($n = 6/124$); V543C ($n = 8/223$); F544C ($n = 19/439$); L545C ($n = 12/181$); L546C ($n = 14/399$); L547C ($n = 8/203$); F548C ($n = 10/279$); L549C ($n = 9/212$); I550C ($n = 8/232$); F551C ($n = 5/152$); and C552 ($n = 7/188$). For unstressed cells: E540C ($n = 4$ fields of view/130 cells); T541C ($n = 7/153$); G542C ($n = 7/188$); V543C ($n = 4/121$); F544C ($n = 4/108$); L545C ($n = 5/101$); L546C ($n = 3/111$); L547C ($n = 4/106$); F548C ($n = 5/143$); L549C ($n = 4/103$); I550C ($n = 5/165$); F551C ($n = 4/108$); and C552 ($n = 3/90$). (G) The area of the detected clusters in the z-projection was determined and plotted. It was 49.9 px for the WT variant, 42.6 px for the cysteine-less variant, and ranged from a minimum of 37.2 px (G542C) to maximum of 48.9 px (V543C) for the single-cysteine variants. The integrated fluorescent intensity of detected clusters was 0.074 (arbitrary units) for the WT, 0.059 for the cysteine-less construct, and ranged from a minimum of 0.046 for the F548C variant to a maximum of 0.059 for the L547C variant. Significance was tested using a Kolmogorov–Smirnov test (*, $P < 0.05$). The segmented and analyzed number of clusters for each construct was as follows: WT: $n = 395$ (raw data in Fig. 1 D); cysteine-less: $n = 211$ (raw data in Fig. 1 D); E540C: $n = 215$; T541C: $n = 158$; G542C: $n = 95$; V543C: $n = 101$; F544C: $n = 224$; L545C: $n = 131$; L546C: $n = 191$; L547C: $n = 121$; F548C: $n = 127$; L549C: $n = 168$; I550C: $n = 121$; F551C: $n = 113$; and C552: $n = 75$. px, pixels.

Downloaded from http://rpress.org/jcb/article-pdf/2020/1078/1418855/jcb_202011078.pdf by guest on 31 January 2023

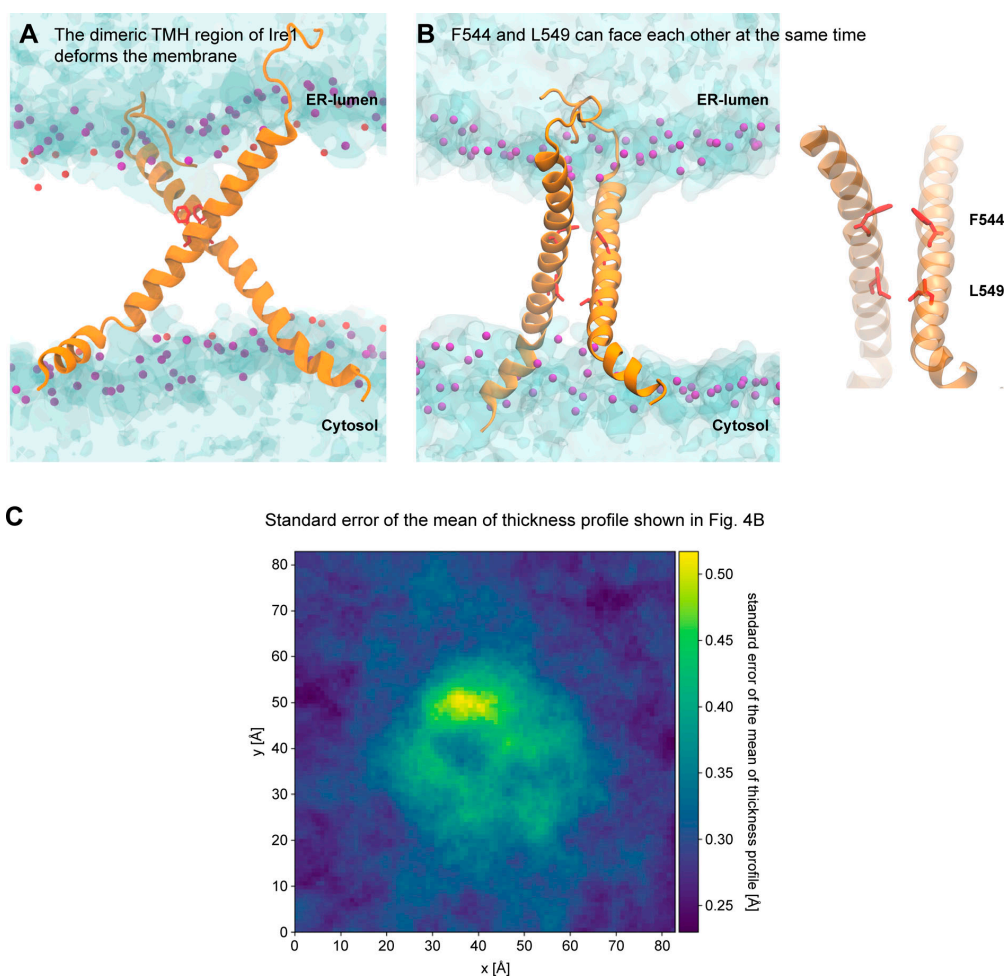


Figure S4. **The dimeric TMH region of Ire1 deforms the membrane.** **(A)** Membrane deformation by the modeled, dimeric TMH region of Ire1. Water is shown in blue tones with a transparent surface representation. The phosphate moieties of POPC are shown as purple beads. **(B)** Configuration of a model TMH dimer obtained from atomistic molecular dynamics simulations. Protomers are shown as an orange ribbon, with the residues F544 and L549 highlighted in red. The phosphate moieties of POPC are shown as purple beads. The hydroxyl groups of cholesterol molecules are shown as red beads. Water is shown with a transparent surface representation. Right: Lipid and water are not shown for clarity. **(C)** The SEM of the thickness profile represented in Fig. 4 B. The thickness fluctuations in the proximity of the TMH dimer (not shown, centered in the middle of the box) give rise to a locally increased SEM of the thickness profile, but is much lower than the actual degree of membrane deformation as plotted in Fig. 4 B.

Downloaded from http://rupress.org/jcb/article-pdf/2018/20/2011078/118855/jcb_202011078.pdf by guest on 31 January 2023

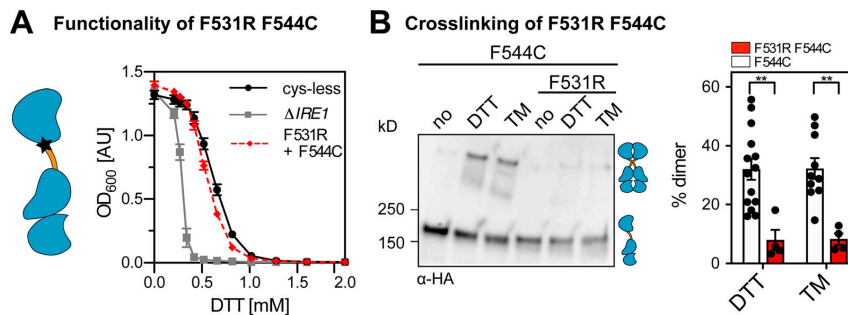


Figure S5. **A mutation of the AH affects Ire1 function and cross-linking propensity.** (A) The ER-stress resistance of cells expressing the AH-disrupting F531R variant of *IRE1*_{3xHA-GFP} containing the F544C single-cysteine was scored using an ER-stress resistance assay. The indicated cells were cultivated and treated as in Fig. 5, A and C. Data for Δ *IRE1* and the cysteine-less construct are identical to data in Fig. 5 A. F531R/F544C ($n = 12$ independent experiments from two individual colonies). (B) The impact of the AH-disrupting F531R mutation of Ire1 on the degree of cross-linking via the single-cysteine variant F544C was determined using the microsome-based cross-linking assay. Cells were cultivated and further treated as described in Fig. 5, B and D. The data are represented as the mean \pm SEM. All data related to the F544C variant are identical to the data in Fig. 3 F. F531R/F544C ($n = 4$ independent experiments from two individual colonies). Significance was tested by an unpaired, two-tailed Student's t test. **, $P < 0.01$.

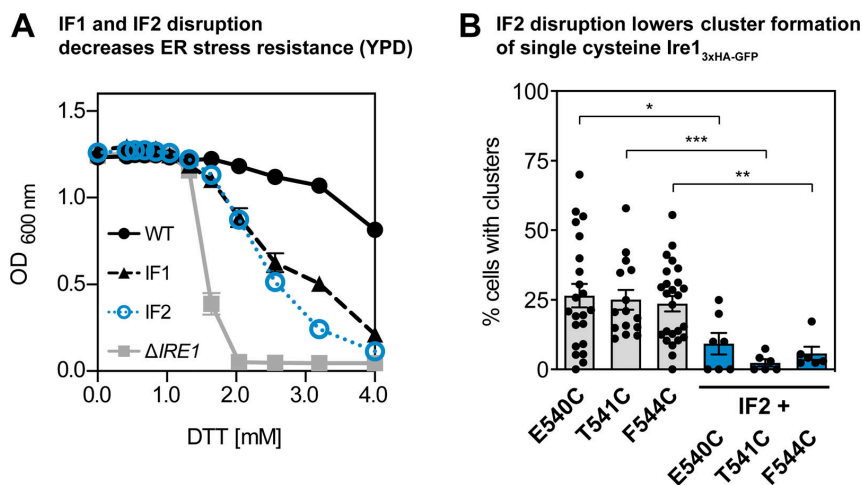


Figure S6. **Disrupting ER-luminal interfaces for dimerization (IF1) and oligomerization (IF2) of Ire1 impairs cellular ER-stress resistance and the formation of Ire1 clusters.** (A) The resistance to DTT of cells expressing the IF1 (T226A/F247A) or IF2 (W426A) variants of *IRE1* with all native cysteines was analyzed in rich medium. The indicated cells were cultivated and treated as in Fig. 5, A and C. Data for Δ *IRE1* (gray squares) and *IRE1* WT knock-in construct with all native cysteines (black circles) are plotted as a reference. WT ($n = 6$) and IF2 ($n = 12$) data were from two individual colonies. IF1 ($n = 4$) and Δ *IRE1* ($n = 6$) data are from a single colony. (B) The percentage of cluster-containing cells was determined for the indicated strains cultivated in SCD medium and stressed with 2 mM DTT for 1 h. We re-used the raw microscopic data from Fig. S3 F for E540C ($n = 15$ fields of view/374 cells), T541C ($n = 9/181$), and F544C ($n = 19/440$), re-analyzed them as described in the Materials and methods, and pooled those with additional data for E540C ($n = 7/281$), T541C ($n = 6/172$), and F544C ($n = 6/213$). We also studied the clustering of E540C/IF2 ($n = 7/98$), T541C/IF2 ($n = 6/150$), and F544C/IF2 ($n = 6/208$). Microscopic images were analyzed using a customized CellProfiler pipeline. The percentage of cluster-containing cells with single cysteine variants of Ire1 is significantly different from any of the cells where the ER-luminal IF2 was disrupted by mutation (W426A). The data are represented as the mean \pm SEM. Significance was tested using a Kolmogorov-Smirnov test (*, $P < 0.05$; **, $P < 0.01$; ***, $P < 0.001$).

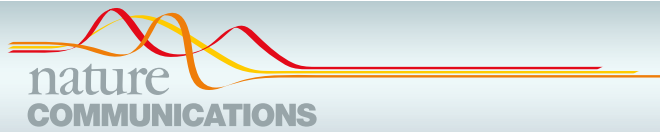


Video 1. **A structural model of the TMH region of Ire1 highlights membrane thinning and water penetration into the bilayer.** The two protomers of Ire1 TMH region are shown as orange ribbons. The residue corresponding to F544 is highlighted in red. The phosphate moieties of the lipid headgroups are shown as red/purple spheres. Water is indicated as shaded region to highlight membrane thinning. Lipid acyl chains are not shown for clarity.

Video 2. **Dynamics of the TMH region of Ire1 dimers over a period of 600 ns.** The two TMH regions are shown as orange ribbons. The residue corresponding to F544 is highlighted in red, while residues T541 to F551 are shown in blue. The phosphate moieties of the lipid headgroups are shown as purple spheres. Water, ions, and lipid acyl chains are omitted for clarity.

Tables S1 and S2 are provided online as separate files. Table S1 shows yeast strains used in this study. Table S2 shows plasmids used in this study.

Downloaded from http://jcb.rupress.org/jcb/article-pdf/2018/2/2011078/118855/jcb_202011078.pdf by guest on 31 January 2023



ARTICLE

<https://doi.org/10.1038/s41467-020-14528-1>

OPEN

Regulation of lipid saturation without sensing membrane fluidity

Stephanie Ballweg^{1,2}, Erdinc Sezgin³, Milka Doktorova⁴, Roberto Covino⁵, John Reinhard^{1,2},
Dorith Wunnicke⁶, Inga Hänel⁶, Ilya Levental⁴, Gerhard Hummer^{5,7} & Robert Ernst^{1,2*}

Cells maintain membrane fluidity by regulating lipid saturation, but the molecular mechanisms of this homeoviscous adaptation remain poorly understood. We have reconstituted the core machinery for regulating lipid saturation in baker's yeast to study its molecular mechanism. By combining molecular dynamics simulations with experiments, we uncover a remarkable sensitivity of the transcriptional regulator Mga2 to the abundance, position, and configuration of double bonds in lipid acyl chains, and provide insights into the molecular rules of membrane adaptation. Our data challenge the prevailing hypothesis that membrane fluidity serves as the measured variable for regulating lipid saturation. Rather, we show that Mga2 senses the molecular lipid-packing density in a defined region of the membrane. Our findings suggest that membrane property sensors have evolved remarkable sensitivities to highly specific aspects of membrane structure and dynamics, thus paving the way toward the development of genetically encoded reporters for such properties in the future.

¹Medical Biochemistry and Molecular Biology, Medical Faculty, Saarland University, Kirrberger Strasse 100, Building 61.4, 66421 Homburg, Germany.

²PZMS, Center for Molecular Signaling (PZMS), Medical Faculty, Saarland University, 66421 Homburg, Germany. ³MRC Human Immunology Unit, MRC Weatherall Institute of Molecular Medicine, University of Oxford, Oxford, UK. ⁴Department of Integrative Biology and Pharmacology, McGovern Medical School at the University of Texas Health Science Center, Houston, Texas, USA. ⁵Department of Theoretical Biophysics, Max Planck Institute of Biophysics, Max-von-Laue-Strasse 3, 60438 Frankfurt, Germany. ⁶Institute of Biochemistry, Goethe University Frankfurt, Max-von-Laue-Strasse 9, 60438 Frankfurt, Germany. ⁷Institute of Biophysics, Goethe University Frankfurt, 60438 Frankfurt, Germany. *email: robert.ernst@uks.eu

Cellular membranes are complex assemblies of proteins and lipids, which collectively determine physical bilayer properties such as membrane fluidity/viscosity, permeability, and the lateral pressure profile^{1–4}. Membrane fluidity determines how easily lipids and proteins can diffuse laterally in the plane of the membrane. We quantify it by measuring the diffusion coefficient of membrane lipids, which is inversely proportional to membrane viscosity. The acyl chain composition of membrane lipids is an important determinant of membrane fluidity and is tightly controlled in bacteria^{5–7}, fungi^{8,9}, worms^{10,11}, flies¹², and vertebrates^{13,14}. Saturated lipid acyl chains tend to form non-fluid, tightly packed gel phases at physiological temperatures, whereas unsaturated lipid acyl chains fluidize the bilayer. Poikilothermic organisms that cannot control their body temperature must adjust their lipid composition during cold stress to maintain membrane functions—a phenomenon referred to as the homeoviscous adaptation^{15–17}. Despite recent advances in identifying candidate sensory machineries, it remains largely unknown how they work on the molecular scale and how they are coordinated for maintaining the physicochemical properties of cellular membranes^{18,19}. The fact that most, if not all, membrane properties are interdependent is a key challenge for this emerging field. How do cells, e.g., balance the need for maintaining membrane fluidity with the need to maintain organelle-specific lateral pressure profiles²⁰? A perturbation of membrane fluidity by genetically targeting fatty acid metabolism, e.g., leads to complex changes throughout the entire lipidome impacting on other bilayer properties, thereby causing endoplasmic reticulum (ER) stress and a disruption of membrane architecture^{21–23}. We lack a unifying theory to accurately predict the properties of a membrane given its composition: each component of a complex biological membrane contributes to its collective physicochemical properties in a non-additive and nonlinear manner^{3,24}. As an important step towards a unifying membrane theory, we need to identify a set of membrane properties that are both minimally correlated and sufficient to uniquely describe the state of a bilayer. Characterizing naturally occurring membrane property sensors, which may exhibit highly specialized sensitivities to specific membrane properties, holds promise to better understand how cells prioritize the maintenance of such orthogonal membrane properties¹⁹.

Eukaryotic cells use sensor proteins possessing refined mechanisms to monitor physicochemical properties of organellar membranes and to adjust lipid metabolism during stress, metabolic adaptation, and development^{10,23,25–30}. These sensor proteins can be categorized into three classes, based on topological considerations^{18,19}. Class I sensors interrogate surface properties of cellular membranes, such as the surface charge and molecular packing density as reported for amphipathic lipid-packing sensor (ALPS) motif-containing proteins and other amphipathic helix-containing proteins³¹. Class II sensors perturb and interrogate the hydrophobic core of the bilayer and have been implicated in the regulation of lipid saturation. Class III sensors are transmembrane proteins acting across the bilayer by locally squeezing, stretching, and/or bending the membrane to challenge selective properties such as thickness or bending rigidity^{18,19}.

The prototypical class II sensor Mga2 is crucial for the regulation of membrane fluidity in baker's yeast^{9,25} (Fig. 1a). Its single transmembrane helix (TMH) senses a physicochemical signal in the ER membrane to control a homeostatic response that adjusts membrane lipid saturation via the essential fatty acid *cis*- Δ 9-desaturase Ole1^{32–34}. Increased lipid saturation triggers the ubiquitylation of three lysine residues in the cytosolic juxta-membrane region of Mga2 by the E3 ubiquitin ligase Rsp5³⁵. This ubiquitylation serves as a signal for the proteasome-dependent processing of the membrane-bound Mga2 precursor (P120) and

the release of a transcriptionally active P90 fragment, which upregulates *OLE1* expression³⁶ (Fig. 1a). This regulated, ubiquitin/proteasome-dependent processing resembles the pathway of ER-associated degradation (ERAD)³⁷ and was first described for Spt23, a close structural and functional homolog of Mga2³⁸. As Ole1 is the only source for the de novo biosynthesis of unsaturated fatty acids (UFAs), its tight regulation is essential for maintaining membrane fluidity in this poikilotherm^{9,34}.

Molecular dynamics (MD) simulations have revealed a remarkable conformational flexibility of the Mga2 transmembrane region²⁵. The TMHs of Mga2 dimerize and rotate against each other, thus forming an ensemble of dimerization interfaces. Importantly, the population of these alternative configurations is affected by the membrane lipid environment: higher proportions of saturated lipid acyl chains stabilize a configuration in which two tryptophan residues (W1042) point toward the dimer interface, whereas higher proportions of unsaturated lipid acyl chains favor a conformation where these residues point away from one another and toward the lipid environment^{9,25}. Based on the remarkable correspondence with genetic and biophysical data, we proposed that the membrane-dependent structural dynamics of the TMHs are coupled to the ubiquitylation and activation of Mga2²⁵. However, it remained unclear whether the reported, relatively subtle changes in the population of short-lived rotational conformations are sufficient to control a robust cellular response. How can the processing of Mga2 be blocked by an increased proportion of unsaturated lipids in the membrane, if the sensory TMHs still explore their entire conformational space? How is the “noisy” signal from the TMH propagated via disordered regions to the site of ubiquitylation in the juxtamembrane region (Fig. 1b)?

As an important step toward answering these questions, we have designed and isolated a minimal sensor construct based on Mga2 that can both sense and respond: it senses the membrane environment and acquires, depending on the membrane lipid composition, a poly-ubiquitylation label as a signal for its activation via proteasomal processing. After reconstituting this sense-and-response construct in liposomes with defined lipid compositions, we demonstrate a remarkable sensitivity of Mga2 to specific changes in the bilayer composition. We provide evidence for functional coupling between the TMH and the site of ubiquitylation using electron paramagnetic resonance (EPR) and Förster resonance energy transfer (FRET). Our data contradict a central assumption of the theory of homeoviscous adaptation and rule out the possibility that Mga2 acts as a sensor for membrane fluidity. Instead, we propose that Mga2 senses the packing density at the level of the sensory tryptophans (W1042)²⁵ and thus a small portion of the lateral compressibility profile in the hydrophobic core of the membrane. Analogous to ALPS motifs that recognize lipid-packing defects in the water-membrane interface by inserting hydrophobic residues into the membrane core³⁹, Mga2 might sense the packing density of hydrogen and carbon atoms in the core of the membrane via the bulky residue W1042. We speculate that this packing-dependent sensing, together with chemical interactions, determines the population of different rotational orientations of the entire TMH of Mga2. Thus, our mechanistic analysis of the membrane lipid saturation sensor Mga2 challenges the common view of membrane fluidity as the critical measured variable in membrane biology.

Results

A minimal reporter of membrane lipid saturation. We proposed that Mga2 uses a rotation-based mechanism to sense membrane lipid saturation²⁵ (Fig. 1a). However, the sensory TMHs of Mga2 are separated from the site of ubiquitylation by a

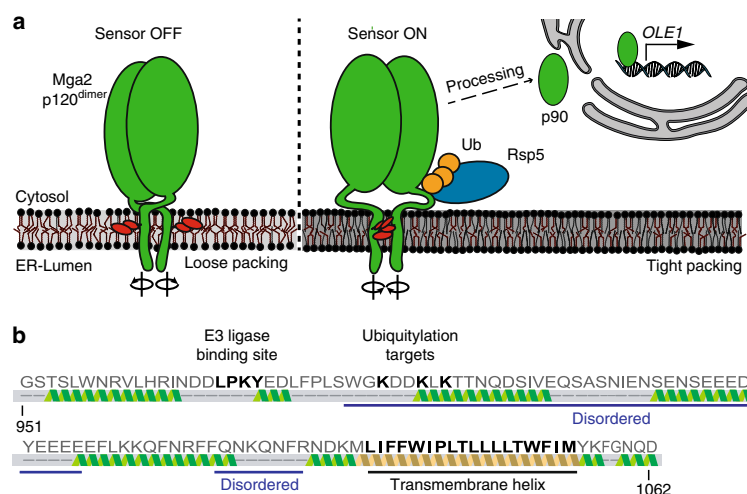


Fig. 1 The activation of Mga2 is controlled by the ER membrane composition. **a** Model of the OLE pathway: the transcription factor Mga2 forms inactive dimers in the ER membrane (Mga2 p120^{dimer}) with highly dynamic TMHs exploring alternative rotational orientations. Loose lipid packing (left) caused by unsaturated lipids stabilizes conformations with two sensory tryptophan residues (W1042; red) pointing away from the dimer interface toward the lipid environment. Tight lipid packing (right) stabilizes alternative rotational conformations with the sensory tryptophans facing each other in the dimer interface (right). The E3 ubiquitin ligase Rsp5 is required to ubiquitylate (Ub) Mga2, thereby facilitating the proteolytic processing by the proteasome and the release of transcriptionally active Mga2 (p90). **b** Secondary structure prediction of the juxtamembrane and transmembrane region (residue 951–1062) of Mga2 using Phyre2⁶⁵. Source data are provided as a Source Data file.

predicted disordered loop and ~50 amino acids (Fig. 1b), thereby posing a question of their functional coupling. How can the conformational dynamics of the TMHs control the ubiquitylation of Mga2? To study the coupling of sensing and ubiquitylation in vitro, we have generated a minimal sense-and-response construct (ZIP-MBP^{Mga2}^{950–1062}) comprising an N-terminal leucine zipper (ZIP) derived from the transcription factor GCN4, the maltose-binding protein (MBP), the juxtamembrane region (950–1036), and the TMH (1037–1058) of Mga2 (950–1062) (Fig. 2a). The N-terminal zipper mimics the IPT (Ig-like, plexin, transcription factor) domain of full-length Mga2 and stabilizes a homo-dimeric state⁴⁰, whereas the MBP was used as a purification and solubility tag²⁵. The juxtamembrane domain of Mga2 comprises the LPKY motif (Mga2^{958–961}) for recruiting the E3 ubiquitin ligase Rsp5⁴¹, three lysine residues K⁹⁸⁰, K⁹⁸³, and K⁹⁸⁵ ubiquitylated in vivo³⁵, and the disordered region linking these motifs to the TMH (Fig. 2a). The construct was recombinantly produced and isolated in the presence of Octyl- β -D-glucopyranoside (OG) using an amylose-coupled affinity matrix and size-exclusion chromatography (SEC) (Fig. 2b and Supplementary Fig. 1a). Expectedly, the N-terminal zipper stabilizes a dimeric form of the sense-and-response construct and supports, at increased concentrations, the formation of higher oligomeric forms as suggested by SEC experiments that also included a zipper-less variant (MBP^{Mga2}^{950–1062}) as a control (Fig. 2c and Supplementary Fig. 1b, c). We reconstituted the sense-and-response construct in liposomes at molar protein-to-lipid ratios between 1:5000 and 1:15,000. As illustrated by the protein-to-lipid ratio of 1:8000 (Supplementary Fig. 1d), we did not detect any sign of protein aggregation in our preparations using sucrose density gradient centrifugations.

We then tested whether the sense-and-response construct could be ubiquitylated in vitro and adapted a strategy established for the ubiquitylation of substrates of the ERAD machinery⁴². We incubated the proteoliposomes with an ATP-regenerating system,

purified 8xHis ubiquitin, and yeast cytosol containing all enzymes required for ubiquitylation (Fig. 2d). Subsequent immunoblot analyses revealed a time-dependent ubiquitylation of the sense-and-response construct, which became apparent as a ladder of MBP-positive signals (Fig. 2e). Control experiments validated the specificity of the ubiquitylation reaction: no ubiquitylation was observed, when the Rsp5-binding site (Δ LPKY) was deleted from the sense-and-response construct (Fig. 2e). Furthermore, despite the presence of 50 lysine residues in the entire construct, the substitution of the three lysine residues (3KR) targeted by Rsp5 in vivo³⁵ was sufficient to prevent the ubiquitylation (Fig. 2e). Notably, these experiments were performed at a relatively high protein-to-lipid ratio of 1:5000, to increase the sensitivity for a potential background ubiquitylation of the control constructs. We conclude that the in vitro ubiquitylation assay is specific, and that the conformational dynamics in the juxtamembrane region are likely to reflect the structural dynamics found in full-length Mga2. Most importantly, this in vitro system also allowed us to test the hypothesis of functional coupling between the sensory TMHs and protein ubiquitylation.

We reconstituted the sense-and-response construct in two distinct membrane environments based on a phosphatidylcholine (PC) matrix but differing in their lipid acyl chain composition. One membrane environment contained 50% unsaturated 18:1 and 50% saturated 16:0 acyl chains (100 mol% 1-palmitoyl-2-oleoyl-*sn*-glycero-3-phosphocholine (POPC); 16:0/18:1), whereas the other was less saturated and contained 75% unsaturated 18:1 and 25% saturated 16:0 acyl chains (50 mol% 1,2-dioleoyl-*sn*-glycero-3-phosphocholine (DOPC); 18:1/18:1, 50 mol% POPC) (Fig. 2f). Notably, this degree of lipid saturation is in the range of the naturally occurring acyl chain compositions reported for baker's yeast cultivated in different conditions^{8,21,43,44}. The sense-and-response construct was efficiently ubiquitylated in the more saturated membrane environment (evidenced by a ladder of bands with lower electrophoretic mobility), but not in the

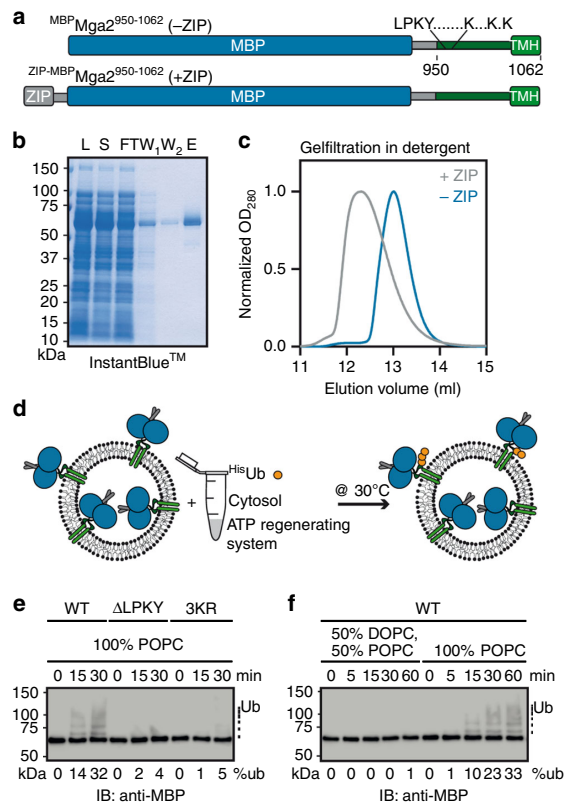


Fig. 2 An in vitro sense-and-response system for membrane lipid saturation. **a** Schematic representation of the sense-and-response constructs. The fusion proteins are composed of the maltose-binding protein (MBP, blue) and Mga2⁹⁵⁰⁻¹⁰⁶² (green) with the Rsp5-binding site (LPKY), three lysine residues as targets of ubiquitylation (K⁹⁸⁰, K⁹⁸³, and K⁹⁸⁵), a predicted disordered juxtamembrane region, and the C-terminal TMH. An optional N-terminal leucine zipper derived from Gcn4 (gray, Gcn4²⁴⁹⁻²⁸¹) supports dimerization. **b** Isolation of the zipped sense-and-response construct by affinity purification. 0.1 OD units of the lysate (L), soluble (S), flow-through (FT), and two wash fractions (W_{1,2}), as well as 1 μg of the eluate were subjected to SDS-PAGE followed by InstantBlue™ staining. The protein was further purified by preparative SEC (Supplementary Fig. 1a). **c** One hundred micrograms in 100 μl of the purified sense-and-response constructs either with (+ZIP) or without zipper (-ZIP) were loaded onto a Superdex 200 10/300 Increase column (void volume 8.8 ml). **d** Schematic representation of the in vitro ubiquitylation assay. Proteoliposomes containing ZIP-MBP-Mga2⁹⁵⁰⁻¹⁰⁶² were mixed with 8xHisUbiquitin (HisUb), an ATP-regenerating system, and cytosol prepared from wild-type yeasts to facilitate Mga2 ubiquitylation at 30 °C. **e** The reaction was performed with the ZIP-MBP-Mga2⁹⁵⁰⁻¹⁰⁶² wild-type (WT) construct, a variant lacking the Rsp5-binding site (ΔLPKY), and a variant with arginine residues instead of the lysine residues K⁹⁸⁰, K⁹⁸³, and K⁹⁸⁵ (3KR), thus lacking the target residues of ubiquitylation. These variants were reconstituted in liposomes composed of 100 mol% POPC at protein-to-lipid ratio of 1:5000. After the indicated times, the reactions were stopped using sample buffer and were subjected to SDS-PAGE. For analysis, an immunoblot using anti-MBP antibodies was performed. **f** Ubiquitylation reactions were performed as in **e** with the WT sense-and-response construct reconstituted in the indicated lipid environments at a molar protein-to-lipid ratio of 1:5000. Source data are provided as a Source Data file.

unsaturated one (Fig. 2f and Supplementary Fig. 1e). This observation highlights the remarkable sensitivity of this class II membrane property sensor and provides strong evidence for a functional coupling between the TMHs and the site of ubiquitylation.

An in vitro strategy to reconstitute membrane lipid sensing. To detect changes of the conformational dynamics in the juxta-membrane region, we established an in vitro FRET assay. We hypothesized that the average distance between the binding site of the E3 ligase Rsp5 (LPKY) and a lysine residue targeted by Rsp5 may be affected by changes in the membrane lipid environment due to a functional coupling with the TMH. We thus generated a donor construct labeled with Atto488 at the position of a lysine residue (K983^D) targeted by the ubiquitylation machinery and an acceptor construct labeled with Atto590 within the Rsp5 recognition site (K969^A) (Förster radius of 59 Å) (Fig. 3a). Notably, the required amino acid substitutions to cysteine at the positions of labeling did not interfere with the activation of full-length Mga2 in vivo (Supplementary Fig. 2a). The individually isolated donor (K983^D) and acceptor (K969^A) constructs exhibited only negligible fluorescence emission at 614 nm in detergent solution upon donor excitation at 488 nm (Fig. 3b). However, a significant emission at 614 nm (from here on referred to as FRET signal) was detectable upon mixing the donor and acceptor constructs (K983^D + K969^A) (Fig. 3b). Notably, a direct excitation of the acceptor at 590 nm (Supplementary Fig. 2b) resulted in equal fluorescence intensities at 614 nm for both K983^D + K969^A and K969^{A,only} samples, but no emission for the K983^{D,only} sample. The normalized FRET signal of the K983^D + K969^A reporter was concentration-dependent in detergent solution (Fig. 3c), thereby suggesting a dynamic equilibrium between monomeric and oligomeric species (presumably dimers) of the labeled sense-and-response construct. To validate this interpretation and to rule out the possibility that the FRET signal was predominantly caused by FRET between stable K983^D-K983^D and K969^A-K969^A dimers bumping into each other, we performed competition experiments. We found that the ratiometric FRET efficiency of the K983^D + K969^A reporter was substantially reduced upon titrating it with an unlabeled sense-and-response construct containing an N-terminal leucine zipper (Fig. 3d). However, it remained unaffected upon titration with an unlabeled construct lacking a zipper (Fig. 3d). This indicates (i) that the zipper centrally contributes to the stability of the dimer, (ii) that individual protomers readily exchange in detergent solution, and (iii) that the FRET signal is mainly due to K983^D-K969^A heterooligomers. In fact, additional titration experiments with the K969^A acceptor revealed that the observed FRET efficiency is a linear function of the molar fraction of the acceptor (Supplementary Fig. 2c, d), thereby indicating that the FRET signal is indeed caused by dimers⁴⁵.

Next, we studied the structural dynamics of the sense-and-response construct in liposomes using the FRET reporter. To this end, we reconstituted K983^{D,only} and the premixed K983^D + K969^A pair in liposomes of defined lipid compositions and recorded fluorescence spectra (Fig. 3e–g). We used a low protein-to-lipid ratio of 1:8000 in these experiments to minimize the contribution of unspecific proximity FRET to the overall signal⁴⁵. We observed a significant FRET signal for the K983^D-K969^A reporter reconstituted in a POPC bilayer (Fig. 3e) evidenced by a decreased donor fluorescence and an increased acceptor emission at 614 nm compared with the K983^{D,only} sample (Fig. 3e). Using this FRET assay, we then studied the impact of the lipid acyl chain composition on the structural dynamics of the juxtamembrane region. The lowest FRET efficiency was observed in a DOPC bilayer containing 100% unsaturated acyl chains

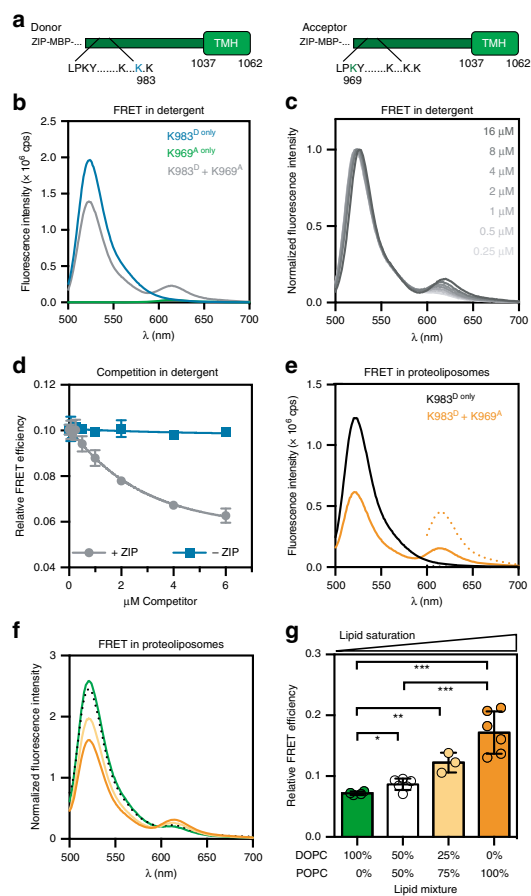


Fig. 3 FRET reveals membrane-dependent conformational changes in the sense-and-response construct. **a** Representation of constructs. The

Atto488 dye is linked to K983C at a position, which is ubiquitinated by Rsp5 in vivo. The Atto590 dye was linked to K969C in the Rsp5-binding site. **b** Fluorescence emission spectra reveal FRET in detergent solution. Each construct ($2\ \mu\text{M}$) were used to record fluorescence emission spectra (ex: 488 nm, em: 500–700 nm) of the donor (K983^D only), acceptor (K969^A only), and the combined (K983^D + K969^A) FRET pair.

c Fluorescence emission spectra were recorded for serial dilutions K983^D + K969^A in detergent solution as in **b**. The spectra were normalized to the maximal intensity at the donor emission. **d** Zipped donor ($2\ \mu\text{M}$) and acceptor ($2\ \mu\text{M}$) pairs were mixed and incubated in detergent solution for 10 min, to allow for protomer exchange and equilibration. This sample was titrated with an unlabeled competitor either with (+ZIP) or without zipper domain (–ZIP). Emission spectra were recorded as in **b**. The relative FRET efficiency was determined from the acceptor-to-donor intensity ratio and plotted as mean \pm SD from two independent experiments. **e** Emission spectra indicate energy transfer within the membrane-reconstituted, dimeric sense-and-response construct. The donor construct was premixed either with an unlabeled (K983^D only) or a labeled acceptor construct (K983^D + K969^A) prior to the reconstitution in POPC liposomes at a protein-to-lipid ratio of 1:8000. Fluorescence emission spectra (em: 500–700 nm) upon donor excitation (ex: 488 nm; solid line) and acceptor excitation (ex: 590 nm; dotted line) are plotted. **f** Donor (K983^D) and acceptor (K969^A) were mixed equimolarly and were incubated in detergent solution prior to a reconstitution in indicated lipid environments. Emission spectra were recorded as in **e** and were normalized to the maximal acceptor emission after direct acceptor excitation (ex: 590 nm). **g** The relative FRET efficiency was derived from the fluorescence spectra in **f** and plotted as mean \pm SD of at least three independent reconstitutions ($n_{\text{DOPC}} = 4$; $n_{1:1}(\text{POPC:DOPC}) = 6$; $n_{3:1}(\text{POPC:DOPC}) = 3$; $n_{\text{POPC}} = 6$). A two-tailed, unpaired *t*-test was performed to test for statistical significance (* $p < 0.05$, ** $p < 0.01$, *** $p < 0.001$). Source data are provided as a Source Data file.

(Fig. 3f, g). At higher proportions of saturated lipid acyl chains in the bilayer, the FRET efficiency increased. These data demonstrate that the acyl chain composition in the hydrophobic core of the membrane imposes structural changes to regions outside the membrane, which have been implicated in signal propagation^{35,41}. Our data establish an intricate functional and structural coupling between the TMH regions and the sites of ubiquitylation.

The Mga2-based reporter does not sense membrane fluidity.

We performed extensive MD simulations illustrating that bilayer properties such as the average area per lipid (Supplementary Fig. 3a), the membrane thickness (Supplementary Fig. 3b), the lateral pressure profile (Supplementary Fig. 3c), and the lipid acyl chain order (Supplementary Fig. 3d) are determined both by the lipid headgroups and the lipid acyl chains.

The remarkable sensitivity of Mga2 to lipid saturation raises the question of whether it is based on membrane fluidity. To test this hypothesis, we first measured the diffusion coefficients of fluorescent lipid analogs (0.01 mol% Atto488-DPPE (Fig. 4a) and 0.01 mol% Abberior Star Red-PEG Cholesterol) (Supplementary Fig. 4a) in giant unilaminar vesicles with different lipid compositions via confocal point fluorescence correlation spectroscopy (FCS). Expectedly, the membrane fluidity decreases slightly with the proportion of saturated lipid acyl chains (from 0% saturated acyl chains for DOPC to 50% for POPC) as evidenced

by decreased diffusion coefficients of the labeled lipids (Fig. 4a and Supplementary Fig. 4a). Notably, this lipid diffusion coefficient is roughly an order of magnitude higher than in giant plasma membrane vesicles⁴⁶ and is ~3- to 5-fold lower than in isolated giant plasma membrane vesicles⁴⁷. Previous reports have identified a central contribution of phosphatidylethanolamine (PE) to membrane fluidity in cells and in vitro⁴⁸. Consistently, we see that a lipid bilayer containing 40 mol% PE (Fig. 4a and Supplementary Fig. 4a gray symbols) is less fluid than a bilayer composed only of PC lipids, despite an identical acyl chain composition (Fig. 4a and Supplementary Fig. 4a white symbols). Intriguingly, the anisotropy of the membrane-probe 1,6-diphenyl 1,3,5-hexatriene (DPH) is barely affected by such changes of the bilayer composition over a broad range of temperatures (Supplementary Fig. 4b). This indicates that subtle changes of membrane fluidity are better detected by analyzing lipid diffusion rather than by the anisotropy of the smaller DPH probe. We further characterized this set of lipid compositions using C-Laurdan spectroscopy, which reports on water penetration into the lipid bilayer⁴⁹. A low degree of water penetration increases the generalized polarization (GP) of C-Laurdan and indicates tighter lipid packing in the lipid headgroup region. Expectedly, we found that lipid packing increases with lipid saturation and upon including PE lipids into the bilayer (Fig. 4b and Supplementary Figs. 3a and 4c).

If Mga2 directly sensed membrane viscosity, the fluidity of the bilayer should dominate the structural dynamics of both the sensory TMHs and at the site of ubiquitylation (Fig. 3). Most importantly, the membrane viscosity should then also control the ubiquitylation of the sense-and-response construct (Fig. 2). We

tested these predictions by using up to 40 mol% of PE in the lipid bilayer to perturb membrane fluidity without changing the composition of its lipid acyl chains (Fig. 4). Notably, PE does not only affect membrane fluidity but also other membrane properties such as lipid packing in the headgroup region (Fig. 4b), the area per lipid, the membrane thickness, and the lateral pressure profile as highlighted in MD simulations (Supplementary Fig. 3).

Nevertheless, EPR spectroscopy indicated that different proportions of PE in the bilayer do not substantially perturb the conformational dynamics in the sensory TMH of Mga2 (Fig. 4c and Supplementary Fig. 4d). We took advantage of a previously established minimal sensor construct, which comprises the TMH of Mga2 (residues 1029–1062) fused to MBP²⁵. Using methanethiosulfonate (MTS) spin labels installed at the position of W1042 in the TMH and continuous wave EPR spectroscopy, we had previously observed a significant impact of lipid saturation on the average interspin distance²⁵. The relatively high protein-to-lipid ratio of 1:500 required for these EPR experiments render the resulting proteoliposomes a bit more similar to cellular membranes, which exhibit protein-to-lipid ratios of ~1:80¹⁸. We show that the inclusion of 20% or 40 mol% of PE in the proteoliposomes has no discernable impact on the resulting EPR spectra (Supplementary Fig. 4d) and the semi-quantitative value for average interspin proximity (the I_{L/I_M} ratio) (Fig. 4c), despite its impact on membrane fluidity (Fig. 4a and Supplementary Fig. 4a, e) and other membrane properties (Fig. 4b and Supplementary Figs. 3 and 4c). Hence, it is unlikely that the previously reported impact of lipid saturation on the structural dynamics of the TMH²⁵ is due to a decreased membrane fluidity (Fig. 4a).

Our FRET reporter (K983^D + K969^A) enabled us to reveal the role of membrane viscosity on the structural dynamics in the region of ubiquitylation (Fig. 3). We determined the average diameter of proteoliposomes containing the FRET reporter by dynamic light scattering (Malvern Zetasizer Nano S90) (Supplementary Fig. 4f). It was slightly larger (~140 nm) for proteoliposomes containing 40 mol% PE than for those generated exclusively from PC lipids (100 mol% DOPC, 50 mol% DOPC and 50 mol% POPC, and 100 mol% POPC) with average diameters between ~60 nm and ~75 nm. Although membrane curvature can have a significant impact on most membrane properties including the lateral pressure profile and lipid packing, we doubt that the curvature in proteoliposomes with diameters > 60 nm manifests substantially enough at the molecular scale to affect the structure and function of Mga2. We then determined the FRET efficiency for the K983^D + K969^A FRET pair, which reports on the average proximity between the binding site of the E3 ubiquitin ligase Rsp5 (K969^A) and a target site of ubiquitylation (K983^D) in the opposing protomer of Mga2. The FRET efficiency in a bilayer with 40 mol% PE was moderately higher than in a PE-free bilayer with an otherwise identical acyl chain composition (50 mol% DOPC, 50 mol% POPC) (Fig. 4d and Supplementary Fig. 4g, h). Expectedly, the inclusion of only 20 mol% PE in the bilayer while maintaining the acyl chain composition affected the FRET efficiency even less (Supplementary Fig. 4h). The highest FRET efficiency was observed for the more saturated membrane (POPC) (Fig. 4d), even though it is less tightly packed (Fig. 4b) and exhibits a similar membrane fluidity as the PE-containing bilayer (Fig. 4a and Supplementary Fig. 4a, e). Thus, the FRET efficiency of this reporter does not correlate with membrane viscosity.

Finally, the functional relevance was studied by an in vitro ubiquitylation assay using the sense-and-response construct (Fig. 4e, f and Supplementary Fig. 4i, j). The highest degree of ubiquitylation was observed for a POPC membrane environment,

which also has the highest degree of lipid saturation. When the sense-and-response construct was reconstituted in a PE-containing bilayer (Supplementary Fig. 4i), which is less saturated but exhibits similar viscosity (Fig. 4a), we observed significantly less ubiquitylation (Fig. 4e, f and Supplementary Fig. 4i, j). Together, these structural and functional data indicate that a key mediator of the homeoviscous response in baker's yeast does not sense membrane fluidity. Instead, they highlight a particular sensitivity of Mga2 to the degree of lipid saturation.

Configuration and position of lipid double bonds affect Mga2.

To gain deeper insight into the contribution of the double bond in unsaturated lipid acyl chains to the activation of Mga2, we employed a different set of lipids. We used PC lipids with two unsaturated (18:1) acyl chains differing either in the position ($\Delta 6$ or $\Delta 9$) or the configuration ($\Delta 9$ -*cis* or $\Delta 9$ -*trans*) of the double bond (Supplementary Fig. 5a). Expectedly, we find that the “kink” introduced by a *cis* double bond supports membrane fluidity (Fig. 5a and Supplementary Fig. 5b, c) by lowering both lipid packing (Fig. 5b) and membrane order (Fig. 5b). Importantly, $\Delta 6$ -*cis* acyl chains render the membrane less fluid than $\Delta 9$ -*cis* acyl chains (Fig. 5a and Supplementary Fig. 5b, c) with no detectable impact on membrane order as studied by C-Laurdan spectroscopy (Fig. 5b and Supplementary Fig. 5d). In contrast, $\Delta 9$ -*trans* 18:1 acyl chains render the bilayer substantially less fluid (Fig. 5a and Supplementary Fig. 5b) and allow for a much tighter packing of lipids (Fig. 5b and Supplementary Fig. 3a) consistent with the higher gel-to-fluid melting temperature of the lipid (12 °C for $\Delta 9$ -*trans* 18:1 PC compared with -18 °C for $\Delta 9$ -*cis* 18:1 PC)⁵⁰. Again, monitoring the changes in fluidity via DPH anisotropy proved less sensitive: increased anisotropies (indicating a decreased mobility) compared with the other bilayer systems were only observed for $\Delta 9$ -*trans* 18:1 acyl chains containing PC lipids and at temperatures below 12 °C, presumably due the formation of gel phases (Supplementary Fig. 5e)⁵⁰. As additional control, we also characterized the fluidity and lipid packing of a PC bilayer with 16:1 acyl chains and $\Delta 9$ -*trans* double bonds (Supplementary Fig. 5c–e). Using these bilayer systems differing by the position and configuration of the double bonds in the lipid acyl chains, we set out their impact on the structure and function of Mga2 in vitro.

First, we studied how the double bond position and configuration affects the structural dynamics of Mga2's TMH region using EPR spectroscopy. Placing the sensor in the tightly packed membrane with $\Delta 9$ -*trans* 18:1 acyl chains caused a substantial broadening of the continuous wave EPR spectra recorded at -115 °C (Fig. 5c) and increased interspin proximities (Fig. 5d). Membrane environments with either $\Delta 6$ -*cis* or $\Delta 9$ -*cis* 18:1 acyl chains caused considerably less spectral broadening (Fig. 5c). This indicates that $\Delta 9$ -*trans* double bonds in lipid acyl chains—more than $\Delta 9$ -*cis* and $\Delta 6$ -*cis* bonds—stabilize a rotational orientation of Mga2's TMH region, where spin labels at the position W1042 face each other in the dimer interface²⁵. Moreover, our data suggest that lipid acyl chains with $\Delta 9$ -*trans* double bonds, which are less kinked than those with $\Delta 9$ -*cis* double bonds, have a similar impact on the structural dynamics of Mga2's TMH as saturated lipid acyl chains.

Next, we tested whether the position and configuration of the double bond in unsaturated lipid acyl chains has an impact on the structural dynamics of Mga2 in the region of ubiquitylation. To this end, we used our FRET reporter (K983^D + K969^A) and reconstituted it successfully in different membrane environments as judged by sucrose density gradients (Supplementary Fig. 5f). The reason for the different buoyant densities of the proteoliposomes remains to be fully explored. The FRET signal (Fig. 5e) and

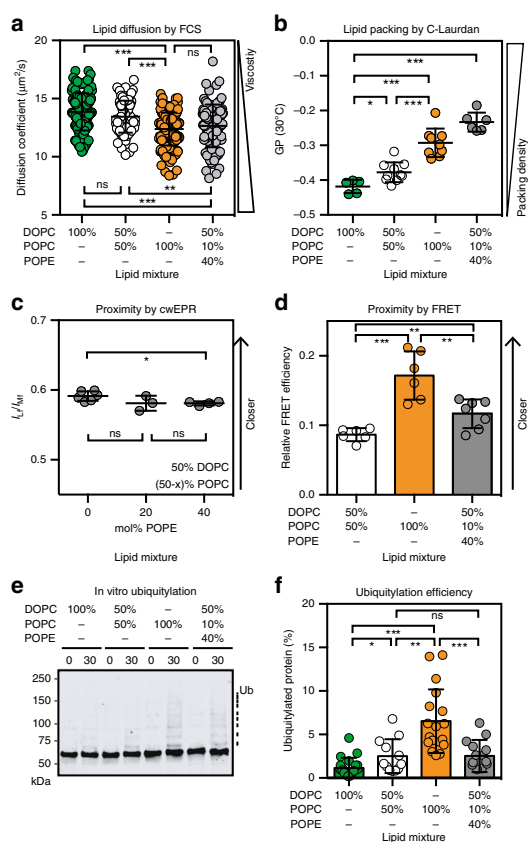


Fig. 4 The conformation and activity of the sense-and-response construct does not correlate with membrane viscosity. **a** Diffusion coefficients of the fluorescent Atto488-DPPE lipid in giant unilamellar vesicles with indicated compositions were determined by confocal point FCS. Data are represented as mean \pm SD ($n_{\text{DOPC}} = 172$; $n_{(1:1)\text{DOPC:POPC}} = 81$; $n_{\text{POPC}} = 153$; $n_{40\%\text{POPE}} = 100$) and subjected to a Kolmogorov-Smirnov test (* $p < 0.05$, ** $p < 0.01$, *** $p < 0.001$). **b** The lipid packing of the indicated lipid compositions were determined by C-Laurdan spectroscopy and expressed as generalized polarization (GP). Data are shown as mean \pm SD ($n_{\text{DOPC}} = 6$; $n_{(1:1)\text{DOPC:POPC}} = 10$; $n_{\text{POPC}} = 9$; $n_{40\%\text{PE}} = 6$) and analyzed using a two-tailed, unpaired t -test (* $p < 0.05$, ** $p < 0.01$, *** $p < 0.001$). **c** cwEPR spectra were recorded at -115°C for a fusion protein composed of MBP and the TMH of Mga2 (MBP-Mga2¹⁰³²⁻¹⁰⁶²) labeled at position W1042C after reconstitution at a molar protein:lipid ratio of 1:500 in indicated liposomes. The semi-quantitative proximity index L_r/L_m indicating the interspin distance was derived from the cwEPR spectra as previously published²⁵. Higher values indicate a lower average interspin distance. Data are plotted as mean \pm SD ($n_{0\%\text{PE}} = 6$; $n_{20\%\text{PE}} = 3$; $n_{40\%\text{PE}} = 4$) and analyzed by a two-tailed, unpaired t -test (* $p < 0.05$; ns not significant). **d** Relative FRET efficiencies calculated from fluorescence emission spectra (ex: 488 nm, em: 500–700 nm) of the (K983^D + K969^A) FRET pair reconstituted in liposomes composed of 50 mol% DOPC, 10 mol% POPC, and 40 mol% POPE. The FRET efficiencies for the other lipid compositions are the same as in Fig. 3g and shown for comparison. Data are plotted as mean \pm SD ($n_{(1:1)\text{DOPC:POPC}} = 6$; $n_{\text{POPC}} = 6$; $n_{40\%\text{PE}} = 7$) and analyzed using a two-tailed, unpaired t -test (** $p < 0.01$, *** $p < 0.001$). **e** In vitro ubiquitylation of the zipped sense-and-response construct (ZIP-MBP-Mga2⁹⁵⁰⁻¹⁰⁶²) reconstituted in liposomes of the indicated lipid compositions at a molar protein-to-lipid ratio of 1:8000. After the reaction was stopped, the samples were subjected to SDS-PAGE and analyzed by immunoblotting using anti-MBP antibodies. **f** Densitometric quantification of ubiquitylation from immunoblots as in **e** was performed using Image StudioTM Lite. Data are plotted as mean \pm SD ($n_{\text{DOPC}} = 20$; $n_{(1:1)\text{DOPC:POPC}} = 12$; $n_{\text{POPC}} = 18$; $n_{40\%\text{PE}} = 14$) and analyzed using a two-tailed, unpaired t -test (* $p < 0.05$, ** $p < 0.01$, *** $p < 0.001$). Source data are provided as a Source Data file.

FRET efficiency (Fig. 5f) of the reporter were low when the sensor was situated in a bilayer with poorly packing $\Delta 9$ -*cis* acyl chains (Figs. 3f, g and 5e, f). This indicates a relatively large distance between the binding site for Rsp5 (K969) and the target site for ubiquitylation in the opposing protomer of Mga2 (K983). The FRET efficiency was only mildly higher in a membrane environment with $\Delta 6$ -*cis* acyl chains (Fig. 5f). This suggests that the position of the *cis* double bond has only a modest impact on the average distance between K969^A and K983^D in the FRET reporter. Significantly higher FRET efficiencies were observed when the reporter was placed in membranes with tightly packing $\Delta 9$ -*trans* 18:1 acyl chains (Fig. 5f) or $\Delta 9$ -*trans* 16:1 acyl chains (Supplementary Fig. 5g, h). These findings demonstrate that the structural dynamics of Mga2 is affected by the configuration and potentially by the position of double bonds in unsaturated lipids. Furthermore, our observations on the $\Delta 9$ -*trans* 16:1 acyl chains indicate a lack of correlation between FRET efficiency (Supplementary Fig. 5g, h), membrane fluidity (Supplementary Fig. 5c), and the lipid-packing density (Supplementary Fig. 5d). Nevertheless, our data suggest a structural coupling and transfer of information from the TMH of Mga2 (Fig. 5c, d) to the site of ubiquitylation (Fig. 5e, f).

To characterize the functional consequences of the proposed membrane-controlled structural dynamics of Mga2, we performed in vitro ubiquitylation assays with the sense-and-response construct (ZIP-MBP-Mga2⁹⁵⁰⁻¹⁰⁶²) reconstituted initially in three distinct membrane environments (Fig. 5g, h). Although we barely detected any ubiquitylation above background when the sense-and-response construct was reconstituted in a loosely packed

bilayer with 18:1 $\Delta 9$ -*cis* acyl chains (DOPC), we observed a robust ubiquitylation when the construct was situated in a bilayer with either $\Delta 9$ -*trans* or $\Delta 6$ -*cis* acyl chains. The highest degree of ubiquitylation of the reporter was observed in the membrane with $\Delta 6$ -*cis* lipid acyl chains, followed by the less fluid and more tightly packed membrane with $\Delta 9$ -*trans* lipid acyl chains. This observation supports our previous conclusion that the ubiquitylation of Mga2 does not correlate with membrane viscosity. Furthermore, we find that the FRET efficiencies of the K969^A and K983^D pair in different bilayers (Fig. 5e, f and Supplementary Fig. 5g, h) do not correlate with the respective ubiquitylation efficiencies (Fig. 5g, h and Supplementary Fig. 5i). This is not entirely surprising, because a single FRET pair cannot describe the entire structural dynamics in the region of ubiquitylation. Although increased FRET efficiencies imply an increased average proximity of the two fluorophores, it does not imply a perfect distance and relative orientation of the target lysine residues K⁹⁸⁰, K⁹⁸³, and K⁹⁸⁵, and the E3 ubiquitin ligase Rsp5.

Together, our data provide strong evidence that Mga2 does not sense the mere presence or absence of double bonds in the lipid acyl chains. Instead, it is highly sensitive to the configuration and position of the double bond with immediate effect on the structural and dynamic properties of the TMH of Mga2 that dictate the ubiquitylation reaction.

Bulkiness of sensor residue determines signaling output. The TMH of Mga2 contains a bulky tryptophan (W1042), which is

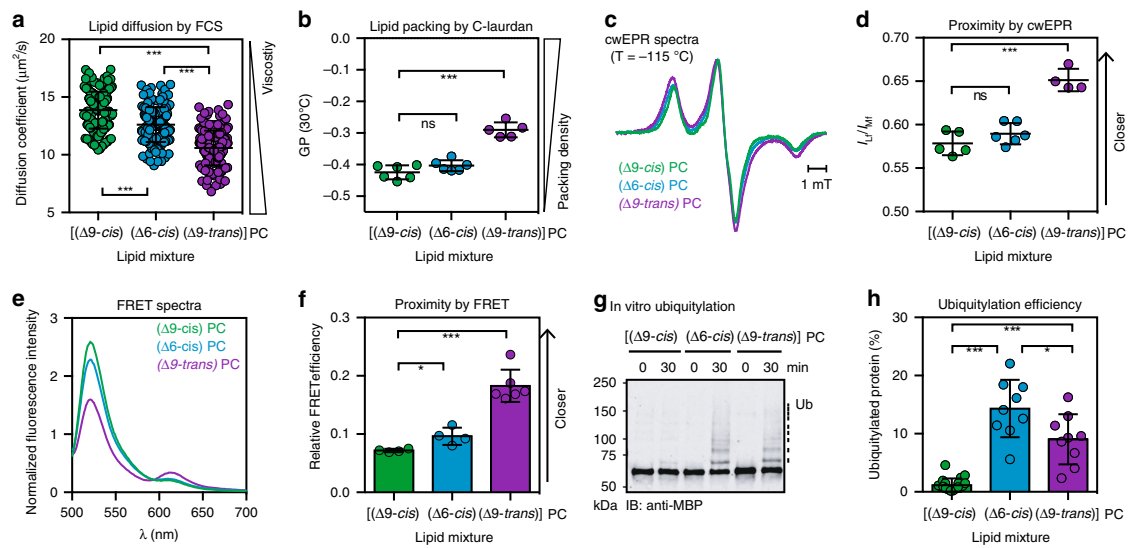


Fig. 5 The double bond in unsaturated lipid acyl chains affects the configuration and activity of the sense-and-response construct. **a** Diffusion coefficients of the fluorescent lipid Atto488-DPPE in GUVs with indicated compositions were determined by confocal point FCS. Data for DOPC ($\Delta 9$ -cis) are the same as in Fig. 4a. Data are plotted as mean \pm SD ($n_{(\Delta 9\text{-cis})} = 172$; $n_{(\Delta 6\text{-cis})} = 162$; $n_{(\Delta 9\text{-trans})} = 163$) and analyzed using Kolmogorov-Smirnov tests ($***p < 0.001$). **b** Lipid packing in liposomes was determined by C-Laurdan spectroscopy. Data for DOPC ($\Delta 9$ -cis) are the same as in Fig. 4b. Data are plotted as mean \pm SD ($n_{(\Delta 9\text{-cis})} = 6$, $n_{(\Delta 6\text{-cis})} = 6$; $n_{(\Delta 9\text{-trans})} = 5$) and analyzed via unpaired two-tailed, Student's *t*-tests ($***p < 0.001$). **c** Intensity-normalized cwEPR spectra recorded at -115°C for MBP^{Mga2}¹⁰³²⁻¹⁰⁶² labeled at position W1042C after reconstitution at a molar protein:lipid ratio of 1:500 in liposomes with indicated composition. **d** Semi-quantitative proximity index I_L/I_M derived from cwEPR spectra. High values indicate low average interspin distances. Data are plotted as mean \pm SD ($n_{(\Delta 9\text{-cis})} = 5$; $n_{(\Delta 6\text{-cis})} = 6$; $n_{(\Delta 9\text{-trans})} = 4$) and analyzed using two-tailed, unpaired *t*-tests ($***p < 0.001$). **e** Fluorescence emission spectra of the membrane-reconstituted FRET pair (K983^D + K969^A) (ex: 488 nm, em: 500-700 nm) are plotted after normalization to the maximal emission upon acceptor excitation (ex: 590 nm). Data for DOPC ($\Delta 9$ -cis PC) are the same as in Fig. 3f. **f** Relative FRET efficiencies were calculated as in **e**, plotted as mean \pm SD ($n_{(\Delta 9\text{-cis})} = 4$; $n_{(\Delta 6\text{-cis})} = 4$; $n_{(\Delta 9\text{-trans})} = 6$), and analyzed by two-tailed, unpaired *t*-tests ($*p < 0.05$; $**p < 0.005$). Data for DOPC ($\Delta 9$ -cis PC) are the same as in Fig. 3g. **g** In vitro ubiquitylation of the zipped sense-and-response construct (^{ZIP}-MBP^{Mga2}⁹⁵⁰⁻¹⁰⁶²) reconstituted in indicated liposomes at a molar protein-to-lipid ratio of 1:8000 and at 30°C . After stopping the reaction, the samples were subjected to SDS-PAGE and analyzed by immunoblotting using anti-MBP antibodies. **h** Densitometric quantification of ubiquitylation at the indicated time points from immunoblots as in **g**. Data are plotted as mean \pm SD ($n_{(\Delta 9\text{-cis})} = 20$; $n_{(\Delta 6\text{-cis})} = 9$; $n_{(\Delta 9\text{-trans})} = 9$). Data for DOPC ($\Delta 9$ -cis PC) are the same as in Fig. 4f. Source data are provided as a Source Data file.

functionally important and might serve as a sensor residue²⁵. Previous MD simulations have shown that W1042 is situated in the hydrophobic core of the bilayer overlapping with the $\Delta 9$ -cis double bonds of unsaturated phospholipids²⁵. We hypothesized that Mga2 senses the lipid-packing density in this region of the lipid bilayer and/or a thin slice of the lateral compressibility profile^{2,18}. The sensitivity of our sense-and-response construct to the position and configuration of the double bond in lipid acyl chains (Fig. 5) is consistent with this idea. Our model predicts that the activation of Mga2 is controlled by the size of the amino acid side chain at position 1042, which also controls the population of alternative, rotational configurations of the sensory TMH in a dynamic equilibrium. An increased packing and a lowered lateral compressibility in this region should cause a relatively large amino acid to “hide” in the dimer interface, thereby stabilizing a productive configuration. A smaller residue should be less sensitive to the membrane environment and populate non-productive configurations.

To test this prediction, we have substituted W1042 with either tyrosine (Y), phenylalanine (F), glutamine (Q), leucine (L), or alanine (A), and assayed the role of the side-chain bulkiness and aromatic character on the signal output in vivo. Expectedly, a $\Delta\text{SPT23}\Delta\text{MGA2}$ double mutant lacking both transcriptional regulators of *OLE1* does not grow unless UFAs were provided with the medium (Fig. 6a)⁵¹. This UFA auxotrophy of

$\Delta\text{SPT23}\Delta\text{MGA2}$ cells is complemented by both wild-type and mutant *MGA2* variants expressed from the endogenous promoter on a *CEN*-based plasmid (Fig. 6a, b). However, the growth of these cells was highly dependent on the amino acid at position 1042 under UFA-limiting conditions (Fig. 6a and Supplementary Fig. 6a, b). We observed a striking correlation between the size of the side chain and the optical density of overnight cultures (Fig. 6b). The only exception to this near-perfect correlation was the W1042Q mutation. Given that intra-membrane glutamines are known to mediate homotypic interactions⁵², we speculate that the W1042Q mutation stabilizes a rotational conformation of the TMHs, where the two Q1042 side chains face each other and interact, thereby stabilizing Mga2 in a productive configuration. Furthermore, the phenotypic differences between the W1042Q, W1042L, and W1042A variants (Fig. 6a–d) show that an aromatic character at the sensory position is not absolutely required for sensing.

Next, we studied the impact of these mutations on the proteolytic processing of full-length Mga2 in cells (Fig. 6c, d). We found a perfect concordance of these immunoblot experiments with the in vivo phenotypes (Fig. 6a, b). The processing of the membrane-bound precursor of Mga2 (P120) to the signaling-active form (P90) was greatly affected by the residue at the position 1042. These data were complemented by functional in vitro experiments using the sense-and-response construct

reconstituted in liposomes (Supplementary Fig. 6c, d). The *in vitro* ubiquitylation in a POPC bilayer was significantly reduced to almost background levels by the W1042A mutation. These data support a central, sensory role of W1042.

Using a previously established MD simulation pipeline²⁵, we analyzed the impact of the W1042Y, W1042Q, W1042F, and W1042A mutations on the structural dynamics of dimeric TMHs derived from Mga2. We performed extensive, coarse-grained MD simulations of these mutant variants in a POPC bilayer (Supplementary Fig. 6e–h), which we have shown to support robust ubiquitylation of Mga2 *in vitro* (Fig. 2e, f). At least three populations of distinct configurations in the TMH region were detected. They correspond to configurations with the two residues at the position 1042 (i) facing each other, (ii) pointing in the same direction, or (iii) pointing away from each other. The population of these configurations were clearly affected by mutations at the position of W1042 (Supplementary Fig. 6f–i). Notably, the mutants with a particularly strong impact on the structural dynamics in the TMH region (W1042F and W1042A) also exhibit a strong functional defect *in vivo* (Fig. 6a–d and Supplementary Fig. 6e–h). Based on these data, we conclude that W1042 acts as a sensor residue and that the size and the chemical character of the amino acid in this position controls the signaling output.

Representing local lipid packing reveals sensing mechanism. As membrane fluidity is unlikely to control the activation of Mga2, and as the size of the residue 1042 determines the functionally relevant structural dynamics in the transmembrane region, we turned our attention to the local packing density of the lipids.

To explore the contribution of lipid headgroups and the lipid acyl chain composition on the investigated bilayer systems, we performed extensive all-atom MD simulations of protein-free bilayers. As a reference, we first characterized a DOPC bilayer containing no saturated lipid acyl chains (Supplementary Fig. 3a–d). This bilayer was compared with three other systems: a 50:50 mixture of DOPC and POPC containing 25% saturated lipid acyl chains, POPC with 50% saturated lipid acyl chains, and a 50:10:40 mixture of DOPC, POPC, and POPE, which contain 25% saturated acyl chains, but almost half of the lipids have a smaller ethanolamine headgroup (Supplementary Fig. 3a–d). We asked whether an increased lipid packing due to changes in the acyl chain composition is qualitatively distinct from increased lipid packing due to different lipid headgroup compositions. Of particular interest is a region between 3 Å and 10 Å from the bilayer center, where the sensory W1042 is situated as previously shown²⁵. We determined the 3-dimensional number density of lipid atoms in small 1 Å × 1 Å × 1 Å voxels (cubes) within the DOPC bilayer as a measure for the local packing density (Fig. 7a) and did the same for the other three bilayer systems (Supplementary Fig. 7). Expectedly, this representation identifies a particularly high density of lipid atoms in the headgroup region and a much lower one in the bilayer center.

As we could not detect any ubiquitylation of the sense-and-response construct in DOPC, but robust ubiquitylation in POPC (Fig. 4e, f), we turned our attention toward the differences between DOPC and the other bilayer systems. We derived difference maps of the local packing density between DOPC and the other three bilayer systems to highlight regions of increased and decreased local number densities (Fig. 7b). We reasoned that any difference in the local packing density, especially in the region of the sensory W1042, might contribute to regulation of Mga2. We find that saturated lipid acyl chains increase the density of lipid atoms relative to DOPC precisely in this region of the bilayer (3 Å–10 Å from the bilayer center) (Fig. 7b). In a bilayer containing 40 mol% PE, we also observe

increased densities along the acyl chain region, but this increase is less pronounced and more delocalized (Fig. 7b). This computational analysis demonstrates that saturated lipid acyl chains increase the local density of lipid atoms precisely and specifically in the region of the sensory tryptophan W1042. Based on these findings and our experimental data, we propose that Mga2 senses a bilayer property at the level of the bulky W1042, which is closely related to the local packing density.

Discussion

We have reconstituted key steps of sensing and communicating lipid saturation by the prototypical type II membrane property sensor Mga2¹⁹. We uncover a unique sensitivity of Mga2 for the lipid acyl chain composition of the ER membrane and provide direct evidence for a functional coupling between the dimeric, sensory TMHs and the sites of ubiquitylation. Our *in vitro* system allowed us to directly test a central assumption underlying the concept of homeoviscous adaptation^{9,15,17}. By investigating the role of membrane fluidity on the ubiquitylation of Mga2, we demonstrate that the core regulator of fatty acid desaturation in baker's yeast^{21,53} is not regulated by the viscosity of the membrane (Figs. 4, and 5). Instead, our data suggest that Mga2 uses a bulky TMH residue (W1042) to sense the packing density, which probably affects the lateral compressibility profile at a specific depth in the ER membrane. Based on our findings, we conclude that membrane fluidity does not serve as the central measured property for regulating the lipid acyl chain composition in baker's yeast and presumably many other eukaryotic species.

Our *in vitro* approach with reconstituted proteoliposomes has provided insights into the sensitivity of Mga2 to physiologically relevant changes of the lipid acyl chain composition^{8,44}. Baker's yeast can synthesize only $\Delta 9$ -*cis* mono-UFA and the average proportion of these unsaturated acyl chains lies between 65% and 75% in glycerophospholipids depending on the temperature of cultivation⁸. The sense-and-response construct cannot be ubiquitylated in a relatively unsaturated membrane (75% $\Delta 9$ -*cis* 18:1 acyl chains), but it is robustly ubiquitylated in POPC, which is slightly more saturated (50% $\Delta 9$ -*cis* 18:1 acyl chains) (Fig. 2f). A simple back-of-an-envelope calculation that considers only the volume of the lipid bilayer highlights the remarkable dose-response relationship of this machinery: the sense-and-response system is OFF, when the concentration of unsaturated lipid acyl chains is ~1.9 M, but it is ON at a concentration of ~1.3 M (assumptions: ~370,000 lipids per 200 nm liposome; $\sim 4.82 \times 10^{-19}$ l membrane volume per liposome). This switch-like response is based on fluctuating signals from the membrane, which are decoded by the sensor protein into an almost binary output.

To better understand the nature of sensing, we have employed a strategy to compare different bilayer systems by means of the local number density of lipid atoms (Fig. 7 and Supplementary Fig. 7). This approach yielded insight into the qualitatively distinct impact of saturated lipids and a perturbed PC-to-PE ratio on the lipid-packing densities in the core of the membrane (Fig. 7b). We find that increased lipid saturation causes a localized, sharp increase of the local packing density, whereas the inclusion of PE into the bilayer causes a rather mild increase of the packing density, which is delocalized along the lipid acyl chains (Fig. 7b and Supplementary Fig. 7). It is well known that the inclusion of PE into a PC-based bilayer causes intrinsic curvature stress and characteristic changes of the lateral pressure profile (Supplementary Fig. 3c), which may be sensed particularly well by hourglass-shaped transmembrane domains^{54–57}. However, the cylindrical TMHs of Mga2 dimers are more sensitive to saturated lipid acyl chains causing an increased packing density in a specific region of the bilayer overlapping with the sensory W1042 residue

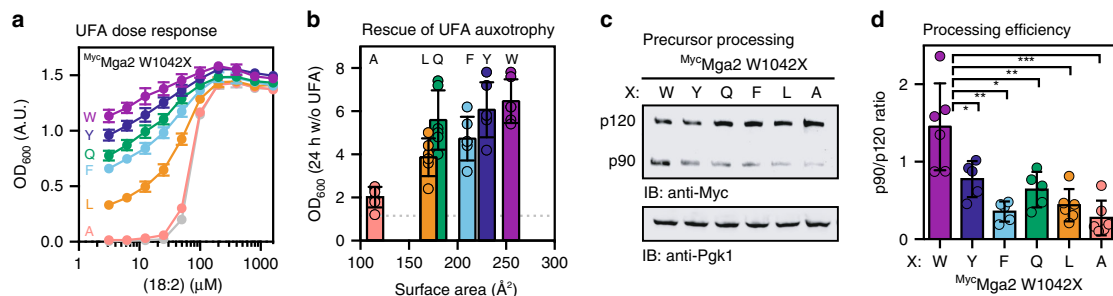


Fig. 6 The activity of Mga2 is tuned by mutations in the sensory TMH. **a** Dose-dependent rescue of UFA auxotrophy by linoleic acid (18:2). Δ SPT23 Δ MGA2 strains carrying CEN-based plasmids to produce MycMga2 variants with the indicated residues at position 1042 were cultivated for 16 h at 30 °C in SCD-Ura medium supplemented with indicated concentrations of linoleic acid in 0.8% tergitol. The density of the culture was determined at 600 nm (OD₆₀₀) and plotted against the concentration of linoleic acid. Cells carrying an empty vector served as control (gray). Plotted is the mean \pm SEM ($n = 8$). **b** Rescue of UFA auxotrophy of Δ SPT23 Δ MGA2 by Mga2 variants. Cells producing mutant Mga2 as in **a** were cultivated for 24 h in the absence of supplemented UFAs in SCD-Ura medium. Cell density was determined as in **a** and was plotted against residue surface area of residues installed at position 1042⁶⁶. Plotted is the mean \pm SEM of five independent experiments. The dotted line indicates the OD measured for an empty vector control. **c** Immunoblot analysis of the Mga2 processing efficiency. Wild-type cells (BY4741) producing the indicated MycMga2 variants at position 1042 were cultivated in full medium (yeast extract–peptone–dextrose; YPD) to the mid-exponential phase. Cell lysates were subjected to SDS-PAGE and analyzed via immunoblotting using anti-Myc antibodies to detect the unprocessed (p120) and the processed, active form (p90) of Mga2. An immunoblot using anti-Pgk1 antibodies served as loading control. **d** Densitometric quantification of the ratio of p90:p120 in immunoblots as in **c**. Signal intensities were quantified using Fiji and plotted as mean \pm SD ($n_W = 6$, $n_Y = 5$, $n_F = 5$, $n_Q = 5$, $n_L = 6$, $n_A = 6$)⁶⁷. A two-tailed, unpaired *t*-test was performed to test for statistical significance (* $p < 0.05$, ** $p < 0.01$, *** $p < 0.001$). Source data are provided as a Source Data file.

(Fig. 7a, b). We thus provide not only a model for lipid sensing by Mga2 but also an approach to dissect the relative impact of lipid headgroup and the acyl chain composition on membrane protein function in general.

Our results lead to the following model of lipid saturation sensing: the lipid acyl chain composition has a profound impact on the distribution of lipid atoms in the hydrophobic core of the membrane (Fig. 7a, b and Supplementary Fig. 7). Mga2 senses increased packing densities via a bulky tryptophan residue (W1042) situated deep in the hydrophobic core of the bilayer (3 Å–10 Å from the bilayer center²⁵). In a more saturated membrane, the packing density increases at the level of the sensory tryptophan (W1042) (Fig. 7b), which then rotates away and “hides” in the dimer interface (Fig. 1a). In a more unsaturated membrane, the lower packing density in this region allows the sensory tryptophan to point on average more often towards the lipid environment²⁵ (Fig. 1a). We would like to stress that the TMHs of Mga2 constantly rotate against each other and explore a large variety of rotational states (Supplementary Fig. 6e–h) in each membrane but the specific lipid composition of the membrane has a significant impact on the structural dynamics in the TMH region by determining the relative probability of these rotational states²⁵. It seems that the fluctuating signals from the membrane are decoded by the structural dynamics of the TMHs and then transmitted to the site of ubiquitylation via a disordered, juxtamembrane region (Figs. 1b and 3g). We speculate that the flexible linkage provides a means to bias the orientation and relative position of two “ubiquitylation zones” around the E3 ubiquitin ligase Rsp5 bound to Mga2, however, with a minimal perturbation of the TMH dynamics. Such “zones of ubiquitylation” have recently been predicted for Rsp5 and implicated into the quality control of misfolded and mistargeted plasma membrane proteins⁵⁸. Supported by our FRET data (Fig. 3f, g), we propose that Rsp5 bound to one protomer of dimeric Mga2 can ubiquitylate specific lysine residues on the other protomer, when it is properly placed and oriented. Effectively, this *trans*-ubiquitylation would be controlled by the physicochemical properties of the ER membrane. The remarkable sensitivity of

Mga2 ubiquitylation to the lipid environment might be sharpened by deubiquitylating enzymes⁵⁹ such as Ubp2⁶⁰ and supported by an activating, *trans*-autoubiquitylation of Rsp5⁶¹.

The assays and tools established here provide handles to better understand the structural and dynamic features that render a protein a good substrate of the E3 ubiquitin ligase Rsp5. Identifying the molecular rules of substrate selection is a major open question, because Rsp5 has been implicated in most diverse aspects of cellular physiology including endocytosis⁵⁸, mitochondrial fusion⁶², and the turnover of heat-damaged proteins in the cytosol⁶³. Our in vitro system using a membrane-reconstituted, conditional substrate of Rsp5 provides a unique opportunity to better understand (i) the contribution of *trans*-autoubiquitylation of Rsp5, (ii) the relevance of structural malleability in Rsp5 substrates, and (iii) the role of deubiquitylating enzymes in defining the selectivity and sensitivity of the Rsp5-mediated ubiquitylation. In the context of the Mga2 sensor, an intriguing question is how “noisy” signals from the TMH region are transduced into robust, almost switch-like ubiquitylation responses.

Two lines of evidence suggest that the rotation-based sensing mechanism of Mga2²⁵ is based on a collective, physical property of the membrane rather than on a preferential, chemical interaction with the double bonds in the lipid acyl chains. First, Mga2 distinguishes robustly between two membrane environments that differ in the configuration of the double bonds (*cis* or *trans*) in the lipid acyl chains, but not in the overall abundance of double bonds (Fig. 5). Second, an aromatic amino acid, which might confer some chemical specificity for double bonds, is not absolutely required at the position of the sensory tryptophan (W1042) in the TMH (Fig. 6). A partial activity of the OLE pathway is preserved when the sensor residue W1042 is substituted with leucine, but not when it is substituted with the smaller alanine (Fig. 6a, b; and Supplementary Fig. 5b). Nevertheless, our data do not rule out an important contribution of chemical specificity to the sensor function. We expect that the high degree of structural malleability in the TMH region and at the site of ubiquitylation is established by a fine balance of chemical interactions and collective, physical membrane properties. In fact, even the rather

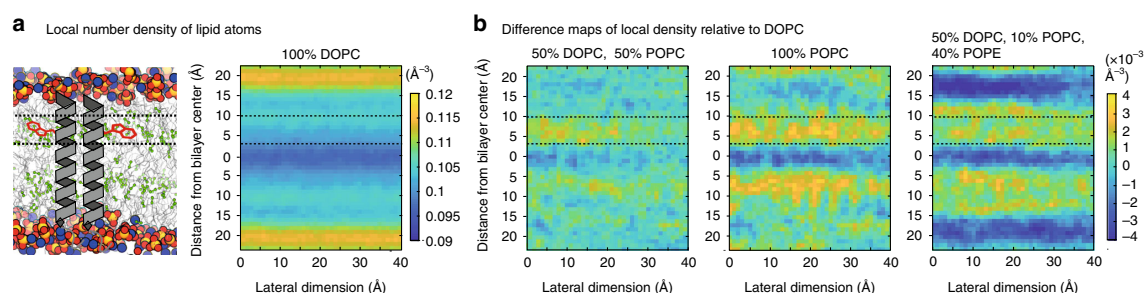


Fig. 7 The local number density of lipid atoms in a specific region of the membrane correlates with Mga2 activation. **a** Snapshot from an all-atom MD simulation of a protein-free DOPC bilayer (left) and the derived local number density of lipid atoms (right). A schematic representation of the dimeric TMH of Mga2 in the left panel is provided to indicate the relative position of the sensory tryptophan W1042 (red sticks and dashed line). The position of double bonds in the lipid acyl chains is given by green spheres, whereas a schematic representation of the Mga2-TMH is given to guide the eye. The number density of lipid atoms in cubic boxes with a side of 1\AA was calculated and plotted (right panel) for different depths in the bilayer (distance for bilayer center) and different lateral positions (lateral dimension). Highest local number densities are indicated in yellow and are observed in the region of the lipid headgroups. Lowest densities are indicated in dark blue and observed in the center of the lipid bilayer. For details see the Supplementary Materials.

b Difference maps of the local density were determined by subtracting the local number density of lipid atoms of DOPC from the one of the indicated bilayer systems. Increased packing densities relative to the DOPC bilayer are indicated in yellow, whereas decreased densities are indicated in blue. The region probed by the sensory tryptophan²⁵ is indicated by two dashed lines. Changes in lipid saturation and the lipid headgroup region have qualitatively distinct impact on the distribution of local packing densities. Source data are provided as a Source Data file.

conservative mutation W1042F has a substantial impact on the structural flexibility in the TMH region (Supplementary Fig. 6e) and on the functionality of the OLE pathway in vivo (Fig. 6a–d).

In conclusion, we have provided detailed mechanistic insight into a sensory system that is centrally important for membrane adaptivity. Our findings challenge the common view of membrane fluidity as pivotal measured variable in eukaryotic cells and have important implications to all processes involving membrane lipid adaptation. Beyond that, our work represents an important step towards identifying the molecular rules of substrate selection by the E3 ubiquitin ligase Rsp5. This work opens a door towards establishing genetically encoded machineries that can sense specific membrane features, which are indiscernible by conventional tools. In the future, these sensors will be exploited to dissect the physical membrane properties of different organelles and cells in vivo and in real-time.

Methods

Plasmids and strains and oligonucleotides. All plasmids and strains used in this study are listed in Supplementary Tables 1 and 2. Oligonucleotides used for molecular cloning are listed in Supplementary Table 3.

Antibodies. Antibodies used for immunoblotting are listed in Supplementary Table 4.

Expression and purification and labeling of MBP^{Mga2} fusions. The ZIP-MBP^{Mga2}^{2950–1062} fusion protein comprising the leucine zipper of the Gcn4 transcription factor (residues 249–281), the MBP from *Escherichia coli*, and the residues G950–D1062 from Mga2 was generated using the pMal-C2x plasmid system. The resulting constructs were produced in *E. coli* and isolated in detergent solution using amylose affinity followed by a preparative SEC (Superdex 200 10/300 Increase). For fluorescent labeling, the K983C and K969C variants were incubated with 1 mM ATTO488 or ATTO590 (ATTO-TEC GmbH) on the affinity purification column for 16 h at 4 °C. The MBP^{Mga2}^{1032–1062} fusion protein containing residue R1032-D1062 from Mga2 and a W1042C mutation was purified and labeled with MTS spin probes. For details, see Supplementary Materials. The proteins were stored in 40 mM HEPES (pH 7.0), 120 mM NaCl, 0.8 mM EDTA, 40 mM OG, and 20% (w/v) glycerol.

Reconstitution of MBP^{Mga2} fusions in proteoliposomes. The spin-labeled MBP^{Mga2}-TMH fusion was reconstituted at a protein:lipid molar ratio of 1:500. For details see Supplementary Materials. The unlabeled or ATTO-labeled ZIP-MBP^{Mga2}^{2950–1062} constructs were reconstituted at different protein–lipid molar ratios of 1 to 5000, 1 to 8000, and 1 to 15,000. To this end, lipids (final

concentration 1 mM) and OG (final concentration 37.5 mM) were mixed with either labeled or unlabeled proteins in a final volume of 1 ml. After 10 min of incubation at room temperature under constant agitation, the detergent was via SM-2 biobeads (two-step removal using 500 mg and 100 mg, respectively).

The yield of the reconstitution was tested after harvesting the proteoliposomes and it was comparable for all the desired protein and lipid compositions used in this study. The average diameter of the proteoliposomes was determined at 25 °C by dynamic light scattering (Malvern Zetasizer Nano S90) in 20 mM Hepes, pH 7.4, 145 mM NaCl, 5 mM MgCl₂, 5% (w/v) glycerol. A detailed description for the reconstitution is provided in the Supplementary Materials.

Diffusion coefficients by FCS. FCS on the GUVs was carried out using Zeiss LSM 880 microscope, $\times 40$ water immersion objective (numerical aperture 1.2)⁴⁷. First, GUVs were labeled by adding fluorescent analogs to a final concentration of 10–50 ng/mL ($\approx 0.01 \text{ mol}\%$). To measure the diffusion on the GUV membrane, vesicles were placed into an eight-well glass-bottom (#1.5) Ibidi chambers coated with bovin serum albumin. GUVs of small sizes ($\approx 10 \mu\text{m}$) were picked for measurements. The laser spot was focused on the top membrane of the vesicles by maximizing the fluorescence intensity. Then, three to five curves were obtained for each spot (5 s each). The obtained curves were fit using the freely available FoCUS-point software using two-dimensional and triplet model⁶⁴.

C-Laurdan spectroscopy. C-Laurdan was used to measure lipid packing⁴⁹. To this end, 333.3 μM lipid was mixed with 0.4 μM C-Laurdan dye in 150 μl 50 mM HEPES pH 7.4, 150 mM NaCl, 5% (w/v) glycerol. The sample was excited at 375 nm and an emission spectrum from 400 to 600 nm was recorded (excitation and emission bandwidth 3 nm). For blank correction, an emission spectrum recorded in the absence of C-Laurdan was used. The GP, which ranges theoretically from +1 for most ordered to -1 for most disordered membranes, was calculated by integrating the intensities between 400 and 460 nm (I_{Ch1}), and 470 and 530 nm (I_{Ch2}), and according to (1).

$$\text{GP} = \frac{I_{\text{Ch1}} - I_{\text{Ch2}}}{I_{\text{Ch1}} + I_{\text{Ch2}}} \quad (1)$$

Recording and analysis of FRET spectra. For FRET measurements, the ZIP-MBP^{Mga2}^{2950–1062} K983ATTO488 and ZIP-MBP^{Mga2}^{2950–1062} K969ATTO590 constructs were used as fluorescence donor and acceptor, respectively. Fluorescence emission spectra were recorded in detergent solution and in proteoliposomes at 30 °C. The samples were excited at 488 nm and 590 nm for donor and acceptor excitation, respectively. The spectra were normalized to the maximal acceptor fluorescence intensity after direct excitation to correct for subtle variations in the reconstitution yields. As the bleed-through for both the donor and acceptor fluorescence was negligible, ratiometric FRET (relative FRET; E_{rel}) was determined as the donor-to-acceptor intensity ratio at 525 nm and 614 nm from the raw data (2) for qualitative

comparisons.

$$E_{\text{rel}} = \frac{I_A}{I_D + I_A} \quad (2)$$

In vitro ubiquitylation assay. Proteoliposomes containing ZIP-MBP^{Mga2⁹⁵⁰⁻¹⁰⁶²}, ^{8xHis}Ubiquitin (see Supplementary Materials for a description of expression and purification), cytosol, and an 10x ATP-regenerating system were mixed on ice in a total volume of 20 μl , to obtain final concentrations of 0.1 μM ZIP-MBP^{Mga2⁹⁵⁰⁻¹⁰⁶²}, 0.1 $\mu\text{g}/\mu\text{l}$ ^{8xHis}Ubiquitin, 1 $\mu\text{g}/\mu\text{l}$ cytosolic proteins, 1 mM ATP, 50 mM creatine phosphate, and 0.2 mg/ml creatine phosphokinase in ubiquitylation buffer (20 mM HEPES pH 7.4, 145 mM NaCl, 5 mM MgCl₂, 10 $\mu\text{g}/\text{ml}$ chymostatin, 10 $\mu\text{g}/\text{ml}$ antipain, 10 $\mu\text{g}/\text{ml}$ pepstatin). Cytosol was prepared from BY4741 cells grown to mid-log phase (OD₆₀₀ = 1) in YPD medium⁴². For details see Supplementary Materials. The ubiquitylation reaction was incubated at 30 °C and stopped by mixing the sample at a ratio of 2:1 with 5x reducing sample buffer (8 M urea, 0.1 M Tris-HCl pH 6.8, 5 mM EDTA, 3.2% (w/v) SDS, 0.15% (w/v) bromophenol blue, 4% (v/v) glycerol, 4% (v/v) β -mercaptoethanol) and boiling it. Protein ubiquitylation was analyzed by SDS-polyacrylamide gel electrophoresis using 4–15% Mini-PROTEAN-TGX gels (BioRad) and immunoblotting using anti-MBP antibodies. Uncropped and unprocessed scans of immunoblots are provided as Source Data file and Supplementary Source Data file.

Molecular dynamics simulations. We characterized the impact of mutations on the assembly of the dimer-forming TMH of Mga2 by performing coarse-grained MD simulations. We modeled the TMHs containing the mutations W1042F, W1042Y, and W1042Q, and simulated their dynamics in a POPC bilayer for 1 ms, 0.93 ms, and 1 ms, respectively²⁵. For details, see Supplementary Materials.

Furthermore, we examined the biophysical properties (lipid packing, acyl chain order, and local density) of the experimentally studied lipid bilayers with all-atom MD simulations. The simulations were constructed, simulated, and analyzed mostly based on existing protocols⁵⁶. For details, see Supplementary Materials. Details on system size, trajectory length, and analysis can be found in Supplementary Table 5.

Reporting summary. Further information on research design is available in the Nature Research Reporting Summary linked to this article.

Data availability

Data supporting the findings of this manuscript are available from the corresponding author upon reasonable request. A reporting summary for this Article is available as a Supplementary Information file.

The source data underlying Figs. 1b, 2b–f, 3b–h, 4a–f, 5a–h, 6a–d and Supplementary Figs. 1a–e, 2a–d, 3a–d, 4a–j, 5b–i, 6b–h provided as a Source Data file.

Received: 16 July 2019; Accepted: 14 January 2020;

Published online: 06 February 2020

References

- Harayama, T. & Riezman, H. Understanding the diversity of membrane lipid composition. *Nat. Rev. Mol. Cell Biol.* **19**, 281–296 (2018).
- Radanović, T., Reinhard, J., Ballweg, S., Pesek, K. & Ernst, R. An emerging group of membrane property sensors controls the physical state of organellar membranes to maintain their identity. *BioEssays* **40**, e1700250 (2018).
- Sezgin, E., Levental, I., Mayor, S. & Eggeling, C. The mystery of membrane organization: composition, regulation and roles of lipid rafts. *Nat. Rev. Mol. Cell Biol.* **18**, 361–374 (2017).
- Lande, M. B., Donovan, J. M. & Zeidel, M. L. The relationship between membrane fluidity and permeabilities to water, solutes, ammonia, and protons. *J. Gen. Physiol.* **106**, 67–84 (1995).
- de Mendoza, D. Temperature sensing by membranes. *Annu. Rev. Microbiol.* **68**, 101–116 (2014).
- Los, D. & Murata, N. Membrane fluidity and its role in the perception of environmental signals. *Biochim. Biophys. Acta* **1666**, 142–157 (2004).
- Sinensky, M. Temperature control of phospholipid biosynthesis in *Escherichia coli*. *J. Bacteriol.* **106**, 449–455 (1971).
- Klose, C. et al. Flexibility of a eukaryotic lipidome - insights from yeast lipidomics. *PLoS ONE* **7**, e35063 (2012).
- Ballweg, S. & Ernst, R. Control of membrane fluidity: the OLE pathway in focus. *Biol. Chem.* **398**, 215–228 (2017).
- Svensk, E. et al. *Caenorhabditis elegans* PAQR-2 and IGLR-2 protect against glucose toxicity by modulating membrane lipid composition. *PLoS Genet.* **12**, e1005982 (2016).

- Ma, D. K. et al. Acyl-CoA dehydrogenase drives heat adaptation by sequestering fatty acids. *Cell* **161**, 1152–1163 (2015).
- Brankatschk, M. et al. A temperature-dependent switch in feeding preference improves *Drosophila* development and survival in the cold. *Dev. Cell* **46**, 781–793.e4 (2018).
- Behan-Martin, M. K., Jones, G. R., Bowler, K. & Cossins, A. R. A near perfect temperature adaptation of bilayer order in vertebrate brain membranes. *Biochim. Biophys. Acta* **1151**, 216–222 (1993).
- Tiku, P., Gracey, A., Macartney, A., Beynon, R. & Cossins, A. Cold-induced expression of $\Delta 9$ -desaturase by transcriptional and post-translational mechanisms. *Science* **271**, 815 (1996).
- Sinensky, M. Homeoviscous adaptation—a homeostatic process that regulates the viscosity of membrane lipids in *Escherichia coli*. *Proc. Natl Acad. Sci. USA* **71**, 522–525 (1974).
- Ernst, R., Ejsing, C. S. & Antonny, B. Homeoviscous adaptation and the regulation of membrane lipids. *J. Mol. Biol.* **428**, 4776–4791 (2016).
- Hazel, J. R. Thermal adaptation in biological-membranes - is homeoviscous adaptation the explanation. *Annu. Rev. Physiol.* **57**, 19–42 (1995).
- Covino, R., Hummer, G. & Ernst, R. Integrated functions of membrane property sensors and a hidden side of the unfolded protein response. *Mol. Cell* **71**, 458–467 (2018).
- Ernst, R., Ballweg, S. & Levental, I. Cellular mechanisms of physicochemical membrane homeostasis. *Curr. Opin. Cell Biol.* **53**, 44–51 (2018).
- Jensen, M. & Mouritsen, O. G. Lipids do influence protein function - the hydrophobic matching hypothesis revisited. *Biochim. Biophys. Acta Biomembr.* **1666**, 205–226 (2004).
- Surma, M. A. et al. A lipid E-MAP identifies Ubx2 as a critical regulator of lipid saturation and lipid bilayer stress. *Mol. Cell* **51**, 519–530 (2013).
- Budin, I. et al. Viscous control of cellular respiration by membrane lipid composition. *Science* **362**, 1186–1189 (2018).
- Halbleib, K. et al. Activation of the unfolded protein response by lipid bilayer stress. *Mol. Cell* **67**, 673–684.e8 (2017).
- Sodt, A. J., Venable, R. M., Lyman, E. & Pastor, R. W. Nonadditive compositional curvature energetics of lipid bilayers. *Phys. Rev. Lett.* **117**, 138104 (2016).
- Covino, R. et al. A eukaryotic sensor for membrane lipid saturation. *Mol. Cell* **63**, 49–59 (2016).
- Hofbauer, H. F. et al. The molecular recognition of phosphatidic acid by an amphipathic helix in Opi1. *J. Cell Biol.* **217**, 3109–3126 (2018).
- Cornell, R. B. Membrane lipid compositional sensing by the inducible amphipathic helix of CCT. *Biochim. Biophys. Acta Mol. Cell Biol. Lipids* **1861**, 847–861 (2016).
- Radhakrishnan, A., Goldstein, J. L., McDonald, J. G. & Brown, M. S. Switch-like control of SREBP-2 transport triggered by small changes in ER cholesterol: a delicate balance. *Cell Metab.* **8**, 512–521 (2008).
- Bigay, J. & Antonny, B. Curvature, lipid packing, and electrostatics of membrane organelles: defining cellular territories in determining specificity. *Dev. Cell* **23**, 886–895 (2012).
- Prévost, C. et al. Mechanism and determinants of amphipathic helix-containing protein targeting to lipid droplets. *Dev. Cell* **44**, 73–86.e4 (2018).
- Giménez-Andrés, M., Copic, A. & Antonny, B. The many faces of amphipathic helices. *Biomolecules* **8**, E45 (2018).
- Martin, C. E., Oh, C.-S. & Jiang, Y. Regulation of long chain unsaturated fatty acid synthesis in yeast. *Biochim. Biophys. Acta Mol. Cell Biol. Lipids* **1771**, 271–285 (2007).
- Zhang, S., Skalsky, Y. & Garfinkel, D. J. MGA2 or SPT23 is required for transcription of the delta9 fatty acid desaturase gene, OLE1, and nuclear membrane integrity in *Saccharomyces cerevisiae*. *Genetics* **151**, 473–483 (1999).
- Stukey, J. E., McDonough, V. M. & Martin, C. E. The OLE1 gene of *Saccharomyces cerevisiae* encodes the delta 9 fatty acid desaturase and can be functionally replaced by the rat stearoyl CoA desaturase gene. *J. Biol. Chem.* **265**, 20144–20149 (1990).
- Bhattacharya, S. et al. Identification of lysines within membrane-anchored Mga2p120 that are targets of Rsp5p ubiquitination and mediate mobilization of tethered Mga2p90. *J. Mol. Biol.* **385**, 718–725 (2009).
- Shcherbik, N., Zoladek, T., Nickels, J. T. & Haines, D. S. Rsp5p is required for ER bound Mga2p120 polyubiquitination and release of the processed/tethered transactivator Mga2p90. *Curr. Biol.* **13**, 1227–1233 (2003).
- Stordeur, C., Puth, K., Sáenz, J. P. & Ernst, R. Crosstalk of lipid and protein homeostasis to maintain membrane function. *Biol. Chem.* **395**, 313–326 (2014).
- Hoppe, T. et al. Activation of a membrane-bound transcription factor by regulated ubiquitin/proteasome-dependent processing. *Cell* **102**, 577–586 (2000).
- Antonny, B. Mechanisms of membrane curvature sensing. *Annu. Rev. Biochem.* **80**, 101–123 (2011).
- Piwko, W. & Jentsch, S. Proteasome-mediated protein processing by bidirectional degradation initiated from an internal site. *Nat. Struct. Mol. Biol.* **13**, 691–697 (2006).

41. Shcherbik, N., Kee, Y., Lyon, N., Huibregtse, J. M. & Haines, D. S. A single PXY motif located within the carboxyl terminus of Spt23p and Mga2p mediates a physical and functional interaction with ubiquitin ligase Rsp5p. *J. Biol. Chem.* **279**, 53892–53898 (2004).
42. Nakatsukasa, K. & Brodsky, J. L. In vitro reconstitution of the selection, ubiquitination, and membrane extraction of a polytopic ERAD substrate kunio. *Methods Mol. Biol.* **619**, 356–376 (2010). <https://doi.org/10.1201/9781351074735-12>
43. Ejsing, C. S. et al. Global analysis of the yeast lipidome by quantitative shotgun mass spectrometry. *Proc. Natl Acad. Sci. USA* **106**, 2136–2141 (2009).
44. Casanovas, A. et al. Quantitative analysis of proteome and lipidome dynamics reveals functional regulation of global lipid metabolism. *Chem. Biol.* **22**, 412–425 (2015).
45. Anbazhagan, V. & Schneider, D. The membrane environment modulates self-association of the human GPa TM domain—Implications for membrane protein folding and transmembrane signaling. *Biochim. Biophys. Acta Biomembr.* **1798**, 1899–1907 (2010).
46. Phillips, R. in *Physics of Biological Membranes* 73–105 (Springer International Publishing, 2018). https://doi.org/10.1007/978-3-030-00630-3_3
47. Schneider, F. et al. Diffusion of lipids and GPI-anchored proteins in actin-free plasma membrane vesicles measured by STED-FCS. *Mol. Biol. Cell* **28**, 1507–1518 (2017).
48. Dawaliby, R. et al. Phosphatidylethanolamine is a key regulator of membrane fluidity in eukaryotic cells. *J. Biol. Chem.* **291**, 3658–3667 (2016).
49. Kaiser, H.-J. et al. Order of lipid phases in model and plasma membranes. *Proc. Natl Acad. Sci. USA* **106**, 16645–16650 (2009).
50. Koynova, R. & Caffrey, M. Phases and phase transitions of the phosphatidylcholines. *Biochim. Biophys. Acta Rev. Biomembr.* **1376**, 91–145 (1998).
51. Chellappa, R. et al. The membrane proteins, Spt23p and Mga2p, play distinct roles in the activation of *Saccharomyces cerevisiae* OLE1 gene expression: fatty acid-mediated regulation of Mga2p activity is independent of its proteolytic processing into a soluble transcription act. *J. Biol. Chem.* **276**, 43548–43556 (2001).
52. Gratkowski, H., Lear, J. D. & DeGrado, W. F. Polar side chains drive the association of model transmembrane peptides. *Proc. Natl Acad. Sci. USA* **98**, 880–885 (2002).
53. Kandasamy, P., Vemula, M., Oh, C. S., Chellappa, R. & Martin, C. E. Regulation of unsaturated fatty acid biosynthesis in *Saccharomyces*: The endoplasmic reticulum membrane protein, Mga2p, a transcription activator of the OLE1 gene, regulates the stability of the OLE1 mRNA through exosome-mediated mechanisms. *J. Biol. Chem.* **279**, 36586–36592 (2004).
54. Cantor, R. S. Lipid composition and the lateral pressure profile in bilayers. *Biophys. J.* **76**, 2625–2639 (1999).
55. Van Den Brink-Van Der Laan, E., Antoinette Killian, J. & De Kruijff, B. Nonbilayer lipids affect peripheral and integral membrane proteins via changes in the lateral pressure profile. *Biochim. Biophys. Acta Biomembr.* **1666**, 275–288 (2004).
56. Doktorova, M., LeVine, M. V., Khelashvili, G. & Weinstein, H. A new computational method for membrane compressibility: bilayer mechanical thickness revisited. *Biophys. J.* **116**, 487–502 (2019).
57. Lee, A. G. How lipids affect the activities of integral membrane proteins. *Biochim. Biophys. Acta Biomembr.* **1666**, 62–87 (2004).
58. Sardana, R., Zhu, L. & Emr, S. D. Rsp5 ubiquitin ligase-mediated quality control system clears membrane proteins mistargeted to the vacuole membrane. *J. Cell Biol.* **218**, 234–250 (2019).
59. Zhang, Z. R., Bonifacino, J. S. & Hegde, R. S. Deubiquitinases sharpen substrate discrimination during membrane protein degradation from the ER. *Cell* **154**, 609–622 (2013).
60. Kee, Y., Lyon, N. & Huibregtse, J. M. The Rsp5 ubiquitin ligase is coupled to and antagonized by the Ubp2 deubiquitinating enzyme. *EMBO J.* **24**, 2414–2424 (2005).
61. Attali, I. et al. Ubiquitylation-dependent oligomerization regulates activity of Nedd4 ligases. *EMBO J.* **36**, 425–440 (2017).
62. Cavellini, L. et al. An ubiquitin-dependent balance between mitofusin turnover and fatty acids desaturation regulates mitochondrial fusion. *Nat. Commun.* **8**, 15832 (2017).
63. Fang, N. N. et al. Rsp5/Nedd4 is the main ubiquitin ligase that targets cytosolic misfolded proteins following heat stress. *Nat. Cell Biol.* **16**, 1227–1237 (2014).
64. Waithe, D., Clausen, M. P., Sezgin, E. & Eggeling, C. FoCuS-point: software for STED fluorescence correlation and time-gated single photon counting. *Bioinformatics* **32**, 958–960 (2016).
65. Kelley, L. A., Mezulis, S., Yates, C. M., Wass, M. N. & Sternberg, M. J. E. The Phyre2 web portal for protein modeling, prediction and analysis. *Nat. Protoc.* **10**, 845–858 (2015).
66. Chothia, C. The nature of the accessible and buried surfaces in proteins. *J. Mol. Biol.* **105**, 1–12 (1976).
67. Schindelin, J. et al. Fiji: an open-source platform for biological-image analysis. *Nat. Methods* **9**, 676–682 (2012).

Acknowledgements

We thank Laura Glück and Kim Wendrich for excellent technical assistance. We acknowledge Jeffrey Brodsky and Volker Dötsch for sharing reagents and protocols, as well as Edward Lyman and Alex Solt for fruitful discussions. This work was supported by the Deutsche Forschungsgemeinschaft (DFG, ER608/2–1) to R.E. and (HA6322/3–1) to I.H., the Volkswagen Foundation (Life?, grant numbers 93089 and 93091) to R.E. and I.L., respectively, and the European Molecular Biology Organization (EMBO, ASTF 451–2014) to S.B. E.S. is funded by British Council Newton-Katip Celebi Fund (#352333122). I.L. and M.D. acknowledge funding from the NIH/National Institute of General Medical Sciences (GM114282, GM124072, and GM120351) and the Human Frontiers Science Program (RGP0059/2019). R.C. and G.H. were supported by the Max Planck Society. This work used the Extreme Science and Engineering Discovery Environment (allocation TG-MCB180168), which is supported by National Science Foundation grant number ACI-1548562. Data regarding the wild-type and the W1042A variant of the Mga2-TMH in Supplementary Fig. 5 are replotted from Covino et al.²⁵, with permission from Elsevier.

Author contributions

Conceptualization: R.E. Experimental design: S.B., E.S., D.W., I.H., R.C., M.C., J.R., and R.E. Performed experiments: S.B., R.C., M.D., E.S., D.W., and J.R. Writing—original draft: S.B. and R.E. Writing—revised draft: R.E., S.B., R.C., and M.D. Funding acquisition: R.E., I.H., E.S., I.L., and G.H. Supervision: R.E., G.H., and I.L.

Competing interests

The authors declare no competing interests.

Additional information

Supplementary information is available for this paper at <https://doi.org/10.1038/s41467-020-14528-1>.

Correspondence and requests for materials should be addressed to R.E.

Peer review information *Nature Communications* thanks the anonymous reviewer(s) for their contribution to the peer review of this work. Peer reviewer reports are available.

Reprints and permission information is available at <http://www.nature.com/reprints>

Publisher's note Springer Nature remains neutral with regard to jurisdictional claims in published maps and institutional affiliations.



Open Access This article is licensed under a Creative Commons Attribution 4.0 International License, which permits use, sharing, adaptation, distribution and reproduction in any medium or format, as long as you give appropriate credit to the original author(s) and the source, provide a link to the Creative Commons license, and indicate if changes were made. The images or other third party material in this article are included in the article's Creative Commons license, unless indicated otherwise in a credit line to the material. If material is not included in the article's Creative Commons license and your intended use is not permitted by statutory regulation or exceeds the permitted use, you will need to obtain permission directly from the copyright holder. To view a copy of this license, visit <http://creativecommons.org/licenses/by/4.0/>.

© The Author(s) 2020

1
2
3
4
5
6
7
8
9
10
11
12
13
14
15
16
17
18
19
20
21
22
23
24
25
26
27
28
29
30
31
32
33
34
35
36
37
38

Supplementary Materials

**for Ballweg *et al.*
Regulation of lipid saturation without sensing membrane fluidity**

**(contains Supplementary Methods, Supplementary Figures 1-7, and
Supplementary Tables 1-5)**

**Correspondence and requests for materials should be addressed to Robert Ernst
(email: robert.ernst@uks.eu)**

39 Supplementary Methods

40

41 Reagents and antibodies.

42 All chemicals and reagents were of analytical or higher grade and obtained from Sigma Aldrich
43 if not stated otherwise. The following antibodies were used: mouse anti-Myc (9E10), mouse
44 anti-Pgk1 (Life Technologies), mouse anti-MBP (NEB), anti-mouse-HRP (Dianova), anti-
45 mouse-IRDye 800CW (LI-COR). Atto488-PE was purchased from AttoTec GmbH. Abberior
46 Star Red-Cholesterol is purchased from Abberior GmbH. It has a PEG linker between
47 cholesterol moiety and the fluorescent tag.

48

49 Cultivation and genetic manipulation of *S. cerevisiae*

50 Plasmids (Table1) were used for the transformation of baker's yeast (Table 2). Overnight
51 cultures were inoculated from single colonies and cultivated in SCD selection medium at 30°C
52 until the stationary phase was reached. The UFA auxotroph $\Delta SPT23\Delta MGA2$ strain was
53 cultivated in the presence of 0.05% sodium linoleate. Main cultures were inoculated to an
54 OD600 of 0.2 in rich medium (YPD) and cultivated to the mid-exponential phase (OD600 \approx
55 1.0). If indicated, the YPD was supplemented with sodium linoleate.

56 A *CEN*-based plasmid expressing 3xmyc-tagged *MGA2* under the control of the *MGA2*
57 promoter for near-endogenous levels was used as described previously ¹. Mutagenesis of
58 *MGA2* was performed using a PCR-based strategy based on the QuikChange® method
59 (Stratagene) using the PHUSION polymerase (NEB). *S. cerevisiae* was transformed using
60 Lithium-Acetate (Ito et al., 1983).

61

62 Molecular cloning

63 Plasmids (Table 1) were generated and modified using oligonucleotides listed in Table 3. In
64 order to generate a minimal sense-and-response construct (^{ZIP-MBP}Mga²⁹⁵⁰⁻¹⁰⁶²), the C-terminal
65 region of *MGA2* containing juxtamembrane region (G950-S1113) and the predicted TMH was
66 cloned into the pMAL-C2x-TEV expression vector via *EcoRI/HindIII* restriction sites. The
67 resulting construct was truncated downstream of the TMH by introducing two consecutive stop
68 codons after the residue at position 1062 by the PCR-based QuikChange® method. The
69 *GCN4*-derived leucine zipper and a flexible linker (GGGS)₂ were introduced N-terminally to the
70 MBP by restriction-based cloning using *NdeI*. Further mutagenesis of this construct and yeast
71 expression vectors was performed either via the QuikChange® or the Q5 mutagenesis
72 approach as indicated in Table 3.

73

74 Preparation of cell extracts and immunoblot analysis

75 Crude cell lysates were prepared as described previously ¹ with minor modifications. Shortly,
76 15 OD600 equivalents of cells grown to the mid-exponential phase (OD600 \approx 1.0) were
77 harvested by centrifugation, washed with phosphate-buffered saline (PBS) supplemented with
78 10 mM NEM and snap-frozen. The cells were resuspended in 0.5 ml lysis buffer (PBS, 10 mM
79 NEM, 5 mM EDTA, 10 μ g/ml chymostatin, 10 μ g/ml antipain, 10 μ g/ml pepstatin) and lysed by
80 bead-beating twice with 200 μ l zirconia beads (Roth) using a Scientific Industries SI™
81 Disruptor Genie™ Analog Cell Disruptor for 5 min each at 4 °C and 1 min pause on ice. For
82 protein denaturation the extract was mixed at a ratio of 2:1 with 5x reducing sample buffer (8
83 M urea, 0.1 M Tris-HCl pH 6.8, 5 mM EDTA, 3.2% (w/v) SDS, 0.15% (w/v) bromphenol blue,
84 4% (v/v) glycerol, 4% (v/v) β -mercaptoethanol) and incubated at 60°C for 10 min.

85 Centrifugation (1 min, 16,000x g, room temperature) cleared protein samples were subjected
86 to a discontinuous SDS-PAGE using 4-15% Mini-PROTEAN-TGX gels (BioRad). After semi-
87 dry Western-Blotting onto nitrocellulose membranes, the target proteins were detected using
88 specific antibodies. A list of antibodies, their used dilutions and source can be found in
89 Supplementary Table 4.

90

91 **Yeast growth assays / rescue of UFA auxotrophy**

92 The UFA auxotroph $\Delta SPT23\Delta MGA2$ strain was generated by Harald Hofbauer (Graz
93 University) and cultivated in SCD-medium supplemented with 0.05% sodium linoleate. The
94 cells were harvested by centrifugation, washed successively with 1% NP40-type tergitol
95 (NP40S Sigma), then ddH₂O and then resuspended in SCD medium lacking any additives to
96 an OD₆₀₀ of 0.2. The cells were either cultivated at 30°C for 5-6 h to starve cells for UFAs prior
97 to perform spotting tests or for 24 h to study the impact of mutations on the final cell density in
98 liquid culture. For spotting tests, the UFA-starved cells were harvested and adjusted to an
99 OD₆₀₀ of 1. Serial 1:10 dilutions were prepared (10^0 , 10^{-1} , 10^{-2} , 10^{-3}) and 5 μ l of each dilution
100 were spotted onto selective agar plates. The plates were incubated for 2-3 days at 30°C until
101 sufficient cell growth became apparent.

102 The impact of linoleate on the final cell density in liquid medium was tested with UFA-depleted
103 cultures that were adjusted to an OD₆₀₀ of 0.05. 50 μ l of these cultures were added to 180 μ l
104 SCD-Ura containing 1% NP40-type tergitol and varying concentrations of linoleic acid. The
105 optical density of the cultures was determined using a microplate reader at 600 nm (OD₆₀₀)
106 after 17 h of cultivation at 30°C.

107

108 **Preparation of yeast cytosol**

109 500 OD equivalents were harvested by centrifugation (5 min, 3000x g), washed with 30 ml ice
110 cold PBS, then with 30 ml cold ubiquitylation buffer. The supernatant was decanted, and the
111 cell pellet was resuspended in the residual liquid by vigorous vortexing. The resulting
112 suspension was subjected dropwise into a tube with liquid nitrogen. The frozen beads of cells
113 crushed with mortar and pestil (4 x 60 s and 1 x 90 s) and the resulting yeast powder was
114 transferred into a cold 50 ml tube. The tube was immersed in water at room temperature and
115 the thawing suspension was quickly adjusted to 1 mM DTT. Unbroken cells and debris were
116 removed from the ice-cold suspension by centrifugation (10 min, 20,000x g, 4 °C). The
117 supernatant of this step was centrifuged again (1 h, 100,000x g, 4 °C) to obtain the soluble,
118 cytosolic fraction from the supernatant.

119

120 **Expression, purification and labeling of MBP Mga2-fusions**

121 Plasmids (Table 1) were used for the heterologous production of sensor construct in *E. coli*.
122 The minimal sensor construct (^{MBP}Mga2¹⁰³²⁻¹⁰⁶²) comprising the residues R1032-D1062 that
123 include the TMH region of Mga2 was described previously ¹. The sense-and-response
124 construct (^{MBP}Mga2⁹⁵⁰⁻¹⁰⁶²) was generated by cloning the coding regions of the JM and TMH
125 region of Mga2 (residues 950-1062) into the pMal-C2x vector. The ^{ZIP}-^{MBP}Mga2⁹⁵⁰⁻¹⁰⁶² construct
126 was generated by fusing the leucine zipper sequence derived from the *GCN4* transcription
127 factor (residues 249-281) in frame to MBP protein. The minimal sensor construct and the
128 sense-and-response construct were overexpressed in the cytosol of *E. coli* BL21(DE3)pLysS
129 and isolated essentially as described previously ^{1,2} with minor modifications. A 500 ml culture
130 in LBrich medium (LB medium supplemented with 2% glucose, 100 mg/ml ampicillin, 34 μ g/ml

131 chloramphenicol) was inoculated 1:50 using an overnight culture and cultivated at 37°C until
132 an OD600 of ~0.6 was reached. Then, protein production was induced by isopropyl-β-D-
133 thiogalactopyranoside (IPTG) at a final concentration of 0.3 mM. After 3 h of cultivation at 37 °C
134 the cells were harvested by centrifugation and washed with PBS. For isolation of the proteins,
135 the cells were resuspended in 40 ml of lysis buffer (50 mM HEPES pH 7.0, 150 mM NaCl,
136 1 mM EDTA, 10 μg/ml chymostatin, 10 μg/ml antipain, 10 μg/ml pepstatin, 2 mM DTT, 5 U/ml
137 Benzonase) per liter of culture and disrupted by sonification using a SONOPULS HD2070
138 ultrasonic homogenizer (Bandelin) (4x 30s, power 30%, pulse 0.7 sec/0.3 sec). The protein
139 was solubilized by gentle agitation in the presence of 50 mM β-Octylglucoside (β-OG) for
140 20 min at 4 °C. Non-solubilized material was pelleted by centrifugation (30 min, 100,000 x g,
141 4° C) and the supernatant was applied to washed and equilibrated amylose beads (NEB) using
142 6 ml of slurry per liter of culture. After binding (20 min at 4 °C) to the amylose column and
143 washing the column with 26 column volumes (CV) wash buffer (50 mM HEPES pH 7.0,
144 200 mM NaCl, 1 mM EDTA, 50 mM β-OG) the protein was either labeled or directly eluted.
145 The labeling of the proteins at single cysteine residues with 1 mM MTS (methanethiosulfonate)
146 (Enzo Life Sciences) or 1 mM ATTO488/ATTO590 dyes (ATTO TEC GmbH) was performed
147 on the amylose column during an overnight incubation at 4 °C including gentle shaking. This
148 step was skipped for the isolation of unlabeled proteins. The fusion protein was eluted with
149 elution buffer (50 mM HEPES pH 7.0, 150 mM NaCl, 1 mM EDTA, 10 mM maltose, 50 mM β-
150 OG). The sense-and-response construct (^{ZIP-MBPMga2⁹⁵⁰⁻¹⁰⁶²}) was further purified by
151 preparative SEC using a Superdex 200 10/300 increase column in SEC-buffer (50 mM HEPES
152 pH 7.0, 150 mM NaCl, 1 mM EDTA, 50 mM β-OG). The purified proteins could be stored
153 at -80°C for extended periods of time in storage buffer (40 mM HEPES pH 7.0, 120 mM NaCl,
154 0.8 mM EDTA, 40 mM β-OG, and 20% (v/v) glycerol).

155 The efficiency of spin-labeling was determined for each construct by double-integration of the
156 EPR resonances and a comparison to the signal of a 100 μM MTS standard. The determined
157 spin-label concentration was put into relation to the protein concentration determined by
158 absorption spectroscopy at A280. The labeling efficiency for W1042C^{MTS} was > 95%.

159 The efficiency of labeling with fluorescent dyes was determined by absorption spectroscopy
160 using the following extinction factors: 9.58*10⁴ l mol⁻¹ cm⁻¹ (unlabeled protein K983 or K969),
161 9*10⁴ l mol⁻¹ cm⁻¹ (ATTO488), 1.2*10⁵ l mol⁻¹ cm⁻¹ (ATTO 590) and the correction factors were
162 0.1 for ATTO488 and 0.44 for ATTO590 according to the manufacturer's specification. Maximal
163 absorption intensities were determined at 505 nm (ATTO488) or 597 nm (ATTO590). The
164 labeling efficiency was ~60% (K983^{ATTO 488}) and ~90% (K969^{ATTO 590}).

165

166 Liposome preparation

167 Liposomes of defined compositions were generated by mixing 1,2-dioleoyl-*sn*-glycero-3-
168 phosphocholine (DOPC), 1-palmitoyl-2-oleoyl-*sn*-glycero-3-phosphocholine (POPC), 2-
169 dipetroselenoyl-*sn*-glycero-3-phosphocholine (18:1 (Δ6-*cis*)PC), 2-dielaidoyl-*sn*-glycero-3-
170 phosphocholine (*trans*DOPC) or 1-palmitoyl-2-oleoyl-*sn*-glycero-3-phosphoethanolamine
171 (POPE) from 20 mg/ml stocks, dissolved in chloroform to obtain following molar compositions:
172 1) 100% DOPC; 2) 50% DOPC, 50% POPC; 3) 25% DOPC, 75% POPC; 4) 100% POPC; 5)
173 100% (18:1 (Δ6-*cis*)PC); 6) 100% *trans*DOPC; 7) 100% (16:1 (Δ9-*trans*)PC); 8) 50% DOPC,
174 30% POPC, 20% POPE; 9) 50% DOPC, 10% POPC, 40% POPE. After evaporation of the
175 organic solvent using a constant stream of nitrogen, the lipid film was dried in a desiccator
176 under vacuum (2 – 4 mbar) for at least 1 h at room temperature. For rehydration, the lipid film

177 was resuspended in reconstitution buffer (20 mM HEPES, pH 7.4, 150 mM NaCl, 5% (w/v)
178 glycerol) to a final lipid concentration of 10 mM, incubated at 60 °C under rigorous shaking for
179 30 min at 1200 rpm, and incubated in a sonication in a water bath at 60°C for 30 min. The
180 resulting multilamellar liposomes were used for reconstitution experiments.

181

182 **Reconstitution of MBP^{Mga2}-fusions in proteoliposomes**

183 For reconstitution of the ZIP-MBP^{Mga2}⁹⁵⁰⁻¹⁰⁶² constructs at a protein:lipid molar ratio of 1:5,000 -
184 1:15,000, 0.1 μmol lipid and 0.2 – 0.067 nmol protein were mixed in reconstitution buffer
185 (20 mM HEPES (pH 7.4), 150 mM NaCl, and 5% (w/v) glycerol), adjusted to 37 mM β-OG in
186 a total volume of 1 ml and incubated for 20 min at room temperature under gentle agitating.
187 For detergent removal, 500 mg of Bio-Beads™ SM-2 Adsorbent Media (BioRad) were added
188 and the resulting mixture was incubated and gently mixed for 120 min at room temperature.
189 The suspension was then transferred to a fresh tube containing 100 mg Bio-Beads™ SM-2
190 Adsorbent Media and further incubated for 60 min. 0.8 ml of the proteoliposome containing
191 suspension was mixed with 2.2 ml Harvesting buffer (20 mM HEPES, pH 7.4, 75 mM NaCl).
192 Proteoliposomes were harvested by centrifugation (200,000x g, 4 °C, 18 h) and resuspended
193 either in the respective assay buffer.

194

195 **DPH anisotropy**

196 Liposomes of different lipid compositions were generated by consecutive extrusions through
197 400 nm and 200 nm filters (21 strokes each) in a LiposoFast (Avestin) extruder. The
198 concentration of lipids was then adjusted to 0.1 mM with PBS. Diphenylhexatriene (DPH) was
199 added to a final concentration of 0.5 μM. The samples were incubated for 20 min in the dark
200 at room temperature. Intensities for each polarized component (I_{hv} , I_{hh} , I_{vv} , I_{vh}) were recorded
201 on a FluoroMax-4 spectrofluorometer using the following settings. The sample was excited at
202 360 nm and the emission was recorded at 430 nm with slit widths of 5 nm. A maximum of 10
203 measurements were performed with standard deviation cutoff of 5 %. The samples were
204 equilibrated for 5 min for each temperature. To correct for scattered light, the intensities for
205 each polarized component of the respective liposome sample before the addition of DPH were
206 subtracted. The G factor and anisotropy (r) were calculated as follows $G = \frac{I_{hv}}{I_{vh}}$, $r = \frac{I_{vv} - G^* I_{vh}}{I_{vv} + 2^* G^* I_{vh}}$.

207

208 **Thin layer chromatography**

209 For lipid extraction, a 60 μl sample of ZIP-MBP^{Mga2}⁹⁵⁰⁻¹⁰⁶²-containing proteoliposomes
210 reconstituted at a protein to lipid ratio of 1:8,000 were used. The sample was mixed with 1 ml
211 of CHCl₃:MeOH (2:1) and an artificial upper phase of 200 μl (48:47:3) MeOH:H₂O:CHCl₃ and
212 constantly agitated for 2 h at 4°C. After centrifugation (3,000 x g, 4°C, 5 min) the aqueous
213 phase was discarded. The organic solvent evaporated from the remaining sample under a
214 constant stream of N₂. Residual traces of the solvent were removed in 30 min using a
215 desiccator and by applying vacuum. The extracted lipids were then taken up in 15 μl
216 CHCl₃:MeOH (2:1). 1 μl of the extract was spotted onto an HPTLC Silica gel 60 (Merck KGaA)
217 and separated using as a mobile phase (97.5:37.5:6) CHCl₃:MeOH:H₂O. As a reference, 1 μl
218 of POPC, DOPC and POPE at a concentration of 20 mg/ml in CHCl₃ were spotted onto the
219 plate. Additionally, a buffer control (50 mM Hepes pH 7.4, 150 mM NaCl, 5% w/v glycerol) was
220 used. The silica plates were stained for 30 min using iodine.

221

222 Sucrose density gradient centrifugation

223 For validation of the reconstitution procedure, 200 μ l of a proteoliposomal preparation were
224 mixed with 400 μ l 60% (w/v) sucrose solution in reconstitution buffer and overlaid with different
225 layers of distinct densities. For protein-to-lipid molar ratios of 1:5,000, 1:8,000, and 1:15,000,
226 the proteoliposome-containing layer was overlaid with each 2.5 ml of 20%, 10%, 5% and 0%
227 (w/v) sucrose in reconstitution buffer. After centrifugation (100,000x g, 4°C, overnight) the
228 gradient was fractionated from top to bottom in 13 fractions of 0.85 ml each. The distribution
229 of the MBP-containing fusion proteins in the gradient was analyzed by SDS-PAGE and
230 subsequent immunoblotting. The lipid content of the individual fractions was estimated by
231 adjusting each fraction to 7 μ M Hoechst 33342 and determination of the fluorescence intensity
232 using a TECAN microplate reader (ex355 nm: em459, bandwidth 20 nm).

233

234

235 Recording and analysis of cwEPR spectra

236 cwEPR spectra were recorded and analyzed as previously described¹.

237

238 Isolation of His⁸ubiquitin

239 8xHis⁸ubiquitin was overproduced in *E. coli* BL21(DE3)pLysS and purified using immobilized
240 metal affinity chromatography (Ni²⁺-NTA matrix). The plasmid encoding the human ubiquitin
241 with an N-terminal 8xHis-tag was derived from a pETM-m60 plasmid and kindly provided by
242 the Volker Dötsch lab. The production of 8xHis⁸ubiquitin was induced at an OD₆₀₀ of ~0.6 at
243 37 °C using 0.3 mM IPTG. After induction, the cells were cultivated for additional 3 h at 30 °C
244 prior to harvesting and washing of the cell pellet using PBS. For purification, the cells were
245 resuspended in 20 ml lysis buffer (50 mM HEPES, pH 8.0, 250 mM NaCl, 20 mM imidazol, 10
246 μ g/ml chymostatin, 10 μ g/ml antipain, 10 μ g/ml pepstatin) and disrupted by sonification (3x
247 30s, power 30%, pulse 0.7 s/ 0.3 s). Unbroken cells, debris, and cellular membranes were
248 removed by centrifugation (1 h, 100,000x g, 4 °C). The cleared lysate was applied to 1 ml Ni²⁺-
249 NTA agarose matrix and incubated for 1 h at 4 °C while rotating to allow for protein binding.
250 The mixture was then transferred into a gravity flow column and the flow-through was collected.
251 The affinity matrix was washed with 30 CV of wash buffer (50 mM HEPES pH 8.0, 250 mM
252 NaCl, 20 mM imidazole). 8xHis⁸ubiquitin was eluted with elution buffer (50 mM HEPES pH 8.0,
253 250 mM NaCl, 400 mM imidazole). The eluate was dialysed against 100-fold volume storage
254 buffer (50 mM HEPES, pH 7.4, 150 mM NaCl) using a dialysis membrane with a molecular
255 weight cutoff of 3.5 kDa (Spectra/Por). After 2 h the storage buffer was refreshed, and the
256 sample was dialyzed overnight at 4°C. For long-term storage, the purified 8xHis⁸ubiquitin was
257 adjusted to 1 mg/ml and 20% (w/v) glycerol in storage buffer.

258

259 Molecular dynamics simulations

260 We performed coarse-grained simulations in the MARTINI v2.2 force field^{3,4}. We modelled
261 TMHs containing the mutations W1042F, W1042Q, and W1042Y with the UCSF Chimera
262 package⁵ (Pettersen et al., 2004), and coarse grained in MARTINI⁴. For each mutation, we
263 inserted two identical TMHs in a POPC lipid bilayer spanning the periodic simulation box in the
264 xy-plane. We obtained simulation boxes containing two TMHs surrounded by approximately
265 560 lipids, 9000 water beads, and 150 mM sodium chloride. After energy minimization and
266 equilibration, we ran 10 independent MD simulations for each system, totaling a simulated time
267 of 1 ms for the W1042F and W1042Q systems each, and 0.93 ms for W1042Y one. All

268 simulations were performed in GROMACS 4.6.7, using a time step of 20 fs. A temperature of
269 303 K and a pressure of 1 atm were maintained with the velocity rescaling thermostat⁶ and the
270 semiisotropic Parrinello-Rahman barostat⁷.

271

272 All-atom simulations of empty bilayers were performed with NAMD⁸, using the CHARMM36
273 force field parameters for lipids^{9,10}. Four bilayer systems were constructed and simulated as
274 indicated in Supplementary Table 5. For the POPC trajectory, we used data from a previous
275 simulation that contained 64 lipids per leaflet, 45 water molecules per lipid and no ions¹¹. All
276 bilayers were simulated at constant temperature of 30°C and constant pressure of 1 atm with
277 the same simulation parameters as previously used¹¹.

278

279 Each trajectory was centered so that the geometric center of all terminal methyl carbons of the
280 lipids was at (x,y,z)=(0,0,0). The last ~270 ns were used for analysis with frames being output
281 every 20 ps. The average area per lipid (APL) was calculated by dividing the lateral area of
282 the simulation box by the number of lipids in one leaflet. Thickness was calculated as the mean
283 distance between the average z position of the phosphate atoms in each leaflet. The errors on
284 both APL and thickness represent the standard deviation of the time series of the respective
285 property.

286

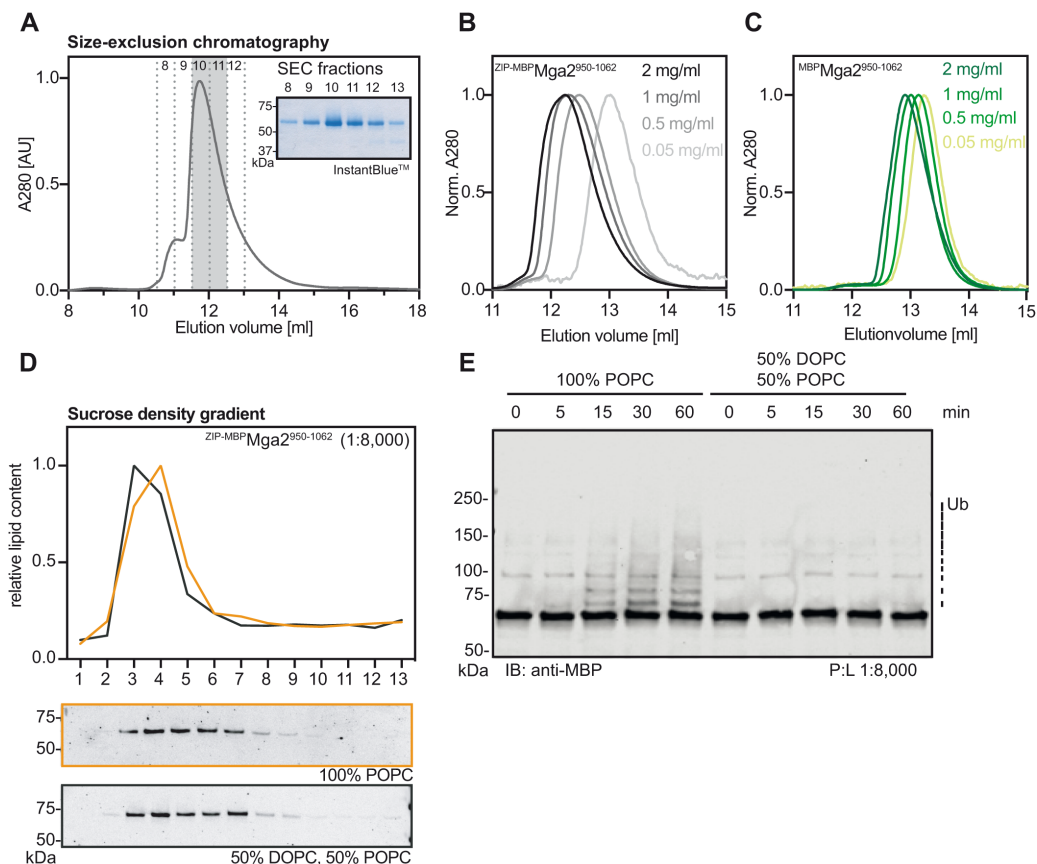
287 Acyl chain order parameters were computed with an in-house tcl script. The order parameter
288 S_{CD} at a carbon position is expressed as $S_{CD} = \frac{1}{2}(3 \cos^2 \theta - 1)$ where $\langle \cdot \rangle$ denotes ensemble
289 average and θ is the angle between a CH bond at that carbon and the bilayer normal (assumed
290 to be the z dimension of the simulation box).

291

292 Local number density of lipid atoms was calculated with the volmap plugin in VMD¹². A fixed
293 region of the bilayer between -23 Å and 23 Å in each dimension was divided into grid points
294 spaced 1×1×1 Å apart. Atoms were represented as normalized gaussians with standard
295 deviation equal to the atom radius. This representation was used to calculate their atomic
296 number density at each grid point. The atomic radii used in the calculation were the default
297 atomic radii in VMD, which mimic the atomic radii in the CHARMM36 force field parameters:
298 carbon 1.5 Å, hydrogen 1.0 Å, nitrogen 1.4 Å, oxygen 1.3 Å. The densities calculated at the
299 grid points were subsequently analyzed with MATLAB to produce the density profiles as a
300 function of z and the heatmap representations in which the data was collapsed on the xz
301 plane by taking the average across all corresponding y values.

302

303 Lateral pressure profiles were calculated from the last 230-250 ns of the trajectories with
304 NAMD as previously explained¹¹. Each profile was symmetrized by means of averaging the
305 pressure profiles of the two leaflets (i.e. above and below z=0) and smoothed with a 7-point
306 moving average window in MATLAB. Bilayer snapshots of the all-atom bilayers were rendered
307 with VMD.

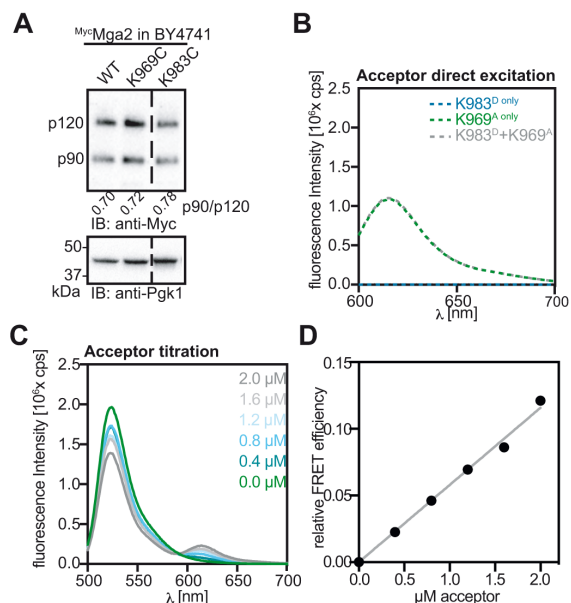


308
309

310 **Supplementary Figure 1. Isolation and functional reconstitution of sense-and-response**
311 **construct.**

312 (A) Purification of the zipped sense-and-response construct ($\text{ZIP-MBP Mga2}^{950-1062}$) by SEC. The
313 eluate of the affinity purification (Figure 2B) was concentrated ~ 10 fold and loaded onto a
314 Superdex 200 10/300 Increase column (void volume 8.8 ml) using a $500 \mu\text{l}$ loop. Fractions of
315 0.5 ml were collected, mixed with non-reducing membrane sample buffer and subjected to
316 SDS-PAGE followed by InstantBlueTM staining. Fraction 10 and 11 were pooled and further
317 used. (B) SEC of the purified $\text{ZIP-MBP Mga2}^{950-1062}$ protein in the detergent-containing SEC-buffer.
318 The protein concentration was adjusted to the indicated concentrations, and $100 \mu\text{l}$ of each of
319 these samples were subjected to SEC using a Superdex 200 10/300 Increase column. (C)
320 SEC of the purified non-zipped $\text{MBP Mga2}^{950-1062}$ protein in SEC-buffer. The protein
321 concentration was adjusted to the indicated concentrations, and $100 \mu\text{l}$ of each of these
322 samples were loaded onto a Superdex 200 10/300 Increase column. (D) Sucrose-density
323 gradients centrifugation for proteoliposomes containing $\text{ZIP-MBP Mga2}^{950-1062}$ at a molar
324 protein:lipid ratio of 1:8,000. The proteoliposome sample was adjusted to 40% w/v sucrose
325 and overlaid with sucrose cushions of different concentrations (20%, 10%, 5%, 0% w/v). After
326 ultracentrifugation, 13 fractions were collected from top to bottom. The relative content of lipids
327 in the individual fractions was determined by Hoechst 33342 fluorescent staining. The amount
328 of MBP Mga2-TMH in the fractions was monitored by immunoblotting using anti-MBP antibodies.
329 (E) *In vitro* ubiquitylation reactions were performed with the WT $\text{ZIP-MBP Mga2}^{950-1062}$ sense-and-

330 response construct reconstituted in the indicated lipid environments at a protein:lipid ratio of
331 1:8,000. After indicated times, the reactions were stopped and subjected to SDS-PAGE. For
332 analysis, an immunoblot using anti-MBP antibodies was performed. Source data are provided
333 as a Source Data file.



334

335

Supplementary Figure 2: Establishing a FRET reporter based on sense-and-response construct.

336

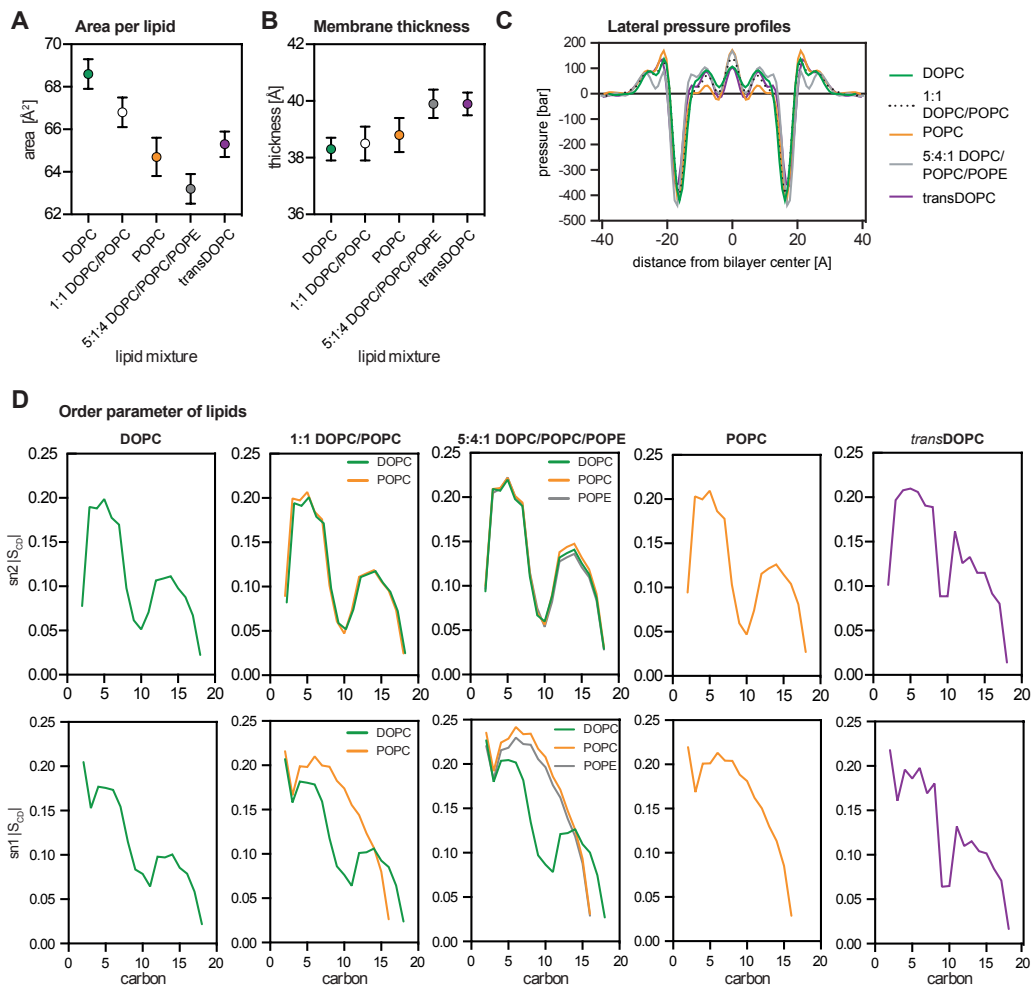
337

(A) Immunoblot analysis of indicated MycMga2 variants produced at near-endogenous levels in the BY4741 wild type background. Cells were cultivated in YPD to the mid-logarithmic growth phase. Crude cell lysates were subjected to SDS-PAGE and analyzed by immunoblotting using anti-Myc antibodies. The Mga2 p90:p120 ratios were determined by densitometric quantification. An anti-Pgk1 immunoblot served as loading control. (B) Fluorescence emission spectra for the samples in shown in Figure 3B upon direct acceptor excitation at 590 nm. (C) 2 μM donor was titrated with the indicated acceptor concentrations and fluorescence emission spectra were measured upon donor excitation. The overall protein concentrations were maintained by the use of unlabeled ZIP-MBPMga2⁹⁵⁰⁻¹⁰⁶². (D) Relative FRET efficiencies were determined from the donor/acceptor intensity ratios in (C). Data were fitted via linear regression. Source data are provided as a Source Data file.

346

347

348



349

350

351 **Supplementary Figure 3: Biophysical properties of lipid bilayers determined from all-**352 **atom simulations. (A)** Plotted is the average area per lipid and **(B)** the phosphate-to-

353 phosphate thickness in different bilayer systems. Acyl chain saturation and the presence of PE

354 lipids increase lipid packing (decrease area per lipid) and have a more modest effect on bilayer

355 thickness. **(C)** Lateral pressure distribution in the bilayers as a function of distance from the

356 bilayer center. Acyl chain saturation increases the pressure at the bilayer midplane while in

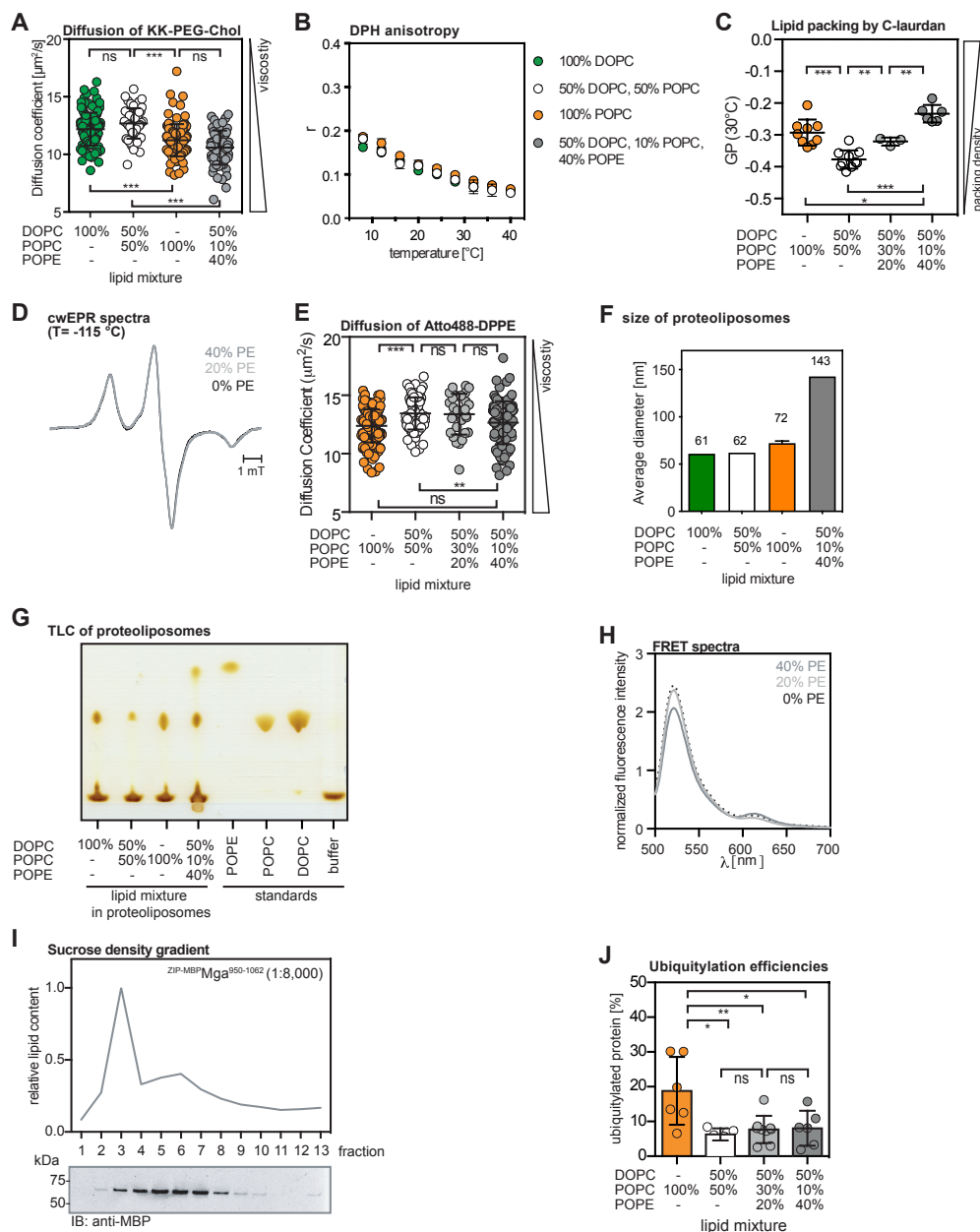
357 the region of the sensory W1042 residue of Mga2 the pressure is similar in all bilayers except

358 for POPC where it is lower. **(D)** Acyl chain order parameter of each lipid type in the different359 bilayers. Minimal changes are observed in the oleoyl *sn*-2 chain of the lipids while more

360 pronounced differences consistent with the changes in lipid packing (A) can be seen in the

361 order parameter of the lipids' *sn*-1 chain. Source data are provided as a Source Data file.

361



362

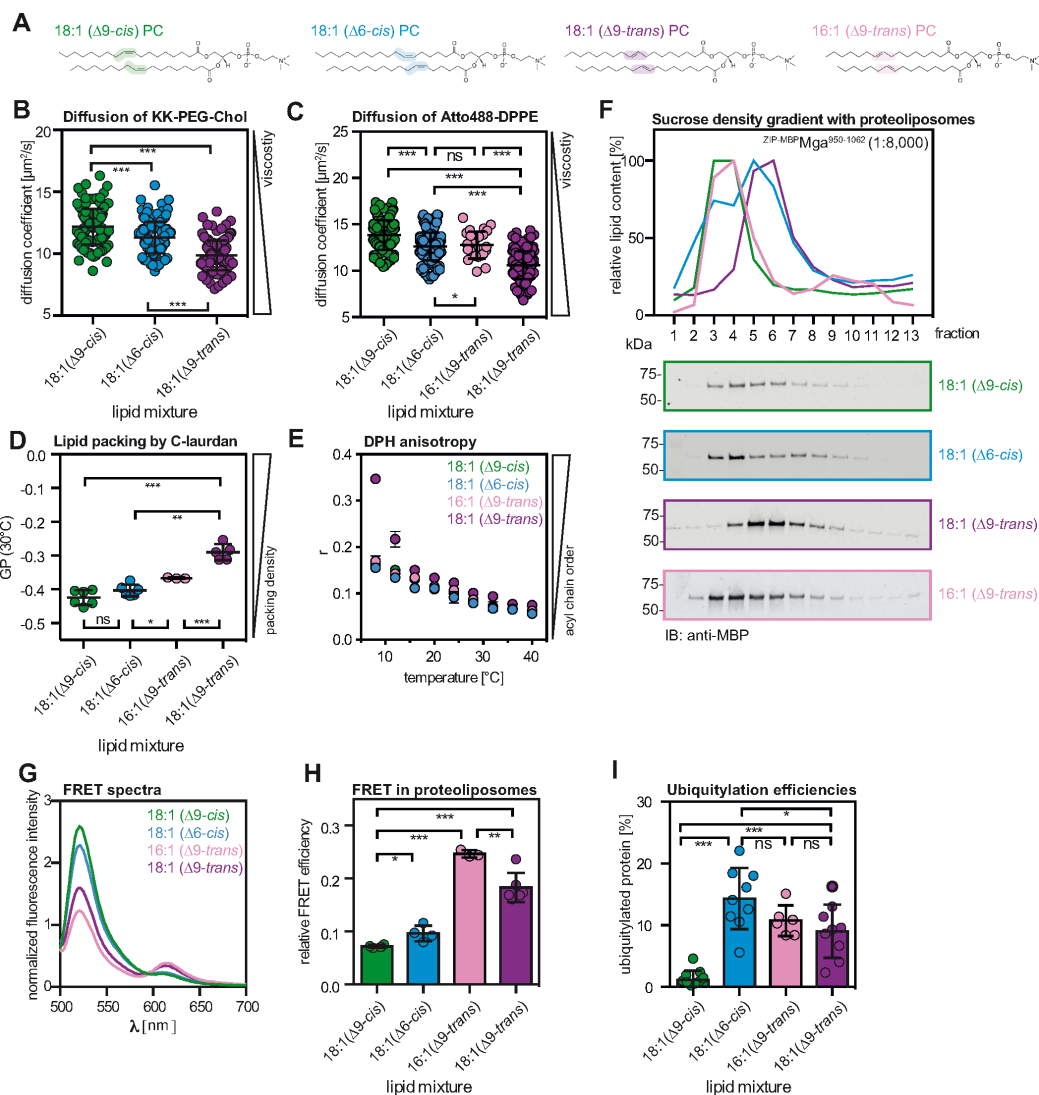
363

Supplementary Figure 4: Reconstituting the sense-and-response construct in PE-containing liposomes.

364

(A) Diffusion coefficients of Star Red-PEG Cholesterol in giant unilaminar vesicles of the indicated lipids were determined by confocal point-FCS. Plotted is the mean \pm SD ($n_{\text{DOPC}}=127$, $n_{(1:1) \text{ DOPC:POPC}}=53$, $n_{\text{POPC}}=110$, $n_{40\% \text{ POPE}}=66$). A Kolmogorov-Smirnov test was performed to test for statistical significance (** $p < 0.001$). (B) The anisotropy of DPH was determined at different temperatures and in liposomes with the indicated compositions. The data are plotted as the mean \pm SD of three independent experiments. (C) The lipid packing in liposomes composed of DOPC:POPC:POPE at a ratio of 5:3:2 was determined via C-Laurdan spectroscopy at 30°C. The GP values shown for POPC, POPC:DOPC at a ratio of 1:1, and

373 DOPC:POPC:POPE at a ratio of 5:1:4 are identical to the data in Figure 4B. The data are
374 plotted as mean \pm SD ($n_{\text{POPC}}=9$; $n_{(1:1)\text{DOPC:POPC}}=10$; $n_{20\%\text{PE}}=3$; $n_{40\%\text{PE}}=6$). An unpaired two-tailed,
375 students t-test was performed to test for statistical significance (* $p<0.05$, ** $p<0.01$,
376 *** $p<0.001$). (D) Intensity normalized cwEPR spectra recorded at -115°C for a fusion protein
377 composed of MBP and the TMH of Mga2 ($^{\text{MBP}}\text{Mga2}^{1032-1062}$) labeled at position W1042C was
378 reconstituted at a molar protein:lipid of 1:500 in liposomes composed of the indicated lipid
379 mixtures. (E) Diffusion coefficients of the fluorescent lipid analogue Atto488-DPPE in giant
380 unilaminar vesicles containing DOPC:POPC:POPE at a molar ratio of 5:3:2 were determined
381 by confocal point FCS. The plotted diffusion coefficients of Atto488-DPPE in liposomes
382 composed of either POPC, POPC:DOPC at molar ratio of 1:1, or DOPC:POPC:POPE at a
383 molar ratio of 5:4:1 are the same as in Figure 4B. The data are represented as mean \pm SD
384 ($n_{\text{DOPC}}=172$; $n_{(1:1)\text{DOPC:POPC}}=81$; $n_{\text{POPC}}=153$; $n_{20\%\text{PE}}=30$ $n_{40\%\text{PE}}=100$). A Kolmogorov-Smirnov test
385 was performed to test for statistical significance (*** $p<0.001$). (F) The average diameter of the
386 proteoliposomes containing the FRET reporter and with the indicated lipid composition was
387 determined by dynamic light scattering (Malvern Zetasizer Nano S90) and plotted. The
388 experiments were performed only once with proteoliposomes from a reconstitution generating
389 membrane environments with DOPC, POPC:DOPC at a molar ratio of 1:1, and
390 DOPC:POPC:POPE at a molar ratio of 5:4:1. They were performed for two independent
391 reconstitutions generating a POPC membrane environment. (G) Thin layer chromatography
392 (TLC) of $^{\text{ZIP-MBP}}\text{Mga2}^{950-1062}$ -containing proteoliposomes with the indicated lipid composition.
393 Lipids were extracted from the proteoliposomes, spotted onto a HPTLC Silica gel 60 plate, and
394 separated using 97.5:37.5:6 CHCl_3 :MeOH:H₂O as a mobile phase prior to iodine staining. As
395 controls served 1 μl of the indicated lipid stocks at a concentration of 20 mg/ml in CHCl_3 or
396 reconstitution buffer (50 mM Hepes pH 7.4, 150 mM NaCl, 5% w/v glycerol). (H) Fluorescence
397 emission spectra of the (K983^D+K969^A) FRET pair reconstituted in liposomes composed of the
398 indicated lipid mixtures were recorded (ex: 488 nm, em: 500-700 nm), normalized to the
399 maximal acceptor emission after direct acceptor excitation (ex: 590 nm), and plotted. The
400 emission spectra were normalized to acceptor emission after direct acceptor excitation. (I)
401 Sucrose-density gradient centrifugation for proteoliposomes containing $^{\text{ZIP-MBP}}\text{Mga2}^{950-1062}$ at a
402 molar protein:lipid ratio of 1:8,000 in a lipid mixture of 50 mol% DOPC, 10 mol% POPC and
403 40 mol% POPE. Samples were adjusted to 40% sucrose and overlaid with decreasing
404 concentrations of sucrose-solution (20%, 10%, 5%, 0%). After ultracentrifugation 13 fractions
405 were recovered from top to bottom. The relative content of lipids in the individual fractions was
406 determined by Hoechst 33342 fluorescent staining. The amount of $^{\text{MBP}}\text{Mga2}$ -TMH in the
407 fractions was monitored by immunoblotting using anti-MBP antibodies. (J) *In vitro*
408 ubiquitylation of the zipped sense-and-response construct ($^{\text{ZIP-MBP}}\text{Mga2}^{950-1062}$) reconstituted in
409 liposomes composed of 50% DOPC, 30% POPC, 20% POPE at a molar protein-to-lipid ratio
410 of 1:8,000 were performed as described in the Supplementary Materials and analyzed by
411 immunoblotting using anti-MBP antibodies. The signal intensities of ubiquitylated species were
412 quantified using Image Studio Lite (LI-COR). Plotted is the mean \pm SD ($n_{(\text{POPC})}=5$; $n_{(50:50)}=5$;
413 $n_{(+20\text{PE})}=7$; $n_{(+40\text{PE})}=5$). Unpaired, two-tailed t-test were performed to test for statistical
414 significance (* $p<0.05$, ** $p<0.01$). Source data are provided as a Source Data file.
415
416



417

418

419

Supplementary Figure 5: Reconstituting the sense-and-response construct in liposomes with different PC-species.

420

421

422

423

424

425

426

427

428

429

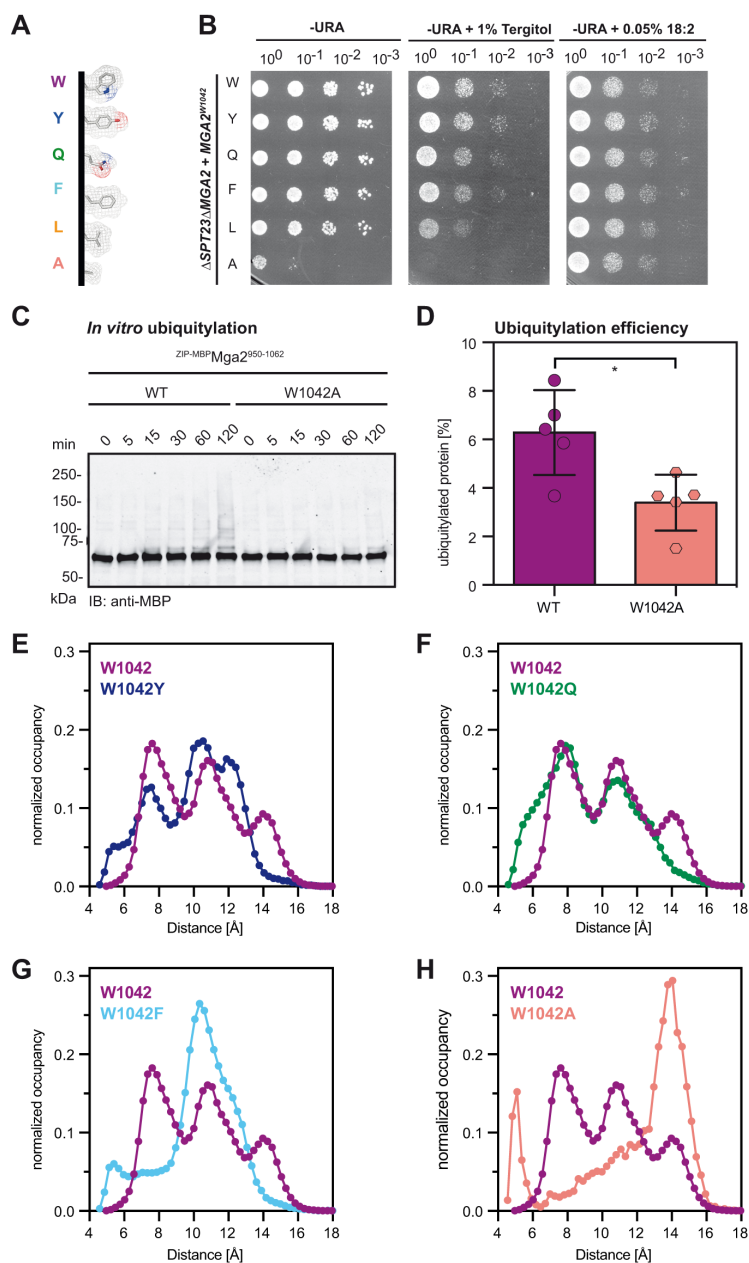
430

431

432

(A) Chemical structure of the four relevant PC lipids with distinct double bonds isomers and positions. All lipids contain a PC head group, two acyl chains of 18 or 16 carbons with one double bond. They differ in the position ($\Delta 9$ or $\Delta 6$) and the orientation of the double bond (*cis* or *trans*). The color code is maintained in (B-I). (Structures adapted from avantlipids.com) (B) Diffusion coefficients of Star Red-PEG Cholesterol in giant unilamellar vesicles of the indicated lipids were determined by confocal point FCS. Plotted is the mean \pm SD ($n_{18:1(\Delta 9\text{-cis})}=127$, $n_{18:1(\Delta 6\text{-cis})}=132$, $n_{18:1(\Delta 9\text{-trans})}=132$). A Kolmogorov-Smirnov test was performed to test for statistical significance (** $p < 0.001$). (C) Diffusion coefficient of the fluorescent lipid analogue Atto488-DPPE in giant unilamellar vesicles composed of 16:1($\Delta 9$ -trans)PC was determined by confocal point FCS. The diffusion coefficients of Atto488-DPPE in DOPC (18:1($\Delta 9$ -cis)), in PC lipids with two 18:1($\Delta 6$ -cis) acyl chains, and PE lipid with two 18:1($\Delta 9$ -trans) acyl chains are identical to the ones shown in Figure 5A. The data are plotted as mean \pm SD ($n_{18:1(\Delta 9\text{-cis})}=172$; $n_{18:1(\Delta 6\text{-cis})}=162$; $n_{16:1(\Delta 9\text{-trans})}=25$; $n_{18:1(\Delta 9\text{-trans})}=163$). A Kolmogorov-Smirnov test was performed

433 to test for statistical significance (* $p < 0.05$, *** $p < 0.001$). **(D)** The lipid packing in liposomes
434 composed of 16:1($\Delta 9$ -*trans*)PC was determined via C-Laurdan spectroscopy at 30°C. GP
435 values of C-Laurdan in DOPC (18:1($\Delta 9$ -*cis*)), in PC lipids with two 18:1($\Delta 6$ -*cis*) acyl chains,
436 and in PC lipids with two 18:1($\Delta 9$ -*trans*) are identical to the ones shown in Figure 5B. The data
437 are plotted as mean \pm SD ($n_{(18:1(\Delta 9-cis))} = 6$, $n_{(18:1(\Delta 6-cis))} = 6$; $n_{(16:1(\Delta 9-trans))} = 3$, $n_{(18:1(\Delta 9-trans))} = 5$). An
438 unpaired two-tailed, students t-test was performed to test for statistical significance (** $p < 0.01$,
439 *** $p < 0.001$). **(E)** Anisotropy of DPH was determined at different temperatures and in liposomes
440 with the indicated lipid compositions. The data are plotted as the mean \pm SD of three
441 independent experiments. **(F)** Sucrose-density gradient centrifugation of proteoliposomes of
442 the indicated lipid composition containing ZIP-MBP^{ZIP-MBP}Mga2⁹⁵⁰⁻¹⁰⁶² reconstituted at a molar
443 protein:lipid ratio of 1:8,000. The proteoliposome samples were adjusted to 40% (w/v) sucrose
444 and overlaid with four containing different concentrations of sucrose (20% (w/v), 10% (w/v),
445 5% (w/v), 0% (w/v)). After centrifugation (100,000x g, 4°C, overnight) the gradient was
446 fractionated from top to bottom. The distribution of lipids and proteins in the gradient was
447 determined as described in the Supplementary Materials. **(G)** The fluorescence emission
448 spectrum of the (K983^D+K969^A) FRET pair reconstituted in liposomes composed of 16:1($\Delta 9$ -
449 *trans*)PC lipids was recorded (ex: 488 nm, em: 500-700 nm) and plotted after normalization to
450 the maximal emission upon direct excitation of the acceptor (ex: 590 nm). The data for DOPC
451 (18:1($\Delta 9$ -*cis*)), PC lipids with either two 18:1($\Delta 6$ -*cis*) or two 18:1($\Delta 9$ -*trans*) acyl chains are
452 identical to the data shown in Figure 5E. **(H)** The relative FRET efficiencies were calculated
453 from fluorescence spectra as in (G). The data are plotted as the mean \pm SD ($n_{(18:1(\Delta 9-cis))} = 4$;
454 $n_{(18:1(\Delta 6-cis))} = 4$; $n_{(16:1(\Delta 9-trans))} = 3$; $n_{(18:1(\Delta 9-trans))} = 6$). A two-tailed, unpaired t-test was performed to
455 test for statistical significance (* $p < 0.05$; ** $p < 0.005$). The data for DOPC (18:1($\Delta 9$ -*cis*)),
456 18:1($\Delta 6$ -*cis*)PC and 18:1($\Delta 9$ -*trans*)PC are identical to the one in Figure 5F. **(I)** *In vitro*
457 ubiquitylation of the zipped sense-and-response construct (ZIP-MBP^{ZIP-MBP}Mga2⁹⁵⁰⁻¹⁰⁶²) reconstituted in
458 liposomes composed of 16:1($\Delta 9$ -*trans*)PC at a molar protein-to-lipid ratio of 1:8,000 were
459 performed as described in the Supplementary Materials. After the reaction was stopped, the
460 samples were subjected to SDS-PAGE and analyzed by immunoblotting using anti-MBP
461 antibodies. The signal intensities of ubiquitylated species were quantified using Image Studio
462 Lite (LI-COR). Plotted is the mean \pm SD ($n_{(18:1(\Delta 9-cis))} = 20$; $n_{(18:1(\Delta 6-cis))} = 9$; $n_{(16:1(\Delta 9-trans))} = 6$; $n_{(18:1(\Delta 9-$
463 *trans*))} = 9). The data for DOPC (18:1($\Delta 9$ -*cis*)PC), 18:1($\Delta 6$ -*cis*)PC and 18:1($\Delta 9$ -*trans*)PC are
464 identical with the data in Figure 5H. Source data are provided as a Source Data file.
465

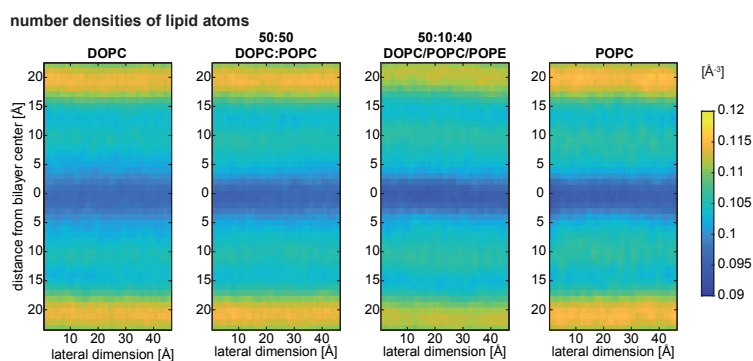


466
467

468 **Supplementary Figure 6: Mutagenesis of sensory residue W1042 and phenotypic**
469 **characterization.**

470 (A) Representations of the amino acids (and substitutions) at position of the sensory W1042
471 in the TMH of Mga2. The side-chain structures were modeled using PyMOL and are shown as
472 sticks with electron meshes. (B) Spotting test for rescue of UFA auxotrophy. The indicated
473 MGA2 variants were expressed from their endogenous promoters on CEN-based plasmids in
474 the $\Delta SPT23 \Delta MGA2$ strain background. Cultures were cultivated in the absence of
475 exogenously provided UFAs for 5 h and then spotted in a ten-fold dilution series on SCD-URA

476 plates with the indicated additives. The resulting colonies were documented after 2 days of
477 cultivation at 30 °C. **(C)** *In vitro* ubiquitylation of the zipped sense-and-response construct ZIP-
478 MBP^{Mga2⁹⁵⁰⁻¹⁰⁶²} wild type (WT) and a W1042A variant reconstituted at a protein:lipid molar ratio
479 of 1:15,000 in POPC. After the reaction was stopped, ubiquitylated species were detected by
480 SDS-PAGE and subsequent immunoblotting using anti-MBP antibodies. **(D)** Densiometric
481 quantification of the *in vitro* ubiquitylation assays as in (C). The fraction of ubiquitylated protein
482 was determined for the indicated time points and for the wildtype (WT) and W1042A variant of
483 the sense-and-response construct. Plotted is the mean \pm SD (n=5). The statistical significance
484 was tested by a two-tailed, unpaired t-test (*p<0.05). **(E-H)** Distribution of distances between
485 the backbone beads of residue 1042 in the TMH dimer of wildtype Mga2 (W1042) and the
486 indicated variants, calculated from coarse-grained MD simulations performed with a POPC
487 bilayer using the MARTINI v2.2 force field^{3,4}. Data for the wildtype Mga2 and the W1042A
488 mutation are re-plotted from a previous study with permission from Elsevier¹. The population
489 of different conformational states is strongly affected by the side chain of the amino acid at the
490 position of the sensory W1042. Notably, mutations with the most prominent impact of the
491 structural dynamics (W1042F and W1042A) have also have the strongest impact on the
492 processing efficiency of Mga2 as experimentally shown in Figure 6D. Source data are provided
493 as a Source Data file.
494



495

496

497

Supplementary Figure 7: The local number density of lipid atoms in different bilayer systems.

498

All-atom MD simulations were performed for the indicated bilayer systems. The number density of lipid atoms in cubic boxes with a side of length 1 \AA was calculated and plotted as a heatmap.

499

The x-axis shows the mean of the local densities in the x and y planes at the respective z

500

position. Highest local number densities are indicated in yellow and observed in the region of

501

the lipid headgroups. Lowest densities are indicated in dark blue and observed in the center

502

of the lipid bilayer. Source data are provided as a Source Data file.

503

504

505

506

507

508

509

510

511

512

513

514

515

516

517

518

519

520

521

522

523

524

525

526

527

528

529

530

531

532

533

534

535

536

537

538

539

540

505 **Supplementary Table 1. Plasmids used in this study.**

Plasmid	Description	Source
<i>in vivo</i>		
pRS316	Empty vector (CEN6-ARS4, URA3, AMP)	EUROSCARF
pRE262	pRS316-3xMyc- <i>MGA2</i> WT	This study and ¹
pRE266	pRS316-3xMyc- <i>MGA2</i> W1042A	This study and ¹
pRE305	pRS316-3xMyc- <i>MGA2</i> W1042L	This study and ¹
pRE333	pRS316-3xMyc- <i>MGA2</i> W1042Y	This study
pRE334	pRS316-3xMyc- <i>MGA2</i> W1042F	This study
pRE335	pRS316-3xMyc- <i>MGA2</i> W1042Q	This study
pRE683	pRS316-3xMyc- <i>MGA2</i> K969C	This study
pRE684	pRS316-3xMyc- <i>MGA2</i> K983C	This study

506

Plasmid	Description	Source
<i>in vitro</i>		
pRE345	pMAL-C2x-MBP- <i>MGA2</i> -TMH W1042C	This study and ¹
pRE496	pETM-m60-8xHis-hUb WT	Provided by V. Dötsch
pRE714	pMAL-C2x-MBP- <i>MGA2</i> -JM-TMH WT	This study
pRE759	pMAL-C2x-ZIP-MBP- <i>MGA2</i> -JM-TMH WT	This study
pRE766	pMAL-C2x-ZIP-MBP- <i>MGA2</i> -JM-TMH Δ LPKY	This study
pRE767	pMAL-C2x-ZIP-MBP- <i>MGA2</i> -JM-TMH W1042A	This study
pRE771	pMAL-C2x-ZIP-MBP- <i>MGA2</i> -JM-TMH K980R, K983R, K985R	This study
pRE848	pMAL-C2x-ZIP-MBP- <i>MGA2</i> -JM-TMH K983C	This study
pRE849	pMAL-C2x-ZIP-MBP- <i>MGA2</i> -JM-TMH K969C	This study

507

508 **Supplementary Table 2. Strains used in this study.**

Strain Number	Description	Genotype	Source	Plasmid
ECRE01	<i>E. coli</i> DH5 alpha	F ⁻ ϕ 80 <i>lacZ</i> Δ M15 Δ (<i>lacZYA-argF</i>) U169 <i>recA endA1 hsdR17</i> (rK ⁻ , mK ⁺) <i>phoA</i> <i>supE44</i> λ ⁻ <i>thi-1 gyrA96 relA1</i>	ThermoFisher EC0112	N/A
ECRE02	<i>E. coli</i> BL21 Star TM (DE3) <i>pLysS</i>	F- <i>ompT hsdSB</i> (rB, mB) <i>galdcmrne131</i> (DE3) <i>pLysS</i> (Cam ^R)	ThermoFisher C602003	<i>pLysS</i>
YRE001	BY4741	MATa; <i>his3</i> Δ 1; <i>leu2</i> Δ 0; <i>met15</i> Δ 0; <i>ura3</i> Δ 0	EUROSCARF ¹³ (Y00000)	N/A
YRE009	Δ UBX2	MATa; <i>his3</i> Δ 1; <i>leu2</i> Δ 0; <i>met15</i> Δ 0; <i>ura3</i> Δ 0; <i>ubx2</i> Δ :: <i>kanMX4</i>	EUROSCARF ¹⁴ (Y00560)	N/A
YRE067	BY4741 3xMyc- <i>MGA2</i> WT	MATa; <i>his3</i> Δ 1; <i>leu2</i> Δ 0; <i>met15</i> Δ 0; <i>ura3</i> Δ 0	This study and ¹	<i>pRE262</i>
YRE068	BY4741 3xMyc- <i>MGA2</i> W1042A	MATa; <i>his3</i> Δ 1; <i>leu2</i> Δ 0; <i>met15</i> Δ 0; <i>ura3</i> Δ 0	This study and ¹	<i>pRE266</i>
YRE071	Δ UBX2 3xMyc- <i>MGA2</i> WT	MATa; <i>his3</i> Δ 1; <i>leu2</i> Δ 0; <i>met15</i> Δ 0; <i>ura3</i> Δ 0; <i>ubx2</i> Δ :: <i>kanMX4</i>	This study and ¹	<i>pRE262</i>
YRE199	BY4741 3xMyc- <i>MGA2</i> W1042L	MATa; <i>his3</i> Δ 1; <i>leu2</i> Δ 0; <i>met15</i> Δ 0; <i>ura3</i> Δ 0	This study and ¹	<i>pRE305</i>
YRE216	BY4741 3xMyc- <i>MGA2</i> W1042Y	MATa; <i>his3</i> Δ 1; <i>leu2</i> Δ 0; <i>met15</i> Δ 0; <i>ura3</i> Δ 0	This study	<i>pRE333</i>
YRE217	BY4741 3xMyc- <i>MGA2</i> W1042F	MATa; <i>his3</i> Δ 1; <i>leu2</i> Δ 0; <i>met15</i> Δ 0; <i>ura3</i> Δ 0	This study	<i>pRE334</i>
YRE228	Δ SPT23, Δ MGA2	MAT α ; <i>his3</i> Δ 1; <i>leu2</i> Δ 0; <i>lys2</i> Δ 0; <i>ura3</i> Δ 0; <i>spt23</i> Δ :: <i>kanMX4</i> ; <i>mga2</i> Δ :: <i>natMX</i>	This study Provided by H. Hofbauer	
YRE295	Δ SPT23, Δ MGA2 3xMyc- <i>MGA2</i> WT	MAT α ; <i>his3</i> Δ 1; <i>leu2</i> Δ 0; <i>lys2</i> Δ 0; <i>ura3</i> Δ 0; <i>spt23</i> Δ :: <i>kanMX4</i> ; <i>mga2</i> Δ :: <i>natMX</i>	This study	<i>pRE262</i>
YRE296	Δ SPT23, Δ MGA2 3xMyc- <i>MGA2</i> W1042A	MAT α ; <i>his3</i> Δ 1; <i>leu2</i> Δ 0; <i>lys2</i> Δ 0; <i>ura3</i> Δ 0; <i>spt23</i> Δ :: <i>kanMX4</i> ; <i>mga2</i> Δ :: <i>natMX</i>	This study	<i>pRE266</i>
YRE297	Δ SPT23, Δ MGA2 3xMyc- <i>MGA2</i> W1042L	MAT α ; <i>his3</i> Δ 1; <i>leu2</i> Δ 0; <i>lys2</i> Δ 0; <i>ura3</i> Δ 0; <i>spt23</i> Δ :: <i>kanMX4</i> ; <i>mga2</i> Δ :: <i>natMX</i>	This study	<i>pRE305</i>
YRE404	BY4741 3xMyc- <i>MGA2</i> W1042Q	MATa; <i>his3</i> Δ 1; <i>leu2</i> Δ 0; <i>met15</i> Δ 0; <i>ura3</i> Δ 0	This study	<i>pRE335</i>
YRE415	BY4741 empty vector <i>pRS316</i>	MATa; <i>his3</i> Δ 1; <i>leu2</i> Δ 0; <i>met15</i> Δ 0; <i>ura3</i> Δ 0	This study	<i>pRS316</i>
YRE572	Δ SPT23, Δ MGA2 3xMyc- <i>MGA2</i> W1042Q	MAT α ; <i>his3</i> Δ 1; <i>leu2</i> Δ 0; <i>lys2</i> Δ 0; <i>ura3</i> Δ 0; <i>spt23</i> Δ :: <i>kanMX4</i> ; <i>mga2</i> Δ :: <i>natMX</i>	This study	<i>pRE335</i>
YRE573	Δ SPT23, Δ MGA2 3xMyc- <i>MGA2</i> W1042F	MAT α ; <i>his3</i> Δ 1; <i>leu2</i> Δ 0; <i>lys2</i> Δ 0; <i>ura3</i> Δ 0; <i>spt23</i> Δ :: <i>kanMX4</i> ; <i>mga2</i> Δ :: <i>natMX</i>	This study	<i>pRE334</i>
YRE574	Δ SPT23, Δ MGA2 3xMyc- <i>MGA2</i> W1042Y	MAT α ; <i>his3</i> Δ 1; <i>leu2</i> Δ 0; <i>lys2</i> Δ 0; <i>ura3</i> Δ 0; <i>spt23</i> Δ :: <i>kanMX4</i> ; <i>mga2</i> Δ :: <i>natMX</i>	This study	<i>pRE333</i>
YRE578	Δ SPT23, Δ MGA2 empty vector <i>pRS316</i>	MAT α ; <i>his3</i> Δ 1; <i>leu2</i> Δ 0; <i>lys2</i> Δ 0; <i>ura3</i> Δ 0; <i>spt23</i> Δ :: <i>kanMX4</i> ; <i>mga2</i> Δ :: <i>natMX</i>	This study	<i>pRS316</i>

509

510 **Supplementary Table 3. Oligonucleotides used for molecular cloning.**

Name	Sequence (5' → 3')	Description
SB1	GGGAATTCGGGTAGTACATCTCTCGAATAGAGTTTAC	GG- <i>EcoRI</i> -MGA2 (bp 2974–2996) forward (f)
SB2	CCCAGCTTCTAACTGACAATTAATCGTTCAACATTC	CCC- <i>HindIII</i> -MGA2 (bp 3437–3465) reverse (r)
RE337	GATAAAATGTTAATATTTTTCTTGATACCCCTTAACACTACTAC	MGA2 W1042L (f); QuikChange
RE338	GTAGTAGTGTTAAGGGTATCAAGAAAAATTAACATTTTATC	MGA2 W1042L (r); QuikChange
RE410	CCATCACGGTCTCGTGCAGATTTTCGTGAAAACCC	8xHis-UB tagging; Q5 (f)
RE411	TGATGGTGATGGTGATGCATGGTATATCTCCTTCTTAAAG	8xHis-UB tagging; Q5 (r)
RE925	GCAACATATGAGAACCACCACCGCTTCGCCAACTAATTTCT	<i>NdeI</i> -SGGG-GCN4 (ZIP) (r)
RE926	AGCGTCCGAGCATCATATGATGAGAATGAAACAACCTGAAGACAA	13 bp- <i>NdeI</i> -GCN4 (ZIP) (f)
RE930	ATCGGAATTCGGTGCGGTTCTGG	ATCG- <i>EcoRI</i> -(GGGS) ₂ -MGA2 (bp3217-3233) (f)
RE931	ACGCAAGCTTTTAATCTTGTTGCCAAATTTGTAC	ACGC- <i>HindIII</i> -MGA2-TMH (bp3311-3333) (r)
RE934	GCGGTGGTGGTCTGGTGGAGGTTCTAAAATCGAAGAAGG	IntGGGS ZIP_MBP; QuikChange (f)
RE935	CCTTCTCGATTTTAGAACCTCCACCAGAACCACCACCGC	IntGGGS ZIP_MBP; QuikChange (r)
RE252	CCGAAATGATAAAATGTTAATATTTTTCGCTATACCCCTAACACTACTACTTTTGACATGG	MGA2 W1042A; QuikChange (r)
RE253	CCATGTCAAAGTAGTAGTGTAAAGGGTATAGCGAAAAATTAACATTTTATCATTTCGG	MGA2 W1042A; QuikChange (f)
RE260	GAGGATCTGTTCCGTTGTCTTGGGGTCTGATGATCGTTTGCCTACCACAAATCAAGACAGTATTGTGGAGCAG	MGA2 K980R, K983R, K985R; QuikChange (f)
RE261	CTGCTCCAATACTGTCTTGATTGTGGTACGCAACGATCATCACGCCCAAGACAACGGGAACAGATCCTC	MGA2 K980R, K983R, K985R; QuikChange (r)
RE471	ACAAAACCTCCGAAATGATAAAATGTTAATATTTTTCTATATACCCCTAACACTACTACTTTTGAC	MGA2 W1042Y; QuikChange (f)
RE472	GTCAAAGTAGTAGTGTAAAGGGTATATAGAAAAATTAACATTTTATCATTTCGGAAGTTTGT	MGA2 W1042Y; QuikChange (r)
RE473	AAAACCTCCGAAATGATAAAATGTTAATATTTTTCTCATACCCCTAACACTACTACTTTTGA	MGA2 W1042F; QuikChange (f)
RE474	TCAAAGTAGTAGTGTAAAGGGTATGAAGAAAAATTAACATTTTATCATTTCGGAAGTTT	MGA2 W1042F; QuikChange (r)
RE541	AATATTTTTCCAAATACCCTAACACTACTACTTTTG	MGA2 W1042Q; Q5 (f)
RE542	AACATTTTATCATTTCGGAAGTTTGT	MGA2 W1042Q; Q5 (r)
RE603	GGCAACCAAGATTGATAAATCAATCATATAAGCG	MGA2 S1063*, S1064*; QuikChange (f)
RE604	CGCTTATATGATTGATTATCAATCTTGGTTGCC	MGA2 S1063*, S1064*; QuikChange (r)
RE764	CGAAATGATAAAATGTTAATATTTTTCTCATACCCCTAACACTACTACTTTTGAC	MGA2 W1042A; QuikChange (f)
RE765	GTCAAAGTAGTAGTGTAAAGGGTATAGCGAAAAATTAACATTTTATCATTTCG	MGA2 W1042A; QuikChange (r)
RE902	GTCATCATAATTCGATGTAAC	ΔLPKY ^{MBP} Mga2-LPKY-TMH; Q5 (f)
RE903	GAGGATCTGTTCCCGTTG	ΔLPKY ^{MBP} Mga2-LPKY-TMH; Q5 (r)
RE904	CGAATTAATGATGACTTACCATGTTATGAGGATCTGTTCCCG	MGA2 K969C; QuikChange (f)

RE905	CGGGAACAGATCCTCATAACATGGTAAGTCATCATTAAATTCG	MGA2 K969C; QuikChange (r)
RE906	CGTTGTCTTGGGGTAAAGATGATTGTTTGAAAACCACAAATCAAGAC	MGA2 K983C; QuikChange (f)
RE907	GTCTTGATTTGGTTTTCAACAATCATCTTACCCCAAGACAACG	MGA2 K983C; QuikChange (r)
TP246	GCGAATCCGAAATGATAAAATGTTAATATTTTTCTGTATACCCCTTAACACTACTACTTTTG	MGA2 W1042C; QuikChange (f)
TP267	CAAAAGTAGTAGTGTAAAGGGTATACAGAAAAATTAACATTTTATCATTTCGGAATTCGC	MGA2 W1042C; QuikChange (r)

512 **Supplementary Table 4. Antibodies used for immunoblotting.**

Antibody	Vendor	Catalogue #	Working dilution
Mouse anti-myc monoclonal (9E10)	Sigma-Aldrich	M4439	1:2,000
mouse anti-Pgk1 monoclonal (22C5)	Invitrogen	459250	1:20,000
mouse anti-MBP, monoclonal	NEB	E8032L	1:30,000
Goat anti-mouse-HRP	Dianova	115-035-146	1:20,000
Goat anti-mouse-IRDye 800CW	Li-COR	926-32210	1:20,000

513 The antibodies used in this study are listed along with the vendor, catalogue number, and the
514 working solution are listed.

515 **Supplementary Table 5. All-atom bilayers simulated in this study.**

Bilayer	Construction	Lipids per leaflet	Waters per lipid	Ions	Simulation Time [ns]
DOPC	built with CHARMM-GUI membrane builder ¹⁵⁻¹⁷	100	45	-	902 (915)
(1:1) DOPC:POPC		100	45	-	1008 (1009)
(5:1:4) DOPC:POPC:POPE		100	45	-	1018 (1018)
<i>trans</i> DOPC	Initial configuration taken from the end of CHARMM-GUI equilibration protocol ¹⁸	100	45	-	973 (1007)

516 All-atom bilayers simulated in this study. Shown are (from left to right): bilayer composition,
517 system construction details, number of lipids per leaflet, number of water molecules per lipid,
518 number of ions in the system and the length of the last portion of the trajectory where the
519 bilayer area is converged as determined by a previously reported algorithm¹⁹. The total
520 simulation length is given in parenthesis.

521

522 **Supplementary References**

523

- 524 1. Covino, R. *et al.* A eukaryotic sensor for membrane lipid saturation. *Mol. Cell*
525 **63**, 49–59 (2016).
- 526 2. Contreras, F.-X. *et al.* Molecular recognition of a single sphingolipid species by
527 a protein's transmembrane domain. *Nature* **481**, 525–529 (2012).
- 528 3. Marrink, S. J., Risselada, H. J., Yefimov, S., Tieleman, D. P. & De Vries, A. H.
529 The MARTINI force field: Coarse grained model for biomolecular simulations.
530 *J. Phys. Chem. B* **111**, 7812–7824 (2007).
- 531 4. Monticelli, L. *et al.* The MARTINI coarse-grained force field: Extension to
532 proteins. *J. Chem. Theory Comput.* **4**, 819–834 (2008).
- 533 5. Pettersen, E. F. *et al.* UCSF Chimera - A visualization system for exploratory
534 research and analysis. *J. Comput. Chem.* **25**, 1605–1612 (2004).
- 535 6. Bussi, G., Donadio, D. & Parrinello, M. Canonical sampling through velocity
536 rescaling. *J. Chem. Phys.* **126**, 014101 (2007).
- 537 7. Parrinello, M. & Rahman, A. Crystal structure and pair potentials: A molecular-
538 dynamics study. *Phys. Rev. Lett.* **45**, 1196–1199 (1980).
- 539 8. Phillips, J. C. *et al.* Scalable molecular dynamics with NAMD. *Journal of*
540 *Computational Chemistry* **26**, 1781–1802 (2005).
- 541 9. Klauda, J. B. *et al.* Update of the CHARMM All-Atom Additive Force Field for
542 Lipids: Validation on Six Lipid Types. *J. Phys. Chem. B* **114**, 7830–7843
543 (2010).
- 544 10. Klauda, J. B., Monje, V., Kim, T. & Im, W. Improving the CHARMM force field
545 for polyunsaturated fatty acid chains. *J. Phys. Chem. B* **116**, 9424–9431
546 (2012).
- 547 11. Doktorova, M., LeVine, M. V, Khelashvili, G. & Weinstein, H. A New
548 Computational Method for Membrane Compressibility: Bilayer Mechanical
549 Thickness Revisited. *Biophys. J.* **116**, 487–502 (2019).
- 550 12. Humphrey, W., Dalke, A. & Schulten, K. VMD: Visual molecular dynamics. *J.*
551 *Mol. Graph.* **14**, 33–38 (1996).
- 552 13. Brachmann, C. B. *et al.* Designer deletion strains derived from *Saccharomyces*
553 *cerevisiae* S288C: A useful set of strains and plasmids for PCR-mediated gene
554 disruption and other applications. *Yeast* **14**, 115–132 (1998).
- 555 14. Giaever, G. *et al.* Functional profiling of the *Saccharomyces cerevisiae*
556 genome. *Nature* **418**, 387–391 (2002).
- 557 15. Lee, J. *et al.* CHARMM-GUI Input Generator for NAMD, GROMACS, AMBER,
558 OpenMM, and CHARMM/OpenMM Simulations Using the CHARMM36
559 Additive Force Field. *J. Chem. Theory Comput.* **12**, 405–413 (2016).
- 560 16. Wu, E. L. *et al.* CHARMM-GUI membrane builder toward realistic biological
561 membrane simulations. *J. Comput. Chem.* **35**, 1997–2004 (2014).
- 562 17. Jo, S., Kim, T., Iyer, V. G. & Im, W. CHARMM-GUI: A web-based graphical
563 user interface for CHARMM. *J. Comput. Chem.* **29**, 1859–1865 (2008).
- 564 18. Doktorova, M., Harries, D. & Khelashvili, G. Determination of bending rigidity
565 and tilt modulus of lipid membranes from real-space fluctuation analysis of
566 molecular dynamics simulations. *Phys. Chem. Chem. Phys.* **19**, 16806–16818
567 (2017).
- 568 19. Chodera, J. D. A Simple Method for Automated Equilibration Detection in
569 Molecular Simulations. *J. Chem. Theory Comput.* **12**, 1799–1805 (2016).

570



A Quantitative Analysis of Cellular Lipid Compositions During Acute Proteotoxic ER Stress Reveals Specificity in the Production of Asymmetric Lipids

John Reinhard^{1,2†}, Carsten Mattes^{1,2†}, Kristina Våth^{1,2†}, Toni Radanović^{1,2}, Michal A. Surma³, Christian Klose³ and Robert Ernst^{1,2*}

¹ Medical Biochemistry and Molecular Biology, Medical Faculty, Saarland University, Homburg, Germany, ² PZMS, Center for Molecular Signaling, Medical Faculty, Saarland University, Homburg, Germany, ³ Lipotype GmbH, Dresden, Germany

OPEN ACCESS

Edited by:

Fernando Antunes,
University of Lisbon, Portugal

Reviewed by:

Guillaume Thibault,
Nanyang Technological University,
Singapore
Yukio Kimata,
Nara Institute of Science
and Technology (NAIST), Japan

*Correspondence:

Robert Ernst
robert.ernst@uks.eu

[†]These authors have contributed
equally to this work

Specialty section:

This article was submitted to
Cellular Biochemistry,
a section of the journal
Frontiers in Cell and Developmental
Biology

Received: 06 May 2020

Accepted: 20 July 2020

Published: 04 August 2020

Citation:

Reinhard J, Mattes C, Våth K,
Radanović T, Surma MA, Klose C and
Ernst R (2020) A Quantitative Analysis
of Cellular Lipid Compositions During
Acute Proteotoxic ER Stress Reveals
Specificity in the Production
of Asymmetric Lipids.
Front. Cell Dev. Biol. 8:756.
doi: 10.3389/fcell.2020.00756

The unfolded protein response (UPR) is central to endoplasmic reticulum (ER) homeostasis by controlling its size and protein folding capacity. When activated by unfolded proteins in the ER-lumen or aberrant lipid compositions, the UPR adjusts the expression of hundreds of target genes to counteract ER stress. The proteotoxic drugs dithiothreitol (DTT) and tunicamycin (TM) are commonly used to induce misfolding of proteins in the ER and to study the UPR. However, their potential impact on the cellular lipid composition has never been systematically addressed. Here, we report the quantitative, cellular lipid composition of *Saccharomyces cerevisiae* during acute, proteotoxic stress in both rich and synthetic media. We show that DTT causes rapid remodeling of the lipidome when used in rich medium at growth-inhibitory concentrations, while TM has only a marginal impact on the lipidome under our conditions of cultivation. We formulate recommendations on how to study UPR activation by proteotoxic stress without interferences from a perturbed lipid metabolism. Furthermore, our data suggest an intricate connection between the cellular growth rate, the abundance of the ER, and the metabolism of fatty acids. We show that *Saccharomyces cerevisiae* can produce asymmetric lipids with two saturated fatty acyl chains differing substantially in length. These observations indicate that the pairing of saturated fatty acyl chains is tightly controlled and suggest an evolutionary conservation of asymmetric lipids and their biosynthetic machineries.

Keywords: UPR, Ire1, lipid bilayer stress, proteotoxic stress, lipidomics, DTT, tunicamycin, asymmetric lipids

INTRODUCTION

Biological membranes are complex assemblies of proteins and lipids forming the boundary of cellular life and compartmentalizing biochemical processes in different organelles (van Meer et al., 2008; Bigay and Antonny, 2012). A major fraction of cellular bioactivity is localized to biological membranes: one third of all proteins and the majority of therapeutic drug targets are either membrane embedded or membrane associated (Uhlén et al., 2015). The interactions, activities, and subcellular localizations of membrane proteins

are modulated by their complex and dynamically regulated environment (Lee, 2004; Phillips et al., 2009; Lorent et al., 2017). The lipidome of a eukaryotic cell comprises hundreds, if not thousands, of lipid species and it can be remodeled upon dietary perturbation, by the growth phase, and in response to external cues such as temperature or nutrient availability (Shevchenko and Simons, 2010; Klose et al., 2012; Casanovas et al., 2015; Han, 2016; Levental et al., 2020). This membrane responsiveness down to the level of individual lipid species is essential to sustain cellular fitness, by maintaining physicochemical membrane properties such as fluidity, permeability, phase behavior, and surface charge density in a regime acceptable for membrane function (Bigay and Antonny, 2012; Sezgin et al., 2017; Ernst et al., 2018; Harayama and Riezman, 2018). Our understanding of these complex remodeling processes, their purposes and the underlying principles, remains rather limited.

The endoplasmic reticulum (ER) is the central hub for membrane biogenesis in eukaryotic cells (van Meer et al., 2008). The vast majority of membrane proteins is targeted to ER-localized machineries for membrane insertion (Aviram and Schuldiner, 2017). Likewise, a major fraction of membrane lipids including sterols, glycerophospholipids, and ceramides is produced in the ER (van Meer et al., 2008). In the past years it became increasingly clear that protein quality control and lipid metabolism are intimately connected both on the cellular and the molecular level (Jonikas et al., 2009; De Kroon et al., 2013; Stordeur et al., 2014; Volmer and Ron, 2015; Fun and Thibault, 2020; Goder et al., 2020).

A prominent example is the unfolded protein response (UPR) (Walter and Ron, 2011). Both an accumulation of unfolded protein in the lumen of the ER and stiffening of the ER membrane due to lipid imbalances serve as activating signals for the UPR (Halbleib et al., 2017; Karagöz et al., 2017; Adams et al., 2019; Preissler and Ron, 2019). How precisely these activating signals from the lumen of the ER and the ER membrane are integrated by the transducers of the UPR is matter of active debate (Volmer and Ron, 2015; Covino et al., 2018; Fun and Thibault, 2020). Once activated, the UPR increases the size of the ER and its folding capacity in order to reestablish ER homeostasis even under adverse conditions (Bernales et al., 2006; Schuck et al., 2009). This is accomplished by a global attenuation of protein production (Walter and Ron, 2011), by upregulating the ER-associated degradation machinery, and by increasing the number of ER chaperones (Cox et al., 1993; Jonikas et al., 2009). At the same time, the UPR induces the expression of a large number of genes involved in membrane-related processes such as lipid biosynthesis, membrane protein sorting, and vesicular traffic (Travers et al., 2000). Unbiased genetic screens and targeted perturbations of lipid metabolism have clearly established the mutual dependency of the UPR and lipid metabolism (Jonikas et al., 2009; Pineau et al., 2009; Schuck et al., 2009; Promlek et al., 2011; Thibault et al., 2012; Surma et al., 2013). Given its central importance for ER homeostasis and cell physiology, it is not surprising that the UPR plays also a crucial role in pathologic processes such as viral infections, neurodegeneration, and cancer (Wang and Kaufman, 2012; Wang and Kaufman, 2014; Hetz et al., 2019). Metabolic

diseases associated with chronic UPR signaling such as type II diabetes and non-alcoholic steatohepatitis (Kaufman, 2002; Fonseca et al., 2009) are historically studied with a focus on the role of unfolded, soluble proteins in the ER lumen while the contribution of signals from the ER membrane remains understudied.

The eukaryotic model organism *Saccharomyces cerevisiae* (*S. cerevisiae*) has facilitated the identification of numerous key components of the secretory pathway, lipid metabolism, and the proteostasis network (Novick et al., 1980; Wolf and Schäfer, 2006; Henry et al., 2012; De Kroon et al., 2013). In contrast to metazoans, the UPR in *S. cerevisiae* relies on a single, ER-localized UPR transducer (Kimata and Kohno, 2011): the Inositol-requiring enzyme 1 (Ire1p). It is conserved from yeast to humans and comprises an N-terminal sensor domain facing the ER-lumen, a single transmembrane helix, and cytosolic effector domains with kinase and RNase functions. The formation of dimers and higher oligomers of Ire1p during stress from unfolded proteins or from the ER membrane (Kimata et al., 2007; Korennykh et al., 2009; Halbleib et al., 2017) triggers the *trans*-autophosphorylation of the cytosolic kinase domain and the activation of the adjacent RNase domain. The RNase activity of Ire1p contributes to an unconventional splicing of the *HAC1* mRNA in the cytosol (Cox and Walter, 1996; Mori et al., 1996) thereby facilitating the production of the active transcription factor Hac1p regulating several hundred UPR-target genes.

For studying and assaying the UPR, it is common practice to stress the cells acutely either with dithiothreitol (DTT), a reducing agent interfering with disulfide bridge formation in the ER-lumen, or tunicamycin (TM), a natural inhibitor of the N-linked glycosylation of proteins in the ER (Azim and Surani, 1979). It is generally assumed that DTT and TM exclusively cause proteotoxic ER stress. However, the impact of DTT and TM on the cellular lipid composition has never been systematically tested.

Here, we have studied the impact of DTT or TM on the lipidome of *S. cerevisiae* in both rich and synthetic medium. Serendipitously, we find evidence for a remarkable selectivity of *S. cerevisiae* in the generation and metabolism of highly asymmetric glycerophospholipids with one saturated, medium fatty acyl chain (C10 or C12) and a long, saturated one (C16 or C18). Despite a high overall abundance of unsaturated fatty acyl chains (C16:1 or C18:1), we find an almost exclusive pairing of two saturated fatty acyl chains in these asymmetric glycerophospholipids, thereby implying a strong, inherent selectivity of acyl chain pairing. With respect to the UPR, we find that (1) DTT and TM impair cellular growth, (2) the medium has a significant impact on the cellular lipidome thereby potentially tuning the sensitivity of the UPR, (3) DTT at growth-inhibitory concentrations causes a substantial and rapid remodeling of the lipidome in rich medium, and (4) TM under our experimental conditions has only a marginal impact on the cellular lipidome in both synthetic and rich medium. Based on these findings, we provide a guideline to predictably and unambiguously activate the UPR by proteotoxic stress, whilst minimizing potential artifacts from lipid bilayer stress.

MATERIALS AND METHODS

Yeast Strains

Yeasts used were the standard laboratory wild-type *S. cerevisiae* strain BY4741 MATa *his3Δ1 leu2Δ0 met15Δ0 ura3Δ0* and the *ire1Δ*-derivative BY4741 MATa; *ura3Δ0; leu2Δ0; his3Δ1; met15Δ0; YHR079c::kanMX4*.

Reagents

Chemicals and solvents of HPLC/LC-MS analytical grade were used. TM (#T7765), DTT (#D0632), and ammonium bicarbonate (#9830) were purchased from Sigma-Aldrich. Ammonium sulfate (#9218) was purchased from Carl Roth.

Media

All media were prepared according to standard protocols (Dymond, 2013). D(+)-Glucose (#HN06, tryptone/peptone (#8952), and yeast extract (#2363) were purchased from Carl Roth. Yeast nitrogen base (YNB) (#CYN0602), agar-agar (#AGA03), and complete supplement mixture (CSM complete) (#DCS0019) were purchased from FORMEDIUM.

Cell Cultivation for Lipidomics

Cells were cultivated under constant agitation at 30°C at 220 rpm, if not stated otherwise. Every lipidomic sample started from an individual, single colony on either yeast peptone dextrose (YPD) or synthetic complete dextrose (SCD) agar plates. A single colony was used to inoculate a pre-culture, which was then cultivated overnight for 21 h in either YPD or SCD liquid medium. The resulting stationary culture was used to inoculate a main culture in fresh medium to a final OD₆₀₀ of 0.1. When the culture reached an OD₆₀₀ of 0.8 ± 0.05, the cells were either stressed with DTT, TM or left untreated. DTT was used at a final concentration 8 mM and 2 mM in YPD and SCD, respectively. TM was used at a final concentration of 1.0 μg/ml and 1.5 μg/ml in YPD and SCD, respectively. After an additional hour of cultivation, 20 OD units of cells were harvested by centrifugation (3,500 × g, 5 min, 4°C), and washed three-times with ice-cold 155 mM ammonium bicarbonate supplemented with 10 mM sodium azide in 1.5 ml reaction tubes using quick centrifugation (10,000 × g, 20 s, 4°C). The resulting cell pellets were snap-frozen with liquid nitrogen and stored for up to 4 weeks at -80°C. Prior to cell lysis, pellets were thawed on ice and then resuspended in 1 ml 155 mM ammonium bicarbonate. 200 μl zirconia beads were added to the suspension and cells were disrupted by vigorous shaking using a DisruptorGenie for 10 min at 4°C. 500 μl of the resulting lysate was snap-frozen and used for further analysis via shotgun mass spectrometry.

Growth Assay – Acute Stress

Cultures in YPD and SCD were inoculated precisely as described for lipidomic experiments. The density of the culture was monitored over a prolonged period of time by determining the OD₆₀₀ for up to 5 h after they had reached an OD₆₀₀ = 0.8. For determining the doubling time of an exponentially growing culture, all data points with an OD₆₀₀ between 0.2 and 2.5 were

considered. The data were fitted to the exponential (Malthusian) growth function using Prism 8 for macOS Version 8.4.1.

Growth Assay – Prolonged Stress

Stationary overnight cultures in YPD were used to inoculate a pre-culture in either YPD or SCD to an OD₆₀₀ of 0.2. The cells were then cultivated for 6 h to reach the exponential growth phase. These cultures were used to inoculate a main culture in a 96-well plate to an OD₆₀₀ of 0.01 using fresh medium (either YPD or SCD) containing different concentrations of DTT. After cultivation for 16 h at 30°C with no agitation, the final OD₆₀₀ was determined after intense mixing of the culture using a microplate reader (Tecan Microplate Reader Spark).

Lipid Extraction for Mass Spectrometry Lipidomics

Mass spectrometry-based lipid analysis was performed by Lipotype GmbH (Dresden, Germany) as described (Ejsing et al., 2009; Klose et al., 2012). Lipids were extracted using a two-step chloroform/methanol procedure (Ejsing et al., 2009). Samples were spiked with internal lipid standard mixture containing: CDP-DAG 17:0/18:1, ceramide 18:1;2/17:0 (Cer), diacylglycerol 17:0/17:0 (DAG), lyso-phosphatidate 17:0 (LPA), lyso-phosphatidylcholine 12:0 (LPC), lyso-phosphatidylethanolamine 17:1 (LPE), lyso-phosphatidylinositol 17:1 (LPI), lyso-phosphatidylserine 17:1 (LPS), phosphatidate 17:0/14:1 (PA), phosphatidylcholine 17:0/14:1 (PC), phosphatidylethanolamine 17:0/14:1 (PE), phosphatidylglycerol 17:0/14:1 (PG), phosphatidylinositol 17:0/14:1 (PI), phosphatidylserine 17:0/14:1 (PS), ergosterol ester 13:0 (EE), triacylglycerol 17:0/17:0/17:0 (TAG), stigmastatrienol, inositolphosphorylceramide 44:0;2 (IPC), mannosyl-inositolphosphorylceramide 44:0;2 (MIPC), mannosyl-di-(inositolphosphoryl)ceramide 44:0;2 (M(IP)₂C). After extraction, the organic phase was transferred to an infusion plate and dried in a speed vacuum concentrator. 1st step dry extract was resuspended in 7.5 mM ammonium acetate in chloroform/methanol/propanol (1:2:4, V:V:V) and 2nd step dry extract in 33% ethanol solution of methylamine in chloroform/methanol (0.003:5:1; V:V:V). All liquid handling steps were performed using Hamilton Robotics STARlet robotic platform with the Anti Droplet Control feature for organic solvents pipetting.

MS Data Acquisition

Samples were analyzed by direct infusion on a QExactive mass spectrometer (Thermo Scientific) equipped with a TriVersa NanoMate ion source (Advion Biosciences). Samples were analyzed in both positive and negative ion modes with a resolution of $R_{m/z} = 200 = 280000$ for MS and $R_{m/z} = 200 = 17500$ for MSMS experiments, in a single acquisition. MSMS was triggered by an inclusion list encompassing corresponding MS mass ranges scanned in 1 Da increments (Surma et al., 2015). Both MS and MSMS data were combined to monitor EE, DAG, and TAG ions as ammonium adducts; PC as an acetate adduct; and CL, PA,

PE, PG, PI, and PS as deprotonated anions. MS only was used to monitor LPA, LPE, LPI, LPS, IPC, MIPC, M(IP)₂C as deprotonated anions; Cer and LPC as acetate adducts and ergosterol as protonated ion of an acetylated derivative (Liebisch et al., 2006).

MS Data Analysis

Data were analyzed by Lipotype GmbH using an in-house developed lipid identification software based on LipidXplorer (Herzog et al., 2011, 2012). Data post-processing and normalization were performed using an in-house developed data management system. Only lipid identifications with a signal-to-noise ratio > 5, and a signal intensity five-fold higher than in corresponding blank samples were considered for further data analysis.

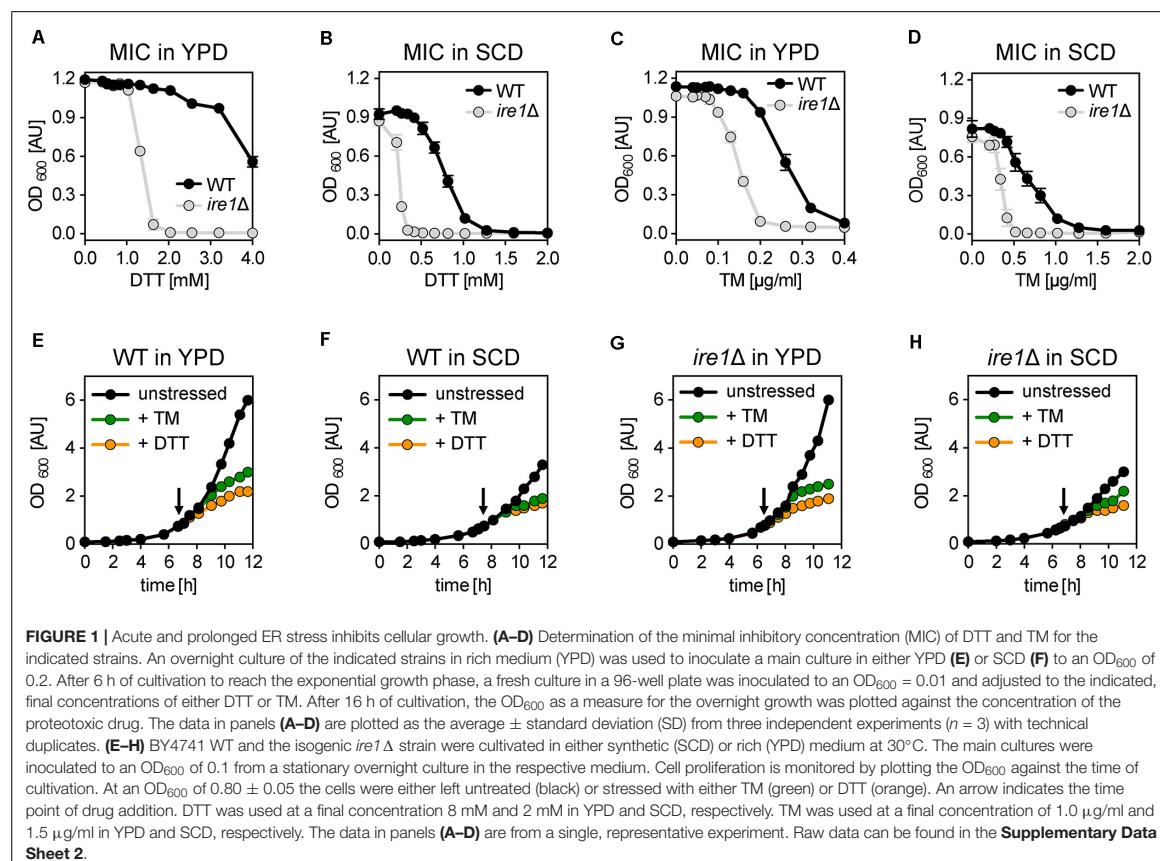
RESULTS

We investigated the impact of two potent, proteotoxic inducers of ER stress, namely DTT and TM, on cellular growth and the cellular lipid composition. Our ultimate goal was to faithfully induce proteotoxic stress in the lumen of the

ER whilst minimizing potential artifacts from aberrant ER lipid compositions.

DTT and TM Inhibit Cellular Growth

We wanted to know the impact of DTT and TM on cellular growth. To this end, we cultivated the *S. cerevisiae* wildtype (WT) strain BY4741 and isogenic *ire1Δ* cells in either rich medium (YPD) or synthetic medium (SCD) to the exponential growth phase. Using these cells, we inoculated fresh cultures in a 96-well plate to an OD₆₀₀ of 0.01 in the respective medium supplemented with various concentrations of DTT and TM. After overnight cultivation, cellular growth was assayed via the OD₆₀₀ (Figures 1A–D). Not surprisingly, WT cells are more resistant to DTT- or TM-induced ER stress than *ire1Δ* in both rich and synthetic medium (Figures 1A–D). This suggests that UPR-activation via Ire1p contributes to cellular fitness under conditions of prolonged proteotoxic stress. Notably, the choice of the medium affects the growth-inhibitory concentrations of DTT and TM such that higher initial concentrations of DTT are required to inhibit overnight growth in rich medium, while lower concentrations are sufficient in minimal medium



(Figures 1A,B). In contrast, lower concentrations of TM are required to block overnight growth in rich versus synthetic medium (Figures 1C,D). The underlying reasons remain unclear. Among other possibilities, the medium might affect the drug *per se* (e.g., DTT oxidation), the uptake and extrusion of the compound, or -via diverse mechanisms- the cellular resistance to proteotoxic stress. Nevertheless, our data help choosing appropriate concentrations to effectively inhibit overnight growth for each medium and both drugs.

Next, we wanted to study the impact of acute ER stress on cellular growth. We cultivated WT cells in rich (YPD) and synthetic (SCD) medium (Figures 1E,F) under conditions most commonly used for studying the biology of *S. cerevisiae* (Sherman, 2002). We inoculated liquid cultures to an OD₆₀₀ of 0.1 using stationary, overnight cultures in the respective medium and then followed the cellular growth over time. When the cultures reached an OD₆₀₀ of 0.75 to 0.8, the cells were either left untreated or stressed with DTT or TM at concentrations causing a near-complete inhibition of overnight growth to account for the different dose-response curves in different media (Figures 1A–D). Specifically, DTT was used at a concentration of 8 mM and 2 mM, while TM was used at a concentration of 1.0 µg/ml and 1.5 µg/ml in rich and synthetic medium, respectively. Notably, 8 mM of DTT has previously been used to study ER membrane expansion in stressed cells, while 1–2 µg/ml of TM are known to reorganize Golgi traffic and mitochondrial enlargement by activating the UPR (Bernales et al., 2007; Schuck et al., 2009; Hsu et al., 2016; Tran et al., 2019).

Expectedly, we find that unstressed cells grow faster in rich medium (doubling time 86 min) than in synthetic medium (doubling time 107 min) (Figures 1E,F), which underscores the previous finding that BY4741 strains requires an additional supplementation of the SCD medium for optimal growth (Hanscho et al., 2012). Furthermore, DTT- and TM-stressed cells grow markedly slower compared to the unstressed cells in both media (Figures 1E,F). Consistent with previous observations (Pincus et al., 2010), the reduced rate of growth becomes apparent as early as 1 h after the addition of the stress-inducing agents (Supplementary Figures S1A,B). Notably, the impact of DTT is more pronounced than the impact of TM at the given concentrations (Figures 1E,F).

Next, we wanted to test if the reduced growth of the stressed cells is due to an activation of the UPR, which is known to peak within 1 h after the addition of DTT or TM to the medium and which largely remodels the cellular transcriptome (Kawahara et al., 1997; Travers et al., 2000; Promlek et al., 2011). Surprisingly, the growth of both stressed and unstressed *ire1Δ* cells was indistinguishable from WT cells in both rich and synthetic medium (Figures 1E–H and Supplementary Figures S1C–H). This suggests that DTT and TM impair cellular growth during this early phase of stress predominantly via their impact on protein folding and not by processes downstream of UPR activation. The slightly higher potency of DTT to impede cellular growth compared to TM at the given concentrations may reflect the fact that these compounds affect the folding of different sets of proteins: proteins with disulfide bonds in the case of DTT and N-linked glycosylated proteins in the case of TM. Furthermore,

DTT can reduce already formed disulfide bonds and is known to directly affect also other cellular processes outside the ER such as the protein import into mitochondria (Mesecke et al., 2005) and protein palmitoylation (Levental et al., 2010). In contrast, TM affects only the glycosylation of freshly synthesized proteins. Our data suggest that the growth inhibition observed in *acutely* stressed cells is independent of UPR activation.

Experimental Outline and Global Insights From Principal Component Analysis

We used shotgun mass spectrometry-based lipidomics to comprehensively and quantitatively dissect the impact of acute proteotoxic stress on the cellular lipid composition. In light of the pronounced impact of DTT and TM on cellular growth, we focused on their immediate effects within 1 h of treatment. We analyzed the lipid composition for six conditions and two different strains each as biological triplicates (Figure 2A). A principal component analysis (PCA) of the entire dataset at the level of individual lipid species revealed a close clustering of all samples from WT and *ire1Δ* cells cultivated in SCD, thereby suggesting UPR activity itself has little impact on their lipidomes (Figure 2B). In contrast, we observed two clusters for cells cultivated in rich medium. One cluster contained samples from WT and *ire1Δ* cells that were either left untreated or stressed with TM, while the other cluster contained samples from cells that were stressed with DTT at concentrations commonly used for UPR activation. This suggests that DTT causes a substantial remodeling of the lipidome, while TM treatments have a lesser impact on the cellular lipid composition. Not surprisingly, the loadings plot suggests a correlation of specific groups of lipids (Supplementary Figure S2A). The total amount of lipids quantified from 1 OD unit of cells (Supplementary Figure S2B) and the amount of storage lipids (Supplementary Figure S2C) highlight a low variability between replicates and show that storage lipids are more abundant in synthetic (SCD) medium. Storage lipids comprise all triacylglycerol (TAG) species and ergosterol esters.

The Impact of YPD and SCD Medium on the Lipidome of *S. cerevisiae*

For representing this complex dataset, we assorted the identified lipid species to one of four major lipid categories: sterols, sphingolipids (SLs), membrane glycerolipids (MGLs), and storage lipids. MGLs comprise all glycerophospholipids and diacylglycerol (DAG) species (Figure 3 and Supplementary Figure S3). Overall, we find a remarkable impact of the medium on the cellular lipid composition (Figure 3A).

Global Impact of the Medium on Sphingolipids

Yeast SLs comprise inositolphosphorylceramide (IPC), mannosyl-inositol phosphorylceramide (MIPC), mannosyl-di-(inositolphosphoryl) ceramide (M(IP)₂C), and - less abundantly - ceramides (Cer). With the exception of Cer, all SLs have a significantly lower level in cells cultivated in rich medium compared to cells cultivated synthetic medium

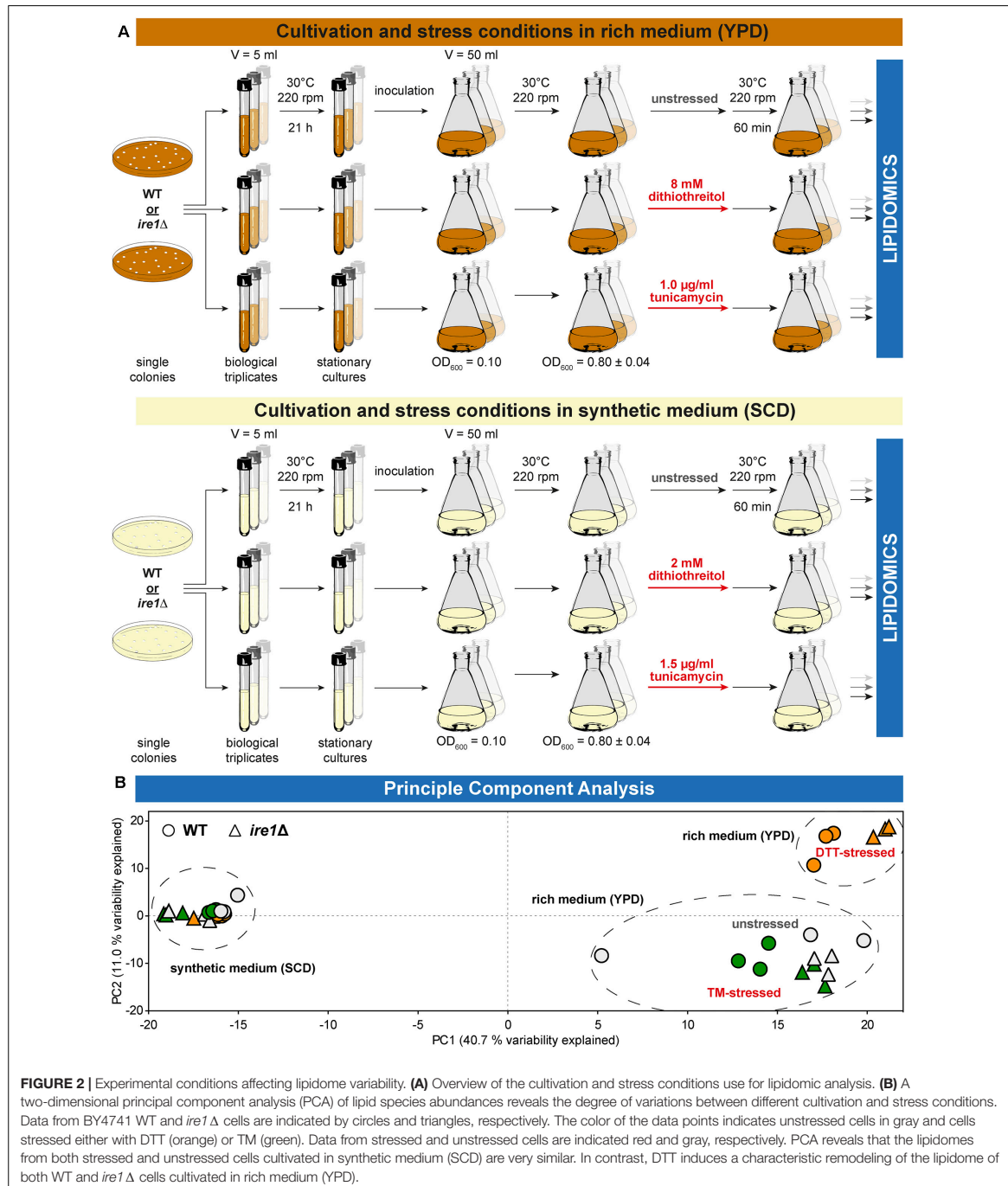


(Figure 3A). The same trend was observed for all SLs in *ire1Δ* cells (Supplementary Figure S3A). Thus, the lower level of sphingolipids in YPD-cultured cells is not due to

possible differences in basal, constitutive UPR signaling. However, because SLs are concentrated along the secretory pathway and highly abundant in the plasma membrane (van

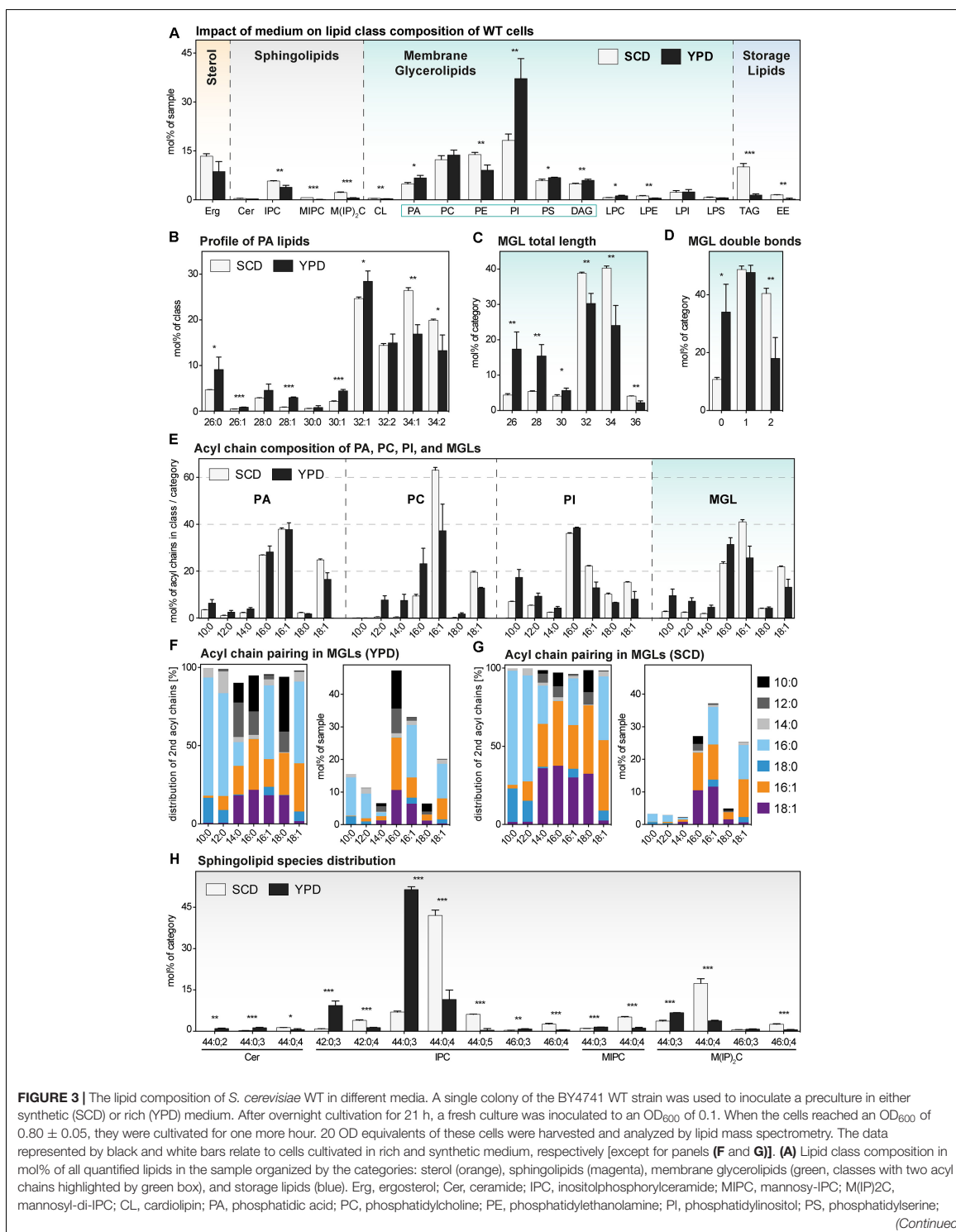


FIGURE 3 | Continued

DAG, diacylglycerol; LPC, lyso-PC; LPE, lyso-PE; LPI, lyso-PI; LPS, lyso-PS; TAG, triacylglycerol; EE, ergosteryl ester. **(B)** Profile of PA lipids in mol% of the class. **(C)** Total length of lipids in a sub-category of membrane glycerolipids (MGLs) including PA, PC, PE, PI, PS, DAG. The total length is given as the sum of carbon atoms in both fatty acyl chains in mol% of this sub-category. **(D)** Total number double bonds in a sub-category of MGLs (PA, PC, PE, PI, PS, DAG) is given as the sum of double bonds in both acyl chains, in mol% of this sub-category. **(E)** The acyl chain composition of PA, PC, PI and of a sub-category of MGLs (PA, PC, PE, PI, PS, DAG) is normalized either to the individual lipid class or the sub-category and given in mol%. **(F,G)** The pairing of fatty acyl chains in MGLs (PA, PC, PE, PI, PS, DAG) is plotted for cells cultivated in **(F)** rich (YPD) and **(G)** synthetic (SCD) medium. The left panel indicates the pairing of fatty acyl chains in a sub-category of MGLs (PA, PC, PE, PI, PS, DAG) normalized to each particular fatty acyl chain and is given as mol%. The right panel indicates the abundance of acyl chain pairs in the sub-category of MGLs and is given in mol%. **(H)** Profile of sphingolipids in mol% of the category. The least abundant species in each panel are omitted for clarity. Each bar represents the average \pm SD from $n = 3$ independent experiments. Statistical significance was tested by an unpaired two-tailed *t*-test using GraphPad Prism, * $p < 0.05$, ** $p < 0.01$, *** $p < 0.001$.

Meer et al., 2008; Klemm et al., 2009; Hannich et al., 2011; Surma et al., 2011) it is tempting to speculate that cells cultivated in rich medium feature a higher abundance of inner membranes relative to the plasma membrane. In fact, the rapidly growing cells in rich medium have a particularly high demand for membrane biogenesis and both ER size and the rate of membrane lipid production can be controlled independently of UPR signaling (Loewen, 2004; Schuck et al., 2009; Henry et al., 2012).

Global Impact of the Medium on Membrane Glycerolipids

Membrane glycerolipids constitute the most abundant lipid category comprising the lipid classes phosphatidic acid (PA), phosphatidylcholine (PC), phosphatidyl-ethanolamine (PE), phosphatidylinositol (PI), phosphatidylserine (PS), and diacylglycerol (DAG) (Henry et al., 2012; Klose et al., 2012). Less abundant are cardiolipin (CL) and the lyso-lipid derivatives of the major glycerophospholipid classes with one fatty acid (FA) chain. We find that phosphatidylinositol (PI) is by far the most abundant lipid class in both WT and *ire1Δ* cells when cultivated in rich medium (**Figure 3A** and **Supplementary Figure S3A**). However, when cells are cultivated in synthetic medium, PI is much less abundant and found at levels comparable with phosphatidylcholine (PC) and phosphatidylethanolamine (PE) (**Figure 3A** and **Supplementary Figure S3A**). This is particularly relevant when studying the UPR: Ire1p has been identified as inositol-requiring enzyme (Nikawa and Yamashita, 1992), it is activated by inositol-depletion (Promlek et al., 2011), and sensitive to the stiffness of the ER membrane (Halbleib et al., 2017) thereby implying an important role of PI lipids. But not only PI, also the abundance of PE is affected by the choice the medium. PE is significantly less abundant in cells cultivated in rich versus synthetic medium (**Figure 3A**). Again, this is likely to affect the sensitivity and activity of the UPR as aberrant PE-to-PC ratios have been firmly implicated in chronic activation of the UPR in yeast, worms, and mammals (Fu et al., 2011; Thibault et al., 2012; Hou et al., 2014).

Although qualitatively consistent with previous reports (Ejsing et al., 2009; Klose et al., 2012; Surma et al., 2013; Casanovas et al., 2015) our observations also highlight an important caveat for the use of rich medium. Because YPD is not a defined medium (in contrast to the synthetic-defined SCD), its use will inevitably lead to inconsistencies with respect to the lipid composition. As a consequence, it is almost impossible to

compare data coming from different laboratories using media from different suppliers or even media batches. It is also impossible to exclude a technical bias as contributing factor for seemingly divergent observations: different procedures for lipid extraction into an organic phase may affect the spectrum of lipids that can be detected, different modes of sample separation and/or detection [such as thin-layer chromatography (TLC), liquid chromatography coupled to mass spectrometry (LC-MS) or the shotgun lipidomics platform used for this study] might bias the detection of some lipids/lipid classes over others. Ideally, the use of internal standards should correct the bias from extraction and detection. Furthermore, only fully quantitative data expressed in absolute units (such as pmol or derived molar fractions) can be compared to each other, as any relative data depend on the experimental setup and reference points applicable only within a given experiment.

Impact of the Medium on Storage Lipids

The choice of the medium has a striking impact on the abundancies of storage lipids. Exponentially growing cells cultivated in rich medium store much less TAGs and EEs than those cultivated in synthetic medium (**Figure 3A**). The same trend is observed in *ire1Δ* cells (**Supplementary Figure S3A**). It is tempting to speculate that rapidly growing cells depend more heavily on the production of membrane lipids than relatively slow growing cells, which can 'afford' to store some lipids for future use. Clearly, the different growth rates in the two media (**Figure 1** and **Supplementary Figure S1**) must be considered in light of the intricate connections between membrane biogenesis, lipid droplet formation, and the UPR (Gaspar et al., 2011; Stordeur et al., 2014; Casanovas et al., 2015). Our data underscore the importance to study the UPR under tightly controlled conditions.

Impact of the Medium on the Lipid Species Level Identifies Asymmetric Lipids

We wanted to know the impact of rich versus synthetic medium on lipid acyl chains and initially focused our attention on the profile of PA lipids (**Figure 3B**). Normally, in *S. cerevisiae*, the fatty acid composition of PA lipids is mostly limited to palmitic (C16:0), palmitoleic (C16:1) and oleic acid (C18:1) with low amounts of shorter fatty acids (Klose et al., 2012). However, the cells cultivated in rich medium exhibited a significantly higher abundance of PA lipids with shorter, saturated acyl chains, as evidenced by the level of PA lipids with a cumulative acyl chain length of C26, C28, and C30

(Figure 3B). A combined analysis of all MGLs with two fatty acyl chains (PA, PC, PE, PI, PS, DAG) further highlighted this general and significant shift toward shorter (Figure 3C) and more saturated lipid species (Figure 3D). Notably, identical trends can be observed for *ire1Δ* cells indicating that a low, basal activation of the UPR does not contribute to this global trend in all MGLs caused by the cultivation in different media (Supplementary Figures S3B–D).

We then studied the usage of different fatty acyl chains in PA, PC, and PI in cells cultivated in both rich and synthetic medium (Figure 3E) and also calculated the abundance of the different fatty acyl chains in all MGLs (with two fatty acyl chains) (Figure 3E). Consistent with previous reports, we find that the distribution of the fatty acyl chains differs between the individual glycerophospholipid classes (Figure 3E) (Ejsing et al., 2009; Klose et al., 2012; Casanovas et al., 2015). Strikingly, our data reveal that saturated, medium fatty acyl chains (C10, C12, and C14) are much more prominently found in cells cultivated in rich medium throughout all glycerophospholipid classes (Figure 3E). Notably, similar asymmetric lipids with two acyl chains differing substantially in length have only recently been found at high abundance in the lipidome of *Schizosaccharomyces japonicus* (Makarova et al., 2020).

In order to gain more insight in the molecular rules that govern the production of asymmetric lipids, we studied the pairing of fatty acyl chains in MGLs. We found an almost exclusive pairing of saturated, medium fatty acyl chains (C10:0 or C12:0) with longer saturated fatty acyl chains (C16:0 or C18:0) in *S. cerevisiae* (Figure 3F; left panel). In fact, we find virtually no pairing of unsaturated fatty acyl chain (C16:1 or C18:1) with medium fatty acyl chains (C10:0 or C12:0). Also when considering the relative abundance of the different fatty acyl chains (C16:0, C16:1 and C18:1 are most abundant), the same, remarkable selectivity for certain pairs of fatty acyl chains becomes clear: medium fatty acyl chains preferentially pair with saturated, but not with unsaturated fatty acyl chains (Figure 3F; right panel). YPD is not a fully defined medium and it may contain minor concentrations of short and medium chain fatty acids. In order to test if *S. cerevisiae* can synthesize asymmetric lipids from scratch, we analyzed the acyl chain pairing in cells cultivated in synthetic medium (Figure 3G). Again, we found a strong preferential pairing of saturated, medium fatty acyl chains with saturated, long fatty acid chains, but not with unsaturated ones (Figure 3G). Our data suggest that tight and evolutionary conserved rules underlie the pairing of fatty acyl chains in these highly asymmetric lipids.

A Medium-Dependent Switch in the Species Distribution of Sphingolipids

Another remarkably specific impact of the medium can be observed in the profile of SLs for both WT (Figure 3H) and *ire1Δ* cells (Supplementary Figure S3E). The most abundant sphingolipid species of cells cultivated in rich medium is IPC 44:0,3 (with three hydroxylations) contributing to more than 50 mol% of all SLs, while IPC 44:0,4 (with four hydroxylations) is much less abundant. In contrast, IPC 44:0,4 is contributing to more than 40 mol% to the pool of SLs and

is the most abundant SL species in SCD-cultured cells. The molecular underpinnings of this remarkable shift in the species composition and its physiological relevance remains to be studied in greater detail.

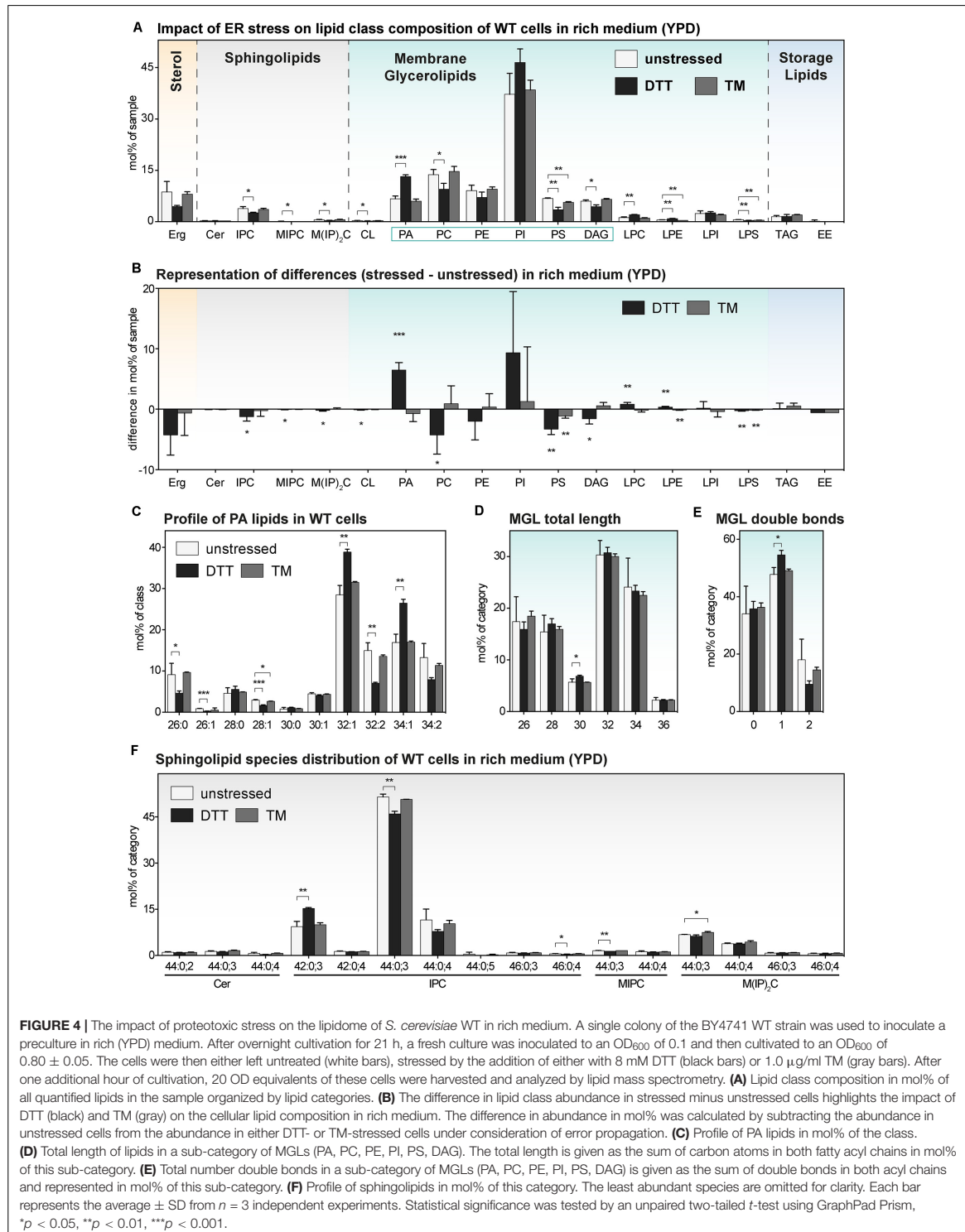
The Impact of DTT and TM on the Lipidome of *S. cerevisiae* in Rich Medium

We wanted to study the impact of DTT and TM on the lipid composition of cells cultivated in both rich medium (Figure 4) and synthetic medium (Figure 5) and focus our attention on an early time point after 1 h of treatment. As important controls, we also determined the lipid compositions of stressed and unstressed *ire1Δ* cells in both media to test a possible contribution of UPR to changes of the lipidome (Supplementary Figures S4, S5).

Consistent with our PCA analysis (Figure 2B), we find that the TM-induced stress has barely any impact on the lipid composition of WT cells (Figure 4A). This lack-of-impact is best evident when representing difference of abundance between stressed and unstressed cells for each lipid class (Figure 4B). There is also barely any impact of TM on the profile of PA lipids (Figure 4C), the length distribution of the fatty acyl chains (Figure 4D), the degree of saturation (Figure 4E), and the species composition of SLs (Figure 4F). Notably, this is true for both for WT and *ire1Δ* cells (Supplementary Figures S4A–F). These data suggest TM can be used as proteotoxic drug in YPD-cultivated cells without severely affecting the cellular lipid composition.

In contrast to that, DTT at the given concentration has a significant impact on the lipidome of YPD-cultured cells (Figure 4A), which is most apparent when plotting the difference of lipid class abundance between stressed and unstressed cells (Figure 4B). Clearly, treating the cells for only 1 h with DTT is sufficient to cause a significant and substantial increase of PA in the stressed cells. Given that PA lipids are important signaling lipids involved in regulating membrane biogenesis (Loewen, 2004; Schuck et al., 2009; Henry et al., 2012; Hofbauer et al., 2018), a two-fold increase of the cellular PA level is likely to have broad impact on lipid metabolism and the cellular transcriptome. Intriguingly, treating the cells with DTT induces also a shift in the profile of PA lipids toward a higher average acyl chain length and more unsaturation for both WT (Figure 4C) and *ire1Δ* cells (Supplementary Figure S4C). While these observations suggest that DTT affects PA lipids either directly (by affecting fatty acid metabolism) or indirectly (by its impact on cellular growth or other means; Supplementary Figure S1A), these trends are not pronounced in the wider group of MGLs with two fatty acyl chains – neither for WT nor *ire1Δ* cells (Figures 4D,E and Supplementary Figures S4D,E). Based on its position in the lipid metabolic network (Henry et al., 2012; Ernst et al., 2016), we speculate that PA is a class of ‘early-responding’ lipids, which change most readily upon an environmental perturbation, while other MGLs are affected only after prolonged periods of stress.

We also find some impact of ER stress on the profile of SLs of WT and *ire1Δ* cells (Figure 4F and Supplementary Figure S4F), but these changes are relatively small. The overall similarity of the lipidomic changes observed for WT and *ire1Δ* cells upon DTT treatments, suggest that most DTT impacts on lipid metabolism



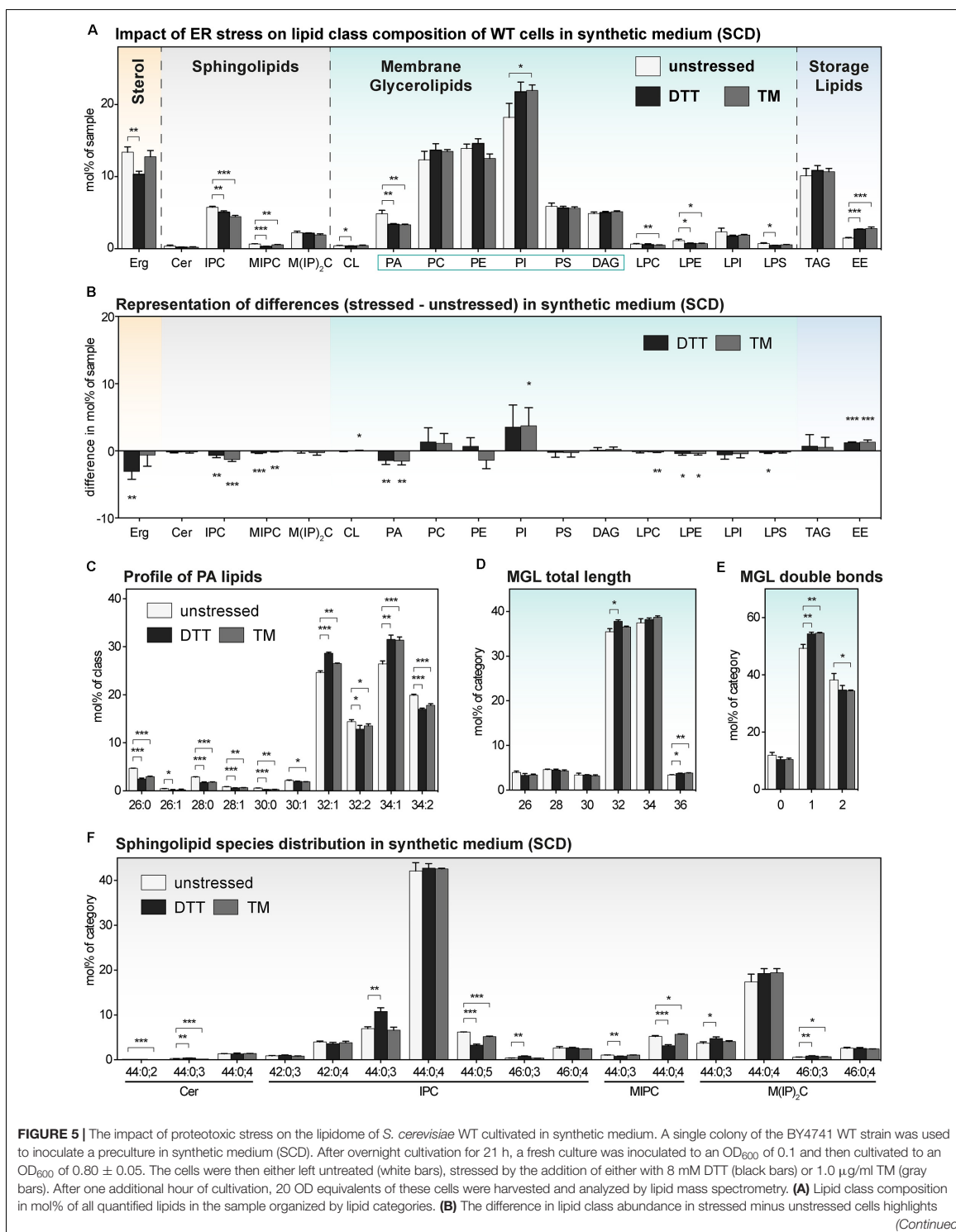


FIGURE 5 | Continued

the impact of DTT (black) and TM (gray) on the cellular lipid composition in synthetic medium. The difference in abundance in mol% was calculated by subtracting the abundance in unstressed cells from the abundance in either DTT- or TM-stressed cells under consideration of error propagation. **(C)** Profile of PA lipids in mol% of the class. **(D)** Total length of lipids in a sub-category of MGLs (PA, PC, PE, PI, PS, DAG). The total length is given as the sum of carbon atoms in both fatty acyl chains in mol% of this sub-category. **(E)** Total number double bonds in a sub-category of MGLs (PA, PC, PE, PI, PS, DAG) is given as the sum of double bonds in both acyl chains and represented in mol% of this sub-category. **(F)** Profile of sphingolipids in mol% of this category. The least abundant species are omitted for clarity. Each bar represents the average \pm SD from $n = 3$ independent experiments. Statistical significance was tested by an unpaired two-tailed *t*-test using GraphPad Prism, * $p < 0.05$, ** $p < 0.01$, *** $p < 0.001$.

are independently of UPR-signaling, at least under the given conditions (Figure 4 and Supplementary Figure S4).

In summary, we find that even a short cultivation in the presence of DTT induces substantial changes of the cellular lipidome.

The Impact of DTT and TM on the Lipidome of *S. cerevisiae* in Synthetic Medium

We wanted to know the impact of DTT and TM on the lipid composition of *S. cerevisiae* cultivated in synthetic medium. We therefore determined the lipidomes of both stressed and unstressed WT and *ire1Δ* cells (Figure 5 and Supplementary Figure S5). Overall, we find an almost identical lipid class composition for cells stressed either with DTT or TM compared to untreated control cells with only minor changes in the abundance of several lipid classes (Figures 5A,B and Supplementary Figures S5A,B). While the changes between stressed and unstressed cells are significant, the difference in abundance seems rather moderate (Figure 5B). For example, the ~30% lower level of PA in both DTT- and TM-stressed cells (Figure 5A), has most probably a lower impact on cellular physiology than the two-fold increase of PA in DTT-treated cells in rich medium (Figure 4A). Other significant, moderate changes are observed for several SLs, Erg, and EEs (Figure 5A). We doubt that these lipidome changes are substantial enough to impact on the activity of the UPR via a membrane-based mechanism. This speculation is supported by the observation that proteotoxic stress clearly dominates over membrane-based stress when cells are treated with either DTT or TM for 1 h or less (Promlek et al., 2011).

Beyond the overall very similar lipid class distribution of stressed and unstressed cells cultivated in synthetic medium, we find significant, but minor stress-induced changes in the PA species composition (Figure 5C), a similar total fatty acyl chain length in MGLs (Figure 5D), a mildly affected degree of lipid saturation (Figure 5E), and a largely similar profile of SLs (Figure 5F). Again, the lipidomes observed for WT and *ire1Δ* cells are extremely similar. In summary, we find, somewhat surprisingly, that the cellular lipidome is quite 'resistant' to perturbations from DTT- and TM-treatments when cells are treated for 1 h in synthetic medium.

Our lipidomic survey of stressed and unstressed *S. cerevisiae* reveals that TM treatments for 1 h are suitable in both rich and synthetic medium to activate the UPR via proteotoxic stress with only little interference from a perturbed lipid composition. However, more precautions should be taken when using DTT.

DISCUSSION

We have performed a systematic, quantitative analysis of the lipidomic changes associated with acute ER stress caused by the proteotoxic agents DTT and TM. Given the central relevance of the UPR for cellular homeostasis and the adverse effects associated with chronic UPR activation, it is crucial to better understand the signals that underlie prolonged and chronic activation of the UPR in the future.

Recommendations for Studying UPR-Activating Signals

Using *S. cerevisiae* as a model, we highlight the importance of tightly controlled cultivation conditions and quantitative lipid analyses for a more holistic approach toward understanding the interplay of UPR-activating signals. We show that (1) the proteotoxic drugs DTT and TM impair cellular growth, thereby confirming previous observations (Pincus et al., 2010), (2) DTT causes within 1 h of treatment substantial changes of the lipidome of YPD-cultured cells, (3) DTT and TM have only a minor impact on the lipidome of SCD-cultured cells, (4) unstressed WT and *ire1Δ* cells feature virtually identical lipidomes under the tested conditions, thereby suggesting that basal, low-level UPR signaling (or lack of thereof) does not substantially affect the cellular lipid composition. Overall, our data are consistent with the general assumption that TM predominantly causes proteotoxic stress, at least within the first hour of treatment (Promlek et al., 2011). The rapid, DTT-dependent remodeling of the lipidome observed in YPD-cultured cells and the strongly impaired growth of stressed cultures, however, may serve as a warning to carefully interpret data derived from acutely stressed cells. We like to stress that we investigated only the impact of a single concentration for each drug in both media on the cellular lipid composition. It is possible that TM, when used at higher concentrations, might have a more severe impact on the cellular lipid composition. Nevertheless, for studying the UPR and its response to proteotoxic signals with little to no interference from a perturbed lipid metabolism, we suggest (1) the use of defined SCD over ill-defined YPD, (2) the use of TM over DTT, because of its more specific impact on protein folding in the ER, and (3) applying TM or DTT stress for a maximum of 1 h.

Membrane Biogenesis in Rapidly Growing Cells – Competition for Lipid Metabolites

Our systematic lipidomic analyses of WT and *ire1Δ* cells in two different media provides insights into the orchestration

of membrane biogenesis by rapidly growing, eukaryotic cells. Even though rich medium provides a rich supply of nutrients, cells cultivated in this medium do not accumulate substantial amounts of storage lipids during the exponential growth phase (Figure 3A). Cells cultivated in synthetic medium, however, accumulate a five times higher level of neutral lipids (TAGs + EEs) although the medium is not as rich (Figure 3A). We speculate that these marked differences are at least partly due to the growth rate, which is substantially higher for YPD-cultured cells. This interpretation is consistent with the previous observation that storage lipids are dynamically regulated in a growth-stage dependent fashion (Klose et al., 2012; Kohlwein et al., 2013; Casanovas et al., 2015) and suggests an increased flux of fatty acids into membrane lipids in rapidly growing cells. In fact, the lipid phenotypes associated with a genetically disrupted fatty acid desaturation are more pronounced in YPD-cultured cells (Surma et al., 2013). The global role of the cellular growth rate on lipid metabolism remains to be established in the future.

Along these lines, we also find that the ratio of SLs to MGLs is low in rapidly growing, YPD-cultured cells, but higher in slow-growing SCD-cultured cells (Figure 3A). While it is clear that many distinct regulatory circuits of the cell are affected by the composition of the medium, we speculate that the low SL-to-MGL ratio reflects an increased global rate of the lipid biosynthesis in the ER and -as a consequence- a low ratio of plasma membrane-to-ER abundance. Notably, our finding that WT and *ire1Δ* cells feature almost identical lipidomes (Supplementary Figure S3) would suggest that ER abundance is controlled independently of the UPR in this case. This is consistent with previous findings that ER proliferation can be uncoupled from the UPR via the Opi1 and Ino2/Ino4 regulatory circuit (Loewen, 2004; Schuck et al., 2009; Henry et al., 2012). Opi1 binding to PA lipids at the ER membrane (Loewen, 2004; Hofbauer et al., 2018) de-represses Ino2/Ino4-regulated genes involved in MGL biosynthesis and tip the balance from storing neutral lipids toward membrane proliferation. In fact, we find an increased level of PA lipids in YPD-cultured cells (Figure 3A and Supplementary Figure S3A). Our findings fuel that idea that the flux of fatty acids into either membrane or storage lipids is affected by the cellular growth rate, which shall investigated by dedicated experiments in the future.

Revealing Acyl Chain Selectivity in Saturated, Asymmetric Lipids

We were surprised by the high content of saturated lipids in YPD-grown cells (Figures 3D,E), which differs from previous studies (Klose et al., 2012; Surma et al., 2013; Casanovas et al., 2015) and which resembles lipid phenotypes observed only in genetically modified *S. cerevisiae* with a disrupted fatty acid desaturation (Pineau et al., 2009; Surma et al., 2013; Ballweg and Ernst, 2017; Budin et al., 2018). The majority of these saturated lipids contain a medium fatty acyl chain (C10:0 or C12:0) paired with a second, long fatty acyl chain (C16:0 or C18:0). Such asymmetric, saturated lipids at even higher abundances have been recently identified in *Schizosaccharomyces japonicus* (Makarova et al., 2020). The length difference of the two acyl

chains may allow for an interdigitation of the acyl chains, which increases lipid packing, whilst maintaining a fluid bilayer (Xu and Huang, 1987; Schram and Thompson, 1995; Makarova et al., 2020). This way, the asymmetric lipids can provide an alternative handle to balance competing demands in the homeostasis of physicochemical membrane properties, e.g., by maintaining membrane barrier function whilst increasing membrane fluidity (Lande et al., 1995; Schram and Thompson, 1995; Radanović et al., 2018). This may become very relevant under conditions when medium-chain fatty acids accumulate in the cell and/or when the desaturation of long-chain fatty acids via the fatty acid desaturase Ole1 becomes limiting (Stukey et al., 1989; Ballweg and Ernst, 2017). How precisely saturated, asymmetric lipids provide a feedback to the production of unsaturated fatty acid via the lipid saturation sensor Mga2 (Covino et al., 2016; Ballweg et al., 2020) is an interesting question for the future. Our finding that asymmetric, saturated lipids can be observed at substantial levels in *S. cerevisiae* suggests that such lipids may play a much wider role than previously anticipated.

The machineries and mechanisms mediating a finely tuned production of asymmetric lipids in *S. cerevisiae* and other fungi are still unknown, but tracking the origin and fate of medium chain fatty acids might help identifying them. Our finding that saturated, asymmetric lipids are produced even upon cultivation in fatty acid-free SCD medium (Figure 3G) suggests that at least a significant portion of the esterified medium chain fatty acids originate from *de novo* biosynthesis. The fungal fatty acid synthase produces fatty acids of different lengths determined by the cellular ratio of acetyl-CoA to malonyl-CoA, which are used for priming and fatty acid elongation (Sumper et al., 1969; Okuyama et al., 1979; Heil et al., 2019). It is possible that a different product spectrum of the fatty acid synthase contributes to the production and abundance of asymmetric lipids in *S. cerevisiae*. Intriguingly, a hyper-active mutation in the rate-limiting enzyme for fatty acid biosynthesis leads to an increased production of malonyl-CoA and increased average fatty acyl chain length in glycerophospholipids (Hofbauer et al., 2014). In line with previous reports (Makarova et al., 2020), we therefore propose that the profile of *de novo* synthesized fatty acids is a major determinant for the abundance of saturated, asymmetric lipids.

Our finding that saturated, medium fatty acyl chain pair almost exclusive with saturated, but not with the more abundant unsaturated fatty acyl chains (Figures 3E–G), reveals a remarkable, inherent selectivity in the biosynthesis and metabolism of asymmetric lipids. It will be intriguing to learn about the processes that contribute to this selectivity and to dissect the contribution of fatty acid biosynthesis and activation, acyl transferases, phospholipases, and substrate channeling (Henry et al., 2012; Ernst et al., 2016; Patton-Vogt and de Kroon, 2020). Because the key enzymes of lipid metabolism and the principle mechanisms of membrane adaptivity are conserved throughout evolution (Henry et al., 2012; Ernst et al., 2016), it will be intriguing to test if similarly specific mechanisms of acyl chain pairing are at work in organisms from bacteria to humans.

CONCLUSION

The UPR has been implicated in a wide array of pathologies and is gaining increasing attention as a potential drug target (Hetz et al., 2019). While the fatal consequences of prolonged ER stress have been intensively studied (Tabas and Ron, 2011), the molecular events that cause chronic UPR activation remain poorly characterized. In the future, it will be crucial to develop new tools and assays to better understand the signals that perpetuate ER stress. Only quantitative information on the ER load with unfolded proteins and on the composition of the ER membrane during acute and prolonged ER stress can unambiguously establish the relative importance of signals from the ER lumen and the ER membrane. As a first step in this direction, we have studied the impact of different media and two UPR-activating, proteotoxic drugs on the cellular lipid composition. Our data will provide an important reference point for future endeavors, and has already proven useful for highlighting possible connections between the cellular growth rate, proteotoxic ER stress, and lipid metabolism. Our finding that *S. cerevisiae* produces asymmetric lipids with two saturated acyl chains of different lengths provides evidence for a remarkable specificity in pairing of saturated fatty acyl chains.

DATA AVAILABILITY STATEMENT

All datasets presented in this study are included in the article/**Supplementary Material**.

REFERENCES

- Adams, C. J., Kopp, M. C., Larburu, N., Nowak, P. R., and Ali, M. M. U. (2019). Structure and molecular mechanism of ER stress signaling by the unfolded protein response signal activator IRE1. *Front. Mol. Biosci.* 6:11. doi: 10.3389/fmolb.2019.00011
- Aviram, N., and Schuldiner, M. (2017). Targeting and translocation of proteins to the endoplasmic reticulum at a glance. *J. Cell Sci.* 130, 4079–4085. doi: 10.1242/jcs.204396
- Azim, M., and Surani, H. (1979). Glycoprotein synthesis and inhibition of glycosylation by tunicamycin in preimplantation mouse embryos: compaction and trophoblast adhesion. *Cell* 18, 217–227. doi: 10.1016/0092-8674(79)90370-2
- Ballweg, S., and Ernst, R. (2017). Control of membrane fluidity: the OLE pathway in focus. *Biol. Chem.* 398, 215–228. doi: 10.1515/hsz-2016-0277
- Ballweg, S., Sezgin, E., Doktorova, M., Covino, R., Reinhard, J., Wunnicke, D., et al. (2020). Regulation of lipid saturation without sensing membrane fluidity. *Nat. Commun.* 11:756. doi: 10.1038/s41467-020-14528-1
- Bernales, S., McDonald, K. L., and Walter, P. (2006). Autophagy counterbalances endoplasmic reticulum expansion during the unfolded protein response. *PLoS Biol.* 4:e423. doi: 10.1371/journal.pbio.0040423
- Bernales, S., Schuck, S., and Walter, P. (2007). ER-Phagy: selective autophagy of the endoplasmic reticulum. *Autophagy* 3, 285–287. doi: 10.4161/auto.3930
- Bigay, J., and Antony, B. (2012). Curvature, lipid packing, and electrostatics of membrane organelles: defining cellular territories in determining specificity. *Dev. Cell* 23, 886–895. doi: 10.1016/j.devcel.2012.10.009
- Budin, I., de Rond, T., Chen, Y., Chan, L. J. G., Petzold, C. J., and Keasling, J. D. (2018). Viscous control of cellular respiration by membrane lipid composition. *Science* 362, 1186–1189. doi: 10.1126/science.aat7925

AUTHOR CONTRIBUTIONS

RE conceived and designed the experiments. JR, CM, KV, MS, and CK performed the experiments. JR, CM, KV, and TR analyzed the data. JR, MS, and CK contributed reagents, materials, and analysis tools. JR, CM, TR, and RE wrote the manuscript. All authors contributed to the article and approved the submitted version.

FUNDING

This work was supported by the Volkswagen Foundation (Life?, 93089 to RE), European Commission (ERC-CoG 866011), and the Deutsche Forschungsgemeinschaft (SFB894, ‘Ca²⁺ Signals: Molecular Mechanisms and Integrative Functions’ and SFB807, ‘Transport and Communication across biological membranes’ to RE).

ACKNOWLEDGMENTS

The authors would like to thank Ilya Levental, James Sáenz, Maya Schuldiner, and Toon de Kroon for insightful discussions.

SUPPLEMENTARY MATERIAL

The Supplementary Material for this article can be found online at: <https://www.frontiersin.org/articles/10.3389/fcell.2020.00756/full#supplementary-material>

- Casanovas, A., Sprenger, R. R., Tarasov, K., Ruckerbauer, D. E., Hannibal-Bach, H. K., Zanghellini, J., et al. (2015). Quantitative analysis of proteome and lipidome dynamics reveals functional regulation of global lipid metabolism. *Chem. Biol.* 22, 412–425. doi: 10.1016/j.chembiol.2015.02.007
- Covino, R., Ballweg, S., Stordeur, C., Michaelis, J. B., Puth, K., Wernig, F., et al. (2016). A eukaryotic sensor for membrane lipid saturation. *Mol. Cell* 63, 49–59. doi: 10.1016/j.molcel.2016.05.015
- Covino, R., Hummer, G., and Ernst, R. (2018). Integrated functions of membrane property sensors and a hidden side of the unfolded protein response. *Mol. Cell* 71, 458–467. doi: 10.1016/j.molcel.2018.07.019
- Cox, J. S., Shamu, C. E., and Walter, P. (1993). Transcriptional induction of genes encoding endoplasmic reticulum resident proteins requires a transmembrane protein kinase. *Cell* 73, 1197–1206. doi: 10.1016/0092-8674(93)90648-A
- Cox, J. S., and Walter, P. (1996). A novel mechanism for regulating activity of a transcription factor that controls the unfolded protein response. *Cell* 87, 391–404. doi: 10.1016/s0092-8674(00)81360-4
- De Kroon, A. I. P. M., Rijken, P. J., and De Smet, C. H. (2013). Checks and balances in membrane phospholipid class and acyl chain homeostasis, the yeast perspective. *Prog. Lipid Res.* 52, 374–394. doi: 10.1016/j.plipres.2013.04.006
- Dymond, J. S. (2013). *Saccharomyces cerevisiae* growth media. *Methods Enzymol.* 533, 191–204. doi: 10.1016/B978-0-12-420067-8.00012-X
- Ejsing, C. S., Sampaio, J. L., Surendranath, V., Duchoslav, E., Ekroos, K., Klemm, R. W., et al. (2009). Global analysis of the yeast lipidome by quantitative shotgun mass spectrometry. *Proc. Natl. Acad. Sci. U.S.A.* 106, 2136–2141. doi: 10.1073/pnas.0811700106
- Ernst, R., Ballweg, S., and Levental, I. (2018). Cellular mechanisms of physicochemical membrane homeostasis. *Curr. Opin. Cell Biol.* 53, 44–51. doi: 10.1016/j.ceb.2018.04.013

- Ernst, R., Ejsing, C. S., and Antonny, B. (2016). Homeoviscous adaptation and the regulation of membrane lipids. *J. Mol. Biol.* 428, 4776–4791. doi: 10.1016/j.jmb.2016.08.013
- Fonseca, S. G., Burcin, M., Gromada, J., and Urano, F. (2009). Endoplasmic reticulum stress in β -cells and development of diabetes. *Curr. Opin. Pharmacol.* 9, 763–770. doi: 10.1016/j.coph.2009.07.003
- Fu, S., Yang, L., Li, P., Hofmann, O., Dicker, L., Hide, W., et al. (2011). Aberrant lipid metabolism disrupts calcium homeostasis causing liver endoplasmic reticulum stress in obesity. *Nature* 473, 528–531. doi: 10.1038/nature09968
- Fun, X. H., and Thibault, G. (2020). Lipid bilayer stress and proteotoxic stress-induced unfolded protein response deploy divergent transcriptional and non-transcriptional programmes. *Biochim. Biophys. Acta* 1865:158449. doi: 10.1016/j.bbali.2019.04.009
- Gaspar, M. L., Hofbauer, H. F., Kohlwein, S. D., and Henry, S. A. (2011). Coordination of storage lipid synthesis and membrane biogenesis: evidence for cross-talk between triacylglycerol metabolism and phosphatidylinositol synthesis. *J. Biol. Chem.* 286, 1696–1708. doi: 10.1074/jbc.M110.172296
- Goder, V., Alanis-Dominguez, E., and Bustamante-Sequeiros, M. (2020). Lipids and their (un)known effects on ER-associated protein degradation (ERAD). *Biochim. Biophys. Acta* 1865:158488. doi: 10.1016/j.bbali.2019.06.014
- Halbleib, K., Pesek, K., Covino, R., Hofbauer, H. F., Wunnicke, D., Hännel, I., et al. (2017). Activation of the unfolded protein response by lipid bilayer stress. *Mol. Cell* 67, 673–684.e8. doi: 10.1016/j.molcel.2017.06.012
- Han, X. (2016). Lipidomics for studying metabolism. *Nat. Rev. Endocrinol.* 12, 668–679. doi: 10.1038/nrendo.2016.98
- Hannich, J. T., Umehayashi, K., and Riezman, H. (2011). Distribution and functions of sterols and sphingolipids. *Cold Spring Harb. Perspect. Biol.* 3:a004762. doi: 10.1101/cshperspect.a004762
- Hansch, M., Ruckerbauer, D. E., Chauhan, N., Hofbauer, H. F., Krahulec, S., Nidetzky, B., et al. (2012). Nutritional requirements of the BY series of *Saccharomyces cerevisiae* strains for optimum growth. *FEMS Yeast Res.* 12, 796–808. doi: 10.1111/j.1567-1364.2012.00830.x
- Harayama, T., and Riezman, H. (2018). Understanding the diversity of membrane lipid composition. *Nat. Rev. Mol. Cell Biol.* 19, 281–296. doi: 10.1038/nrm.2017.138
- Heil, C. S., Wehrheim, S. S., Paithankar, K. S., and Grininger, M. (2019). Fatty acid biosynthesis: chain-length regulation and control. *ChemBioChem* 20, 2298–2321. doi: 10.1002/cbic.201800809
- Henry, S. A., Kohlwein, S. D., and Carman, G. M. (2012). Metabolism and regulation of glycerolipids in the yeast *Saccharomyces cerevisiae*. *Genetics* 190, 317–349. doi: 10.1534/genetics.111.130286
- Herzog, R., Schuhmann, K., Schwudke, D., Sampaio, J. L., Bornstein, S. R., Schroeder, M., et al. (2012). LipidXplorer: a software for consensual cross-platform lipidomics. *PLoS One* 7:e29851. doi: 10.1371/journal.pone.0029851
- Herzog, R., Schwudke, D., Schuhmann, K., Sampaio, J. L., Bornstein, S. R., Schroeder, M., et al. (2011). A novel informatics concept for high-throughput shotgun lipidomics based on the molecular fragmentation query language. *Genome Biol.* 12:R8. doi: 10.1186/gb-2011-12-1-r8
- Hetz, C., Axten, J. M., and Patterson, J. B. (2019). Pharmacological targeting of the unfolded protein response for disease intervention. *Nat. Chem. Biol.* 15, 764–775. doi: 10.1038/s41589-019-0326-2
- Hofbauer, H. F., Gecht, M., Fischer, S. C., Seybert, A., Frangakis, A. S., Stelzer, E. H. K., et al. (2018). The molecular recognition of phosphatidic acid by an amphipathic helix in Opi1. *J. Cell Biol.* 217, 3109–3126. doi: 10.1083/jcb.201802027
- Hofbauer, H. F., Schopf, F. H., Schleifer, H., Knittelfelder, O. L., Pieber, B., Rechberger, G. N., et al. (2014). Regulation of gene expression through a transcriptional repressor that senses acyl-chain length in membrane phospholipids. *Dev. Cell* 29, 729–739. doi: 10.1016/j.devcel.2014.04.025
- Hou, N. S., Gutschmidt, A., Choi, D. Y., Pather, K., Shi, X., Watts, J. L., et al. (2014). Activation of the endoplasmic reticulum unfolded protein response by lipid disequilibrium without disturbed proteostasis *in vivo*. *Proc. Natl. Acad. Sci. U.S.A.* 111, E2271–E2280. doi: 10.1073/pnas.1318262111
- Hsu, J. W., Tang, P. H., Wang, I. H., Liu, C. L., Chen, W. H., Tsai, P. C., et al. (2016). Unfolded protein response regulates yeast small GTPase Arl1p activation at late Golgi via phosphorylation of Arf GEF Syt1p. *Proc. Natl. Acad. Sci. U.S.A.* 113, E1683–E1690. doi: 10.1073/pnas.1518260113
- Jonikas, M. C., Collins, S. R., Denic, V., Oh, E., Quan, E. M., Schmid, V., et al. (2009). Comprehensive characterization of genes required for protein folding in the endoplasmic reticulum. *Science* 323, 1693–1697. doi: 10.1126/science.1167983
- Karagöz, G. E., Acosta-Alvear, D., Nguyen, H. T., Lee, C. P., Chu, F., and Walter, P. (2017). An unfolded protein-induced conformational switch activates mammalian IRE1. *eLife* 6:e30700. doi: 10.7554/eLife.30700
- Kaufman, R. J. (2002). Orchestrating the unfolded protein response in health and disease. *J. Clin. Invest.* 110, 1389–1398. doi: 10.1172/jci16886
- Kawahara, T., Yanagi, H., Yura, T., and Mori, K. (1997). Endoplasmic reticulum stress-induced mRNA splicing permits synthesis of transcription factor Hac1p/Ern4p that activates the unfolded protein response. *Mol. Biol. Cell* 8, 1845–1862. doi: 10.1091/mbc.8.10.1845
- Kimata, Y., Ishiwata-Kimata, Y., Ito, T., Hirata, A., Suzuki, T., Oikawa, D., et al. (2007). Two regulatory steps of ER-stress sensor Ire1 involving its cluster formation and interaction with unfolded proteins. *J. Cell Biol.* 179, 75–86. doi: 10.1083/jcb.200704166
- Kimata, Y., and Kohno, K. (2011). Endoplasmic reticulum stress-sensing mechanisms in yeast and mammalian cells. *Curr. Opin. Cell Biol.* 23, 135–142. doi: 10.1016/j.ceb.2010.10.008
- Klemm, R. W., Ejsing, C. S., Surma, M. A., Kaiser, H. J., Gerl, M. J., Sampaio, J. L., et al. (2009). Segregation of sphingolipids and sterols during formation of secretory vesicles at the trans-Golgi network. *J. Cell Biol.* 185, 601–612. doi: 10.1083/jcb.200901145
- Klose, C., Surma, M. A., Gerl, M. J., Meyenhofer, F., Shevchenko, A., and Simons, K. (2012). Flexibility of a eukaryotic lipidome - insights from yeast lipidomics. *PLoS One* 7:e35063. doi: 10.1371/journal.pone.0035063
- Kohlwein, S. D., Veenhuis, M., and van der Klei, I. J. (2013). Lipid droplets and peroxisomes: key players in cellular lipid homeostasis or a matter of fat-store'em up or burn'em down. *Genetics* 193, 1–50. doi: 10.1534/genetics.112.143362
- Korenykh, A. V., Egea, P. F., Korostelev, A. A., Finer-Moore, J., Zhang, C., Shokat, K. M., et al. (2009). The unfolded protein response signals through high-order assembly of Ire1. *Nature* 457, 687–693. doi: 10.1038/nature07661
- Lande, M. B., Donovan, J. M., and Zeidel, M. L. (1995). The relationship between membrane fluidity and permeabilities to water, solutes, ammonia, and protons. *J. Gen. Physiol.* 106, 67–84. doi: 10.1085/jgp.106.1.67
- Lee, A. G. (2004). How lipids affect the activities of integral membrane proteins. *Biochim. Biophys. Acta* 1666, 62–87. doi: 10.1016/j.bbame.2004.05.012
- Levental, I., Lingwood, D., Grzybek, M., Coskun, Ü., and Simons, K. (2010). Palmitoylation regulates raft affinity for the majority of integral raft proteins. *Proc. Natl. Acad. Sci. U.S.A.* 107, 22050–22054. doi: 10.1073/pnas.1016184107
- Levental, K. R., Malmberg, E., Symons, J. L., Fan, Y. Y., Chapkin, R. S., Ernst, R., et al. (2020). Lipidomic and biophysical homeostasis of mammalian membranes counteracts dietary lipid perturbations to maintain cellular fitness. *Nat. Commun.* 11:1339. doi: 10.1038/s41467-020-15203-1
- Liebisch, G., Binder, M., Schifferer, R., Langmann, T., Schulz, B., and Schmitz, G. (2006). High throughput quantification of cholesterol and cholesteryl ester by electrospray ionization tandem mass spectrometry (ESI-MS/MS). *Biochim. Biophys. Acta* 1761, 121–128. doi: 10.1016/j.bbali.2005.12.007
- Loewen, C. J. R. (2004). Phospholipid metabolism regulated by a transcription factor sensing phosphatidic acid. *Science* 304, 1644–1647. doi: 10.1126/science.1096083
- Lorent, J. H., Diaz-Rohrer, B., Lin, X., Spring, K., Gorge, A. A., Levental, K. R., et al. (2017). Structural determinants and functional consequences of protein affinity for membrane rafts. *Nat. Commun.* 8:1219. doi: 10.1038/s41467-017-01328-3
- Makarova, M., Peter, M., Balogh, G., Glatz, A., MacRae, J. I., Lopez Mora, N., et al. (2020). Delineating the rules for structural adaptation of membrane-associated proteins to evolutionary changes in membrane lipidome. *Curr. Biol.* 30, 367–380.e8. doi: 10.1016/j.cub.2019.11.043
- Mesecke, N., Terziyska, N., Kozany, C., Baumann, F., Neupert, W., Hell, K., et al. (2005). A disulfide relay system in the intermembrane space of mitochondria that mediates protein import. *Cell* 121, 1059–1069. doi: 10.1016/j.cell.2005.04.011

- Mori, K., Kawahara, T., Yoshida, H., Yanagi, H., and Yura, T. (1996). Signalling from endoplasmic reticulum to nucleus: transcription factor with a basic-leucine zipper motif is required for the unfolded protein-response pathway. *Genes Cells* 1, 803–817. doi: 10.1046/j.1365-2443.1996.d01-274.x
- Nikawa, J., and Yamashita, S. (1992). IRE1 encodes a putative protein kinase containing a membrane-spanning domain and is required for inositol phototrophy in *Saccharomyces cerevisiae*. *Mol. Microbiol.* 6, 1441–1446. doi: 10.1111/j.1365-2958.1992.tb00864.x
- Novick, P., Field, C., and Schekman, R. (1980). Identification of 23 complementation groups required for post-translational events in the yeast secretory pathway. *Cell* 21, 205–215. doi: 10.1016/0092-8674(80)90128-2
- Okuyama, H., Saito, M., Joshi, V. C., Gunsberg, S., and Wakil, S. J. (1979). Regulation by temperature of the chain length of fatty acids in yeast. *J. Biol. Chem.* 254, 12281–12284.
- Patton-Vogt, J., and de Kroon, A. I. P. M. (2020). Phospholipid turnover and acyl chain remodeling in the yeast ER. *Biochim. Biophys. Acta* 1865:158462. doi: 10.1016/j.bbali.2019.05.006
- Phillips, R., Ursell, T., Wiggins, P., and Sens, P. (2009). Emerging roles for lipids in shaping membrane-protein function. *Nature* 459, 379–385. doi: 10.1038/nature08147
- Pincus, D., Chevalier, M. W., Aragón, T., van Anken, E., Vidal, S. E., El-Samad, H., et al. (2010). BiP binding to the ER-stress sensor Ire1 tunes the homeostatic behavior of the unfolded protein response. *PLoS Biol.* 8:e1000415. doi: 10.1371/journal.pbio.1000415
- Pineau, L., Colas, J., Dupont, S., Beney, L., Fleurat-Lessard, P., Berjeaud, J. M., et al. (2009). Lipid-induced ER stress: synergistic effects of sterols and saturated fatty acids. *Traffic* 10, 673–690. doi: 10.1111/j.1600-0854.2009.00903.x
- Preissler, S., and Ron, D. (2019). Early events in the endoplasmic reticulum unfolded protein response. *Cold Spring Harb. Perspect. Biol.* 11:a033894. doi: 10.1101/cshperspect.a033894
- Promlek, T., Ishiwata-Kimata, Y., Shido, M., Sakuramoto, M., Kohno, K., and Kimata, Y. (2011). Membrane aberrancy and unfolded proteins activate the endoplasmic reticulum stress sensor Ire1 in different ways. *Mol. Biol. Cell* 22, 3520–3532. doi: 10.1091/mbc.E11-04-0295
- Radanović, T., Reinhard, J., Ballweg, S., Pesek, K., and Ernst, R. (2018). An emerging group of membrane property sensors controls the physical state of organellar membranes to maintain their identity. *Bioessays* 40:e1700250. doi: 10.1002/bies.201700250
- Schram, V., and Thompson, T. E. (1995). Interdigitation does not affect translational diffusion of lipids in liquid crystalline bilayers. *Biophys. J.* 69, 2517–2520. doi: 10.1016/s0006-3495(95)80122-0
- Schuck, S., Prinz, W. A., Thorn, K. S., Voss, C., and Walter, P. (2009). Membrane expansion alleviates endoplasmic reticulum stress independently of the unfolded protein response. *J. Cell Biol.* 187, 525–536. doi: 10.1083/jcb.200907074
- Sezgin, E., Levental, I., Mayor, S., and Eggeling, C. (2017). The mystery of membrane organization: composition, regulation and roles of lipid rafts. *Nat. Rev. Mol. Cell Biol.* 18, 361–374. doi: 10.1038/nrm.2017.16
- Sherman, F. (2002). Getting started with yeast. *Methods Enzymol.* 350, 3–41. doi: 10.1016/S0076-6879(02)50954-X
- Shevchenko, A., and Simons, K. (2010). Lipidomics: coming to grips with lipid diversity. *Nat. Rev. Mol. Cell Biol.* 11, 593–598. doi: 10.1038/nrm2934
- Stordeur, C., Puth, K., Sáenz, J. P., and Ernst, R. (2014). Crosstalk of lipid and protein homeostasis to maintain membrane function. *Biol. Chem.* 395, 313–326. doi: 10.1515/hsz-2013-0235
- Stukey, J. E., McDonough, V. M., and Martin, C. E. (1989). Isolation and characterization of OLE1, a gene affecting fatty acid desaturation from *Saccharomyces cerevisiae*. *J. Biol. Chem.* 264, 16537–16544.
- Sumper, M., Riepertinger, C., Lynen, F., and Oesterheld, D. (1969). Die Synthese verschiedener Carbonsäuren durch den Multienzymkomplex der Fettsäuresynthese aus Hefe und die Erklärung ihrer Bildung. *Eur. J. Biochem.* 10, 377–387. doi: 10.1111/j.1432-1033.1969.tb00701.x
- Surma, M. A., Herzog, R., Vasilij, A., Klose, C., Christinat, N., Morin-Rivron, D., et al. (2015). An automated shotgun lipidomics platform for high throughput, comprehensive, and quantitative analysis of blood plasma intact lipids. *Eur. J. Lipid Sci. Technol.* 117, 1540–1549. doi: 10.1002/ejlt.201500145
- Surma, M. A., Klose, C., Klemm, R. W., Ejsing, C. S., and Simons, K. (2011). Generic sorting of raft lipids into secretory vesicles in yeast. *Traffic* 12, 1139–1147. doi: 10.1111/j.1600-0854.2011.01221.x
- Surma, M. A., Klose, C., Peng, D., Shales, M., Mrejen, C., Stefanko, A., et al. (2013). A lipid E-MAP identifies Ubx2 as a critical regulator of lipid saturation and lipid bilayer stress. *Mol. Cell* 51, 519–530. doi: 10.1016/j.molcel.2013.06.014
- Tabas, I., and Ron, D. (2011). Integrating the mechanisms of apoptosis induced by endoplasmic reticulum stress. *Nat. Cell Biol.* 13, 184–190. doi: 10.1038/ncb0311-184
- Thibault, G., Shui, G., Kim, W., McAlister, G. C., Ismail, N., Gygi, S. P., et al. (2012). The membrane stress response buffers lethal effects of lipid disequilibrium by reprogramming the protein homeostasis network. *Mol. Cell* 48, 16–27. doi: 10.1016/j.molcel.2012.08.016
- Tran, D. M., Ishiwata-Kimata, Y., Mai, T. C., Kubo, M., and Kimata, Y. (2019). The unfolded protein response alongside the diauxic shift of yeast cells and its involvement in mitochondria enlargement. *Sci. Rep.* 9:12780. doi: 10.1038/s41598-019-49146-5
- Travers, K. J., Patil, C. K., Wodicka, L., Lockhart, D. J., Weissman, J. S., and Walter, P. (2000). Functional and genomic analyses reveal an essential coordination between the unfolded protein response and ER-associated degradation. *Cell* 101, 249–258. doi: 10.1016/S0092-8674(00)80835-1
- Uhlén, M., Fagerberg, L., Hallström, B. M., Lindskog, C., Oksvold, P., Mardinoglu, A., et al. (2015). Tissue-based map of the human proteome. *Science* 347:1260419. doi: 10.1126/science.1260419
- van Meer, G., Voelker, D. R., and Feigenson, G. W. (2008). Membrane lipids: where they are and how they behave. *Nat. Rev. Mol. Cell Biol.* 9, 112–124. doi: 10.1038/nrm2330
- Volmer, R., and Ron, D. (2015). Lipid-dependent regulation of the unfolded protein response. *Curr. Opin. Cell Biol.* 33, 67–73. doi: 10.1016/j.cob.2014.12.002
- Walter, P., and Ron, D. (2011). The unfolded protein response: from stress pathway to homeostatic regulation. *Science* 334, 1081–1086. doi: 10.1126/science.1209038
- Wang, M., and Kaufman, R. J. (2014). The impact of the endoplasmic reticulum protein-folding environment on cancer development. *Nat. Rev. Cancer* 14, 581–597. doi: 10.1038/nrc3800
- Wang, S., and Kaufman, R. J. (2012). The impact of the unfolded protein response on human disease. *J. Cell Biol.* 197, 857–867. doi: 10.1083/jcb.201110131
- Wolf, D. H., and Schäfer, A. (2006). CPY* and the power of yeast genetics in the elucidation of quality control and associated protein degradation of the endoplasmic reticulum. *Curr. Top. Microbiol. Immunol.* 300, 41–56. doi: 10.1007/3-540-28007-3_3
- Xu, H., and Huang, C. H. (1987). Scanning calorimetric study of fully hydrated asymmetric phosphatidylcholines with one acyl chain twice as long as the other. *Biochemistry* 26, 1036–1043. doi: 10.1021/bi00378a009

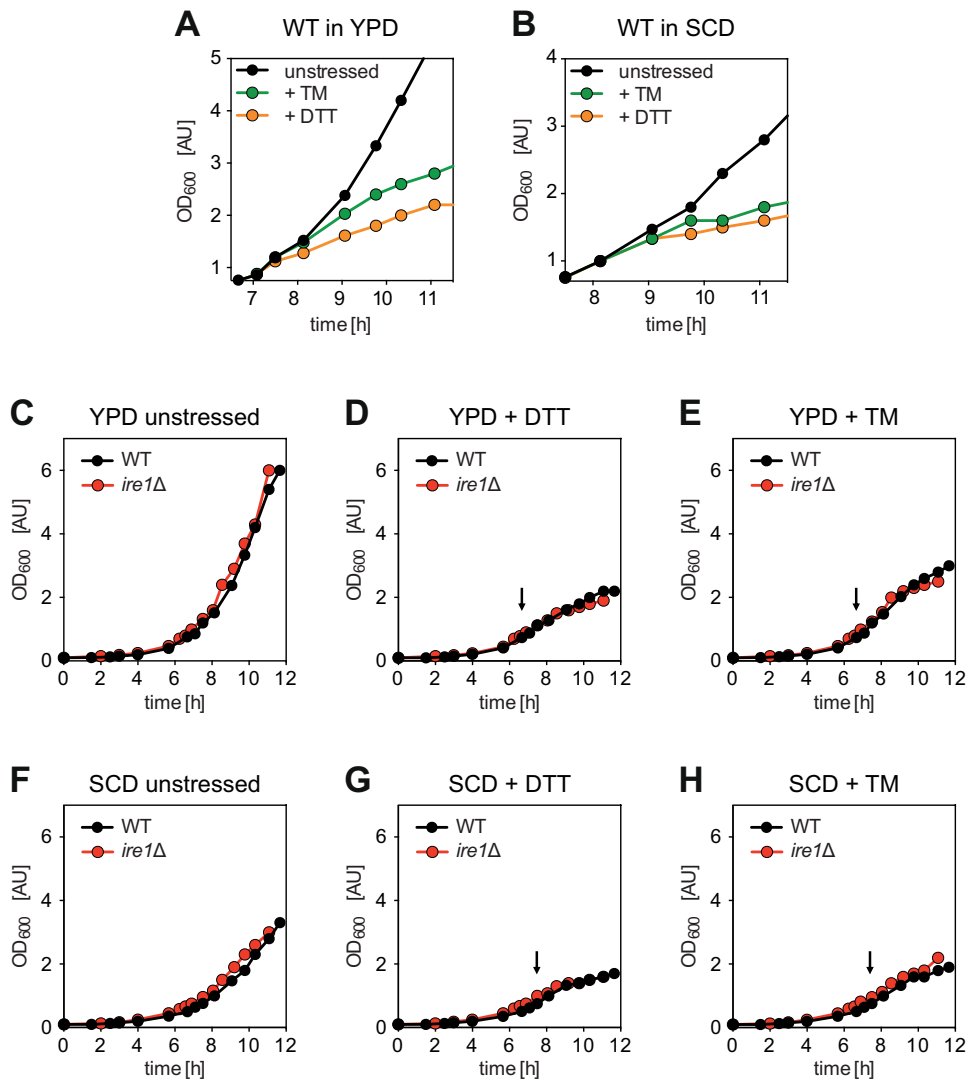
Conflict of Interest: MS and CK were employed by the company Lipotype GmbH, Dresden.

The remaining authors declare that the research was conducted in the absence of any other commercial or financial relationships that could be construed as a potential conflict of interest.

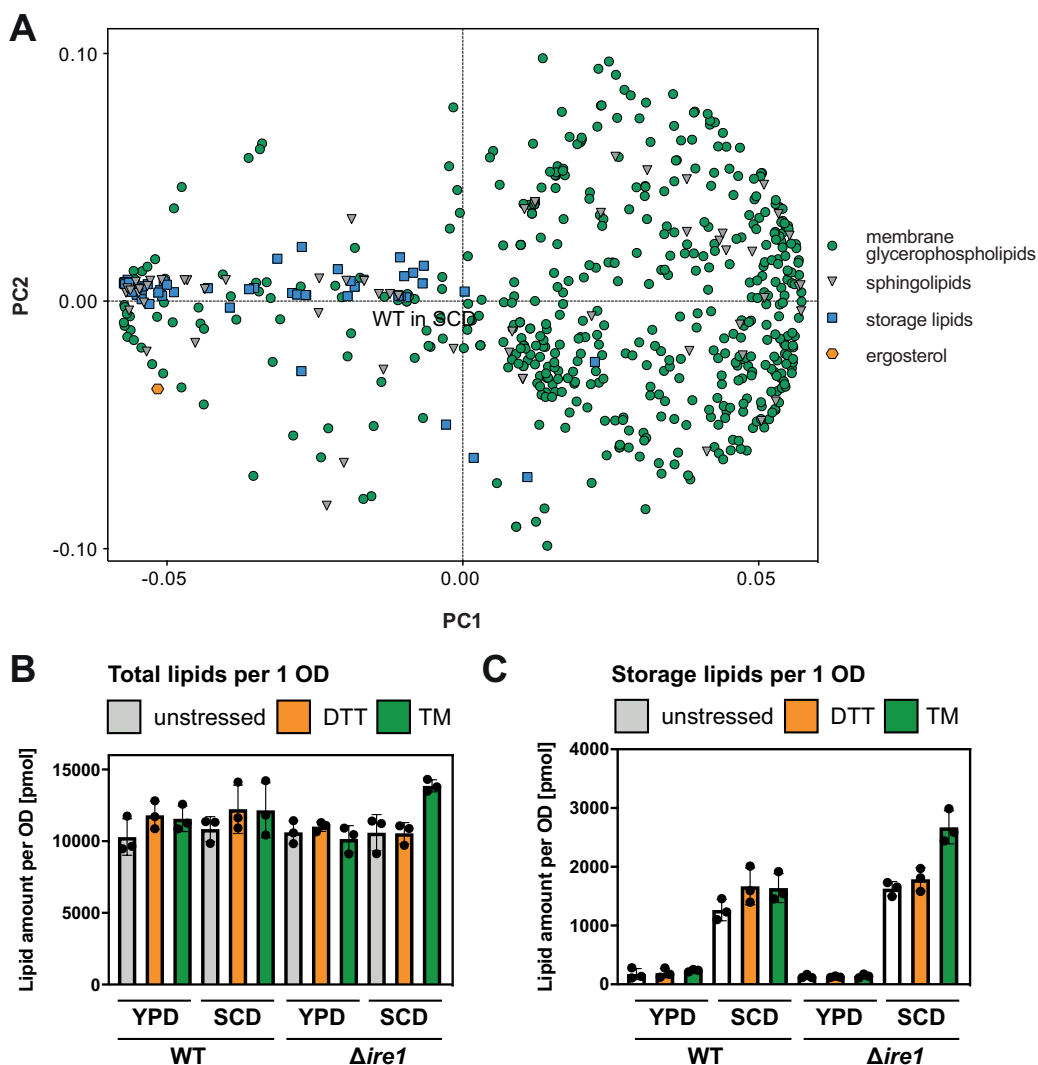
Copyright © 2020 Reinhard, Mattes, Väh, Radanović, Surma, Klose and Ernst. This is an open-access article distributed under the terms of the Creative Commons Attribution License (CC BY). The use, distribution or reproduction in other forums is permitted, provided the original author(s) and the copyright owner(s) are credited and that the original publication in this journal is cited, in accordance with accepted academic practice. No use, distribution or reproduction is permitted which does not comply with these terms.



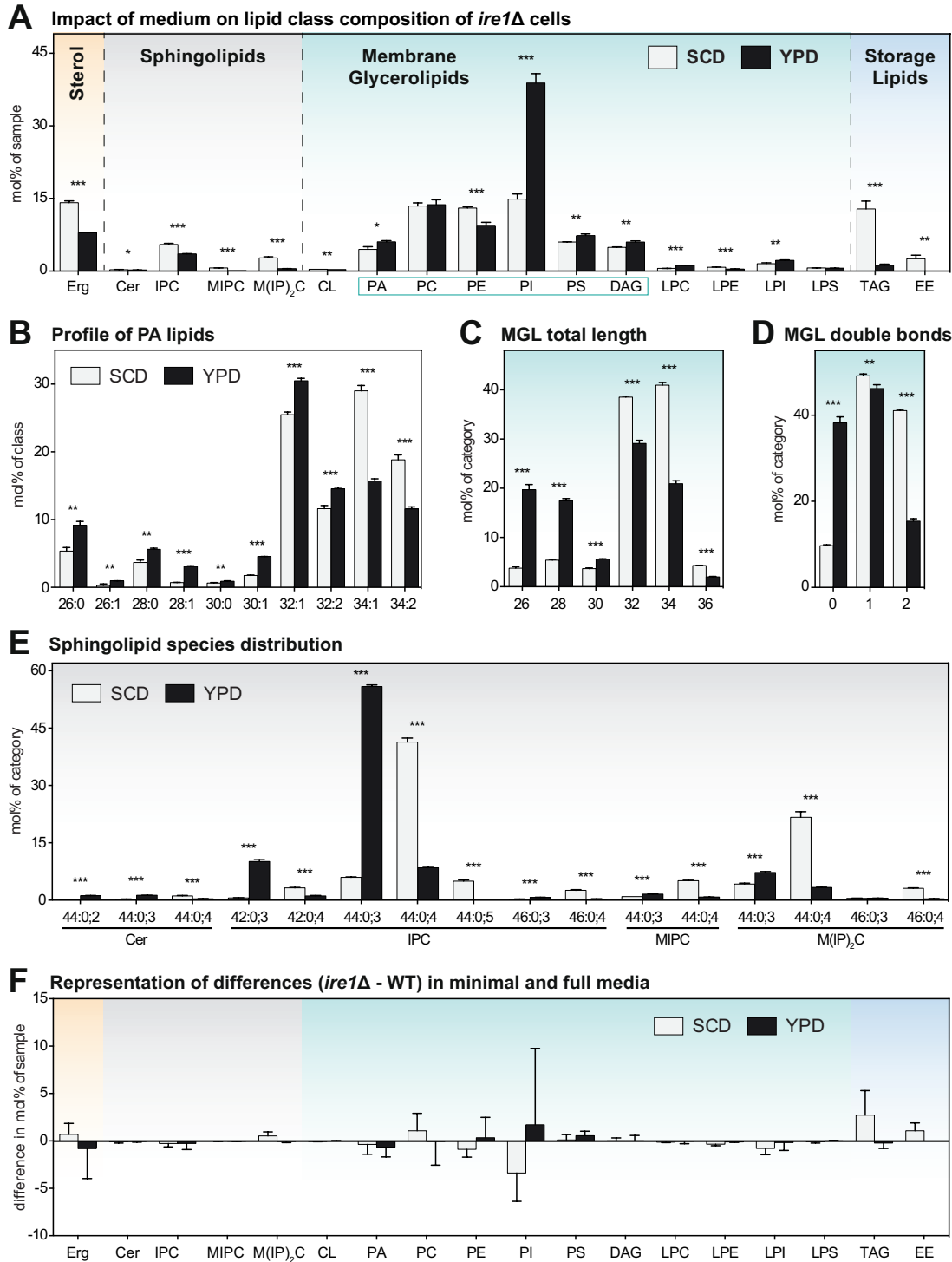
Supplementary Material



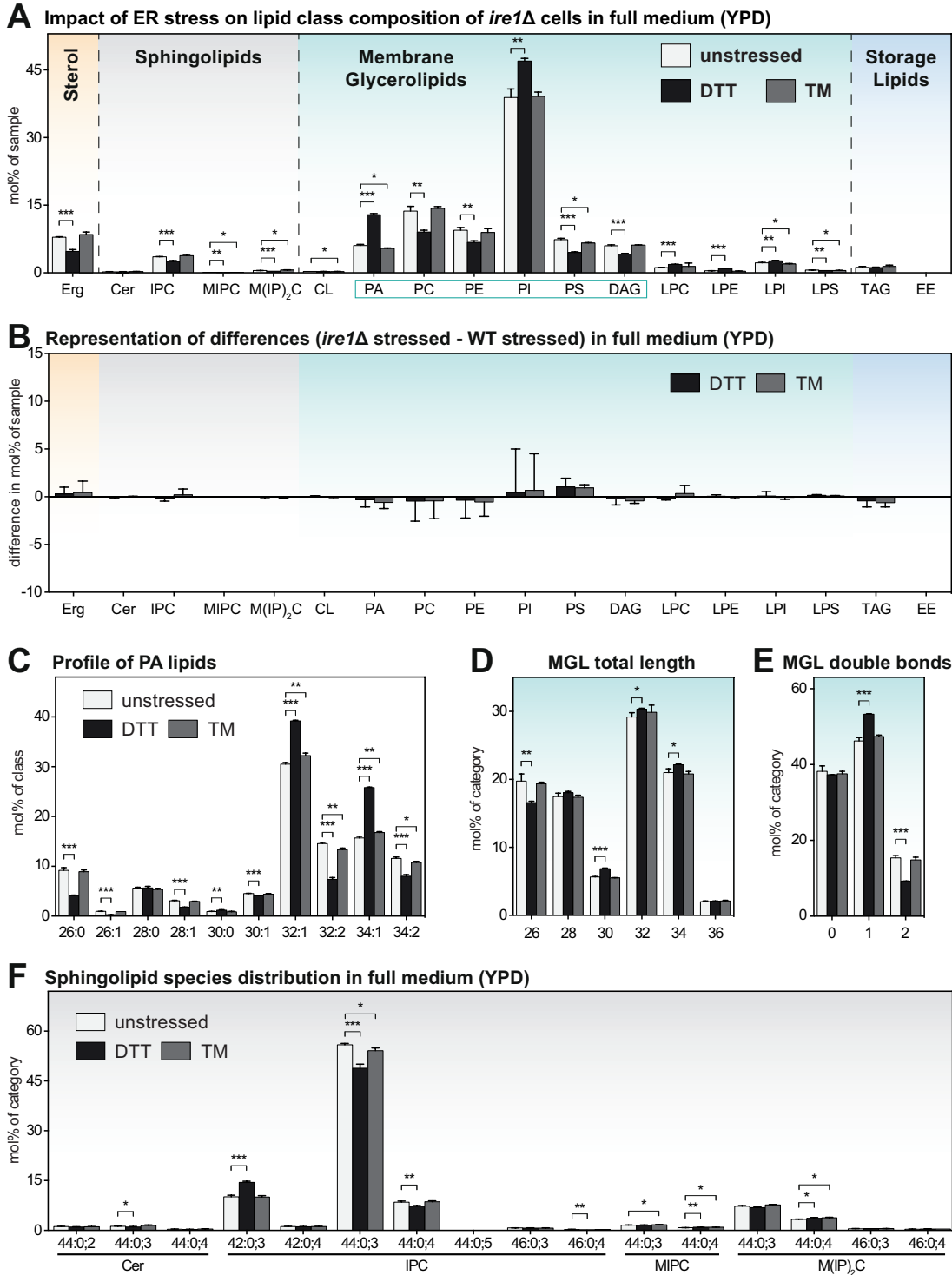
Supplementary Figure S1. Acute growth defect by UPR inducing drugs is predominantly a consequence of proteotoxic stress independent of UPR activation. (A),(B) The data are replotted from Figure 1E-F. Only a subset of data is represented with a particular focus on the period the cells were either stressed by DTT (orange), TM (green) or left untreated (black). The first datapoint corresponds to the moment of adding the proteotoxic drug. (C)-(H) The data are replotted from Figure 1E-H to highlight the similar growth of BY4741 WT and *ire1Δ* cells. The arrow indicates the moment of adding the proteotoxic drug (6.7 h and 7.5 h in YPD and SCD, respectively). All data in this Figure are derived from a single, representative experiment.



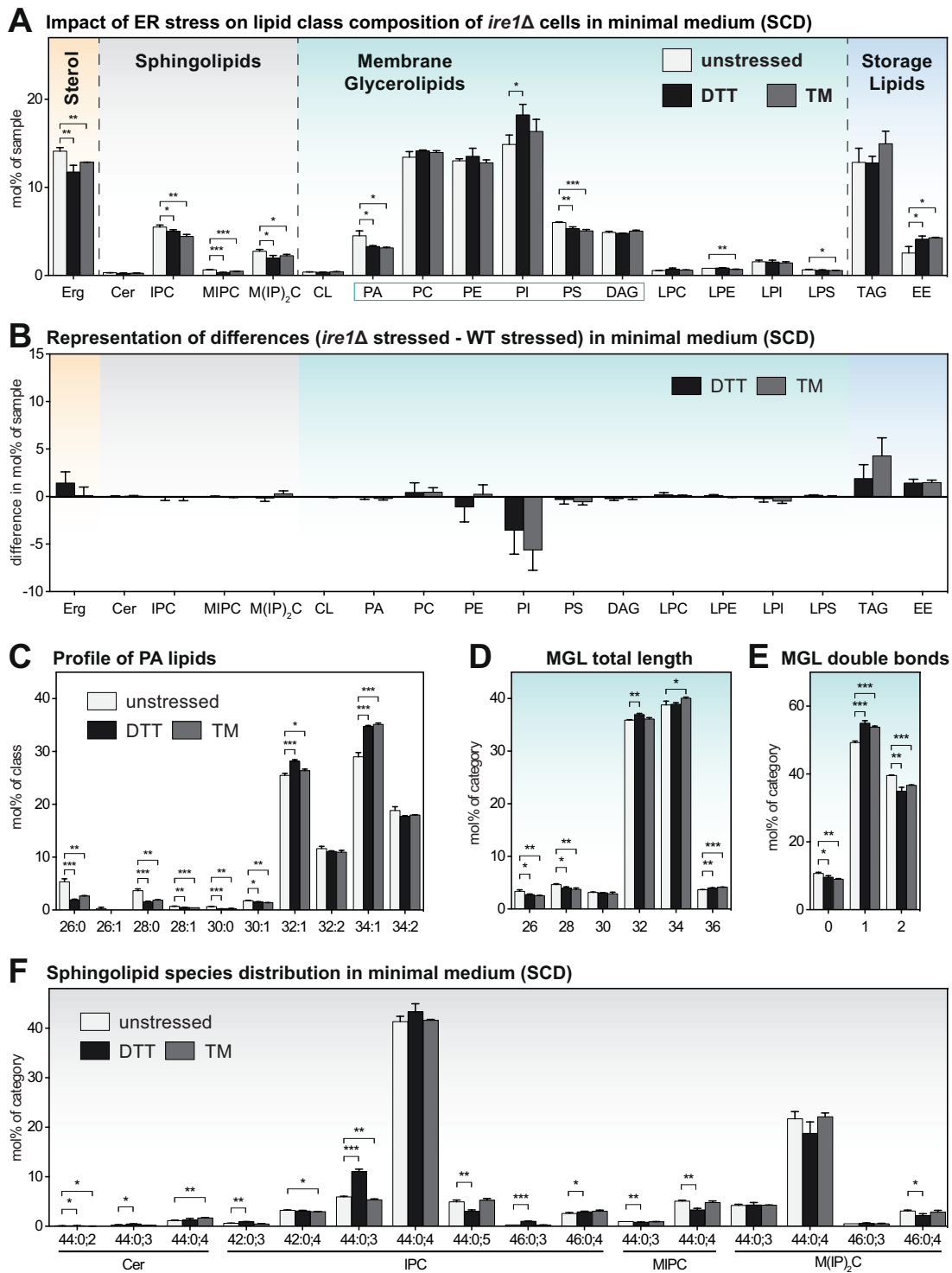
Supplementary Figure S2. Loadings plot of the entire dataset. (A) The loadings plots indicate the contribution (loadings) of individual lipid species to the principle components 1 and 2 from Figure 2B. For clarity, only membrane glycerolipids with two acyl chains were considered. The data suggest low, negative loadings of most storage lipids (SL, blue squares), sphingolipids (gray triangles) and ergosterol (orange hexagons) on principle component 1. In contrast, the majority of membrane glycerophospholipids (green circles) have low, positive loadings on principle component 1. (B),(C) The total amount of lipids (A) and the amount of storage lipids (B) quantified from 1 OD unit of cells is plotted for different cells and media as indicated. The color code indicates unstressed (gray), DTT-stressed (orange), and TM-stressed (green) cells.



Supplementary Figure S3. The lipid composition of *ire1Δ* cells in different media. A single colony of *ire1Δ* cells was used to inoculate a preculture in either minimal (SCD) or full (YPD) medium. After overnight cultivation for 21 hours, a fresh culture was inoculated to an OD₆₀₀ of 0.1. When the cells reached an OD₆₀₀ of 0.80 ± 0.05, they were cultivated for one more hour. 20 OD equivalents of these cells were harvested and analyzed by lipid mass spectrometry. The data represented by black and white bars relate to cells cultivated in full and minimal medium, respectively. **(A)** Lipid class composition in mol% of all quantified lipids in the sample organized by lipid categories. **(B)** Profile of PA lipids in mol% of the class. **(C)** Total length of lipids in a sub-category of MGLs (PA, PC, PE, PI, PS, DAG). The total length is given as the sum of carbon atoms in both fatty acyl chains in mol% of this sub-category. **(D)** Total number double bonds in a sub-category of MGLs (PA, PC, PE, PI, PS, DAG) is given as the sum of double bonds in both acyl chains and represented in mol% of this sub-category. **(E)** Profile of sphingolipids in mol% of this category. **(F)** The difference in lipid class abundance in mol% between WT and *ire1Δ* is both SCD and YPD was determined and is plotted. The difference was calculated by subtracting the lipid class abundance in WT cells from the abundance in *ire1Δ* under consideration of error propagation. The least abundant species in each panel are omitted for clarity. Each bar represents the average ± SD from n = 3 independent experiments. Statistical significance was tested by an unpaired two-tailed t-test using GraphPad Prism, *p<0.05, **p<0.01, ***p<0.001.



Supplementary Figure S4. The impact of proteotoxic stress on the lipidome of *ire1Δ* cells in full medium. A single colony of *ire1Δ* cells was used to inoculate a preculture in full (YPD) medium. After overnight cultivation for 21 hours, a fresh culture was inoculated to an OD₆₀₀ of 0.1 and then cultivated to an OD₆₀₀ of 0.80 ± 0.05. The cells were then either left untreated (white bars), stressed by the addition of either with 8 mM DTT (black bars) or 1.0 μg/ml TM (gray bars). After one additional hour of cultivation, 20 OD equivalents of these cells were harvested and analyzed by lipid mass spectrometry. **(A)** Lipid class composition in mol% of all quantified lipids in the sample organized by lipid categories. **(B)** The difference in lipid class abundance in stressed minus unstressed cells highlights the impact of DTT (black) and TM (gray) on the cellular lipid composition in full medium. The difference in abundance in mol% was calculated by subtracting the abundance in unstressed cells from the abundance in either DTT- or TM-stressed cells under consideration of error propagation. **(C)** Profile of PA lipids in mol% of the class. **(D)** Total length of lipids in a sub-category of MGLs (PA, PC, PE, PI, PS, DAG). The total length is given as the sum of carbon atoms in both fatty acyl chains in mol% of this sub-category. **(E)** Total number double bonds in a sub-category of MGLs (PA, PC, PE, PI, PS, DAG) is given as the sum of double bonds in both acyl chains and represented in mol% of this sub-category. **(F)** Profile of sphingolipids in mol% of this category. The least abundant species are omitted for clarity. Each bar represents the average ± SD from n = 3 independent experiments. Statistical significance was tested by an unpaired two-tailed t-test using GraphPad Prism, *p<0.05, **p<0.01, ***p<0.001.











Supplementary Figure S5 The impact of proteotoxic stress on the lipidome of *ire1Δ* cells in minimal medium. A single colony of *ire1Δ* cells was used to inoculate a preculture in minimal (SCD) medium. After overnight cultivation for 21 hours, a fresh culture was inoculated to an OD₆₀₀ of 0.1 and then cultivated to an OD₆₀₀ of 0.80 ± 0.05. The cells were then either left untreated (white bars), stressed by the addition of either with 8 mM DTT (black bars) or 1.0 μg/ml TM (gray bars). After one additional hour of cultivation, 20 OD equivalents of these cells were harvested and analyzed by lipid mass spectrometry. **(A)** Lipid class composition in mol% of all quantified lipids in the sample organized by lipid categories. **(B)** The difference in lipid class abundance in stressed minus unstressed cells highlights the impact of DTT (black) and TM (gray) on the cellular lipid composition in minimal medium. The difference in abundance in mol% was calculated by subtracting the abundance in unstressed cells from the abundance in either DTT- or TM-stressed cells under consideration of error propagation. **(C)** Profile of PA lipids in mol% of the class. **(D)** Total length of lipids in a sub-category of MGLs (PA, PC, PE, PI, PS, DAG). The total length is given as the sum of carbon atoms in both fatty acyl chains in mol% of this sub-category. **(E)** Total number double bonds in a sub-category of MGLs (PA, PC, PE, PI, PS, DAG) is given as the sum of double bonds in both acyl chains and represented in mol% of this sub-category. **(F)** Profile of sphingolipids in mol% of this category. The least abundant species are omitted for clarity. Each bar represents the average ± SD from n = 3 independent experiments. Statistical significance was tested by an unpaired two-tailed t-test using GraphPad Prism, *p<0.05, **p<0.01, ***p<0.001.

Resource



MemPrep, a new technology for isolating organellar membranes provides fingerprints of lipid bilayer stress

John Reinhard ^{1,2}, Leonhard Starke³, Christian Klose⁴, Per Haberkant⁵, Henrik Hammarén ⁶, Frank Stein ⁵, Ofir Klein ⁷, Charlotte Berhorst^{1,2}, Heike Stumpf^{1,2}, James P Sáenz ⁸, Jochen Hub ³, Maya Schuldiner ⁷ & Robert Ernst ^{1,2}✉

Abstract

Biological membranes have a stunning ability to adapt their composition in response to physiological stress and metabolic challenges. Little is known how such perturbations affect individual organelles in eukaryotic cells. Pioneering work has provided insights into the subcellular distribution of lipids in the yeast *Saccharomyces cerevisiae*, but the composition of the endoplasmic reticulum (ER) membrane, which also crucially regulates lipid metabolism and the unfolded protein response, remains insufficiently characterized. Here, we describe a method for purifying organelle membranes from yeast, MemPrep. We demonstrate the purity of our ER membrane preparations by proteomics, and document the general utility of MemPrep by isolating vacuolar membranes. Quantitative lipidomics establishes the lipid composition of the ER and the vacuolar membrane. Our findings provide a baseline for studying membrane protein biogenesis and have important implications for understanding the role of lipids in regulating the unfolded protein response (UPR). The combined preparative and analytical MemPrep approach uncovers dynamic remodeling of ER membranes in stressed cells and establishes distinct molecular fingerprints of lipid bilayer stress.

Keywords ER Stress; UPR; Lipid Bilayer Stress; MemPrep; Organelle Lipidomics

Subject Categories Membranes & Trafficking; Organelles
<https://doi.org/10.1038/s44318-024-00063-y>

Received 14 September 2022; Revised 16 February 2024;

Accepted 26 February 2024

Published online: 15 March 2024

Introduction

Biological membranes are complex assemblies of lipids and proteins. Their compositions and properties are dynamically

regulated in response to stress and as well as more subtle physical and metabolic cues (Harayama and Riezman, 2018; Ernst et al, 2018). A prominent example is the homeoviscous adaptation, where the lipid composition is adapted to temperature for maintaining membrane fluidity and membrane phase behavior (Sinensky, 1980; Ernst et al, 2016; Harayama and Riezman, 2018). Even mammals, which maintain a constant body temperature, can readily adjust their membrane composition in response to dietary perturbation with major impact on collective bilayer properties such as fluidity, thickness, surface charge or compressibility (Bigay and Antonny, 2012; Levental et al, 2020). Eukaryotic cells face the challenge of maintaining the properties of the plasma membrane and several coexisting organelle membranes each featuring characteristic lipid compositions as well as constantly exchanging membrane material with other organelles. Despite recent advances to manipulate and follow membrane properties (John Peter et al, 2022; Renne et al, 2022; Tsuchiya et al, 2023; preprint: Jiménez-Rojo et al, 2022), we know little about how stressed cells coordinate membrane adaptation between organelles whilst maintaining organelle identity and functions.

The endoplasmic reticulum (ER) spans eukaryotic cells as a continuous membrane network, including the nuclear envelope and the peripheral ER consisting of flat cisternae and narrow tubules (Phillips and Voeltz, 2016). It is a hotspot for lipid biosynthesis (Zinser et al, 1991; Henry et al, 2012) and provides an entry site for soluble and transmembrane proteins to the secretory pathway. The flux of proteins and lipids through the secretory pathway is controlled by the unfolded protein response (UPR) (Travers et al, 2000; Walter and Ron, 2011). When the protein folding capacity of the ER is overwhelmed, the type I membrane protein Ire1 responds to an increase in protein misfolding by multimerizing thereby facilitating the association and activation of its cytosolic kinase/RNase domains (Walter and Ron, 2011). The cleavage of the *HAC1* mRNA in *Saccharomyces cerevisiae* (from here on “yeast”) by the activated RNase domain is the committed step for UPR activation and leads to the formation of the Hac1 transcription factor, which

¹Saarland University, Medical Biochemistry and Molecular Biology, Homburg, Germany. ²Saarland University, Preclinical Center for Molecular Signaling (PZMS), Homburg, Germany. ³Saarland University, Theoretical Physics and Center for Biophysics, Saarbrücken, Germany. ⁴Lipotype GmbH, Dresden, Germany. ⁵EMBL Heidelberg, Proteomics Core Facility, Heidelberg, Germany. ⁶EMBL Heidelberg, Genome Biology, Heidelberg, Germany. ⁷Weizmann Institute of Science, Department of Molecular Genetics, Rehovot, Israel. ⁸Technische Universität Dresden, B CUBE, Dresden, Germany. ✉E-mail: robert.ernst@uks.eu

regulates hundreds of UPR target genes (Travers et al, 2000; Ho et al, 2020). Once activated, the UPR lowers global protein synthesis, whilst upregulating the ER-luminal folding machinery, ER-associated protein degradation, and lipid biosynthesis enzymes (Travers et al, 2000; Walter and Ron, 2011). Intriguingly, Ire1 can also sense ER membrane aberrancies referred to as lipid bilayer stress via a hydrophobic mismatch-based mechanism (Halbleib et al, 2017). This responsiveness of the UPR to lipid bilayer stress is evolutionarily conserved (Volmer et al, 2013; Hou et al, 2014; Ho et al, 2018; Pérez-Martí et al, 2022). A diverse set of lipid metabolic perturbations trigger the UPR: inositol depletion (Cox et al, 1997; Promlek et al, 2011; Halbleib et al, 2017), increased lipid saturation (Pineau et al, 2009; Surma et al, 2013), increased sterol levels (Feng et al, 2003; Pineau et al, 2009), misregulated sphingolipid metabolism (Han et al, 2010), and a disrupted conversion of phosphatidylethanolamine (PE) to phosphatidylcholine (PC) (Thibault et al, 2012; Ho et al, 2020; Ishiwata-Kimata et al, 2022). Even prolonged proteotoxic stresses, misfolded membrane proteins, and exhaustion of the culture medium have been associated with UPR activation via this membrane-based mechanism (Promlek et al, 2011; Tran et al, 2019b; Váth et al, 2021; Ishiwata-Kimata et al, 2022). Little is known how these conditions of lipid bilayer stress affect the molecular composition of the ER membrane.

Advances in quantitative lipidomics (Ejsing et al, 2009) have provided deep insights into the flexibility and adaptation of the cellular lipidome to various metabolic and physical stimuli in both yeast and mammals (Klose et al, 2012; Casanovas et al, 2015; Levental et al, 2020; Surma et al, 2021). However, unless these analytical platforms are paired with powerful techniques for isolating organellar membranes from stressed and unstressed cells, they lack the subcellular resolution, which is essential to understand how lipid metabolism is organized between organelles. Even though tremendous and pioneering efforts have been invested in characterizing organellar membranes from yeast (Zinser and Daum, 1995; Schneider et al, 1999; Klemm et al, 2009; Surma et al, 2011; Reglinski et al, 2020), we still lack comprehensive and quantitative information on the ER membrane. This is probably due to the extensive membrane contact sites formed between the ER and other organelles, making isolation technically challenging (English and Voeltz, 2013; Scorrano et al, 2019).

Here, we describe a protocol for the isolation of highly enriched organellar membranes, MemPrep. We demonstrate its utility by the successful isolation of both ER and vacuolar membranes from yeast and provide a molecular toolkit to make this method applicable to other organelles. Using quantitative lipidomics, we reveal specific characteristics of these membranes. In the ER, we observe a high proportion of monounsaturated fatty acyl chains and a low level of ergosterol. The vacuole membrane, on the other hand, is virtually devoid of phosphatidic acid (PA). By analyzing the lipid composition of the stressed ER, we establish molecular fingerprints of lipid bilayer stress, provide evidence for a general contribution of low membrane compressibility to UPR activation, and identify a potential role of anionic lipids as negative regulators of the UPR. Despite these common denominators, our data demonstrate that lipid bilayer stress comes in different flavors provided by vastly distinct lipid and protein compositions of the ER membrane. The MemPrep approach sets the stage for a better understanding of the organelle-specific membrane adaptations to metabolic, proteotoxic, and physical stresses in the future.

Results

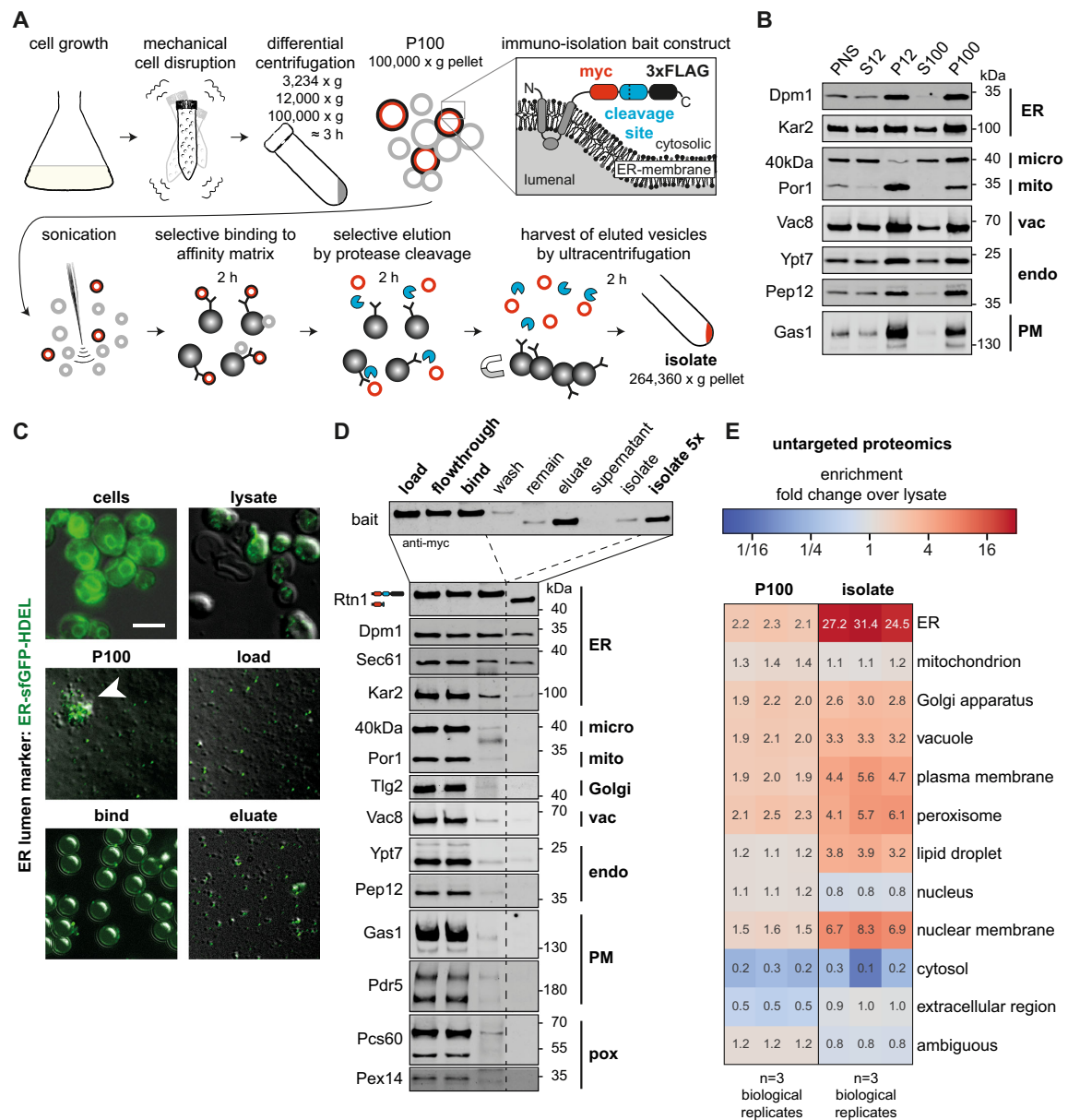
Creation of a rapid and clean approach for yeast organelle isolation, MemPrep

In the past, systematic organelle isolation from yeast has been carried out predominantly by differential sedimentation and density centrifugation (Zinser and Daum, 1995; Schneider et al, 1999). Affinity purification methods that work well in mammalian cells cannot be translated easily into yeast work, especially when the organelle-of-interest forms extensive membrane contact sites (Takamori et al, 2006; Klemm et al, 2009; Abu-Remaileh et al, 2017; Ray et al, 2020; Fasimoye et al, 2023). We sought to create a versatile, yeast-specific affinity purification method, MemPrep, for obtaining highly enriched organelle membrane fractions. We reasoned that important aspects of MemPrep would be the capacity to bind organellar membranes with high specificity and the ability to release them selectively after intense washing. Hence, we constructed a tagging cassette that can equip an open reading frame in yeast with a sequence encoding for a C-terminal bait tag comprising a myc epitope, a recognition site for the human rhinovirus (HRV) 3C protease, and the 3xFLAG epitope (Fig. 1A). Following proof of concept of the validity of MemPrep (see below) and to enable our approach to be widely used by the yeast community regardless of which organelle is of interest, we created a systematic collection of strains in which every yeast protein is tagged with the bait sequence (see some examples for each organelle in Appendix Fig. S1A). To do this, we used the SWAT Tag (SWAT) approach (Yofe et al, 2016; Meurer et al, 2018; Weill et al, 2018) coupled with automated library creation strategies (Tong and Boone, 2006; Weill et al, 2018). The library or any individual strain is freely distributed.

MemPrep yields highly enriched ER membrane vesicles

To showcase MemPrep, we initially focused on the largest organelle in the cell, the ER, which is a particularly challenging target. It forms physical contact sites with almost every other membrane-bound organelle (English and Voeltz, 2013), and previous attempts to isolate ER membranes suffered from significant mitochondrial contaminations (Schneider et al, 1999; Reglinski et al, 2020). An ideal bait protein should be a highly abundant transmembrane protein, feature an accessible C-terminus, and localize exclusively to a single organelle. Initially, we used Rtn1 as a bait, which is a structural determinant of the tubular ER. Rtn1 is a small (~33 kDa) and highly abundant reticulon protein (~37,100 copies per cell), which stabilizes membrane curvature in the tubular ER (Ghaemmaghami et al, 2003; Voeltz et al, 2006). Rtn1 has four predicted transmembrane helices with both N- and C-terminus facing the cytosol and a C-terminal amphipathic helix, which inserts into the cytosolic leaflet of the ER membrane to generate a high spontaneous membrane curvature (De Craene et al, 2006; Hu et al, 2008).

Several experimental factors are important to ensure the successful isolation of ER membranes (Fig. 1A): First, cells are mechanically disrupted, thereby minimizing potential artifacts from the ongoing lipid metabolism and ER stress that would occur during the enzymatic digestion of the cell wall under reducing conditions (Zinser and Daum, 1995). Second, after a differential



centrifugation to obtain a crude microsome fraction, organellar fragments were disrupted by sonication. This is because a major fraction of the ER membrane surface forms physical contacts to other organelles (Phillips and Voeltz, 2016), which would hamper the subsequent ER isolation. We reasoned that large ER fragments are more likely to contain such contact sites, while enough small ER fragments might facilitate higher purity if membrane mixing can be avoided. Third, we employ harsh washing conditions with urea-containing buffers to remove peripherally attached proteins and to

destabilize membrane contact sites. Fourth, the isolated membrane vesicles are selectively eluted from the affinity matrix thereby providing a straightforward coupling to various mass spectrometry-based analytical platforms following previous paradigms (Klemm et al, 2009).

Enrichments of organellar membranes relies first on differential centrifugation and only then on affinity purification. To decide on the exact fraction best to utilize for membrane pull-downs, we performed immunoblotting experiments after differential

Figure 1. Immunoisolation of the ER via MemPrep.

(A) Schematic representation of the immunoisolation protocol. Cells are cultivated in SCD_{complete} medium and mechanically disrupted by vigorous shaking with zirconia/glass beads. Differential centrifugation at 3234 × *g*, 12,000 × *g*, and 100,000 × *g* yields crude microsomes in the P100 fraction originating from different organelles. The immunoisolation bait tag installed at the C-terminal end of Rtn1 is depicted in the inset (myc-tag, human rhinovirus (HRV) 3C protease cleavage site, 3xFLAG tag). Sonication segregates clustered vesicles and decreases the vesicle size. ER-derived vesicles are specifically captured by anti-FLAG antibodies bound to Protein G on magnetic beads. After rigorous washing, the ER-derived vesicles are selectively eluted by cleaving the bait tag with the HRV3C protease (blue sectors). The eluted ER-derived vesicles (red circles) are harvested and concentrated by ultracentrifugation. (B) Distribution of the indicated organellar markers in the fractions of a differential centrifugation procedure: Supernatant after 3234 × *g* centrifugation (post nuclear supernatant, PNS), supernatant after 12,000 × *g* centrifugation (S12), pellet after 12,000 × *g* centrifugation (P12), supernatant after 100,000 × *g* centrifugation (S100), pellet after 100,000 × *g* centrifugation (P100). Dpm1 and Kar2 are ER markers, the 40 kDa protein (40 kDa) is a marker for light microsomes (Zinser et al, 1991), Por1 is a marker of the outer mitochondrial membrane, Vac8 is a vacuolar marker, Ypt7 and Pep12 mark endosomes, and Gas1 serves as plasma membrane marker. In total, 7.8 μg total protein loaded per lane. (C) Overlay of fluorescence micrographs and differential interference contrast images of cells expressing an ER-luminal marker (ER-sfGFP-HDEL) and fractions from immunoisolation. Intact cells (cells) show typical ER staining. Mechanical cell disruption leads to fragmentation and release of intracellular membranous organelles (lysate). The crude microsomal fraction (P100) contains aggregates of GFP-positive and GFP-negative vesicles (white arrowhead). Segregation by sonication yields more homogenous size distribution of vesicles (load). Individual ER-luminal marker containing vesicles are bound to the surface of much larger magnetic beads (bind). Selective elution by protease cleavage releases vesicles from the affinity matrix (eluate). Scale bar for all panels: 5 μm. (D) Immunoblot analysis of immunoisolation fractions for common organellar markers (ER endoplasmic reticulum, micro light microsomal fraction, mito mitochondria, Golgi Golgi apparatus, vac vacuole, endo endosomal system, PM plasma membrane, pox peroxisomes). Overall, 0.2% of each fraction loaded. (E) Untargeted protein mass spectrometry analysis showing enrichment of P100 and isolate fractions over whole-cell lysate. The enrichment of proteins over the cell lysate (fold change) is based on uniquely annotated subcellular locations and provided for each biological replicate. The illustrated numbers represent the median enrichment for unique annotated genes from *n* = 3 biological replicates. Source data are available online for this figure.

centrifugation (Fig. 1B). Membrane markers for the ER (Dpm1), mitochondria (Por1), endosomes (Ypt7, Pep12), the vacuole (Vac8), and the plasma membrane (Gas1) were all enriched in the pellets of a centrifugation at 12,000 × *g* (P12) and 100,000 × *g* (P100), while the light microsomal 40 kDa protein (40 kDa) was predominantly found in the P100 fraction (Fig. 1B). The marker for the outer mitochondrial membrane (Por1) was significantly enriched in P12 relative to P100 (Fig. 1B). To minimize contaminations from mitochondrial membranes we decided to use the crude microsomal P100 fraction for isolating ER membrane vesicles. By doing so, we discard a significant fraction of ER membrane with the P12 fraction (Fig. 1B). We cannot formally rule out the possibility that the discarded ER membrane vesicles in the P12 fraction have a different composition than the rest of the ER, which we subsequently isolate. The ER-luminal chaperone Kar2 was found both in the supernatant and the pellet after centrifugation at 100,000 × *g* (S100). This suggests that a significant portion of ER-luminal content is released during cell disruption.

To ensure that our choice of P100 is optimal and to uncover the extent of loss of ER-luminal proteins, we followed the entire procedure from cell disruption to the elution of the isolated vesicles in a control experiment using fluorescence microscopy. To this end, we used cells expressing both an ER bait protein, but also an ER-targeted, superfolder-GFP variant equipped with a HDEL sequence for ER retrieval (Fig. 1C) (Lajoie et al, 2012). By following the fluorescent ER-luminal marker, we realized that the crude microsomal P100 fraction contains large clumps of GFP-positive and GFP-negative vesicles (Fig. 1C; P100, white arrowhead). Due to the loss of ER-luminal proteins, the GFP-negative vesicles could be derived from the ER but may also be from other organelles. We decided to reduce the size of the microsomes by sonication, which also separated larger clumps of aggregated vesicles (Fig. 1A,C).

Sonication transiently disrupts lipid bilayers and can theoretically induce lipid mixing or a transient fusion of adjacent lipid bilayers. Because this would obscure our measurement of the ER membrane composition, we performed control experiments to rule this out. We utilized small unilamellar vesicles of ~100 nm containing POPC, NBD-PE, and Rho-PE at a ratio of 98:1:1. The

two fluorescent lipid analogs form a Förster resonance energy transfer (FRET) pair (Appendix Fig. S1B). We sonicated these synthetic liposomes in the presence of a ~15.4-fold excess of microsomal membranes (P100) based on membrane phospholipid content. Because fusion between the synthetic liposomes and microsomal membranes would “dilute” the fluorescent lipid analogs, a decrease of the relative FRET efficiency would be expected upon membrane mixing or upon the exchange of individual fluorescent lipid molecules. However, the 10 cycles of sonication as used during MemPrep procedure for dissociating vesicle aggregates do not lead to a significant change of the FRET efficiency. Lower FRET efficiencies indicative for lipid exchange or membrane fusion, was only observed after 100 cycles of sonication, which also leads to sample warming, and upon incubation for 30 min at RT with either 18 mM methyl-β-cyclodextrin, which facilitates lipid exchange, or with 40% w/v PEG 8000, which supports membrane fusion (Appendix Fig. S1B) (Lentz, 1994; Cheng et al, 2009). Expectedly, we observed a dramatic drop of the relative FRET efficiency upon the addition of SDS, which dissolves both the liposomal and microsomal membranes (Appendix Fig. S1B). These data suggest that the sonication as used in the MemPrep procedure does not cause a significant degree of membrane mixing from fusion and/or lipid exchange.

After having optimized sample homogenization, we turned our attention to the immunoisolation procedure. We decided on magnetic dynabeads coated with Protein G and sparsely decorated with anti-FLAG antibodies. Notably, the low density of antibodies is required to lower avidity effects, which would impede the elution of membrane vesicles from the matrix. The capturing of GFP-positive, ER-derived vesicles to the affinity matrix was validated by fluorescence microscopy (Fig. 1C, bind). After extensive washing with 0.6 M urea-containing buffers, the isolated vesicles were eluted by cleaving the bait tag (Fig. 1C; eluate) as validated by immunoblotting using anti-myc antibodies (Fig. 1D; eluate). The isolated membrane material was harvested and concentrated by ultracentrifugation (264,360 × *g*, 2 h, 4°C) (Fig. 1A). Immunoblotting demonstrated the co-purification of the bait (Rtn1) with other ER membrane proteins (Dpm1, Sec61) (Fig. 1D), while most of the

ER-luminal chaperone Kar2 is lost during the isolation. Remarkably, all markers for other organelles including the mitochondrial marker Por1 remained undetected in the final isolate (Fig. 1D). Even the light microsomal marker 40 kDa protein (40 kDa), whose subcellular localization is not fully established, is lost during the preparation (Zinser et al, 1991). Hence, MemPrep yields highly enriched ER membrane preparations. While previous approaches for isolating organelles such as the Lyso-IP were optimized for speed (Abu-Remaileh et al, 2017; Ray et al, 2020; Fasimoye et al, 2023), we established a technique that also allows for the elution of the isolated membrane vesicles. This approach does not only increase the purity of our preparation, it also provides a significant advantage for coupling the isolation to analytical platforms such as quantitative lipidomics, proteomics, or fluorescence spectroscopy. Overall, the MemPrep procedure provides high purity of organelle-derived membranes at the expense of low yields (83 mg protein in the cell lysate yields ~30 µg of protein in the isolate via the Rtn1-bait). Assuming the ER accounts for 20% of the total cell protein (Zinser and Daum, 1995), we estimate that >99.8% of ER protein is lost during the isolation.

Quantitative proteomics validates the performance of MemPrep with distinct bait proteins

Demonstrating the loss of several specific organelle markers by immunoblotting is often used as a “gold standard” for validating organelle isolations, however, this validation is limited by the detection sensitivity of the antibody as well as the specific abundance of the organelle marker utilized. Hence, for a more rigorous validation, we measured the level of cleanliness of our preparations by TMT-multiplexed, untargeted protein mass spectrometry (Fig. 1E). We also compared the enrichment of the ER over the cell lysate with that of other organelles using a total of 1670 proteins uniquely annotated for cellular compartments with gene ontology terms (GO terms) (Fig. 1E, Source Data file: Fig. 1E_annotations). The mean enrichment of 213 ER-specific proteins was 27.7-fold in the immuno-isolate over the cell lysate, which is also consistent with semi-quantitative, immunoblotting data (Appendix Fig. S1C). This quantitative approach revealed an efficient depletion of cytosolic and nucleoplasmic proteins and a strong enrichment over mitochondrial proteins, which represented a major contaminant in microsome preparations in the past (Schneider et al, 1999; Reglinski et al, 2020). A moderate enrichment of markers from other organelles of the endomembrane system (Golgi apparatus, vacuole, etc.) was found as expected since they pass through the ER on their route to their subcellular destination and because the efficient removal of soluble proteins alone causes an enrichment of organelle membrane markers. In line with the procedure that is intended to enrich for the membrane fraction, ER membrane proteins were substantially more enriched than ER-luminal, soluble proteins or proteins from other organelles (Appendix Fig. S1D). Only a few proteins annotated to other organelles are enriched >20-fold over the lysate (Appendix Fig. S1D) and for most of these there is evidence that they in fact localize to the ER or the nuclear envelope, which is continuous with the ER membrane. Hence, Osm1, Yur1, Ist2, Ygr026w, Pex30, Pex29, Slc1, Uip6, Brr6, and She10 were falsely annotated as non-ER proteins (Appendix Fig. S1D). A dual localization including the ER and another organelle has been reported for

Osm1, Yur1, Pex31, Slc1, Cst26, Svp26, Ept1, and Cbr1. Likewise, there is evidence for an ER localization for the non-annotated proteins Ybr096w, Gta1, Msc1, and Hlj1. This suggests that MemPrep and quantitative proteomics can even predict ER membrane localization.

The ER forms an extended membrane network composed of sheets and tubules. We assayed whether MemPrep is suitable to isolate ER subdomains by an appropriate choice of the bait or if ER membranes isolated by this approach are representative for the “entire” ER membrane? To address this question, we compared the isolates using the Rtn1-bait localizing to the tubular ER with those using the Elo3-bait, which is enriched in the nuclear ER membrane (Fig. EV1A). Quantitative proteomics reveals that fusing the bait tag to either Rtn1 or Elo3 has no impact on the overall cellular proteome (Fig. EV1B) and that ER proteins can be enriched by MemPrep using either of the two baits (Fig. EV1C,D) with an estimated yield of 0.19% and 0.08% of the input material for the Rtn1- and Elo3-bait, respectively. We included an additional carbonate wash of the P100 microsomes prior to the immunoprecipitation procedure to further decrease contaminations from soluble proteins and to potentially increase the coverage of membrane proteins in the subsequent proteomics experiment. A direct comparison of the proteomes from the two isolates identified stunningly few differences: While 3013 proteins were detected and analyzed, only 12 proteins showed a >20-fold difference between Rtn1-bait and Elo3-bait-derived ER isolates (Fig. EV1E). This suggests that MemPrep yields preparations, which rather represent the “entire” ER membrane than a specific ER subdomain. Yet, we cannot exclude that the portion of the ER that is lost/discarded during the preparation may have a different composition. We speculate that the harsh mechanical disruption of the cell, which is required to break the cell wall, causes a fragmentation of the ER network that disrupts lateral specializations. While we know from our work with mammalian cells that ER subdomains can be isolated via MemPrep, we are convinced that preparations representative of the “entire” organelle membranes have practical advantages for studying inter-organelle transport processes by lowering the minimally required sample number for proteomics and lipidomics experiments as indicated by first applications using the MemPrep technology and variations thereof (Reinhard et al, 2023; preprint: Koch et al, 2023).

The lipid composition of the ER

Previous attempts to establish the ER membrane lipid composition in yeast were hampered by mitochondrial contaminations (Schneider et al, 1999; Reglinski et al, 2020). Having established the isolation of ER-derived membranes via the Rtn1-bait, we were interested in determining their lipid composition using quantitative lipidomics (Fig. 2A–C). Compared to whole-cell lysates, the ER membrane features (1) substantially lower levels of neutral storage lipids (ergosterol esters (EEs) and triacylglycerols (TAGs)), (2) significantly more diacylglycerol (DAG), PC and PE, but (3) less phosphatidylinositol (PI) lipids. Notably, the same lipid composition was observed for ER membranes isolated via the Elo3-bait (Fig. EV2A–C). Hence, the ER maintains a characteristic lipid composition even though it readily exchanges membrane material with other organelles (Wong et al, 2019). Remarkably, the level of ergosterol in the ER (9.7 mol%) is barely distinct from the level in

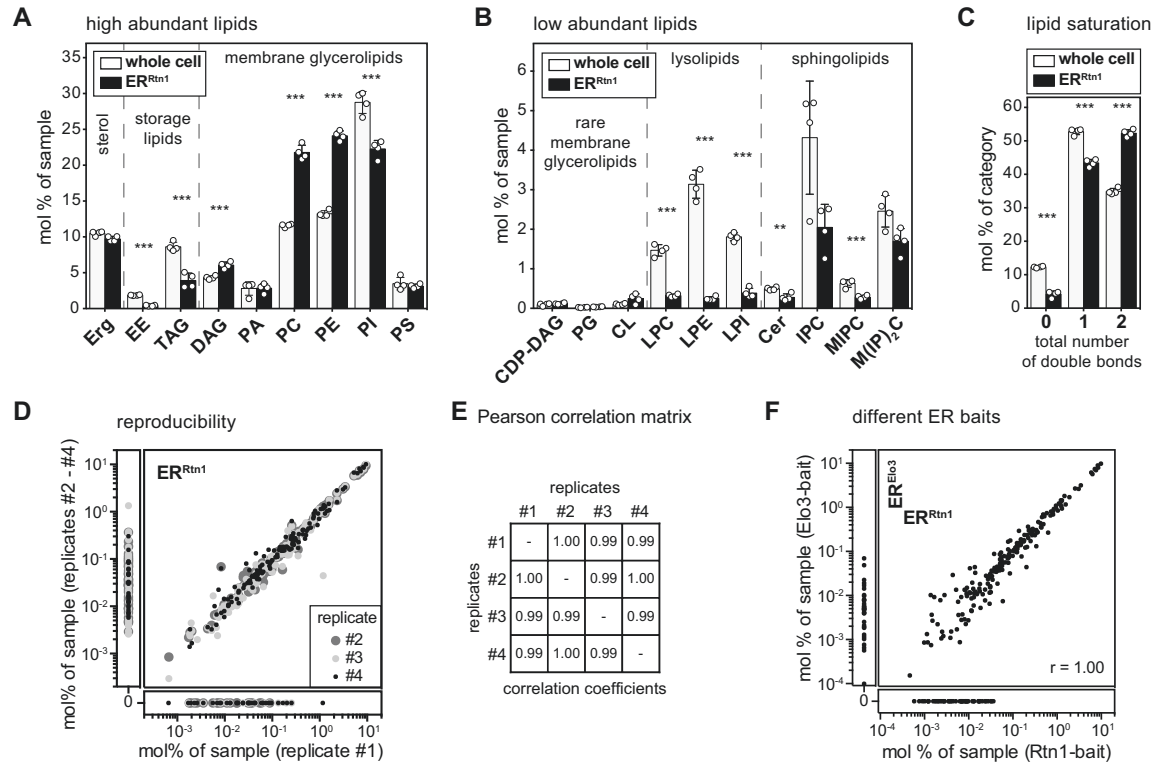


Figure 2. Lipid composition of the ER membrane of *S. cerevisiae* determined by MemPrep via Rtn1-bait.

SCD_{complete} medium was inoculated to an OD₆₀₀ of 0.1 using stationary overnight cultures of cells expressing the bait protein. Cells were cultivated to an OD₆₀₀ of 1.0, harvested, frozen, stored, thawed, and then subjected to the MemPrep procedure. (A) Quantitative lipidomics reveals the lipid class composition given as mol% of all identified lipids in the sample. Classes are categorized into sterol (Erg ergosterol), storage lipids (EE ergosteryl ester, TAG triacylglycerol), membrane glycerolipids (DAG diacylglycerol, PA phosphatidic acid, PC phosphatidylcholine, PE phosphatidylethanolamine, PI phosphatidylinositol, PS phosphatidylserine) ($n = 4$ biological replicates). (B) Lipid class composition of rare membrane glycerolipids (CDP-DAG cytidine diphosphate diacylglycerol, PG phosphatidylglycerol, CL cardiolipin), lysolipids (LPC lyso-phosphatidylcholine, LPE lyso-phosphatidylethanolamine, LPI lyso-phosphatidylinositol), and sphingolipids (Cer ceramide, IPC inositolphosphorylceramide, MIPC mannosyl-IPC, M(IP)₂C mannosyl-di-IPC) given as mol% of all lipids in the sample ($n = 4$ biological replicates). (C) The total number of double bonds in membrane glycerolipids except for CL (i.e. CDP-DAG, DAG, PA, PC, PE, PG, PI, PS) as mol% of this category ($n = 4$ biological replicates). (D) Reproducibility of immuno-isolated ER lipidome data shown as the correlation of mol% of sample values of all detected lipid species between replicate 1 and replicates 2–4. (E) Pearson correlation coefficients of lipidomics data for all combinations of replicate samples. (F) Correlation of mol% of sample values of all detected lipid species from Rtn1-bait and Eloc3-bait derived ER membranes. Data information: Data from $n = 4$ biological replicates in (A–C) are presented as individual data points and as mean \pm SD. ** $P \leq 0.01$, *** $P \leq 0.001$ (multiple t tests, corrected for multiple comparisons using the method of Benjamini, Krieger, and Yekutieli, with $Q = 1\%$, without assuming consistent SD). Nonsignificant comparisons are not highlighted. Source data for this figure are available online.

whole cells (10.5 mol%) (Fig. 2A) or in the *trans*-Golgi network/endosome (TGN/E) system (9.8 mol%) (Klemm et al, 2009), but much lower than in the plasma membrane (>44 mol%) (Surma et al, 2011). Notably, the absence of a steep sterol gradient in the early secretory pathway is not in conflict with previous studies (Zinser et al, 1991, 1993) and has important implications for the sorting of transmembrane proteins based on hydrophobic thickness (Bretscher and Munro, 1993; Ridsdale et al, 2006; Herzig et al, 2012). Complex sphingolipids such as inositolphosphorylceramide (IPC), mannosyl-IPC (MIPC), and mannosyl-di-(IP)C (M(IP)₂C) are found, as expected, at a significantly lower level in the ER (Figs. 2B and EV2B). While we cannot rule out that a minor fraction of these lipids may originate from contaminating

organelles, these data suggest a significant retrograde transport of complex sphingolipids from the Golgi apparatus to the ER, likely via COP-I vesicles together with ER-resident proteins bound to the HDEL receptor (Aguilera-Romero et al, 2008). A closer look at the fatty acyl chain composition of ER lipids reveals a particularly low level (<5 mol%) of tightly packing, saturated lipids and a significant enrichment of loosely packing, unsaturated lipids (Figs. 2C and EV2C). Loose lipid packing and high membrane compressibility are likely contributing to the remarkable ability of the ER to accept and fold the entire diversity of transmembrane proteins differing substantially in shape and hydrophobic thicknesses (Sharpe et al, 2010; Quiroga et al, 2013; Lorent et al, 2020; Renne and Ernst, 2023). Future work will be dedicated to quantifying also

phosphoinositides such as phosphatidylinositol-4,5-bisphosphate (PIP2), or phosphatidylinositol-3,4,5-triphosphate (PIP3).

In summary, our molecular analysis of the ER membrane reveals surprising insights, which are nevertheless consistent with previous findings and our current understanding of the properties and functions of the ER. The robustness and reproducibility of our MemPrep approach coupled to lipidomic platforms is demonstrated by the remarkable correlation of lipid abundances reported in four independent experiments with the Rtn1-bait (Fig. 2D,E) or between the isolates using the Rtn1- and the Elo3-bait (Fig. 2F).

Stable lipid compositions after cell lysis contrasts ER lipid remodeling in living cells

While our isolation process is shorter than many previously employed methods for organelle purification, it still takes 8 h from cell lysis to finish. Hence, we wanted to exclude that ongoing lipid metabolism during the isolation procedure distorts the measured lipid composition. Consequently, we performed a control experiment in which we split a crude microsomes preparation (P100) into two equal samples. The first sample was directly snap-frozen in liquid N₂ while the second one was frozen only after incubation at 4 °C for 8 h. A comparison of the two samples revealed remarkably similar lipid compositions (Appendix Fig. S2A–C). Only the low abundant lyso-PC, lyso-PE, and lyso-PI lipids showed some differences (Appendix Fig. S2B), suggesting a loss of lysolipids over time, which is consistent with their role as intermediates of lipid degradation (Harayama and Riezman, 2018). Hence, ongoing lipid metabolism has only a minor impact on the cellular lipidome.

A molecular fingerprint of lipid bilayer stress during inositol depletion

Having successfully coupled the MemPrep technology to quantitative lipidomics, we turned our attention to the stressed ER. Lipid bilayer stress is a collective term for aberrant ER membrane compositions activating the UPR (Surma et al, 2013; Ho et al, 2018; Radanović and Ernst, 2021). It is expected that an acute depletion of inositol from the medium causes UPR activation without triggering a substantial accumulation of misfolded proteins (Cox et al, 1997; Promlek et al, 2011; Lajoie et al, 2012). We scored UPR activity in stressed and unstressed cells by determining the relative abundance of the spliced *HAC1* mRNA (Fig. EV3A) and the mRNA abundance of the UPR target genes *PDI1* and *KAR2* by RT-qPCR (Fig. EV3B,C). Depletion of inositol from the medium, but not supplementation with choline, triggered a robust UPR in both the Rtn1-bait strain and the respective wild-type yeast (BY4741) (Fig. EV3A–C). Hence, the bait tag attached to Rtn1 does not interfere with the ability of the cell to respond to lipid bilayer stress. We then isolated ER membranes via the Rtn1-bait and performed quantitative proteomics experiments. The ER membrane proteome remains remarkably unperturbed by inositol depletion: only 12 out of 2655 robustly detected proteins showed increased abundances in ER isolates upon inositol depletion (Fig. 3A). Among these, we found the myo-inositol transporter *Itr1* (Nikawa et al, 1993), the glycerophosphoinositol permease *Git1* (Patton-Vogt and Henry, 1998), and the soluble Inositol-3-phosphate synthase *Ino1* (Hirsch and Henry, 1986), known to be transcriptionally upregulated in response to inositol depletion (Jesch et al, 2006).

Our main goal was establishing a molecular fingerprint of lipid bilayer stress in the ER (Fig. 3). Immuno-isolated ER membranes revealed, somewhat unsurprisingly, that inositol depletion causes a substantial drop of inositol-containing PI lipids in the ER (Fig. 3B) accompanied by a drastic accumulation of CDP-DAG lipids, which serve as direct precursors for PI synthesis via *Pis1* (Fig. 3C,D) (Henry et al, 2012). Even the penultimate precursor of PI synthesis, PA, accumulates in the ER upon inositol depletion (Fig. 3B) (Henry et al, 2012). Inositol-containing sphingolipids, however, are not depleted under this condition (Fig. 3C). This implies distinct rates of PI and sphingolipid metabolism under this condition. Overall, the molecular lipid fingerprint of the lipid bilayer stress caused by inositol depletion is characterized by substantial changes in the abundance of anionic lipids, PI in particular (Fig. 3B,C).

We further dissected the compositional changes of the ER membrane lipidome upon inositol depletion at the level of the lipid acyl chains and observed a minor, nonsignificant trend toward more saturated glycerophospholipids (Fig. 3E). While these changes are likely to fine-tune the physicochemical properties of the ER membrane, it is unlikely that they alone are sufficient to trigger the UPR by activating *Ire1* (Halbleib et al, 2017). Hence, we speculate that the overall reduction of anionic lipids might contribute to lipid bilayer stress. Our data provide a quantitative basis for studying the contribution of anionic lipids and collective membrane properties to chronic ER stress *in vitro* after reconstituting UPR transducers in native-like membrane environments.

An increased PC-to-PE ratio does not cause lipid bilayer stress in yeast

Increased cellular PC-to-PE ratios have been associated with chronic ER stress in mammalian cells (Fu et al, 2011), while a decreased production of PC from PE causes lipid bilayer stress in yeast (Thibault et al, 2012; Ho et al, 2020; Ishiwata-Kimata et al, 2022). Because cells cultivated in a synthetic medium and challenged with 2 mM choline do not activate the UPR (Fig. EV3), we were interested in the ER lipidome under this condition. We isolated ER membranes via the Rtn1-bait and determined the resulting lipid composition (Appendix Fig. S3A–C). Choline can be activated to CDP-choline and then transferred onto diacylglycerol (DAG) to yield PC (Appendix Fig. S3D) (Kennedy and Weiss, 1956). Expectedly, the ER of choline-challenged cells features substantially higher levels of PC lipids at the expense of PE and causes an increase of the PC-to-PE ratio from ~1.1 to ~2.4 (Appendix Fig. S3A). This increased PC-to-PE ratio in the ER of choline-challenged cells is neither associated with changes in lipid saturation (Appendix Fig. S3C) nor with UPR activation (Fig. EV3A–C). Lipid metabolism and the PC-to-PE ratio may have been more affected if different concentrations of choline and inositol had been used (Hirsch and Henry, 1986; Gaspar et al, 2006). Nevertheless, our data show that even a grossly increased PC-to-PE ratio, which likely affects the lateral pressure profile and ER membrane fluidity (van den Brink-van der Laan et al, 2004; Marsh, 2007; Dawaliby et al, 2016) does not cause lipid bilayer stress in yeast.

Lipid bilayer stress caused by proteotoxic agents Dithiothreitol (DTT) and Tunicamycin (TM)

Instances of acute proteotoxic stress disrupt protein folding in the ER and activate the UPR without causing substantial alterations to

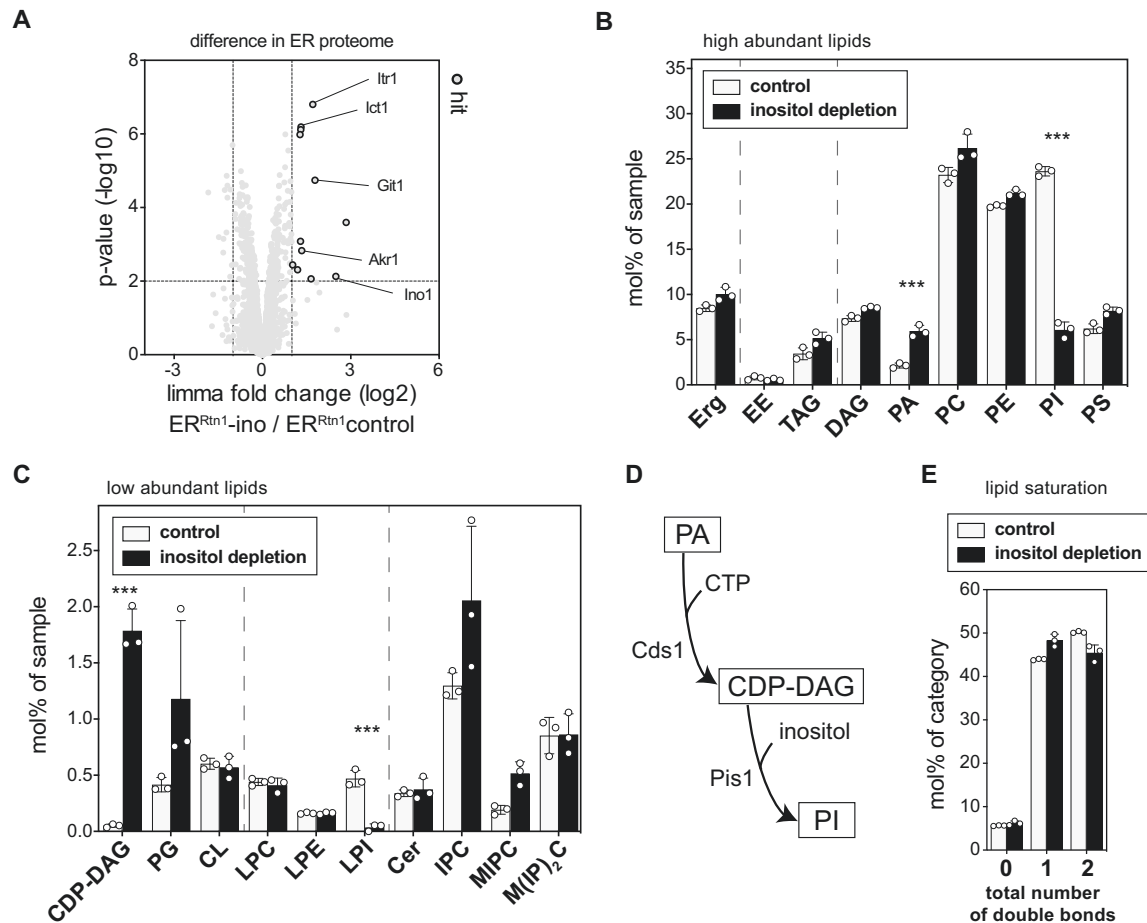


Figure 3. Molecular fingerprints of lipid bilayer stress.

SCD_{complete} medium was inoculated with Rtn1-bait cells to an OD₆₀₀ of 0.003 from an overnight pre-culture and grown to an OD₆₀₀ of 1.2. Cells were washed with inositol-free medium and then cultivated for an additional 2 h in either inositol-free (inositol depletion) or SCD_{complete} medium (control) starting with an OD₆₀₀ of 0.6. Note that the culturing conditions for the unstressed control was different from that used to determine the steady-state ER lipid composition in Fig. 2. ER-derived membranes were purified by differential centrifugation and immunoprecipitation and subsequently analyzed by TMT-labeling proteomics or quantitative shotgun lipidomics. (A) To increase the proteomics coverage for membrane proteins, P100 membranes were carbonate-washed before performing immunoprecipitation. Limma analysis of TMT-labeling proteomics. Highlighted are proteins that are more abundant in ER samples upon lipid bilayer stress by inositol depletion (ER^{Rtn1-ino}). (B) Lipid class composition given as mol% of all lipids in the sample. Erg ergosterol, EE ergosterol ester, TAG triacylglycerol, DAG diacylglycerol, PA phosphatidic acid, PC phosphatidylcholine, PE phosphatidylethanolamine, PI phosphatidylinositol, PS phosphatidylserine ($n=3$ biological replicates). (C) Class distribution of low abundant lipids CDP-DAG cytidine diphosphate diacylglycerol, PG phosphatidylglycerol, CL cardiolipin, LPC lyso-phosphatidylcholine, LPE lyso-phosphatidylethanolamine, LPI lyso-phosphatidylinositol, Cer ceramide, IPC inositolphosphorylceramide, MIPC mannosyl-IPC, M(IP)₂C mannosyl-di-IPC ($n=3$ biological replicates). (D) Lipid metabolic pathway of PI biogenesis. (E) The total number of double bonds in membrane glycerolipids (except CL which has four acyl chains) as mol% of this category ($n=3$ biological replicates). Data information: Data from $n=3$ biological replicates in (A) are presented as the mean. We used the moderated t-test limma to test for differential enrichment. P values were corrected for multiple testing with the method from Benjamini and Hochberg. The data from three biological replicates are presented as individual points in (B, C, E) and as the mean \pm SD. *** $P \leq 0.001$ (multiple t tests, corrected for multiple comparisons using the method of Benjamini, Krieger, and Yekutieli, with $Q=1\%$, without assuming consistent SD). Nonsignificant comparisons are not highlighted. Source data are available online for this figure.

cellular lipidomes (Reinhard et al, 2020). However, prolonged proteotoxic stress triggers the UPR through a membrane-based mechanism (Promlek et al, 2011; Våth et al, 2021), with the underlying molecular basis remaining largely unexplored. Even prolonged yeast cultivation without external stressors transiently

triggers the UPR around the time of the diauxic shift (Tran et al, 2019a). To replicate these observations in our experimental context, we investigated the impact of DTT, TM, and extended cultivation on UPR activity (Fig. EV4). Cells exposed to 2 mM DTT or 1.5 μ g/ml TM for 4 h exhibited potent UPR activity, as evidenced by

increased mRNA abundance of spliced *HAC1*, *PDI1*, and *KAR2* compared to cells harvested before exposure to the proteotoxic agents (Fig. EV4A–C; pre-stress). As expected, TM failed to induce a UPR in *ire1Δ* cells (Fig. EV4A–C). Prolonged cultivation in the absence of proteotoxic agents triggered a mild UPR in both wild-type yeast and the Rtn1-bait strain (Fig. EV4A–C).

We sought to understand how prolonged proteotoxic stress and extended cultivation without external stressors affected the lipid composition of wild-type and *ire1Δ* cells (Fig. 4A). Comprehensive analyses revealed that DTT and TM have a remarkably similar impact on the cellular lipid composition (Fig. 4A, see Source Data for full dataset). Stressed cells, compared to exponentially growing cells before the proteotoxic insult, showed elevated levels of PC, DAG, ergosterol esters (EEs), and TAGs, but reduced levels of PE and PI (Fig. 4A). If the increased levels of storage lipids reflect an increased abundance in the ER membrane or a more intimate interaction of the ER with lipid droplets, which accumulate under ER stress (Stordeur et al, 2014; Garcia et al, 2021), remains to be investigated.

Prolonged cultivation in the absence of supplemented proteotoxic agents also resulted in significant remodeling of the cellular lipidome and much lower EE and PI levels compared to DTT- or TM-treated cells (Fig. 4A; untreated versus TM or DTT). Because standard SCD medium contains only 11 μM inositol and because the BY4741 is particularly dependent on inositol for normal growth (Hanscho et al, 2012) it is possible that prolonged cultivation of this strain leads to a “natural” inositol depletion. The increased abundances of precursors of PI biosynthesis, PA and CDP-DAG, also point in this direction. While it is likely that the mildly reduced levels of PI contribute to the membrane-based ER stress upon prolonged DTT or TM treatments, our data suggest a more complex remodeling of the cellular lipidome, which is distinct from the effects of inositol depletion and prolonged cultivation. This conclusion is corroborated by a principal component analysis of whole-cell lipidomic data showing distinct clustering of the data derived from pre-stressed, untreated, inositol-depleted, and the DTT- or TM-stressed cells (Fig. 4B). Notably, *ire1Δ* cells exhibited nearly identical lipidomic changes as their wild-type counterparts regardless of the treatment, and the respective data from wild-type and *ire1Δ* cells co-clustered in principal component analyses (Fig. 4B). Thus, lipidome remodeling cannot be attributed to UPR signaling in this context but may be involved in UPR induction (Fig. EV4A–C). Instead, lipidome remodeling may be related to the strong growth defect that is induced by both drugs (Reinhard et al, 2020).

Given our interest in the molecular basis of UPR activation by lipid bilayer stress, we focused on the impact of prolonged DTT and TM treatments on ER membrane composition. These treatments trigger a robust UPR by a membrane-based mechanism (Fig. EV4A–C) (Promlek et al, 2011; Vāth et al, 2021) and induce severe remodeling of the cellular lipidome (Fig. 4B). We aimed to provide a quantitative description of the ER membrane composition from stressed cells, hoping it would facilitate a direct comparison of different types of lipid bilayer stress and reveal both commonalities and differences. Even though DTT and TM have different modes of action, they have a remarkably similar impact on ER membrane composition (Fig. 4D,E). The stressed ER features a lower content of unsaturated membrane lipids (Fig. 4C) and exhibits higher levels of storage lipids (EEs and TAGs)

(Fig. 4D), possibly due to reduced growth rates (Reinhard et al, 2020) and increased fatty acid flux into storage lipids, or a gradual depletion of lipid metabolites such as inositol from the medium (Listenberger et al, 2003; Vevea et al, 2015; Henne et al, 2018; Reinhard et al, 2020). The elevated levels of lipid metabolic intermediates CDP-DAG and DAG in the stressed ER support both possibilities (Fig. 4D,E). In fact, inositol depletion is a possible contributor to the membrane-based activation of the UPR under this condition. However, the most notable change was observed in the abundant lipid classes PC and PE. In the unstressed ER, the PC-to-PE ratio was 1.0, while the DTT- and TM-stressed ER featured PC-to-PE ratios of 2.8 and 3.1, respectively (Fig. 4D). The UPR transducer Ire1 is unlikely to be directly activated by increased PC-to-PE ratios, as artificially increasing it by choline supplementation to ~2.4 does not activate the UPR (Appendix Fig. S3A; Fig. EV3A–C), whereas inositol depletion triggers the UPR without perturbing the PC-to-PE ratio (Figs. 3B and EV3) (Fu et al, 2011; Gao et al, 2015; Ho et al, 2020; Ishiwata-Kimata et al, 2022). Instead, the ER membrane of DTT- and TM-stressed cells features lower levels of negatively charged, inositol-containing lipids (PI, LPI, IPC, MIPC), which is only partially compensated by increased levels of PA and CDP-DAG (Fig. 4D,E). The molecular fingerprints of lipid bilayer stress provide a crucial framework for dissecting the modulatory role of anionic lipids in UPR activation in the future.

Characterizing complex ER-like lipid mixtures in vitro and in silico

Based on lipidomic data on isolated ER membranes and using twelve commercially available lipids, we established ER-like lipid compositions mimicking the stressed and unstressed ER (Appendix Fig. S4A). For each condition, these mixtures match the lipid class composition, the overall degree of lipid saturation, and the acyl chain composition of each lipid class. We assessed the molecular lipid packing density of these ER-like lipid mixtures in large unilamellar vesicles (LUVs) using the solvatochromic probe C-laurdan (Appendix Fig. S4B), which reports on water penetration into the membrane (Kim et al, 2007). Liposomes mimicking the ER upon inositol depletion featured higher generalized polarization (GP_s) values than those mimicking the unstressed ER and the ER exposed to prolonged proteotoxic stresses. Hence, there is no correlation between lipid packing in the water-membrane interface as measured by C-laurdan (Appendix Fig. S4B) and UPR activity (Figs. EV3 and EV4). This also means that lipid packing in this region of the bilayer is not the dominant modulator of UPR activity, which is consistent with the proposed hydrophobic mismatch-based mechanism of Ire1 that predicts a contribution of lipid packing across the entire lipid bilayer (Halbleib et al, 2017; Covino et al, 2018). All-atom molecular dynamics (MD) simulations revealed substantial differences between different ER-like lipid bilayers and those composed solely of PC lipids in terms of membrane thickness (Appendix Fig. S4D), lipid packing defects (Appendix Fig. S4E), and free volume profile (Appendix Fig. S4F). This highlights that PC-dominated membrane mixtures are not an accurate mimic for the ER membrane. Compared to a lipid composition mimicking the unstressed ER, the stressed ER (induced by DTT/TM or inositol depletion) was significantly thicker (Appendix Fig. S4D), aligning with the notion that

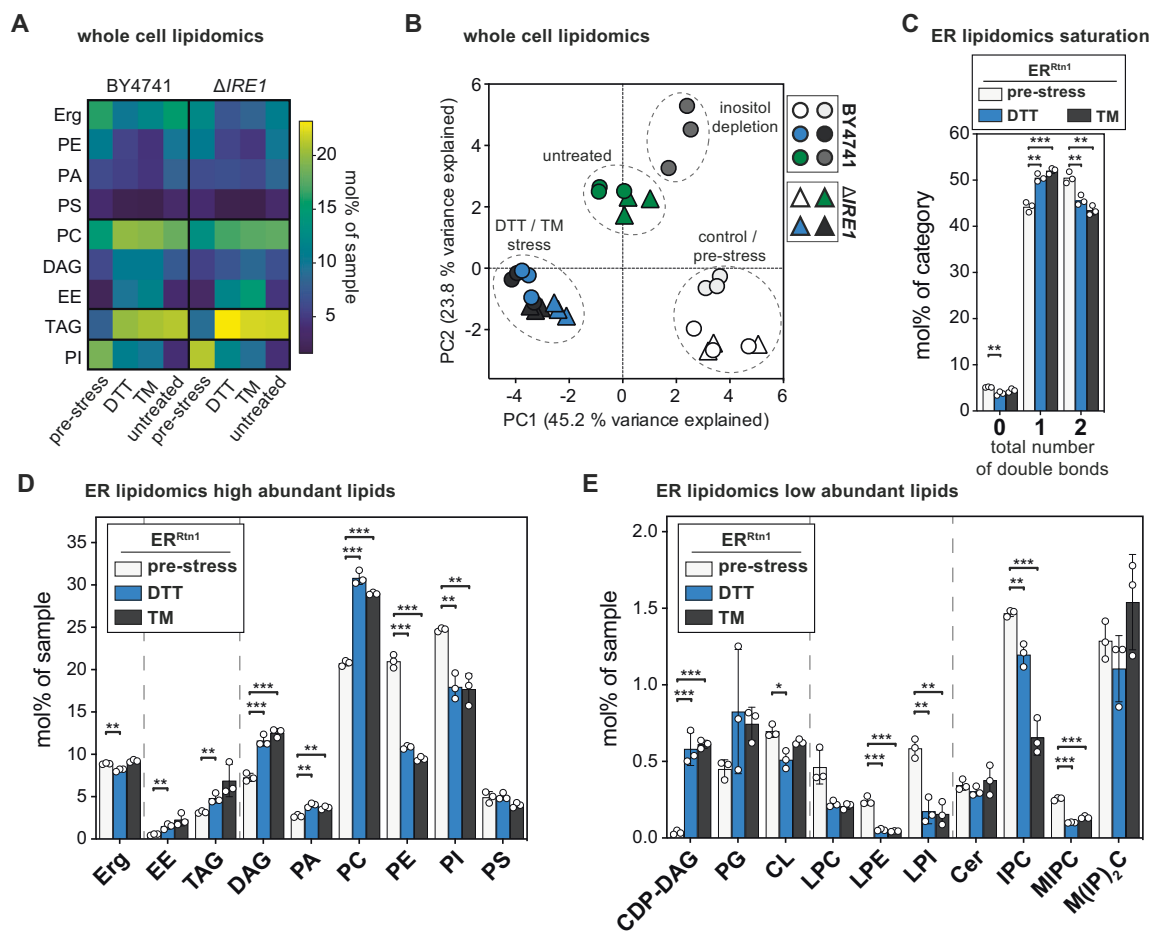


Figure 4. ER stress induced by DTT and TM manifests in a distinct lipid fingerprint on the whole cell and ER level.

(A) SCD_{complete} medium was inoculated with BY4741 wild-type or $\Delta IRE1$ cells to an OD₆₀₀ of 0.1 from an overnight pre-culture. Cells were grown to an OD₆₀₀ of 0.8 and then stressed by the addition of either 2 mM DTT or 1.5 μ g/ml TM or left untreated for 4 h. The lipidome of whole cells was determined by quantitative shotgun mass spectrometry. Mean abundance from three biologically independent replicates is shown as mol% of all lipid classes identified in the sample. Only classes with significant changes are shown and clustered by their abundance pattern. Erg, PE, PA, PS are decreased in DTT- and TM-stressed cells. PC, DAG, EE are increased in stressed cells. TAG increases in all three conditions (DTT/TM stress, untreated). PI is slightly decreased in DTT- and TM-stressed cells and strongly decreased in untreated cells. (B) Principal component analysis (PCA) of whole-cell lipidomics data from wild-type (BY4741, circles) and $\Delta IRE1$ (triangles) cells. Cells were subjected to prolonged proteotoxic stress by DTT or TM or left untreated. PCA includes whole-cell lipidomes of direct lipid bilayer stress by inositol depletion. Lipidomes of DTT and TM stress cluster together, indicating a high degree of similarity. Lipidomes of untreated cells form a distinct cluster different from pre-stressed and DTT- or TM-stressed conditions. Lipidomes of inositol depletion form a distinct cluster, the respective control condition is close to the pre-stress cluster. Cells for inositol depletion were grown as described in Fig. 3. Interestingly, lipidomes of $\Delta IRE1$ cells cluster with their respective wild-type counterparts, indicating little influence of UPR activity on the cellular lipidome under these conditions. (C) Rtn1-bait cells were grown as described for (A). ER-derived membranes were purified by MemPrep and subsequently analyzed by quantitative shotgun lipid mass spectrometry. Total number of double bonds in membrane glycerolipids (without CL) given as mol% of this category ($n = 3$ biological replicates). (D) Lipid class distribution of sterol, storage lipids and abundant membrane glycerolipids in ER-derived vesicles from cells that were either challenged with 2 mM dithiothreitol (DTT) or 1.5 μ g/ml TM for 4 h. The ER lipidome undergoes significant remodeling upon ER stress ($n = 3$ biological replicates). (E) Lipid class distribution of rare membrane glycerolipids, lysolipids, and sphingolipids ($n = 3$ biological replicates). Data information: Data from $n = 3$ biological replicates in (A) are shown as the mean. Data from $n = 3$ biological replicates in (C-E) are presented as individual data points and as the mean \pm SD. * $P \leq 0.05$, ** $P \leq 0.01$, *** $P \leq 0.001$ (multiple t tests, corrected for multiple comparisons using the method of Benjamini, Krieger, and Yekutieli, with $Q = 1\%$, without assuming consistent SD). Nonsignificant comparisons are not highlighted. Source data are available online for this figure.

Ire1 senses lipid bilayer stress through a hydrophobic mismatch-based mechanism (Halbleib et al, 2017; Covino et al, 2018). A particularly intriguing difference between stressed and unstressed ER-like mixtures was the distinct distribution of positive and negative charges in the water-membrane interface (Appendix Fig. S4G) reflecting the different abundance of anionic lipids in the stressed ER (Fig. EV4D; Appendix Fig. S4C). These observations suggest that membrane thickness and membrane compressibility regulate the activity of the UPR and identify anionic lipids as potential modulators. The underlying mechanisms, however, remain to be dissected by *in vitro* experiments. Beyond that, our lipidomic data on the stressed and unstressed ER do not only establish lipid fingerprints of the stressed ER, but also provide a resource for studying the structure, folding, and function of ER membrane proteins in more realistic membrane environments.

DTT and TM have similar yet distinct impact on the ER proteome

Next, we were interested in the repercussions of prolonged proteotoxic stress on the ER proteome. To this end, we isolated ER membranes from stressed and unstressed cells for a quantitative analysis via untargeted proteomics. Prior to subjecting microsomal membranes to the immunoprecipitation procedure, we washed the microsomes with sodium carbonate to remove loosely attached peripheral proteins and contaminating cytosolic proteins even more efficiently. Membrane contact sites are remodeled during ER stress in both yeast and mammalian cells (Vevea et al, 2015; Liu et al, 2017; Kwak et al, 2020; Liao et al, 2022). To exclude that any of the observed proteomic changes are due to increased contaminations with other organelles, we first assessed the impact of DTT and TM on the quality of our ER preparations by immunoblotting. Expectedly, the GPI-anchored cell wall protein Gas1 accumulates as a ~105 kDa precursor in the ER of TM-stressed cells, but not in the ER or DTT-stressed cells (Fig. EV5A) (Fankhauser and Conzelmann, 1991; Wang et al, 2024). The purity of the ER isolations was assessed by determining the enrichment of marker proteins for the ER, the vacuole, mitochondria, and endosomes (Fig. EV5A–C). While the Rtn1-bait and the ER membrane protein Dpm1 were several-fold enriched in the immunoprecipitation step starting from microsomes, the markers for the vacuole (Vph1), mitochondria (Por1), and endosomes (Pep12) were depleted relative to the microsomal P100 fraction (Fig. EV5A–C). Hence, MemPrep allows for the isolation of both the unstressed and the stressed ER.

Using untargeted, quantitative proteomics on ER isolates a total of 2952 proteins were robustly detected in three biological replicates of both the stressed and unstressed ER. Prolonged proteotoxic stresses cause a major remodeling of the ER proteome that involves hundreds of proteins (Fig. 5A,B). Notably, this is in stark contrast to inositol depletion, which affects the abundance of only a few proteins in the ER (Fig. 3A).

Globally, the ER proteomes of DTT- and TM-stressed cells are similar to each other (Pearson correlation coefficient $r = 0.82$, Fig. EV5D). Canonical UPR targets, including ER-luminal (co-) chaperones Kar2, Sil1, and Lhs1, proteins involved in disulfide bridge formation Eug1 and Ero1, and the lipid metabolic enzyme Ino1 were upregulated in the stressed ER (Fig. 5A,B) (Travers et al,

2000; Jesch et al, 2006). The increased abundance of various lipid metabolic enzymes such as Plb1, Plb3, and Cld1 for acyl chain remodeling may contribute to the lipidomic changes observed for the stressed ER and reflect, at least in part, homeostatic responses to maintain ER membrane function upon stress (Renne et al, 2015). Furthermore, major reorganizations of the secretory pathway in response to both DTT- and TM treatments can be inferred from the ER accumulation of the HDEL receptor Erd2 and crucial components of the COP-I (Emp46, and Sly1) and COP-II (Ret2) machinery.

To functionally annotate the complex proteomic changes, we determined the enrichment of gene ontology terms (GO terms) in all upregulated proteins (Fig. 5C). While DTT seems to act more prominently on vesicular transport and autophagic processes (regulation of macroautophagy) (Fig. 5C), TM affects more selectively hydrolytic enzymes and carbohydrate-related metabolic processes thereby leading to an aberrant ER accumulation of vacuolar proteins and cell wall proteins. This can be expected because TM is crucial for the maturation of N-glycosylated proteins and GPI-anchored proteins. To further investigate the differences of DTT- and TM-induced changes of ER proteomes, we performed K-means clustering of the proteomic data (Fig. EV5D). The analysis of GO term enrichments for the individual clusters revealed a small group of proteins that were accumulated in the DTT-stressed ER but depleted in the ER from TM-stressed cells (Fig. EV5D,E, cluster 2). These proteins are involved in copper and iron transport (Fre7, Ctrl1, and Fre1), which is interesting because iron affects the clustering propensity of Ire1 and the amplitude of UPR signaling (Cohen et al, 2017).

Taken together, our proteomics data suggest that DTT and TM treatments induce globally similar, yet qualitatively distinct forms of stress, which are reflected in distinct ER proteomes. Both forms of ER stress cause an accumulation of non-ER proteins in the ER, whose contribution to UPR activation remains to be systematically investigated.

Different forms of lipid bilayer stress leave different marks in the lipid acyl chain region

Prolonged proteotoxic stress and inositol depletion exert discrete effects on the ER proteome (Figs. 3A and 5A,B) and the lipid class composition in the ER (Figs. 3A,B and 4C–E). These discrete effects also extend to the lipid acyl chains (Appendix Fig. S5). Upon inositol depletion, a nuanced shift toward shorter and more saturated acyl chains is observed across major glycerophospholipid classes (Appendix Fig. S5A). This contrasts with the impact of an increased PC-to-PE ratio enforced by choline supplementation, which barely leaves any marks in the lipid acyl chain composition (Appendix Fig. S5B). Moreover, prolonged proteotoxic stress induced by DTT or TM elicits distinctive impacts on the composition of lipid acyl chains (Appendix Fig. S5C,D). In this context, the acyl chains demonstrate a tendency throughout most lipid classes to become slightly longer and more saturated. Collectively, these observations underscore the notion that different forms of lipid bilayer stress are based on unique molecular signatures despite having common denominators. Consequently, targeted perturbations in lipid metabolism designed to ameliorate specific types of lipid bilayer stress may prove detrimental in other metabolic contexts.

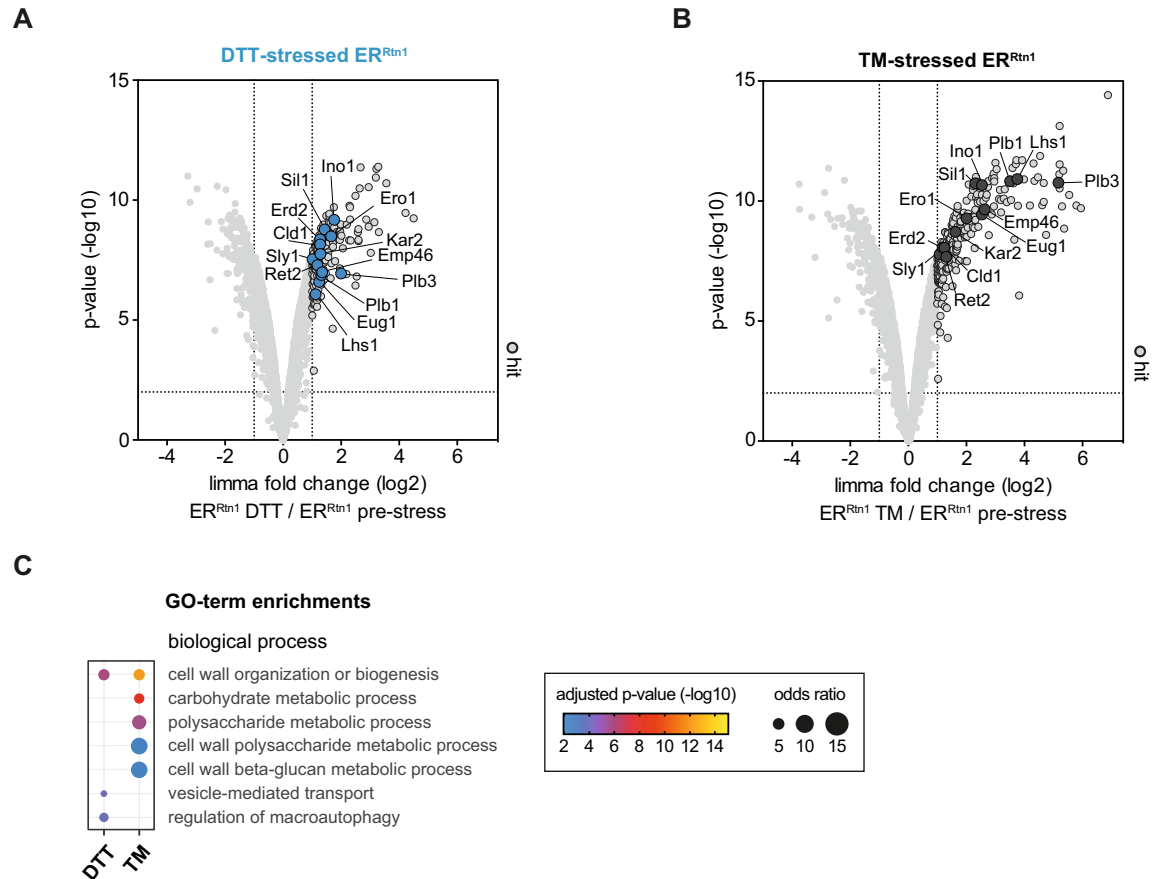


Figure 5. The proteome of the ER under conditions of prolonged proteotoxic stress.

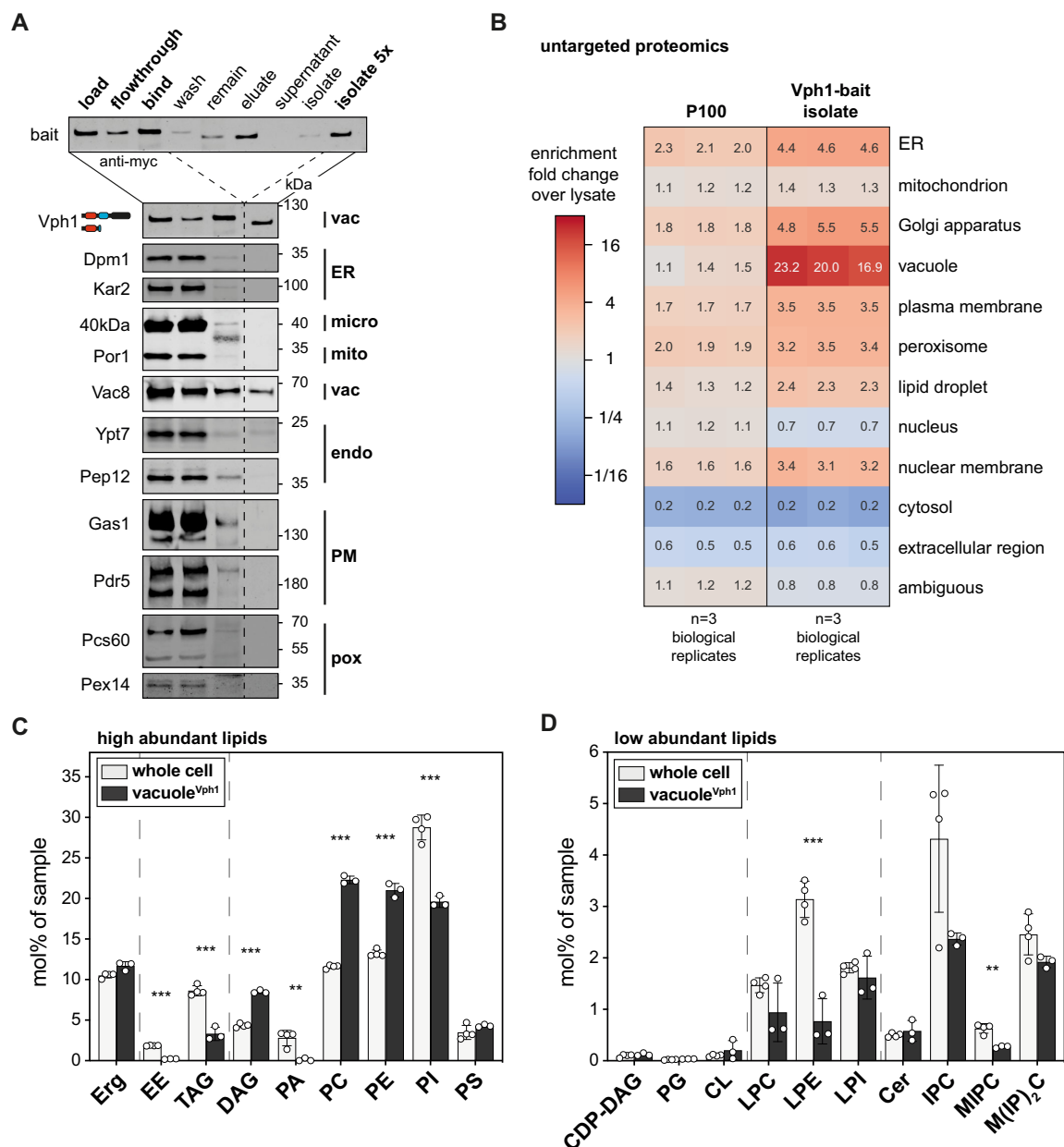
ER-derived vesicles were isolated by MemPrep and subsequently analyzed by untargeted proteomics. An additional sodium carbonate wash step was performed on P100 to remove soluble proteins from the membrane preparation. (A) Limma analysis identified proteins that are accumulating in ER preparations after prolonged DTT-induced stress (top right quadrant of volcano plot). Proteins that are discussed in the text are indicated. The enrichment of proteins in preparations of the stressed ER membrane was considered significant when they were at least twofold enriched compared to their abundance in pre-stress conditions with a P value < 0.01 ($n = 3$ biological replicates). (B) Limma analysis showing proteins that are accumulating in the ER upon prolonged TM-induced ER stress (top right quadrant of volcano plot). All proteins discussed in the text are labeled. The enrichment of proteins in the preparations of the stressed ER was considered significant when they were enriched at least twofold compared to their abundance in pre-stress conditions with a P value < 0.01 ($n = 3$ biological replicates). (C) Enriched gene ontology terms (GO terms) in the list of enriched proteins. GO terms are grouped by categories, FDR $< 1\%$ ($n = 3$ biological replicates). Data information: Data in (A, B) are presented as the mean from three biological replicates. We used the moderated t-test limma to test for differential enrichment. P values were corrected for multiple testing with the method from Benjamini and Hochberg. Data in (C) presented as mean from three biological replicates. P values were derived from a Fisher-test and corrected for multiple testing with the method of Benjamini and Hochberg. Source data are available online for this figure.

Demonstrating the broad applicability of MemPrep on vacuolar membranes

While MemPrep was initially designed and optimized for the isolation of ER membranes, our objective was to develop its applicability for isolating membranes from various organelles. This versatility was validated by successfully isolating vacuolar membranes (Fig. 6A,B). Given that the vacuole receives membrane material via the secretory pathway, endocytosis, macroautophagy, lipophagy, and direct lipid transfer, it was unclear what the lipid

composition of the vacuole would be even though its lipid composition has been partially addressed before (Schneiter et al, 1999; González Montoro et al, 2018).

To investigate the lipid composition of the vacuole, we utilized a bait-tagged variant of Vph1, a subunit of the abundant ATP-driven proton pump in the vacuole. Employing the same procedures as for the ER isolation but with increased starting material, we conducted the subcellular fractionation (Appendix Fig. S6A) and immunolysis (Fig. 6A). Immunoblot analysis of the final isolate confirmed the presence of two vacuolar membrane proteins (the



Vph1-bait and the palmitoylated Vac8), while markers for other organelles remained undetectable, underscoring the broad applicability of MemPrep for organelle membrane isolation (Fig. 6A).

Untargeted proteomics robustly detected 3264 proteins in all three biological replicates and revealed a >20-fold enrichment of many annotated vacuolar proteins (both soluble and membrane proteins) in the final isolate (Fig. 6B). Only a few proteins

annotated to other organelles were enriched >20-fold in the final isolate (Appendix Fig. S6B). Apart from Sys1, which is well-characterized as membrane protein in the Golgi apparatus, all other proteins (Adp1, the uncharacterized Ypr003c, Syg1, Fet5, and Tul1) have previously been observed to localize to the vacuole, affirming the accuracy of our isolation method (Breker et al, 2013, 2014; Yofe et al, 2016; Weill et al, 2018). More specifically, the iron oxidase

◀ **Figure 6. Lipid composition after MemPrep of the vacuolar membrane.**

(A) Immunoblot analysis of fractions after immunoisolation via a vacuolar bait protein (Vph1-bait). Common organellar markers are shown: ER, endoplasmic reticulum (Dpm1 and Kar2); micro, microsomal fraction (40 kDa); mito, mitochondria (Por1); vac, vacuole (Vac8); endo, endosomal system (Ypt7 and Pep12); PM, plasma membrane (Gas1 and Pdr5); pox, peroxisomes (Pcs60 and Pex14). 0.2% of each fraction loaded per lane. (B) Untargeted protein mass spectrometry analysis showing enrichment of P100 and isolate fractions over whole-cell lysate. The enrichment of proteins over the cell lysate (fold change) is based on uniquely annotated subcellular locations and provided for each of $n = 3$ biological replicates. The illustrated numbers represent the median enrichment for each biological replicate. (C) Lipid class composition given as mol% of all lipids in the sample. Classes are categorized into sterol (Erg ergosterol), storage lipids (EE ergosteryl ester, TAG triacylglycerol), membrane glycerolipids (DAG diacylglycerol, PA phosphatidic acid, PC phosphatidylcholine, PE phosphatidylethanolamine, PI phosphatidylinositol, PS phosphatidylserine). Whole-cell lipid data are identical with the data presented in Fig. 2A,B ($n = 4$ biological replicates for whole cell; $n = 3$ biological replicates for vacuole^{vph1}). (D) Continuation of lipid class composition given as mol% of all lipids in the sample. Classes are categorized into rare membrane glycerolipids (CDP-DAG cytidine diphosphate diacylglycerol, PG phosphatidylglycerol, CL cardiolipin), lysolipids (LPC lyso-phosphatidylcholine, LPE lyso-phosphatidylethanolamine, LPI lyso-phosphatidylinositol) and sphingolipids (Cer ceramide, IPC inositolphosphorylceramide, MIPC mannosyl-IPC, M(IP)₂C mannosyl-di-IPC). Whole-cell lipid data are identical with the data presented in Fig. 2B. Data information: Data in (B) are presented as the median enrichment of uniquely annotated genes for $n = 3$ biological replicates. Data in (C, D) are presented as individual data points and the mean \pm SD. ** $P \leq 0.01$, *** $P \leq 0.001$ (multiple t tests, corrected for multiple comparisons using the method of Benjamini, Krieger, and Yekutieli, with $Q = 1\%$, without assuming consistent SD). Nonsignificant comparisons are not highlighted. Source data are available online for this figure.

Fet5 was demonstrated to reside in the vacuole (Urbanowski and Piper, 1999), while Tull1 is part of the yeast Dsc E3 ubiquitin ligase complex that localizes, depending on its exact composition, to the Golgi apparatus, endosomes, or the vacuole (Yang et al, 2018). These observations collectively support the conclusion that the MemPrep procedure can yield highly pure vacuole membranes.

Further analysis through shotgun lipidomics unveiled substantial differences in lipid composition between vacuolar membranes and whole-cell lysate (Fig. 6C,D), as well as the plasma membrane (Surma et al, 2011). Noteworthy similarities with the ER, such as the abundance of PC, PI, and complex sphingolipids, were observed (Appendix Fig. S6C,D). However, distinct features included significantly higher levels of ergosterol and DAGs in the vacuole membrane, as well as an almost complete absence of PA lipids (Appendix Fig. S6C). These findings align with previous studies using alternative protocols for vacuole isolation (González Montoro et al, 2018; Kim and Budin, 2024) and our own work utilizing Mam3 as an alternative bait protein (Reinhard et al, 2023).

In line with its function of the vacuole as a lipid-degrading organelle, elevated levels of lysolipids (LPC, LPE, and LPI) were detected in the vacuole compared to the ER membrane (Appendix Fig. S6D). In addition, the lipid fatty acyl chains are more saturated in the vacuole compared to the ER membrane (Appendix Fig. S6E). These findings underscore the remarkable versatility of the MemPrep immunoisolation procedure and its suitability for organellar lipidomics.

Discussion

Understanding the homeostasis and adaptation of organellar membranes to metabolic perturbation and cellular stress is one of the key challenges in membrane biology. We developed MemPrep for the isolation of organellar membranes and a quantitative characterization of their composition. The versatility of this approach is demonstrated by the immunoisolation of membrane vesicles from two organelles in yeast: the ER and the vacuole. Using state-of-the-art lipidomics we provide a comprehensive, molecular description of their membrane composition and establish a baseline for dissecting the role of lipids in transmembrane protein folding, trafficking, and function. Atomistic molecular dynamics (MD) simulations highlight the difference between ER-mimetic

membranes and PC-based lipid bilayers with respect to membrane thickness, lipid packing, the free volume profile, and surface charge distribution (Appendix Fig. S4C–G). The biochemical reconstitution of ER proteins in more realistic membrane environments is now feasible and will become particularly relevant for the characterization of membrane property sensors and the machineries that insert and extract membrane proteins into and out of the ER, respectively (Covino et al, 2018; Wu and Rapoport, 2021).

MemPrep overcomes the challenges associated with extensive membrane contact sites for purifying organelle membranes. In contrast to recent strategies optimized for a rapid precipitation of organelles from yeast and mammalian cells (Liao et al, 2018; Melero et al, 2018; Ray et al, 2020; Higuchi-Sanabria et al, 2020), MemPrep maximizes purity at the expense of low yields and provides full access to the eluted membrane vesicles for a straightforward coupling to quantitative, analytical platforms. Using the Rtn1-bait, MemPrep facilitates a mean enrichment of 27.7 for over 213 tested ER-resident proteins. This is remarkable, because even a sevenfold enrichment over the cell lysate has been considered as sufficient or even optimal in the past (Zinser and Daum, 1995). While we cannot rule out the possibility that certain lipids redistribute during cell disruption and organelle isolation, our proteomic and lipidomic data identify organelle-specific compositions that exclude a global mixing of organelle membranes or a broad equilibration of lipids during these procedures. Nevertheless, lateral specializations of the ER membrane such as sheets and tubules collapse during the preparation, as isolates via the Rtn1-bait and the Elo3-bait feature almost identical proteomes (Fig. EV1) and lipidomes (Fig. EV2). Based on these observations, we think that MemPrep reports rather on the “global” ER membrane composition, whereas ER sub-compartments in vivo may establish local, specialized compositions.

Quantitative lipidomics demonstrates that the ER membrane has a remarkably high content of unsaturated fatty acyl chains (~74 mol%) and a low level of ergosterol (9.7 mol%). The resulting low degree of lipid packing is a crucial determinant of ER identity and renders it highly compressible (Bigay and Antonny, 2012; Holthuis and Menon, 2014; Renne and Ernst, 2023). Lipid packing in the ER membrane is continuously monitored by lipid saturation sensors (Covino et al, 2016; Ballweg et al, 2020) and actively maintained by the OLE pathway that regulates the production of unsaturated fatty acids and sterols (Hoppe et al, 2000; Rice et al,

2010). Maintaining ER membrane compressibility, on the other hand, is important to facilitate the insertion and folding of membrane proteins that differ substantially in their hydrophobic thicknesses and surface roughness depending on their subcellular distribution along the secretory pathway (Sharpe et al, 2010; Quiroga et al, 2013; Lorent et al, 2017, 2020). The machineries that insert and remove membrane proteins into and from the ER, respectively, induce a local membrane thinning, presumably to lower the energy barrier for insertion and extraction (Wu and Rapoport, 2021). Consequently, aberrantly high sterol levels or increased lipid saturation inhibit the insertion of transmembrane proteins in model membranes, the mammalian ER, and bacterial membranes (Nilsson et al, 2001; Brambillasca et al, 2005; Kamel et al, 2022). Therefore, it comes as no surprise that the compressibility and thickness of the ER membrane is continuously monitored by the UPR for regulating the relative rate of protein and lipid biosynthesis (Halbleib et al, 2017; Schuck et al, 2009; Covino et al, 2018).

Our lipidomic data are fully consistent with a gradual increase of lipid saturation along the secretory pathway (Van Meer et al, 2008; Bigay and Antonny, 2012), thereby complementing previous work on the composition of the trans-Golgi network/endosomal (TGN/E) system, secretory vesicles, and the plasma membrane in yeast (Klemm et al, 2009; Surma et al, 2011). Likewise, the ergosterol level of 9.7 mol% in the yeast ER membrane is consistent with previous estimations (Zinser and Daum, 1995; Schneiter et al, 1999; Van Meer et al, 2008) and parallels findings in mammalian cells, for which a resting cholesterol level in the ER between 7 and 8 mol% has been reported along with a switch-like regulation of sterol response element binding protein (SREBP) processing, when the level of cholesterol drops below 5 mol% in the ER (Radhakrishnan et al, 2008; Sokoya et al, 2022). From a cell biological viewpoint, our data suggest that the sterol gradient along the secretory pathway is rather flat from the ER (9.7 mol%) to the TGN/E system (9.8 mol%) (Klemm et al, 2009). If this is indeed the case, our findings support the view that active transport of sterols by lipid transfer proteins (Mesmin et al, 2013) aids lipid and protein sorting at the level of the TGN (Klemm et al, 2009). A flat sterol gradient in the early secretory pathway and a step-wise increase at the level of the TGN has important implications for the sorting of transmembrane proteins (Sharpe et al, 2010; Herzig et al, 2012; Quiroga et al, 2013; Lorent et al, 2017) and is consistent with recent models that favor sterol-enriched vesicular carriers (Borgese, 2016) or sterol-based, selective diffusion barriers for membrane proteins in the early secretory pathway (Weigel et al, 2021). This would be reminiscent of ceramide-based diffusion barriers for membrane proteins in the ER of dividing cells, which limits the access for 'old', potentially damaged membrane proteins to the daughter cell (Clay et al, 2014; Megyeri et al, 2019). Significant levels of complex sphingolipids in the ER, on the other hand, have previously been observed and are not surprising, even though the de novo biosynthesis of these lipids occurs in the Golgi apparatus (Hechtberger et al, 1994; Schneiter et al, 1999) (Fig. 2B). In fact, complex sphingolipids can be transported to the ER at substantial rates, in part for their degradation to ceramide by the phospholipase Isc1 in the context of a sphingolipid salvage pathway (Matmati and Hannun, 2008).

The lipid composition of the vacuole is vastly distinct from that of the plasma membrane (Surma et al, 2011) despite a substantial intake of membrane material via the endocytic route (Wendland

et al, 1998). The vacuolar membrane is also distinct from the ER membrane both in terms of lipid saturation (71 mol% unsaturated lipid acyl chains) and sterol content (11.7 mol%). It is possible that a tighter lipid packing in the vacuole membrane is required to reduce membrane permeability and to support vacuolar acidification. Most strikingly, however, is the near complete absence of PA lipids in the vacuole membrane (Fig. 6C), which is consistent with recent observations using alternative means of organelle isolation (González Montoro et al, 2018; Kim and Budin, 2024). Intriguingly, PA lipids are important signaling molecules in the ER membrane that regulate lipid biosynthesis by sensing the cytosolic pH, which in turn is crucially regulated by the vacuolar proton pump (Young et al, 2010; Hofbauer et al, 2018). The higher level of lysolipids observed in vacuolar versus ER membranes is consistent with the role of the vacuole as a lipid-degrading organelle (Henry et al, 2012). Notably, due to the large head-to-tail volume ratio, lysolipids exhibit large positive intrinsic curvature that would favor the formation of membrane defects (Ting et al, 2018). Hence, the high levels of the negatively curved DAG may be required to counterbalance undesired effects from lysolipids on membrane stability.

We have established and employed MemPrep to identify molecular fingerprints of lipid bilayer stress. While lipid metabolic changes of the ER membrane have been firmly associated with chronic ER stress (Hotamisligil, 2010), the underlying molecular changes remain understudied. We show that distinct conditions of lipid bilayer stress, namely inositol depletion and prolonged proteotoxic stresses, are associated with significant changes of the ER composition (Figs. 3 and 4) and identify an increased membrane thickness as a common denominator of the membrane-based UPR activation (Appendix Fig. S4D). This is in line with the prevailing model that Ire1 senses lipid bilayer stress via a hydrophobic mismatch-based mechanism (Halbleib et al, 2017). Our unbiased approach provides the surprising insight that a reduced abundance of anionic lipids in the ER membrane correlates with UPR activation. A general role of negatively charged lipids as attenuators of the UPR would have important physiological implications, because the level of PI and other anionic lipids change substantially in different growth stages (Casanovas et al, 2015). In fact, the availability of inositol is limiting for optimal growth of the commonly used strain BY4741 (Hanscho et al, 2012) and its prolonged cultivation in synthetic medium containing only 11 μ M causes UPR activation even in the absence of exogenous stressors (Fig. EV4) when the cellular level of anionic PI lipids is low (Fig. 4A). Integrating information on the membrane composition and properties, either directly or indirectly, is crucial for Ire1 to orchestrate membrane biogenesis by balancing the production of proteins and lipids in different stages of growth (Covino et al, 2018). Now, it is possible to study the role of anionic lipids on Ire1 oligomerization by systematic reconstitution experiments using realistic membrane environments.

MemPrep also facilitates a direct comparison of different forms of lipid bilayer stress on the level of the proteome. Inositol depletion affects the abundance of only a handful of proteins, which are involved in handling either inositol or inositol-containing lipids (Fig. 3A). In stark contrast, DTT and TM cause a broader and more complex remodeling of the ER proteome (Figs. 5 and EV5D,E). This is not surprising as these potent proteotoxic agents can rapidly trigger the UPR and maintain UPR activity upon prolonged treatments via a membrane-based

mechanism (Promlek et al, 2011; Vath et al, 2021). Many proteins accumulating in the ER of DTT- or TM-stressed cells are known UPR targets, including ER chaperones, oxidoreductases, and lipid metabolic enzymes (Figs. 5 and EV5) (Travers et al, 2000; Jesch et al, 2006). While this accumulation likely reflects the duration of UPR activity, our proteomic analyses of the stressed ER are in line with the proposition that proteotoxic and lipid bilayer stress are associated with distinct transcriptional programs (Ho et al, 2020). Nevertheless, it is remarkable that DTT and TM, which establish somewhat similar but clearly distinct ER proteomes (Figs. 5 and EV5D,E), have virtually identical ER lipid fingerprints even down to the level of lipid acyl chains (Fig. 4C–E; Appendix Fig. S5).

Our quantitative data address an open question on the role of the PC-to-PE ratio in the ER as a potential driver of the UPR. PC and PE lipids are key determinants of the lateral pressure profile and curvature stress in cellular membranes, thereby affecting the conformational dynamics of membrane proteins (Marsh, 2007; van den Brink-van der Laan et al, 2004; Phillips et al, 2009). Aberrantly increased PC-to-PE ratios in the ER were suggested to cause chronic ER stress in obese mice (Fu et al, 2011), but the general validity of this interpretation has been controversially discussed (Gao et al, 2015). We employed MemPrep, quantitative lipidomics, and sensitive UPR assays to investigate this point in yeast. Prolonged proteotoxic stress is associated with a dramatically increased PC-to-PE ratio in the ER, which goes well beyond the range of physiological variation observed in cells at different growth stages (Klose et al, 2012; Janssen et al, 2000; Casanovas et al, 2015; Tran et al, 2019a). In contrast, artificially increasing the PC-to-PE ratio in the ER by supplementing choline to the medium is not sufficient to trigger the UPR (Fig. EV3). Inositol depletion, on the other hand, triggers a robust UPR without significantly perturbing the PC-to-PE ratio (Fig. EV3). Hence, an increased PC-to-PE ratio is not sufficient to activate the UPR in yeast. Instead, we favor the idea that a reduced PC-to-PE ratio and the accumulation of lipotoxic intermediates trigger the UPR by activating Ire1 either directly or indirectly (Ho et al, 2020; Ishiwata-Kimata et al, 2022). In summary, our quantitative analysis of the ER membrane composition isolated from stressed and metabolically challenged cells provides important insights to tackle mechanistic questions related to the chronic activation of the UPR.

Combining MemPrep with quantitative proteomics and lipidomics unlocks a toolbox to study the inter-organelle transport of both proteins and lipids. It is now feasible to investigate membrane protein targeting and sorting comprehensively and with organellar resolution. A variation of the MemPrep approach has been employed to establish a crucial role of the endoplasmic reticulum-mitochondria encounter structure (ERMES) for the delivery of mitochondrial preproteins via the ER surface to the mitochondrial import machinery (preprint: Koch et al, 2023). There are also fascinating examples of inter-organelle communication between the ER, lipid droplets, mitochondria, peroxisomes, and the vacuole in dealing with ER stress and lipotoxicity (Listenberger et al, 2003; Piccolis et al, 2019; Garcia et al, 2021). Here, the exchange of lipids between organelles provides a means to adapt to cellular stress and metabolic cues (Scorrano et al, 2019). While changes in lipid abundance can be readily identified by whole-cell lipidomics, it is not possible to study their redistribution in cells from one organelle to another unless individual organelle

membranes can be isolated and analyzed. This is now becoming feasible. Naturally, it is also possible in this context to combine gene deletions with organelle-specific bait strains for studying the role of a specific gene on the lipid composition of an individual organelle.

There are, however, also limitations to the MemPrep approach, which has been optimized for highest purity. The yields of the preparation are low, which can make the isolation of membranes from low abundant organelles less feasible. While MemPrep provides a comprehensive snapshot of a specific organelle membrane, the associated preparative efforts are significant, and the benefit of extensive time-course experiments should be carefully evaluated. Because lateral specializations of the ER membrane and membrane contact sites are disrupted during the preparation, the MemPrep approach is not suitable to isolate membrane contact sites or other lateral membrane specializations such as the outer or inner nuclear membrane. For these purposes, proximity labeling approaches and a selective solubilization of membrane proteins are promising developments (Kwak et al, 2020; van 't Klooster et al, 2020).

Elegant approaches have provided a first glimpse at the rate of lipid exchange between individual certain organelles (John Peter et al, 2022), but there is a great need for new preparative and analytical tools to obtain a comprehensive map of lipids at a given time. The combination of biosensors providing high spatial and temporal resolution with MemPrep, which provides quantitative and comprehensive snapshots of a given organelle at a certain time, surfaces as a promising approach to study membrane adaptation in a holistic fashion. We make MemPrep accessible to the community and have generated a collection of strains that facilitates the isolation of any organellar membrane of interest, as demonstrated for the ER and the vacuolar membrane.

Methods

Generation of MemPrep library

The C-terminus SWAp Tag (SWAT) library from yeast was used to generate a library with a C-terminal myc-HRV3C-3xFLAG tag as previously published (Meurer et al, 2018). In short, a SWAT donor strain (yMS2085) was transformed with a donor plasmid (pMS1134) containing the myc-HRV3C-3xFLAG cassette and then SWATted as described. The final library genotype is his3Δ1 leu2Δ0 met15Δ0 ura3Δ0, can1Δ::GAL1pr-SceI-NLS::STE2pr-SpHIS5, lyp1Δ::STE3pr-LEU2, XXX-L3-MYC-HRV3C-3xFLAG-ADH1ter-TEFpr-KANMXR-TEFter-L4]. Once generated, to check proper integration of the cassette into the genome, random proteins were tested by polymerase chain reaction (PCR) and sodium dodecyl sulfate-polyacrylamide gel electrophoresis (SDS-PAGE), confirming their in-frame tagging.

Manual generation of bait-tag strains

DNA sequences of *HRV3C site-GSG* and *myc-GSG* were introduced via primers in two consecutive steps between *6xGLY* and *3xFLAG* encoding regions on plasmid pFA6a-6xGLY-3xFLAG-kanMX6 (Funakoshi and Hochstrasser, 2009) (Addgene plasmid #20754) using Gibson assembly to yield pRE866. The DNA sequence of the

Reagents and tools table

Reagent/resource	Reference or source	Identifier or catalog number
Experimental models		
BY4741 (<i>S. cerevisiae</i>)	Euroscarf	MATa <i>his3Δ1 leu2Δ0 met15Δ0 ura3Δ0</i>
ΔIRE1 (<i>S. cerevisiae</i>)	Euroscarf	MATa <i>his3Δ1 leu2Δ0 met15Δ0 ura3Δ0 IRE1::KANMX4</i>
Rtn1-bait, RESC000796 (<i>S. cerevisiae</i>)	This study	MATa <i>his3Δ1 leu2Δ0 met15Δ0 ura3Δ0 RTN1-MYC-3C-3xFLAG-KANMX6</i> + pRE512
Elo3-bait, RESC000799 (<i>S. cerevisiae</i>)	This study	MATa <i>his3Δ1 leu2Δ0 met15Δ0 ura3Δ0 ELO3-MYC-3C-3xFLAG-KANMX6</i>
Vph1-bait, RESC000798 (<i>S. cerevisiae</i>)	This study	MATa <i>his3Δ1 leu2Δ0 met15Δ0 ura3Δ0 VPH1-MYC-3C-3xFLAG-KANMX6</i>
Rtn1-bait + ER-sfGFP-HDEL, RESC000797 (<i>S. cerevisiae</i>)	This study	MATa <i>his3Δ1 leu2Δ0 met15Δ0 ura3Δ0 RTN1-MYC-3C-3xFLAG-KANMX6</i> + pRE512
Recombinant DNA		
<i>Indicate species for genes and proteins when appropriate</i>		
pRE866	This study	pFA6a-KANMX6 containing the MYC-3C-3xFLAG tag for bait tagging
pRE512	Eric Snapp	pRS415-ER-sfGFP-HDEL (ER-luminal marker)
Antibodies		
Anti-FLAG, mouse monoclonal M2	Sigma-Aldrich	F1804
Anti-myc, mouse monoclonal 9E10 (1:1000)	Sigma-Aldrich	M4439
Anti-Dpm1, mouse monoclonal 5C5A7 (1:2000)	Fisher Scientific	A6429
Anti-Sec61, rabbit antiserum (1:1000)	Karin Römisch	
Anti-Kar2, rabbit polyclonal y-115 (1:1000)	Santa Cruz	sc-33630
Anti-40kDa, rabbit antiserum (1:10,000)	Sepp Kohlwein	
Anti-Por1, rabbit antiserum (1:10,000)	Sepp Kohlwein	
Anti-Tlg2, rabbit antiserum (1:1000)	Susan Ferro-Novick	
Anti-Vac8, rabbit antiserum (1:10,000)	Christian Ungermann	
Anti-Ypt7, rabbit antiserum (1:1000)	Christian Ungermann	
Anti-Pep12, mouse monoclonal 2C3 (1:1000)	Thermo Fisher Scientific	
Anti-Gas1, rabbit antiserum (1:2000)	Howard Riezman	
Anti-Pdr5, rabbit antiserum (1:10,000)	Karl Kuchler	
Anti-Pcs60, rabbit antiserum (1:5000)	Ralf Erdmann	
Anti-Pex14, rabbit antiserum (1:2000)	Ralf Erdmann	
Anti-Vph1, mouse monoclonal (1:2000)	Abcam	ab113683
Anti-rabbit, goat IRDye 680LT (1:15,000)	LI-COR	926-68021

Reagent/resource	Reference or source	Identifier or catalog number
Anti-rabbit, goat IRDye 800CW (1:15,000)	LI-COR	926-32211
Anti-mouse, goat IRDye 680LT (1:2000)	LI-COR	926-68020
Anti-mouse, goat IRDye 800CW (1:15,000)	LI-COR	926-32210
Oligonucleotides and sequence-based reagents		
RE1012 (tag Rtn1 with bait from pRE866 fwd)	This study	GAAAAGTACAAAAAAGCTTGC AAAATGAATTGGAAAAAACAACGCTgggggaggcgggggtgga
RE1013 (tag Rtn1 with bait from pRE866 rev)	This study	CAAAAGTTAGCTATTCTTTGAAATGAAAAAAGCACTCAgaattcgagctgtttaaac
RE1014 (tag Vph1 with bait from pRE866 fwd)	This study	GGAAGTCGCTGTTGCTAGTGCAAGCTCTCCGCTTCAAGCgggggaggcgggggtgga
RE1015 (tag Vph1 with bait from pRE866 rev)	This study	GAAGTACTTAAATGTTTCGCTTTTTTAAAAGTCTCAAATTTAgaattcgagctgtttaaac
RE1018 (tag Elo3 with bait from pRE866 fwd)	This study	CTGGTGCAAGACCTCTAACACCAAGTCTCTCCAGGAAAGCTgggggaggcgggggtgga
RE1019 (tag Elo3 with bait from pRE866 rev)	This study	CATTTAATTTTTTCTTTTTCATTCGCTGTCAAAAATTCGCTTCTATTGAgaattcgagctgtttaaac
Chemicals, enzymes, and other reagents		
NBD-PE, 1,2-dioleoyl-sn-glycero-3-phosphoethanolamine-N-(7-nitro-2,1,3-benzoxadiazol-4-yl)	Avanti Polar Lipids	810145
Rho-PE, 1,2-dioleoyl-sn-glycero-3-phosphoethanolamine-N-(lissamine rhodamine B sulfonyl)	Avanti Polar Lipids	810150
DPDG, 1,2-dipalmitoyl-sn-glycerol	Avanti Polar Lipids	800816
PODG, 1-palmitoyl-2-oleoyl-sn-glycerol	Avanti Polar Lipids	800815
DODG, 1-2-dioleoyl-sn-glycerol	Avanti Polar Lipids	800811
Erg, Ergosterol	Sigma-Aldrich	PHR1512
16:1-PE, 1,2-dipalmitoleoyl-sn-glycero-3-phosphoethanolamine	Avanti Polar Lipids	850706
POPE, 1-palmitoyl-2-oleoyl-sn-glycero-3-phosphoethanolamine	Avanti Polar Lipids	850757
16:1-PC, 1,2-dipalmitoleoyl-sn-glycero-3-phosphocholine	Avanti Polar Lipids	850358
POPC, 1-palmitoyl-2-oleoyl-glycero-3-phosphocholine	Avanti Polar Lipids	850457
POPI, 1-palmitoyl-2-oleoyl-sn-glycero-3-phosphoinositol	Avanti Polar Lipids	850142
POPA, 1-palmitoyl-2-oleoyl-sn-glycero-3-phosphate	Avanti Polar Lipids	840857

Reagent/resource	Reference or source	Identifier or catalog number
DOPA, 1,2-dioleoyl-sn-glycero-3-phosphate	Avanti Polar Lipids	840875
POPS, 1-palmitoyl-2-oleoyl-sn-glycero-3-phospho-L-serine	Avanti Polar Lipids	840034
DOPS, 1,2-dioleoyl-sn-glycero-3-phospho-L-serine	Avanti Polar Lipids	840035

bait-tag cassette (Appendix Supplementary Methods) was amplified by PCR from plasmid pRE866 using primers RE1012/RE1013, RE1018/RE1019, RE1014/RE1015 for tagging Rtn1, Elo3, and Vph1, respectively. Primers contain homologous regions for C-terminal tagging at the endogenous loci (*RTN1*, *ELO3*, *VPH1*). PCR products were used to transform wild-type yeast strain BY4741 by the lithium-acetate method (Ito et al, 1983).

Fluorescence microscopy

In total, 3 μ l of a yeast cell suspension ($OD_{600} = 50$), crude cell lysates or a fraction from the isolation procedure were placed on a thin agarose pad (1% agarose prepared in SCD) and then covered with a coverslip. Images were acquired on an Axio Observer Z1 equipped with a Rolera em-c2 camera (QImaging) and a Colibri 7 (Zeiss) light source for fluorescence excitation. Using either an EC Plan-Neofluar 100 \times /1.3 or an EC Plan-Apochromat 63 \times /1.4 objective in combination with a 1.6 \times tube lens (Zeiss), GFP fluorescence was excited using a 475-nm LED module and a 38 HE filter (Zeiss). Differential interference contrast (DIC) images were acquired using a translight LED light source. Image contrasts were adjusted linearly using Fiji (Schindelin et al, 2012).

Immunofluorescence

Yeast cells for immunofluorescence were grown to $OD_{600} = 1.0$. 20 OD_{600} units were fixed in 1 ml PBS containing 4% paraformaldehyde at RT for 2 h. Fixed cells were then washed with SP buffer (25 mM HEPES pH 7.4, 1 mM EDTA, 1.2 M sorbitol) and subsequently incubated in SP buffer containing 2% (v/v) 2-mercaptoethanol and 0.1 mg/ml Zymolyase 20 T (amsbio, 120491-1) at RT for 15 min to generate spheroblasts. 10 μ l of washed spheroblast solution was placed on a round 10 mm coverslip, previously coated with poly-L-lysine (Sigma-Aldrich, P8920), and incubated at RT for 30 min. Cells were permeabilized by incubation in ice-cold methanol for 5 min and then acetone for 30 s. After brief air-drying, coverslips were immediately placed in 12-well plates and incubated with 1 ml of PBS-B (PBS, 1% BSA) for 30 min. Samples were then incubated with primary anti-FLAG (1:500) in PBS-BT (PBS, 1% BSA, 0.1% Tween-20) at RT for 1 h. After washing with PBS-B, samples were incubated with secondary anti-mouse IRDye 680LT (1:2000) in PBS-BT at RT for 1 h. After washing with PBS-B, PBS and rinsing in 95% ethanol, samples were mounted with 4 μ l Fluoromount-G (Thermo Fisher Scientific) on glass slides. Images were acquired on an Axio Observer Z1 equipped with a Rolera em-c2 camera (QImaging) and a Colibri 7 (Zeiss) light source for fluorescence excitation. Using an EC Plan-Neofluar 100 \times /1.3 objective, GFP and IRDye fluorescence were

excited using a 475 nm and 630 nm LED module with filters 38 HE and 90 HE (Zeiss), respectively. Image contrasts were adjusted linearly using Fiji (Schindelin et al, 2012).

Cell cultivation

Cells were cultivated at 30 °C in SCD_{complete} medium (0.79 g/l complete supplement mixture (Formedium, batch no: FM0418/8363, FM0920/10437), 1.9 g/l yeast nitrogen base without amino acids and without ammonium sulfate (YNB) (Formedium, batch no: FM0A616/006763, FM0718/8627), 5 g/l ammonium sulfate (Carl Roth) and 20 g/l glucose (ACS, anhydrous, Carl Roth)) and constantly agitated by shaking the cultures at 220 rpm. Unless stated otherwise, overnight cultures (21 h) were used to inoculate a main culture to an OD_{600} of 0.1. Cells were harvested by centrifugation (3000 \times g, 5 min, room temperature (RT)) at an OD_{600} of 1.0, washed with 25 ml ice-cold phosphate-buffered saline (PBS), snap-frozen in liquid nitrogen, and stored at -80 °C until further use. In each case ER and vacuolar membranes were isolated from a total of 2000 and 4000 OD_{600} units, respectively. This general procedure for cell cultivation and harvesting was also employed for stressed cells, with minor adaptations. For isolating the ER from cells before and after the induction of prolonged proteotoxic stresses, the cells were cultivated in the absence of stress to an OD_{600} of 0.8 and a "pre-stress" sample was harvested. The residual culture was supplemented with either 2 mM dithiothreitol (DTT) or 1.5 μ g/ml tunicamycin (TM) and cultivated for another 4 h prior to harvesting the cells. For isolating the ER from inositol-depleted cells, a first culture was inoculated to an OD_{600} of 0.003 and cultivated overnight to an OD_{600} of 1.2. Cells from this culture were pelleted (3000 \times g, 5 min, RT), washed twice with 100 ml pre-warmed inositol-free medium (SCD_{complete-ino} prepared using yeast nitrogen base lacking inositol (YNB-ino) [Formedium batch no: FM0619/9431]). The washed cells were then resuspended in either inositol-containing SCD_{complete} (control) or in SCD_{complete-ino} (inositol depletion) medium to an OD_{600} of 0.6 and cultivated for another 2 h prior to harvesting the cells.

Cell lysis and differential centrifugation

Frozen cell pellets of 1000 OD_{600} units were thawed on ice, resuspended in microsome preparation (MP) buffer (25 mM HEPES pH 7.0, 600 mM mannitol, 1 mM EDTA, 0.03 mg/ml protease inhibitor cocktail containing equal weights of pepstatin, antipain, chymotrypsin and 12.5 units/ml benzonase nuclease (Sigma-Aldrich)) and mechanically disrupted in 15 ml reaction tubes previously loaded with 13 g zirconia/silica beads (0.5 mm diameter, Carl Roth) using a FastPrep-24 bead beater (5 m/s, 10

cycles of 15 s beating and 45 s of cooling in an ice bath). Cell lysates were centrifuged twice ($3234 \times g$, 5 min, 4 °C) in a swinging bucket rotor to remove unbroken cells, cell debris and nuclei. The resulting post nuclear supernatant (PNS) was centrifuged ($12,000 \times g$, 20 min, 4 °C) in a Beckman type 70 Ti rotor to remove large organelle fragments. Using the same rotor, the resulting supernatant (S12) was centrifuged ($100,000 \times g$, 1 h, 4 °C) to obtain microsomes in the pellet. Microsomes were resuspended in 1 ml MP buffer per 1000 OD₆₀₀ units of original cell mass, snap-frozen in liquid nitrogen, and stored at -80 °C until further use. For subsequent proteomics analyses of samples from pre-stressed and stressed cells, microsomes were additionally resuspended in MP buffer containing 200 mM sodium carbonate (pH 10.6) and incubated rotating overhead at 3 rpm and 4 °C for 1 h to remove soluble and membrane-associated proteins. Carbonate-washed microsomes were neutralized by the addition of concentrated HCl, sedimented by ultracentrifugation ($100,000 \times g$, 1 h, 4 °C), resuspended in 1 ml MP buffer per 1000 OD₆₀₀ units original cell mass, snap-frozen in liquid nitrogen, and stored at -80 °C until further use.

Immunoisolation

The entire isolation procedure was performed on ice or at 4 °C. Microsomes were thawed in 1.5-ml reaction tubes and then dissociated using a sonotrode (MS72) on a Bandelin Sonopuls HD 2070 with 50% power and 10 pulses of each 0.7 s (duty cycle 0.7). While sonication may affect the sidedness of ER-derived vesicles, this step was crucial for maximizing the purity of the preparation. After sonication, the microsomes were centrifuged ($3000 \times g$, 3 min, 4 °C). In total, 700 μ l of the resulting supernatant (corresponding to 700 OD₆₀₀ units) were mixed with 700 μ l immunoprecipitation (IP) buffer (25 mM HEPES pH 7.0, 150 mM NaCl, 1 mM EDTA) and loaded onto magnetic beads (dynabeads, protein G, 2.8 μ m diameter, Invitrogen), which were previously decorated with sub-saturating quantities of a monoclonal anti-FLAG antibody (M2, F1804, Sigma-Aldrich). Specifically, the affinity matrix was prepared by using 800 μ l of magnetic bead slurry per 700 OD₆₀₀ units of cells, which were incubated overnight at 4 °C with 3.2 μ g of the anti-FLAG antibody using an overhead rotor at 20 rpm. Subsequently, microsomes were loaded on the antibody-decorated magnetic beads and allowed to bind for 2 h at 4 °C using an overhead rotor at 3 rpm.

The bound membrane vesicles were washed two times with 1.4 ml of wash buffer (25 mM HEPES pH 7.0, 75 mM NaCl, 600 mM urea, 1 mM EDTA) and twice with 1.4 ml of IP buffer. Specific elution was performed by resuspension of the affinity matrix in 700 μ l elution buffer (PBS pH 7.4, 0.5 mM EDTA, 1 mM DTT, and 0.04 mg/ml affinity-purified GST-HRV3C protease) per 700 OD₆₀₀ units of original cell mass followed by incubation for 2 h at 4 °C on an overhead rotor at 3 rpm. The eluate was centrifuged ($264,360 \times g$, 2 h, 4 °C) in a Beckman TLA 100.3 rotor to harvest the ER- or vacuole-derived vesicles. The membrane pellet was resuspended in 200 μ l PBS per 1400 OD₆₀₀ units of original cell mass (isolate), snap-frozen, and stored at -80 °C until lipid extraction and lipidomics analysis. For proteomics experiments, the membrane pellet was resuspended in 40 μ l PBS-SDS (1%) per 1400 OD₆₀₀ units.

Protein concentration determination, SDS-PAGE, and immunoblotting

Protein concentrations of all fractions from the immunoisolation were determined using the microBCA protein assay (Thermo Fisher Scientific #23235) following the manufacturer's recommendations. For SDS-PAGE, 1 volume membrane sample buffer (8 M urea, 0.1 M Tris-HCl, pH 6.8, 5 mM EDTA, 3.2% (w/v) SDS, 0.05% (w/v) bromphenol blue, 4% [v/v] glycerol, and 4% (v/v) β -mercaptoethanol) was mixed with two volumes of the immunoisolation fraction, incubated at 60 °C for 10 min, and loaded onto 4–15% mini-PROTEAN TGX precast protein gels (Bio-Rad). Proteins were separated at 185 V for 35 min. After separation, proteins were transferred by semi-dry Western blotting onto nitrocellulose membranes (Amersham Protran Premium 0.45 μ m). The proteins of interest were detected using specific primary antibodies and fluorescent secondary antibodies (see "Reagents and tools table") on a fluorescence imager (LI-COR, Odyssey DLx). Signal intensities on immunoblots were quantified using ImageStudioLite.

Liposome integrity and fusion assay

POPC-based, multilamellar liposomes containing 1 mol% 1,2-dioleoyl-sn-glycero-3-phosphoethanolamine-N-(7-nitro-2-1,3-benzoxadiazol-4-yl) (NBD-PE) and 1 mol% 1,2-dioleoyl-sn-glycero-3-phosphoethanolamine-N-(lissamine rhodamine B sulfonyl) (Rho-PE) as a FRET pair (Weber et al, 1998) were prepared by rehydrating dried lipids in MP buffer without protease inhibitors and benzonase (25 mM HEPES pH 7.0, 600 mM mannitol, 1 mM EDTA). Multilamellar liposomes were extruded through 0.4 μ m and then 0.1- μ m filters with each 21 strokes to yield large unilamellar vesicles (LUVs). LUVs were mixed with a 15.4 ± 1.3 -fold excess of unlabeled P100 microsomes as quantified by a total phosphate determination after lipid extraction and acid hydrolysis based on classical protocols (Chen et al, 1956; Bligh and Dyer, 1959; Rouser et al, 1970). In brief, lipids from 100 μ l of LUV or microsome solution were mixed with 100 μ l MP buffer without protease inhibitors and benzonase (25 mM HEPES pH 7.0, 600 mM mannitol, 1 mM EDTA) and extracted in two steps by addition of first 750 μ l chloroform:methanol (1:2) and then 750 μ l chloroform and 250 μ l ABC buffer (155 mM ammonium bicarbonate) at RT. The organic phase was recovered, and the solvent was evaporated using a centrifugal evaporator. Dried lipids were resuspended in 100 μ l chloroform:methanol (1:2). 25 μ l of this lipid extract was transferred to a pyrex glass tube, and the solvent was evaporated. The resulting lipid cake was treated with 300 μ l 70% perchloric acid at 180 °C. Subsequently, 1 ml Milli-Q water, 0.4 ml of 5% (w/v) ascorbic acid, and 0.4 ml of 1.25% (w/v) ammonium molybdate were added and the resulting sample was boiled for 15 min. Absorbance at 797 nm was measured at RT after the sample cooled down. To test if sonication might potentially induce lipid exchange between liposomes and microsomes or even membrane fusion, the suspension was either sonicated for 10 s (Sonotrode MS72; Bandelin Sonopuls HD 2070 with 50% volume as 70% pulses) to match the MemPrep procedure or for 100 s to validate the impact of a much harsher treatment. As a positive control for lipid exchange, the suspension was mixed with 18 mM methyl- β -

cyclodextrin and incubated for 30 min at RT. To induce membrane fusion between the liposomes and microsomes as a control, we adjusted the mix to 40% (w/v) PEG 8000 and incubated for 30 min at RT. Full solubilization of the liposomes and the microsomes was achieved by adjusting the suspension to 1% SDS. Fluorescence emission spectra were recorded between 500 and 700 nm (step size of 2 nm) upon excitation at 467 nm using an Infinite 200 Pro (Tecan) plate reader. Bandwidths for the excitation and emission were set to 10 nm. Acceptor fluorescence upon donor excitation in the absence of a donor fluorophore (crosstalk) was determined using LUVs containing only the acceptor fluorophore (99 mol% POPC and 1 mol% Rho-PE) and subtracted from raw spectra of samples containing the FRET pair to yield background-corrected spectra. To aid spectral unmixing, we recorded fluorescence emission spectra of LUVs containing only the donor fluorophore (99 mol% POPC and 1 mol% NBD-PE) excited at 467 nm and of LUVs containing only the acceptor fluorophore (99 mol% POPC and 1 mol% Rho-PE) excited at 520 nm. Both, the background-corrected spectrum of the FRET pair and the two reference spectra were normalized by setting the area under the curve to 1 and decomposed using the software *ale* by FluorTools to determine the relative contribution of the donor (NBD-PE) and the acceptor (Rho-PE) to the overall spectrum. Relative FRET efficiencies were calculated as $I_{\text{Rho-PE}} / (I_{\text{NBD-PE}} + I_{\text{Rho-PE}})$ with $I_{\text{Rho-PE}}$ being the acceptor and $I_{\text{NBD-PE}}$ the donor component after decomposition of the spectrum recorded from 500 to 700 nm.

C-laurdan fluorescence spectroscopy

Lipid films were generated by drying lipid mixtures in chloroform under a stream of nitrogen at 50 °C and constant agitation at 400 rpm. Subsequently, residual chloroform was removed in an evacuated desiccator at RT for 1 h. Multilamellar liposomes were generated by the swelling method in liposome buffer (25 mM HEPES pH 7.0, 150 mM NaCl) at 1200 rpm shaking, 60 °C for 1 h. After sonication in a sonication bath for 20 min, the resulting multilamellar vesicles were snap-frozen in liquid nitrogen and stored at -80 °C. After thawing, the multilamellar vesicles were subjected to sonication using the sonotrode MS72 on a Bandelin Sonopuls HD 2070 with 50% power for 10 pulses of each 0.7 s. Liposomes were diluted (0.1 mM lipid) in liposome buffer and equilibrated in black 96-well plates in an Infinite 200 Pro (Tecan) plate reader at 30 °C. Background fluorescence emission spectra were recorded at 400–530 nm in 2 nm steps with 40 μ s integration time, excitation at 375 nm and both bandwidths set to 10 nm. In total, 0.2 μ M C-laurdan was added and incubated for 15 min before recording a fluorescence spectrum with the same settings. Generalized polarization was calculated as $GP = (I_1 - I_2) / (I_1 + I_2)$ with I_1 being the background-corrected signal sum between 400 and 460 nm and I_2 the background-corrected signal sum between 470 and 530 nm.

Lipid extraction for mass spectrometry lipidomics

Mass spectrometry-based lipid analysis was performed by Lipotype GmbH (Dresden, Germany) as described (Ejsing et al, 2009; Klose et al, 2012). Lipids were extracted using a two-step chloroform/methanol procedure (Ejsing et al, 2009). Samples were spiked with internal lipid standard mixture containing: CDP-DAG 17:0/18:1, ceramide 18:1/2/17:0

(Cer), diacylglycerol 17:0/17:0 (DAG), lyso-phosphatidate 17:0 (LPA), lyso-phosphatidylcholine 12:0 (LPC), lyso-phosphatidylethanolamine 17:1 (LPE), lyso-phosphatidylinositol 17:1 (LPI), lyso-phosphatidylserine 17:1 (LPS), phosphatidate 17:0/14:1 (PA), phosphatidylcholine 17:0/14:1 (PC), phosphatidylethanolamine 17:0/14:1 (PE), phosphatidylglycerol 17:0/14:1 (PG), phosphatidylinositol 17:0/14:1 (PI), phosphatidylserine 17:0/14:1 (PS), ergosterol ester 13:0 (EE), triacylglycerol 17:0/17:0/17:0 (TAG), stigmastatrienol, inositolphosphorylceramide 44:0;2 (IPC), mannosyl-inositolphosphorylceramide 44:0;2 (MIPC) and mannosyl-di-(inositolphosphoryl)ceramide 44:0;2 (M(IP)2C). After extraction, the organic phase was transferred to an infusion plate and dried in a speed vacuum concentrator. 1st step dry extract was resuspended in 7.5 mM ammonium acetate in chloroform/methanol/propanol (1:2:4, V:V:V) and 2nd step dry extract in 33% ethanol solution of methylamine in chloroform/methanol (0.0035:1; V:V:V). All liquid handling steps were performed using Hamilton Robotics STARlet robotic platform with the Anti Droplet Control feature for organic solvents pipetting.

Mass spectrometry (MS) data acquisition for lipidomics

Samples were analyzed by direct infusion on a QExactive mass spectrometer (Thermo Scientific) equipped with a TriVersa NanoMate ion source (Advion Biosciences). Samples were analyzed in both positive and negative ion modes with a resolution of $R_{m/z=200} = 280,000$ for MS and $R_{m/z=200} = 17,500$ for MSMS experiments, in a single acquisition. MS/MS was triggered by an inclusion list encompassing corresponding MS mass ranges scanned in 1 Da increments (Surma et al, 2015). Both MS and MSMS data were combined to monitor EE, DAG, and TAG ions as ammonium adducts; PC as an acetate adduct; and CL, PA, PE, PG, PI, and PS as deprotonated anions. MS only was used to monitor LPA, LPE, LPI, LPS, IPC, MIPC, M(IP)2C as deprotonated anions; Cer and LPC as acetate adducts and ergosterol as protonated ion of an acetylated derivative (Liebisch et al, 2006).

Data analysis and post-processing for lipidomics

Data were analyzed with in-house developed lipid identification software based on LipidXplorer (Herzog et al, 2011; Herzog et al, 2012). Data post-processing and normalization were performed using an in-house developed data management system. Only lipid identifications with a signal-to-noise ratio >5, and a signal intensity fivefold higher than in corresponding blank samples were considered for further data analysis.

Sample preparation for proteomics via liquid chromatography (LC)-MS/MS

Lysates were adjusted to 1% SDS and a final concentration 1 mg/ml. 5 μ g of cell lysates and 10 μ g of ER membrane were subjected to an in-solution tryptic digest using a modified version of the Single-Pot Solid-Phase-enhanced Sample Preparation (SP3) protocol (Hughes et al, 2014; Moggridge et al, 2018). In total, three biological replicates were prepared including control, wild-type and mutant-derived lysates ($n = 3$). Lysates were added to Sera-Mag Beads (Thermo Scientific, #4515-2105-050250, 6515-2105-050250) in 10 μ l 15% formic acid and 30 μ l of ethanol. Binding of proteins was achieved by shaking for 15 min at room temperature. SDS was removed by 4 subsequent washes with 200 μ l of 70% ethanol. Proteins were

digested overnight at room temperature with 0.4 µg of sequencing grade modified trypsin (Promega, #V5111) in 40 µl HEPES/NaOH, pH 8.4 in the presence of 1.25 mM TCEP and 5 mM chloroacetamide (Sigma-Aldrich, #C0267). Beads were separated, washed with 10 µl of an aqueous solution of 2% DMSO and the combined eluates were dried down. Peptides of ER membranes were reconstituted in 10 µl of H₂O and reacted for 1 h at room temperature with 80 µg of TMT10plex (Thermo Scientific, #90111) (Werner et al, 2014) label reagent dissolved in 4 µl of acetonitrile. Peptides of cell lysates were reconstituted in 10 µl of H₂O and reacted for 1 h at room temperature with 50 µg of TMT16proTM label reagent (Thermo Scientific, #A44521) dissolved in 4 µl of acetonitrile. Excess TMT reagent was quenched by the addition of 4 µl of an aqueous 5% hydroxylamine solution (Sigma, 438227). Peptides were reconstituted in 0.1% formic acid, mixed to achieve a 1:1 ratio across all TMT-channels and purified by a reverse phase clean-up step (OASIS HLB 96-well µElution Plate, Waters #186001828BA). Peptides were subjected to an off-line fractionation under high pH conditions (Hughes et al, 2014). The resulting 12 fractions were then analyzed by LC-MS/MS on an Orbitrap Fusion Lumos mass spectrometer.

LC-MS/MS analysis of ER membranes and cell lysates

Peptides were separated using an Ultimate 3000 nano RSLC system (Dionex) equipped with a trapping cartridge (Precolumn C18 PepMap100, 5 mm, 300 µm i.d., 5 µm, 100 Å) and an analytical column (Acclaim PepMap100, 75 × 50 cm C18, 3 mm, 100 Å) connected to a nanospray-Flex ion source. The peptides were loaded onto the trap column at 30 µl per min using solvent A (0.1% formic acid) and, for analysis of ER membranes, eluted using a gradient from 2 to 38% Solvent B (0.1% formic acid in acetonitrile) over 52 min and then to 80% at 0.3 µl per min (all solvents were of LC-MS grade). Peptides for analysis of cell lysates were eluted using a gradient from 2 to 80% Solvent B over 2 h at 0.3 µl per min. The Orbitrap Fusion Lumos was operated in positive ion mode with a spray voltage of 2.4 kV and capillary temperature of 275 °C. Full-scan MS spectra with a mass range of 375–1500 *m/z* were acquired in profile mode using a resolution of 60,000 or 120,000 for analysis of ER membranes or cell lysates respectively, with a maximum injection time of 50 ms, AGC operated in standard mode and a RF lens setting of 30%.

Fragmentation was triggered for 3 s cycle time for peptide-like features with charge states of 2–7 on the MS scan (data-dependent acquisition). Precursors were isolated using the quadrupole with a window of 0.7 *m/z* and fragmented with a normalized collision energy of 36% for analysis of ER membranes (34% for analysis of cell lysates). Fragment mass spectra were acquired in profile mode and a resolution of 30,000 in profile mode. Maximum injection time was set to 94 ms or an AGC target of 200%. The dynamic exclusion was set to 60 s.

Analysis of proteomics data

Acquired data were analyzed using IsobarQuant (Franken et al, 2015) and Mascot V2.4 (Matrix Science) using a reverse UniProt FASTA *Saccharomyces cerevisiae* database (UP000002311), including common contaminants and the following Rtn1-myc-3C-3xFLAG-tagged (bait) protein employed for the enrichment of subcellular membranes:

```
sp|P1707_RE|P1707_RE
MSASAQHSQAQQQQKSCNCDLLWRNPVQTGKYFGG
SLLALLLKKVNLITFFLKVAYTILFTTGSIEFVSKLFLGQGLIT-
KYGPKECPNIAGFIKPHIDEALKQLPVFQAHIRKTVFAQVP
KHTFKTAVALLLHKFFSWFSIWTIVFVADIFTFLPVYHSY-
KHEIDATVAQGVSEISKQKTQEF SQMACEKTKPYLDKVESKLG-
PISNLVKSKTAPVSTAGPQTASTSKLAADVPLEPESKAYTSSA
QVMPEVPQHEPSTTQEFNVDELSNELKKSTKNLQNELEKNN
GGGGGGGEQKLISEEDLGLGLEVLVFGPGSGDYKDHGDYKDH
DIDYKDDDDK
```

The following modifications were considered: Carbamidomethyl (C, fixed), TMT10plex (K, fixed), Acetyl (N-term, variable), Oxidation (M, variable) and TMT10plex (N-term, variable). TMT16plex labeled samples The TMT16plex (K, fixed) and TMT16plex (N-term, variable) labels were considered as modifications. The mass error tolerance for full-scan MS spectra was set to 10 ppm and for MS/MS spectra to 0.02 Da. A maximum of two missed cleavages were allowed. A minimum of two unique peptides with a peptide length of at least seven amino acids and a false discovery rate below 0.01 were required on the peptide and protein level (Savitski et al, 2015).

Enrichment calculation based on untargeted proteomics and clustering

For enrichment calculations, IsobarQuant output data were analyzed on a gene symbol level in R (<https://www.R-project.org>) using in-house data analysis pipelines. In brief, data were filtered to remove contaminants and proteins with less than two unique quantified peptide matches. Subsequently, log₂ transformed protein reporter ion intensities (“signal sum” columns) were first cleaned for batch effects using the “removeBatchEffects” function from the limma package (Ritchie et al, 2015) and further normalized within the TMT set using the vsn package (Huber et al, 2002). UniProt annotations of subcellular location were retrieved from UniProt (accessed 27.01.2023).

For clustering analyses, proteins were tested for differential expression using the limma package. The replicate information was added as a factor in the design matrix given as an argument to the “lmFit” function of limma. A protein was annotated as a hit with a false discovery rate (fdr) smaller 5% and a fold change of at least 100% and as a candidate with a fdr below 20% and a fold change of at least 50%. Proteins classified as hits and candidates as well as a positive fold changes of the “pre” condition were clustered into nine clusters (method k-means) based on the Euclidean distance between normalized TMT reporter ion intensities divided by the median of the “pre-stress” condition.

Molecular dynamics (MD) simulations

All-atom MD simulations were set up and carried out using the GROMACS software (Páll et al, 2020). Lipid topologies and structures were taken from the CHARMM-GUI web server (Jo et al, 2009). Bilayers were then generated using MemGen (Knight and Hub, 2015). Three different ER compositions were used (Appendix Fig. S4A) as well as a reference membrane composed of 50% POPC and 50% DOPC. Each system contained 100 lipids per leaflet and 60 water molecules per lipid. Na⁺ and Cl⁻ ions were added to reach an ionic concentration of 0.15 M. Taken together each system contained approximately 60000 atoms. Simulations

were carried out using the CHARMM36m forcefield (Huang et al, 2017) and the CHARMM-modified TIP3P water model (Jorgensen et al, 1983). The system was kept at 303 K using velocity recording (Bussi et al, 2007). Semi-isotropic pressure coupling at 1.0 bar was applied using the Berendsen barostat (Berendsen et al, 1984) for equilibration and the Parrinello-Rahman barostat using a coupling time constant of $\tau = 2$ ps (Parrinello and Rahman, 1981) during production runs. Electrostatic interactions were calculated using the particle-mesh Ewald method (Essmann et al, 1995). A cutoff of 1.2 nm according to CHARMM36 specifications (Best et al, 2012) was used for the non-bonded interactions, while the Lennard-Jones interactions were gradually switched off between 1.0 and 1.2 nm. Bond constraints involving hydrogen atoms were implemented using LINCS (Hess, 2008), thus a 2 fs time step was chosen. Each system was initially equilibrated for 50 ns followed by three independent production runs of at least 700 ns.

For the analysis, the first 100 ns of each production run was discarded. Mass density profiles were calculated along the z axis (membrane normal) using the Gromacs module `gmx density`. The membrane thickness was extracted from the density profiles using a threshold of 500 kg/m³. Errors were obtained by averaging and calculating the SEM over independent simulations segments. An in-house modified version of the Gromacs module `freevolume` was used to calculate the free volume profile as a function of z . The module estimates the accessible free volume by inserting probe spheres of radius R at random positions, while testing the overlap with the Van der Waals radii of all simulated atoms. Here, we used a probe radius or $R = 0$, thereby obtaining the total free volume. Errors for each individual simulation were obtained by multiple independent insertion rounds carried out by `gmx freevolume`, the overall error for the averaged curves was calculated using standard error propagation. Surface packing defects were calculated using the program `PackMem` (Gautier et al, 2018). The program uses a grid-based approach to identify surface defects and distinguishes between deep and shallow defects based on the distance to the mean glycerol position (everything below a threshold of 1 Å was considered a deep defect). By fitting a single exponential to the obtained defect area distribution, the defect size constant was determined for each defect type. To achieve converged results, trajectory snapshots taken every 100 ps were used. Error estimation was conducted by block averaging dividing each simulation into three blocks of equal size, and calculating the SEM over all blocks.

RNA preparation, cDNA synthesis, and RT-qPCR analysis

UPR activation was measured by determining the mRNA levels of spliced *HAC1*, *PDI*, and *KAR2*. For each experimental condition total RNA was prepared from five OD₆₀₀ units of cells using the RNeasy Plus RNA Isolation Kit (Qiagen). Synthesis of cDNA was performed using 500 ng of prepared RNA, Oligo(dT) primers, and the Superscript II RT protocol (Invitrogen). RT-qPCR was performed using the ORA qPCR Green ROX L Mix (HighQu) and a Mic qPCR cyclor (Bio Molecular Systems) using a reaction volume of 20 μ l. Primers were used at a final concentration of 400 nM to determine the Ct values of the housekeeping gene *TAF10* and the genes of interest: spliced *HAC1* forward: 5'-TACCTGCCGTAGACAACAAC-3'; spliced *HAC1* reverse: 5'-ACTGCGCTTCTGGATTAC-3'; *PDI* forward: 5'-TTCCCTCTATTTGCCATCCAC-3'; *PDI* reverse: 5'-GCCTTAGACTCCAACAGATC-3'; *KAR2* forward: 5'-TGCTGTCTGTTACTGTTCTCTG-3'; *KAR2* reverse: 5'-GATTATCCAAACCGTAGGCAATG-3'; *TAF10* forward: 5'-ATATCCAGGATCAGTT

CTTCCGTAGC-3'; *TAF10* reverse: 5'-GTAGTCTTCTCATTCTGTTGATGTTGTTGTTG-3'.

The qPCR program consisted of the following steps: (1) 95 °C, 15 min; (2) 95 °C, 20 s; (3) 62 °C, 20 s; (4) 72 °C, 30 s; and (5) 72 °C, 5 min; steps 2–4 were repeated 40 times. We used the comparative $\Delta\Delta C_t$ method with normalization to the Ct values recorded for *TAF10* to assess the relative levels of the spliced *HAC1*, *PDI*, and *KAR2* mRNAs.

Data availability

The mass spectrometry proteomics data from this publication have been deposited to the ProteomeXchange Consortium via the PRIDE [http://www.ebi.ac.uk/pride] partner repository with the dataset identifier PXD048553 (Perez-Riverol et al, 2022). Other datasets are included in the source data file.

Expanded view data, supplementary information, appendices are available for this paper at <https://doi.org/10.1038/s44318-024-00063-y>.

Peer review information

A peer review file is available at <https://doi.org/10.1038/s44318-024-00063-y>

References

- Abu-Remaileh M, Wyant GA, Kim C, Laqtom NN, Abbasi M, Chan SH, Freinkman E, Sabatini DM (2017) Lysosomal metabolomics reveals V-ATPase- and mTOR-dependent regulation of amino acid efflux from lysosomes. *Science* 358:807–813
- Aguilera-Romero A, Kaminska J, Spang A, Riezman H, Muñiz M (2008) The yeast p24 complex is required for the formation of COPI retrograde transport vesicles from the Golgi apparatus. *J Cell Biol* 180:713–720
- Ballweg S, Sezgin E, Doktorova M, Covino R, Reinhard J, Wunnicke D, Hänelt I, Levental I, Hummer G, Ernst R (2020) Regulation of lipid saturation without sensing membrane fluidity. *Nat Commun* 11:756
- Berendsen HJC, Postma JPM, Van Gunsteren WF, Dinola A, Haak JR (1984) Molecular dynamics with coupling to an external bath. *J Chem Phys* 81:3684–3690
- Best RB, Zhu X, Shim J, Lopes PEM, Mittal J, Feig M, Mackerell AD (2012) Optimization of the additive CHARMM all-atom protein force field targeting improved sampling of the backbone ϕ , ψ and side-chain $\chi(1)$ and $\chi(2)$ dihedral angles. *J Chem Theory Comput* 8:3257–3273
- Bigay J, Antonny B (2012) Curvature, lipid packing, and electrostatics of membrane organelles: defining cellular territories in determining specificity. *Dev Cell* 23:886–895
- Bligh EG, Dyer WJ (1959) A rapid method of total lipid extraction and purification. *Can J Biochem Physiol* 37:911–917
- Borgese N (2016) Getting membrane proteins on and off the shuttle bus between the endoplasmic reticulum and the Golgi complex. *J Cell Sci* 129:1537–1545
- Brambillasca S, Yabal M, Soffientini P, Stefanovic S, Makarow M, Hegde RS, Borgese N (2005) Transmembrane topogenesis of a tail-anchored protein is modulated by membrane lipid composition. *EMBO J* 24:2533–2542
- Breker M, Gymrek M, Moldavski O, Schuldiner M (2014) LoQAtE—localization and quantitation Atlas of the yeast proteome. A new tool for multiparametric

- dissection of single-protein behavior in response to biological perturbations in yeast. *Nucleic Acids Res* 42:D726–D730
- Breker M, Gymrek M, Schuldiner M (2013) A novel single-cell screening platform reveals proteome plasticity during yeast stress responses. *J Cell Biol* 200:839–850
- Bretscher MS, Munro S (1993) Cholesterol and the Golgi apparatus. *Science* 261:1280–1281
- Bussi G, Donadio D, Parrinello M (2007) Canonical sampling through velocity rescaling. *J Chem Phys* 126:014101
- Casanovas A, Sprenger RR, Tarasov K, Ruckerbauer DE, Hannibal-Bach HK, Zanghellini J, Jensen ON, Ejsing CS (2015) Quantitative analysis of proteome and lipidome dynamics reveals functional regulation of global lipid metabolism. *Chem Biol* 22:412–425
- Chen PS, Toribara TY, Warner H (1956) Microdetermination of phosphorus. *Anal Chem* 28:1756–1758
- Cheng H-T (2009) Preparation and properties of asymmetric vesicles that mimic cell membranes. *J Biol Chem* 284:6079–6092
- Clay L, Caudron F, Denoth-Lippuner A, Boettcher B, Buvelot Frei S, Snapp EL, Barral Y (2014) A sphingolipid-dependent diffusion barrier confines ER stress to the yeast mother cell. *eLife* 3:e01883
- Cohen N, Breker M, Bakunts A, Pesek K, Chas A, Argemí J, Orsi A, Gal L, Chuartzman S, Wigelman Y, Jonas F, Walter P, Ernst R, Aragón T, van Anken E, Schuldiner M (2017) Iron affects Ire1 clustering propensity and the amplitude of endoplasmic reticulum stress signaling. *J Cell Sci* 130:3222–3233
- Covino R, Ballweg S, Stordeur C, Michaelis JB, Puth K, Wernig F, Bahrami A, Ernst AM, Hummer G, Ernst R (2016) A eukaryotic sensor for membrane lipid saturation. *Mol Cell* 63:49–59
- Covino R, Hummer G, Ernst R (2018) Integrated functions of membrane property sensors and a hidden side of the unfolded protein response. *Mol Cell* 71:458–467
- Cox JS, Chapman RE, Walter P (1997) The unfolded protein response coordinates the production of endoplasmic reticulum protein and endoplasmic reticulum membrane. *Mol Biol Cell* 8:1805–1814
- Dawaliby R, Trubbia C, Delporte C, Noyon C, Ruyschaert J-M, Van Antwerpen P, Govaerts C (2016) Phosphatidylethanolamine is a key regulator of membrane fluidity in eukaryotic cells. *J Biol Chem* 291:3658–3667
- De Craene J-O, Coleman J, Estrada de Martin P, Pypaert M, Anderson S, Yates JR, Ferro-Novick S, Novick P (2006) Rtn1p is involved in structuring the cortical endoplasmic reticulum. *Mol Biol Cell* 17:3009–3020
- Ejsing CS, Sampaio JL, Surendranath V, Duchoslav E, Ekroos K, Klemm RW, Simons K, Shevchenko A (2009) Global analysis of the yeast lipidome by quantitative shotgun mass spectrometry. *Proc Natl Acad Sci USA* 106:2136–2141
- English AR, Voeltz GK (2013) Endoplasmic reticulum structure and interconnections with other organelles. *Cold Spring Harb Perspect Biol* 5:a013227
- Ernst R, Ballweg S, Levental I (2018) Cellular mechanisms of physicochemical membrane homeostasis. *Curr Opin Cell Biol* 53:44–51
- Ernst R, Ejsing CS, Antonny B (2016) Homeoviscous adaptation and the regulation of membrane lipids. *J Mol Biol* 428:4776–4791
- Essmann U, Perera L, Berkowitz ML, Darden T, Lee H, Pedersen LG (1995) A smooth particle mesh Ewald method. *J Chem Phys* 103:8577–8593
- Fankhauser C, Conzelmann A (1991) Purification, biosynthesis and cellular localization of a major 125-kDa glycoposphatidylinositol-anchored membrane glycoprotein of *Saccharomyces cerevisiae*. *Eur J Biochem* 195:439–448
- Fasimoye R, Dong W, Nirujogi RS, Rawat ES, Iguchi M, Nyame K, Phung TK, Bagnoli E, Prescott AR, Alessi DR, Abu-Remaih M (2023) Golgi-IP, a tool for multimodal analysis of Golgi molecular content. *Proc Natl Acad Sci USA* 120:e2219953120
- Feng B, Yao PM, Li Y, Devlin CM, Zhang D, Harding HP, Sweeney M, Rong JX, Kuriakose G, Fisher EA, Marks AR, Ron D, Tabas I (2003) The endoplasmic reticulum is the site of cholesterol-induced cytotoxicity in macrophages. *Nat Cell Biol* 5:781–792
- Franken H, Mathieson T, Childs D, Sweetman GMA, Werner T, Tögel I, Doce C, Gade S, Bantscheff M, Drewes G, Reinhard FBM, Huber W, Savitski MM (2015) Thermal proteome profiling for unbiased identification of direct and indirect drug targets using multiplexed quantitative mass spectrometry. *Nat Protoc* 10:1567–1593
- Fu S, Yang L, Li P, Hofmann O, Dicker L, Hide W, Lin X, Watkins SM, Ivanov AR, Hotamisligil GS (2011) Aberrant lipid metabolism disrupts calcium homeostasis causing liver endoplasmic reticulum stress in obesity. *Nature* 473:528–531
- Funakoshi M, Hochstrasser M (2009) Small epitope-linker modules for PCR-based C-terminal tagging in *Saccharomyces cerevisiae*. *Yeast* 26:185–192
- Gao X, van der Veen JN, Vance JE, Thiesen A, Vance DE, Jacobs RL (2015) Lack of phosphatidylethanolamine N-methyltransferase alters hepatic phospholipid composition and induces endoplasmic reticulum stress. *Biochim Biophys Acta Mol Basis Dis* 1852:2689–2699
- Garcia EJ, Liao PC, Tan G, Vevea JD, Sing CN, Tsang CA, McCaffery JM, Boldogh IR, Pon LA (2021) Membrane dynamics and protein targets of lipid droplet microautophagy during ER stress-induced proteostasis in the budding yeast, *Saccharomyces cerevisiae*. *Autophagy* 17:2363–2383
- Gaspar ML, Aregullin MA, Jesch SA, Henry SA (2006) Inositol induces a profound alteration in the pattern and rate of synthesis and turnover of membrane lipids in *Saccharomyces cerevisiae*. *J Biol Chem* 281:22773–22785
- Gautier R, Bacle A, Tiberti ML, Fuchs PF, Vanni S, Antonny B (2018) PackMem: a versatile tool to compute and visualize interfacial packing defects in lipid bilayers. *Biophys J* 115:436–444
- Ghaemmaghami S, Huh WK, Bower K, Howson RW, Belle A, Dephoure N, O'Shea EK, Weissman JS (2003) Global analysis of protein expression in yeast. *Nature* 425:737–741
- González Montoro A, Auffarth K, Hönscher C, Bohnert M, Becker T, Warscheid B, Reggiori F, van der Laan M, Fröhlich F, Ungermann C (2018) Vps39 interacts with Tom40 to establish one of two functionally distinct vacuole-mitochondria contact sites. *Dev Cell* 45:621–636.e7
- Halbleib K, Pesek K, Covino R, Hofbauer HF, Wunnicke D, Hänel I, Hummer G, Ernst R (2017) Activation of the unfolded protein response by lipid bilayer stress. *Mol Cell* 67:673–684.e8
- Han S, Lone MA, Schneiter R, Chang A (2010) Orm1 and Orm2 are conserved endoplasmic reticulum membrane proteins regulating lipid homeostasis and protein quality control. *Proc Natl Acad Sci USA* 107:5851–5856
- Hanscho M, Ruckerbauer DE, Chauhan N, Hofbauer HF, Krahulec S, Nidetzky B, Kohlwein SD, Zanghellini J, Natter K (2012) Nutritional requirements of the BY series of *Saccharomyces cerevisiae* strains for optimum growth. *FEMS Yeast Res* 12:796–808
- Harayama T, Riezman H (2018) Understanding the diversity of membrane lipid composition. *Nat Rev Mol Cell Biol* 19:281–296
- Hechtberger P, Zinser E, Saf R, Hummel K, Paltauf F, Daum G (1994) Characterization, quantification and subcellular localization of inositol-containing sphingolipids of the yeast, *Saccharomyces cerevisiae*. *Eur J Biochem* 225:641–649
- Henne WM, Reese ML, Goodman JM (2018) The assembly of lipid droplets and their roles in challenged cells. *EMBO J* 37:e98947
- Henry SA, Kohlwein SD, Carman GM (2012) Metabolism and regulation of glycerolipids in the yeast *Saccharomyces cerevisiae*. *Genetics* 190:317–349

- Herzig Y, Sharpe HJ, Elbaz Y, Munro S, Schuldiner M (2012) A systematic approach to pair secretory cargo receptors with their cargo suggests a mechanism for cargo selection by Erv14. *PLoS Biol* 10:e1001329
- Herzog R, Schuhmann K, Schwudke D, Sampaio JL, Bornstein SR, Schroeder M, Shevchenko A (2012) LipidXplorer: a software for consensual cross-platform lipidomics. *PLoS ONE* 7:e29851
- Herzog R, Schwudke D, Schuhmann K, Sampaio JL, Bornstein SR, Schroeder M, Shevchenko A (2011) A novel informatics concept for high-throughput shotgun lipidomics based on the molecular fragmentation query language. *Genome Biol* 12:R8
- Hess B (2008) P-LINCS: a parallel linear constraint solver for molecular simulation. *J Chem Theory Comput* 4:116–122
- Higuchi-Sanabria R, Shen K, Kelet N, Frankino PA, Durieux J, Bar-Ziv R, Sing CN, Garcia EJ, Homentcovschi S, Sanchez M, Wu R, Tronnes SU, Joe L, Webster B, Ahilon-Jeronimo A, Monshietehadi S, Dallarda S, Pender C, Pon LA, Zoncu R et al (2020) Lysosomal recycling of amino acids affects ER quality control. *Sci Adv* 6:eaz9805
- Hirsch JP, Henry SA (1986) Expression of the *Saccharomyces cerevisiae* inositol-1-phosphate synthase (INO1) gene is regulated by factors that affect phospholipid synthesis. *Mol Cell Biol* 6:3320–3328
- Ho N, Xu C, Thibault G (2018) From the unfolded protein response to metabolic diseases—lipids under the spotlight. *J Cell Sci* 131:ics199307
- Ho N, Yap WS, Xu J, Wu H, Koh JH, Goh WWB, George B, Chong SC, Taubert S, Thibault G (2020) Stress sensor Ire1 deploys a divergent transcriptional program in response to lipid bilayer stress. *J Cell Biol* 219:e201909165
- Hofbauer HF, Gecht M, Fischer SC, Seybert A, Frangakis AS, Stelzer EHK, Covino R, Hummer G, Ernst R (2018) The molecular recognition of phosphatidic acid by an amphipathic helix in Opi1. *J Cell Biol* 217:3109–3126
- Holthuis JCM, Menon AK (2014) Lipid landscapes and pipelines in membrane homeostasis. *Nature* 510:48–57
- Hoppe T, Matuschewski K, Rape M, Schlenker S, Ulrich HD, Jentsch S (2000) Activation of a membrane-bound transcription factor by regulated ubiquitin/proteasome-dependent processing. *Cell* 102:577–586
- Hotamisligil GS (2010) Endoplasmic reticulum stress and the inflammatory basis of metabolic disease. *Cell* 140:900–917
- Hou NS, Gutschmidt A, Choi DY, Pather K, Shi X, Watts JL, Hoppe T, Taubert S (2014) Activation of the endoplasmic reticulum unfolded protein response by lipid disequilibrium without disturbed proteostasis in vivo. *Proc Natl Acad Sci USA* 111:E2271–E2280
- Hu J, Shibata Y, Voss C, Shemesh T, Li Z, Coughlin M, Kozlov MM, Rapoport TA, Prinz WA (2008) Membrane proteins of the endoplasmic reticulum induce high-curvature tubules. *Science* 319:1247–1250
- Huang J, Rauscher S, Nawrocki G, Ran T, Feig M, de Groot BL, Grubmüller H, MacKerell AD (2017) CHARMM36m: an improved force field for folded and intrinsically disordered proteins. *Nat Methods* 14:71–73
- Huber W, von Heydebreck A, Sülthmann H, Poustka A, Vingron M (2002) Variance stabilization applied to microarray data calibration and to the quantification of differential expression. *Bioinformatics* 18:S96–S104
- Hughes CS, Foehr S, Garfield DA, Furlong EE, Steinmetz LM, Krijgsvelde J (2014) Ultrasensitive proteome analysis using paramagnetic bead technology. *Mol Syst Biol* 10:757
- Ishiwata-Kimata Y, Le QG, Kimata Y (2022) Induction and aggravation of the endoplasmic-reticulum stress by membrane-lipid metabolic intermediate phosphatidyl-N-monomethylethanolamine. *Front Cell Dev Biol* 9:743018
- Ito H, Fukuda Y, Murata K, Kimura A (1983) Transformation of intact yeast cells treated with alkali cations. *J Bacteriol* 153:163–168
- Janssen MJ, Koorengel MC, de Kruijff B, de Kroon AI (2000) The phosphatidylcholine to phosphatidylethanolamine ratio of *Saccharomyces cerevisiae* varies with the growth phase. *Yeast* 16:641–650
- Jesch SA, Liu P, Zhao X, Wells MT, Henry SA (2006) Multiple endoplasmic reticulum-to-nucleus signaling pathways coordinate phospholipid metabolism with gene expression by distinct mechanisms. *J Biol Chem* 281:24070–24083
- Jiménez-Rojo N, Feng S, Morstein J, Pritzl SD, Harayama T, Asaro A, Vepřek NA, Arp CJ, Reynders M, Novak AJE, Kanshin E, Ueberheide B, Lohmüller T, Riezman H, Trauner D (2022) Optical control of membrane fluidity modulates protein secretion. Preprint at bioRxiv <https://doi.org/10.1101/2022.02.14.480333>
- Jo S, Lim JB, Klauda JB, Im W (2009) CHARMM-GUI Membrane Builder for mixed bilayers and its application to yeast membranes. *Biophys J* 97:50–58
- John Peter AT, Petrunaro C, Peter M, Kornmann B (2022) METALIC reveals interorganelle lipid flux in live cells by enzymatic mass tagging. *Nat Cell Biol* 24:996–1004
- Jorgensen WL, Chandrasekhar J, Madura JD, Impey RW, Klein ML (1983) Comparison of simple potential functions for simulating liquid water. *J Chem Phys* 79:926–935
- Kamel M, Löwe M, Schott-Verdugo S, Gohlke H, Kedrov A (2022) Unsaturated fatty acids augment protein transport via the SecA:SecYEG translocon. *FEBS J* 289:140–162
- Kennedy EP, Weiss SB (1956) The function of cytidine coenzymes in the biosynthesis of phospholipides. *J Biol Chem* 222:193–214
- Kim H, Budin I (2024) Intracellular sphingolipid sorting drives membrane phase separation in the yeast vacuole. *J Biol Chem* 300:105496
- Kim HM, Choo H, Jung S, Ko Y, Park W, Jeon S, Kim CH, Joo T, Cho BR (2007) A two-photon fluorescent probe for lipid raft imaging: C-Laurdan. *ChemBioChem* 8:553–559
- Klemm RW, Ejsing CS, Surma MA, Kaiser H-J, Gerl MJ, Sampaio JL, de Robillard Q, Ferguson C, Proszynski TJ, Shevchenko A, Simons K (2009) Segregation of sphingolipids and sterols during formation of secretory vesicles at the trans-Golgi network. *J Cell Biol* 185:601–612
- Klose C, Surma MA, Gerl MJ, Meyenhofer F, Shevchenko A, Simons K (2012) Flexibility of a Eukaryotic lipidome—insights from yeast lipidomics. *PLoS ONE* 7:e35063
- Knight CJ, Hub JS (2015) MemGen: a general web server for the setup of lipid membrane simulation systems. *Bioinformatics* 31:2897–2899
- Koch C, Räschele M, Prescianotto-Baschong C, Spang A & Herrmann JM (2023) The ER-SURF pathway uses ER-mitochondria contact sites for protein targeting to mitochondria. Preprint at bioRxiv <https://doi.org/10.1101/2023.08.10.552816>
- Kwak C, Shin S, Park J-S, Jung M, Nhung TTM, Kang M-G, Lee C, Kwon T-H, Park SK, Mun JY, Kim J-S, Rhee H-W (2020) Contact-ID, a tool for profiling organelle contact sites, reveals regulatory proteins of mitochondrial-associated membrane formation. *Proc Natl Acad Sci USA* 117:12109–12120
- Lajoie P, Moir RD, Willis IM, Snapp EL (2012) Kar2p availability defines distinct forms of endoplasmic reticulum stress in living cells. *Mol Biol Cell* 23:955–964
- Lentz BR (1994) Polymer-induced membrane fusion: potential mechanism and relation to cell fusion events. *Chem Phys Lipids* 73:91–106
- Levental KR, Malmberg E, Symons JL, Fan Y-Y, Chapkin RS, Ernst R, Levental I (2020) Lipidomic and biophysical homeostasis of mammalian membranes counteracts dietary lipid perturbations to maintain cellular fitness. *Nat Commun* 11:1339
- Liao P-C, Boldogh IR, Siegmund SE, Freyberg Z, Pon LA (2018) Isolation of mitochondria from *Saccharomyces cerevisiae* using magnetic bead affinity purification. *PLoS ONE* 13:e0196632
- Liao P-C, Yang EJ, Borgman T, Boldogh IR, Sing CN, Swayne TC, Pon LA (2022) Touch and go: membrane contact sites between lipid droplets and other organelles. *Front Cell Dev Biol* 10:852021
- Liebisch G, Binder M, Schifferer R, Langmann T, Schulz B, Schmitz G (2006) High throughput quantification of cholesterol and cholesteryl ester by electrospray

- ionization tandem mass spectrometry (ESI-MS/MS). *Biochim Biophys Acta* 1761:121-128
- Listenberger LL, Han X, Lewis SE, Cases S, Farese RV, Ory DS, Schaffer JE (2003) Triglyceride accumulation protects against fatty acid-induced lipotoxicity. *Proc Natl Acad Sci USA* 100:3077-3082
- Liu L-K, Choudhary V, Toulmay A, Prinz WA (2017) An inducible ER-Golgi tether facilitates ceramide transport to alleviate lipotoxicity. *J Cell Biol* 216:131-147
- Lorent JH, Diaz-Rohrer B, Lin X, Spring K, Gorfe AA, Levental KR, Levental I (2017) Structural determinants and functional consequences of protein affinity for membrane rafts. *Nat Commun* 8:1219
- Lorent JH, Levental KR, Ganesan L, Rivera-Longworth G, Sezgin E, Doktorova M, Lyman E, Levental I (2020) Plasma membranes are asymmetric in lipid unsaturation, packing and protein shape. *Nat Chem Biol* 16:644-652
- Marsh D (2007) Lateral pressure profile, spontaneous curvature frustration, and the incorporation and conformation of proteins in membranes. *Biophys J* 93:3884-3899
- Matmati N, Hannun YA (2008) Thematic review series: sphingolipids. ISC1 (inositol phosphosphingolipid-phospholipase C), the yeast homologue of neutral sphingomyelinases. *J Lipid Res* 49:922-928
- Megyeri M, Prasad R, Volpert G, Sliwa-Gonzalez A, Haribowo AG, Aguilera-Romero A, Riezman H, Barral Y, Futerman AH, Schuldiner M (2019) Yeast ceramide synthases, Lag1 and Lac1, have distinct substrate specificity. *J Cell Sci* 132:jcs228411
- Melero A, Chiaruttini N, Karashima T, Riezman I, Funato K, Barlowe C, Riezman H, Roux A (2018) Lysophospholipids facilitate COPII vesicle formation. *Curr Biol* 28:1950-1958.e6
- Mesmin B, Bigay J, Moser von Filseck J, Lacas-Gervais S, Drin G, Antony B (2013) A four-step cycle driven by PI(4)P hydrolysis directs sterol/PI(4)P exchange by the ER-Golgi tether OSBP. *Cell* 155:830-843
- Meurer M, Duan Y, Sass E, Kats I, Herbst K, Buchmuller BC, Dederer V, Huber F, Kirmaier D, Steffl M, Van Laer K, Dick TP, Lemberg MK, Khmelinskii A, Levy ED, Knop M (2018) Genome-wide C-SWAT library for high-throughput yeast genome tagging. *Nat Methods* 15:598-600
- Moggridge S, Sorensen PH, Morin GB, Hughes CS (2018) Extending the compatibility of the SP3 paramagnetic bead processing approach for proteomics. *J Proteome Res* 17:1730-1740
- Nikawa J, Hosaka K, Yamashita S (1993) Differential regulation of two myo-inositol transporter genes of *Saccharomyces cerevisiae*. *Mol Microbiol* 10:955-961
- Nilsson IM, Ohvo-Rekilä H, Slotte JP, Johnson AE, Von Heijne G (2001) Inhibition of protein translocation across the endoplasmic reticulum membrane by sterols. *J Biol Chem* 276:41748-41754
- Páll S, Zhmurov A, Bauer P, Abraham M, Lundborg M, Gray A, Hess B, Lindahl E (2020) Heterogeneous parallelization and acceleration of molecular dynamics simulations in GROMACS. *J Chem Phys* 153:134110
- Parrinello M, Rahman A (1981) Polymorphic transitions in single crystals: a new molecular dynamics method. *J Appl Phys* 52:7182-7190
- Patton-Vogt JL, Henry SA (1998) GIT1, a gene encoding a novel transporter for glycerophosphoinositol in *Saccharomyces cerevisiae*. *Genetics* 149:1707-1715
- Pérez-Martí A, Ramakrishnan S, Li J, Dugourd A, Molenaar MR, De La Motte LR, Grand K, Mansouri A, Parisot M, Lienkamp SS, Saez-Rodriguez J, Simons M (2022) Reducing lipid bilayer stress by monounsaturated fatty acids protects renal proximal tubules in diabetes. *eLife* 11:e74391
- Perez-Riverol Y, Bai J, Bandla C, Garcia-Seisdedos D, Hewapathirana S, Kamatchinathan S, Kundu DJ, Prakash A, Frericks-Zipper A, Eisenacher M, Walzer M, Wang S, Brazma A, Vizcaino JA (2022) The PRIDE database resources in 2022: a hub for mass spectrometry-based proteomics evidences. *Nucleic Acids Res* 50:D543-D552
- Phillips MJ, Voeltz GK (2016) Structure and function of ER membrane contact sites with other organelles. *Nat Rev Mol Cell Biol* 17:69-82
- Phillips R, Ursell T, Wiggins P, Sens P (2009) Emerging roles for lipids in shaping membrane-protein function. *Nature* 459:379-385
- Piccolis M, Bond LM, Kampmann M, Pulimeno P, Chitruju C, Jayson CBK, Vaites LP, Boland S, Lai ZW, Gabriel KR, Elliott SD, Paulo JA, Harper JW, Weissman JS, Walther TC, Farese RV (2019) Probing the global cellular responses to lipotoxicity caused by saturated fatty acids. *Mol Cell* 74:32-44.e8
- Pineau L, Colas J, Dupont S, Beney L, Fleurat-Lessard P, Berjeaud JM, Bergès T, Ferreira T (2009) Lipid-induced ER stress: synergistic effects of sterols and saturated fatty acids. *Traffic* 10:673-690
- Promlek T, Ishiwata-Kimata Y, Shido M, Sakuramoto M, Kohno K, Kimata Y (2011) Membrane aberrancy and unfolded proteins activate the endoplasmic reticulum stress sensor Ire1 in different ways. *Mol Biol Cell* 22:3520-3532
- Quiroga R, Trenchi A, Montoro AG, Taubas JV, Maccioni HJF (2013) Short transmembrane domains with high-volume exoplasmic halves determine retention of type II membrane proteins in the Golgi complex. *J Cell Sci* 126:5344-5349
- Radanović T, Ernst R (2021) The unfolded protein response as a guardian of the secretory pathway. *Cells* 10:2965
- Radhakrishnan A, Goldstein JL, McDonald JG, Brown MS (2008) Switch-like control of SREBP-2 transport triggered by small changes in ER cholesterol: a delicate balance. *Cell Metab* 8:512-521
- Ray GJ, Boydston EA, Shortt E, Wyant GA, Lourido S, Chen WW, Sabatini DM (2020) A PEROXO-Tag enables rapid isolation of peroxisomes from human cells. *iScience* 23:101109
- Reglinski K, Steinfort-Effelsberg L, Sezgin E, Klose C, Platta HW, Girzalsky W, Eggeling C, Erdmann R (2020) Fluidity and lipid composition of membranes of peroxisomes, mitochondria and the ER from oleic acid-induced *Saccharomyces cerevisiae*. *Front Cell Dev Biol* 8:574363
- Reinhard J, Leveille CL, Cornell CE, Merz AJ, Klose C, Ernst R, Keller SL (2023) Remodeling of yeast vacuole membrane lipidomes from the log (one phase) to stationary stage (two phases). *Biophys J* 122:1043-1057
- Reinhard J, Mattes C, Vath K, Radanović T, Surma MA, Klose C, Ernst R (2020) A quantitative analysis of cellular lipid compositions during acute proteotoxic ER stress reveals specificity in the production of asymmetric lipids. *Front Cell Dev Biol* 8:756
- Renne MF, Bao X, Hokken MW, Bierhuizen AS, Hermansson M, Sprenger RR, Ewing TA, Ma X, Cox RC, Brouwers JF, De Smet CH, Ejsing CS, de Kroon AI (2022) Molecular species selectivity of lipid transport creates a mitochondrial sink for di-unsaturated phospholipids. *EMBO J* 41:e106837
- Renne MF, Bao X, De Smet CH, de Kroon AIPM (2015) Lipid acyl chain remodeling in yeast. *Lipid Insights* 8:33-40
- Renne MF, Ernst R (2023) Membrane homeostasis beyond fluidity: control of membrane compressibility. *Trends Biochem Sci* 48:963-977
- Rice C, Cooke M, Treloar N, Vollbrecht P, Stuke J, McDonough V (2010) A role for MGA2, but not SPT23, in activation of transcription of ERG1 in *Saccharomyces cerevisiae*. *Biochem Biophys Res Commun* 403:293-297
- Ridsdale A, Denis M, Gougeon PY, Ngsee JK, Presley JF, Zha X (2006) Cholesterol is required for efficient endoplasmic reticulum-to-Golgi transport of secretory membrane proteins. *Mol Biol Cell* 17:1593-1605
- Ritchie ME, Phipson B, Wu D, Hu Y, Law CW, Shi W, Smyth GK (2015) limma powers differential expression analyses for RNA-sequencing and microarray studies. *Nucleic Acids Res* 43:e47-e47
- Rouser G, Fleischer S, Yamamoto A (1970) Two dimensional thin layer chromatographic separation of polar lipids and determination of phospholipids by phosphorus analysis of spots. *Lipids* 5:494-496

- Savitski MM, Wilhelm M, Hahne H, Kuster B, Bantscheff M (2015) A scalable approach for protein false discovery rate estimation in large proteomic data sets. *Mol Cell Proteomics* 14:2394–2404
- Schindelin J, Arganda-Carreras I, Frise E, Kaynig V, Longair M, Pietzsch T, Preibisch S, Rueden C, Saalfeld S, Schmid B, Tinevez JY, White DJ, Hartenstein V, Eliceiri K, Tomancak P, Cardona A (2012) Fiji: an open-source platform for biological-image analysis. *Nat Methods* 9:676–682
- Schneider R, Brügger B, Sandhoff R, Zellnig G, Leber A, Lampl M, Athenstaedt K, Hrastrnik C, Eder S, Daum G, Paltauf F, Wieland FT, Kohlwein SD (1999) Electrospray ionization tandem mass spectrometry (ESI-MS/MS) analysis of the lipid molecular species composition of yeast subcellular membranes reveals acyl chain-based sorting/remodeling of distinct molecular species en route to the plasma membrane. *J Cell Biol* 146:741–754
- Schuck S, Prinz WA, Thorn KS, Voss C, Walter P (2009) Membrane expansion alleviates endoplasmic reticulum stress independently of the unfolded protein response. *J Cell Biol* 187:525–536
- Scorrano L, De Matteis MA, Emr S, Giordano F, Hajnóczky G, Kornmann B, Lackner LL, Levine TP, Pellegrini L, Reinisch K, Rizzuto R, Simmen T, Stenmark H, Ungermann C, Schuldiner M (2019) Coming together to define membrane contact sites. *Nat Commun* 10:1287
- Sharpe HJ, Stevens TJ, Munro S (2010) A comprehensive comparison of transmembrane domains reveals organelle-specific properties. *Cell* 142:158–169
- Sinensky M (1980) Adaptive alteration in phospholipid composition of plasma membranes from a somatic cell mutant defective in the regulation of cholesterol biosynthesis. *J Cell Biol* 85:166–169
- Sokoya T, Parolek J, Foged MM, Danylchuk DI, Bozan M, Sarkar B, Hilderink A, Philippi M, Botto LD, Terhal PA, Mäkitie O, Piehler J, Kim Y, Burd CG, Klymchenko AS, Maeda K, Holthuis JCM (2022) Pathogenic variants of sphingomyelin synthase SMS2 disrupt lipid landscapes in the secretory pathway. *eLife* 11:e79278
- Stordeur C, Puth K, Sáenz JP, Ernst R (2014) Crosstalk of lipid and protein homeostasis to maintain membrane function. *Biol Chem* 395:313–326
- Surma MA, Gerl MJ, Herzog R, Helppi J, Simons K, Klose C (2021) Mouse lipidomics reveals inherent flexibility of a mammalian lipidome. *Sci Rep* 11:19364
- Surma MA, Herzog R, Vasilij A, Klose C, Christinat N, Morin-Rivron D, Simons K, Masoodi M, Sampaio JL (2015) An automated shotgun lipidomics platform for high throughput, comprehensive, and quantitative analysis of blood plasma intact lipids. *Eur J Lipid Sci Technol* 117:1540–1549
- Surma MA, Klose C, Klemm RW, Ejsing CS, Simons K (2011) Generic sorting of raft lipids into secretory vesicles in yeast. *Traffic* 12:1139–1147
- Surma MA, Klose C, Peng D, Shales M, Mrejen C, Stefanko A, Braberg H, Gordon DE, Vorkel D, Ejsing CS, Farese R, Simons K, Krogan NJ, Ernst R (2013) A lipid E-MAP identifies Ubx2 as a critical regulator of lipid saturation and lipid bilayer stress. *Mol Cell* 51:519–530
- Takamori S, Holt M, Stenius K, Lemke EA, Grønborg M, Riedel D, Urlaub H, Schenck S, Brügger B, Ringler P, Müller SA, Rammner B, Gräter F, Hub JS, De Groot BL, Mieskes G, Moriyama Y, Klingauf J, Grubmüller H, Heuser J et al (2006) Molecular anatomy of a trafficking organelle. *Cell* 127:831–846
- Thibault G, Shui G, Kim W, McAlister GC, Ismail N, Gygi SP, Wenk MR, Ng DTW (2012) The membrane stress response buffers lethal effects of lipid disequilibrium by reprogramming the protein homeostasis network. *Mol Cell* 48:16–27
- Ting CL, Awasthi N, Müller M, Hub JS (2018) Metastable prepores in tension-free lipid bilayers. *Phys Rev Lett* 120:128103
- Tong AHY, Boone C (2006) Synthetic genetic array analysis in *Saccharomyces cerevisiae*. In: John M. Walker (ed) *Yeast protocols*. New Jersey, Humana Press, pp 171–192
- Tran DM, Ishiwata-Kimata Y, Mai TC, Kubo M, Kimata Y (2019a) The unfolded protein response alongside the diauxic shift of yeast cells and its involvement in mitochondria enlargement. *Sci Rep* 9:12780
- Tran DM, Takagi H, Kimata Y (2019b) Categorization of endoplasmic reticulum stress as accumulation of unfolded proteins or membrane lipid aberrancy using yeast Ire1 mutants. *Biosci Biotechnol Biochem* 83:326–329
- Travers KJ, Patil CK, Wodicka L, Lockhart DJ, Weissman JS, Walter P (2000) Functional and genomic analyses reveal an essential coordination between the unfolded protein response and ER-associated degradation. *Cell* 101:249–258
- Tsuchiya M, Tachibana N, Nagao K, Tamura T, Hamachi I (2023) Organelle-selective click labeling coupled with flow cytometry allows pooled CRISPR screening of genes involved in phosphatidylcholine metabolism. *Cell Metab* 35:1072–1083.e9
- Urbanowski JL, Piper RC (1999) The iron transporter Fth1p forms a complex with the Fet5 iron oxidase and resides on the vacuolar membrane. *J Biol Chem* 274:38061–38070
- van den Brink-van der Laan E, Antoinette Killian J, de Kruijff B (2004) Nonbilayer lipids affect peripheral and integral membrane proteins via changes in the lateral pressure profile. *Biochim Biophys Acta Biomembr* 1666:275–288
- Van Meer G, Voelker DR, Feigenson GW (2008) Membrane lipids: where they are and how they behave. *Nat Rev Mol Cell Biol* 9:112–124
- van 't Klooster JS, Cheng T-Y, Sikkema HR, Jeucken A, Moody B, Poolman B (2020) Periprotein lipidomes of *Saccharomyces cerevisiae* provide a flexible environment for conformational changes of membrane proteins. *eLife* 9:e57003
- Väth K, Mattes C, Reinhard J, Covino R, Stumpf H, Hummer G, Ernst R (2021) Cysteine cross-linking in native membranes establishes the transmembrane architecture of Ire1. *J Cell Biol* 220:e202011078
- Vevea JD, Garcia EJ, Chan RB, Zhou B, Schultz M, Di Paolo G, McCaffery JM, Pon LA (2015) Role for lipid droplet biogenesis and micropinophagy in adaptation to lipid imbalance in yeast. *Dev Cell* 35:584–599
- Voeltz GK, Prinz WA, Shibata Y, Rist JM, Rappoport TA (2006) A class of membrane proteins shaping the tubular endoplasmic reticulum. *Cell* 124:573–586
- Volmer R, van der Ploeg K, Ron D (2013) Membrane lipid saturation activates endoplasmic reticulum unfolded protein response transducers through their transmembrane domains. *Proc Natl Acad Sci USA* 110:4628–4633
- Walter P, Ron D (2011) The unfolded protein response: from stress pathway to homeostatic regulation. *Science* 334:1081–1086
- Wang Y, Ruan L, Li R (2024) GPI-anchored Gas1 protein regulates cytosolic proteostasis in budding yeast. *G3 Genes Genomes Genet* <https://doi.org/10.1093/g3journal/jkad263>
- Weber T, Zemelman BV, McNew JA, Westermann B, Gmachl M, Parlati F, Söllner TH, Rothman JE (1998) SNAREpins: minimal machinery for membrane fusion. *Cell* 92:759–772
- Weigel AV, Chang C-L, Shtengel G, Xu CS, Hoffman DP, Freeman M, Iyer N, Aaron J, Khuon S, Bogovic J, Qiu W, Hess HF, Lippincott-Schwartz J (2021) ER-to-Golgi protein delivery through an interwoven, tubular network extending from ER. *Cell* 184:2412–2429.e16
- Weill U, Yofe I, Sass E, Stynen B, Davidi D, Natarajan J, Ben-Menachem R, Avihou Z, Goldman O, Harpaz N, Chuartzman S, Kniazev K, Knoblach B, Laborenz J, Boos F, Kowarzyk J, Ben-Dor S, Zalckvar E, Herrmann JM, Rachubinski RA et al (2018) Genome-wide SWAp-Tag yeast libraries for proteome exploration. *Nat Methods* 15:617–622
- Wendland B, Emr SD, Riezman H (1998) Protein traffic in the yeast endocytic and vacuolar protein sorting pathways. *Curr Opin Cell Biol* 10:513–522
- Werner T, Sweetman G, Savitski MF, Mathieson T, Bantscheff M, Savitski MM (2014) Ion coalescence of neutron encoded TMT 10-plex reporter ions. *Anal Chem* 86:3594–3601

- Wong LH, Gatta AT, Levine TP (2019) Lipid transfer proteins: the lipid commute via shuttles, bridges and tubes. *Nat Rev Mol Cell Biol* 20:85–101
- Wu X, Rapoport TA (2021) Translocation of proteins through a distorted lipid bilayer. *Trends Cell Biol* 31:473–484
- Yang X, Arines FM, Zhang W, Li M (2018) Sorting of a multi-subunit ubiquitin ligase complex in the endolysosome system. *eLife* 7:e33116
- Yofe I, Weill U, Meurer M, Chuartzman S, Zalckvar E, Goldman O, Ben-Dor S, Schütze C, Wiedemann N, Knop M, Khmelinskii A, Schuldiner M (2016) One library to make them all: streamlining the creation of yeast libraries via a SWAp-Tag strategy. *Nat Methods* 13:371–378
- Young BP, Shin JH, Orij R, Chao JT, Li SC, Guan XL, Khong A, Jan E, Wenk MR, Prinz WA, Smits GJ, Loewen CJR (2010) Phosphatidic acid is a pH biosensor that links membrane biogenesis to metabolism. *Science* 329:1085–1088
- Zinser E, Daum G (1995) Isolation and biochemical characterization of organelles from the yeast, *Saccharomyces cerevisiae*. *Yeast* 11:493–536
- Zinser E, Paltauf F, Daum G (1993) Sterol composition of yeast organelle membranes and subcellular distribution of enzymes involved in sterol metabolism. *J Bacteriol* 175:2853–2858
- Zinser E, Sperka-Gottlieb CDM, Fasch EV, Kohlwein SD, Paltauf F, Daum G (1991) Phospholipid synthesis and lipid composition of subcellular membranes in the unicellular eukaryote *Saccharomyces cerevisiae*. *J Bacteriol* 173:2026–2034

Acknowledgements

The authors wish to thank Michael Knop for generously providing the C' SWAT library. We would like to thank Sepp Kohlwein, Karin Römisch, Christian Ungermann, Howard Riezman, Karl Kuchler, and Ralf Erdmann for providing antibodies and Sarah L. Keller, Georg Pabst, Sebastian Schuck as well as Chris Stefan for fruitful discussions and helpful comments. We thank Cynthia Alsayyah for an informative control experiment. This work was funded by the VW foundation (Life?, #93089, #93092, #93090) to RE, MS, and JS, by the Deutsche Forschungsgemeinschaft in the framework of the SFB894 to RE and the SFB1027 to both JH and RE, and by the European Research Council under the European Union's Horizon 2020 research and innovation program (grant agreement no. 866011) to RE. MS is an incumbent of the Dr. Gilbert Omenn and Martha Darling Professorial Chair in Molecular Genetics.

Author contributions

John Reinhard: Resources; Data curation; Formal analysis; Validation; Investigation; Visualization; Methodology; Writing—original draft; Writing—review and editing. **Leonhard Starke:** Data curation; Software; Formal analysis; Validation; Visualization; Methodology; Writing—review and editing. **Christian Klose:** Data curation; Formal analysis; Validation; Methodology. **Per Haberkant:**

Resources; Data curation; Software; Validation; Visualization. **Henrik Hammarén:** Resources; Data curation; Software; Validation; Visualization. **Frank Stein:** Resources; Data curation; Software; Validation; Visualization. **Ofir Klein:** Resources; Investigation; Methodology. **Charlotte Berhorst:** Investigation; Methodology. **Heike Stumpf:** Investigation; Methodology. **James P Sáenz:** Funding acquisition; Investigation. **Jochen Hub:** Resources; Data curation; Software; Formal analysis; Supervision; Validation; Visualization; Writing—review and editing. **Maya Schuldiner:** Resources; Data curation; Investigation; Methodology; Writing—review and editing. **Robert Ernst:** Conceptualization; Data curation; Supervision; Funding acquisition; Validation; Visualization; Methodology; Writing—original draft; Project administration; Writing—review and editing.

Funding

Open Access funding enabled and organized by Projekt DEAL.

Disclosure and competing interests statement

CK declares competing financial interests related to the publication of this study, including being chief technology officer at Lipotype GmbH, Dresden. The remaining authors declare no competing interests.

Open Access This article is licensed under a Creative Commons Attribution 4.0 International License, which permits use, sharing, adaptation, distribution and reproduction in any medium or format, as long as you give appropriate credit to the original author(s) and the source, provide a link to the Creative Commons licence, and indicate if changes were made. The images or other third party material in this article are included in the article's Creative Commons licence, unless indicated otherwise in a credit line to the material. If material is not included in the article's Creative Commons licence and your intended use is not permitted by statutory regulation or exceeds the permitted use, you will need to obtain permission directly from the copyright holder. To view a copy of this licence, visit <http://creativecommons.org/licenses/by/4.0/>. Creative Commons Public Domain Dedication waiver <http://creativecommons.org/public-domain/zero/1.0/> applies to the data associated with this article, unless otherwise stated in a credit line to the data, but does not extend to the graphical or creative elements of illustrations, charts, or figures. This waiver removes legal barriers to the re-use and mining of research data. According to standard scholarly practice, it is recommended to provide appropriate citation and attribution whenever technically possible.

© The Author(s) 2024

Expanded View Figures

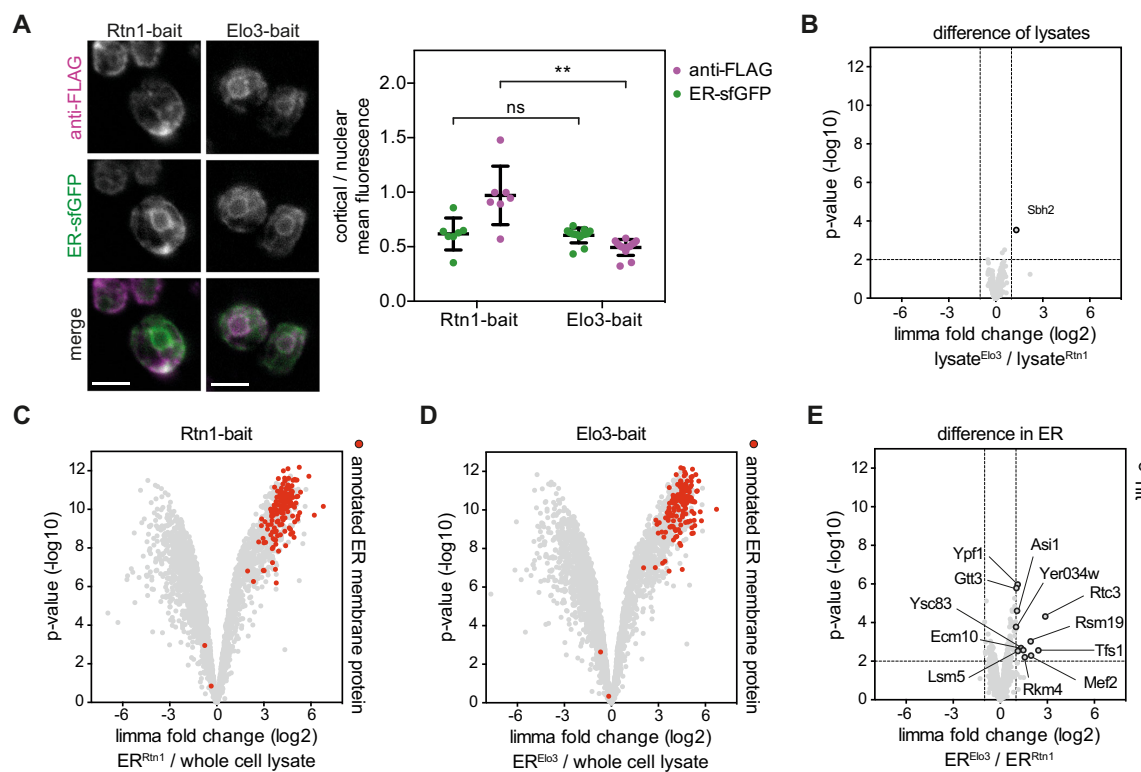


Figure EV1. ER MemPrep via two different bait proteins.

(A) Immunofluorescence showing the localization of two different ER membrane bait proteins (Rtn1-bait, Elo3-bait) relative to the ER-luminal marker ER-sfGFP-HDEL. Scale bar indicates 5 μ m. Quantification of fluorescence distribution. Cell and nuclear areas were chosen manually. Cortical area was defined as total cellular area minus nuclear area. The ER-luminal marker ER-sfGFP-HDEL shows the same cortical-to-nuclear distribution in both bait strains. Rtn1-bait has a stronger preference for the cortical ER, compared to Elo3-bait. $n = 7$ cells for Rtn1-bait, $n = 14$ cells for Elo3-bait. Data from individual cells are represented as data points yielding the average \pm SD. $^{***}P > 0.05$, $^{**}P \leq 0.01$ (unpaired parametric t test with Welch's correction). (B) Limma analysis of TMT-labeling proteomics reveals that the proteome of Rtn1-bait and Elo3-bait whole-cell lysates is identical except for a single outlier (Sbh2) ($n = 3$ biological replicates). (C) To increase the proteomics coverage for membrane proteins, P100 membranes were carbonate-washed before performing immunoprecipitation. MemPrep via Rtn1-bait enriches ER membrane proteins in the isolate (ER^{Rtn1}) ($n = 3$ biological replicates). (D) ER membrane proteins are enriched to the same extent by MemPrep via the bait protein Elo3-bait ($n = 3$ biological replicates). (E) MemPrep via Rtn1-bait and Elo3-bait yields almost identical sample composition with only 12 proteins that are enriched in the Elo3-bait derived ER. Data information: Data in (B-E) are presented as the mean from $n = 3$ biological replicates. A moderated t -test limma to test for differential enrichment was used. P values were corrected for multiple testing with the method from Benjamini and Hochberg. Source data are available online for this figure.

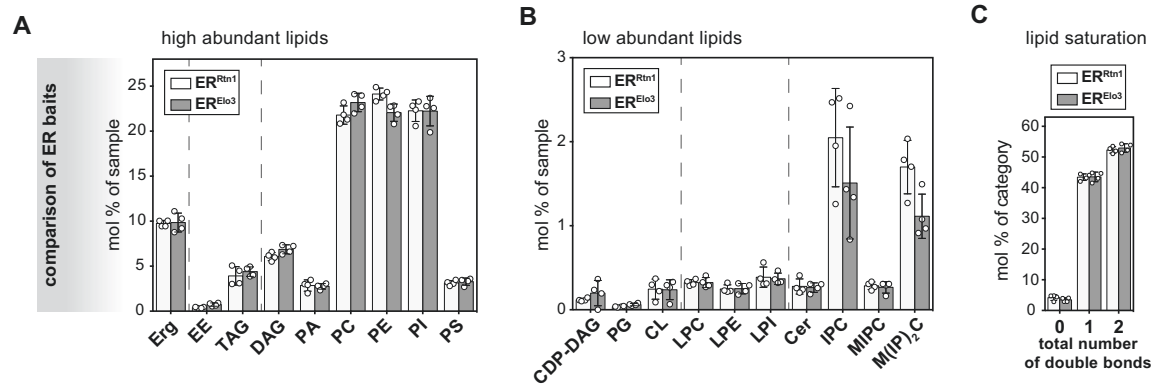


Figure EV2. The lipidome of Rtn1-bait and Elo3-bait derived ER membranes is identical.

Quantitative lipidomics of ER membranes derived via two different bait proteins. (A) Distribution of lipid classes with high abundance. Erg ergosterol, EE ergosteryl ester, TAG triacylglycerol, DAG diacylglycerol, PA phosphatidic acid, PC phosphatidylcholine, PE phosphatidylethanolamine, PI phosphatidylinositol, PS phosphatidylserine ($n = 4$ biological replicates). (B) Distribution of lipid classes with low abundance. CDP-DAG cytidine diphosphate diacylglycerol, PG phosphatidylglycerol, CL cardiolipin, LPC lyso-phosphatidylcholine, LPE lyso-phosphatidylethanolamine, LPI lyso-phosphatidylinositol, Cer ceramide, IPC inositolphosphorylceramide, MIPC mannosyl-IPC, M(IP)₂C mannosyl-di-IPC ($n = 4$ biological replicates). (C) Total number of double bonds in membrane glycerolipids, except for CL, (i.e., CDP-DAG, DAG, PA, PC, PE, PG, PI, PS) as mol% of this category. Lipid data of Rtn1-bait derived membranes are identical with the data presented in Fig. 2A-C. Data information: In (A-C), data from $n = 4$ biological replicates are presented as individual data points and as mean \pm SD. All differences of ER^{Rtn1} versus ER^{Elo3} were nonsignificant with $P > 0.05$ (multiple t tests, corrected for multiple comparisons using the method of Benjamini, Krieger and Yekutieli, with $Q = 1\%$, without assuming consistent SD). Nonsignificant comparisons are not highlighted. Source data are available online for this figure.

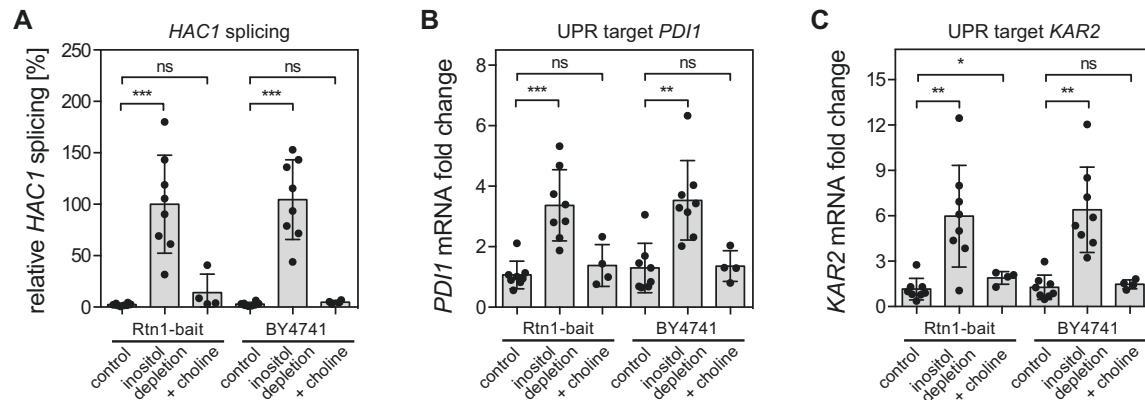
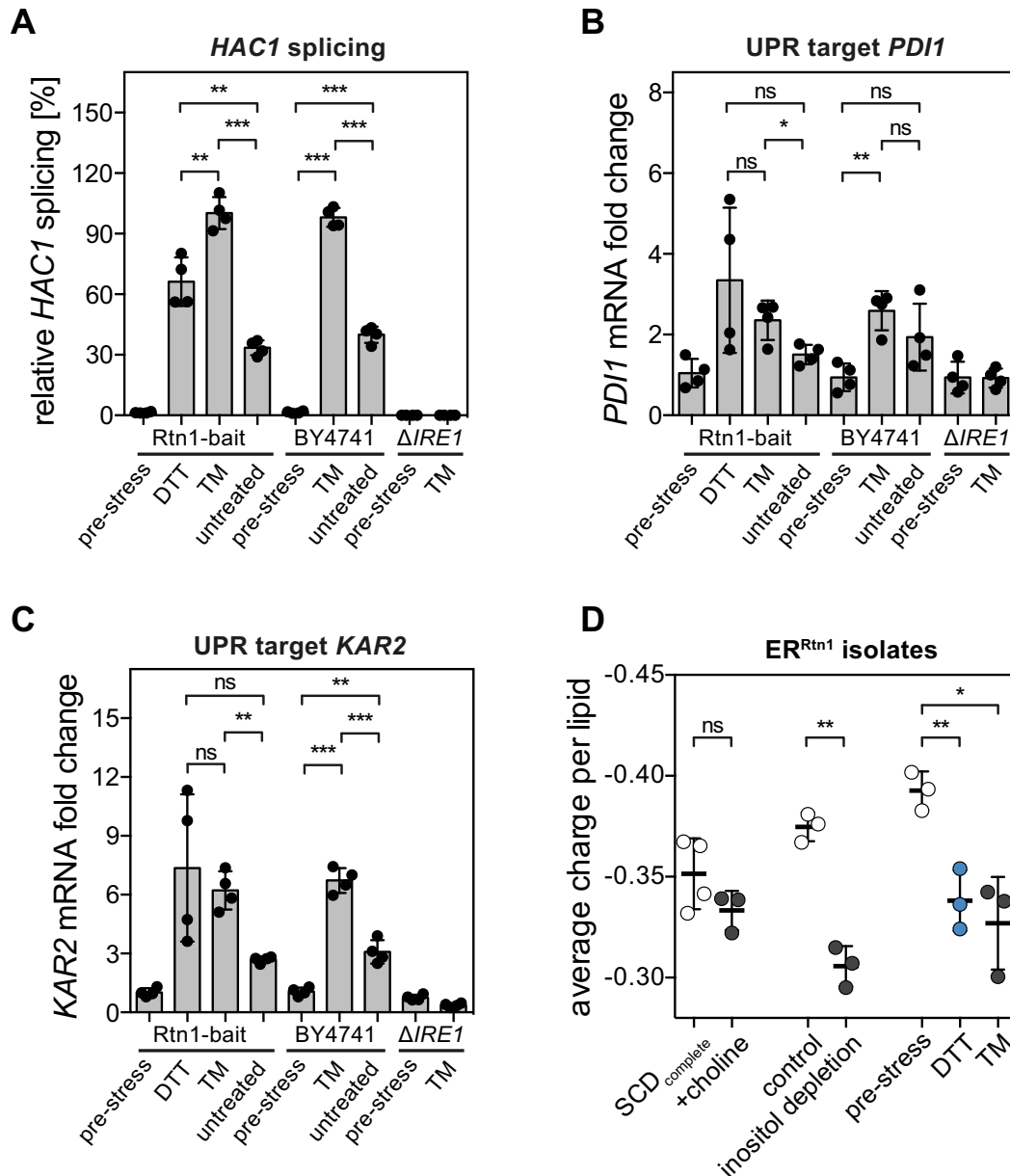


Figure EV3. Activation of the UPR by lipid bilayer stress.

SCD_{complete} medium was inoculated with Rtn1-bait cells to an OD₆₀₀ of 0.003 from an overnight pre-culture and grown to an OD₆₀₀ of 1.2. Cells were washed with inositol-free medium and then cultivated for an additional 2 h in either inositol-free (inositol depletion) or SCD_{complete} medium (control) starting with an OD₆₀₀ of 0.6. Another perturbation of lipid metabolism was achieved by addition of choline. For '+choline' conditions, SCD_{complete} medium was inoculated to an OD₆₀₀ of 0.1 using stationary overnight cultures. Cells were then cultivated to an OD₆₀₀ of 1.0 in the presence of 2 mM choline. (A) UPR activation was measured by determining the levels of spliced HAC1 mRNA. Data for relative HAC1 splicing was normalized to the inositol depletion Rtn1-bait condition ($n = 8$ biological replicates based on two technical replicates for Rtn1-bait control, Rtn1-bait inositol depletion, BY4741 control and BY4741 inositol depletion, but $n = 4$ biological replicates based on two technical replicates for Rtn1-bait + choline and BY4741 + choline). (B) mRNA upregulation of the downstream UPR target gene *PDI1*. *PDI1* mRNA fold change was calculated as $2^{\Delta\Delta Ct}$ and normalized to Rtn1-bait control condition ($n = 8$ biological replicates based on two technical replicates for the Rtn1-bait control, Rtn1-bait inositol depletion, BY4741 control, and BY4741 inositol depletion, but $n = 4$ biological replicates based on two technical replicates for Rtn1-bait + choline and BY4741 + choline). (C) Upregulation of mRNA of the downstream UPR target gene *KAR2* calculated as $2^{\Delta\Delta Ct}$ and normalized to Rtn1-bait control condition ($n = 8$ biological replicates based each on two technical replicates for Rtn1-bait control, Rtn1-bait inositol depletion, BY4741 control, and BY4741 inositol depletion, but $n = 4$ biological replicates based on two technical replicates for Rtn1-bait + choline and BY4741 + choline). Data information: All data from biological replicates are presented in (A-C) as individual data points with the mean \pm SD. $^{ns}P > 0.05$, $^{*}P \leq 0.05$, $^{**}P \leq 0.01$, $^{***}P \leq 0.001$ (unpaired parametric *t* test with Welch's correction). Nonsignificant comparisons are not highlighted. Source data are available online for this figure.



◀ **Figure EV4. Activation of the UPR upon prolonged proteotoxic stress.**

Cells were grown as described above. UPR activation was measured by determining the levels of (A) spliced *HAC1* mRNA and the mRNA of the downstream UPR target gene ($n = 4$ biological replicates based on two technical replicates) (B) *PDI1* ($n = 4$ biological replicates based on two technical replicates) and (C) *KAR2* before and after 4 h of DTT or TM treatment ($n = 4$ biological replicates based on two technical replicates). Data for relative *HAC1* splicing was normalized to the TM-treated Rtn1-bait condition. *PDI1* and *KAR2* mRNA fold changes were calculated as $2^{-\Delta\Delta Ct}$ and normalized to Rtn1-bait pre-stress. (D) Calculation of the average charge per lipid from ER lipidomics data shown in Appendix Fig. S3A,B (SCD_{complete} + choline), Fig. 3B,C (control, inositol depletion), and Fig. 4D,E (pre-stress, DTT, TM). Conditions with active UPR show reduced negative lipid charges compared to their respective controls. Net charges of the lipid classes were considered as follows: Erg O, EE O, TAG O, DAG O, PA -1, PC O, PE O, PI -1, PS -1, CDP-DAG -2, PG -1, CL -2, Cer O, IPC -1, MIPC -1, M(IP)₂C-2 ($n = 4$ biological replicates for SCD_{complete} and $n = 3$ biological replicates for all other conditions). Data information: All data are presented as individual data points and the mean \pm SD. ^{ns} $P > 0.05$, * $P \leq 0.05$, ** $P \leq 0.01$, *** $P \leq 0.001$ (unpaired parametric *t* test with Welch's correction). Source data are available online for this figure.

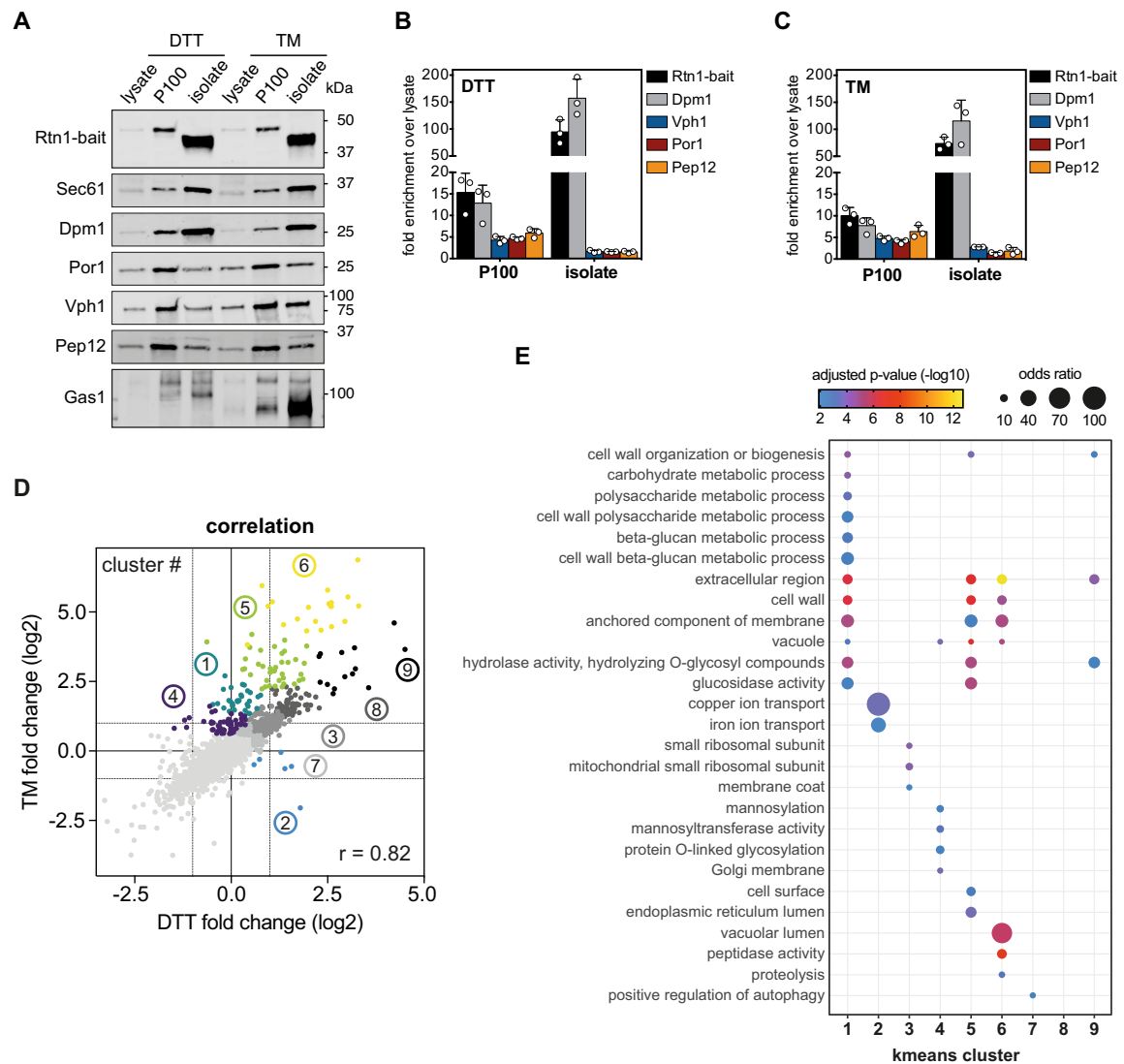


Figure EV5. Enrichment of stressed ER membranes by MemPrep.

(A) Immunoblot analysis of the indicated organellar markers in whole-cell lysates (lysate), crude membranes (P100), and MemPrep isolates (isolate). ER membranes were immuno-isolated via the Rtn1-bait protein. Sec61 and Dpm1 are prototypical ER membrane markers. Por1 is a marker for the outer mitochondrial membrane, Vph1 is a vacuolar marker. Pep12 marks endosomes and Gas1 serves as plasma membrane marker. 1 μ g total protein loaded per lane. (B) Quantification of the organellar markers Dpm1, Vph1, Por1, Pep12 and the Rtn1-bait protein from three immunoblots of independent replicate ER MemPreps after prolonged proteotoxic stress induced by DTT ($n = 3$ biological replicates). (C) Quantification of three immunoblots from independent replicate ER MemPreps after prolonged proteotoxic stress induced by TM. Error bars indicate standard deviations ($n = 3$ biological replicates). (D) Correlation of DTT- and TM-induced fold changes, after Limma analysis, over pre-stress with a Pearson correlation coefficient $r = 0.82$. K-means clusters are indicated by colored groups and their respective cluster number ($n = 3$ biological replicates). (E) Gene ontology term enrichments in K-means clusters ($n = 3$ biological replicates). Data information: Data in (B, C), data from three biological replicates are presented as individual data points and as the mean \pm SD. Data in (E) from $n = 3$ biological replicates are presented as the mean. P values were derived from a Fisher-test and corrected for multiple testing with the method of Benjamini and Hochberg. Source data are available online for this figure.

APPENDIX

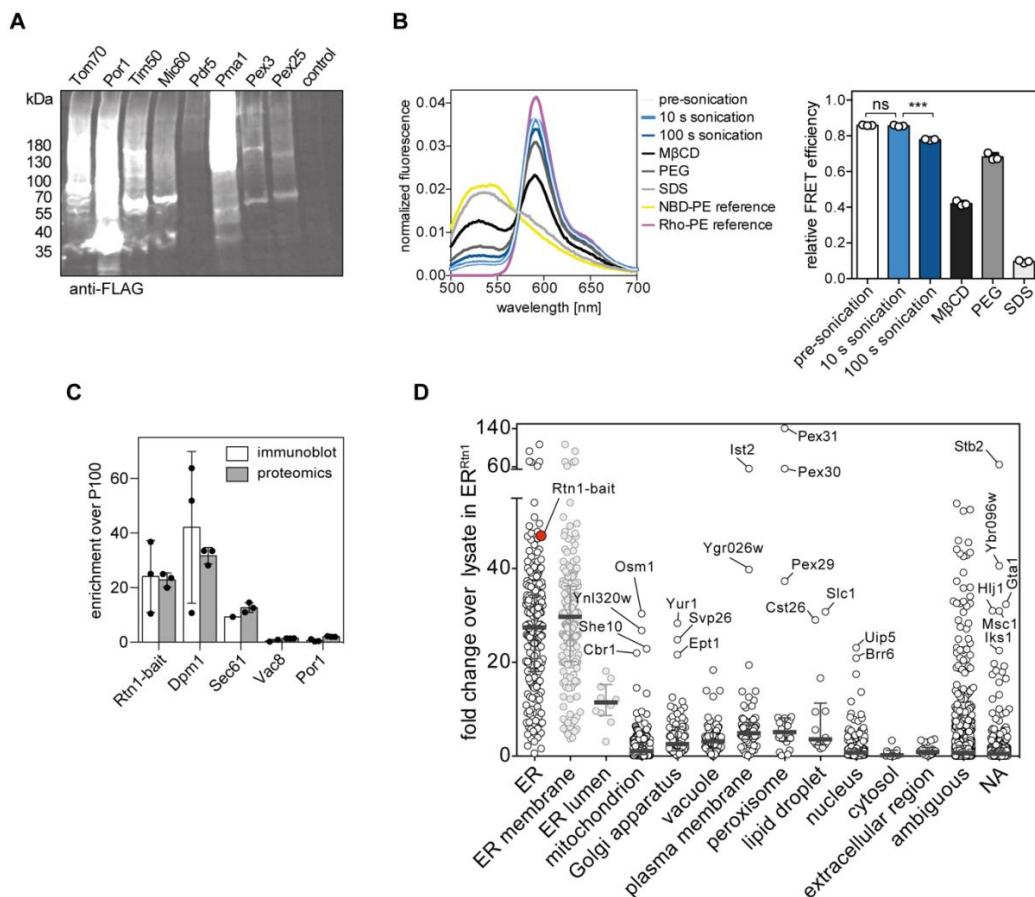
A new technology for isolating organellar membranes provides fingerprints of lipid bilayer stress

Authors: John Reinhard, Leonhard Starke, Christian Klose, Per Haberkant, Henrik Hammarén, Frank Stein, Ofir Klein, Charlotte Berhorst, Heike Stumpf, James P. Sáenz, Jochen Hub, Maya Schuldiner, Robert Ernst

Correspondence to: robert.ernst@uks.eu

Table of contents

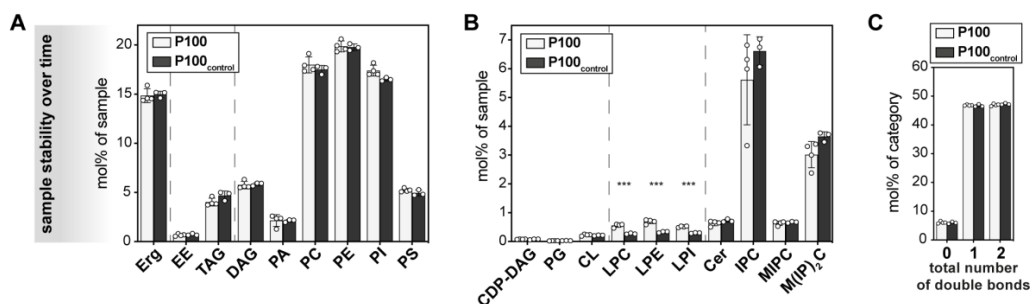
1. Appendix Figure S1	page 2
2. Appendix Figure S2	page 4
3. Appendix Figure S3	page 5
4. Appendix Figure S4	page 6
5. Appendix Figure S5	page 8
6. Appendix Figure S6	page 9
7. Appendix Supplementary Methods	page 10



Appendix Figure S1. Analytical data from MemPrep-derived samples has predictive power. (A)

From a systematic collection of strains in which every protein is tagged with a C-terminal bait tag (myc-3C-3xFLAG) we generated cell lysates for exemplary strains embedded in different organellar membranes. (B) Fluorescence spectra and calculation of relative FRET efficiencies in mixtures of labeled liposomes and a ~15.4-fold excess (based on membrane phospholipid content) of unlabeled P100 microsomes after sonication as performed during MemPrep procedure (10 s sonication), after extensive sonication (100 s sonication), or upon incubation with 18 mM methyl beta cyclodextrin (M β CD), 40% (w/v) polyethylene glycol 8000 (PEG 8000), or 1% sodium dodecyl sulfate (SDS). A low relative FRET efficiency is the result of decreased average proximity of the two FRET-pair fluorophores and indicative for either fusion of labeled liposomes with unlabeled P100 microsomes or lipid exchange between vesicles. Data are presented as individual data points and mean \pm SD ($n = 3$ independent experiments). Statistical significance was tested using an unpaired parametric t test with Welch's correction. ns: not significant; *** $p \leq 0.001$. (C) Correlation of mean enrichments of organellar markers in ER membranes derived by MemPrep over P100 microsomes determined by either immunoblot analysis or proteomics. Immuno-isolation bait protein (myc-Rtn1), ER markers Dpm1 and Sec61, vacuole marker Vac8, and outer mitochondrial membrane marker Por1. Error bars indicate SD ($n = 3$ for Rtn1-bait, Dpm1, and Por1 immunoblot; $n = 1$ for Sec61 immunoblot; $n = 2$ for Vac8 immunoblot; $n = 3$ for all markers in proteomics data). (D) Mean enrichment (fold change over lysate) of each individual identified protein in our untargeted TMT-labeling proteomics data (Figure 1E, $n = 3$). The bait protein 'Rtn1-bait' via which MemPrep was performed is indicated. Several proteins that were highly enriched in our ER membrane preparation via the Rtn1-bait are uniquely annotated to other organelles. Annotations of subcellular location were retrieved from UniProt (accessed 27.01.2023). A subsequent consultation of the *Saccharomyces* Genome Database gene description and GOterms (accessed 03.01.2024)

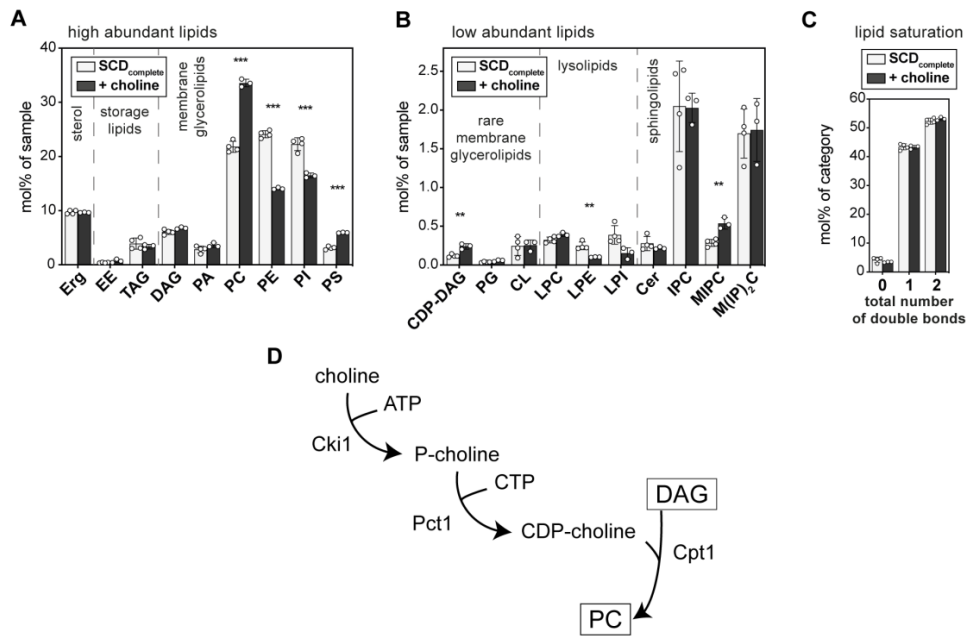
reveals that many of those highly enriched proteins annotated to other organelles were previously observed in the ER or the nuclear envelope (Ist2, Pex30, Pex29, Brr6, She10, YBR096W, YEL043W, Hlj1, YGR026W), or feature a dual localization to the ER and other organelles (Osm1, Slc1, Svp26, Yur1, Ept1, Pex31, Msc1). 'NA' stands for no annotation for subcellular location. Source data for this figure are available online.



Appendix Figure S2. Lysolipids are depleted from the samples during the isolation procedure.

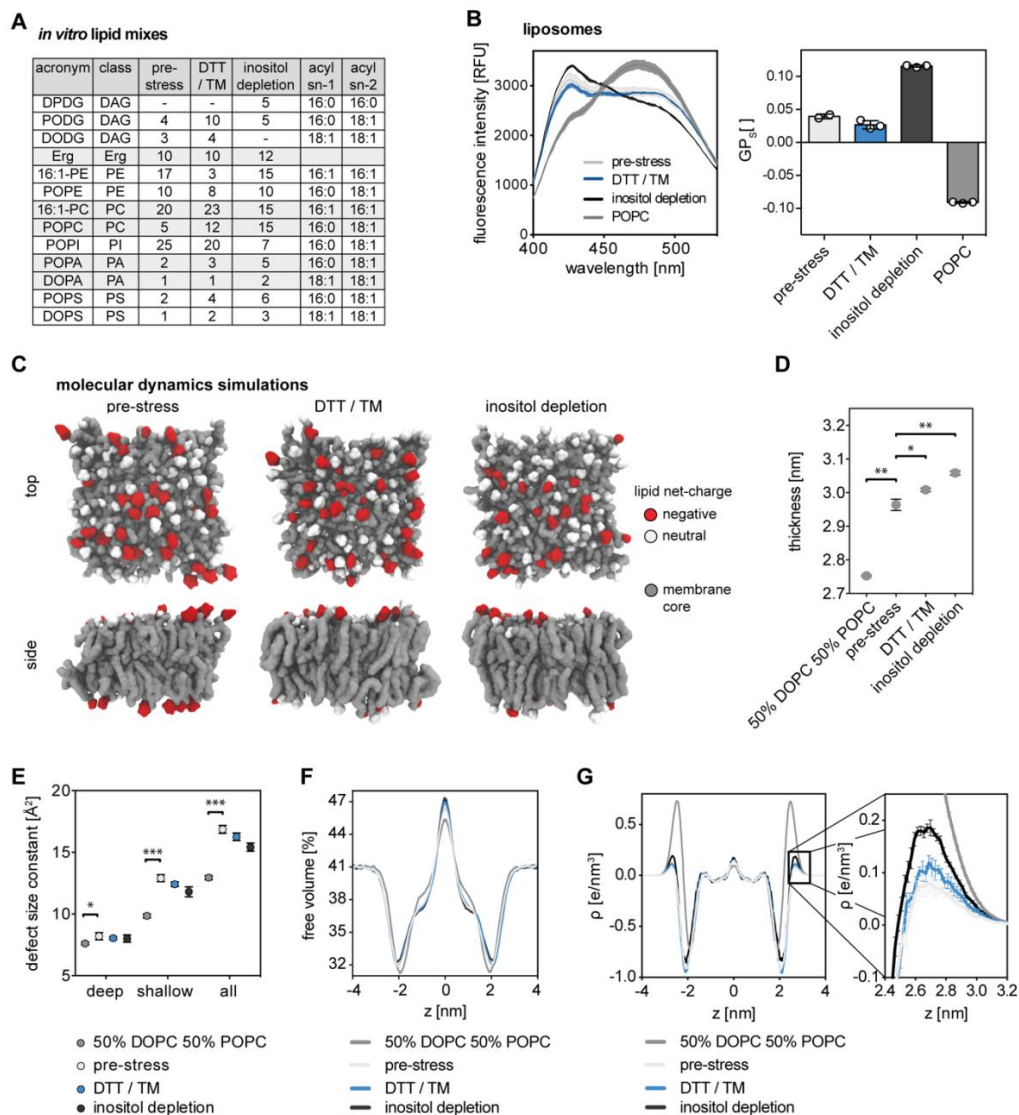
To control stability of the sample an aliquot of P100 microsomes was incubated at 4 °C and overhead rotation (P100_{control}) while the remaining sample was purified by immuno-isolation. **(A)** Abundance of detected lipid classes in microsomes (P100) and control microsomes after incubation for 8 h at 4 °C (P100_{control}). **(B)** Lipid class distribution showing significantly less lyso-phospholipids in control microsomes (P100_{control}). **(C)** The total number of double bonds in membrane glycerolipids is not changed.

In (A-C), data are presented as individual data points and mean \pm SD (P100, n = 4 biological replicates; P100_{control}, n = 3 biological replicates). Statistical significance was tested by multiple t tests correcting for multiple comparisons using the method of Benjamini, Krieger and Yekutieli, with Q = 1%, without assuming consistent standard deviations. ***p \leq 0.001. Source data for this figure are available online.



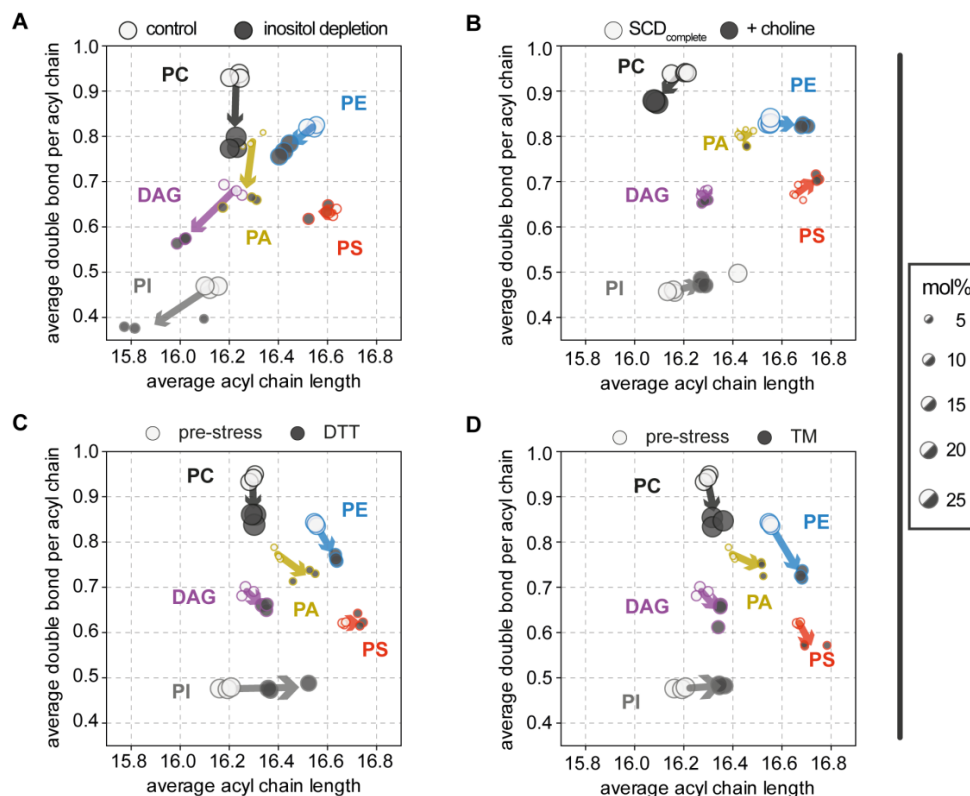
Appendix Figure S3. Metabolic interference with choline induces dramatic lipidome changes without activation of the UPR. SCD_{complete} medium containing 2 mM choline (+ choline) was inoculated with Rtn1-bait cells to an OD₆₀₀ of 0.1 from an overnight pre-culture and cells were harvested at an OD₆₀₀ of 1.0. ER derived membranes were purified by differential centrifugation and immuno-isolation and subsequently analyzed by quantitative shotgun lipidomics. **(A)** Lipid class composition given as mol% of all lipids in the sample. **(B)** Less abundant classes. **(C)** Total number of double bonds in membrane glycerolipids (except CL which has four acyl chains) as mol% of this category. Lipid data for SCD_{complete} in panel A-C are identical with the data presented in Figure 2A-C (ER^{Rtn1}). **(D)** Lipid metabolic map of PC biosynthesis from external choline sources.

In (A-C), data are presented as individual data points and mean \pm SD (SCD_{complete}, n = 4 biological replicates; + choline, n = 3 biological replicates). Statistical significance was tested by multiple t tests correcting for multiple comparisons using the method of Benjamini, Krieger and Yekutieli, with Q = 1%, without assuming consistent standard deviations. **p \leq 0.01, ***p \leq 0.001. Source data for this figure are available online.

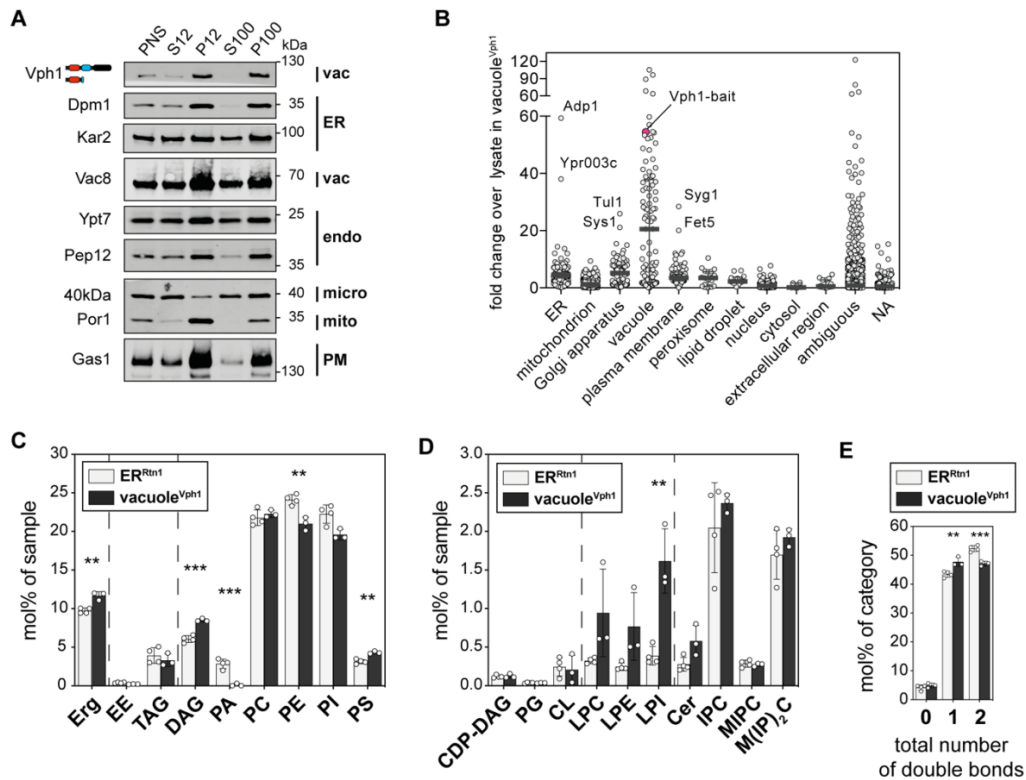


Appendix Figure S4. An *in vitro* lipid mixture that mimics the ER membrane under prolonged proteotoxic and lipid bilayer stresses. (A) Based on our ER membrane lipidomics data we propose commercially available lipid mixtures that mimic the ER under non-stress (pre-stress), prolonged proteotoxic stress (DTT / TM) or lipid bilayer stress conditions (inositol depletion). (B) Unilamellar liposomes were prepared by rehydrating dried lipids and extrusion. General polarization (GP) of fluorescence spectra using the membrane probe C-laurdan ranging from +1 (most ordered membrane) to -1 (most disordered) indicate that the proposed lipid mixtures have distinct physical properties. Data are presented as individual data points and mean \pm SD ($n = 3$ independent liposome preparations). (C) Molecular dynamics (MD) simulations of proposed commercially available *in vitro* ER membrane lipid mixes for non-stress ER (pre-stress) and ER under two different lipid bilayer stress conditions (DTT / TM, inositol depletion). Snapshots were taken after 100 ns. (D) Thickness measurements taken from MD simulations. Data are presented as mean \pm SEM ($n = 3$). Statistical significance was tested using an unpaired parametric t test with Welch's correction. * $p \leq 0.05$, ** $p \leq 0.01$. (E) Determination of defect size constants in MD simulation of model membranes. Data are presented as mean \pm SEM ($n = 3$). Statistical significance was tested using an unpaired parametric t test with Welch's correction. * $p \leq 0.05$, *** $p \leq 0.001$. (F) Free volume calculations from MD simulations. Data are presented as mean \pm SEM ($n = 3$).

= 3). The SEM is within the range of the thickness of the plotted line. **(G)** Charge distribution computed from partial charge density during MD simulations. Data are presented as mean \pm SEM (n = 3). Source data for this figure are available online.



Appendix Figure S5. Changes of average acyl chain length and unsaturation in abundant glycerolipid classes under conditions of ER stress. Arrow diagrams showing changes in acyl chain composition (average number of double bonds per acyl chain, average length per acyl chain) for each glycerolipid class in our ER lipidome data ($n = 3$ biological replicates for all conditions except 'SCD_{complete}', where $n = 4$). **(A)** Acyl chain changes upon lipid bilayer stress by inositol depletion (based on data from Figure 3B, C). Lipid acyl chains from all measured classes tend to get shorter and more saturated. **(B)** Acyl chain changes upon addition of 2 mM choline (based on data from Appendix Figure S3A, B). Acyl chains of PC lipids tend to get shorter and more saturated. Acyl chains of PE, PS and PI lipids tend to get longer. **(C)** Acyl chain changes after prolonged proteotoxic stress by DTT (based on data from Figure 4D, E). **(D)** Acyl chain changes after prolonged proteotoxic stress by TM (based on data from Figure 4D, E). Similar changes are measured for both proteotoxic stress inducers, DTT and TM. PC acyl chains get more saturated, PI acyl chains get longer. Acyl chains in the other lipid classes tend to become longer and more saturated. Circle diameters are proportional to abundance of the respective lipid class in the ER membrane of indicated growth condition. Source data for this figure are available online.



Appendix Figure S6. Lipidomics of the vacuole. SCD_{complete} medium was inoculated with Vph1-bait cells to an OD₆₀₀ of 0.1 from an overnight pre-culture and cells were harvested at an OD₆₀₀ of 1.0. Membranes of the vacuole were purified by MemPrep and subsequently analyzed by TMT-labeling proteomics and quantitative shotgun lipidomics. **(A)** Differential centrifugation yields a crude membrane fraction (P100) that is subsequently used as input for immuno-isolation. **(B)** Mean enrichment (fold change over lysate) of each individual identified protein in our untargeted TMT-labeling proteomics data (Figure 6B, n = 3). The bait protein 'Vph1-bait' via which MemPrep was performed is indicated. Our vacuole membrane preparation seemed to contain several enriched proteins with annotations of non-vacuole organelles. Annotations of subcellular location were retrieved from UniProt (accessed 27.01.2023). A subsequent consultation of the *Saccharomyces* Genome Database gene description and GOterms (accessed 03.01.2024) reveals that many of those highly enriched proteins annotated to other organelles were previously observed in the vacuole or feature a dual localization to the vacuole and other organelles (Tul1, Syg1, Fet5, Adp1). **(C)** Lipid class composition given as mol% of all lipids in the sample. **(D)** Less abundant classes. **(E)** Total number of double bonds in membrane glycerolipids (except CL which has four acyl chains) as mol% of this category.

In (C-E), lipid data for ER^{Rtn1} are identical with the data presented in Figure 2A-C. Lipid data for vacuole^{Vph1} in panel C and D are identical with the data presented in Figure 6C and D. Data are presented as individual data points and mean ± SD (n = 3 biological replicates). Statistical significance was tested by multiple t tests correcting for multiple comparisons using the method of Benjamini, Krieger and Yekutieli, with Q = 1%, without assuming consistent standard deviations. **p ≤ 0.01, ***p ≤ 0.001. Source data for this figure are available online.

Appendix Supplementary Methods

Bait-tagging cassette on plasmid pRE866 coding regions:

myc-HRV 3C site-3xFLAG (amino acids)

GGGGGGEQKLISEEDLGSGLVLFQGGPGSGDYKDHDGDYKDHDIDYKDDDDK*

KanR (aminoglycoside phosphotransferase) (amino acids)

MGKEKTHVSRPRLNSNMDADLYGYKWARDNVGQSGATIYRLYGKPDAPFLKHGKGSVA
 NDVTDEMVRNLNWLTEFMPLPTIKHFIRTPDDAWLLTTAIPGKTAFQVLEEYPDSGENIVDALA
 VFLRRLHSIPVCNCPFNSDRVFRLAQAQSRMNNGLVDASDFDDERNGWPVEQVWKEMHK
 LLPFSPDSVVTHGDFSLDNLIFDEGKLGICIDVGRVGIADRYQDLAILWNCLGEFSPSLQKRL
 FQKYGIDNPDMNKLQFHLMLDEFF*

DNA sequence

gggggaggggggggggagaacaaaaagttgatttctgaagaagattgggggtcagggtctggaagtctgtccagggggcccgga
 tctggcgactacaaagaccatgacgggtgattataaagatcatgacatcgactacaaggatgacgatgacaagtagggcgcc
 acttctaaataagcgaattcttatgattatgattttattataaataagttataaaaaaaataagtgatacaaatitaaagtgacttt
 aggttttaaacgaaaattcttattcttgagtaactcttctgtaggtcagggtgctttctcaggatagatgaggctccttattgacc
 acaccttaccggcagatccgctaggataacagggaatagatctgtagcttgcctcgtccccgcccgggtcaccggcca
 ggcacatggaggccagaataccctccttgacagcttgacgtgagcagctcaggggcatgatgtgactgtgcccgtacatttag
 cccatacatccccatgataatcattgcatccatacatttgatggccgcacggcggaagcaaaaattacggctcctcgtgag
 acctgagcagggaaacgctcccctcacagacgctggaattgtccccagccgcccctgtagagaaataaaaaggta
 ggattgcccactgaggttcttctcatatacttctttaaaatctgtaggatacagttctcacatcacatccgaacataaacaacca
 tgggtaaggaaaagactcacggttcgaggccgcatgaaatccaacatggatgctgatttatagggtataaatgggctcgcgata
 atgtcgggcaatcagggtgcaaatctatcgattgatgggaagcccgatgcccagagttgtttctgaaacatggcaaggtag
 cgttgccaatgatgttacagatgagatggcagactaaactggctgacggaattatgcctctccgaccatcaagcatttatccgta
 ctctgatgatgcatggtactaccactgcgatccccggcaaaacagcattccaggattagaagaatatcctgattcagggtgaa
 aatattgtgatgctgctggcagtgcttctgcgcccgggtgcattcgattcctgttgtaattgtcctttaacagcgatcgcgtattcgtctc
 ctgagggcaatcacgaatgaataacggttggtgatgagtgatgacgagcgaatggctggcctgttgaacaagctc
 ggaaagaaatgcataagccttgcattctcaccggattcagctgctcactatgggtattctcacttgataacctatittgacgagg
 gaaattaataggttgattgatgttgacgagtcggaatcgagaccgataaccaggatcttgccatcctatggaactgcctcgggtga
 gtttctcctcattacagaaacggcttttcaaaaataggtatigataatcctgatataaataatgcagttcatttgatgctgatga
 gttttctaaatcagtagtacaataaaaagattctgtttcaagaactgtcattgtatagtttttatattgtagttctatttaatacaaat
 gttagcgtgatttatatttttgcctcgacatcatctgccagatgcgaagtaagtgccagaaagtaatatcatgctcaatcgt
 atgtgaatgctggtcgtatactg

Please cite this article in press as: Reinhard et al., Remodeling of yeast vacuole membrane lipidomes from the log (one phase) to stationary stage (two phases), *Biophysical Journal* (2023), <https://doi.org/10.1016/j.bpj.2023.01.009>

Biophysical Journal

Article



Remodeling of yeast vacuole membrane lipidomes from the log (one phase) to stationary stage (two phases)

John Reinhard,^{1,2} Chantelle L. Leveille,³ Caitlin E. Cornell,³ Alexey J. Merz,⁴ Christian Klose,⁵ Robert Ernst,^{1,2,*} and Sarah L. Keller^{3,*}

¹Medical Biochemistry and Molecular Biology, Medical Faculty, Saarland University, Homburg, Germany; ²PZMS, Center for Molecular Signaling, Medical Faculty, Saarland University, Homburg, Germany; ³Department of Chemistry, University of Washington, Seattle, WA; ⁴Department of Biochemistry, University of Washington, Seattle, WA; and ⁵Lipotype GmbH, Am Tatzberg 47, Dresden, Germany

ABSTRACT Upon nutrient limitation, budding yeast of *Saccharomyces cerevisiae* shift from fast growth (the log stage) to quiescence (the stationary stage). This shift is accompanied by liquid-liquid phase separation in the membrane of the vacuole, an endosomal organelle. Recent work indicates that the resulting micrometer-scale domains in vacuole membranes enable yeast to survive periods of stress. An outstanding question is which molecular changes might cause this membrane phase separation. Here, we conduct lipidomics of vacuole membranes in both the log and stationary stages. Isolation of pure vacuole membranes is challenging in the stationary stage, when lipid droplets are in close contact with vacuoles. Immuno-isolation has previously been shown to successfully purify log-stage vacuole membranes with high organelle specificity, but it was not previously possible to immuno-isolate stationary-stage vacuole membranes. Here, we develop Mam3 as a bait protein for vacuole immuno-isolation, and demonstrate low contamination by non-vacuolar membranes. We find that stationary-stage vacuole membranes contain surprisingly high fractions of phosphatidylcholine lipids (~40%), roughly twice as much as log-stage membranes. Moreover, in the stationary stage, these lipids have higher melting temperatures, due to longer and more saturated acyl chains. Another surprise is that no significant change in sterol content is observed. These lipidomic changes, which are largely reflected on the whole-cell level, fit within the predominant view that phase separation in membranes requires at least three types of molecules to be present: lipids with high melting temperatures, lipids with low melting temperatures, and sterols.

SIGNIFICANCE When budding yeast shift from growth to quiescence, the membrane of one of their organelles (the vacuole) undergoes liquid-liquid phase separation. What changes in the membrane's lipids cause this phase transition? Here, we conduct lipidomics of immuno-isolated vacuole membranes. We analyze our data in the context of lipid melting temperatures, inspired by observations that liquid-liquid phase separation in model membranes requires a mixture of lipids with high melting temperatures, lipids with low melting temperatures, and sterols. We find that phase-separated vacuole membranes have higher concentrations of phosphatidylcholine lipids, and that those lipids have higher melting temperatures. To conduct our experiments, we developed a tagged version of a protein (Mam3) for immuno-isolation of vacuole membranes.

INTRODUCTION

During normal growth, cells undergo enormous changes as they adapt to their environment and pass through a sequence of distinct metabolic states (1). For example, when certain nutrients become limiting, *Saccharomyces cerevisiae*

(henceforth “yeast”) transition away from fermentative, exponential growth (log stage), through respiratory growth (diauxic shift), to reach a quiescent state (stationary stage) (2). The shift from the logarithmic to the stationary stage is accompanied by striking changes in the yeast vacuole, the functional equivalent of the lysosome in higher eukaryotes. Multiple, small vacuoles fuse so that most cells contain only one large vacuole ((3), and reviewed in (4)), and the vacuole membrane undergoes liquid-liquid phase separation (Fig. 1) (5). As a result, in the stationary stage, the vacuole membrane contains micrometer-scale domains that are

Submitted October 8, 2022, and accepted for publication January 9, 2023.

*Correspondence: robert.ernst@uks.eu or slkeller@uw.edu

John Reinhard and Chantelle L. Leveille contributed equally to this work.

Editor: Jeanne Stachowiak.

<https://doi.org/10.1016/j.bpj.2023.01.009>

© 2023 Biophysical Society.

This is an open access article under the CC BY-NC-ND license (<http://creativecommons.org/licenses/by-nc-nd/4.0/>).

Please cite this article in press as: Reinhard et al., Remodeling of yeast vacuole membrane lipidomes from the log (one phase) to stationary stage (two phases), *Biophysical Journal* (2023), <https://doi.org/10.1016/j.bpj.2023.01.009>

Reinhard et al.

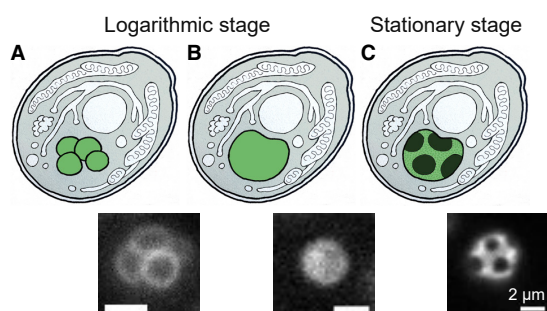


FIGURE 1 (A) In nutrient-rich media, yeast cultures grow exponentially. In this logarithmic stage, each cell contains multiple small vacuoles, the lysosomal organelle of yeast. (B) As nutrients become limited, vacuoles fuse. (C) Eventually, yeast enter the stationary stage in which the vacuole membrane phase separates into micrometer-scale, coexisting liquid phases. Corresponding fluorescence micrographs are shown below each schematic, with scale bars representing 2 μm . To see this figure in color, go online.

enriched in particular lipids and proteins (6–9). This phase transition is reversible, with a transition temperature roughly 15°C above the yeast’s growth temperature (10). Recent studies suggest that phase-separated domains in vacuole membranes regulate the metabolic response of yeast to nutrient limitation through the TORC1 pathway, which regulates protein synthesis, autophagy, lipophagy, and other processes (8,9,11–14).

An outstanding question in the field has been what the molecular basis is for phase separation in the vacuole membrane. Here, we investigate changes in the lipidome of the vacuole as yeast enter the stationary stage. We expect the lipidome to be important because the mutations that perturb phase separation of the vacuole involve lipid trafficking and metabolism (8,9,15). Although our experiments do not address the potential contribution of proteins to membrane phase separation (16,17), we note that treatment of cells with cycloheximide, which inhibits protein translation, increases the prevalence of phase-separated vacuoles within 3 h (18).

We expect to observe changes in vacuole lipidomes from the log to the stationary stage because log-stage vacuole membranes do not phase separate over large shifts in temperature from 30°C to 5°C, whereas stationary-stage vacuole membranes do, even when they are grown over a range of growth temperatures (10). However, we do not necessarily expect the lipidomic changes that drive phase separation to be large. Phase transitions are an effective means of amplifying small signals.

What types of changes do we expect to see in the lipidome? In the past, researchers have focused on ergosterol, the predominant sterol in fungi and many protozoans. Multi-component model membranes containing ergosterol can separate into coexisting liquid phases (19). Moreover, phase separation in isolated vacuoles is reversed through changes in ergosterol levels (8,10,20). Klose et al. measured whole-

cell lipidomes through the growth cycle and found that ergosterol decreased from ~14 mol % of total lipids in the log stage to ~10 mol % in the stationary stage (21). However, because most ergosterol is highly enriched in the plasma membrane, it has remained unclear how and to what extent ergosterol in the vacuolar membrane may contribute to membrane phase separation during the stationary stage.

Previous attempts to measure changes in vacuole lipidomes have been limited by the technical challenge of separating vacuole membranes from the membranes of other organelles. This challenge is formidable because vacuoles form stable membrane contacts with other organelles, such as the nuclear envelope, which can co-purify with vacuoles (22,23). Here, we employ an immuno-isolation technique called MemPrep to efficiently separate vacuole membranes from those of other organelles (24–28). We first identify a bait protein that resides only in the membrane of interest and then genomically fuse a cleavable epitope tag to that bait protein. To achieve roughly equal immuno-isolation efficiencies in the log and stationary stages, we use the membrane protein Mam3 as our bait, which isolates highly enriched membranes from both growth stages at sufficient yields for quantitative lipidomic analyses. This allows us to map the differences in the lipid profiles of the vacuole membrane in the logarithmic and the stationary stages. We then put our lipidomic data into context of existing data of the physical properties of lipids.

MATERIALS AND METHODS

Yeast cell culture and microscopy

For lipidomics experiments, we used the plasmid pRE866 (28) and the primers 5'-GAACCTCCAATTATGATGCCAACGGCTCCTCGTGACCAT AAAAAGAGGGGGAGGGCGGGGGTGA-3' and 5'-GGTTATTATGATGCA TGGCAATTCTTTGGCATAATCTCTCAGATGGCGGGCTAGTATCG-3', and we generated a *S. cerevisiae* strain with a bait tag targeted to the C terminus of Mam3 (a vacuolar membrane protein involved in Mg^{2+} sequestration) (29). A Mam3-bait strain is also available from the MemPrep library (28). The bait tag for immuno-isolation contains a linker region followed by a Myc epitope tag for detection in immunoblotting analysis, a specific cleavage site for the human rhinovirus (HRV) 3C protease for selective elution from the affinity matrix, and three repeats of an FLAG epitope that ensures binding to the affinity matrix. The complete amino acid sequence of the bait tag is: GGGGGGEQKLISEEDLGSGLVLFQGP GSGDYKDHDG DYKDHDIDYKDDDDK.

From a single colony on a YPD (yeast extract peptone dextrose) agar plate, 3 mL of synthetic complete medium was inoculated. Cells were cultivated for 20 h at 30°C, producing a starter culture. From this starter culture, we inoculated 4 L of synthetic complete medium to an optical density at 600 nm (OD_{600}) = 0.1 and cultivated the cells at 30°C and 220 rpm constant agitation. For yeast in the log stage, cells were cultivated for approximately 8 h, until they reached OD_{600} = 1 (yielding a total of 4000 OD_{600} ·mL). For cultivating yeast to the stationary stage, 2 L of synthetic complete medium were inoculated to OD_{600} 0.1 and cultivated for 48 h. The final OD_{600} was 8.6 ± 0.4 (yielding a total of 17,200 OD_{600} ·mL). We used more biomass for isolations from stationary cells because mechanical cell disruption is less efficient at the stationary stage. In the stationary stage, roughly 80% of vacuole membranes undergo phase separation into micrometer-scale domains (8–10, 15).

Please cite this article in press as: Reinhard et al., Remodeling of yeast vacuole membrane lipidomes from the log (one phase) to stationary stage (two phases), Biophysical Journal (2023), <https://doi.org/10.1016/j.bpj.2023.01.009>

Lipidome log and stat vacuole membranes

Yeast were imaged by fluorescence microscopy as described in the supplemental methods section of the Supporting Materials.

Immuno-isolation of microsomes

Microsomes of vacuole membranes and solutions of magnetic beads were produced as briefly described in Fig. 2 and as fully described in the Supporting Materials. Next, 700 μ L of the sonicated, crude microsomal vesicle fraction were added to 700 μ L of the solution of magnetic beads in immunoprecipitation (IP) buffer (25 mM HEPES pH 7.0, 1 mM EDTA, 150 mM NaCl), for a total volume of 1.4 mL. Vesicles were allowed to bind to the beads (Fig. 2 B) by rotating the tubes for 2 h at 4°C in an overhead rotor at 3 rpm, which avoided excessive formation of air bubbles.

Magnetic beads and the membranes bound to them were collected after a series of washes (Fig. 2 B). To this end, the tubes were placed in a magnetic rack and the supernatants were removed. The magnetic beads were washed twice with 1.4 mL of wash buffer (25 mM HEPES, pH 7.0, 1 mM EDTA, 75 mM NaCl, 0.6 M urea), which destabilizes many unspecific protein-protein interactions, and then twice with 1.4 mL of IP buffer. After these washes, the magnetic beads were transferred to a fresh 1.5-mL tube and resuspended with 700 μ L of elution buffer (PBS pH 7.4, 0.5 mM EDTA, 1 mM DTT, and 0.04 mg/mL GST-HRV-3C protease).

To elute vesicles from the affinity matrix (Fig. 2 B), the samples were incubated by rotating overhead at 3 rpm for 2 h at 4°C with the HRV-3C protease. The tubes were then placed in a magnetic rack to precipitate

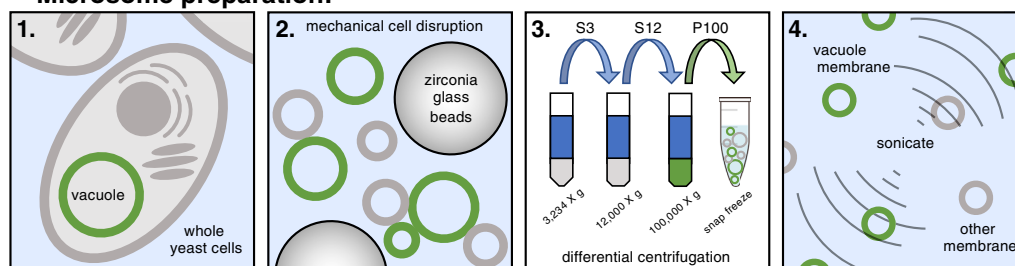
the magnetic beads, and the supernatant (eluate) containing the purified vacuole membranes was transferred to fresh tubes. To concentrate the membrane vesicles and to exchange the buffer, the sample was diluted in PBS and transferred to ultracentrifuge tubes. After centrifugation at $264,360 \times g$ for 2 h at 4°C using a Beckman TLA 100.3 rotor, the supernatant was discarded and the pellet containing purified vacuole membranes was resuspended in 200 μ L of PBS. Resuspended pellets were transferred to fresh microcentrifuge tubes, snap frozen in liquid nitrogen, and stored at -80°C until lipid extraction and mass spectrometry analysis. Procedures for lipid extraction, acquisition of lipidomics data, and processing of lipidomics data are described in the Supporting Materials.

RESULTS

Mam3 is a robust bait protein for immuno-isolation of vacuole membranes

We identified several membrane proteins as candidate “bait proteins” for immuno-isolation of vacuoles in *both* the log stage and the stationary stage of growth. Immuno-isolation with bait proteins provides a high level of organelle selectivity that is not available by standard flotation methods (30,31). One end of the bait protein (the C terminus) is

A Microsome preparation:



B Immunoisolation:

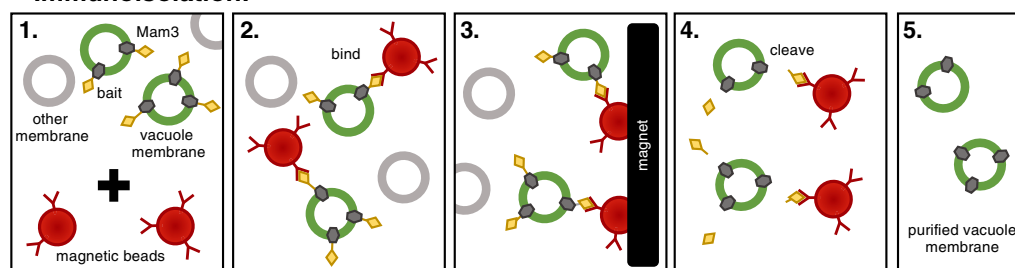


FIGURE 2 (A) 1) Yeast cells are cultivated to either the log or stationary stage. 2) Cells are mechanically fragmented with zirconia glass beads using a FastPrep-24 bead beater. 3) A differential centrifugation procedure at $3234 \times g$, $12,000 \times g$, and $100,000 \times g$ is performed to deplete cell debris and membranes from other organelles, thereby enriching vacuole membranes in the microsomal fraction. The fraction containing vacuole membranes (either the supernatant, S, or the pellet, P, is retained). 4) Controlled pulses of sonication separates clumps of vesicles and produces smaller microsomes for immuno-isolation (28). Items are not drawn to scale. (B) 1) Top: the microsome solution is enriched in vacuole membranes, which are labeled with a bait tag (myc-3C-3xFLAG) attached to the Mam3 protein. Bottom: microsomes are mixed with magnetic beads coated at sub-saturating densities with a mouse anti-FLAG antibody. 2) Antibody-coated magnetic beads bind to Mam3 in vacuole membranes, but not to other membranes. 3) For washing, the affinity matrix (magnetic beads) is immobilized by a magnet, the buffer with all unbound material is removed, and fresh, urea-containing buffer is added. The affinity matrix is serially washed and agitated in the absence of a magnetic field to ensure proper mixing and removal of unbound membrane vesicles. 4) Vacuole membranes are cleaved from the beads with affinity-purified HRV-3C protease. 5) Removal of the magnetic beads leaves purified vacuole membranes for lipidomics. To see this figure in color, go online.

Please cite this article in press as: Reinhard et al., Remodeling of yeast vacuole membrane lipidomes from the log (one phase) to stationary stage (two phases), *Biophysical Journal* (2023), <https://doi.org/10.1016/j.bpj.2023.01.009>

Reinhard et al.

equipped with a molecular bait (the construct myc-3C-3xFLAG). The bait protein and the membrane in which it resides bind to magnetic beads decorated with anti-FLAG antibodies (Fig. 2 B). The beads are magnetically immobilized and washed extensively with urea-containing buffers. The isolated membranes are then cleaved from the beads (using the GST-HRV-3C protease) and analyzed by shotgun lipidomics. For our application, a robust bait protein (1) must have its C terminus available in the cytosol, (2) contain an intramembrane domain anchoring it to the membrane, (3) localize only to the vacuole, and (4) be expressed at high levels in both the log and stationary stage. Initial guesses can be made about whether given proteins are good candidates for bait proteins by consulting the YeastGFP fusion localization database (<https://yeastgfp.yeastgenome.org/>), and then fusions must be tested in the lab (32,33).

An obvious candidate for a bait protein was Vph1, which has high expression levels in the log stage (8,34). Vph1 has been extensively used for visualizing vacuole domains (5,7–10,15), and was previously used by us to demonstrate the utility of MemPrep for isolating vacuole membranes in the log stage (28). However, in the stationary stage, both the expression level of Vph1 and the efficacy of cell lysis are lower (Fig. S1 A–E), resulting in an insufficient yield of membranes upon immuno-isolation via the Vph1-bait construct.

In contrast, Mam3 (~3230–5890 molecules per cell) proved to be an excellent bait protein (34). We confirmed previous reports that Mam3 localizes to the vacuole membrane (35) by showing that Mam3 colocalizes with FM4-64, a styryl dye that selectively stains vacuole membranes (Fig. S2). In the log stage, when vacuoles do not exhibit domains, Mam3 distributes uniformly on the vacuole membrane. In stationary-stage yeast, Mam3 partitions to only one of the two phases of vacuole membranes (Figs. 3 A–B and S3). Specifically, Mam3 partitions to the same phase as Vph1, which Toulmay and Prinz identified as a liquid

disordered (Ld) phase (Fig. S4) (8). Expression levels of Mam3 are high in both the log and stationary stages (Fig. 3 C). Mam3 outperformed four other candidates for bait proteins (Ypq2, Sna4, Ybt1, and YBR241C) carrying the same myc-3C-3xFLAG bait tag. We would expect all of these proteins to preferentially partition to the Ld phase.

For completeness, we attempted to find complementary bait proteins that preferentially partition to the opposite phase (the liquid ordered (Lo) phase) of vacuole membranes in the stationary stage. None were found to be good candidates. For example, the protein Gtr2 partitions to the Lo phase in yeast vacuole membranes (8). We find that membrane fragments isolated with a bait attached to Gtr2 proteins contain low amounts of proteins known to reside in vacuole membranes (Vph1 and Vac8); the Gtr2 bait protein does not isolate enough vacuole membrane to analyze by lipidomics (Fig. S5). To date, the only other protein known to preferentially partition to the Lo phase of vacuole membranes is Ivy1 (8). Because Ivy1 is an inverted BAR protein rather than a transmembrane protein, it is an unsuitable bait protein.

Low contamination by non-vacuolar proteins and lipids

A key challenge in isolating pure organellar membranes is that most organelles are in physical contact with other organelles, which can contaminate membrane samples. Most previous isolation attempts have been based on the protocol pioneered by Uchida et al. in which yeast are converted into spheroplasts and mildly lysed, and then vacuole membranes are enriched by differential centrifugation and density centrifugation (30, 36, 37) (see Table S1 for comparisons). Zinser et al. noted that lipid droplets “seemed to adhere” to vacuole membranes isolated by this method (7, 31). The density gradient method of separating vacuole membranes is relatively insensitive to contamination by other

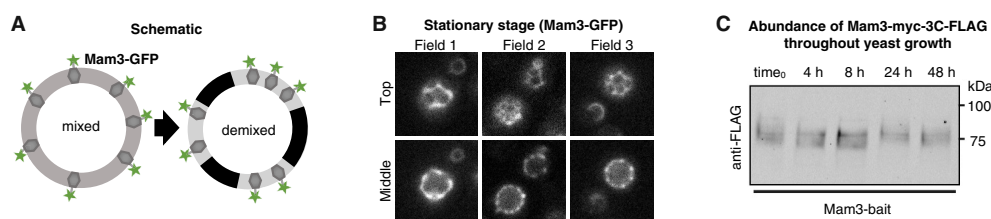


FIGURE 3 (A) In the log stage of growth, lipids and proteins appear uniformly distributed in vacuole membranes of yeast. Mam3, a transmembrane protein in the vacuole membrane, was produced from its endogenous promoter and equipped at its C terminus either with a bait tag for immuno-isolation or with GFP for fluorescence microscopy. (B) In vivo fluorescence micrographs of yeast showing that, in the stationary stage (after 48 h of growth), the vacuole membrane phase separates into two liquid phases. Mam3-GFP partitions into only one of these phases (identified as the Ld phase). Micrographs were taken at room temperature at both the top (“Top”) and the midplane (“Middle”) of vacuoles for each field of view. Wider, representative fields of view are shown in Fig. S3, and corresponding images for Vph1-GFP are in Fig. S4. (C) Immunoblot showing robust and stable expression levels of Mam3-bait. Synthetic complete medium was inoculated to an OD₆₀₀ of 0.1 and cells were harvested by centrifugation after cultivation for 0, 4, 8, 24, and 48 h. The immunoblot was visualized using anti-FLAG and fluorescently labeled secondary antibodies, which bind the myc-3C-3xFLAG bait tag on Mam3. Bands for Mam3-bait are shown in the log (early times) and stationary stage (late times), and positions of molecular weight markers are indicated for reference. To see this figure in color, go online.

Please cite this article in press as: Reinhard et al., Remodeling of yeast vacuole membrane lipidomes from the log (one phase) to stationary stage (two phases), *Biophysical Journal* (2023), <https://doi.org/10.1016/j.bpj.2023.01.009>

Lipidome log and stat vacuole membranes

types of organelles. When Tuller et al. isolated vacuole membranes, and they found 0.5% contamination by plasma membranes and 5.5% contamination by cardiolipins, a lipid specific to mitochondria (37). Likewise, Schneiter et al. reported that a vacuolar marker protein was enriched ~15-fold in their vacuolar membrane preparations, with some contamination from the ER and the outer mitochondrial membrane (25).

Here, we couple a classical differential centrifugation approach with a sonication step that breaks up vesicle aggregates and produces smaller microsomes, from which vacuolar membranes are then purified by immuno-isolation (Fig. 2). We benchmark the purity of isolated vacuole membranes by verifying that protein markers for vacuoles are enriched in post-immuno-isolation fractions and that markers for other organelles are depleted. For example, Dpm1, which localizes to the endoplasmic reticulum, and Por1, which localizes to the mitochondrial outer membrane, are initially present after sonication of microsomes (Fig. 4 B; “load”) and are removed after immuno-isolation (Fig. 4 B; “eluate”). In contrast, Vac8 and Vph1, which localize to the vacuole, are enriched in the immuno-isolation eluate relative to other proteins (Fig. 4 B,C). Mam3 was not used to evaluate enrichment because the FLAG epitope is cleaved off to release vacuole membranes from the magnetic beads, which means that the Mam3 bait protein cannot be detected with anti-FLAG antibodies after elution.

We also evaluated the purity of isolated vacuole membranes by assessing contamination by lipids known to reside in other organelles. We find that only ~1% of lipids in isolated membranes ($0.8\% \pm 0.4\%$) contain cardiolipins from mitochondria. Similarly, TAG (triacylglycerol) and ergosterol esters are “storage lipids” found in the hydrophobic core of lipid droplets (9). For yeast in the log stage, we find that only ~2.5% of all lipids of immuno-isolated vacuoles are TAG, and <1% are ergosterol esters (Fig. S6). In

comparison, in whole-cell extracts of the same cells, we find 9% TAG and 5% ergosterol esters (Fig. S7), in agreement with literature values of $10\% \pm 1\%$ TAG for equivalent yeast and conditions (38). A characteristic feature of vacuole membranes in the log stage of growth is the almost complete absence of phosphatidic acid (PA) (28), which we confirm for vacuole membranes isolated using the Mam3 bait (Fig. 5 A).

Isolation of pure vacuole membranes is particularly challenging in the stationary stage, when lipid droplets are produced in high numbers and are in intimate contact with vacuole membranes (7,9,15,39,40). Uptake of lipid droplets into the vacuole lumen, referred to as lipophagy (39) or microlipophagy (41), occurs upon nitrogen starvation or acute glucose limitation and is associated with liquid-liquid phase separation of vacuole membranes (39,41–45).

Nevertheless, we still find low contamination in immuno-isolated vacuole membranes from yeast in the stationary stage, which contain ~13% TAG and ~0.5% ergosterol esters (Fig. S6). In comparison, in whole-cell extracts from the same cells, we find three times more TAG (>35%) and an order of magnitude more ergosterol esters (>6%) (Fig. S7). High levels of ergosterol esters persist in vacuoles separated by density gradient methods from log-stage yeast grown in YPD media (31), and may be even higher for equivalent yeast grown in synthetic complete media (38). These data highlight the value of isolating vacuole membranes by immuno-isolation. The difference in depletion levels between TAG and ergosterol ester in our vacuole membrane preparations compared with the corresponding whole-cell lipidomes (~threefold for TAGs and >10-fold for ergosterol esters) may reflect different rates of lipophagy for TAG- and ergosterol ester-enriched lipid droplets, and/or different turnover rates of these storage lipids in vacuoles. Because the amount of TAG we observe in stationary-stage vacuole preparations exceeds the solubility of TAG in

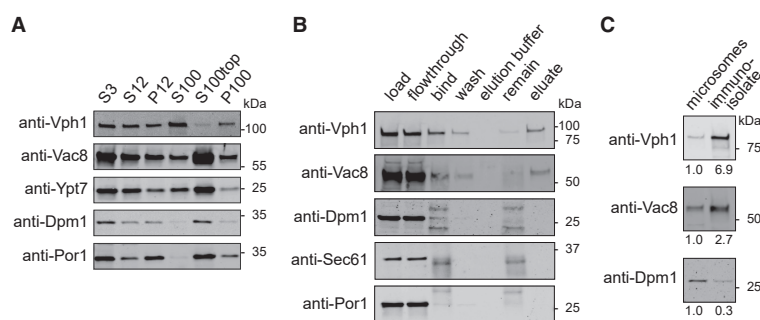


FIGURE 4 Immuno-isolation from cells expressing the Mam3-bait construct. (A) After differential centrifugation, proteins that reside in membranes of the endoplasmic reticulum (Dpm1) and mitochondria (Por1) are present in microsome preparations of yeast (P100 column), as reported by anti-Dpm1 and anti-Por1 immunoblots. (B) P100 microsomes are sonicated and used as input for the immuno-isolation (load). Bands for vacuole markers (Vph1 and Vac8) show binding to antibody-coated magnetic beads (“bind” column), mitigating substantial loss in the flowthrough step (“flowthrough” column). The anti-Dpm1 immunoblot shows two additional bands in the fractions containing magnetic beads (in the “bind” and “remain” columns) originating from the FLAG antibody light chain (~25 kDa) and the coating

of protein G (~37 kDa). Protein G also leads to a band in the anti-Sec61 and anti-Por1 immunoblots. Immuno-isolation removes membranes of the endoplasmic reticulum and mitochondria (seen by an absence of Dpm1, Sec61, and Por1 in the “eluate” column) and retains only vacuole membranes for lipidomics (seen by bands for Vac8 and Vph1 in the eluate column). (C) Enrichment of organelle protein markers in immuno-isolates over crude microsomes was quantified from immunoblot signals loaded from equal amounts of total protein (0.45 μ g).

Please cite this article in press as: Reinhard et al., Remodeling of yeast vacuole membrane lipidomes from the log (one phase) to stationary stage (two phases), *Biophysical Journal* (2023), <https://doi.org/10.1016/j.bpj.2023.01.009>

Reinhard et al.

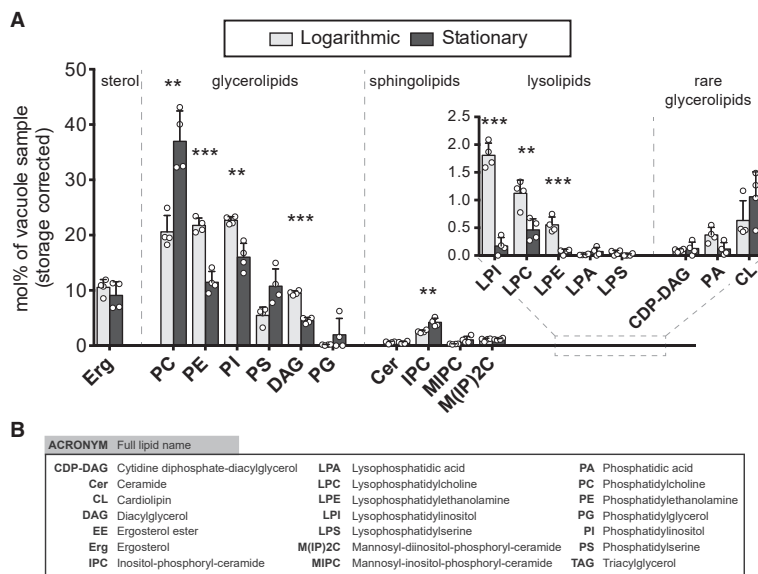


FIGURE 5 (A) Abundances of membrane lipids in yeast vacuole membranes in the logarithmic and stationary stages of growth. A large increase is observed in PC lipids. Concomitant decreases are observed in PE, PI, and DAG lipids. Error bars are standard deviations of four vacuole samples immuno-isolated on different days; individual data points are shown by white circles. Data exclude storage lipids (ergosterol ester and triacylglycerol), which are attributed to lipid droplets. Corresponding graphs that include storage lipids are in Fig. S6 and full datasets are in the supporting information. Statistical significance was tested by multiple *t*-tests correcting for multiple comparisons (method of Benjamini et al. (50)), with a false discovery rate $Q = 1\%$, without assuming consistent standard deviations. * $p < 0.05$, ** $p < 0.01$, and *** $p < 0.001$. (B) Acronyms of lipid types.

bilayers, which is $\sim 3\%$ in glycerolipid membranes and likely even lower in membranes containing sterols (46,47), some of the TAG (and perhaps, to a lesser extent, some other lipid types) in our stationary-stage samples likely originates from lipid droplets. In the sections below, we consider storage lipids as non-membrane lipids and exclude them from the discussion.

In general, breaking contact sites between organelles within the MemPrep strategy for immuno-isolation produces highly purified organelle-specific membrane preparations. For example, the strategy results in an unprecedented ~ 25 -fold enrichment of ER proteins over the cell lysate (28). However, like every technique, it has tradeoffs. As noted by Zinser and Daum, “rupture of intact vacuoles may liberate proteases” (48). Therefore, we perform all steps of MemPrep at 4°C ; every increase in temperature of 10°C doubles the rate at which proteases degrade proteins. This constraint prevents us from isolating membranes from the same population of vacuoles at two temperatures. In the future, we hope to find a way to isolate membranes at both a low temperature (at which the membrane phase separates) and a high temperature (at which the membrane is uniform).

Logarithmic stage lipidomes have high levels of PC, PE, and PI lipids

We quantified the lipidome for ~ 400 individual lipid species, in ~ 20 lipid classes. The list of relevant lipids is shorter in yeast than in many other cell types because yeast can synthesize only mono-unsaturated fatty acids, such that yeast glycerolipids typically contain at most two unsaturated

bonds, one in each chain (49). In general, the phosphatidylcholine (PC), phosphatidylethanolamine (PE), and phosphatidylinositol (PI) lipid classes each constitute $\sim 20\%$ of the log-stage vacuole lipidome (Fig. 5). Lipidomes of log-stage vacuole membranes immuno-isolated using the Mam3-bait are in excellent agreement with those we previously isolated with a Vph1-bait (Fig. S8) (28). It is difficult to assess whether these lipidomes agree with data determined by more traditional methods. Although Zinser et al. (31) reported that levels of PC lipids were twice the level of PE or PI lipids in log-stage vacuoles, it is unclear if the yeast they used were grown to early log stage or a later stage. Whole-cell lipidomes by Reinhard et al. (38) imply that the difference cannot be simply ascribed to the use of YPD media by Zinser and coworkers versus the synthetic complete media used here.

The importance of isolating vacuoles from whole-cell mixtures is reflected in differences between their lipidomes. For log-stage cells grown in synthetic complete medium, the fraction of IPC (inositolphosphoryl-ceramide) and PA lipids are roughly two and 10 times greater in the whole cell, respectively, whereas the fraction of DAG (diacylglycerol) lipids is roughly two times higher in the vacuole than the whole cell (21,38).

Phase separation in vacuole membranes is not likely due to an increase in ergosterol

A central question is why log-stage vacuole membranes do not phase separate, whereas stationary-stage membranes do. Ergosterol is the major sterol in yeast, and it has been suggested that phase separation of vacuole membranes could be

Please cite this article in press as: Reinhard et al., Remodeling of yeast vacuole membrane lipidomes from the log (one phase) to stationary stage (two phases), *Biophysical Journal* (2023), <https://doi.org/10.1016/j.bpj.2023.01.009>

Lipidome log and stat vacuole membranes

due to an increase in ergosterol (8). An increase in ergosterol would be consistent with a report that the ratio of filipin staining of sterols in vacuole versus plasma membranes is higher in the stationary stage than the log stage, although vacuole and plasma membrane levels were not measured independently (10,15). It would also be consistent with the expectation that esterified sterols in lipid droplets are mobilized in the stationary stage by lipophagy, which is required for the maintenance of phase separation in the vacuole membrane (20,24,36,40).

Here, we find statistically equal mole fractions of ergosterol in vacuole membranes in the log and stationary stages: $10\% \pm 1\%$ in the log stage and $9\% \pm 2\%$ in the stationary stage (Fig. 5). Uncertainties represent standard deviations for four independent experiments of each type, and the data exclude storage lipids of ergosterol esters and TAGs. Sterol concentrations in this range ($\sim 10\%$) are often sufficient for separation of model membranes into two liquid phases (51–57). Higher levels are not necessarily better at promoting coexisting liquid phases; the solubility limit of ergosterol in membranes of lipids with an average of one unsaturation is only 25%–35% (58–61), and solubility may be lower when lipid unsaturation is higher, as in biological membranes.

We find that ergosterol fractions in yeast whole-cell extracts, as opposed to only the vacuole membrane, are also $\sim 10\%$ in both the log stage and the stationary stage (Fig. S7). Similarly, Klose et al. reported mole fractions of ergosterol of 13% and 11% in whole-cell extracts from the log and stationary stage, respectively, with uncertainties on the order of 0.5% (21).

We cannot rule out that immuno-isolation with Mam3 under-samples the Lo phase (which contains higher concentrations of ergosterol per unit area than the Ld phase, based on brighter staining by filipin (8)). Nevertheless, our conclusion that vacuole phase separation is not likely driven by an increase in ergosterol is consistent with other results in yeast; we previously found that log-stage vacuole membranes phase separate upon depletion (rather than addition) of ergosterol (10). Other results in the literature are more difficult to interpret. It is not known whether ergosterol and other lipids move into yeast vacuoles or out of them when sterol synthesis and transport are impaired (9,11,12,15), when lipid droplets are perturbed (9,13), or when drugs are applied to manipulate sterols (8,20) (all of which can disrupt the formation or maintenance of vacuole membrane domains).

Results from other cell types are not necessarily applicable to yeast. As in yeast vacuoles, depletion of sterol from modified Chinese hamster ovary cells results in plasma membrane domains, and recovery of photobleached lipids is consistent with the domains and the surrounding membrane both being fluid (62). Similarly, depletion of sterol from giant plasma membrane vesicles (GPMVs) of NIH/3T3 murine fibroblasts causes phase separation to persist to higher

temperatures (63). Membrane domains in other types of sterol-depleted cells (e.g., (64)) may also prove to be due to phase separation, although it is always important to verify that cells are still living (as in (64)) and to identify when membrane properties such as lipid diffusion, dye partitioning, domain shape, and/or domain coalescence reflect liquid rather than solid phases (as in (65–67)). Different results are observed in vesicles derived from other cell types. Depletion of sterol from GPMVs of RBL cells restricts phase separation to lower temperatures (68). Similarly, when phase separation is restricted to lower temperatures in zebrafish GPMVs (because the cells are grown at lower temperature), sterol levels are lower (69). Results from these different cell types are not in conflict; addition and depletion of sterol have been suggested to drive membranes toward opposite ends of tie-lines (away from phase separation and toward a single, uniform phase), based on observations in GPMVs of RBL-2H3 cells (70), CH27 cells (71), and model membranes (19,51,63,72).

Changes in the vacuole lipidome from the log stage to the stationary stage

If phase separation in vacuole membranes is not due to an increase (or even a change) in the fraction of ergosterol, could it be due to changes in other lipids? In the remainder of this paper, commencing with Fig. 5, we explore how the changes in the vacuole lipidome from the log stage to the stationary stage might contribute to membrane phase separation in the vacuole membrane. A first impression from Fig. 5 is that the lipid populations “are more alike than they are different” (to quote Burns et al. (69), who compared lipidomes from zebrafish GPMVs that phase separate with ones that do not). It makes sense that the two lipidomes are similar, because the cells from which they are extracted are separated by only 2 days of cultivation.

Nevertheless, significant changes in the lipidomes are apparent. The most dramatic change is the increase in the fraction of PC lipids. This jump is notable because PCs are a large fraction of the vacuole’s lipids. We observe concomitant minor decreases in PE, PI, and DAG lipids, which mirror decreases in the whole-cell lipidome (Figs. S6 and S7). Sphingolipids constitute a much smaller fraction of vacuole membrane lipids; we find that the total mole fraction is in the range of only 5%–10%, even in the stationary stage. That said, within this small fraction, there is an increase in IPC sphingolipids from about 2% to 4% from the log stage to the stationary stage (Fig. 5). This increase is not reflected in whole-cell lipid extracts, of which $\sim 2\%$ are IPC sphingolipids in the stationary stage (Fig. S7). Even though the fraction of sphingolipids is small, they have often been associated with membrane domains in the literature. For example, model membranes containing sphingolipids exhibit phase behavior at higher temperatures

Please cite this article as: Reinhard et al., Remodeling of yeast vacuole membrane lipidomes from the log (one phase) to stationary stage (two phases), *Biophysical Journal* (2023), <https://doi.org/10.1016/j.bpj.2023.01.009>

Reinhard et al.

than their counterparts with PC lipids of equal chain lengths (52). Similarly, although 10% of GUVs phase separate at 25°C when they are made from whole lipid extracts of yeast (which is admittedly a small percentage), none of the GUVs phase separate when the yeast undergo mutations that reduce sphingolipids and long-chain fatty acids (*elo4*) or prevent C4 hydroxylation of sphingoid bases (*sur2Δ*) (73).

What about the fatty acid chains of the lipids? Roughly 30 mol % of the acyl chains found in vacuolar lipids are saturated (with no double bonds), in both the logarithmic and stationary stage (Fig. S14). Stated another way, the average number of double bonds per lipid acyl chain in vacuolar membrane lipids (excluding TAG, ergosterol esters, and ergosterol) remains constant from the log stage (0.66 ± 0.01) to the stationary stage (0.65 ± 0.00). Even when we restrict the analysis to glycerolipids with two fatty acyl chains, only a minor increase in lipid saturation is apparent (Fig. 6A).

Few lipids in vacuole membranes have more than one chain that is saturated (Fig. 6). This leads to the question of whether a Lo phase could arise in a membrane that has few fully saturated lipids. The answer is yes, for two reasons. The first is tautological: coexisting liquid phases have previously been found in GUVs reconstituted from rat synaptic membranes (74) and in GPMV membranes derived from zebrafish cells (69) and RBL cells (68), all of which have few fully saturated lipids. The second is that biological membranes contain substantial amounts of protein (75), which may increase lipid order (76).

Although the percentage of saturated fatty acid chains remains roughly constant from the log stage to the stationary stage, there is a large shift in how these chains are distributed between different lipid types (Fig. S14). This result highlights that it is essential to evaluate different lipid classes, because average values can obscure shifts. For example, when PC lipids are analyzed on their own (because there is a large increase in PC lipids from the log to the stationary stage), the percentage of PC lipids that contain only one unsaturated chain significantly increases from $17\% \pm 3\%$ in the log-stage vacuoles to $44\% \pm 1\%$ in the stationary-stage vacuoles (Fig. 6C). A concomitant decrease in lipids with two unsaturated chains occurs, from $83\% \pm 3\%$ in the log stage to $54\% \pm 1\%$ in the stationary stage (Fig. 6C).

Similarly, the average length per lipid chain for all lipids in the vacuole (excluding TAG, ergosterol esters, and ergosterol) remains constant from the log stage (16.6 ± 0.1 carbons) to the stationary stage (16.9 ± 0.2 carbons), whereas, by restricting the data to glycerolipids with two chains (Fig. 6B) or PC lipids (Fig. 6D), it is clear that chain lengths slightly increase for these lipids, largely due to a decrease in lipids with a total acyl chain length of 32 carbons, in favor of longer lipids. Yeasts employ various mechanisms to remodel their lipidomes. Synthesis of PC lipids can occur via the PE-methylation pathway or the Kennedy pathway, resulting in different lipid profiles (77). Remodeling of ex-

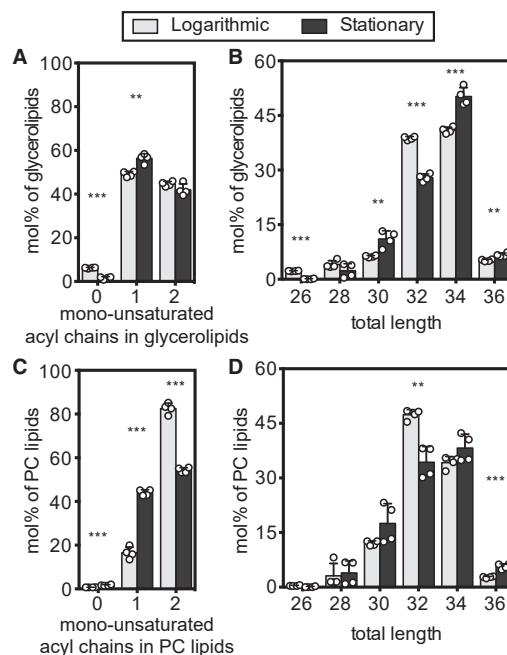


FIGURE 6 Molecular features of glycerolipids and PC lipids in vacuole membranes. (A) Number of mono-unsaturated fatty acyl chains in glycerolipids that have two acyl chains (CDP-DAG, DAG, PA, PC, PE, PG, PI, PS) in the log (gray) and stationary (black) stages. These lipids constitute $81\% \pm 2\%$ and $82\% \pm 4\%$ of all membrane lipids in the log- and stationary-stage vacuole membrane, respectively. (B) Total length of both acyl chains in glycerolipids with two chains. A shift from the log stage to the stationary stage is accompanied by a small increase in lipid chain lengths. (C) Total number of double bonds in PC lipids (PC). Number of mono-unsaturated fatty acyl chains in PC lipids. A shift from the log to the stationary stage is accompanied by a large decrease in the proportion of PC lipids with two mono-unsaturated acyl chains. (D) Total length of acyl chains in PC lipids. Statistical significance was tested by multiple *t*-tests correcting for multiple comparisons (method of Benjamini et al. (50)), with a false discovery rate $Q = 1\%$, without assuming consistent standard deviations. * $p < 0.05$, ** $p < 0.01$, and *** $p < 0.001$.

isting populations of PC lipids can occur through exchange of acyl chains after cleavage by phospholipase A or B, or, to a smaller extent, lipid turnover (78–80).

PC lipids shift to higher melting temperatures in the stationary stage

PC lipids are abundant. Like PE and PI, this lipid class constitutes a large fraction (20%–25%) of all lipids in log-stage vacuole membranes. When yeast transition to the stationary stage, the proportion of PC lipids shoots up to $\sim 40\%$ of vacuolar lipids, the largest increase of any lipid type. A similar increase in the PC-to-PE ratio occurs in the lipidome of whole yeast cells (81). In both cases, the increase may be due to increased availability of methionine for PE-methylation to form PC when protein synthesis declines

Please cite this article in press as: Reinhard et al., Remodeling of yeast vacuole membrane lipidomes from the log (one phase) to stationary stage (two phases), Biophysical Journal (2023), <https://doi.org/10.1016/j.bpj.2023.01.009>

Lipidome log and stat vacuole membranes

(81). Therefore, it seems likely that the onset of phase separation of vacuole membranes is linked to changes in the fraction of PC lipids and their acyl chain compositions. This result is consistent with the observation that yeast knockouts of *OPI3* and *CHO2* (which diminish synthesis of PC lipids (82,83)) exhibit a smaller proportion of vacuoles with domains (8). The mole fractions of every PC lipid in log and stationary-stage vacuoles are provided in Data File S1, with the caveat that fatty acids with odd numbers of carbons should be excluded. We confirmed that these odd-numbered fatty acids are not relevant by analyzing tandem mass spectrometry (MS/MS) fatty acid and headgroup fragmentation.

To gain intuition about how the membrane properties of vacuole membranes might be influenced by their diverse set of PC lipids, we mapped the lipidomics data onto a physical parameter, the temperature at which each lipid melts from the gel to the fluid phase (T_{melt}). Melting temperatures are related to phase separation. Model membranes phase separate into micrometer-scale domains when at least three types of lipids are present: a sterol, a lipid with a high T_{melt} , and a lipid with a low T_{melt} (51,52,54–56,72,84). High and low should be interpreted as relative values rather than absolute values, based on results from model GUV membranes (51) and cell-derived GPMVs (69).

Lipid melting temperatures are affected by the lipid's headgroup, chain length, and chain unsaturation (85–87). When only one of the lipids in a model membrane is varied, a linear relationship can result between the lipid's T_{melt} and the temperature at which the membrane demixes into liquid phases (51,88). Of course, yeast vacuole membranes experience changes in more than one lipid type and in the relative fractions of lipid headgroups, which likely breaks simple relationships between T_{melt} of lipids and the membrane's mixing temperature (51,52,89). However, we are unaware of any single physical parameter that is more relevant than T_{melt} for characterizing lipid mixtures that phase separate.

The formidable task of compiling T_{melt} values of all PC lipids is less onerous for yeast vacuoles than for other cell types because each carbon chain of a yeast glycerolipid has a maximum of one double bond (49). This fact provides a straightforward way to evaluate measurement uncertainties because nonzero entries for polyunsaturated phospholipids in Data File S1 (typically well below 0.2%) must be due to error in the process of assigning lipid identities to mass spectrometry data or are due to fatty acids from the medium. Some T_{melt} values are available in the literature (85,87,90–92). For many others, we estimated T_{melt} values from experimental trends (Tables S2–S4 and Fig. S9). This procedure yielded T_{melt} values for 95% of PC lipids in log-stage vacuoles, and 94% in stationary-stage vacuoles.

By compiling all our data on PC lipids (Fig. 7), we find that they undergo significant acyl chain remodeling from the log stage to the stationary stage in terms of their melting temperatures. Values of T_{melt} are higher for vacuole PC

lipids in the stationary stage compared with the log stage (the weighted average T_{melt} is -31°C in the log stage and -24°C in the stationary stage). Graphically, Fig. 7 A shows this shift as an increase in the mole percent of lipids with high T_{melt} (dark bands).

The increase in T_{melt} correlates with an increase in lipid saturation. In the shift from the log to the stationary stage, PC lipids with two unsaturated chains (lower T_{melt}) become less abundant, and PCs with one unsaturated chain (higher T_{melt}) become more abundant (Figs. 7 B and S10). This large increase in saturation of PC lipids is not reflected in all types of glycerolipids found in vacuole membranes (Fig. S11). Nevertheless, we observe a general trend for each glycerophospholipid and sphingolipid species toward longer acyl chains in the stationary phase (Fig. S11).

The observed increase in average T_{melt} of PC lipids is robust to any possible oversampling of the Ld phase by the Mam3 immuno-isolation procedure. Because Lo phases typically contain higher fractions of lipids with higher melting temperatures and orientational order (51,93) sampling more of the Lo phase would be expected to further increase average T_{melt} values.

The spread in the distribution of lipid melting temperatures is likely to be as important as the average. This is because phase separation persists to higher temperatures in model membranes when the highest T_{melt} is increased (51,89) and when the lowest T_{melt} is decreased (88), at least when those lipids have PC headgroups and do not have methylated tails. These literature reports are consistent with work by Levental et al. showing that phase separation persists to higher temperatures in GPMVs of RBL cells when the two phases are the most different, as measured

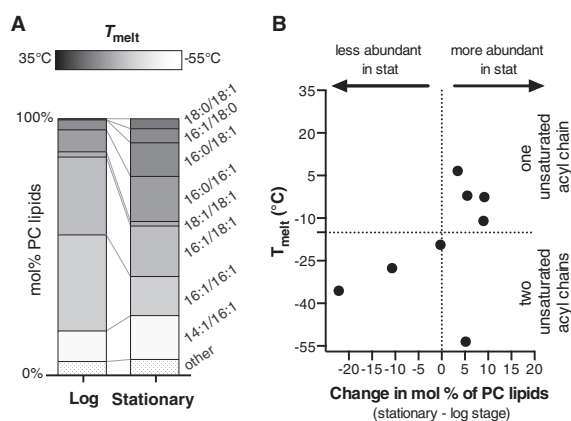


FIGURE 7 Melting temperatures of PC lipids in vacuole membranes. (A) T_{melt} values (represented by gray scale) are higher for PC lipid in the stationary stage than the log stage. Lipids contributing less than 1 mol % are categorized as “other.” (B) From the log to the stationary stage, there is an overall loss of PC lipids with low values of T_{melt} (lower left quadrant) and a gain of PC lipids with high values of T_{melt} (upper right quadrant). Fig. S10 presents an alternative way of plotting these data.

Please cite this article in press as: Reinhard et al., Remodeling of yeast vacuole membrane lipidomes from the log (one phase) to stationary stage (two phases), *Biophysical Journal* (2023), <https://doi.org/10.1016/j.bpj.2023.01.009>

Reinhard et al.

by the generalized polarization of a C-laurdan probe (68). These results can be put into broader context that the addition of any molecule that partitions strongly to only one phase (e.g., a high- T_{melt} lipid to the Lo phase and a low- T_{melt} lipid to the Ld phase) should lower the free energy required for phase separation (94–96).

In the left column of Fig. 7 A, PC lipids in log-stage vacuole membranes cluster around intermediate values of T_{melt} . In the stationary stage, some lipids are replaced by lipids with higher values of T_{melt} , and some are replaced by lipids with lower values. If the vacuole membrane contained only PC lipids, we would conclude that those membranes would be more likely to phase separate in the stationary stage, because their overall melting temperatures are higher and because the distribution of melting temperatures is broader.

PE lipids have similar melting temperatures in log and stationary stage

PE lipids undergo the largest decrease (from ~20% to ~10%) of all lipids in yeast vacuoles. We found melting temperatures of the PE lipids in yeast vacuoles by compiling values in the literature (85,86,97,98) or estimating them (Tables S2 and S3; Fig. S12).

In contrast to PC lipids, the acyl chain composition of PE lipids is not heavily remodeled from the log stage to the stationary stage. This result is seen as a clustering of data points along the vertical dashed line in Fig. 8 B. Accordingly, the melting temperatures of PE lipids change only mildly: the weighted average T_{melt} is -9°C and -5°C in the log and stationary stages, respectively. Similarly, by eye from Fig. 8 A, the distribution of T_{melt} values for PE lipids are similar in the log stage and the stationary stage.

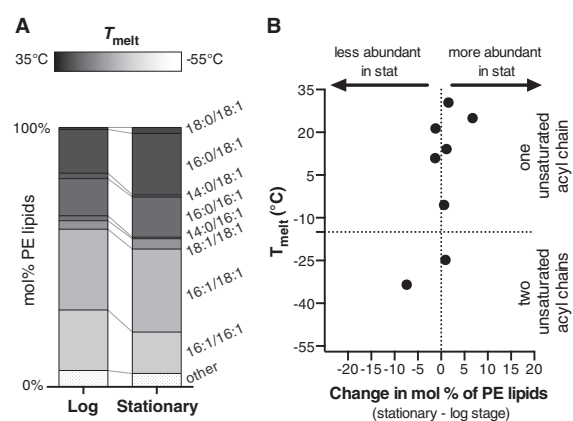


FIGURE 8 Melting temperatures of PE lipids in vacuole membranes. (A) T_{melt} values (represented by gray scale) are similar for vacuole PE lipids in the stationary stage and the log stage. Lipids contributing less than 1 mol % are categorized as “other.” (B) Changes in mol % of PE lipids (x axis) with each melting temperature (y axis) are small; data cluster along the vertical line for zero change in mol %.

Trends in T_{melt} for every glycerolipid

Literature values for lipid melting temperatures are not available for all lipid types, so plots such as Figs. 7 and 8 cannot be reproduced for all headgroups. The next best option is to apply known trends of how lipid chain length and saturation affects lipid T_{melt} ((85,87) and Table S3). We estimate changes in T_{melt} from the log to the stationary stage for each lipid headgroup separately because it is not clear that combining datasets for all lipids would yield insight about whether a membrane would be more likely to phase separate. This is because two lipids can have the same melting temperature, but membranes containing those lipids can phase separate at different temperatures. For example, pure bilayers of palmitoyl sphingomyelin, 16:0SM, and dipalmitoyl PC, di(16:0)PC, have the same T_{melt} (85,99), but multicomponent model membranes containing 16:0SM phase separate at a higher temperature than membranes containing di(16:0)PC (51,52), possibly because sphingomyelins have additional opportunities to hydrogen bond with the sterol (100,101). Similarly, even though PE lipids have higher melting temperatures than equivalent PC lipids (Fig. S13), sterol (cholesterol) partitioning is lower in PE membranes than in PC membranes (102), implying that interactions between sterols and PE lipids are less favorable.

Changes in lipid saturation have much larger effects on melting temperatures than changes in chain length. We find that increasing the average, summed length of both lipid chains by one carbon results in an increase in T_{melt} of 3.6°C for PC and PE lipids (because increasing the total length from 32 to 34 carbons results in an increase in T_{melt} of 7.2°C , as in Table S5). Increasing the saturation of the lipid by one bond results in an increase in T_{melt} of 30.3°C . Therefore, an increase in T_{melt} of, say, 5°C can be achieved either by increasing the average total chain length by $5/3.6 = 1.4$ carbons or by increasing the average saturation by $5/30.3 = 0.17$ bonds (dashed line in Fig. 9).

We know how chain length and saturation changes from the log to stationary stage for all abundant glycerolipids in yeast vacuoles (PC, PE, PI, PS, PG, and DAG) (Figs. 9 and S11). By assuming that the melting temperatures of all these lipids follow similar trends, we find that T_{melt} likely increases for most lipid types during the shift from log to stationary stage. In Fig. 9, changes in chain length or saturation that result in an increase in T_{melt} fall within the shaded region toward the top right of the graph, and the area of each symbol represents the abundance (in mol %) of the lipid type in the stationary stage. The largest increase in T_{melt} is for PC lipids, which are the most abundant lipids in the stationary stage. Lipids for which T_{melt} likely decreases (DAG) have relatively low abundance. Increases in lipid saturation (and, hence, increases in lipid T_{melt} and orientational order) have previously been correlated with phase separation persisting to higher temperatures in GPMVs of zebrafish cells (69).

Please cite this article in press as: Reinhard et al., Remodeling of yeast vacuole membrane lipidomes from the log (one phase) to stationary stage (two phases), Biophysical Journal (2023), <https://doi.org/10.1016/j.bpj.2023.01.009>

Lipidome log and stat vacuole membranes

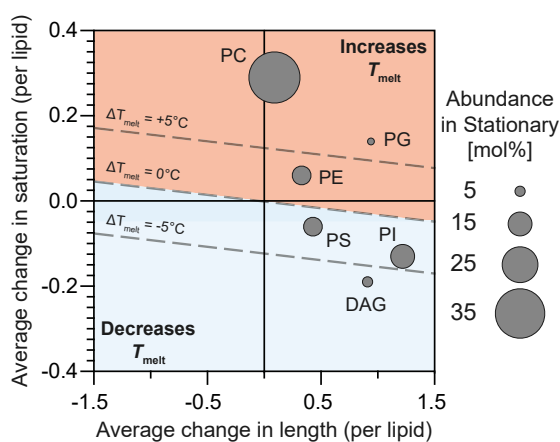


FIGURE 9 At the origin, there is no change in average lipid length (x axis) and no change in average lipid saturation (y axis). Each point represents a different glycerolipid species, and each lipid experiences a change in both length and saturation. The size of each point represents the relative abundance of that lipid class in the stationary stage. Lipids located above the diagonal line of " $\Delta T_{\text{melt}} = 0$ " are expected to experience an increase in T_{melt} . Those below the line are expected to experience a decrease. To see this figure in color, go online.

An alternative mechanism by which eukaryotic cells may influence lipid melting temperatures is through the introduction of highly asymmetric chains. Although highly asymmetric lipids can appear in *S. cerevisiae* membranes (38), here we find no significant change of highly asymmetric lipids in vacuole membranes from the stationary stage (Table S6). In contrast, Burns et al. find that zebrafish GPMVs with lower transition temperatures have more highly asymmetric lipids (69). Similarly, when *Schizosaccharomyces japonicus* fission yeast cannot produce unsaturated lipids (due to anoxic environments), they increase the fraction of lipids with asymmetric acyl tails, which may maintain membrane fluidity (103). Some yeast (e.g., *Schizosaccharomyces pombe*) appear to be biochemically unable to use this strategy (103).

It is also possible that sphingolipids contribute to membrane phase separation in stationary-phase vacuoles, even though they are present at low mole percentages. We find an increase in the length and hydroxylation of the sphingolipids (Fig. S11). We previously noted an increase in IPC sphingolipids from $\sim 2\%$ to $\sim 4\%$ from the log to the stationary stage (Fig. 5), which is noteworthy because its T_{melt} is relatively high (53.4°C as reported by (73)).

Addition of ethanol to isolated, log-stage vacuoles does not cause membrane phase separation

Yeast membranes undergo many changes from the log to the stationary stage that are not captured by lipidomics. For example, as yeast consume glucose, they produce ethanol,

some of which partitions into yeast membranes. In model membranes, addition of ethanol results in disordering of lipid acyl chains (104). Lipidomics does not quantify the percent ethanol in membranes. Nevertheless, we can assess whether ethanol on its own is sufficient to cause log-stage vacuole membranes to phase separate. Here, yeast were grown at 30°C in synthetic complete medium (with 4% glucose) for <24 h until the culture reached an optical density of 0.984. Vacuoles were isolated as in (5), incubated on ice in either 10% v/v ethanol for 1.5 h or 20% v/v ethanol for 2 h, and then imaged at room temperature. Neither population of vacuoles showed evidence of phase separation; only one vacuole showed clear evidence of membrane phase separation, which could not be attributed to the addition of ethanol. The result showing that ethanol, on its own, is not sufficient to cause log-stage vacuole membranes to phase separate is consistent with literature reports. Although ethanol enhances phase separation in vacuole membranes in model membranes (by increasing the temperature at which coexisting Lo and Ld phases persist) (96), it suppresses phase separation in GPMVs from rat basal leukemia cells, which have lipid compositions more similar to yeast vacuole membranes (95).

DISCUSSION

This special issue is dedicated to Klaus Gawrisch, who directed the first experiments to quantify ratios of lipids in Lo and Ld phases of ternary model membranes with high accuracy (93). NMR data from those experiments showed that Lo and Ld phases differed primarily in their fractions of phospholipids with high and low melting temperatures (rather than the amount of sterol). This result was previously surmised from semi-quantitative estimates of lipid compositions from area fractions of Lo and Ld phases (51), but the concept that the two phases could be primarily distinguished by their phospholipid content did not gain traction in the community until high quality data from Klaus's NMR spectrometers were published.

Here, we report a complementary result: demixing of yeast vacuoles into coexisting Lo and Ld phases, which occurs upon a transition from the log to the stationary stage of growth, is accompanied by significant changes in the phospholipid compositions of yeast vacuoles. The fraction of PC lipids roughly doubles. Among the PC lipids, there is a significant increase (7°C) in the average T_{melt} of the lipids. PE lipids, which also exhibit an increase in the average T_{melt} (4°C), are roughly halved in mole fraction.

In this manuscript, we have analyzed the differences in the vacuole lipidome at two growth stages (the log and the stationary stage) in the context of a single physical variable (the mixing temperature) and how it might affect a single membrane attribute (demixing of the membrane into coexisting liquid phases). Of course, membrane phase separation is only one of many relevant physiological parameters.

Please cite this article in press as: Reinhard et al., Remodeling of yeast vacuole membrane lipidomes from the log (one phase) to stationary stage (two phases), *Biophysical Journal* (2023), <https://doi.org/10.1016/j.bpj.2023.01.009>

Reinhard et al.

Cellular lipidomes are also affected by temperature, growth medium, carbon source, anoxia, ethanol adaptation, mutations, and cell stress (69,103,105–110). Cells have the potential to adjust their membrane compositions to meet a broad list of inter-related constraints, including lipid packing, thickness, compression, viscosity, permeability, charge, asymmetry, monolayer and bilayer spontaneous curvatures, and avoidance of (and proximity to) nonlamellar phases (69,110–122). Likewise, the lipidome is only one of many biochemical attributes that a cell might vary (e.g., the asymmetry, charge, tension, and adhesion of the membrane; the abundance, crowding, condensation, and crosslinking of proteins; and the conditions of the solvent) to enhance or suppress liquid-liquid phase separation of its membranes (57,123–127).

Not all lipidomic changes that we observe in the vacuole are reflected across the whole cell (21), highlighting the importance of isolating organelles. Our ability to isolate yeast vacuoles with low levels of contamination by non-vacuole organelles leverages advances in immuno-isolation (28) and our discovery that Mam3 is a robust bait protein in both the log and stationary stages. Recent advances in simulating the molecular dynamics of complex membranes with many lipid types over long timescales are equally exciting (128,129). We hope that sharing our lipidomic data (Data File S1) will be useful to future modelers in elucidating why stationary-stage vacuole membranes phase separate, whereas log-stage membranes do not.

CONCLUSIONS

Here, we establish that Mam3 is a robust bait protein for immuno-isolation of vacuole membranes. Expression levels of Mam3 are high throughout the yeast growth cycle. In the stationary stage, Mam3 partitions into the Ld phase. By conducting lipidomics on isolated vacuole membranes, we find that the shift from the log to the stationary stage of growth is accompanied by large increases in the fraction of PC lipids in the membrane, and that these lipids become longer and more saturated. The resulting increase in melting temperature of these lipids may contribute to demixing of stationary-stage vacuole membranes to form coexisting liquid phases.

SUPPORTING MATERIAL

Supporting material can be found online at <https://doi.org/10.1016/j.bpj.2023.01.009>.

AUTHOR CONTRIBUTIONS

A.J.M., C.E.C., C.L.L., J.R., R.E., and S.L.K. designed the research. C.E.C., C.L.L., C.K., and J.R. performed the research. C.L.L., J.R., C.K., R.E., and S.L.K. analyzed the data. A.J.M., C.L.L., J.R., R.E., and S.L.K. wrote the paper.

ACKNOWLEDGMENTS

This research was supported by NSF grant MCB-1925731 to S.L.K., NIH grants GM077349 and GM130644 to A.J.M., European Union's Horizon 2020 research and innovation program (grant agreement no. 866011) to R.E., Deutsche Forschungsgemeinschaft in the framework of the SFB894 to R.E., Volkswagen Foundation grant #93089 to R.E. and J.R., and a travel grant by The Company of Biologists to C.L.L.

This manuscript is dedicated to Klaus Gawrisch, whose contributions to the biophysical community go beyond his rigorous NMR measurements. His open-mindedness to consider and test unpopular ideas, his generosity in sharing credit through collaborations, and his dedication to mentoring of early-career researchers have continuously elevated the quality of scientific results and the collegiality of scientific culture.

DECLARATION OF INTERESTS

C.K. is employed by Lipotype GmbH, a company that conducts quantitative lipidomic services.

REFERENCES

- Casanovas, A., R. R. Sprenger, ..., C. S. Ejsing. 2015. Quantitative analysis of proteome and lipidome dynamics reveals functional regulation of global lipid metabolism. *Chem. Biol.* 22:412–425.
- Werner-Washburne, M., E. Braun, ..., R. A. Singer. 1993. Stationary phase in the yeast *Saccharomyces cerevisiae*. *Microbiol. Rev.* 57: 383–401.
- Wiemken, A., P. Matile, and H. Moor. 1970. Vacuolar dynamics in synchronously budding yeast. *Arch. Mikrobiol.* 70:89–103.
- Jones, E. W. 1997. Biogenesis and function of the yeast vacuole. *Molecular and Cellular Biology of the Yeast Saccharomyces*. 3:363–470.
- Rayermann, S. P., G. E. Rayermann, ..., S. L. Keller. 2017. Hallmarks of reversible separation of living, unperturbed cell membranes into two liquid phases. *Biophys. J.* 113:2425–2432.
- Moor, H., and K. Mühlethaler. 1963. Fine structure in frozen-etched yeast cells. *J. Cell Biol.* 17:609–628.
- Moeller, C. H., and W. W. Thomson. 1979. An ultrastructural study of the yeast tonoplast during the shift from exponential to stationary phase. *J. Ultrastruct. Res.* 68:28–37.
- Toulmay, A., and W. A. Prinz. 2013. Direct imaging reveals stable, micrometer-scale lipid domains that segregate proteins in live cells. *J. Cell Biol.* 202:35–44.
- Wang, C.-W., Y.-H. Miao, and Y.-S. Chang. 2014. A sterol-enriched vacuolar microdomain mediates stationary phase lipophagy in budding yeast. *J. Cell Biol.* 206:357–366.
- Leveille, C. L., C. E. Cornell, S. L. Keller, ..., 2022. Yeast cells actively tune their membranes to phase separate at temperatures that scale with growth temperatures. *Biophys. J.*:119:e2116007119.
- Murley, A., R. D. Sarsam, ..., J. Nunnari. 2015. Ltc1 is an ER-localized sterol transporter and a component of ER-mitochondria and ER-vacuole contacts. *J. Cell Biol.* 209:539–548.
- Murley, A., J. Yamada, ..., J. Nunnari. 2017. Sterol transporters at membrane contact sites regulate TORC1 and TORC2 signaling. *J. Cell Biol.* 216:2679–2689.
- Seo, A. Y., P.-W. Lau, ..., J. Lippincott-Schwartz. 2017. AMPK and vacuole-associated Atg14p orchestrate μ -lipophagy for energy production and long-term survival under glucose starvation. *Elife*. 6, e21690.
- Hatakeyama, R., M. P. Péli-Gulli, ..., C. De Virgilio. 2019. Spatially distinct pools of TORC1 balance protein homeostasis. *Mol. Cell.* 73:325–338.e8.

Please cite this article in press as: Reinhard et al., Remodeling of yeast vacuole membrane lipidomes from the log (one phase) to stationary stage (two phases), Biophysical Journal (2023), <https://doi.org/10.1016/j.bpj.2023.01.009>

Lipidome log and stat vacuole membranes

15. Tsuji, T., M. Fujimoto, ..., T. Fujimoto. 2017. Niemann-Pick type C proteins promote microautophagy by expanding raft-like membrane domains in the yeast vacuole. *Elife*. 6, e25960.
16. Chatterjee, S., D. Maltseva, ..., S. H. Parekh. 2022. Lipid-driven condensation and interfacial ordering of FUS. *Sci. Adv.* 8, eabm7528.
17. Wang, H. Y., S. H. Chan, ..., I. Levental. 2022. Coupling of protein condensates to ordered lipid domains determines functional membrane organization. Preprint at bioRxiv:2022.08.02.502487.
18. Toulmay, A., and W. A. Prinz. 2013. Direct imaging reveals stable, micrometer-scale lipid domains that segregate proteins in live cells. *J. Cell Biol.* 202:35–44.
19. Beattie, M. E., S. L. Veatch, ..., S. L. Keller. 2005. Sterol structure determines miscibility versus melting transitions in lipid vesicles. *Biophys. J.* 89:1760–1768.
20. Seo, A. Y., F. Sarkleti, ..., J. Lippincott-Schwartz. 2021. Vacuole phase-partitioning boosts mitochondria activity and cell lifespan through an inter-organellar lipid pipeline. Preprint at bioRxiv:2021.04.11.439383.
21. Klose, C., M. A. Surma, ..., K. Simons. 2012. Flexibility of a eukaryotic lipidome – insights from yeast lipidomics. *PLoS One*. 7, e35063.
22. Pan, X., P. Roberts, ..., D. S. Goldfarb. 2000. Nucleus–vacuole junctions in *Saccharomyces cerevisiae* are formed through the direct interaction of Vac8p with Nvj1p. *Mol. Biol. Cell.* 11:2445–2457.
23. Bisinski, D. D., I. Gomes Castro, ..., A. González Montoro. 2022. Cvm1 is a component of multiple vacuolar contact sites required for sphingolipid homeostasis. *J. Cell Biol.* 221:e202103048.
24. Franzusoff, A., E. Lauzé, and K. E. Howell. 1992. Immuno-isolation of Sec7p-coated transport vesicles from the yeast secretory pathway. *Nature*. 355:173–175.
25. Schneiter, R., B. Brügger, ..., S. D. Kohlwein. 1999. Electrospray ionization tandem mass spectrometry (ESI-MS/MS) analysis of the lipid molecular species composition of yeast subcellular membranes reveals acyl chain-based sorting/remodeling of distinct molecular species en route to the plasma membrane. *J. Cell Biol.* 146:741–754.
26. Klemm, R. W., C. S. Ejsing, ..., K. Simons. 2009. Segregation of sphingolipids and sterols during formation of secretory vesicles at the trans-Golgi network. *J. Cell Biol.* 185:601–612.
27. Surma, M. A., C. Klose, ..., K. Simons. 2011. Generic sorting of raft lipids into secretory vesicles in yeast. *Traffic*. 12:1139–1147.
28. Reinhard, J., L. Starke, ..., R. Ernst. 2022. A new technology for isolating organellar membranes provides fingerprints of lipid bilayer stress. Preprint at bioRxiv:2022.09.15.508072.
29. Tang, R. J., S.-F. Meng, ..., S. Luan. 2022. Conserved mechanism for vacuolar magnesium sequestration in yeast and plant cells. *Native Plants*. 8:181–190.
30. Uchida, E., Y. Ohsumi, and Y. Anraku. 1988. Purification of yeast vacuolar membrane H⁺-ATPase and enzymological discrimination of three ATP-driven proton pumps in *Saccharomyces cerevisiae*. In *Methods in Enzymology* Academic Press, pp. 544–562.
31. Zinser, E., C. D. Sperka-Gottlieb, ..., G. Daum. 1991. Phospholipid synthesis and lipid composition of subcellular membranes in the unicellular eukaryote *Saccharomyces cerevisiae*. *J. Bacteriol.* 173:2026–2034.
32. Gupta, M. N., and I. Roy. 2021. Three Phase Partitioning: Applications in Separation and Purification of Biological Molecules and Natural Products. Elsevier.
33. Ghaemmaghami, S., W.-K. Huh, ..., J. S. Weissman. 2003. Global analysis of protein expression in yeast. *Nature*. 425:737–741.
34. Ho, B., A. Baryshnikova, and G. W. Brown. 2018. Unification of protein abundance datasets yields a quantitative *Saccharomyces cerevisiae* proteome. *Cell Syst.* 6:192–205.e3.
35. Huh, W.-K., J. V. Falvo, ..., E. K. O’Shea. 2003. Global analysis of protein localization in budding yeast. *Nature*. 425:686–691.
36. Zinser, E., F. Paltauf, and G. Daum. 1993. Sterol composition of yeast organelle membranes and subcellular distribution of enzymes involved in sterol metabolism. *J. Bacteriol.* 175:2853–2858.
37. Tuller, G., T. Nemeč, ..., G. Daum. 1999. Lipid composition of subcellular membranes of an FY1679-derived haploid yeast wild-type strain grown on different carbon sources. *Yeast*. 15:1555–1564.
38. Reinhard, J., C. Mattes, ..., R. Ernst. 2020. A quantitative analysis of cellular lipid compositions during acute proteotoxic ER stress reveals specificity in the production of asymmetric lipids. *Front. Cell Dev. Biol.* 8:756.
39. van Zutphen, T., V. Todde, ..., S. D. Kohlwein. 2014. Lipid droplet autophagy in the yeast *Saccharomyces cerevisiae*. *Mol. Biol. Cell.* 25:290–301.
40. Moeller, C. H., and W. W. Thomson. 1979. Uptake of lipid bodies by the yeast vacuole involving areas of the tonoplast depleted of intramembranous particles. *J. Ultrastruct. Res.* 68:38–45.
41. Vevea, J. D., E. J. Garcia, ..., L. A. Pon. 2015. Role for lipid droplet biogenesis and microlipophagy in adaptation to lipid imbalance in yeast. *Dev. Cell.* 35:584–599.
42. Garcia, E. J., J. D. Vevea, and L. A. Pon. 2018. Lipid droplet autophagy during energy mobilization, lipid homeostasis and protein quality control. *Front. Biosci.* 23:1552–1563.
43. Wang, C. W., Y. H. Miao, and Y. S. Chang. 2014. A sterol-enriched vacuolar microdomain mediates stationary phase lipophagy in budding yeast. *J. Cell Biol.* 206:357–366.
44. Seo, A. Y., P. W. Lau, ..., J. Lippincott-Schwartz. 2017. AMPK and vacuole-associated Atg14p orchestrate μ -lipophagy for energy production and long-term survival under glucose starvation. *Elife*. 6:e21690.
45. Tsuji, T., M. Fujimoto, ..., T. Fujimoto. 2017. Niemann-Pick type C proteins promote microautophagy by expanding raft-like membrane domains in the yeast vacuole. *Elife*. 6:e25960.
46. Hamilton, J. A., and D. M. Small. 1981. Solubilization and localization of triolein in phosphatidylcholine bilayers: a ¹³C NMR study. *Proc. Natl. Acad. Sci. USA*. 78:6878–6882.
47. Spooner, P. J., and D. M. Small. 1987. Effect of free cholesterol on incorporation of triolein in phospholipid bilayers. *Biochemistry*. 26:5820–5825.
48. Zinser, E., and G. Daum. 1995. Isolation and biochemical characterization of organelles from the yeast, *Saccharomyces cerevisiae*. *Yeast*. 11:493–536.
49. Henry, S. A., S. D. Kohlwein, and G. M. Carman. 2012. Metabolism and regulation of glycerolipids in the yeast *Saccharomyces cerevisiae*. *Genetics*. 190:317–349.
50. Benjamini, Y., A. M. Krieger, and D. Yekutieli. 2006. Adaptive linear step-up procedures that control the false discovery rate. *Biometrika*. 93:491–507.
51. Veatch, S. L., and S. L. Keller. 2003. Separation of liquid phases in giant vesicles of ternary mixtures of phospholipids and cholesterol. *Biophys. J.* 85:3074–3083.
52. Veatch, S. L., and S. L. Keller. 2005. Miscibility phase diagrams of giant vesicles containing sphingomyelin. *Phys. Rev. Lett.* 94, 148101.
53. Veatch, S. L., K. Gawrisch, and S. L. Keller. 2006. Closed-loop miscibility gap and quantitative tie-lines in ternary membranes containing diphytanoyl PC. *Biophys. J.* 90:4428–4436.
54. Zhao, J., J. Wu, ..., G. W. Feigenson. 2007. Phase studies of model biomembranes: complex behavior of DSPC/DOPC/cholesterol. *Biochim. Biophys. Acta*. 1768:2764–2776.
55. Ionova, I. V., V. A. Livshits, and D. Marsh. 2012. Phase diagram of ternary cholesterol/palmitoylsphingomyelin/palmitoyloleoyl-phosphatidylcholine mixtures: spin-label EPR study of lipid-raft formation. *Biophys. J.* 102:1856–1865.
56. Bezlyepkina, N., R. S. Gracià, ..., R. Dimova. 2013. Phase diagram and tie-line determination for the ternary mixture DOPC/eSM/Cholesterol. *Biophys. J.* 104:1456–1464.
57. Blosser, M. C., J. B. Starr, ..., S. L. Keller. 2013. Minimal effect of lipid charge on membrane miscibility phase behavior in three ternary systems. *Biophys. J.* 104:2629–2638.

Please cite this article in press as: Reinhard et al., Remodeling of yeast vacuole membrane lipidomes from the log (one phase) to stationary stage (two phases), *Biophysical Journal* (2023), <https://doi.org/10.1016/j.bpj.2023.01.009>

Reinhard et al.

58. Stevens, M. M., A. R. Honerkamp-Smith, and S. L. Keller. 2010. Solubility limits of cholesterol, lanosterol, ergosterol, stigmaterol, and β -sitosterol in electroformed lipid vesicles. *Soft Matter*. 6:5882–5890.
59. Mannock, D. A., R. N. A. H. Lewis, and R. N. McElhaney. 2010. A calorimetric and spectroscopic comparison of the effects of ergosterol and cholesterol on the thermotropic phase behavior and organization of dipalmitoylphosphatidylcholine bilayer membranes. *Biochim. Biophys. Acta*. 1798:376–388.
60. Hsueh, Y.-W., M.-T. Chen, ..., J. Thewalt. 2007. Ergosterol in POPC membranes: physical properties and comparison with structurally similar sterols. *Biophys. J.* 92:1606–1615.
61. Urbina, J. A., S. Pekarar, ..., E. Oldfield. 1995. Molecular order and dynamics of phosphatidylcholine bilayer membranes in the presence of cholesterol, ergosterol and lanosterol: a comparative study using ^2H - ^{13}C - and ^{31}P -NMR spectroscopy. *Biochim. Biophys. Acta*. 1238:163–176.
62. Hao, M., S. Mukherjee, and F. R. Maxfield. 2001. Cholesterol depletion induces large scale domain segregation in living cell membranes. *Proc. Natl. Acad. Sci. USA*. 98:13072–13077.
63. Levental, I., F. J. Byfield, ..., P. A. Janmey. 2009. Cholesterol-dependent phase separation in cell-derived giant plasma-membrane vesicles. *Biochem. J.* 424:163–167.
64. Mahammad, S., J. Dinic, ..., I. Parmryd. 2010. Limited cholesterol depletion causes aggregation of plasma membrane lipid rafts inducing T cell activation. *Biochim. Biophys. Acta*. 1801:625–634.
65. Vrljic, M., S. Y. Nishimura, ..., H. M. McConnell. 2005. Cholesterol depletion suppresses the translational diffusion of class II major histocompatibility complex proteins in the plasma membrane. *Biophys. J.* 88:334–347.
66. Samsonov, A. V., I. Mihalov, and F. S. Cohen. 2001. Characterization of cholesterol-sphingomyelin domains and their dynamics in bilayer membranes. *Biophys. J.* 81:1486–1500.
67. Baumgart, T., A. T. Hammond, ..., W. W. Webb. 2007. Large-scale fluid/fluid phase separation of proteins and lipids in giant plasma membrane vesicles. *Proc. Natl. Acad. Sci. USA*. 104:3165–3170.
68. Levental, K. R., J. H. Lorent, ..., I. Levental. 2016. Polyunsaturated lipids regulate membrane domain stability by tuning membrane order. *Biophys. J.* 110:1800–1810.
69. Burns, M., K. Wisser, ..., S. L. Veatch. 2017. Miscibility transition temperature scales with growth temperature in a zebrafish cell line. *Biophys. J.* 113:1212–1222.
70. Zhao, J., J. Wu, and S. L. Veatch. 2013. Adhesion stabilizes robust lipid heterogeneity in supercritical membranes at physiological temperature. *Biophys. J.* 104:825–834.
71. Stone, M. B., S. A. Shelby, ..., S. L. Veatch. 2017. Protein sorting by lipid phase-like domains supports emergent signaling function in B lymphocyte plasma membranes. *Elife*. 6:e19891.
72. Veatch, S. L., and S. L. Keller. 2002. Organization in lipid membranes containing cholesterol. *Phys. Rev. Lett.* 89, 268101.
73. Klose, C., C. S. Ejsing, ..., K. Simons. 2010. Yeast lipids can phase-separate into micrometer-scale membrane domains. *J. Biol. Chem.* 285:30224–30232.
74. Tulodziecka, K., B. B. Diaz-Rohrer, ..., I. Levental. 2016. Remodeling of the postsynaptic plasma membrane during neural development. *Mol. Biol. Cell*. 27:3480–3489.
75. Dupuy, A. D., and D. M. Engelman. 2008. Protein area occupancy at the center of the red blood cell membrane. *Proc. Natl. Acad. Sci. USA*. 105:2848–2852.
76. Jähnig, F. 1979. Structural order of lipids and proteins in membranes: evaluation of fluorescence anisotropy data. *Proc. Natl. Acad. Sci. USA*. 76:6361–6365.
77. Boumann, H. A., M. J. A. Damen, ..., A. I. P. M. de Kroon. 2003. The two biosynthetic routes leading to phosphatidylcholine in yeast produce different sets of molecular species. Evidence for lipid remodeling. *Biochemistry*. 42:3054–3059.
78. Patton-Vogt, J., and A. I. P. M. de Kroon. 2020. Phospholipid turnover and acyl chain remodeling in the yeast ER. *Biochim. Biophys. Acta, Mol. Cell Biol. Lipids*. 1865, 158462.
79. de Kroon, A. I. P. M., P. J. Rijken, and C. H. De Smet. 2013. Checks and balances in membrane phospholipid class and acyl chain homeostasis, the yeast perspective. *Prog. Lipid Res.* 52:374–394.
80. van der Harst, D., D. de Jong, ..., A. Brand. 1990. Clonal B-cell populations in patients with idiopathic thrombocytopenic purpura. *Blood*. 76:2321–2326.
81. Janssen, M. J., M. C. Koorengel, ..., A. I. de Kroon. 2000. The phosphatidylcholine to phosphatidylethanolamine ratio of *Saccharomyces cerevisiae* varies with the growth phase. *Yeast*. 16:641–650.
82. McGraw, P., and S. A. Henry. 1989. Mutations in the *Saccharomyces cerevisiae* *opi3* gene: effects on phospholipid methylation, growth and cross-pathway regulation of inositol synthesis. *Genetics*. 122: 317–330.
83. Kodaki, T., and S. Yamashita. 1987. Yeast phosphatidylethanolamine methylation pathway. Cloning and characterization of two distinct methyltransferase genes. *J. Biol. Chem.* 262:15428–15435.
84. Dietrich, C., L. A. Bagatolli, ..., E. Gratton. 2001. Lipid rafts reconstituted in model membranes. *Biophys. J.* 80:1417–1428.
85. Silvius, J. R. 1982. Thermotropic phase transitions of pure lipids in model membranes and their modifications by membrane proteins. *Lipid-protein interactions*. 2:239–281.
86. Koynova, R., and M. Caffrey. 1994. Phases and phase transitions of the hydrated phosphatidylethanolamines. *Chem. Phys. Lipids*. 69:1–34.
87. Koynova, R., and M. Caffrey. 1998. Phases and phase transitions of the phosphatidylcholines. *Biochim. Biophys. Acta*. 1376:91–145.
88. García-Sáez, A. J., S. Chiantia, and P. Schwille. 2007. Effect of line tension on the lateral organization of lipid membranes. *J. Biol. Chem.* 282:33537–33544.
89. Bleecker, J. V., P. A. Cox, ..., S. L. Keller. 2016. Thickness mismatch of coexisting liquid phases in noncanonical lipid bilayers. *J. Phys. Chem. B*. 120:2761–2770.
90. Tada, K., E. Miyazaki, ..., S. Kaneshina. 2009. Barotropic and thermotropic bilayer phase behavior of positional isomers of unsaturated mixed-chain phosphatidylcholines. *Biochim. Biophys. Acta*. 1788:1056–1063.
91. Ichimori, H., T. Hata, ..., S. Kaneshina. 1999. Effect of unsaturated acyl chains on the thermotropic and barotropic phase transitions of phospholipid bilayer membranes. *Chem. Phys. Lipids*. 100:151–164.
92. Goto, M., S. Ishida, ..., S. Kaneshina. 2009. Chain asymmetry alters thermotropic and barotropic properties of phospholipid bilayer membranes. *Chem. Phys. Lipids*. 161:65–76.
93. Veatch, S. L., I. V. Polozov, ..., S. L. Keller. 2004. Liquid domains in vesicles investigated by NMR and fluorescence microscopy. *Biophys. J.* 86:2910–2922.
94. Meerschaert, R. L., and C. V. Kelly. 2015. Trace membrane additives affect lipid phases with distinct mechanisms: a modified Ising model. *Eur. Biophys. J.* 44:227–233.
95. Machta, B. B., E. Gray, ..., S. L. Veatch. 2016. Conditions that stabilize membrane domains also antagonize n-alcohol anesthesia. *Biophys. J.* 111:537–545.
96. Cornell, C. E., N. L. C. McCarthy, ..., S. L. Keller. 2017. n-Alcohol length governs shift in Lo-Ld mixing temperatures in synthetic and cell-derived membranes. *Biophys. J.* 113:1200–1211.
97. Wang, Z. Q., H. N. Lin, ..., C. H. Huang. 1994. Calorimetric studies and molecular mechanics simulations of monounsaturated phosphatidylethanolamine bilayers. *J. Biol. Chem.* 269:23491–23499.
98. Matsuki, H., S. Endo, ..., S. Kaneshina. 2017. Thermotropic and barotropic phase transitions on diacylphosphatidylethanolamine bilayer membranes. *Biochim. Biophys. Acta Biomembr.* 1859:1222–1232.
99. Estep, T. N., D. B. Mountcastle, ..., T. E. Thompson. 1979. Thermal behavior of synthetic sphingomyelin-cholesterol dispersions. *Biochemistry*. 18:2112–2117.

14 *Biophysical Journal* 122, 1–15, March 21, 2023

Please cite this article in press as: Reinhard et al., Remodeling of yeast vacuole membrane lipidomes from the log (one phase) to stationary stage (two phases), *Biophysical Journal* (2023), <https://doi.org/10.1016/j.bpj.2023.01.009>

Lipidome log and stat vacuole membranes

100. Barenholz, Y., and T. E. Thompson. 1980. Sphingomyelins in bilayers and biological membranes. *Biochim. Biophys. Acta.* 604:129–158.
101. Van Duyl, B. Y., D. Ganchev, ..., J. A. Killian. 2003. Sphingomyelin is much more effective than saturated phosphatidylcholine in excluding unsaturated phosphatidylcholine from domains formed with cholesterol. *FEBS Lett.* 547:101–106.
102. Niu, S. L., and B. J. Litman. 2002. Determination of membrane cholesterol partition coefficient using a lipid vesicle–cyclodextrin binary system: effect of phospholipid acyl chain unsaturation and head-group composition. *Biophys. J.* 83:3408–3415.
103. Panconi, L., C. D. Lorenz, ..., M. Makarova. 2022. Phospholipid tail asymmetry allows cellular adaptation to anoxic environments. Preprint at [bioRxiv:2022.08.04.502790](https://doi.org/10.1101/2022.08.04.502790).
104. Barry, J. A., and K. Gawrisch. 1994. Direct NMR evidence for ethanol binding to the lipid-water interface of phospholipid bilayers. *Biochemistry.* 33:8082–8088.
105. Marr, A. G., and J. L. Ingraham. 1962. Effect of temperature on the composition of fatty acids in *Escherichia coli*. *J. Bacteriol.* 84:1260–1267.
106. Kates, M., and R. M. Baxter. 1962. Lipid composition of mesophilic and psychrophilic yeasts (*Candida* species) as influenced by environmental temperature. *Can. J. Biochem. Physiol.* 40:1213–1227.
107. Hunter, K., and A. H. Rose. 1972. Lipid composition of *Saccharomyces cerevisiae* as influenced by growth temperature. *Biochim. Biophys. Acta.* 260:639–653.
108. Beaven, M. J., C. Charpentier, and A. H. Rose. 1982. Production and tolerance of ethanol in relation to phospholipid fatty-acyl composition in *Saccharomyces cerevisiae* NCYC 431. *Microbiology.* 128: 1447–1455.
109. Rousseaux, and Charpentier. Ethanol adaptation mechanisms in *Saccharomyces cerevisiae*. *Appl. Biochem. Biotechnol.*
110. Levental, K. R., E. Malmberg, ..., I. Levental. 2020. Lipidomic and biophysical homeostasis of mammalian membranes counteracts dietary lipid perturbations to maintain cellular fitness. *Nat. Commun.* 11:1339.
111. Huang, L., S. K. Lorch, ..., A. Haug. 1974. Control of membrane lipid fluidity in *Acholeplasma laidlawii*. *FEBS Lett.* 43:1–5.
112. Sinensky, M. 1974. Homeoviscous adaptation—a homeostatic process that regulates the viscosity of membrane lipids in *Escherichia coli*. *Proc. Natl. Acad. Sci. USA.* 71:522–525.
113. Cullis, P. R., M. J. Hope, and C. P. Tilcock. 1986. Lipid polymorphism and the roles of lipids in membranes. *Chem. Phys. Lipids.* 40: 127–144.
114. Lindblom, G., I. Brentel, ..., A. Wieslander. 1986. Phase equilibria of membrane lipids from *Acholeplasma laidlawii*: importance of a single lipid forming nonlamellar phases. *Biochemistry.* 25:7502–7510.
115. Österberg, F., L. Rilfors, ..., S. M. Gruner. 1995. Lipid extracts from membranes of *Acholeplasma laidlawii* A grown with different fatty acids have a nearly constant spontaneous curvature. *Biochim. Biophys. Acta.* 1257:18–24.
116. Morein, S., A. Andersson, G. Lindblom, ..., 1996. Wild-type *Escherichia coli* cells regulate the membrane lipid composition in a “window” between gel and non-lamellar structures. *J. Biol. Chem.* 271:6801–6809.
117. Halbleib, K., K. Pesek, ..., R. Ernst. 2017. Activation of the unfolded protein response by lipid bilayer stress. *Mol. Cell.* 67:673–684.e8.
118. Bigay, J., and B. Antonny. 2012. Curvature, lipid packing, and electrostatics of membrane organelles: defining cellular territories in determining specificity. *Dev. Cell.* 23:886–895.
119. Diaz-Rohrer, B., K. R. Levental, and I. Levental. 2014. Rafting through traffic: membrane domains in cellular logistics. *Biochim. Biophys. Acta.* 1838:3003–3013.
120. Ballweg, S., E. Sezgin, ..., R. Ernst. 2020. Regulation of lipid saturation without sensing membrane fluidity. *Nat. Commun.* 11:756.
121. Ernst, R., S. Ballweg, and I. Levental. 2018. Cellular mechanisms of physicochemical membrane homeostasis. *Curr. Opin. Cell Biol.* 53:44–51.
122. Ernst, R., C. S. Ejsing, and B. Antonny. 2016. Homeoviscous adaptation and the regulation of membrane lipids. *J. Mol. Biol.* 428:4776–4791.
123. Collins, M. D., and S. L. Keller. 2008. Tuning lipid mixtures to induce or suppress domain formation across leaflets of unsupported asymmetric bilayers. *Proc. Natl. Acad. Sci. USA.* 105:124–128.
124. Portet, T., S. E. Gordon, and S. L. Keller. 2012. Increasing membrane tension decreases miscibility temperatures; an experimental demonstration via micropipette aspiration. *Biophys. J.* 103:L35–L37.
125. Liu, A. P., and D. A. Fletcher. 2006. Actin polymerization serves as a membrane domain switch in model lipid bilayers. *Biophys. J.* 91:4064–4070.
126. Hammond, A. T., F. A. Heberle, ..., G. W. Feigenson. 2005. Cross-linking a lipid raft component triggers liquid ordered-liquid disordered phase separation in model plasma membranes. *Proc. Natl. Acad. Sci. USA.* 102:6320–6325.
127. Knorr, R. L., J. Steinkühler, and R. Dimova. 2018. Micron-sized domains in quasi single-component giant vesicles. *Biochim. Biophys. Acta Biomembr.* 1860:1957–1964.
128. Ingólfsson, H. I., C. Neale, ..., F. H. Streitz. 2022. Machine learning-driven multiscale modeling reveals lipid-dependent dynamics of RAS signaling proteins. *Proc. Natl. Acad. Sci. USA.* 119, e2113297119.
129. Marrink, S. J., V. Corradi, ..., M. S. P. Sansom. 2019. Computational modeling of realistic cell membranes. *Chem. Rev.* 119:6184–6226.

Biophysical Journal, Volume 122

Supplemental information

Remodeling of yeast vacuole membrane lipidomes from the log (one phase) to stationary stage (two phases)

John Reinhard, Chantelle L. Leveille, Caitlin E. Cornell, Alexey J. Merz, Christian Klose, Robert Ernst, and Sarah L. Keller

Supporting Material

Remodeling of vacuole membrane lipidome
from the log stage (1-phase) to stationary stage (2-phases)

John Reinhard,^{1,2,6} Chantelle L. Leveille,^{3,6} Caitlin E. Cornell,³ Alexey J. Merz,⁴ Christian Klose,⁵
Robert Ernst,^{1,2*} Sarah L. Keller^{3*}

1 Medical Biochemistry and Molecular Biology, Medical Faculty, Saarland University, Homburg, Germany

2 PZMS, Center for Molecular Signaling, Medical Faculty, Saarland University, Homburg, Germany

3 Department of Chemistry, University of Washington, Seattle, WA, USA

4 Department of Biochemistry, University of Washington, Seattle, WA, USA

5 Lipotype GmbH, Am Tatzberg 47, Dresden, Germany

6 These authors contributed equally to this work

**Correspondence: skeller@uw.edu, robert.ernst@uks.eu*

This PDF file includes

Caption for Data File S1

Supplemental Methods

Figures S1 to S14

Tables S1 to S6

Caption for Data File S1

Raw data for abundances of all lipids in vacuoles immuno-isolated with a Mam3 bait protein from yeast in the log stage (light gray), stationary stage (dark gray) and whole cell data from stationary cells (blue). Additional data of log stage whole cell lipidomes (Fig. S7, Logarithmic) and log stage lipidomes of vacuole membranes immuno-isolated via a Vph1 bait protein (Fig. S8, Vph1-bait) are taken from (1) and highlighted in green. Data in Figure S8 (Mam3-bait) are replotted from Figure S6 (Logarithmic). Tabs in the data file show calculated and plotted values for respective figures.

Supplemental Methods

Microscopy

Saccharomyces cerevisiae BY4741 (2, 3) expressing a Mam3-GFP fusion protein from its endogenous locus and promoter was used for fluorescence microscopy experiments. Live yeast cells were immobilized on a coverslip coated with 3 μ L of 1 mg/mL concanavalin-A (EPC Elastin Products Co. catalog no. C2131) in buffer (50 mM HEPES at pH 7.5, 20 mM calcium acetate, and 1 mM MnSO₄). Immediately prior to use, the coverslips were washed with MilliQ water and dried with compressed air. Cells were diluted for imaging in an isosmotic solution of conditioned medium from the yeast culture. To produce conditioned medium, 1 mL of culture was centrifuged at 3,400 \times g. The supernatant was collected and centrifuged again at 3,400 \times g to remove all remaining cells. To decrease refractive index mismatch (4), 200 μ L of OptiPrep (60% OptiPrep Density Gradient Medium; Sigma catalog no. D1556) was added to 800 μ L of medium and vortexed. Samples of 3 μ L of cells were diluted into 3 μ L of conditioned medium containing 12% OptiPrep and placed onto the concanavalin-A-coated coverslip. A second coverslip was added to the top. Cells were allowed to adhere to the coated coverslip for 10 min before imaging. Unless otherwise noted, images were acquired on a Nikon TE2000 microscope equipped with a Teledyne Photometrics Prime 95BSI camera. Using an oil-immersion objective (100 \times , 1.4 numerical aperture), GFP was excited with an X-Cite 110 light-emitting diode light source and filtered through an infrared cut filter to prevent aberrant heating of the sample from the optics. Brightness and contrast were adjusted linearly using ImageJ software (<https://imagej.nih.gov/ij/>).

Preparation of magnetic beads

Dynabeads with Protein G (Thermo Fisher Scientific #10009D) from 1.6 mL of slurry were washed with 1.6 mL phosphate buffered saline containing 0.02 % Tween-20 (PBS-T). After resuspension in 1.6 mL fresh PBS-T, 10 μ L of anti-FLAG antibody (M2, monoclonal mouse IgG1, affinity isolated, F1804, 1 mg/ml) was added to the Dynabeads to yield a sub-saturating coverage of the beads with antibody. The resulting mix was incubated overnight at 4°C with an overhead rotation at 20 rpm. The supernatant was removed and the antibody-coated magnetic beads were washed once with 1.6 mL of PBS-T and twice with 1.6 mL IP buffer (25 mM HEPES pH 7.0, 1 mM EDTA, 150 mM NaCl). Immediately before use in immuno-isolation, the supernatant was again discarded and replaced with 700 μ L of fresh IP buffer.

Lipid extraction, lipidomics data acquisition and post-processing

Mass spectrometry-based shotgun lipidomics was performed by Lipotype GmbH (Dresden, Germany) as described (5, 6). Lipids were extracted using a two-step chloroform/methanol procedure (5). Samples were spiked with internal lipid standards for major lipid classes in which the lipids contain combinations of acyl chains not found in biological samples, as previously described (1). After extraction, the organic phase was transferred to an infusion plate and dried in a speed vacuum concentrator. 1st step dry extract was re-suspended in 7.5 mM ammonium acetate in chloroform/methanol/propanol (1:2:4, V:V:V) and 2nd step dry extract in 33 % ethanol solution of methylamine in chloroform/methanol (0.003:5:1; V:V:V). All liquid handling steps were performed using Hamilton Robotics STARlet robotic platform with the Anti Droplet Control feature for organic solvents pipetting.

Samples were analyzed by direct infusion on a QExactive mass spectrometer (Thermo Scientific) equipped with a TriVersa NanoMate ion source (Advion Biosciences). Samples were analyzed in both positive and negative ion modes with a resolution of $Rm/z=200=280000$ for MS and $Rm/z=200=17500$ for MSMS experiments, in a single acquisition. MS/MS was triggered by an inclusion list encompassing corresponding MS mass ranges scanned in 1 Da increments (7). Both MS and MSMS data were combined to monitor ergosterol-esters (EE), diacylglycerol (DAG) and triacylglycerol (TAG) ions as ammonium adducts; Phosphatidylcholine (PC) as an acetate adduct; and cardiolipin (CL), phosphatidic acid (PA), phosphatidylethanolamine (PE), phosphatidylglycerol (PG), phosphatidylinositol (PI) and phosphatidylserine (PS) as deprotonated anions. MS only was used to monitor the lyso-lipids of PA, PE, PI, and PS, as well as inositolphosphorylceramide (IPC), mannosyl-inositolphosphorylceramide (MIPC), and mannosyl-di-(inositolphosphoryl)ceramide (M(IP)2C) as deprotonated anions; ceramine (Cer) and lyso-PC

(LPC) as acetate adducts and ergosterol as protonated ion of an acetylated derivative (8). One source of error that can arise is when fatty acids form an adduct with other molecules in the sample. This type of error is more likely when longer, multi-step procedures are used to isolate membrane lipids, as in immuno-isolation as opposed to a fast extraction of all lipids from the entire cell.

Data were analyzed with in-house developed lipid identification software based on LipidXplorer (9, 10). Data post-processing and normalization were performed using an in-house developed data management system. Only lipid identifications with a signal-to-noise ratio >5, and a signal intensity 5-fold higher than in corresponding blank samples were considered for further data analysis.

Microsomal preparation

Throughout microsomal preparation and immuno-isolation procedures (Fig. 2 of the main text), samples from the supernatant and pellet fractions were retained for a subsequent immunoblot analysis. Break points are indicated where samples can be stored at -80°C. 4,000 OD₆₀₀·mL of yeast cells were required as starting material for isolating vacuole membranes from log stage cells. For stationary stage cells, whose mechanical disruption is less efficient (Fig. S1E), 17,200 OD₆₀₀·mL were used. Cells were harvested from the culture by centrifugation at 3,000 x g for 5 min at room temperature. The resulting pellet was resuspended in 25 mL of pre-chilled phosphate buffered saline (PBS) and placed on ice. Cell suspensions corresponding to 1,000 OD₆₀₀·mL (8,600 OD₆₀₀·mL for stationary stage) were transferred to 50 ml tubes and centrifuged at 3,000 x g for 5 min at 4°C. After discarding the supernatants, the cell pellets were snap frozen in liquid nitrogen and stored at -80°C until further use.

A cell pellet corresponding to 1,000 OD₆₀₀·mL (2,150 OD₆₀₀·mL for stationary stage) was thawed on ice and then resuspended in 10 mL of microsome preparation (MP) buffer (25 mM HEPES at pH 7.0, 1 mM EDTA, 0.6 M mannitol, to which 30 µg/ml protease inhibitor cocktail (10 µg/mL of pepstatin, antipain, chymotrypsin each) and 12.5 units/mL benzonase was added freshly). To mechanically lyse the cells (Fig. 2A), 13 g pre-chilled zirconia glass beads (0.5 mm diameter) were combined with cell suspension in a 15 mL tube. Additional MP buffer was added to the suspension to fill the reaction tube and to avoid the formation of air bubbles during mechanical agitation. Using a FastPrep-24 bead beater at 4°C, cells were subjected to 10 cycles of shaking for 15 s at 5 m/s, followed by 45 s of cooling on ice. The resulting cell lysates were transferred to fresh 15 mL tubes. 2 mL MP buffer were used to wash the zirconia glass beads and then combined with the previous lysates.

Differential centrifugation was performed to separate a crude microsomal membrane fraction from both cell debris and soluble proteins, thereby enriching cellular membranes including vacuole membranes (Fig. 2A). Cell lysates were spun at 3,234 x g and 4°C for 5 min in a swinging bucket rotor. The supernatant was transferred to a fresh 15 ml tube and re-centrifuged at 3,234 x g and 4°C for 5 min. The resulting supernatant (S3) was then transferred to ultracentrifuge bottles (26.3 mL polycarbonate bottle assemblies, Beckman Coulter #355618), balanced with MP buffer and centrifuged (rotor Type 70 Ti) at 12,000 x g and 4°C for 20 min. The resulting supernatant (S12) was transferred to a fresh ultracentrifuge bottle, balanced with MP buffer, and centrifuged at 100,000 x g at 4°C for 60 min. Although vacuole markers Vph1 and Vac8 are also found in the pellet after 12,000 x g centrifugation (P12) and in the supernatant after 100,000 x g centrifugation (S100), we chose to work with the pellet after 100,000 x g centrifugation (P100) because it contains smaller vesicles that are less likely connected to mitochondria and lipid droplets. To avoid contamination of the microsome pellet (P100) by lipid droplets floating on top of the supernatant (S100), the supernatant was removed by vacuum from the ultracentrifuge tube, working carefully from the top to the bottom. The pellet containing crude microsomes (P100) was rinsed with 15 mL of MP buffer to remove remnants of the supernatant before resuspending it in 1 mL MP buffer, snap freezing the sample in liquid nitrogen, and storage at -80°C until further use.

Pellets from the microsomal preparation were thawed from -80°C slowly on ice and then sonicated to segregate aggregated membrane vesicles and to break vacuoles into smaller vesicles (Fig. 2A of the main text) (1). A tip sonicator (MS72 sonotrode on a Bandelin Sonopuls HD 2070) was used for 10 s, with a duty cycle of 0.7 at 50% amplitude, keeping the samples on ice. Previous experiments revealed that this treatment does not cause membrane mixing (1). Notably, sonication cleared the originally cloudy suspension. After centrifugation at 3,000 x g at 4°C for 3 min, the supernatant containing microsomes was used for subsequent immunisolations procedures.

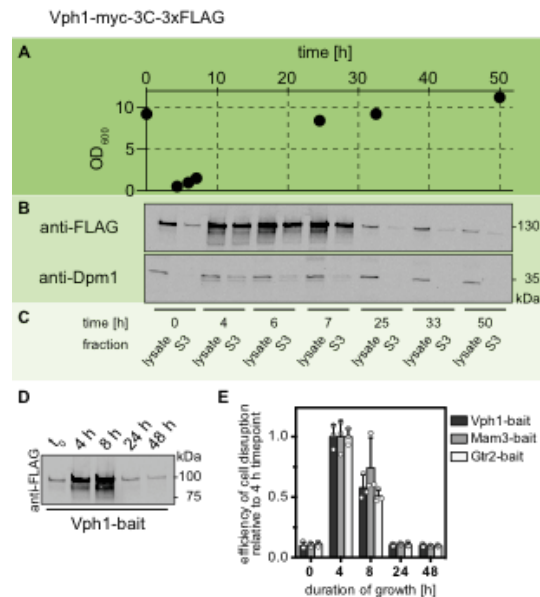


Figure S1: The level of the Vph1-bait protein (Vph1-myc-3C-3xFLAG) is low in the stationary stage compared to the log stage. (A) Yeast growth curve through time, where OD₆₀₀ is the optical density at 600 nm, a proxy for the density of cells. The sample at time “0” is a preculture after 19 hours of the preculture’s growth. The preculture was then diluted to OD₆₀₀ = 0.1 and allowed to grow into the log (early time points), and stationary stage (late time points). **(B-C)** At each timepoint, an immunoblot was performed for the cell lysate (left columns) and supernatant (“S3”, right columns). The supernatant corresponds to S3 in Fig. 2, which is collected from the supernatant after the first step of microsome preparation, a 3,234 x g centrifugation. The presence of Vph1-bait was visualized by anti-FLAG primary and fluorescent secondary antibodies. In the log stage, Vph1 is abundant (timepoints 1-3) in the cell lysate and S3 samples. This result is consistent with reported values of > 50,000 copies/cell, which likely applies only to the log stage (up to ~10 hours of growth) (11, 12). In the stationary stage (timepoints 4-6), Vph1 is significantly reduced in the cell lysate and further reduced after centrifugation step S3. Dpm1, a protein that is a marker for the endoplasmic reticulum, is used as a control. Dpm1 is reported to have < 2,000 copies/cell (11). It maintains a roughly constant abundance throughout the growth cycle. **(D)** A minimal experiment reproducing the results in panel B, with time points similar to Fig. 3C. **(E)** The efficiency of mechanical cell disruption differs with the growth stage. Cell disruption efficiency was estimated by measuring the protein concentration in the post-nuclear supernatant (after a 3,234 x g centrifugation) of cell lysates. The measured protein concentrations are normalized to the concentration measured for cells cultivated for 4 h prior to cell harvest and cell lysis. Experiments were performed in biological triplicates for yeast strains containing one of three distinct immuno-isolation baits (Vph1-bait, Mam3-bait, Gtr2-bait).

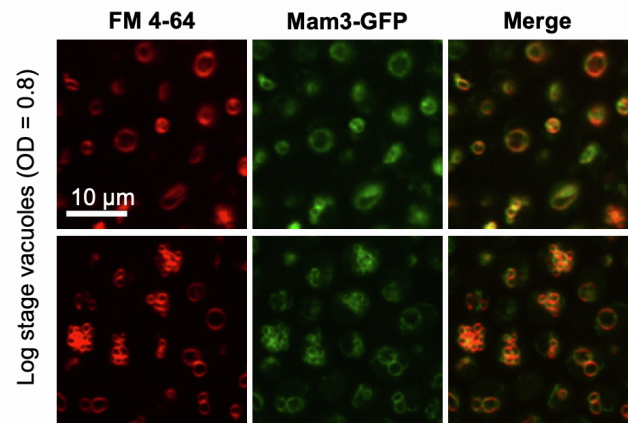


Figure S2: Mam3-GFP localizes to the vacuole membrane. The protein Mam3-GFP (middle column) colocalizes with FM 4-64 (left column), which is known to label vacuole membranes. All yeast in the field of view are living and in the logarithmic stage; no micron-scale domains appear in their membranes. Images were taken at room temperature.

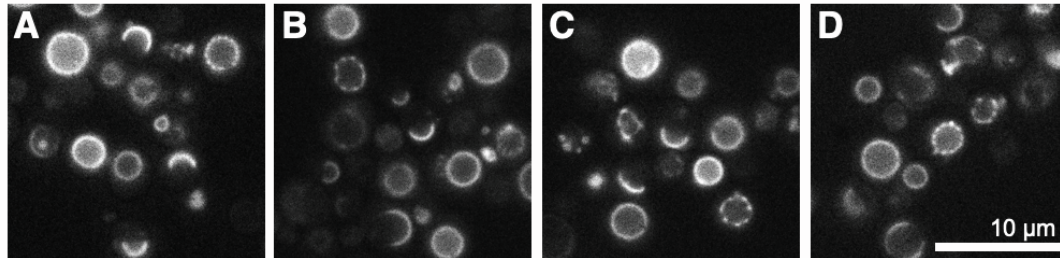


Figure S3: Stationary stage vacuoles phase separate as shown via Mam3-GFP. (A-D) Four fields of view of vacuole membranes in living yeast cells in the stationary stage after 48 hours of cultivation, under conditions equivalent to the cells in Figure S2. Bright areas of the membranes contain the fluorescent protein Mam3-GFP, which was endogenously labeled. Most vacuole membranes in the field of view have phase-separated into co-existing micron-scale domains. Images were taken at room temperature.

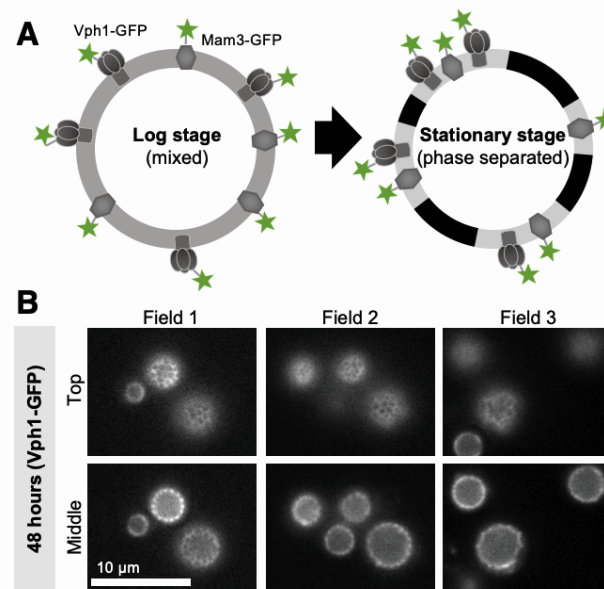


Figure S4: Stationary stage vacuoles phase separate as shown via Vph1-GFP. **(A) Left:** For yeast in the logarithmic stage, lipids and proteins appear uniformly distributed across the surface of vacuole membranes. Two of the proteins, Vph1 and Mam3, can be endogenously labeled with GFP (as shown here) or equipped with a C-terminal bait tag for subsequent immuno-isolations. **Right:** In the stationary stage, the vacuole membrane separates into two liquid phases. Vph1-GFP and Mam3-GFP preferentially partition to the same phase. **(B)** After 48 hours of growth, yeast are in the stationary stage and most vacuole membranes have phase separated. The proteins Mam3 (Fig. 3) and Vph1 partition into only one of the phases, shown at both the top and the midplane of the vacuoles in each field of view. Images are of living cells and were taken at room temperature.

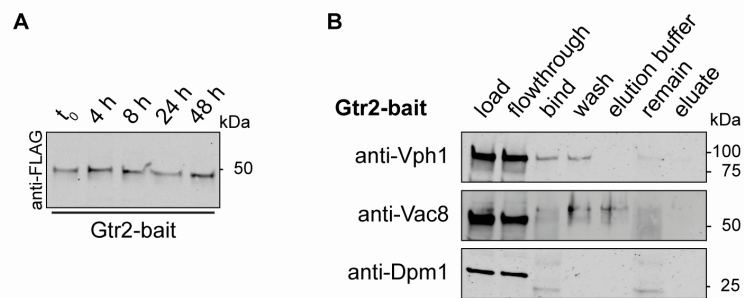


Figure S5: Immuno-isolation via the Gtr2-bait does not work. Gtr2 is a membrane-associated protein anchored to the vacuole membrane via a lipid anchor. In phase-separated, stationary stage vacuole membranes, it resides in the Lo phase (13). **(A)** The Gtr2-bait protein is equally abundant throughout the logarithmic and stationary growth stages. **(B)** We were not able to immuno-isolate any membranes via the Gtr2-bait protein using the MemPrep technology as described in Figure 2. In immunoblot analyses, the vacuole markers Vph1 and Vac8 are not detectable in the eluate. A corresponding figure for isolation via the Mam3-bait protein can be found in Figure 4.

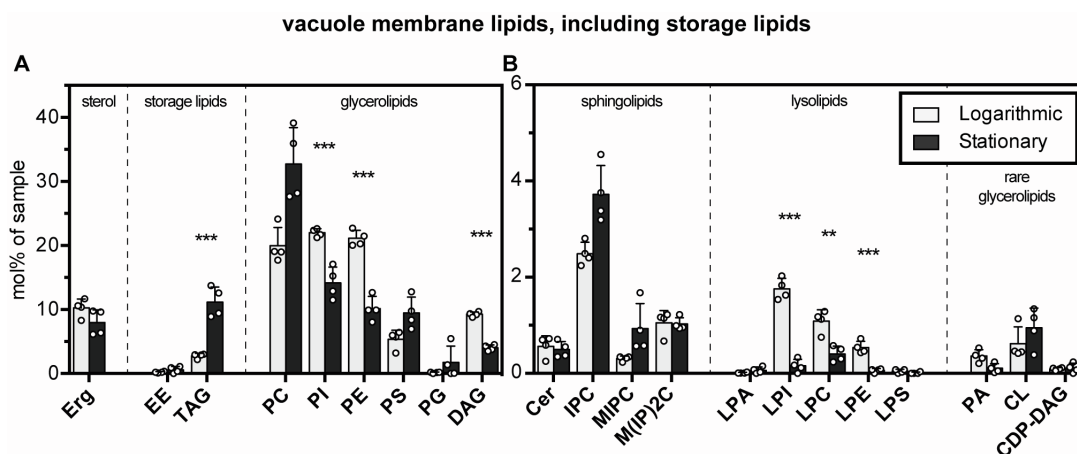


Figure S6: Lipids in log stage and stationary stage vacuole membranes immuno-isolated via a Mam3-bait protein, including storage lipids of ergosterol esters and TAG. Acronyms of lipid names are listed in Figure 5B. **(A)** Ergosterol, storage lipids and abundant glycerolipids. **(B)** Sphingolipids, lysolipids and rare glycerolipids. Note that the y-axis range covers a different range in panel (B) compared to panel (A) to highlight also low abundant lipids. Error bars are standard deviations of vacuole samples immuno-isolated on four different days. Data in this figure include the storage lipids of ergosterol esters and TAG, which are predominantly found in lipid droplets. For yeast in the log stage, we find that ergosterol esters constitute 0.3% of all isolated lipids, in contrast to 4.2% found by Zinser *et al.* (14). Specifically, Zinser *et al.* find a molar ratio of ergosterol to phospholipids of 0.18 and a molar ratio of ergosterol ester to ergosterol of 0.29 (14). Statistical significance was tested by multiple t-tests correcting for multiple comparisons (method of Benjamini *et al.* (15)), with a false discovery rate $Q = 1\%$, without assuming consistent standard deviations. The symbols *, **, and *** denote $p < 0.05$, $p < 0.01$, and $p < 0.001$, respectively.

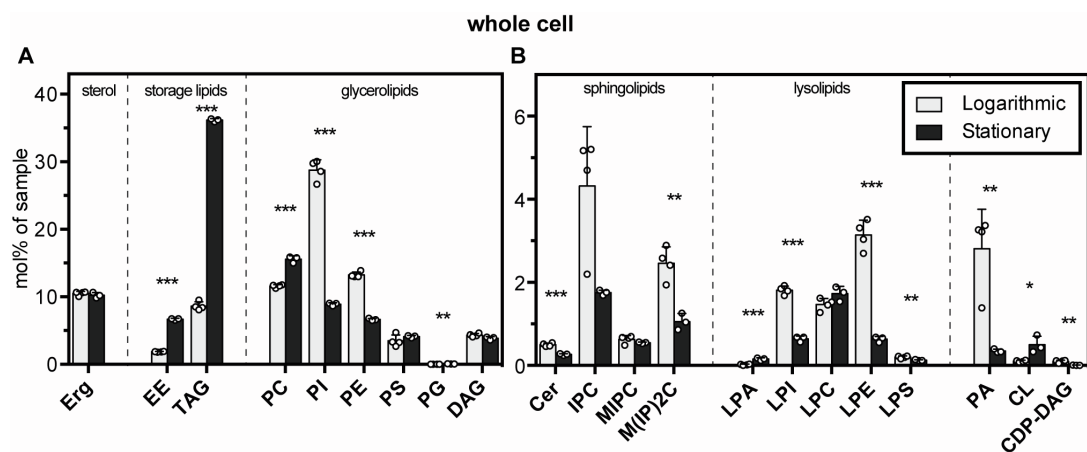


Figure S7: Whole cell lipidomes of cells in the log and the stationary stage. (A) Ergosterol, storage lipids and abundant glycerolipids. (B) Sphingolipids, lysolipids and rare glycerolipids. Error bars represent standard deviations of four independent experiments in the logarithmic stage and three independent experiments in the stationary stage. The data from logarithmic cells are taken from (1). Statistical significance was tested by multiple t-tests correcting for multiple comparisons (method of Benjamini *et al.* (15)), with a false discovery rate $Q = 1\%$, without assuming consistent standard deviations. The symbols *, **, and *** denote $p < 0.05$, $p < 0.01$, and $p < 0.001$, respectively.

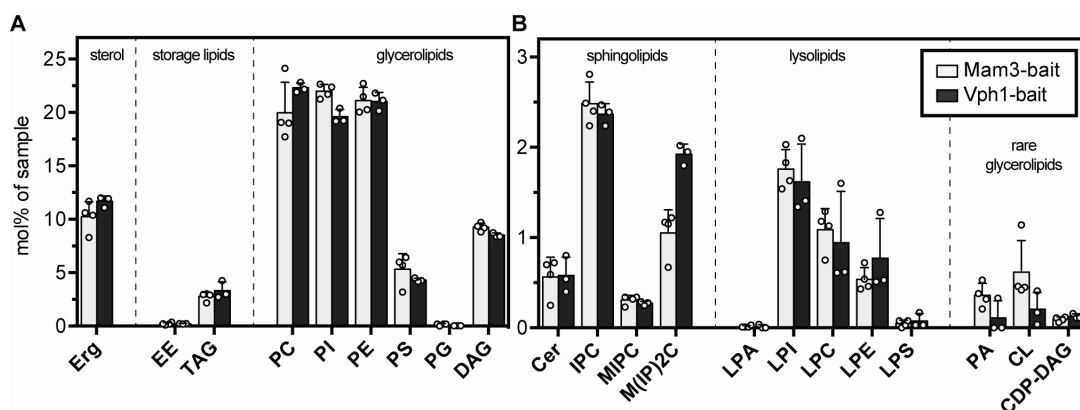
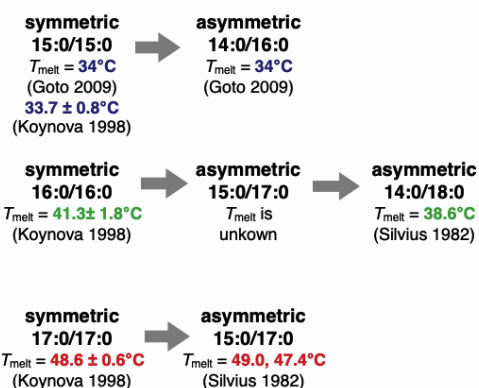


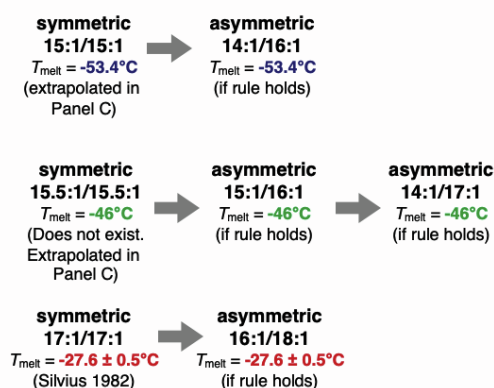
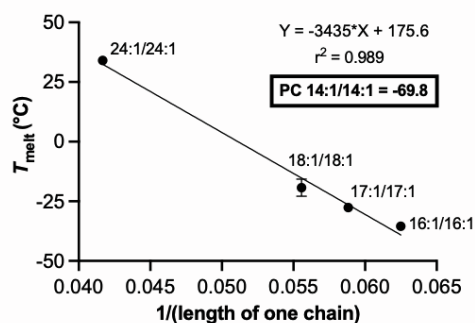
Figure S8: Comparison of lipidomes of vacuole membranes from yeast in the log stage isolated either with the Mam3-bait or the Vph1-bait. Data from membrane preparations via the Vph1-bait are replotted from Reinhard *et al.* (1). Mam3 data are replotted from Figure S6 (Logarithmic). Error bars represent the standard deviations of data from independent immuno-isolations performed on different days. Overall, the two lipidomes are in close agreement. The only apparent differences are in the amount of M(IP)2C (which may be inconsequential because it is in low abundance and which can change rapidly in its abundance during the log stage of growth (16)). These differences might reflect real disparities in how vacuole membranes are isolated by Vph1 and Mam3 baits, or they might reflect experimental variation. Full Vph1 data are presented and discussed in (1). **(A)** Three classes of lipids (glycerolipids, sterol and storage lipids) represent a majority of the lipidome. **(B)** Other classes of lipids (e.g. sphingolipids and ceramides) are much less abundant. Note that the y-axis range is roughly an order of magnitude smaller in panel B than in panel A. Statistical significance was tested by multiple t-tests correcting for multiple comparisons using the method of Benjamini *et al.* (15), with a false discovery rate $Q = 1\%$, without assuming consistent standard deviations. All differences are non-significant.

A. Saturated PC-lipids follow a trend:

For asymmetric, doubly-saturated PC-lipids, when the *sn*-1 chain is shorter than the *sn*-2 chain, T_{melt} is almost equal to T_{melt} of the symmetric lipid.

**B. Unsaturated PC-lipids:**

We can estimate T_{melt} values of asymmetric, doubly-unsaturated PC-lipids if we assume that the same rule holds.

**C.****Symmetrical doubly unsaturated PC lipids****D.**

PC-Lipid	T_{melt}	Source
18:1/18:0	8.7°C	Tada et al. (2009)
18:0/18:1	6.7°C	Tada et al. (2009)
18:1/16:0	-3.2°C	Tada et al. (2009)
16:0/18:1	-1.6°C	Ichimori et al. (1999)
16:1/18:0	-2°C	Estimated based on 18:1/16:0 and 16:0/18:1 pair

Figure S9: Experimental trends used to estimate melting temperatures for PC-lipids.

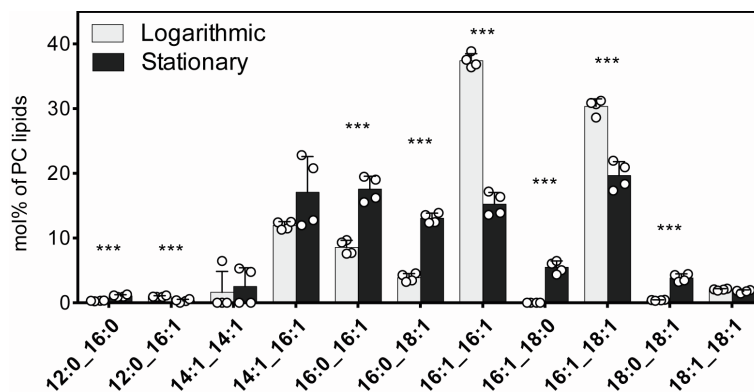


Figure S10: The species composition of vacuolar PC is distinct between log and stationary stage. The mole percent of PC lipids with different acyl chains in immuno-isolated vacuole membranes from yeast in the logarithmic and stationary stages are shown. Data are from four independent immuno-isolations with the error bars indicating the standard deviation. Data for lipids contributing less than 1 mol% in both the log and stationary stage are not shown. Statistical significance was tested by multiple t-tests correcting for multiple comparisons (method of Benjamini *et al.* (15)), with a false discovery rate $Q = 1\%$, without assuming consistent standard deviations. The symbols *, **, and *** denote $p < 0.05$, $p < 0.01$, and $p < 0.001$, respectively.

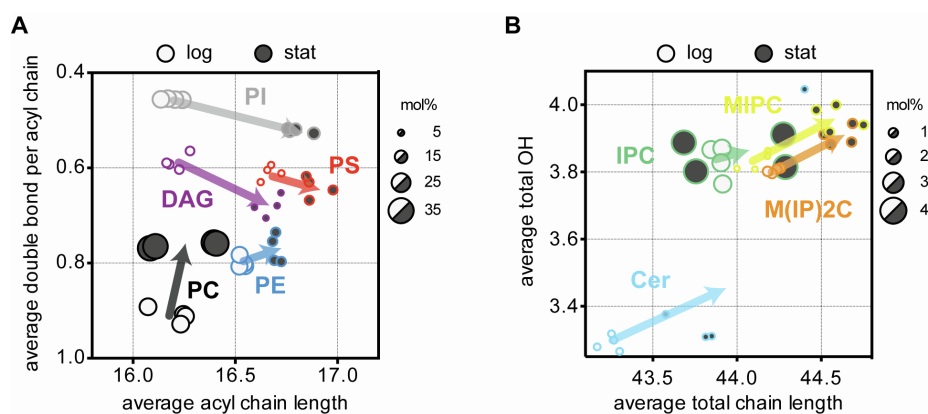


Figure S11: Remodeling of the lipid acyl chain composition in membrane lipids from log to stationary stage. (A) Average number of double bonds per acyl chain and average acyl chain length in the log (open circle) and stationary stage (filled circle) for several lipid types. The size of the circles corresponds to lipid abundance (in mol%) in immuno-isolated vacuole membranes for PC, PE, DAG, PS, and PI, excluding storage lipids such as triacylglycerols and ergosterol esters. Individual data points are derived from four independent immuno-isolations performed on different days. The arrows highlight changes in lipid saturation and the acyl chain length in the indicated lipid classes. **(B)** The same type of representation as in (A) for low abundance lipids of Cer, IPC, MIPC, and M(IP)₂C. Note that the y-axis in Panel B shows the average number OH groups in the lipid acyl chain region and that the x-axis shows the total chain length of the two lipid acyl chains of the respective sphingolipid.

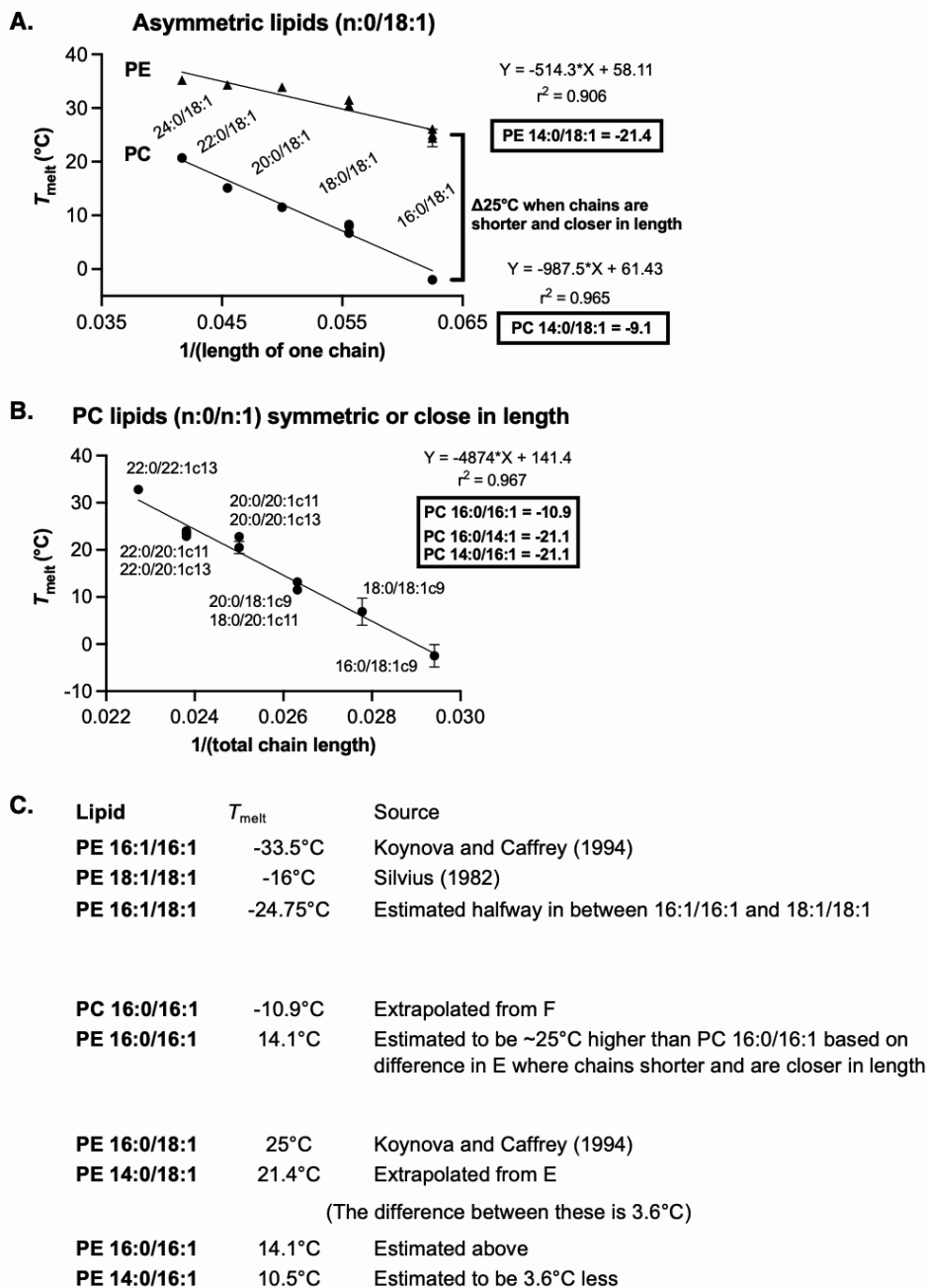


Figure S12: Trends used to estimate melting temperatures for PE-lipids.

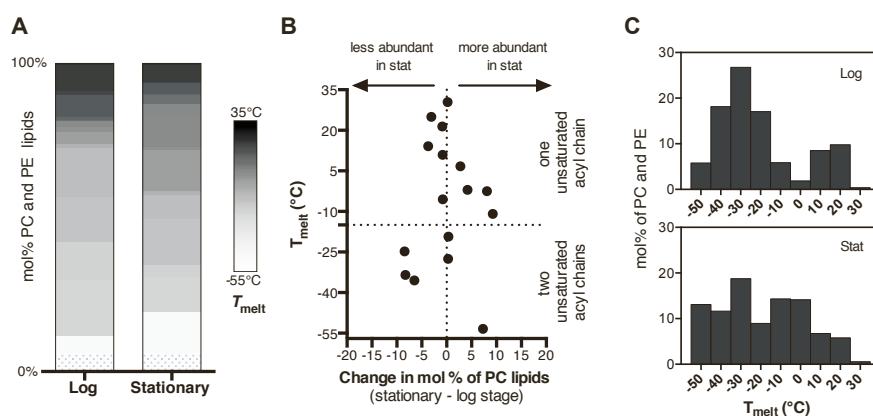


Figure S13: (A) Distributions of melting temperatures for PC and PE lipids of yeast vacuoles, in ratios corresponding to log and stationary stage vacuoles. In other words, the data are weighted to account for the increase in PC lipids and the decrease in PE lipids from the log stage to the stationary stage. (B) Changes in mol% of PC and PE lipids (x-axis) for each melting temperature (y-axis). The change in average lipid T_{melt} due to PC lipids is offset by a decrease in the fraction of PE lipids. (C) Histograms of the percent of PC and PE lipids at each melting temperature, in the log and stationary stages of growth. If we treat the data in the histograms as if they are independent points in a scatterplot, then the values would have standard deviations of 17°C in the log stage and 21°C in the stationary stage.

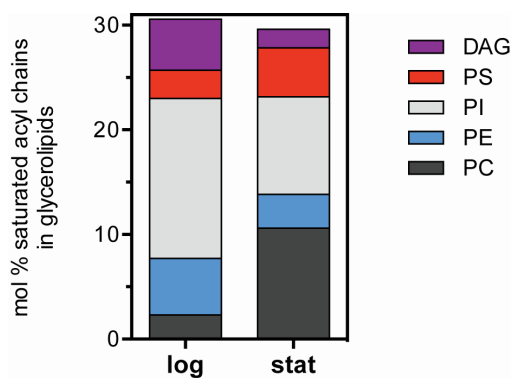


Figure S14: The total molar fraction of saturated fatty acyl chains in glycerolipids with two acyl chains is ~30 mol% in both the logarithmic and stationary stages. Data in the bar charts show that the distribution of saturated fatty acyl chains among different glycerolipid classes shifts from the logarithmic (log) to the stationary (stat) phase. For example, chains of PC lipids become much more saturated. Data are shown only for glycerophospholipid classes with an abundance of at least 0.5 mol%. Colors in the bar chart are in the same order, from top to bottom, as in the legend.

Table S1: Mole percent phospholipids in log-stage, isolated vacuole membranes
(Renormalized to sum all phospholipids to 100%)

Source	PC	PE	PI	PS	PA	Lyso	CL	Other	Method
Zinser 1991	46.5	19.4	18.3	4.4	2.1		1.6	7.7	density gradient
	39.2	26.6	24.4	3.9	2.5	1.6	0.4	1.4	
Tuller 1999	± 3.3	± 1.5	± 1.8	± 1.0	± 0.8	± 0.8	± 0.1	± 0.1	density gradient
	31.4	29.6	27.6	6.1	0.2	4.7	0.3	0.2	
Reinhard 2022	± 1.0	± 1.5	± 0.6	± 0.3	± 0.3	± 1.9	± 0.3	± 0.0	immuno-isolation
	27.3	28.9	30.2	7.3	0.5	4.7	0.8	0.2	
This work	± 3.0	± 1.0	± 1.6	± 2.2	± 0.2	± 0.2	± 0.4	± 0.1	immuno-isolation

Conditions for the experiments above:

	Strain	Glucose	Temp	Media	OD	Stage/Hours
Zinser 1991	X-2180	3%	–	YPD	–	–
Tuller 1999	FY1679	2%	30°C	YPD	?	Late log (~16 h)
Reinhard 2022	BY4741	2%	30°C	SCD	1	Mid log (8 h)
This work	BY4741	2%	30°C	SCD	1	Mid log (8 h)

Notes: Uncertainties are standard deviations. Zinser *et al.* did not provide values of uncertainties (14). Tuller *et al.* note that FY1679 cells are atypical in their high fractions of palmitic acid (16:0) carbon chains and low fraction of oleic acid (18:1) chains (17), implying that comparisons between strains may not always be valid. A contamination of 0.4% cardiolipin in vacuoles isolated by Tuller *et al.* represents 5.5% contamination by mitochondrial membranes (of which $7.2 \pm 0.2\%$ of lipids are cardiolipin) (17). In the row titled “This work”, the entry for “Other” denotes PG lipids. If sphingolipids (IPC, MIPC, and MI(IP)2C) are included in “Other”, the mole percent of other lipids for this work increases to $5.0 \pm 0.8\%$

Table S2: Values of T_{melt} for lipids in yeast vacuole membranes

PC Lipid:	T_{melt} (°C)	Source of T_{melt} value
14:1/14:1	-69.8	Extrapolated in Fig. S9, panel C
14:1/16:1	-53.4	Estimated in Fig. S9, panel B
16:0/16:1	-10.9	Estimated in Fig. S9, panel B
16:0/18:1	-2.5 ± 2.4	Koynova & Caffrey (1998), (18)
16:1/16:1	-35.5	Silvius (1982), (19)
16:1/18:0	-2	Estimated in Fig. S9, panel D
16:1/18:1	-27.5 ± 0.6	Silvius (1982), (19)
18:0/18:1	6.7	Tada (2009), (20)
18:1/18:1	-19.3 ± 3.6	Silvius (1982),(19)

PE Lipid:	T_{melt} (°C)	Source of T_{melt} value
14:0/16:1	10.5	Estimated in Fig. S12, panel C
14:0/18:1	21.4	Extrapolated in Fig. S12, panel A
16:0/16:1	14.1	Estimated in Fig. S12, panel C
16:0/18:1	25	Wang (1994), (21)
16:1/16:1	-33.5	Koynova & Caffrey (1994), (22)
16:1/18:1	19.5	Estimated in Fig. S12, panel C
18:0/18:1	30.4	Silvius (1982), (19)
18:1/18:1	-5.5 ± 0.5	Matsuki <i>et al.</i> (2017), (23)

When values of lipid melting temperatures are directly available in the literature, the reference is given. Values that are not directly available from the literature were extrapolated or estimated in Fig. S9 and S12.

Table S3: Literature values of T_{melt} for PC-lipids(Used for estimating T_{melt} values for vacuole lipids)

Chain length : unsaturation	T_{melt} (°C)	Reference	Reference #
13:0/13:0 PC	13.5	Silvius (1982)	(19)
14:0/14:0 PC	24	Goto <i>et al.</i> (2009)	(24)
15:0/15:0 PC	34 33.7 ± 0.8	Goto <i>et al.</i> (2009) Koynova & Caffrey (1998)	(18, 24)
16:0/16:0 PC	41.3 ± 1.8	Koynova & Caffrey (1998)	(18)
17:0/17:0 PC	48.6 ± 0.6	Koynova & Caffrey (1998)	(18)
14:0/16:0 PC	34	Goto <i>et al.</i> (2009)	(24)
14:0/18:0 PC	38.6	Silvius (1982)	(19)
15:0/17:0 PC	49.0, 47.4	Silvius (1982)	(19)
16:1/16:1 PC	-35.5, -36	Silvius (1982)	(19)
17:1/17:1 PC	-27.6 ± 0.5	Silvius (1982)	(19)
18:1/18:1 PC	-19.3 ± 3.6	Silvius (1982)	(19)
24:1c9/24:1c9 PC	34	Koynova & Caffrey (1998)	(18)
16:0/18:1 PC	-1.6	Ichimori <i>et al.</i> (1999)	(25)
18:1/16:0 PC	-3.2	Tada <i>et al.</i> (2009)	(20)
18:0/18:1 PC	6.7	Tada <i>et al.</i> (2009)	(20)
18:1/18:0 PC	8.7	Tada <i>et al.</i> (2009)	(20)
20:0/18:1 PC	11.5 ± 0.5	Koynova & Caffrey (1998)	(18)
22:0/18:1 PC	15.1	Koynova & Caffrey (1998)	(18)
18:0/20:1c11 PC	13.2	Koynova & Caffrey (1998)	(18)
20:0/20:1c11 PC	20.5 ± 1.3	Koynova & Caffrey (1998)	(18)
20:0/20:1c13 PC	22.8	Koynova & Caffrey (1998)	(18)
22:0/20:1c11 PC	22.9	Koynova & Caffrey (1998)	(18)
22:0/20:1c13 PC	23.5, 24	Koynova & Caffrey (1998)	(18)
22:0/22:1c13 PC	32.8	Koynova & Caffrey (1998)	(18)

Table S4: Literature values of T_{melt} for PE-lipids(Used for estimating T_{melt} values for vacuole lipids)

Chain length : unsaturation	T_{melt} (°C)	Reference	Reference #
16:0/18:1 PE	24.41 ± 1.63 26.1	Koynova & Caffrey (1994) Wang <i>et al.</i> (1994)	(18)
18:0/18:1 PE	31.5 30.4	Wang <i>et al.</i> (1994) Silvius (1982)	(19, 21)
20:0/18:1 PE	33.9	Wang <i>et al.</i> (1994)	(21)
22:0/18:1 PE	34.3	Wang <i>et al.</i> (1994)	(21)
24:0/18:1 PE	35.2	Wang <i>et al.</i> (1994)	(21)
16:1/16:1 PE	-33.5	Koynova & Caffrey (1994) Silvius (1982)	(18) (19)
18.1/18.1 PE	-5.5 ± 0.5	Matsuki <i>et al.</i> (2017)	(23)

Table S5: How changes in lipid chain length and unsaturation affect T_{melt}
(Values are from Tables S2-S4)

Headgroup	Lipid 1, T_{melt}	Lipid 2, T_{melt}	Change in the average number of carbons (over both chains)	Change in the average saturation (over both chains)	Change in T_{melt} (per lipid)
PC	di(16:0)PC, 41.3°C	di(17:0)PC, 48.6°C	2	–	7.3°C
PC	16:0/18:1PC, -1.6°C	18:0/18:1PC, 6.7°C	2	–	8.3°C
PE	16:0/18:1PE, ~25°C	18:0/18:1PE, ~31°C	2	–	6°C
AVERAGE EFFECT OF ADDING ONE CARBON PER LIPID					~ 7.2°C
PC	18:1/18:1PC, -19.3°C	18:0/18:1PC, 6.7°C	–	1	26°C
PC	18:1/18:1PC, -19.3°C	18:1/18:0PC, 8.7°C	–	1	28°C
PE	18:1/18:1PE, -5.5	18:0/18:1PE, 31.0 ± 0.8°C	–	1	37°C
AVERAGE EFFECT OF ADDING ONE SATURATED BOND PER LIPID					~ 30.3°C

Table S6: Differences in length of *sn*-1 and *sn*-2 chains of lipids from vacuoles in the log and stationary stages

Difference in number of carbons	Log stage (average \pm standard deviation)	Stationary stage (average \pm standard deviation)
0 carbons	42.2 \pm 1.1%	34.6 \pm 2.6%
1 carbon	1.4 \pm 0.3%	1.4 \pm 0.9%
2 carbons	46.8 \pm 0.7%	61.0 \pm 2.1%
3 carbons	0.9 \pm 0.5%	0.2 \pm 0.1%
4 carbons	5.3 \pm 0.3%	2.4 \pm 0.1%
5 carbons	0.0 \pm 0.0%	0.0 \pm 0.0%
6 carbons	2.8 \pm 0.1%	0.3 \pm 0.2%
7 carbons	0.0 \pm 0.0%	0.0 \pm 0.0%
8 carbons	0.5 \pm 0.2%	0.1 \pm 0.1%
9 carbons	0.0 \pm 0.0%	0.0 \pm 0.0%
10 carbons	0.0 \pm 0.0%	0.1 \pm 0.1%

SUPPLEMENT REFERENCES

1. Reinhard, J., L. Starke, C. Klose, P. Haberkant, H. Hammarén, F. Stein, O. Klein, C. Berhorst, H. Stumpf, J.P. Sáenz, J. Hub, M. Schuldiner, and R. Ernst. 2022. A new technology for isolating organellar membranes provides fingerprints of lipid bilayer stress. *bioRxiv*. 2022.09.15.508072.
2. Brachmann, C.B., A. Davies, G.J. Cost, E. Caputo, J. Li, P. Hieter, and J.D. Boeke. 1998. Designer deletion strains derived from *Saccharomyces cerevisiae* S288C: a useful set of strains and plasmids for PCR-mediated gene disruption and other applications. *Yeast*. 14:115–132.
3. Huh, W.-K., J.V. Falvo, L.C. Gerke, A.S. Carroll, R.W. Howson, J.S. Weissman, and E.K. O’Shea. 2003. Global analysis of protein localization in budding yeast. *Nature*. 425:686–691.
4. Boothe, T., L. Hilbert, M. Heide, L. Berninger, W.B. Huttner, V. Zaburdaev, N.L. Vastenhouw, E.W. Myers, D.N. Drechsel, and J.C. Rink. 2017. A tunable refractive index matching medium for live imaging cells, tissues and model organisms. *Elife*. 6.
5. Ejsing, C.S., J.L. Sampaio, V. Surendranath, E. Duchoslav, K. Ekroos, R.W. Klemm, K. Simons, and A. Shevchenko. 2009. Global analysis of the yeast lipidome by quantitative shotgun mass spectrometry. *Proc. Natl. Acad. Sci. U. S. A.* 106:2136–2141.
6. Klose, C., M.A. Surma, M.J. Gerl, F. Meyenhofer, A. Shevchenko, and K. Simons. 2012. Flexibility of a Eukaryotic Lipidome – Insights from Yeast Lipidomics. *PLoS ONE*. 7:e35063.
7. Surma, M.A., R. Herzog, A. Vasilij, C. Klose, N. Christinat, D. Morin-Rivron, K. Simons, M. Masoodi, and J.L. Sampaio. 2015. An automated shotgun lipidomics platform for high throughput, comprehensive, and quantitative analysis of blood plasma intact lipids. *Eur. J. Lipid Sci. Technol.* 117:1540–1549.
8. Liebisch, G., M. Binder, R. Schifferer, T. Langmann, B. Schulz, and G. Schmitz. 2006. High throughput quantification of cholesterol and cholesteryl ester by electrospray ionization tandem mass spectrometry (ESI-MS/MS). *Biochim. Biophys. Acta*. 1761:121–128.
9. Herzog, R., K. Schuhmann, D. Schwudke, J.L. Sampaio, S.R. Bornstein, M. Schroeder, and A. Shevchenko. 2012. LipidXplorer: a software for consensual cross-platform lipidomics. *PLoS One*. 7:e29851.
10. Herzog, R., D. Schwudke, K. Schuhmann, J.L. Sampaio, S.R. Bornstein, M. Schroeder, and A. Shevchenko. 2011. A novel informatics concept for high-throughput shotgun lipidomics based on the molecular fragmentation query language. *Genome Biol.* 12:R8.
11. Ghaemmaghami, S., W.-K. Huh, K. Bower, R.W. Howson, A. Belle, N. Dephoure, E.K. O’Shea, and J.S. Weissman. 2003. Global analysis of protein expression in yeast. *Nature*. 425:737–741.
12. Ho, B., A. Baryshnikova, and G.W. Brown. 2018. Unification of Protein Abundance Datasets Yields a Quantitative *Saccharomyces cerevisiae* Proteome. *Cell Syst.* 6:192–205.e3.

13. Toulmay, A., and W.A. Prinz. 2013. Direct imaging reveals stable, micrometer-scale lipid domains that segregate proteins in live cells. *J. Cell Biol.* 202:35–44.
14. Zinser, E., C.D. Sperka-Gottlieb, E.V. Fasch, S.D. Kohlwein, F. Paltauf, and G. Daum. 1991. Phospholipid synthesis and lipid composition of subcellular membranes in the unicellular eukaryote *Saccharomyces cerevisiae*. *J. Bacteriol.* 173:2026–2034.
15. Benjamini, Y., A.M. Krieger, and D. Yekutieli. 2006. Adaptive linear step-up procedures that control the false discovery rate. *Biometrika.* 93:491–507.
16. Casanovas, A., R.R. Sprenger, K. Tarasov, D.E. Ruckerbauer, H.K. Hannibal-Bach, J. Zanghellini, O.N. Jensen, and C.S. Ejsing. 2015. Quantitative analysis of proteome and lipidome dynamics reveals functional regulation of global lipid metabolism. *Chem. Biol.* 22:412–425.
17. Tuller, G., T. Nemeč, C. Hrastnik, and G. Daum. 1999. Lipid composition of subcellular membranes of an FY1679-derived haploid yeast wild-type strain grown on different carbon sources. *Yeast.* 15:1555–1564.
18. Koynova, R., and M. Caffrey. 1998. Phases and phase transitions of the phosphatidylcholines. *Biochim. Biophys. Acta.* 1376:91–145.
19. Silvius, J.R. 1982. Thermotropic phase transitions of pure lipids in model membranes and their modifications by membrane proteins. *Lipid-protein interactions.* 2:239–281.
20. Tada, K., E. Miyazaki, M. Goto, N. Tamai, H. Matsuki, and S. Kaneshina. 2009. Barotropic and thermotropic bilayer phase behavior of positional isomers of unsaturated mixed-chain phosphatidylcholines. *Biochim. Biophys. Acta.* 1788:1056–1063.
21. Wang, Z.Q., H.N. Lin, S. Li, and C.H. Huang. 1994. Calorimetric studies and molecular mechanics simulations of monounsaturated phosphatidylethanolamine bilayers. *J. Biol. Chem.* 269:23491–23499.
22. Koynova, R., and M. Caffrey. 1994. Phases and phase transitions of the hydrated phosphatidylethanolamines. *Chem. Phys. Lipids.* 69:1–34.
23. Matsuki, H., S. Endo, R. Sueyoshi, M. Goto, N. Tamai, and S. Kaneshina. 2017. Thermotropic and barotropic phase transitions on diacylphosphatidylethanolamine bilayer membranes. *Biochim. Biophys. Acta Biomembr.* 1859:1222–1232.
24. Goto, M., S. Ishida, N. Tamai, H. Matsuki, and S. Kaneshina. 2009. Chain asymmetry alters thermotropic and barotropic properties of phospholipid bilayer membranes. *Chem. Phys. Lipids.* 161:65–76.
25. Ichimori, H., T. Hata, H. Matsuki, and S. Kaneshina. 1999. Effect of unsaturated acyl chains on the thermotropic and barotropic phase transitions of phospholipid bilayer membranes. *Chem. Phys. Lipids.* 100:151–164.

DANKSAGUNG

I want to express my gratitude to Robert Ernst, whose guidance and incredible support have been invaluable throughout the entirety of my academic career. Your expertise and mentorship have been tremendously motivating and your example always reminds me that science is also a lot of fun. Thank you for always pointing out the positive aspect of every result. The inspiring curiosity and intensity with which you approach scientific questions left a great imprint on me as a scientist and human being.

Many many thanks to all co-authors and collaborators. I firmly believe that science is a social endeavor and a big team effort. I am very grateful for all the amazing people I got the chance to work with. Without Chantelle Leveille, Sarah Keller, and Caitlin Cornell the phase separation project could not have been successful. I gladly remember the time when we initiated it with your visit in Homburg that generated a lot of happiness and laughter, we did get a fire going. A special thanks goes to Kristina V ath and Carsten Mattes, for the great collaborative atmosphere, sharing of ideas, and discussions of results that shaped our projects into what they are today. I want to thank Christian Klose and the team from Lipotype for their tireless work on our samples, and Michal Surma who was very important in the initial phase of getting lipidomics data. For sharing their great expertise in proteomics, I want to thank Per Haberkant, Frank Stein, and Henrik Hammar en from the EMBL in Heidelberg. Likewise, I thank Jochen Hub and Leonhard Starke from the Saarland University for performing molecular dynamics simulations. You clearly enriched the MemPrep manuscript, and also widened my personal horizon with new and fascinating perspectives. I want to thank Heike Stumpf for her steadfast support for anything related to qPCR and Ofir Klein and Maya Schuldiner for generating the MemPrep bait library. A special thanks deserves Charlotte Berhorst, who helped to improve MemPrep as a Master student in the lab.

I want to say a huge thank you to the members of the Ernst group, past and present. Steffi, Kristina, Julia, Heike, Toni, Carsten, Aamna, Charlotte, Cynthia, Mike, Alex, Jona, Claudia, Louis, Daniel, Philipp, S oren, Martina, Viola. I am very thankful for such inspiring, kind, and sociable colleagues and peers. I will not forget the engaging discussions we had, the one or other drink, the epic table tennis battles, Wikingerschach and boardgame gatherings. The party office will always be a place of good memories. A special thanks goes to Harry Hofbauer for teaching me almost everything I know about yeast and lipids. Thanks to all the people from the Medical Biochemistry and PZMS in Homburg, especially Bianca Schrul, David Mick, Martin van der Laan, Martin Jung and the members of their labs for generating a stimulating science campus culture. Thanks to Elmar Krause, Jens Rettig, Yvonne

Danksagung

Schwarz and Dieter Bruns for giving introductions and granting access to excellent microscopes on campus.

Furthermore, I wish to thank GradUS and the international office of the Saarland University for a generous travel grant that supported my participation in the Physiology Course at the MBL in Woods Hole. Thanks to Robert Tampé and Nina Morgner for helpful discussions and guidance in the initial phase of the MemPrep project. Thanks to Katharina Dolata and the TRAM for financial support and the organization of stimulating summer and winter schools.

I also want to say thanks to Ayelén González Montoro for sharing her knowledge on the vacuole and her visit in our lab which turned to be a very productive time. Thanks to Ilya Levental and Dimitrios Papagiannidis, meeting you at conferences and discussing science with you always means good times.

Ein besonderer Dank gebührt meiner Familie, allen voran meiner Mutter, meinen beiden Omas und meinem Opa Bernd, der früh den Wissenschaftler in mir geweckt hat. Ohne euren Fleiß, eure Entbehrungen und eure Stärke wäre das alles nicht möglich gewesen. Danke für eure Unterstützung und euer unerschütterliches Vertrauen in mich. Von ganzem Herzen möchte ich außerdem meiner Laura danken. Danke, dass du immer an mich glaubst und ich mit dir zusammen durchs Leben spazieren darf. Zu guter Letzt möchte ich meine Freunde Lukas, Nici, Nils, Johnny, Dominik und Johannes nicht unerwähnt lassen. Ihr seid eine Bereicherung und eure motivierenden Worte haben auch zur Entstehung dieser Arbeit beigetragen.

EIDESSTATTLICHE VERSICHERUNG

Ich erkläre hiermit an Eides statt, dass ich die vorliegende Arbeit ohne unzulässige Hilfe Dritter und ohne Benutzung anderer als der angegebenen Hilfsmittel angefertigt habe. Die aus anderen Quellen direkt oder indirekt übernommenen Daten und Konzepte sind unter Angabe der Quelle gekennzeichnet.

Weitere Personen waren an der inhaltlich-materiellen Erstellung der vorliegenden Arbeit nicht beteiligt. Insbesondere habe ich nicht die Hilfe von Vermittlungs- bzw. Beratungsdiensten (Promotionsberater*innen oder andere Personen) in Anspruch genommen. Niemand hat von mir unmittelbar oder mittelbar geldwerte Leistungen für Arbeiten erhalten, die im Zusammenhang mit dem Inhalt der vorliegenden Dissertation stehen.

Die Arbeit wurde bisher weder im Inland noch im Ausland in gleicher oder in ähnlicher Form in einem anderen Verfahren zur Erlangung des Doktorgrades einer anderen Prüfungsbehörde vorgelegt.

Ich versichere an Eides statt, dass ich nach bestem Wissen die Wahrheit gesagt und nichts verschwiegen habe.

Die Bedeutung der eidesstattlichen Erklärung und die strafrechtlichen Folgen einer unrichtigen oder unvollständigen eidesstattlichen Erklärung sind mir bekannt.

Ort, Datum

Wien, 04.05.2024

Unterschrift des Promovierenden



Aus datenschutzrechtlichen Gründen wird der Lebenslauf in der elektronischen Fassung der Dissertation nicht veröffentlicht.